Synthesis and Surface Modification of Inorganic Nanoparticles for Application in Physics and Medicine

Dissertation

zur

Erlangung des Doktorgrades

der Naturwissenschaften

(Dr. rer. nat.)

dem

Fachbereich Physik

der Philipps-Universität Marburg

vorgelegt von

Atif Masood

aus Mirpurkhas, Pakistan

Marburg, 2018

Vom Fachbereich Physik der Philipps-Universität (Hochschulkennziffer: 1180) als Dissertation angenommen am 14.06.2018

Erstgutachter: Prof. Dr. Wolfgang J. Parak

Zweitgutachter: Prof. Dr. Wolfram Heimbrodt

Prüfer: Prof. Dr. Andreas Schrimpf

Prüfer: Prof. Dr. Gregor Witte

Tag der mündlichen Prüfung: 20.09.2018

Die Vorliegende Arbeit wurde am Fachbereich Physik

der Philipps-Universität Marburg unter Anleitung von

Herrn Prof. Dr. Wolfgang. J. Parak

In der Zeit von Oktober 2014 bis September 2018 angefertigt.

Abstract

The core focus of this cumulative thesis is the synthesis, the characterization, and the polymer coating or the surface modification of different types of inorganic nanoparticles (NPs), e.g., semiconductor, magnetic, plasmonic, and titanium oxide NPs. These NPs are used in the field of physics, biotechnology, and in nanomedicine or life sciences for both diagnosis and therapy. The applications of these NPs depend on their unique properties, which are correlated to their size, shape, and the material composition.

The colloidal stability of these nanocrystals or NPs in different media (e.g. organic, water, cell culture media) was achieved by means of capping agents or by wrapping suitable ligands or surfactants around the core of the NPs. The colloidal NPs that were synthesised during this research work were capped with hydrophobic ligands (e.g. oleic acid, oleylamine, etc.) to keep them stable in the organic media, e.g., toluene, chloroform, etc. The phase transfer from organic to aqueous is a mandatory step prior to their use in the few desired applications, especially when these NPs are exposed to aqueous medium or cell media. This is carried out by wrapping the NPs with an amphiphilic polymer, i.e., poly(isobutylene-alt-maleic anhydride) (Mw= 6000 Da) that is grafted with hydrophobic side chains of dodecylamine.

The mentioned four types of produced NPs were: (i) Semiconductor NPs which include the hydrophobic cadmium sulfide (CdS) quantum dots (QDs) that are used: for organic scintillation neutrino detection experiments; for PPO (2, 5-diphenyloxazole) styrene based plastic scintillator detectors; for time resolved spectral measurement, and for fluorescence studies with different surface coatings; additionally, water soluble CdS, manganese doped CdS, and zinc sulphide (ZnS) with and without manganese doping were synthesized and engineered to run several experiments on nanomaterials' (NMs) behavior in environmental media, e.g., river and lake water; (ii) magnetic NPs (MNPs) that include core only (iron oxide, e.g. magnetite) and core shell composite iron oxide magnetic NPs combined with cobalt and manganese ferrites; (iii) plasmonic NPs such as gold and silver NPs that were used in combination with iron-oxide NPs (4 nm each) for toxicity screening and dose determination assays, and (vi) titanium dioxide

(TiO_2) NPs with different sizes and shapes (i.e. cube, rods, plates, and bipyramids), which were used for in vivo experiments: To evaluate the bio-distribution, organ accumulation, biological barrier passage, and potential organ toxicity after a single intravenous administration of TiO_2 NPs, and to assess the influence of the TiO_2 NPs shape and geometry on the mentioned effects. Furthermore TiO_2 NPs were also used to perform few more in vivo studies to investigate: (i) The effect of biological environment (e.g. lung lining liquid, saliva, gastric/intestinal fluids) on NPs' behaviour and toxicity, using complex co-culture systems for the intestine and alveoli, (ii) the effect of NPs on the activation of the inflammasome, and (iii) the influence of NPs on the maturation and activation of dendritic cells.

In addition to above mentioned experiments for synthesis and surface modification another study was carried out with the aim to transfer three different types of NPs (i.e. plasmonic, fluorescent and magnetic) in aqueous phase to be employed in hydrogels, aerogels, and heterogels applications. In this study bimetallic (gold-copper) plasmonic nanocubes, fluorescent (cadmium selenide/CdS) core shell nanorods and magnetic iron oxide (Fe_3O_4) nanospheres were successfully transferred to the aqueous phase irrespective of their different sizes ranging from 5-40 nm in at least one dimension.

All water soluble NPs were cleaned by means of gel electrophoresis or by ultracentrifugation to get rid of micelles (empty polymer) followed by sterilization for all in vivo studies. The qualitative and quantitative analyses all of these NPs were performed by means of different characterization techniques, e.g., ultraviolet-visible spectroscopy, fluorescence spectroscopy, dynamic light scattering, zeta potential measurements gel electrophoresis, transmission electron microscopy, inductively coupled plasma mass spectrometry, and the X-ray diffraction analysis.

Zusammenfassung

Der Schwerpunkt dieser kumulativen Dissertation liegt in der Synthese, der Charakterisierung und der Polymerbeschichtung oder der Oberflächenmodifizierung verschiedener Arten von anorganischen Nanopartikeln (NPs), z. B. Halbleiter-, magnetischen, plasmonischen und Titanoxid-Nanopartikeln. Diese NPs werden auf dem Gebiet der Physik, der Biotechnologie, der Nanomedizin oder der Biowissenschaften sowohl für die Diagnose als auch für die Therapie eingesetzt. Die Anwendungen dieser NPs hängen von ihren einzigartigen Eigenschaften ab, welche mit ihrer Größe, Form und der Materialzusammensetzung korrelieren.

Die kolloidale Stabilität dieser Nanokristalle oder Nanopartikel in verschiedenen Medien (z. B. organische Lösungen, Wasser und Zellkulturmedien) wurde mithilfe von Verkappungsmitteln oder durch Umhüllen des Nanopartikel Kernes mit geeigneten Liganden oder Tensiden erreicht. Die kolloidalen NPs, die während dieser Forschungsarbeit synthetisiert wurden, wurden mit hydrophoben Liganden (z.B. Ölsäure, Oleylamin usw.) funktionalisiert, um sie in organischen Lösungen, wie z.B. Toluol und Chloroform, stabil zu halten. Für einige Anwendungen aber ist ein vorheriger Transfer der NPs von organischen zu wässrigen Lösungen erforderlich, insbesondere wenn die NPs Zellkulturmedien oder anderen wässrigen Medien ausgesetzt werden sollen. Dazu werden die NPs mit einem amphiphilen Polymer umhüllt. Als Polymer wird Poly(isobutylen-alt-maleinsäureanhydrid) (Molekülmasse: 6000 Da) verwendet, welches mit hydrophoben Seitenketten aus Dodecylamin gepfropft ist.

Die erwähnten vier Arten von hergestellten NPs waren: (i) Halbleiter-NPs, dazu gehören die hydrophoben Cadmiumsulfid(CdS)-Quantenpunkte (QDs), die verwendet werden für organische Szintillations-Neutrino-Detektionsexperimente; für PPO(2,5-Diphenyloxazol)-Styrol-basierte Kunststoff-Szintillationsdetektoren; für zeitaufgelöste Spektralmessungen und für Fluoreszenzstudien mit verschiedenen Oberflächenbeschichtungen; zusätzlich wurden wasserlösliche CdS, Mangan-dotierte CdS und Zinksulfid (ZnS) Nanopartikel mit und ohne Mangan-Dotierung synthetisiert und konstruiert, um verschiedene Experimente zum Verhalten von Nanomaterialien (NMs) in Umweltmedien, wie z. B. Fluss- und Seewasser, durchzuführen; (ii) magnetische NPs (MNPs), die nur aus einem Kern (Eisenoxide Magnetit) bestehen und

magnetische Kern-Schale-Eisenoxid-NPs mit Kobalt- und Manganferriten; (iii) plasmonische NPs wie Gold- und Silber-NPs, die in Kombination mit Eisenoxid-NPs (jeweils 4 nm) für Toxizitäts-Screening- und Dosisbestimmungstests verwendet wurden, und (vi) Titandioxid(TiO_2)-NPs mit unterschiedlichen Größen und Formen (d. h. Würfel, Stäbchen, Platten und Doppelpyramiden), die für folgende In-vivo-Experimente verwendet wurden: Die Bewertung der Bio-Verteilung, Ansammlung organischer Stoffe, biologische Barriere-durchlässigkeit und mögliche Organtoxizität nach einmaliger intravenöser Gabe von TiO_2-NP, und Untersuchung des Einfluss von Form und Geometrie der TiO_2 NPs auf die genannten Effekte. Zusätzlich zu den oben erwähnten In-vivo-Studien wurden einige andere In-vivo-Experimente durchgeführt um folgende Punkte zu analysieren: (i) den Einfluss der biologischen Umgebung (z.B. Lungenflüssigkeit, Speichel und Magen- / Darmflüssigkeit) auf das Verhalten und die Toxizität der NPs, unter Verwendung komplexer Co-Kultursysteme für den Darm und die Alveolen, (ii) die Wirkung von NPs auf die Aktivierung des Inflammasoms und (iii) den Einfluss von NPs auf die Reifung und Aktivierung dendritischer Zellen.

Zusätzlich zu den oben erwähnten Experimenten zur Synthese und Oberflächenmodifizierung wurde eine weitere Studie mit dem Ziel durchgeführt, drei verschiedene Arten von NPs (d. h. plasmonische, fluoreszierende und magnetische) in wässrige Phase zu transferieren, für die Verwendung in Hydrogel-, Aerogel- und Heterogel-Anwendungen. In dieser Studie wurden bimetallische (Gold-Kupfer) plasmonische Nano Cubes, fluoreszierende (Cadmiumselenid / CdS) Kern-Schalen-Nanostäbchen und magnetische Eisenoxid (Fe_3O_4) Nanokügelchen erfolgreich in die wässrige Phase übertragen, unabhängig von ihren unterschiedlichen Größen von 5-40 nm in mindestens einer Dimension.

Wasserlösliche NPs wurden mittels Gelelektrophorese oder Ultrazentrifugation von Micellen (leeres Polymer) gereinigt und anschließend für alle in vivo-Studien sterilisiert. Die qualitative und quantitative Analyse all dieser NPs wurde mittels verschiedener Charakterisierungstechniken durchgeführt, wie z. B. UV/VIS-Spektroskopie, Fluorimetrie, dynamischer Lichtstreuung, Gelelektrophorese, Transmissionselektronenmikroskopie, Massen-spektrometrie mit induktiv gekoppelte Plasma und Röntgenbeugungsanalyse.

I would like to dedicate my thesis to:

my father, my mother (late),

my sibblings

my teachers,

my life partner , Aiza

my lovely kids Junaid & Amal

Acknowledgements

First and foremost, I would like to express my sincere gratitude to my advisor Prof. Wolfgang J. Parak for the continuous support of my Ph.D. study, related research. His guidance and appreciations helped me during research work and while thesis writing. I could not have imagined having a better advisor and mentor for my Ph.D. study. To be very honest it was an honour for me to work in Biophotonic research group at Philipps-Universität Marburg under his supervision.

I am really thankful to Prof. Wolfram Heimbrodt for his kind supervision and support in all matters during the entire period after my supervisor Prof. Parak left Philipps Universtät Marburg and joined Universität Hamburg.

I am also grateful to my co-supervisor, Dr. Pablo del Pino and Dr. Beatriz Pelaz Garcia, for their continuous guidance and for their generous support that they offered me during my research work. I also want to express my gratitude to both of them for their valuable helping hands in fixing the problems that I encountered while I was running my experiments and I am also thankful for the proof reading my thesis to put it in a good shape.

I want to thank everyone at Biophotonik to make me feel happy during my stay in lab while doing experiments with some cracking jokes, chit chats and making things easy. I don't want to forget Dr. Qian Zhang as she taught me everything from the scratch. I really appreciate Dr. Neus Feliu Torres, Dr. Carolina Carrillo Carrión, Dr. Indranath Chakraborty, Dr. Nadeem Sabir, Dr Mahmoud Soliman, and Dr. Daniel Valdeperez Toledo for their support, sharing their experience in lab work as well as their guidance. Many thanks are due to Dr. Asrar Ahmad for his suggestions and proofreading that considerably improved the quality of this thesis. I am also thankful to Mikko Wilhelm for translating the abstract of my thesis in German.

I want to say bundles of thanks to Marta Gallego Gonzalez for doing the TEM measurements in San Sebastián, Spain and also to Dr. Indranath Chakraborty and Karsten Kantner for ICP-MS measurement.

Many thanks are due to Stefanie Kramer for resolving the administrative issues and also due to Andreas Rentzos for all the technical support he provided me during my stay at Biophotonik.

I would like to thank especially to my funding agencies, Higher Education Commission of Pakistan (HEC) and German Academic Exchange Service (DAAD) as well as

my parent organization Karachi Institute of Radiotherapy and Nuclear Medicine (KIRAN), PAEC, Karachi, for their financial support and granting me study leave to pursue PhD study.

I would like to express my gratitude for every teacher, my mentors, my relatives, friends, and all of them who contributed in my life to achieve this target: a big round of applause for all of you.

At last, I am grateful to whole of my family (parents, brothers and sisters) for their moral support; I have no words to express my gratitude for the encouragement and prayers that I received during my stressful times. I am really proud of the earliest mentor I got in the shape of my father. How he raised me is exceptional: Thank you Baba Jani. My heart bleeds while missing my late mother (may her soul rest in peace), and I remember word for word her last advice to me "whatever happens to me you have to complete your degree". Dear Mom, I wish that you would have been alive today to see that this goal is successfully achieved. I do not forget you my friend, my dear brother Saleem Masood, while saying bundles of thanks to you for everything that you have done for me.

Thanks are due to my life partner Aiza for always taking care of me during my ailment and lifting me up during depressing times; thank you Aiza for taking care of me and my home, specially my two lovely kids Junaid and Amal. The achievement of this milestone would have been really tough without your support; thanks a lot my better half, Aiza.

Table of Contents

1. Introduction

Nanoscience is characterized as the investigation of wonders and control of materials at nuclear, sub-atomic, and macromolecular scales, where properties contrast altogether from those at bigger scale counterparts. Nanotechnology is an integral technology that is related to all basic sciences, e.g., physics, chemistry, biology. This technology deals with structures which have dimensions below than a hundred nanometres, in addition it is also related to engineering their surface to enhance the biocompatibility or other features (e.g. surface chemistry, net charge, hydrophobicity, elasticity, etc.) in order to obtain the best response for their applicability for example in life sciences. Since 1990's, nanotechnology gained a lot of attention from scientists due to the specific properties related to their size ranging between 1-100 nm at least in one of its dimensions[1-2]. These nanomaterials (NMs) include nanoclusters, nanoparticles (NPs), or quantum dots (QDs) among others. As the change in fundamental properties and characteristics at this size cannot be described by the classical theories, quantum laws are needed to explain the behaviour and properties of the nanostructures. Quantum effect does not come into play by going from macro to micro dimensions rather it starts dominating the behaviour of a material at the nanoscale especially in the range of single to double digit of nanometer scale which affects the optical, electrical and magnetic behaviour of material[3]. The characteristics which makes particles special at nanometer size, are the possibility of detection, observation, labelling and surface modification (area/charge). At nanometer scale the surface area to volume ratio increases drastically which can make materials more chemically reactive that leads to vast majority of applications. The intentional manipulation of NPs´ surface enhances the colloidal stability, providing them with stability against the degradation, aggregation and precipitation when exposed to different media (organic, aqueous or cell media). The colloidal stability of these NPs is defined as the uniform mixture of NPs substances and the NPs suspended in that mixture are known as colloids. Ideally colloids are evenly and uniformly dispersed, distributed in a solvent, dispersant or medium for longer times without requiring some extra forces. The colloidal stability is also determined by the size of the NPs, as the size decreases less than 100 nm therefore the influence of gravitational force becomes negligible and the electromagnetic forces and Van der Waals forces forces mainly dominates, but when the size of the NPs increase beyond a certain limit the gravitational force starts influencing the colloidal stability and consequently the NPs starts losing their colloidal stability[4, 5,6].

The chemical and physical properties of the inorganic NPs are specifically size and shape dependent, as the size changes their physical, optical and chemical properties also

changes[7] for example, if small size QDs that emits fluorescence in the UV range (e.g. blue color) increase their size their emission will be shifted to longer wavelengths such as orange red or near infrared colour from these bigger QDs[8-9]. These properties related to their nanometric size also happened to occur for magnetic and plasmonic NPs. Magnetic NPs (MNPs) can exhibit superparamagnetic properties that would be affected by changes in the size, shape or composition, typically when the size of NPs of certain composition is around 10-20 nm, then every single NP exhibit a single magnetic domain and behaves as a superparamagnetic NP, which results in superparamagnetic behaviour [10,11]. Same happens for the plasmonic ones, in which the absorption wavelength is related to the size and shape of the NPs, i.e., for spherical gold NPs (GNPs) the absorption spectra have one peak located in the visible region but gold nanorods have 2 absorption peaks one in visible region corresponding to electron oscillations along the shorter axis (transversal) and a second one located in the near infrared region corresponding to electron oscillations along the longer axis (longitudinal)[12,13,14].

1.1 Approaches for synthesis NPs

There are several methods for the synthesis of NPs; furthermore, naturally occurring NPs are also available. In general, there are two approaches for the fabrication of NMs. The first approach is based on the breakdown of bulk materials using heat, chemical, mechanical, or other forms of energy to achieve the desired nanostructures. This method is called top-down approach and is based on attrition/milling processes. The second approach to get nanostructures is the bottom-up is the second approach to get nanostructures, which includes the miniaturization of elements, substances or materials components reaching until atomic or molecular level with further self- assembly process leading to the formation of nanostructures, bottom-up synthesis approaches commence with basic building blocks, i.e., atoms or molecules to attain nanostructures. Few examples of bottom-up approaches are the thermal decomposition, pyrolysis, inert gas condensation, solvo-thermal reaction, sol-gel fabrication and structured media[15-16]. There are further classifications for synthesis of NPs in terms of physical (cutting, etching, grinding, ball milling, lithographic techniques: photo lithography, electron beam lithography) chemical (chemical vapour deposition, sol-gel method, pyrolysis) and biological (mycosynthesis, phytonanotechnology) and a lot more can also be listed here[15-17,18].

During this research work thermal decomposition method was adopted for the synthesis of different NPs and QDs. Thermal decomposition, also known as thermolysis, is

the thermal decomposition of organometallic precursors in organic solvents with surfactant capping agents (ligands) in an inert atmosphere. These precursors are heated up to a certain temperature within certain time period at a specific positive ramp, to produce small particles. After the decomposition of chemical bonds from the metallic compounds to metal atoms that would form small metallic nuclei that will grow into NPs. The proper control of the synthesis conditions will lead to get the NCs/NPs of homogeneous size and shape. This synthetic approach provides a versatile platform for the synthesis of inorganic NPs which includes MNPs, plasmonic NPs, and QDs with better control over the size, monodispersity, and shape[10,19,20].

The synthesis of NPs is a two stage process, i.e., nucleation and growth. During thermal decomposition, nucleation is a process in which nuclei (seeds) act as templates for crystal growth[21]. This process of nucleation further described as the series of atomic or molecular processes by which the atoms or molecules of precursors reorganize into a collection of clusters (seeds). The nucleation can be homogenous in the absence of impurities or can be heterogeneous in the presence of impurities, which are collectively known as primary nucleation. This process of nucleation and growth of new crystal was explained by LaMer and Dinegar in 1950[22] as shown in Figure 1.1.

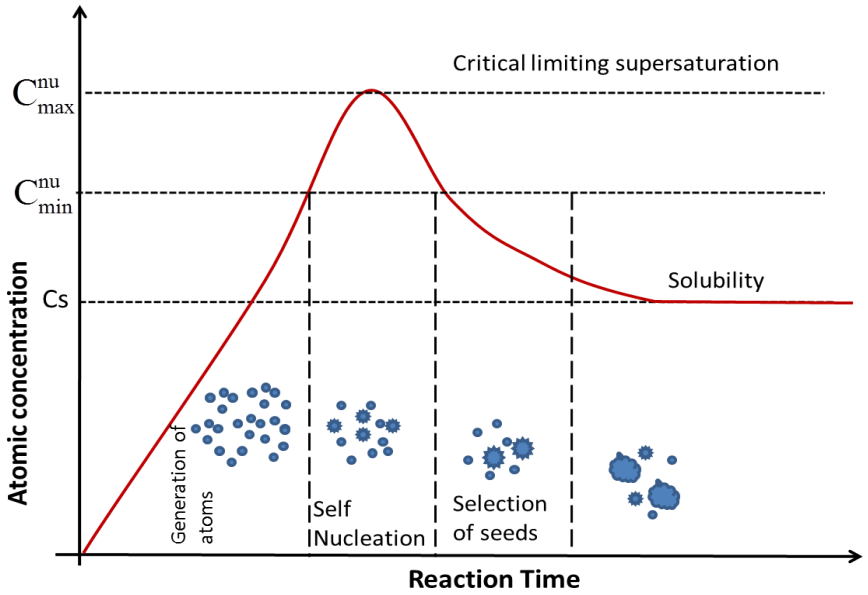

Figure 1.1: Schematic representation of the LaMer model for nucleation and size growth of NPs

The driving force needed for the nucleation and growth of a crystal is referred to as super saturation and is defined as the difference in chemical potential between a molecule in solution (μ_s) and that in the bulk of the crystal phase (μ_c).

$$\Delta\mu = \mu_s - \mu_c \quad (1)$$

Where μ_s is the chemical potential of a molecule in solution and μ_c is the chemical potential of the molecule in the bulk crystal. The most important thing is the stability of these particles to avoid agglomeration and also to control the size of the NPs immediately after nucleation, which is achieved by adding some specific surfactants that binds to the surface of the NPs which result in the protection of the NPs from further nucleation and size growth. There are two types of stabilization process, the steric stabilization is achieved by the long chains of organic molecules(e.g., dodecylamine, hexadecylamine, oleylamine (OLAM), oleic acid (OLAC), trioctyl phosphine (TOP), trioctyl phosphine oxide (TOPO), etc.) that are attached or adsorbed to the surface, and the electrostatic stabilization, which is done by attaching the cations or anions for example H^+, OH^-, SO_4^{2-}, NO_3^-, $RCOO^-$, RSO_3^-, R_4N^+ specifically to the NPs surface[19]. These all stabilizers attached to the surface of NPs are known as surfactants or ligands, these stabilizers are also helpful in achieving colloidal stability of NPs in some solvents and solutions (further details are presented in section 1.7). Another way to achieve monodispersity of the particles is known as Ostwald ripening which is observed when smaller particles diffuse to large particle by vigorous stirring in the solutions, which results in the monodispersity of the NPs[23].Figure 1.2 schematically represents the processes of nucleation and crystal growth and stabilization process.

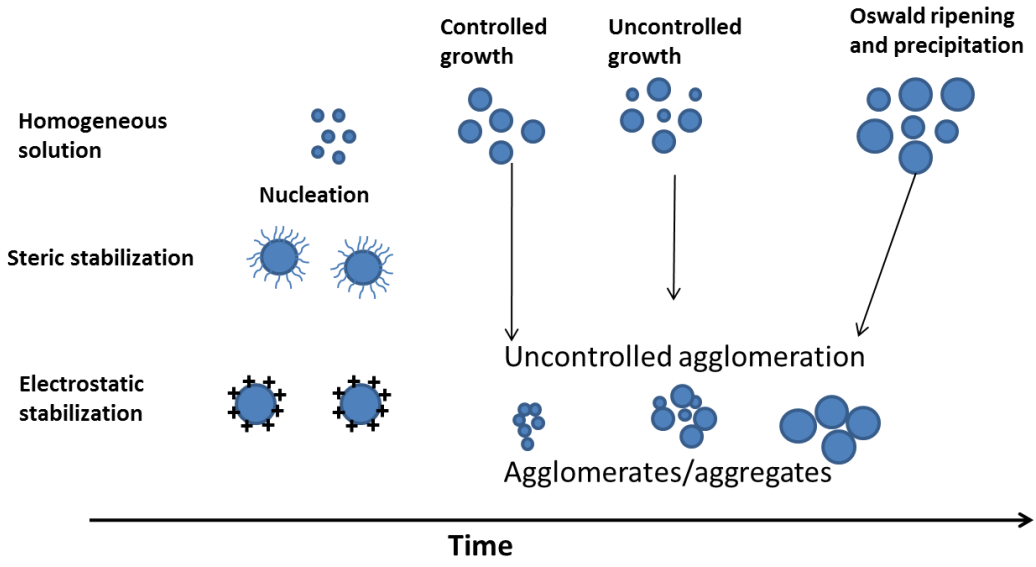

Figure 1.2: Schematic representation of nucleation, steric, electrostatic stabilization, controlled and uncontrolled growth of NCs[19]

1.2 Types of NPs and their properties

There are naturally occurring NPs and they are also produced artificially according to the application and requirements. For example, NCs of salt are found in ocean air, diesel engines emit carbon NPs, cigarette smoke, burning candles, and chimneys also emit NPs. A wide variety of NPs are also produced artificially such as magnetic NPs, QDs, carbon nanofibres, plasmonic NPs, etc. Naturally occurring NPs are difficult to compare with artificially produced NPs as both of them have different characteristics and they also have contrasting physical and chemical properties[24-25]. The aim of this study was to synthesize, characterize, analyse and purposeful surface modification of few of these artificially produced NPs which include QDs/fluorescent NPs (CdS, ZnS, manganese doped CdS and Mn@ZnS), MNPs (iron oxide, composite iron oxide), plasmonic NPs (silver and gold), and catalytic NPs (TiO_2).

1.3 Quantum dots

QDs are special kind of highly fluorescent semiconductor NMs. QDs were first discovered by the Russian physicist Alexei Ekimov in 1980[26]. These are very tiny particles on the order of few nanometres ranging from 2-10 nm in size[27]. Typically, a single QD contains few hundreds to few thousand atoms of a single element or a combination of different elements to form a nanocrystal (NC). These QDs are also classified as inorganic NCs. QDs have broader absorption with emission at fixed positions which is quite in contrast to organic dyes. Their composition, small size, tunable dimensions, and unique opto-electronic properties make these dots significantly important for different applications. The QDs are able to absorb light at a wavelength shorter than the one corresponding to the band gap energy, and reemit light (fluorescence) but in a color roughly corresponding to the band gap energy. This allows the QDs to be excited over a broad range while emitting at a finite position, yielding true colour emission. The emission potential of the QDs is dependent upon the quality and size distribution of the NCs in solution. Most commonly available QDs have cadmium, sulphur, zinc, selenide, silicon, and germanium. They are also distinguished according to their elemental position in the periodic table, e.g., II-VI (ZnS, ZnSe, CdSe, CdTe, CdS, HgS), III-V (GaAs, GaN, InP, InAs, InGaAs), and IV-VI (PbS, PbSe)[19,28,29]. These NCs are also identified as artificial atoms, because of their atom-like discrete electronic structure resulting from quantum confinement this unique property makes them distinct from other types of NPs and that is due to quantum effect the same property usually single atoms have[30]. This property of QDs can easily be tuned during synthesizing or

fabrication process. As the size of the QDs increase the band gap between conduction band and valence band decreases or vice versa this leads to the change in the absorption and emission spectra of these QDs. This effect can be explained by quantum laws of physics, i.e., when the size of these nanostructure reaches typically 10 nm or less in at least one of its dimensions, the free electrons get limited to small well usually called quantum box and also when the radii of these NCs/QDs is less than exciton Bohr radius, then QDs will behave more likely as atoms instead of bulk materials because of discrete energy levels. The orbital electrons in the NCs move to these energy level during excitation and relaxation process. These molecular electrons in NCs lying in highest occupied molecular orbital (HOMO) energy level of valence band move to least unoccupied molecular orbital (LUMO) of conduction band after absorbing some energy and later come back (relax) to HOMO after releasing some energy in form of fluorescence[28]. It means that NCs with the same composition but different sizes can generate fluorescence at different wavelength; this capability will allow estimating the size of QDs NCs[31,32]. The effect of change in the QD size to the energy band gap is represented schematically in Figure 1.3.

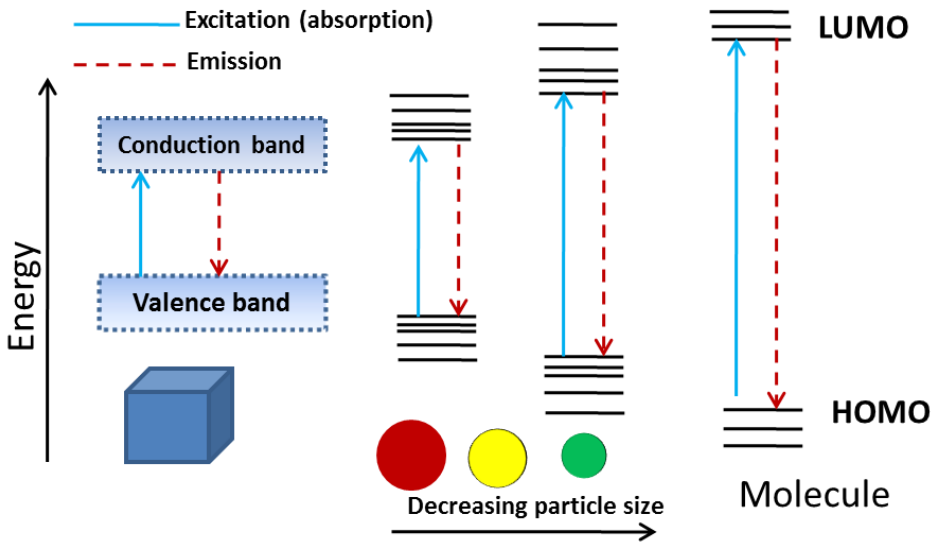

Figure 1.3: Schematic description of size dependency of energy levels, where QDs size is correlated to band gap energy between highest occupied molecular orbital and lowest unoccupied molecular orbitals.

Semiconductor NCs are of great interest for both fundamental research and industrial development. QDs have a wide variety of applications in biology, biotechnology, computing, photovoltaic cells, LEDs and in physics like scintillation detectors. One more quality of these QDs is their strong resistance to photobleaching, which make them superior over traditional fluorophores and dyes for biosensing applications. They are widely used to study intracellular

processes, tumour targeting, in vivo observation of cell trafficking, diagnostics, and high resolutions cellular imaging[33,34].

The properties, characteristics, applications and surface modification along with their characterization of synthesized CdS, ZnS, ZnO and manganese doped CdS, ZnS QDs is presented below.

1.3.1 CdS and manganese doped CdS QDs

CdS QDs are inorganic semiconductors NCs from group of II-VI of the periodic table; they have a Bohr radius of 2.4 nm[35-36], typically the size of these QDs ranging from 2 to 7 nm. The emission spectrum of these QDs lies in between UV (350 nm) and green (500 nm) region[35,37]. Usually the surface of these QDs is capped with long organic chains (e.g. OLAC, decylamine, etc.), which is known as outer surface coating ligands or surfactants. High quality CdS NCs are always area of interest for the researchers and scientists because of their applications. The formation of high-quality semiconductor NCs, with well-controlled size and shape, as well as well confined surface passivation, can be achieved by controlling the thermodynamics and kinetics during the nucleation and growth of NCs. The uniqueness of these CdS QDs arise from their optical/electronic properties with respect to their size, these properties can easily be tuned during the synthesis.

The CdS QDs usually do not have very high conversion efficiency therefore to improve the efficiency shell coating with larger band gap semiconductor material (e.g. ZnS) is usually adopted. The photo-electronic and magnetic properties can also be altered by doping different metals without altering the basic crystals structure of these inorganic semiconductor NCs. The dopant elements can be manganese, chromium, cobalt, nickel, copper and mercury[38,39,40,41,42,43]. The presence of these dopant elements introduces different energy levels which help to absorb incident light at broader wavelengths. The doping of these transitional metals also helps to widen the range of fluorescence properties additionally opto-electronic characteristics and magnetic properties. This alternative approach is used to enhance the efficiency by doping the QDs with optically active transition metal ions such as manganese to create long-lived photogenerated charge carriers and reduce the electron-hole recombination. Moreover manganese alters the optical properties of NCs by creating another option of recombination which results dual fluorescence in the same NCs[44-45].

The CdS QDs have promising applications in a variety of fields ranging from biomedical to fluxtronics, optoelectronic devices such as, high efficiency thin film transistors, light-emitting diodes, electron-beam pumped lasers, and electroluminescent devices[37,46].

Doping of CdS semiconductor QDs with manganese have gained a lot of attraction for both basic research and advanced applications, especially in solar cell applications[43].

1.3.2 Application of CdS QDs

1.3.2.1 CdS QDs for neutrino detectors

A neutrino is a sub atomic particle with no electric charge. It is quite like an electron (ē) but with extreme low mass and no charge[47]. A neutrino (denoted by the Greek letter ν) is a fermion (an elementary particle with half-integer spin). Neutrinos are one of the fundamental particles which make up the universe. It interacts only via the weak subatomic force and gravity. The mass of the neutrino is much smaller than that of the other known elementary particles, e.g., protons, neutrons, etc. The neutrino was first predicted by Wolfgang Pauli in 1931[48]. He predicted that in certain radioactive decays the energy and momentum is not conserved and this missing energy might be carried off by undetectable neutral particle. This particle was later named "neutrino" in 1933, by Fermi. The first experimental detection of neutrino was done by Clyde Cowan and Frederick Reines in the Cowan–Reines neutrino experiment in 1956 at the Savannah River Site in South Carolina[47-48]. In 1943 it was suggested by Sakata and Inouë[48] that there might be more than one types of neutrino exists. Later at different time points in history three different types of neutrinos were discovered, and finally by means of experiments that were performed in 2000 at CERN it was established that there are exactly three families of 'electron-like' but charge less particles (leptons), those are electron neutrino (νe), muon neutrino (νμ) and tau neutrino (ντ) discovered in 1956, 1962 and 1980s respectively.

It is very difficult to detect neutrinos, as they are neutral and have negligible mass therefore they cannot produce ionization directly in the materials they are passing through. The possibility of neutrino interaction with matter is extremely low; it is sensitive to only weak interaction. A neutrino penetrating in matter will only interact when it comes within a distance of 10^{-18} m of one of the quarks present in the neutrons or protons inside the nuclei. The interaction cross-section of neutrino is usually of the order 10^{-42} to 10^{-36} cm^2 [49]. For example, a beam of neutrinos can travel upto 2 years in a lead block before it gets stopped. The mean free path of a 1 MeV neutrino in iron amounts to about 30 light years[48-50]. The effective size of neutrino can be described using their electroweak cross-section which is usually measured in nanobarns (nb) and it is 10^{-33} or 10^{-37} approximately 1billionth the size of uranium nucleus[51].

Neutrinos are produced during the process known as beta negative decay (β^-), and antineutrinos (the antiparticles of neutrinos) are produced in beta positive (β^+) decay, in this process a neutron decays into a proton, electron, and antineutrino[50]. The production equations of neutrino or antineutrino are stated below with examples

$$ {}^{A}_{Z}X \rightarrow {}^{A}_{Z-1}Y' + e^{+} + \nu_e \tag{2} $$

$$ {}^{22}_{11}Na \rightarrow {}^{22}_{10}Ne + e^{+} + \nu_e \tag{3} $$

$$ {}^{A}_{Z}X \rightarrow {}^{A}_{Z+1}Y' + e^{-} + \bar{\nu}_e \tag{4} $$

$$ {}^{137}_{55}Cs \rightarrow {}^{137}_{56}Ba + e^{-} + \bar{\nu}_e \tag{5} $$

As stated above the detection of neutrinos is very difficult as they are not directly ionizing particle therefore a distinctive approach is used which also known as inverse beta decay (IBD), i.e., the interaction of an electron antineutrino ($\bar{\nu}_e$) and a proton (p) produces a positron (e^+) and a neutron, as illustrated by Eq. 6 below

$$ \bar{\nu}_e + p \rightarrow n + e^{+} \tag{6} $$

The minimum threshold kinetic energy required by antineutrino for an IBD reaction is 1.806 MeV. This minimum threshold energy is the difference between the mass of the interacting particle (antineutrino, proton) and resultant products (neutron, positron)[52]. The resultant positron annihilates and causing the production of two photons of 0.511 MeV in opposite directions which is detected by two oppositely placed scintillation detectors. This scheme was used by Reines and Cowan in 1956 to identify antineutrinos using the scintillation detectors. The IBD scheme is also depicted in Figure 1.4

All detection methods require the neutrinos to carry minimum threshold energy, i.e., 1.8 MeV. The detection of neutrinos requires very large scale detector in order to detect a significant number of neutrinos. Neutrino detectors are often built underground in order to isolate the detector from cosmic rays and other background radiation. For example, Super-Kamiokande is a neutrino observatory located under Mount Ikeno near the city of Hida, Gifu Prefecture, Japan, in which large volume of water surrounded by photomultiplier tubes (PMTs), that watches for the Cherenkov radiation emitted when an incoming neutrino creates an electron or muon in the water. This detector contains 50,000 ton tank of water; located approximately 1 km underground. The water in the tank acts as both the target for neutrinos and the detecting medium for the by-products of neutrino interactions. The inside surface of the tank is lined with 11,146 PMTs of 50 cm diameter[53]. An additional layer of water called

the outer detector is also instrumented with light sensors to detect any charged particles entering the central volume, and to shield it by absorbing any neutrons produced in the nearby rock.

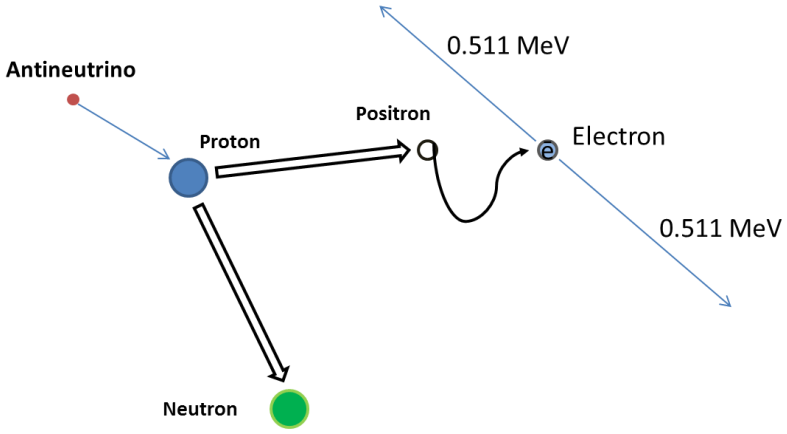

Figure 1.4: Pictorial illustration of inverse beta decay

Scintillator detectors have been widely used for the detection of fundamental particles, especially during last few decades liquid scintillator (LS) gained a lot of attention in astroparticle branch of physics and were particularly fruitful in neutrino detection experiments. In the case of antineutrino detection the resultant particle (i.e. positron) annihilates and the resultant photons of 0.511 MeV energy pass through the scintillator while exciting and ionizing atoms along their path, which leads to energy loss and absorption of photons. Then the rapid relaxation of the scintillator atoms or molecules produces visible photons to PMT or photocathodes, which can be detected. There are two kind of scintillation materials one inorganic scintillator (e.g. crystalline form, mostly doped NaI(Tl), etc.) and organic scintillator (crystalline and liquid form). Organic LS are commonly used as a target material for low-energy neutrino experiments and they are particularly suitable for the detection of neutrinos with energy less than 5 MeV. Organic scintillators are mainly a combination of two types of organic materials that are one or more scintillators compound (solute) and an organic solvent[54]. These scintillators are typically aromatic hydrocarbons, containing benzene ring structures interconnected in different ways. The scintillation arises after the absorption of ionizing energy of incident particles or radiations, most of this energy initially absorbed by the solvents and then transferred to solutes (the scintillation material). The valence band electrons of these scintillating molecules are responsible for scintillation light. These electrons are not particularly associated with a single atom rather a whole molecule, and are lying in molecular orbitals. For example, benzene (C_6H_6) is an aromatic hydrocarbon and it also represents most of the solvents used in organic LS. In this benzene structure carbon provides 4 valence electrons and one electron is provided by the hydrogen.

The six carbon atoms form a regular hexagon. Two valence electrons from each carbon atom form a sigma bond with other carbon atom which results in a benzene ring contains six equally, covalent overlapping Csp^2-Csp^2 sigma (σ) bonds. One valence electron of each carbon atom attached with one valence electron of hydrogen, now from each carbon atom one unhybridized valence electron is left with in the p-orbitals which results in π (pi) bond that is distributed above and below the ring[54]. As shown in the Figure 1.5.

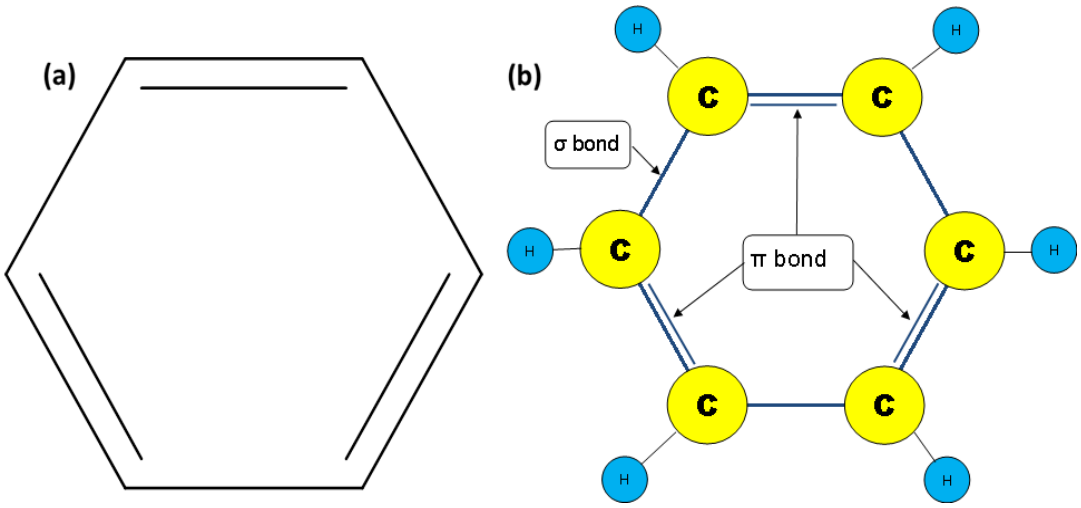

Figure 1.5: (a) Benzene ring structure (b) pictorial illustration of sigma (σ) and pi (π) bond along with position and bonding of carbon and hydrogen

These π-bond electrons get excited and ionized by annihilation photons (0.511 MeV) during their propagation through the organic LS solvents in neutrino detectors. The ionization energy of these weekly bound electrons is approximately 5-9 eV[55]. This process of transfer of energy to scintillation is very efficient and very quick of the order of few nanoseconds. To explain the absorption and relaxation scenario, Jablonski pictorial illustration (Figure 1.6) is really helpful. Where S_0 is singlet ground and S_1, S_2 are singlet excited states, these ground and excited states can have more subdivided vibrational states, e.g., 0, 1, and 2. The organic aromatics molecules are excited to either S_1 or S_2 vibrational level after absorption of energy as indicated by the brown and blue lines in the Figure 1.6. Due to internal conversion phenomenon excited molecules get relaxed within few picoseconds (10^{-12} seconds) to the lowest possible excited vibrational level as indicated by black dashed arrow lines. Then these molecules come to singlet ground states with some emission which is known as fluorescence, as shown by green lines. The relaxation time for fluorescence is of the order of 10^{-9} to 10^{-7} seconds[54,56]. When molecules in S_1 undergo a spin conversion from singlet to triplet state that change is called intersystem crossing, The energy transition from excited triplet states T_1 to singlet ground states S_0 is referred as phosphoresce of the molecules with a life time in

between 10^{-4} to 10^{-1} seconds, The emission wavelengths of phosphorescence are usually greater than the fluorescence wavelengths[56,57].

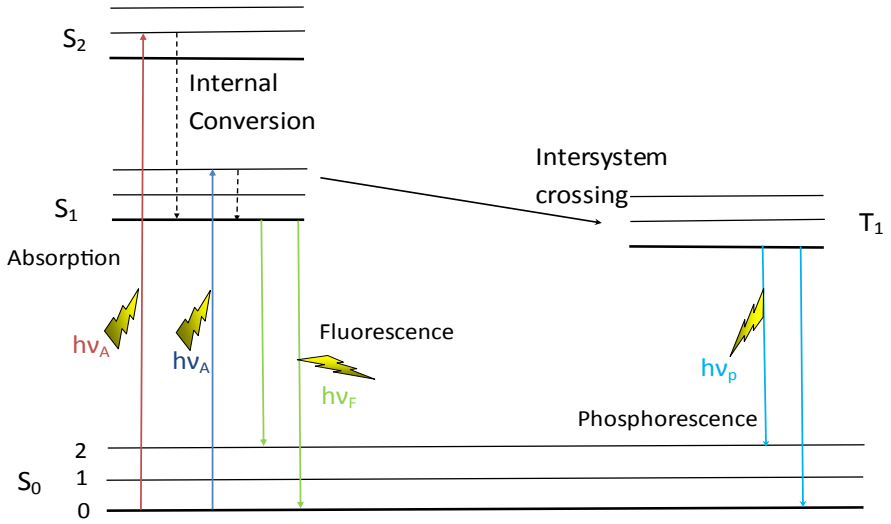

Figure 1.6: The Jablonski diagram illustrates the fluorescence and phosphorescence phenomenon, where brown and blue arrow lines represent the absorption of light, green line and light blue lines represents emission of light in the fluorescence and phosphorescence respectively and black lines represents the orbital energy levels in conduction band (So) and valence band (S_1, S_2).

In some of the flourophores and scintillator the absorption and emission wavelength overlap at certain points which subsequently reduce the intensity of fluorescence reaching to the photo detectors or PMTs specially in the case of large volume detectors, this problem of significant energy loss can be resolved by avoiding reabsorption of emitted photons with the addition of wavelength shifter. These wave shifters are added in low concentrations to minimize their self-absorption also as their main task is to avoid self-quenching effect.

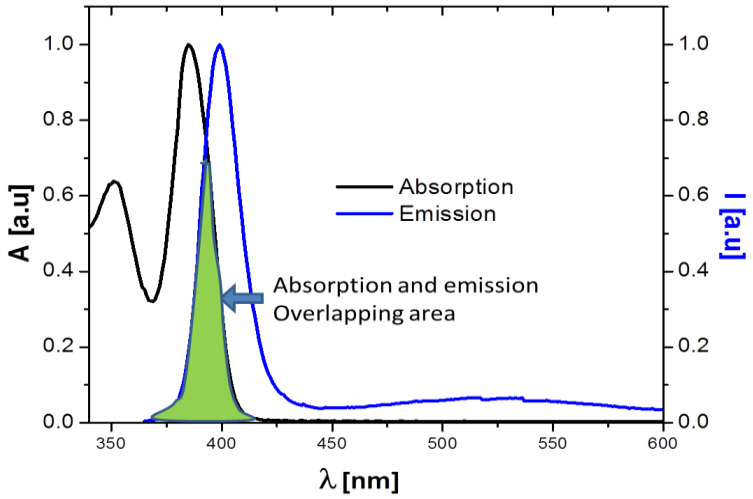

Figure 1.7: Pictorial representation of overlapping area (green) in absorption (black) and emission (blue) spectra of CdS QDs

Some of the most commonly used scintillators (fluorophores) are p-terphenyl, 2-(4-Biphenylyl)-5-phenyl-1,3,4-oxadiazole (PBD), butyl PBD , 2,5-Diphenyloxazole (PPO), inorganic QDs and mostly used solvents are 1,2,4-trimethylbenzene, linear alkylbenzene, and toluene.

Recent developments of fabrication approaches in nanotechnology and synthesis of high quality QDs lead to incorporation of these QDs in organic LS detectors as scintillators (flourophors)[58-59]. These inorganic scintillators QDs are intended to act as wavelength shifters in LS detectors. The main advantage of QDs as compared to other flourophores (e.g. PPO) is their narrow emission peaks. When these inorganic QDs are surrounded by the hydrophobic surfactants that leads to very good dispersion in organic solvents such as toluene, 1,2,4-trimethybenzene, etc., which also helps very good colloidal stability over a period of time by avoiding the aggregation and oxidation of these inorganic NPs. QDs are usually synthesized from binary alloys for example CdS, CdSe, CdTe, and ZnS. Cd based scintillator is more interesting to investigate and to use as doping material for organic LS because of its Cd-113 isotope has the highest thermal neutron capture cross-section, which is 20,000 barn making it ideal for antineutrino measurements using IBD (Eq-5). Another reason which makes the cadmium more prominent candidate as doping material in scintillation detectors is its two other isotopes Cd-116 that under goes double β^- decay and Cd-106 is one isotope that along with other five elements have the characteristics of double β^+ decay and double electron capture[60]. Other elements such as selenide, tellurium and zinc are very suitable matchmakers with cadmium as they are also double beta decay candidates. During this research work we have prepared large amount of CdS QDs to investigate organic LS loaded with semiconductor QDs.

1.3.2.2 CdS QDs for Plastic scintillators

Another form of scintillator detectors widely used in nuclear, particle physics, and homeland security applications are plastic scintillators. Because of the ease, simple, low manufacturing cost, and quick reaction time, plastic scintillator materials have become prominent detection tools[61]. Plastic scintillators are most universally employed as first line of detection because of their ease of use for ionizing radiation surveillance detectors. Plastic scintillators have a fast decay time of 2-3 nanoseconds with high light output.

The styrene based plastic scintillators can be fabricated by employing the thermal polymerization method while using PPO, POPOP and QDs as the dopants. The QDs with exceptional size dependent quality of fluorescence make them very suitable candidate to work as wave shifter. As it has already been explained that increase in the size of QDs results

in a red shift which means the color of the light emission from QDs changes from blue to red as the size of QDs increase which can be perfectly designed according to quantum efficiency of different photo sensors like PMTs, photo-diodes, avalanche photo-diodes, and charge coupled devices (CCDs). The high quality CdS QDs are also suitable candidate to serve as secondary solutes or wave shifters as they can have emission from 350 nm to 500 nm and can be applied to fabricate CdS QDs doped PPO styrene based plastic scintillators.[28,61,62,147].

1.3.2.3 Role of CdS QDs in capping and gatekeeping of mesoporous silica NPs

Mesoporous silica NPs are very significant drug carrier for the delivery of chemotherapeutics and many other drugs. Mesoporous silica NPs are fabricated by using hexagonal surfactant micelles as a template and coating these micelles with silica leading to the formation of silica NPs[63]. After surfactants removal, it leaves behind porous silica NPs. The pore size can be varied from 2-10 nm and to provide suitable and enlarged surface area to drug and gene entrapment for delivery. Leaking and premature release of chemotherapeutics before reaching the sight of action is another challenge. This problem can be resolved by capping the pore opening after loading of drug in porous silica NPs. Small NPs in the range of 2-4 nm can be helpful in capping the pore opening and to provide a gatekeeping support to prevent the premature leakage of the drug during circulation.

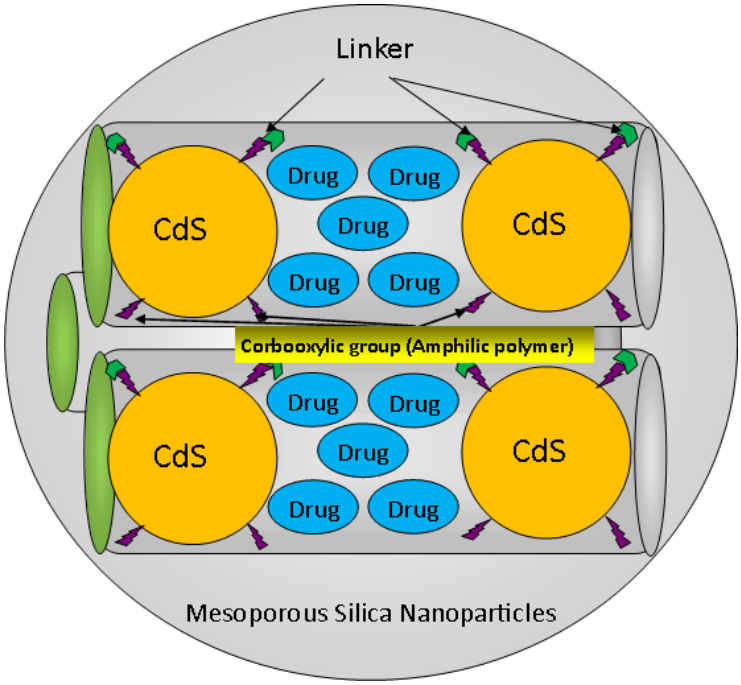

Figure 1.8: Schematic representation of the CdS QDs as gate keeper in mesoporous silica NPs for controlld drug release.

Cadmium sulfide (CdS) particles in the range of 2-4 nm can be used for the controlled release of drug from mesoporous silica NPs. Surface modification of mesoporous silica NPs

at pore opening and CdS particles helps in chemical interaction. CdS surface can be modified with a polymer having a carboxylic group and mesoporous silica nanoparticle surface can be modified with an amide group. This interaction between carboxylic group (CdS particle) and amide group (pore opening of mesoporous silica NPs) leads to the capping of pore and prevention of premature leaking of chemotherapeutics and other materials[64]. The CdS QDs after polymer coating with PMA will be helpful in achieving this target of the controlled release of loaded drugs in mesoporous silica NPs as depicted in Figure 1.8

1.3.2.4 Time resolved photo luminescence (TRPL) spectroscopy of CdS QDs

CdS QDs can be used to understand the interaction between the QDs and semiconductor substrates. The colloidal CdS QDs can be linked via van der Waals interaction to the substrate to enable an easy deposition of large quantities on the surface, which might be useful for their possible applications as gas sensors, photo sensors or solar cells. The aim is to investigate a possible energy and charge transfer between the QDs and the burrowed quantum well (QW) and to gain a deeper understanding of underlying physical processes. The CdS QDs are deposited via drop casting on top of the semiconductor substrate. These hybrid structures are investigated with continuous wave (CW) and time resolved PL measurements in the pico and nanosecond range.

Other than above mentioned investigations performed with CdS QDs, they can also be used for some other miscellaneous experiments such as, fluorescence measurements of CdS QDs with different surface modifications to study the behaviour of different surface coatings, study about behaviour of water soluble CdS QDs and manganese doped CdS QDs in the environmental media.

1.3.3 ZnS and manganese doped ZnS QDs

ZnS is one of the important semiconductor materials and it is most abundantly available compound in nature as source of zinc. It is also like CdS from II-VI semiconductor compound with important photoluminescence, electroluminescence, and photocatalytic characteristics[41]. The wide-band gap energy of 3.6 eV makes ZnS semiconductor materials vital for a set of applications including ultraviolet light-emitting diodes, injection lasers, flat panel displays, electroluminescent devices and infrared (IR) windows and sensors[65,66]. There are different synthetic approaches to produce different sizes of ZnS NCs. A variety of colloidally stable ZnS NCs can be synthesised with different surface coatings or various surfactant ligands (e.g. OLAM, PEG, TOPO, etc.)[65,67]. Due to the lower toxicity of ZnS

compared to Cd-based QDs such as cadmium telluride (CdTe) and cadmium selenide (CdSe), they are usually replacing them in latest in biomedical applications.

The photoluminescence properties of ZnS can be altered by adding suitable doping elements (manganese). Comparing undoped ZnS, manganese doped ZnS QDs have successfully overcome the intrinsic disadvantages of self-quenching due to small ensemble stokes shift and thermal chemical and photochemical sensitivity problems. Manganese doped ZnS makes a potential test-bed for a variety of applications in optoelectronics and especially in nanobiotechnology as bio-markers due to low toxicity[68,69].

1.3.4 Environmental applications of QDs

Applications for metal based NPs are increasing drastically, leading to concerns related to their effects in the environment. The synthesis and use of different NPs and QDs is on the rise and they are somehow released in environmental media (e.g. lake and river) through waste water passages. The toxicity of these QDs and NMs should be thoroughly investigated to assess the potential hazards to the environmental species. In this research work we have presented the toxicity screening using different QDs along with their physicochemical characterization for the better assessment of effects of these QDs on the environment. It was performed using two bacterial species Pseudomonas putida and Escherichia coli in a controlled environment. CdS, ZnS, manganese doped CdS and ZnS was used as test beds for these toxicity screenings[70,71].

1.3.5 ZnO QDs

Zinc is a period 4 element while oxygen is a period 2 element same as CdS and ZnS QDs of group II-VI. ZnO is an n-type semiconductor. ZnO NPs also known as ZnO QDs or NCs. In comparison to other variety of semiconducting materials, it exists in the form of hexagonal wurtzite crystalline structure[72,73,74]. ZnO is a distinctive electronic and photonic compound with the direct band gap energy of 3.37 eV and a high exciton binding energy of 60 meV at room temperature[72,75]. The characteristic emission of ZnO QDs due to free excitation electrons recombination is peaked at 390 nm[76].In addition to this characteristic emission ZnO NPs have another photoluminescence in green region centred at 590 nm, for bulk materials, this fluorescence lies in yellow and peaked at 620 nm[77,78].The green fluorescence in ZnO NMs arises due to the atomic deficiency of oxygen and the fluorescence in yellow or orange region produced due to access of oxygen atoms in the bulk materials. The synthesis approaches usually used to produce ZnO NCs are sol-gel, micro emulsion, thermal decomposition, electrodeposition, ultrasonic, microwave-assisted techniques, chemical vapor

deposition (CVD), hydrothermal synthesis, precipitation spray pyrolysis or electro-chemical[76,79]. These NPs reveal antiseptic, antibacterial anti-corrosive, antifungal and UV filter properties[80]. ZnO have widespread applications in electronics, photoelectronics, sensors and catalysis. ZnO is now extensively used as a nanocrystalline additive to sunscreen, with further anticipated applications such as, cosmetics, paints, plastics photovoltaic devices and nanomechanical components which result in drastic increase in the production of ZnO during the last decade[81,82].

1.3.5.1 Application of ZnO QDs

Luminescent ZnO NPs has useful applications when they are integrated in a matrix based on organic-organic hybrid polymers in order to develop a humidity sensor coating for drug packaging. The humidity in the package could result from the passage of steam through the package material or through the dehydration of the medicine itself. This humidity leads to a fluorescence quenching of the luminescent ZnO NPs and that effect can be detected. The second function of this coating should increase the counterfeit protection. As it is possible to use ZnO NPs with different colours, a colour code could be generated on the packaging for this purpose.

1.3.6 CdSe/CdS nanorods,

CdSe is n-type semiconducting material. CdSe related NCs has been thoroughly investigated due to their excellent optical properties, i.e., bright and spectrally narrow photoluminescence characteristics. They have applications in the field of opto-electronic devices, laser diodes, biomedical imaging, nanosensing, high-efficiency solar cells and thin-film transistors. CdSe have band gap energy of 1.74 eV. CdSe NCs have excellent quantum yield when combined with CdS NMs along with very good size distribution (monodispersity). When CdS NCs are grown as shell on CdSe nanostructure, they have quantum yield of up to 75% for longitudinal shapes (nanorods). These nanostructures CdSe and CdS produces heterogeneous carrier confinement when fabricated together in single NCs, which means that holes will remain, trapped in CdSe nanostructure while the electrons can move freely between CdS and CdSe NCs. The creation of heterogeneous carrier confinement leads to reduction in radiative recombination that finally results in a good quantum yield[83,84,85].

1.4 Magnetic NPs

Magnetic NPs (MNPs) gained a lot of attention by scientists and researchers during the last couple of decades due to their distinct magnetic and catalytic properties. MNPs are so special due to their distinct tuneable magnetic properties which are in contrast to their bulk

counterparts. The unique property of magnetism expressed by these NPs arises from their size, shape and composition, i.e., as the size, composition and geometry changes the magnetism characteristics also differ. The magnetism of MNPs can depict their size[86,87].

All elements in nature experience magnetism, some more strongly than others, and the strength of their magnetic behaviour strongly depends on their atomic structure and the temperature. Magnetism in any material arises from the net magnetic dipole moment of the elementary particles (electrons) and the dipole moment from the electron spin (spin magnetic moment) and the orbital motion (orbital magnetic moment) of the electrons around the nucleus. These electrons have the property of angular moment (spin) and they have the tendency to form pairs at atomic or molecular levels. In paired electrons that are continuously moving (spin or orbital movement) in opposite direction the net magnetization is zero; therefore, no magnetism is observed. But when there is enough unpaired electron aligned in a same spin direction they results in a strong magnetic field and magnetism is felt at macrolevel. The degree of magnetism exhibited by any material in the presence of external magnetic field is also dependent on the sum of all spin and orbital magnetic moments inside the atom [86,88,89,90].

All materials are classified in-to five categories according to their weak or strong response to external magnetic gradients: Diamagnetic, paramagnetic, ferromagnetic, ferrimagnetic, and antiferromagnetic. Diamagnetism is a fundamental property of all the materials, though it is usually very weak. Diamagnetic materials produce an opposite magnetic field when they brought closer to an external magnetic field. Paramagnetic materials show magnetism only, when they put in the external magnetic field, usually the magnetic dipoles are aligned at random, with overall resultant zero magnetic state, but when the external magnetic field is applied the dipole moments immediately becomes in alignment to the direction of magnetic field applied, which result in some net magnetization. If we see the periodic table diamagnetism and paramagnetism are the two most common types of magnetism for most of the elements at room temperature. From periodic table most of the elements do not experience magnetism at room temperature therefore they usually refer to as non-magnetic whereas those which experience very strong magnetism called ferromagnetic[90-98]. Ferromagnetic materials are those which get magnetized very strongly in the presence of an external field. The direction of magnetism is the same as of the applied external magnetic field. In ferromagnetism all the magnetic domains align in the same direction and parallel to each other to produce strong permanent magnets. These materials also demonstrate magnetisation in the absence of magnetic field, this property of

ferromagnetic material is known as spontaneous magnetisation. Iron, cobalt, nickel and manganese are some of the examples of ferromagnetic bulk metallic materials. If the dipoles align themselves antiparallel to each other but the magnitude of the dipoles is not equal the net magnetization will not be zero and then materials exhibits net magnetisation. These types of materials are known as ferrimagnetic and this form of magnetism is called ferrimagnetism. Ferrimagnetism occurs in oxides of iron which is usually referred as ferrite. Iron oxides, (e.g. $MgFe_2O_4$, $NiFe_2O_4$, Fe_3O_4, $CoFe_2O_4$, Fe_7S_8, Fe_7S_4, etc.) are the examples of ferrimagnetic materials. The ferromagnetism and ferrimagnetism are similar forces but the difference arises at microscopic level and at Curie temperature (T_C). The Curie temperature also known as Curie point is the temperature above which the ferromagnetic materials experience abrupt change in their magnetic properties[91,92]. Below the T_C, the ferromagnetism is efficient and above T_C is lost. If the material is antiferromagnetic and it loses its magnetic properties becoming paramagnetic after a certain temperature then this temperature is known as Néel temperature or magnetic ordering temperature. [90,93,94]. Whereas in the antiferromagnetic materials the electrons align parallel and antiparallel to each other, and present opposite magnetic moment to one another, this parallel and antiparallel arrangement combination results into zero net magnetization. As all dipoles are of equal magnitude, the net magnetisation is zero, which is opposite to ferromagnetic materials as the name also represents antiferromagnetic. Its examples are FeS, Fe_2O_3, αFe_2O_3, Fe_2OTiO_2, Cr, and NiO[86,88].

In contrast to the bulk counterparts the properties of MNPs are a result of both the intrinsic properties of the particles and the interactions between them. MNPs below a critical size exhibit different behaviour, at nanometric scale the magnetic materials can be tailored to be soft or hard magnetic materials by designing the nanostructure of such materials, such as super paramagnetic particle of single magnetic domain. The hard and soft magnetic material is defined by the coercive field (H_C) of hysteresis curve, for hard magnetic materials the Hc is big and it is smaller for a soft magnetic material. H_C is defined as the capacity of a ferromagnetic material to refuse to become demagnetised under the external applied field[90,94]. The tuning ability of H_C while playing with size and composition makes MNPs attractive for a vast variety of applications.

The properties of MNPs can be also tuned by varying the size of the NPs because there are two main parameters dominated for the magnetic properties of NPs related to size variability. First, the finite-size effects which leads to various special features, the finite size effects arises from the quantum confinement of the electrons and also the single and multi-

domain structures. Second, the typical surface effects which results from the symmetry breaking of the crystal structure at the surface or boundary of each NP, oxidation, dangling bonds existence of surfactants, surface strain and also from the different physico-chemical and crystalline structure of the core and the shell around it[95,96,97].

In bulk ferromagnetic materials and bigger MNPs, there are multiple domain magnetic moments, in these multi domain structures there are identical and uniform magnetization areas which are separated by domain walls. The balance between external magnetostatic energy (ΔE_{MS}) and the domain wall energy (E_{dw}) creates these domain walls. The ΔE_{MS} is proportional to the increases in the volume of the materials and the E_{dw} increases proportionally to the interfacial area between wall domains. The enhancement in the volume of the materials allows increasing the ΔE_{MS} (stray field) while broader interfacial area between domains helps to increase in the domain wall energy[95, 98,99].

MNPs below a critical diameter cannot support more than one domain, and are thus described as single domain NPs. The existence of single domain (SD) and multiple domains (MD) depends on the size and composition of the NPs, when the size or volume of NP is less than a certain critical value at which it requires more energy to produce domain walls as compared to support ΔE_{MS}. The critical size diameter (D_C) can range up to few tens of nm depending on the material (i.e. ferro- and ferrimagnet's nature) and temperature. The SD exists less than this critical size (D_C) and the MD exists above D_C. SD NPs (depending on material) with sizes below a certain critical value, for which magnetic reversal can be thermally activated, are typically called superparamagnetic (SPM) particles. In SD particles all the spins are aligned in one direction and the whole magnetic NP is homogeneously magnetized. The magnetization at which all the moments are aligned to external field is referred to as the saturation magnetization (Ms). When the external magnetic field is removed the magnetically saturated material still exhibit some remnant magnetization (M_R), the applied magnetic field in reverse direction to make this (M_R) zero is known as coercitivity (H_C) as represented in Figure 1.10. The maximum coercivity for a given material occurs within its SD range. Above D_C for larger particles sizes, H_C decreases because of the creation of multiple domains and for smaller particles, H_C again decreases, but this time due to the randomizing effects of thermal energy. To create multiple domains in a NP its size should be more than the thickness of domain walls[101,104]. The response of single and multi-domain particles to external magnetic field applied, is schematically presented Figure 1.9.

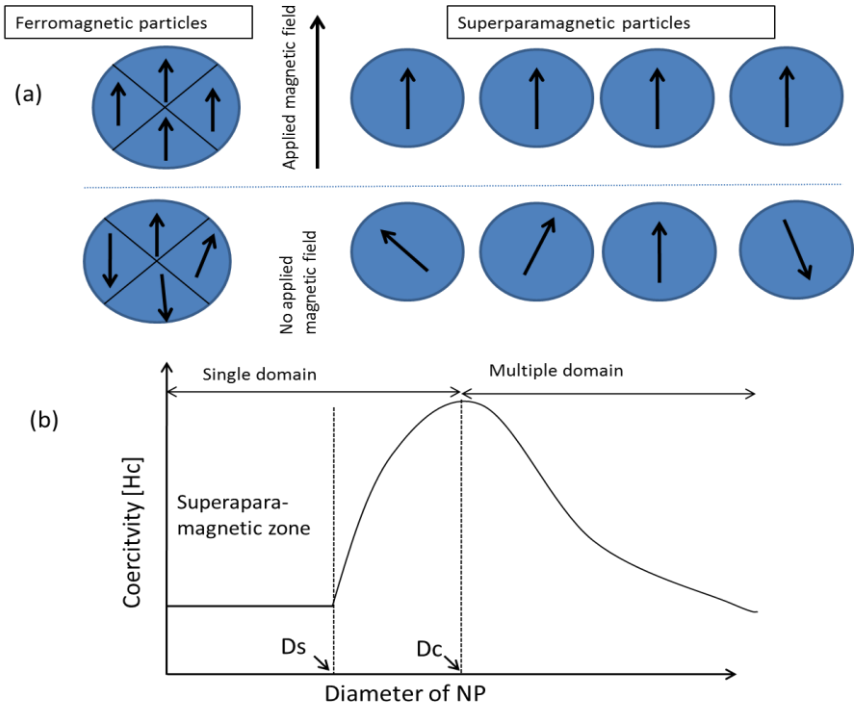

Figure 1.9: (a) Response of magnetic moments in MD-FM particles and SD-SPM (SD) when no field applied and external magnetic field applied (b) Coercivity (Hc) response with respect to magnetic particle size (diameter) for FM and SPM particles, Ds is the size diameter below which the MNPs exhibit SPM behaviour and Dc 'critical' size diameter below which MNP behaviour changes from SD to MD or vice versa.

High coercivity of small NPs is due to two reasons, first one is the spin rotation and the second is the shape anisotropy. For the spherical NPs the coercitvity is smaller. SD NPs usually behave like SPM materials and their all magnetic moments are rotating randomly, for SPM NPs with no external magnetic field they exhibits zero magnetization when the temperature is above blocking temperature while there is a presence of external field there is a statistical magnetization. This behaviour of MNPs is illustrated in the hysteresis diagram Figure 1.10

Single domain NPs produces the magnetization when the applied magnetic field reaches coercive field (Hc) and also the saturation magnetization (Ms) is achieved at higher magnetic field strengths. When the applied external field is removed there is still a significant magnetization is still observed which is called residual magnetization (M_R). It is because of the hysteresis phenomenon. For superparamagnetic NPs, however there is no such remanence and coercivity. For a perfect SPM NPs there is zero magnetization for no applied magnetic field but magnetic saturation is gained at very low magnitude of applied external magnetic fields as shown in Figure 1.10. Superparamagetism is a property strictly coupled to MNP and arises when the thermal energy is adequately high to overcome the magnetic stabilization

energy of the MNPs[95,100]. This property makes them ideal for heating application using alternating magnetic field (AMF).

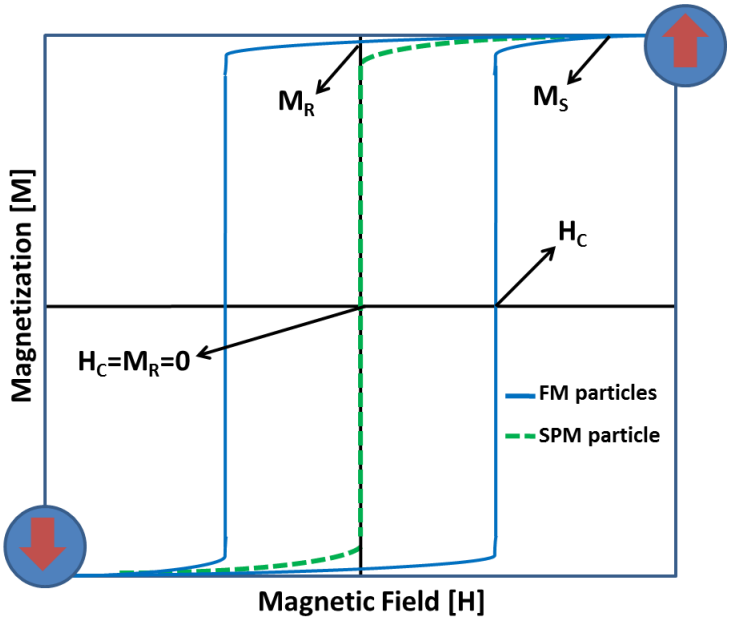

Figure 1.10: Hysteresis image illustrating magnetization (M), magnetic saturation (M_S), magnetic remanance (M_R) and coercivity field (H_C) for FM particles by blue sold line and SPM particle by green dotted line [96]

The MNPs can get oxidise when they are exposed to air for longer periods of time. There are several ways to overcome the oxidation which can be size control, changes in the structure and composition of NPs, furthermore to avoid the oxidation of MNPs surface coating of these NPs with some suitable oxidation resistant polymers and molecules can be applied, such as carboxyl groups, biotin, poly(isobutylene-alt-maleic andydride), starch, dextran and polyethylene glycol (PEG)[98,101,102]. The surface modification of these MNP is also dependent on the application or area of use.

MNPs have a wide range of applications, including ultra-high-density magnetic recording, magnetic fluids recording, catalysis, biotechnology/biomedicine, material sciences, photocatalysis, electrochemical and bioeletrochemical sensing, array-based assaying, microwave absorption, data storage, environmental remediation and, as an electrode for super-capacitors and lithium ion batteries (LIB) [103,104,105].

The special characteristic of these MNPs is that they can be handled by an external magnetic field, makes them a suitable candidate for imaging and therapy in medicine, e.g. contrast enhancement in existing magnetic resonance imaging (MRI) techniques, localized treatment options such as targeted drug delivery and hyperthermia. For example Rodríguez-Luccioni et al. applied an AMF to MNP in MCF-7 breast cancer cell cultures and presented substantial reduction in cells viability compared to hot water-induced hyperthermia[106,107,].

Magnetic NPs have gained a lot of interest because of their intrinsic properties. Researchers have developed different ways to increase the functionality of these NPs and they are continuously trying to improve the optimal response of MNPs under the influence of external magnetic field.

1.5 Plasmonic NPs

Another form of metallic NPs is plasmonic NPs, usually these NPs are gold (GNPs), silver, copper and platinum. These metallic NPs, especially GNPs, are in use since centuries but during the last century they attracted lot of attention due to their optical and catalytic properties, that can be applied to number of applications, e.g., drug delivery, photothermal therapy, optoacoustic imaging, biosensing, biotechnology, nanomedicine, and photovoltaics[108,109,110,111]. The application of these plasmonic NPs is mainly dependent on their size, shape, surface chemistry, surface charge and colloidal stability. By controlling, tailoring and manipulating all these parameters the physicochemical properties of these metallic particles can differ resulting change in applied area. For instance, the optical absorption and scattering of these NPs is largely dependent on their size, i.e., the ratio of the scattering to absorption increases dramatically for larger size of particles. For a 20 nm GNP, the total extinction is nearly all contributed by absorption but when the size increases to 80 nm, the extinction is contributed by both absorption and scattering in a similar degree. This fact can guide the choice of GNPs for biomedical applications. While larger NPs are preferred for imaging because of higher scattering efficiency, smaller NPs are preferred for photothermal therapy[112] as the light is mainly absorbed by the particles and thus efficiently converted to heat for cell and tissue destruction.

These metallic NMs exhibit a special resonance property at specific wavelengths, a resonant combined oscillation of the conduction band electrons of NPs known as plasmon resonance[111]. This plasmon resonance is a unique phenomenon to highly conductive metals (Au, Ag, Cu) of nanometer size particles and it arises, when an electromagnetic radiation (light) induces a collective oscillation in free conduction band electrons. For nanometer size particles the free conduction electrons oscillate along the particle surface, therefore it is termed as localized surface plasmon resonance (LSPR)[113,114]. The optical properties of plasmonic NPs are also size and shape dependent subsequently on LSPR because change in the size, shape and composition also changes the LSPR. This illustration is also shown in Figure 1.11.

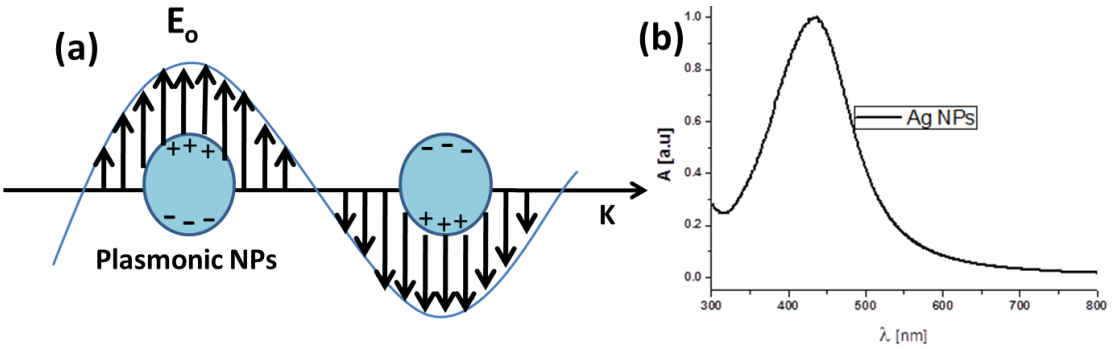

Figure 1.11 (a) Schematic diagram illustrating the interaction of polarized electromagnetic radiation with a metallic NP to generate a LSPR. (b) UV-Vis absorption spectra for silver NPs, which have one SPR band in the visible region and its maximum of absorption is peaked at 436 nm

The intensity and frequency of light at which metal NPs reveals maximum plasmon resonance is highly dependent on the size, geometry, composition (material), local environment, surrounding medium and dispersant of the NPs, which influences the electron charge density on the NPs' surface[115,116]. For example, spherical NPs (SNPs) of gold the LSPR is peaked around 520 nm and for silver the SPR frequency peaked around 435 nm but when the shape of these NPs changes LSPR wavelength also changes[115]. For instance, gold with anisotropic structure (rods-shape) have two SPR peaks, one is located in the visible region and called transversal SPR, due to the oscillation of conduction electrons along the shorter axis of NPs and the second is located in the near infrared region and called longitudinal SPR, due to the oscillation of conduction electrons along the shorter axis of NPs [117].

There are wide varieties of synthetic routes for the preparation of plasmonic NPs. These routes include sol-gel method, thermal decomposition of metallic compounds, chemical reduction of metallic precursors, etc.[12,15,16,115]. The reduction or decomposition of metallic salts is the most commonly used method to synthesize colloidal plasmonic NPs[16]. During the reduction method, the atoms of these metallic elements (Gold, silver or copper) are reduced from multivalent to zero-valent atoms, and these zero-valent metallic atoms are the main constituent of these metallic NPs. This reduction approach can be employed to produce colloidal metallic NPs under the presence of suitable stabilizing agents which supports the colloidal stability in organic or aqueous environments to avoid the aggregation and oxidation. These modern colloidal synthesis methods help scientist and researchers to tune the fabrication conditions in order to achieve required shape, size and with good control over monodispersity (size distribution). The manipulation of surface chemistry of the metallic NPs can be achieved by adding suitable stabilizing agents (e.g. CTAB, PEG, DDA, 1-

dodecanethiol or other thiol modified ligands, etc.) during or after the synthesis using ligand exchange methods which results in a suitable surface chemistry[101,111].

In nanobiotechnology plasmonic NPs are applied in combination with compatible biomacromolecules such as DNA, proteins, antibodies, peptides, etc. The combination of these biomacromolecules to NPs often is referred as bioconjugates. The modification of GNPs with thiolated ligands is straight forwards; however the linkage of biomacromolecules requires the use of bioconjugation strategies. The functionality provided by these molecules also has improved the applicability of NPs in fields such as medicine and biotechnology[115,118].

1.5.1 Bimetallic (Au-Cu) NPs

Alloy NPs have been studied extensively because of their unique synergistic effects derived from the parent metals on optical, catalytic, and magnetic properties. These combined properties can be enhanced by controlling their size, shape, and composition. Gold and copper NMs are plasmonic NPs. Bimetallic gold and copper NPs with tuneable sizes and compositions provide wider control over their plasmonic properties than single metallic NCs. Incorporation of copper in gold NCs lattice increases catalytic property of gold and enhances the use of AuCu NPs for catalysis applications[119,120]. These Au-Cu bimetallic NPs were studied in this research work in connection with their use in hydrogels and aerogels applications.

1.6 TiO_2 NPs

Titanium dioxide (TiO_2) is also known with the name Titania or Titanium (IV) oxide, which was discovered in 1791 by William Gregor from ilmenite. Rutile, anatase and brookite are three most abundantly available ores of TiO_2 in nature[121,122,123]. Titanium dioxide (TiO_2) belongs to the family of transition metal oxides. Being n-type semiconductor and having very high band gap energy of approximately 3.2 eV along with very good optical properties (excellent optical transmittance, high refractive index of 2.6-2.9) and chemical stability makes TiO_2 very suitable for the application in the area of photocatalysis and photoelectrochemistry[121,122]. Titanium is one of the ninth most abundant naturally occurring metals. A great percentage of its production is used for white pigments while nearly about 2% is used for making titanium metal, welding rod coatings, fluxes, and other products[123,124]. TiO_2 has nowadays become a part of our daily life with an extensive variety of applications ranging from fabric industry to makeup industry, for example paints colors, pigments, varnishes, dyes, paper, plastics, coloring agents, food, toothpastes, medicines, and paving

stones[121-125]. Due to good absorbance of ultraviolet light by TiO_2 NPs it is widely used in sun-blocks, sun-screens, and a wide variety of other cosmetic products[126]. TiO_2 is widely used in pigment industrial application because of its poor solubility, brightness and high refractive index. The photocatalytic characteristics of TiO_2 have been employed to handle different environmental issues, specially to get rid of contaminants from both air and water[127]. In comparison to organic UV protecting material, its inorganic nature makes TiO_2 superior in terms of safety for health and nature. TiO_2 is also produced and synthesized at nanometer scale in different shapes and sizes. TiO2 NPs are 100 times smaller in size and they are produced in amounts that are less than 1% in comparison to pigments[128].

Scientist has developed different methods to synthesize TiO_2 NPs, for example hydrothermal, solvothermal, microemulsion technique, Sol-gel technique, electrochemical process, precipitation, biological synthesis, direct oxidation method, chemical vapor deposition (CVD), electrodeposition, sonochemical method, aerosol synthesis in a furnace, liquid flame spray (LFS) and microwave method,[128,129,130]. TiO_2 NPs can be synthesized by the above listed synthesis techniques. The selection of any of these synthesis routes depends on required, shape, size, type, and intended application. Some conventional methods have limitations in terms of fine crystallinity and good size distribution. For example, TiO_2 NPs produced with sol-gel process are amorphous and require more calcinations treatment to achieve better crystallinity[124]. There is some application in which these NPs are coated with some polymers to avoid any side effects, for example TiO_2 NPs are coated with alumina or silica to avoid production of hydroxyl radicals during direct contact of TiO_2 NPs with skin which helps to prevent the hazardous carcinogenic[131,132]. The size, shape and surface chemistry of these NPs are usually optimized during the synthesis process. The surface chemistry of synthesized TiO_2 nanostructures can also be tuned with several methods such as ligand exchange and polymer coating.

1.6.1 TiO_2 NPs for in vivo study

TiO_2 NPs has been extensively investigated during recent decade for sub-pathological and pathological effects in biological matrices. TiO_2 NPs are most robust; chemically stable and hard to dissolve among other different kind of NMs. Therefore inertness and persistence inside the body is a critical issue for this robust NP. The interaction mechanism of NPs with biological matrices is not exclusively related to the administered dose but also there are some other features of these NPs which play their part, these players can be administration technique, shape, composition, surface charge and biological target. Shape and geometry of the NPs play a minor role as compared to surface chemistry (charge and the presence of

different sized molecules, chemical groups, and molecular conformations) on the interaction with extracellular matrix. Surface chemistry of the NPs is, therefore a key player as compared to shape of the NPs. However, after the chemical composition and state of the NP, next player is shape because it affects molecular arrangement[133,134,135].

The proposed in vivo study plan was carried out with different shape (cube, rods, plates) while maintaining the surface chemistry of all these NPs identical. The study was aimed to determine the role of dose in organ distribution and organ pathology. In addition to determining the influence of dose response, the three main objectives of the study were:

1. To evaluate the effect of a single intravenous administration of TiO_2 NPs in terms of biodistribution, organ accumulation, and biological barrier passage;
2. to evaluate the effect of a single intravenous administration of TiO_2 NPs in terms of TiO_2 potential organ toxicity, and
3. to evaluate the influence of the TiO_2 NPs geometry on the above effects.

Furthermore there are also some other in vivo experiments performed with replacement of cube shaped with bipyramids shaped TiO_2 NPs along with rod, and plate TiO_2 NPs. The rationale behind to perform these in vivo experiments is to investigate

i. the effect of biological environment (e.g. lung lining liquid, saliva, gastric/intestinal fluids) on NP's behaviour and toxicity using complex co-culture systems for the intestine and alveoli;
ii. the effect of NPs on the activation of the inflammasome;
iii. the influence of NPs on the maturation and activation of dendritic cells.

1.7 Stabilization and surface modification of NPs

The NPs synthesised in organic solution or capped with organic surfactant are usually stable only in non-polar solvents or in organic media, e.g., toluene, chloroform, hexane, etc. These long chain organic surfactants also help to control the size during nucleation process. These surfactants are usually aliphatic side chains (described in section 1.1, page number. 3) which contain hydrocarbon as the number of hydrocarbon increase the hydrophobicity increases, which support the colloidal stability of the NPs. These NPs were synthesized usually by thermal decomposition. The schematic diagram of some of surfactant, ligands or capping agents used for inorganic NPs are shown in the Figure 1.12.

These NPs have a lot more biological application which requires the NPs to be stable in the water or cell media. The stability of these NPs in aqueous phase can be achieved by capping the NPs core with a suitable surfactant or ligand; this surfactant stabilizes the NPs in aqueous phase by electrostatic forces or steric repulsion. If the surfactant molecules cannot stabilize the NPs individually the NPs gets aggregated which means they are no more single

NP, but they become unwanted bunch of NPs. To avoid these agglomeration or aggregation, sufficient electrostatic or steric forces are required, which can be introduced by suitable surface engineering.

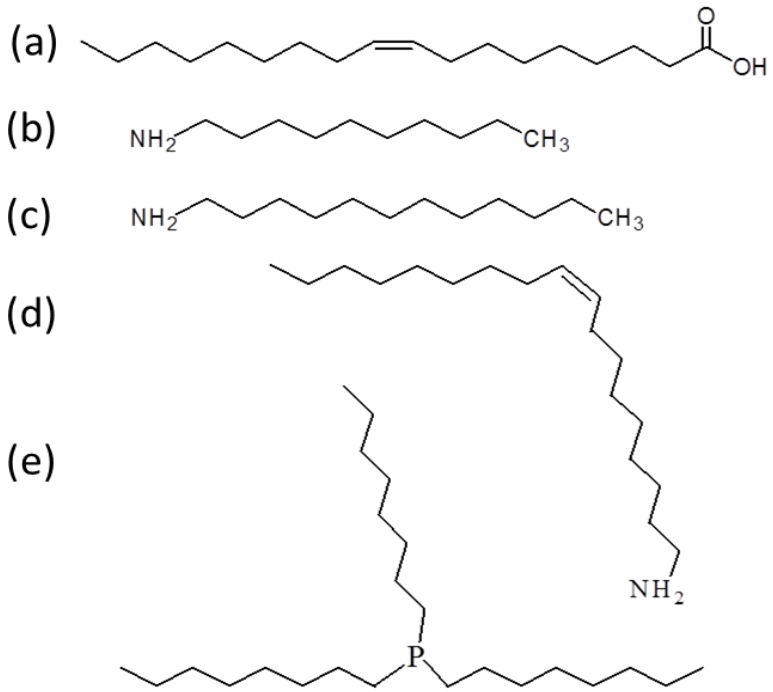

Figure 1.12: Schematic diagrams of (a) oleic acid, (b) decylamine, (c) dodecylamine, (d) oleylamine, and (e) trioctylphosphine

To transfer the hydrophobic capped NPs in aqueous phase from organic phase different approaches have been developed. In general there are two methods[136]. Most commonly used: (i) Introduction of charges at the surface of the NP as same charges repel and helps to maintain single NP stability by electrostatic repulsion, and (ii) the suitable ligands exchange (removal of organic ligands by hydrophilic) at the surface of NP's core, which stabilizes the NPs in the aqueous solution by steric repulsion. The hydrophobic surfactants/ligands are replaced by hydrophilic molecules which ultimately help to turn hydrophobic NPs into hydrophilic NPs. This illustration of stabilization of NPs is depicted in the schematic diagram Figure 1.13.

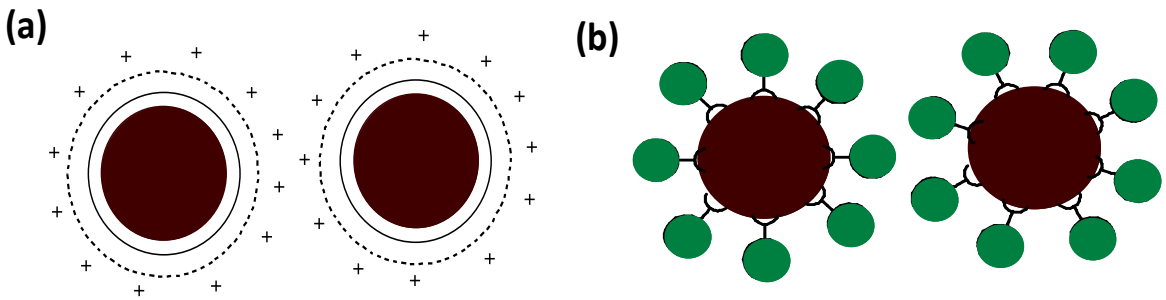

Figure 1.13: Schematic diagram representing NPs stabilized by (a) electrostatic repulsion and (b) steric repulsion

The surface modification by introducing the charges is also done by suitable coating of amphiphilic polymer which has sufficient charge values to avoid the agglomeration by electrostatic repulsion of same charges around the NPs. These polymers usually consist of two parts one hydrophilic and second hydrophobic. The polymer used during this research work was developed [101] by attaching the side chains of dodecylamine with poly(isobutylene-alt-maleic anhydride) (PMA), where maleic anhydride rings reacted with amine group of dodecylamine. Approximately 75% of the rings get reacted according to the amount of hydrophobic side chains and hydrophilic backbone used as presented in Figure 1.14. The rest 25% unreacted rings can further be utilized for attachment of some other functional groups as in this study we have used Cyanin-5-amin (Cy5) dye, which also contains amine group.

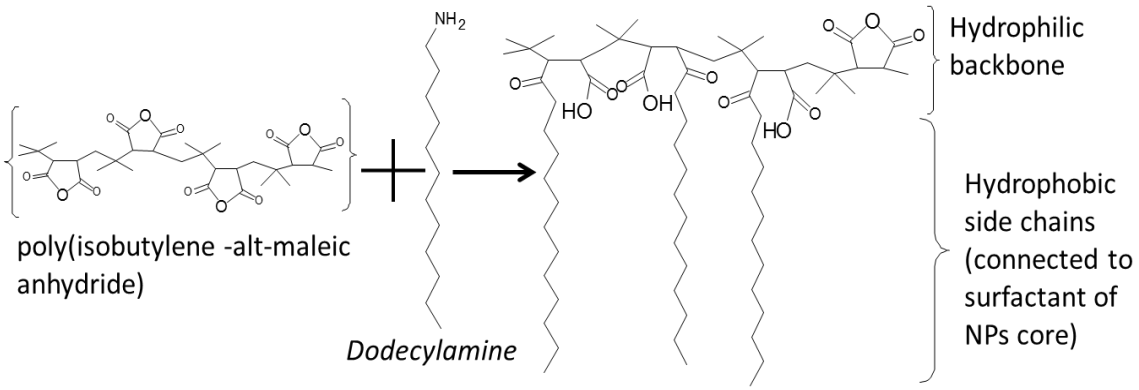

Figure 1.14: Schematic diagram of amphiphilic polymer with hydrophobic side chains

During the phase transfer from organic to aqueous medium the hydrophobic parts interact with the hydrophobic surfactants that are attached to core of the NPs, as shown in the Figure 1.17. When NPs coated with PMA, that contains enough carboxylic groups (-COOH) on the outer surface of NPs, which results in the sufficient negative charge to avoid the agglomeration of these polymer coated NPs and support good colloidal stability.

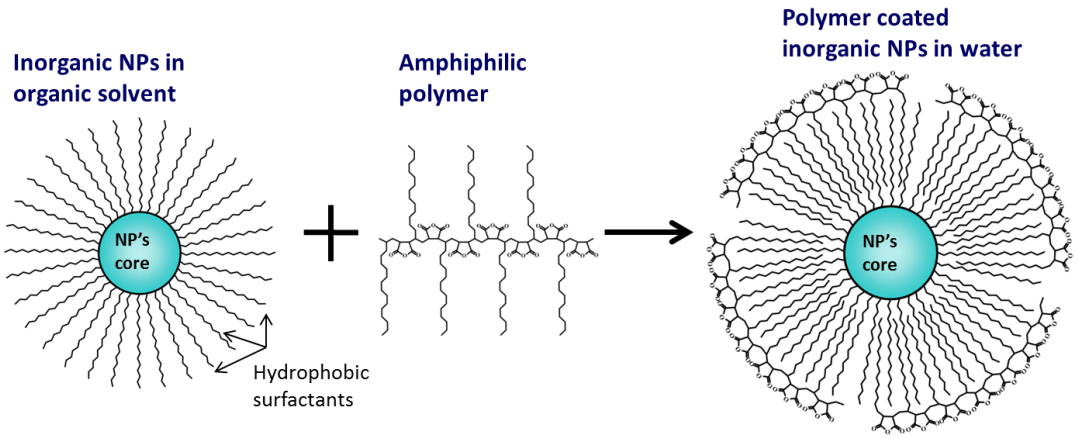

Figure 1.15: Schematic representation of polymer coating NPs

During the polymer coating procedure several empty polymers are formed which contain no NP. The cleaning of NPs from these free or empty polymers (micelles) can be performed with gel electrophoresis. As the polymer coated NPs are negatively charged because of negative corbooxylic (COOH) groups at the surface of NPs, they are attracted towards the positive electrode (anode) of the gel electrophoresis cell. The carboxylic groups can be further modified with primary amine ($-NH_2$) groups via 1-ethyl-3-(3-dimethylaminopropyl) carbodiimide (EDC chemistry)[101] as schematically represented in Figure 1.16. Using this functionalization method the number of PEG molecules attached to the NPs' core can be controlled as depicted in Figure 1.17 (c), i.e., from (ii) to (ix) represents the number of PEG molecules attached to the IONP.

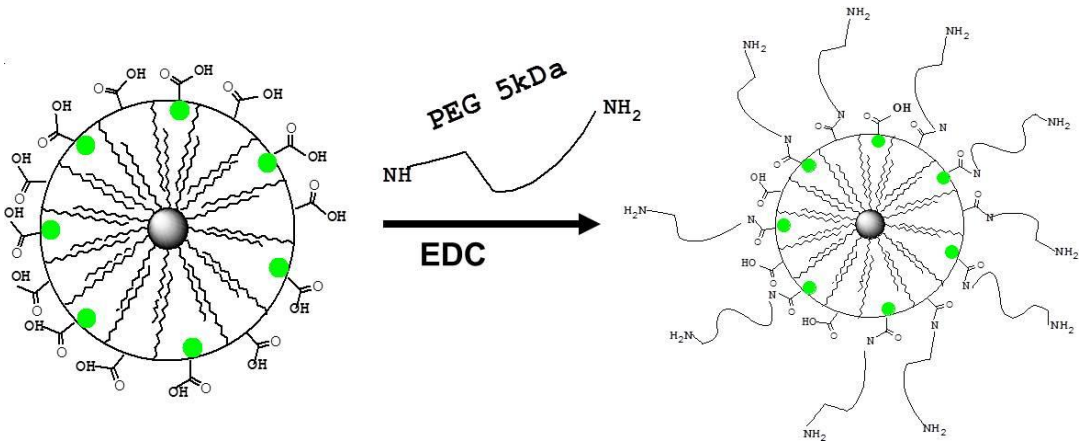

Figure 1.16: Schematic diagram of carboxylic group's functionalization with 5kDa amino PEG

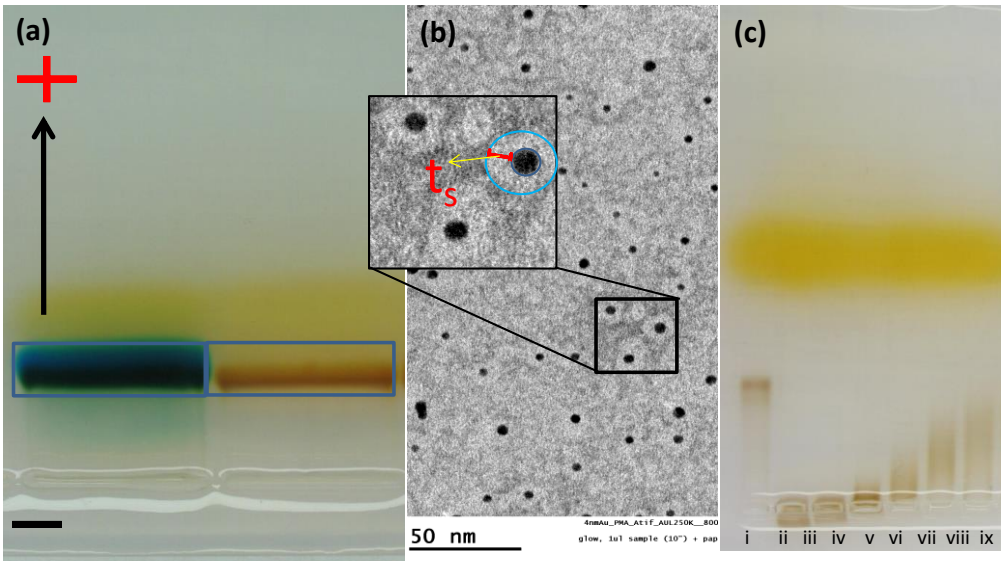

Figure 1.17: (a) Gel electrophoresis image of polymer coated Ag NPs with Cy5 flourofour (left) and without (right), (b) TEM image of GNPs showing polymer shell thickness (t_s) around the NPs, and (c) IONPs with further surface modification using EDC chemistry for the attachment of 5 kDa PEG, running in 2% agarose gel, (i)

represents without PEG molecule, (ii) represents highest number of attached molecule to (ix) least number of attached molecule.

The polymer coated NPs can also be cleaned from free polymer or micelles by precipitation method using ultracentrifugation for lighter particle, along with micelles there is also a possibility that there are some aggregated NPs, these aggregated NPs can be filtered by syringe filters.

1.8 Aim of the Ph.D. thesis

In the field of nanotechnology researches are finding various ways to synthesize stable colloidal NPs having a wide variety of applications in physics, chemistry, biology, biotechnology and medicine. The aim of this thesis was to synthesize various kinds of NPs with their compatible surface chemistry that met the requirements of diverse collaborative research projects. The surface of these NPs was also engineered to make them useful for a variety of applications few of them has been already discussed.

There were several rationale behind the synthesis of CdS QDs: First, it will be used for the detection of neutrinos using organic LS and CdS QDs as wave shifters along with different organic flourophor, the main reason was that the CdS QDs can bear the potential to increase the optical properties of current LS significantly; second, they can be used to fabricate CdS QDs doped PPO styrene based plastic scintillators by thermal polymerization; third, time resolved photo luminescence (TRPL) investigations of the CdS QDs by attaching them to a ZnSe substrate via spin-coating; fourth, polymer coated CdS QDs in the range of 2-4 nm with amphiphilic polymer having carboxylic groups on the outer surface can work as gate keeping NPs for the controlled release of drug from mesoporous silica NPs; fifth, water soluble polymer (i.e. PMA) coated CdS QDs were also used to perform several experiments along with manganese doped CdS QDs, ZnS QDs and manganese doped ZnS QDs, on nanomaterial's (NMs) behaviour in the environmental media (river and lake water). Luminescent ZnO NPs are useful when integrated in a matrix based on an organic-organic hybrid polymer in order to develop a humidity sensor coating for drug packaging.

Initially it was aimed at to study magnetic behaviour of these MNP under alternating magnetic fields and also to calculate the maximum specific power loss (SPL) for localized hyperthermia related applications by incorporating them in poly electrolyte capsules.

Several toxicity screenings and dose determination assays were performed by water soluble IONP, GNPs, and silver NPs, each of size 4 nm, and the silver NPs were coated with Cyanine-5 (organic flourophor) additionally.

Cubical TiO2 (ca. 10 nm) NPs were synthesised with the purpose to be a part of TiO2 NPs library that includes rod, plate and bipyramid of different sizes to be used for various in vivo studies. These in vivo studies were performed to investigate toxicity, biodistribution response in biological matrices with respect to dose administration, size and shape of TiO2. Another in vivo study was aimed at to investigate the effects of biological media (lung lining liquid, saliva, gastric/intestinal fluids) on NPs' behaviour and toxicity using complex co-culture systems for the intestine and for the alveoli, the effects of NPs on the activation of the inflammasome, and the influence of NPs on the maturation and activation of dendritic cells.

Another study was performed with the aim to phase transfer of the hydrophobic NPs while retaining all their optical, magnetic and plasmonic properties. After polymer coating these NPs, they will be employed in Aerogels, hydrogels and heterogels. These polymer-coated NPs will be used for the elaboration of NPs based hydro and aerogels. These NPs were of different sizes (5-40 nm), shapes (rods, spheres and cubes) and composition or physical properties (photo-luminescent, magnetic and plasmonic). These NPs were surface coated with amphiphilic polymer to present that this unique phase transfer route is adopted irrespective of the size, shape and composition of NPs.

2. Synthesis, surface modification, and characterization of the NPs and QDs

2.1 Synthesis and polymer coating of CdS QDs

CdS QDs were synthesized in inert atmosphere using schlenk line to avoid any oxidation of NCs; these synthesis procedures were performed according to different published protocols with some modifications[28,137,138]. In brief cadmium oxide (CdO) 0.126 g, OLAC 2.02 g, and 1-octadecence (ODE) 12.0 mL were taken in a three neck flask along with magnetic stirring and heated up to 120 ^{o}C with a heating mantle, at this temperature vacuum is applied for approximately 10 min, then temperature of the flask is raised up to 300 °C under nitrogen reflux. After few minutes CdO start to decompose and the brown colour solution turns to transparent. When the solution in the flask is completely transparent then a solution of sulfur in ODE (2.0 mL, 0.25 M), which was prepared in another bottle injected via syringe immediately into the mixture and the temperature of solution slumps around 250 °C. After the injection of sulfur-ODE the color of the solution turns yellow from transparent which shows the growth of QDs. The size of QDs is dependent on the time allowed for the growth of these NCs. After achievement of required size of QDs the heating mantle is removed and the solution allowed to cool down. This solution of QDs was cleaned from free ligands OLAC, ODE and nondissolved sulphur and CdO with addition of acetone and precipitation. The precipitate is redispersed in toluene and cleaned several time with subsequent addition of ethanol. Finally, after couple of cleaning it is dissolved in chloroform or toluene and characterized by absorption and emission spectra initially.

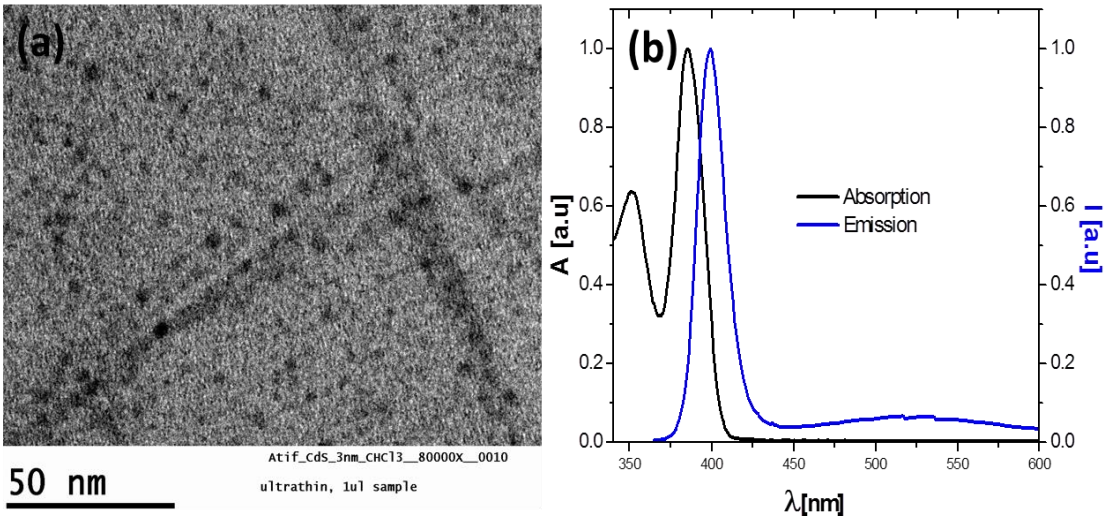

Figure 2.1: CdS QDs in toluene (a) TEM image of CdS QDs, (b) absorption peaked at 393 nm and emission peaked at 403 nm of these QDs

The synthesized CdS QDs were with variable sizes in order to meet the desired optical properties for LS detectors, plastic scintillators, TRPL spectroscopy of CdS QDs with emission spectra peaked in the range of 381 nm to 457 nm. The absorption (Figure 2.2) and emission (Figure 2.3) spectra for few of these high quality CdS QDs are presented below in Figure 2.2and Figure 2.3

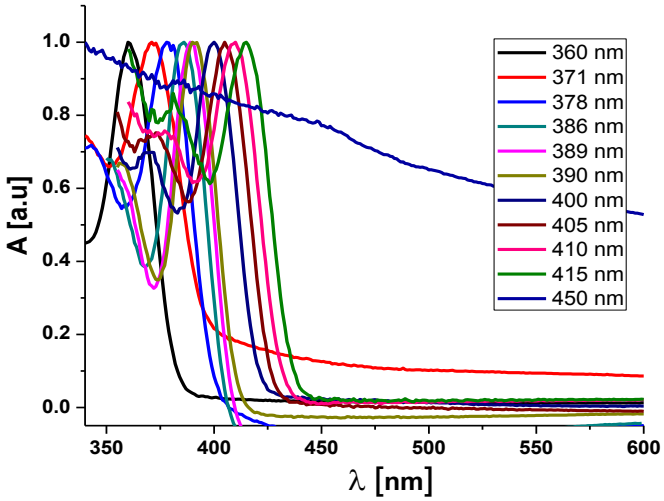

Figure 2.2: Absorption spectra peaked (360-450 nm) of different size of CdS QDs

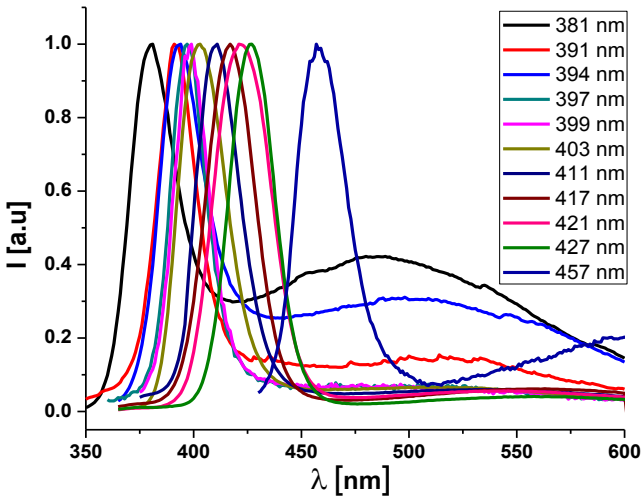

Figure 2.3: Emission Spectra peaked (381-457 nm) for different size of CdS QDs

Scintillation application for neutrino detection requires significant amount of these CdS QDs to be used as wave shifter or secondary scintillators. The proposed study requires minimum 13 mL sample with 65 mg of CdS QDs which is approximately 5 g of CdS QD per liter dissolved in the aromatic solvents (toluene, pseudocumene, and linear alkylbenzene). Normal laboratory scale synthesis protocol does not provide this much of amount with extreme purity because during the cleaning process a significant amount of CdS QDs are lost, to achieve this high concentration target of CdS QDs different synthesis routes and parameters were extensively investigated[28,137,138]. This high concentration of CdS QDs was a

result of multiple synthesis experiment with the aim to get same optical properties every time, the same optical characteristics achieved during these synthesis experiments is presented below Figure 2.4, Figure 2.5, and Figure 2.6.

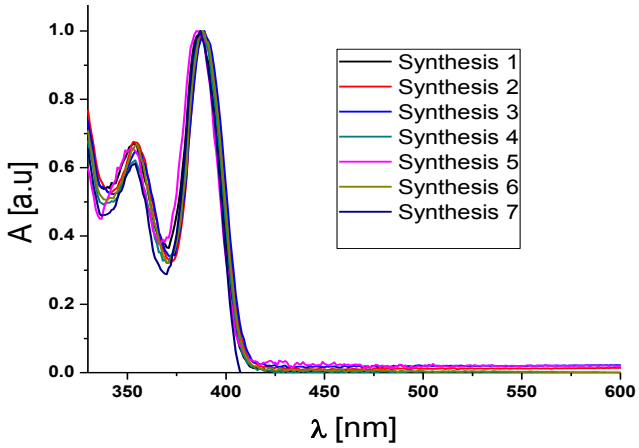

Figure 2.4: Absorption spectra of multiple synthesis experiment with similar absorption peak.

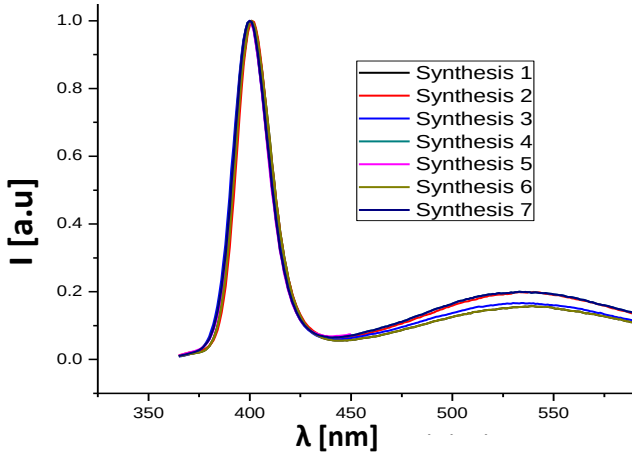

Figure 2.5: Emission spectra of CdS QDs with smiliar emission peak for multiple syntheses

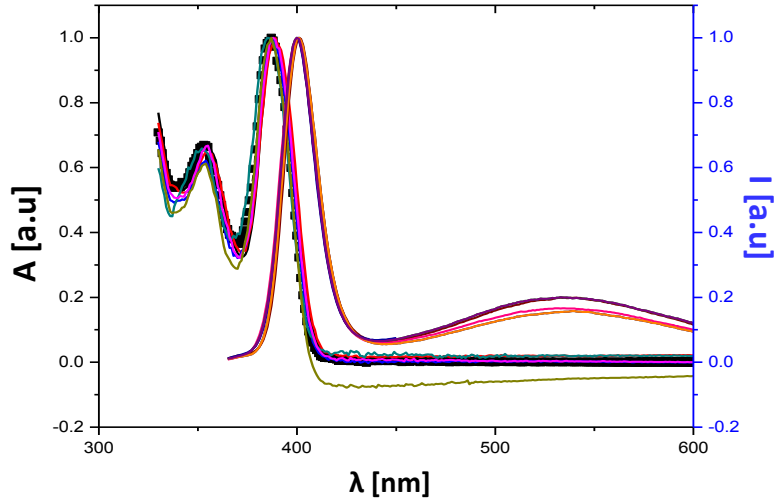

Figure 2.6: Combined absorption and emission spectra of CdS QDs for multiple syntheses

CdS QDs synthesized with thermal decomposition method consist of hydrophobic surfactants which are soluble in organic solvents like toluene, hexane and chloroform. For the biological applications water soluble NCs are required, to achieve water soluble QDs, surface modification amphiphilic shell or polymer coating with PMA was performed. The polymer coating is more advantageous over other methods of phase transfer from organic to aqueous phase because polymer coating retains the nanoscopic properties of NPs due to only a thin shell is grown over NP's surface. This phenomenon is already explained in detail earlier in section 1.3 and also by Lin et al.[101]. The characterization of CdS QDs after polymer coating is presented in Figure 2.7

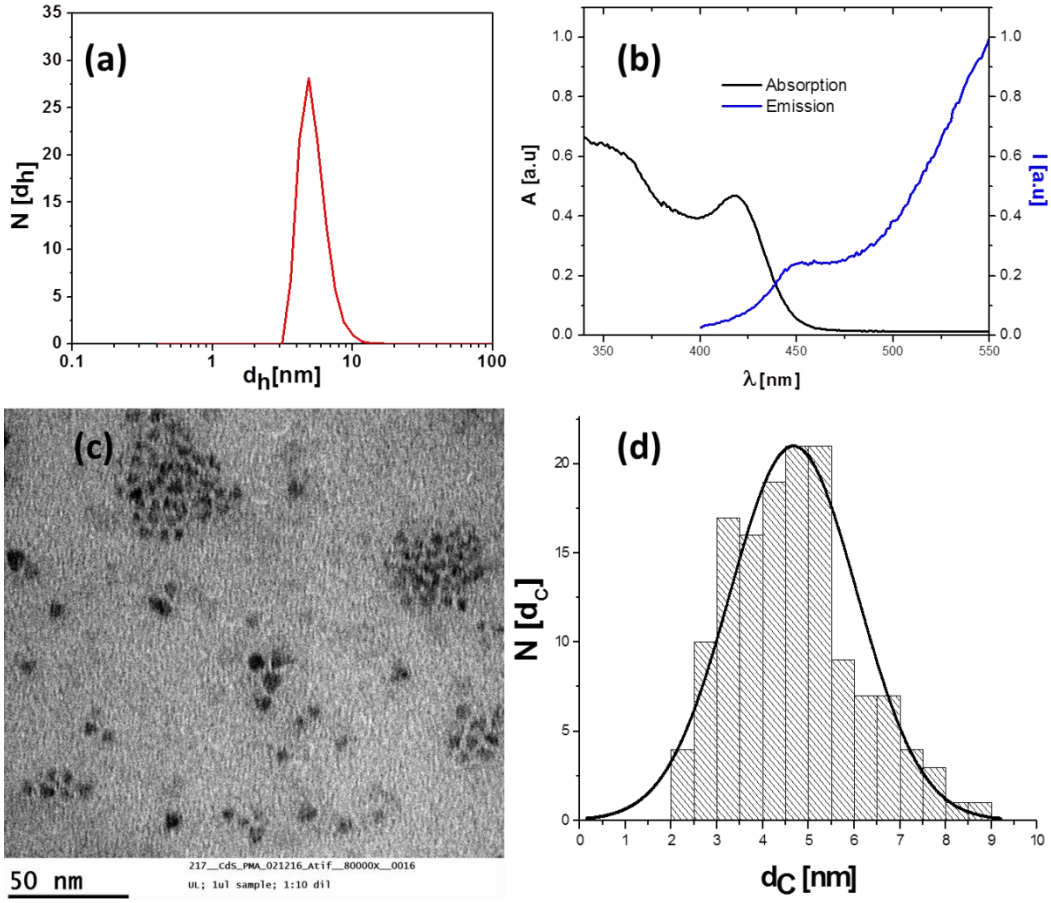

Figure 2.7: CdS QDs after polymer coating (a) hydrodynamic (d_H) size in number using DLS 5.79 ± 0.54 nm, (b) absorption and emission spectra after polymer coating, (c) TEM image in water, and (d) Size distribution histogram 4.68±1.40 nm.

2.2 Synthesis and polymer coating of manganese doped CdS QDs

CdS QDs were doped with manganese ion (Mn^{+2}) according to published protocols[137,138]. Briefly already synthesised CdS QDs dispersed in chloroform or hexane or dried powder form were taken in a three neck flask along with 2 mL of OLAM, and 6 mL ODE, both in volume to volume ratio of 1:3 in total 8 mL. The solution mixture of CdS NCs,

OLAM and ODE was connected to schlenk line under nitrogen environment and then heated up to 120 ^{o}C at this temperature the solvent of CdS NCs for example chloroform or hexane was removed by applying vacuum for few seconds. Then the mixture is heated up to 180 ^{o}C to 280 ^{o}C to add the dopant solution already prepared according to protocol[137]. When the temperature is reached around 250 ^{o}C, 0.22 mL of dopant $Mn(S_2CNEt_2)_2$ dropwise added to the solution and left for 20 mins with vigorous stirring under nitrogen flow. After this 20 mins of stirring the heat source was removed and QDs' mixture allowed to cool down at room temperature. Manganese doped CdS NCs from this yellow color solution was extracted, cleaned, purified then later polymer coated as described in section 2.1. The characterization data of CdS QDs before doping and after manganese doping in toluene is presented in Figure 2.8 (a) and Figure 2.8 (b) respectively and the characterization data of water soluble CdS QDs is presented in Figure 2.9.

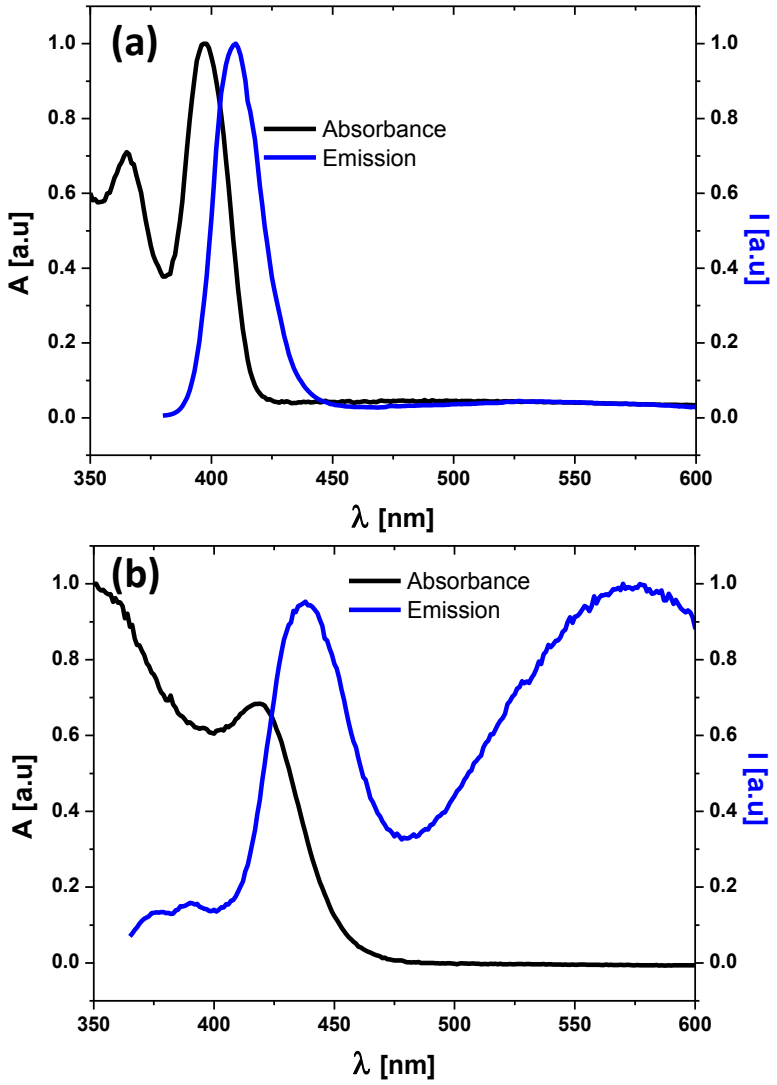

Figure 2.8: Absorption and emission spectra of CdS QDs in toluene (a) before manganese doping (b) after doping of manganese

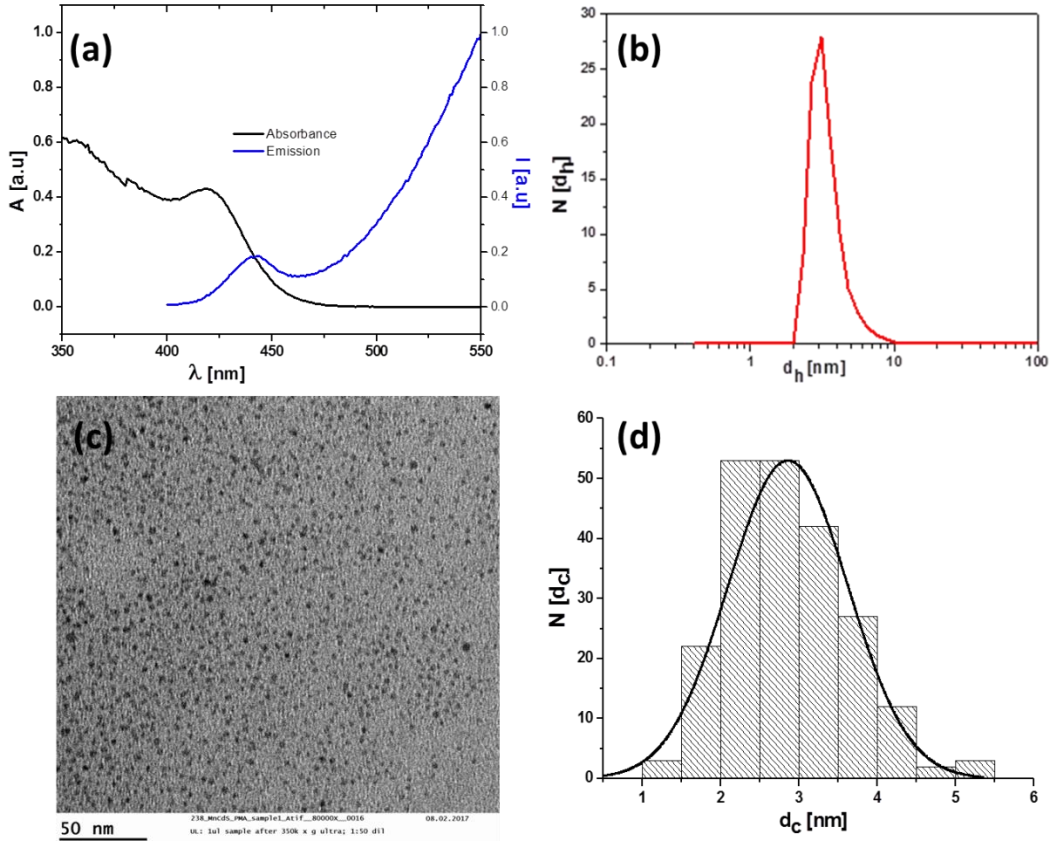

Figure 2.9: Manganese doped CdS QDs in water after polymer coating (a) hydrodynamic, (d_H) size in number using DLS 2.98±0.41 nm, (b) absorption and emission spectra after polymer coating, (c) TEM image in water, and (d) Size distribution histogram 2.87±0.80 nm.

2.3 Synthesis and polymer coating of ZnS QDs

ZnS NCs were synthesized by slightly modifying the already published protocol by Zhang et al.[69] by replacing the manganese strearate with stearic acid. Briefly, stearic acid 0.028 g, 1-dodecanethiol (DTT), 1 mL and ODE 3 mL were loaded into a three-neck flask and heated up to 120 ^{o}C then degassed under vacuum for 15 min, and then heated up to 250 °C under N_2 flow with stirring, meanwhile in another glass bottle a solution of Sulfur-ODE 0.4 M prepared by dissolving sulfur powder in ODE at 120 °C, When the temperature of flask reaches 250 ^{o}C, 0.5 mL of S-ODE (0.4 M) injected into the reaction solution. After 2 min, 1 mL of Zn stock solution (explained in section 2.4) injected dropwise to the stirring solution in a period of ca. 20 min. Zn stock solution was prepared according to protocol[69]. The color of the solution gets slight yellow, which is an indication of growth of ZnS QDs. The temperature of the mixture is lowered up to 230 ^{o}C, then another 1 mL of Zn stock solution was added. This additional 1 mL of Zn stock solution will be used to grow another ZnS shell. This reaction continued for another 20 min to utilize all of the Zn precursor stock solution. Then the heating source is removed and the stirring mixture is allowed to cool down

to room temperature. The ZnS QDs were purified using methanol/hexane extraction with the ZnS QDs in the hexane layer. The hexane was slowly evaporated in a rotavap system for ca. 30 min at 40 °C, and the resulting dried QDs were redissolved in toluene, these ZnS further purified by addition of ethanol and precipitation by centrifugation at 2700 rcf. The characterization is shown below in Figure 2.10

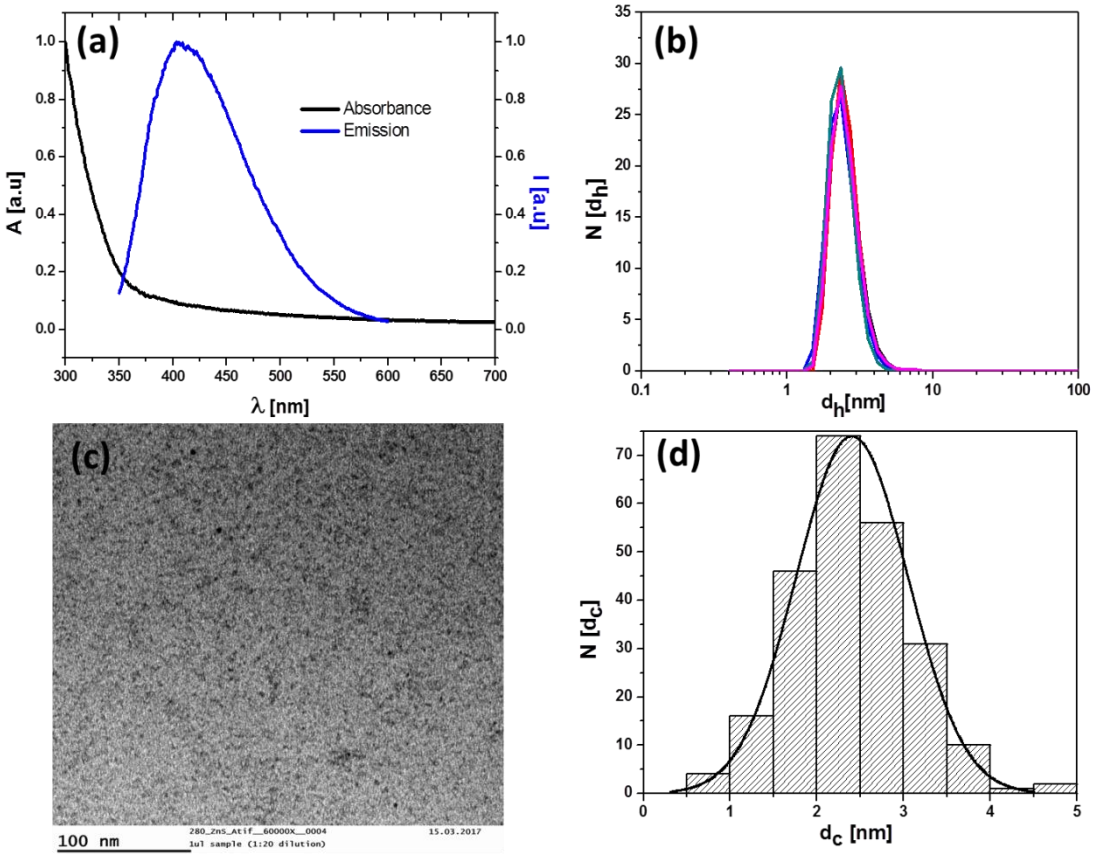

Figure 2.10: ZnS QDs in water after polymer coating (a) hydrodynamic (d_H) size in number using DLS zetasizer 2.48 ±0.07 nm, (b) absoption (black line) and emission spectra (blue line) after polymer coating, (c) TEM image in water, and (d) size distribution histogram 2.40±0.64 nm

2.4 Synthesis and polymer coating of manganese doped ZnS QDs

Manganese doped ZnS NCs were synthesized by two steps nucleation-doping approach using an already published protocol described by Zhang et al. [69]. Initially manganese precursor and zinc stock solution was prepared following the protocol as mentioned. The manganese precursor, manganese stearate ($MnSt_2$), was prepared by dissolving stearic acid in 35 mL of methanol and heated until this mixture becomes transparent solution. In another round flask, tetramethylammonium hydroxide pentahydrate (TMAH) was dissolved in 15 mL of methanol, and then both solutions were mixed together using strong stirring, a solution of manganese chloride ($MnCl_2$) in 15 mL of methanol

prepared in a falcon tube and added. This solution was added drop wise to the round flask with vigorous stirring, after few minutes a white precipitate of $MnSt_2$ slowly flocculated. This precipitate ($MnSt_2$) was repeatedly purified with methanol and dried under vacuum to be used for the synthesis of manganese doped ZnS NCs.

The zinc stock solution (0.5 M) for ZnS shell growth was prepared by dissolving zinc acetate ($Zn(OAc)_2$, 2.195 g, in a mixture of 6 mL of OLAM, and 14 mL of ODE, at 160 °C under nitrogen flow using schlenk line inside a glove box. When the mixture is completely clear and slight yellow in color the heating source and nitrogen turned OFF. This zinc stock solution is stored at 50 ^oC for further use during the synthesis of manganese doped ZnS QDs.

Synthesis of manganese doped ZnS QDs. In a three-neck flask 0.062 g of $MnSt_2$, 1 mL of DDT and 3 mL of ODE were mixed together by applying nitrogen along with heating, when the temperature reaches 120 ^oC the mixture was degassed under vacuum for 15 min, and then heated up to 250 °C under N_2 flow to get a colorless transparent solution. Then 0.5 mL of S solution in ODE (S-ODE, 0.4 M), obtained by dissolving sulfur powder in ODE at 120 °C, was then injected, observing the color change to faint yellow as consequence of the formation of MnS nanoclusters. Two min later S-ODE solution was injected; later 1 mL the Zn stock solution was added drop wise to the reaction system under vigorous stirring in a period of ca. 20 min. Soon after adding the Zn stock solution color of the reaction solution turned to golden yellow, which indicates the growth of the ZnS shell. Then, the temperature was lowered down to 230 °C for the further overgrowth of ZnS shell with addition of another 1 mL of Zn stock solution. After finishing the addition of stock solution, the reaction mixture stayed at 230 °C for another 20 min to make sure the maximum consumption of the Zn precursor. Finally, the solution was allowed to cool down to room temperature by turning off the heating mantle. The NCs were purified using methanol and hexane extraction with these QDs in hexane layer. The hexane was removed slowly using Rotavap, when the MnZnS NCs get dried they were again dissolved in toluene or chloroform to be used for polymer coating. There is additional cleaning step to clean and purify the MnZnS by adding ethanol in a same ratio of QDs solvent and then collecting the MnZnS QDs by precipitation. Then these QDs were polymer coated as described in previous sections. After polymer coating these NCs were characterized as shown in Figure 2.11.

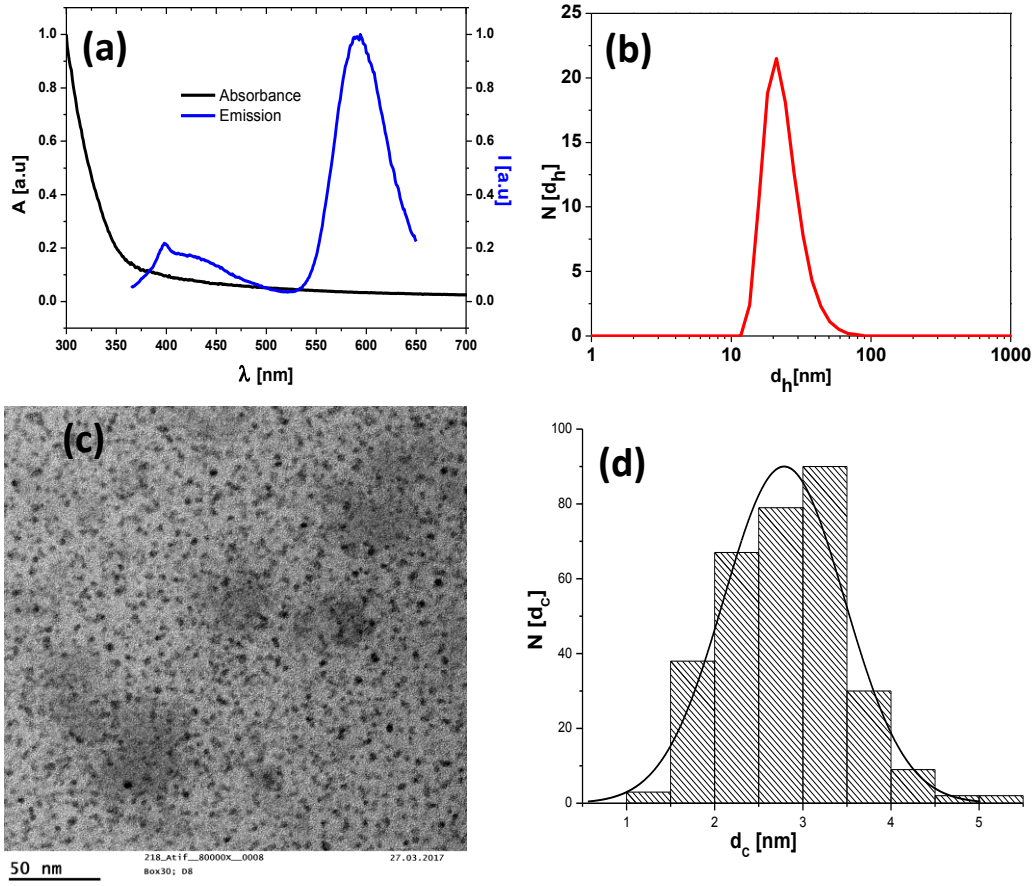

Figure 2.11: MnZnS QDs in water (a) hydrodynamic (dH) size in number using DLS zetasizer 26.78±3.07 nm, (b) absoption and emission spectra after polymer coating, (c) TEM image in water, and (d) Size distribution histogram 2.78±0.68 nm

2.5 Synthesis and polymer coating of ZnO QDs

Hydrophobic ZnO QDs were synthesized following an already published protocol by Abdelmonem et al.[74]. Briefly 1.46 g Zinc acetate dihydrate ($Zn(Ac)_2{\cdot}2H_2O$), was dissolved in 62.5 mL of methanol at a temperature of 60 °C. In a tube 0.7 g of potassium hydroxide (KOH) was dissolved in 32.5 mL methanol and added drop-wise to the $Zn(Ac)_2{\cdot}2H_2O$ solution over a time period of about 10 mins under vigorous stirring. Within a few minutes after of the KOH addition, $Zn(OH)_2$ precipitates and the solution become cloudy. The stirring was continued after the complete addition of the KOH solution, and the mixture becomes transparent in ca. 30 mins which illustrates the formation ZnO NCs. To cap ZnO with hydrophobic OLAC surfactants, this solution was sonicated for 10 mins and 1 mL of OLAC was added, followed by 5 min of again sonication and later strong stirring for 10 mins at 60 ^{o}C. The NCs were allowed to cool down by turning off the heat source and stopping the stirring. The OLAC capped ZnO NCs purified by precipitating using centrifugation at a speed of 2000 rpm (1283 rcf) for 5 min. The ZnO particles were collected from pallet and redispersed in chloroform. These NCs again cleaned by adding methanol and chloroform

followed by centrifugation, this cleaning step was performed couple of times to get rid of nonreactive precursors and free surfactants. Finally, the hydrophobic ZnO QDs were dissolved in 25 mL organic solvent, e.g., hexane, chloroform or toluene leading to a clear transparent solution. In order to transfer them from organic to aqueous phase, these NPs were coated with an amphiphilic polymer, as described previously. The characterization these NPs is shown in Figure 2.12.

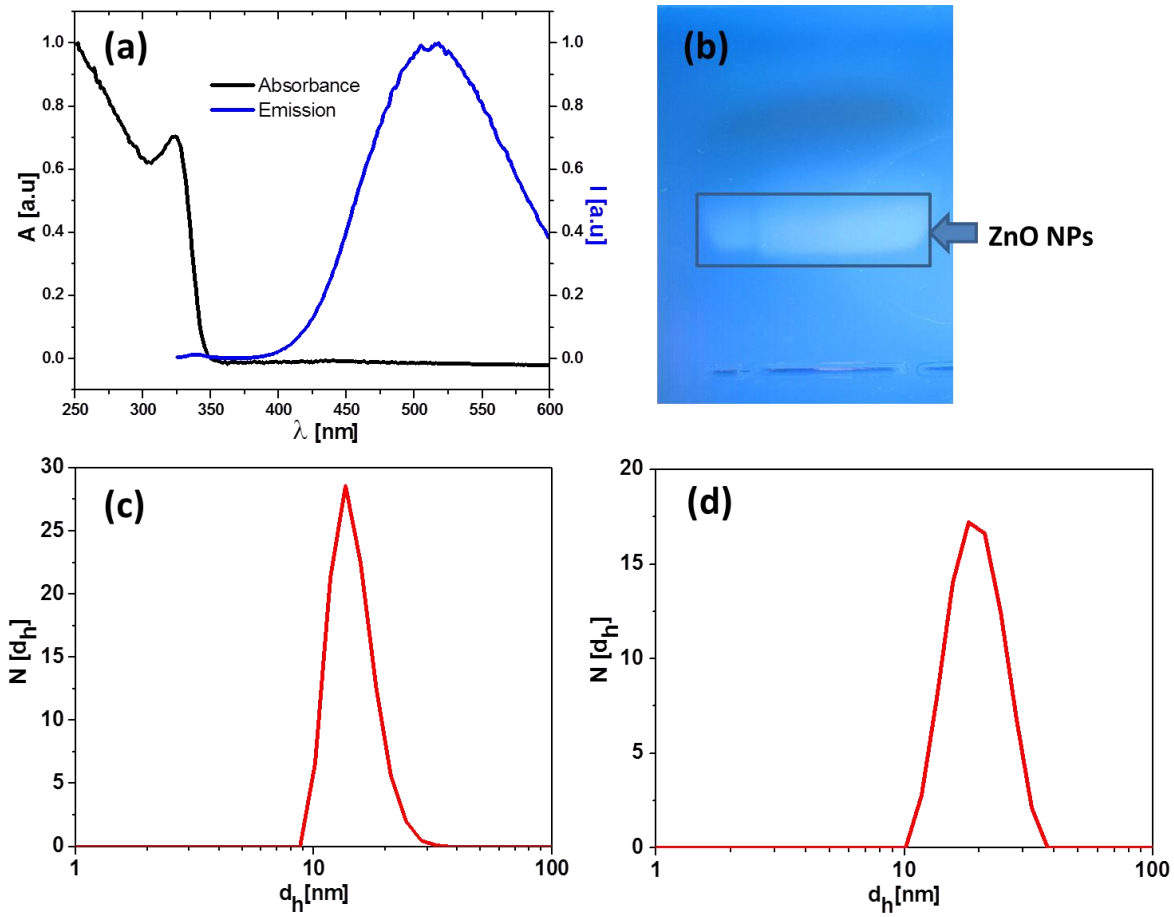

Figure 2.12: ZnO NPs (a) hydrodynamic (d_H) size in number using DLS zetasizer by number 13.84±0.2 nm, (b) size using DLS zetasizer nm by intensity 21.13±0.28 nm, (c) absorption and emission spectra in chloroform, and (d) 2 % agarose gel image of the polymer coated ZnO NPs run at 100 V for 1h.

2.6 Synthesis and polymer coating of magnetic NPs

Monodisperse iron oxide and composite iron oxide NPs were synthesised by slightly modifying the published protocols by Sun et al.[139,140,141]. All these synthesis were carried out in air and water free nitrogen environment inside a glovebox, which yields high monodisperse hydrophobic NPs. Following are the synthetic approaches used to produce MNPs of various sizes and composition along with their characterization.

Synthesis of ca. 4 nm Fe_3O_4 NPs: Magnetic 4 nm IONP were prepared by mixing 0.7 g of iron acetylacetonate $Fe(acac)_3$, 2.58 g of 1-2 hexadecanediol 1.69 g of OLAC, 1.6 g

OLAM and 20 mL of phenyl ether in a 100 mL, two neck glass flask then this mixture was heated upto 120 ^{o}C under nitrogen environment and then degassed for 10 mins, after this the temperature of the flask was raised to 200 ^{o}C at rate of 3.3 ^{o}C/min, then the mixture was kept stirring at this temperature for 30 mins then again raised to 265 ^{o}C with same rate 3.3 ^{o}C/min, at 265 ^{o}C the mixture kept stirring for 30 mins. After this the heating source removed and the mixture allowed to cool down at room temperature. The resulted dark brown solution was dissolved in toluene and precipitated by adding ethanol and centrifuging at 2500 rcf for 10 mins, the precipates again dissolved in toluene along with approximately 50-100 µL of OLAM and OLAC in ratio 1:1 and then again centrifuged at same speed then the supernatant taken to another bottle and then again centrifuged after adding ethanol. The precipitate finally is collected and redispersed in toluene to be used further. All these washing and cleaning steps were performed to get rid of unreacted precursors, free surfactants, and aggregates of NPs. The polymer-coating is done with same standard procedure as explained earlier.

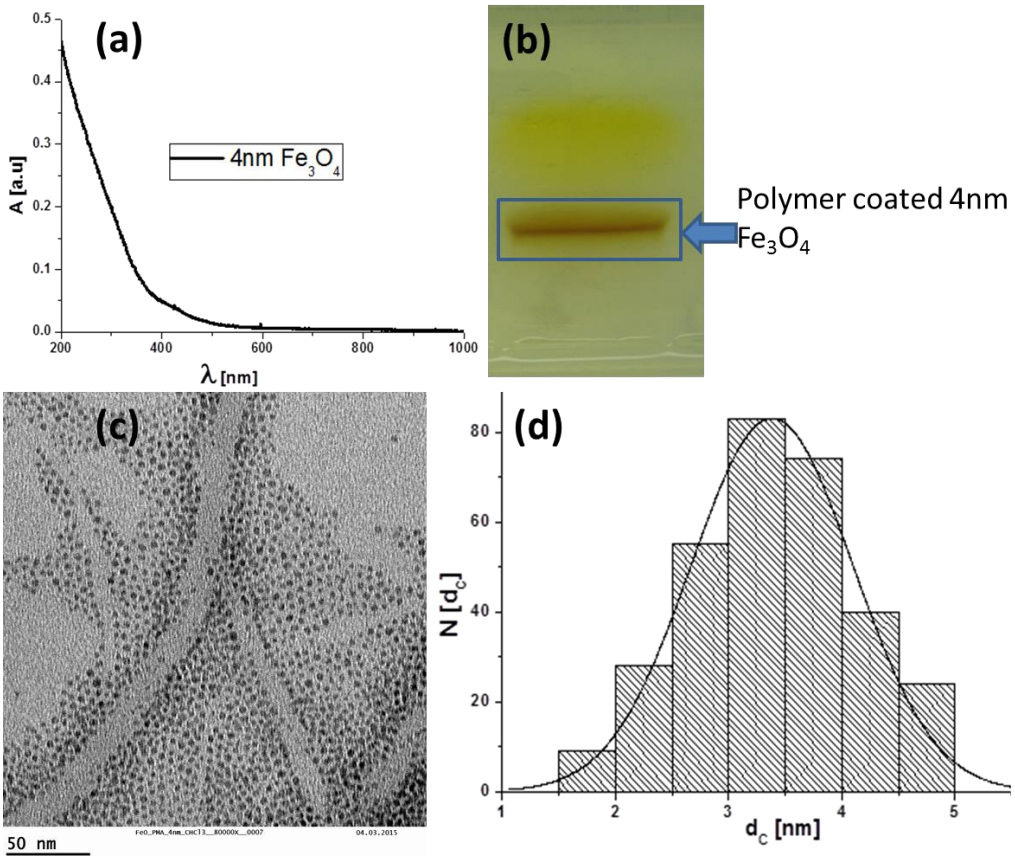

Figure 2.13: Fe_3O_4 NPs (ca. 4 nm) (a) UV-Vis absorption spectra, (b) gel electrophoresis image of the polymer coated ca. 4 nm IONPs on 2 % agarose gel, 100 volts applied for 60 mins, and (c) TEM image (d) size distribution 3.38±0.71 nm

Synthesis of ca. 6 nm Fe_3O_4 NPs: Approximately 6 nm monodisperse IONPs were prepared slightly modifying the synthesis approach of 4 nm. Briefly 0.7 g of iron acetylacetonate $Fe(acac)_3$, 2.58 g of 1-2 hexadecanediol 1.69 g of OLAC, 1.6 g OLAM and 20 mL of benzyl

ether were taken in 2 neck 100 mL round flask then this mixture was heated upto 120 ^{o}C under nitrogen environment and then degassed for 10 min, after this the temperature of the flask was raised to 200 ^{o}C at rate of 3.3 ^{o}C/min, then the mixture was kept stirring at this temperature for 120mins then again raised to 300 ^{o}C with same rate 3.3 ^{o}C/min, at 300 ^{o}C the mixture was kept stirring for 30 mins. After this the heating source removed and the mixture allowed cooling down to room temperature. The cleaning and polymercoating is done with same standard procedure as explained earlier. The basic characterization data is shown in Figure 2.14

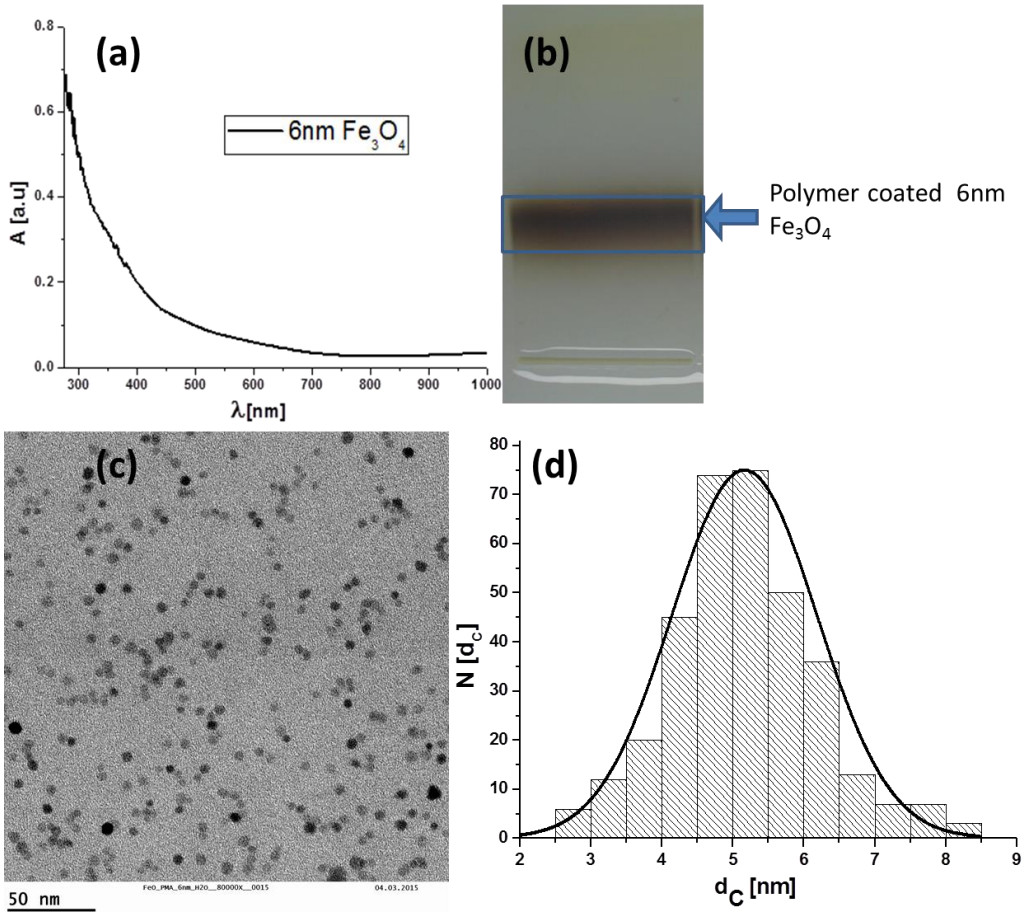

Figure 2.14: Fe_3O_4 NPs (ca. 6 nm) (a) Uv-Vis absorption spectra, (b) gel electrophoresis image of the polymer coated ca. 6 nm IONPs on 2 % agarose gel when 100 volts applied for 60 mins, (c) TEM image, and (d) Size distribution histogram 5.16±1.02 nm

Synthesis of ca. 10 nm Fe_3O_4 NPs: Synthesis of ca. 10 nm IONPs is done by almost same as of 6 nm Fe_3O_4 NPs except the amount of benzyl ether reduced to 10 mL. The cleaning and polymer coating procedure of these NPs remains the same as presented in earlier sections. The characterization for synthesized NPs is shown in Figure 2.15

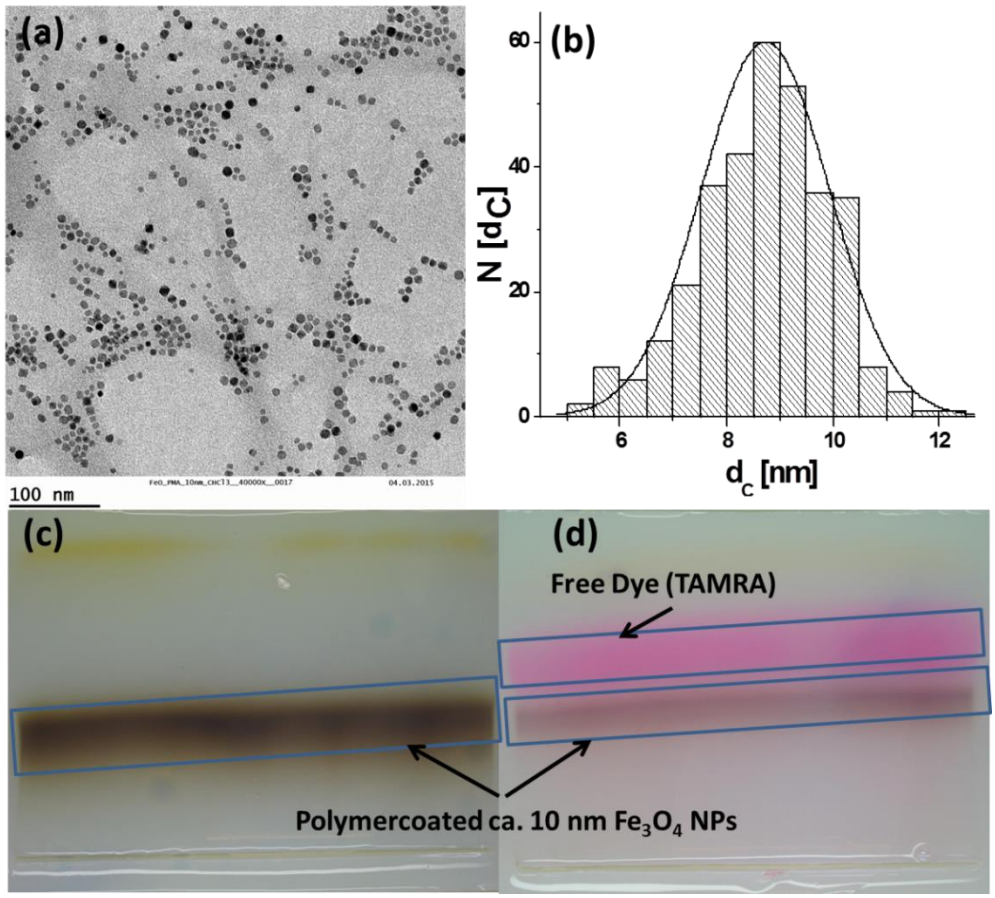

Figure 2.15: Fe_3O_4 NPs (ca. 10 nm) (a) TEM image in chloroform, and (b) size distribution histogram 8.67±1.24 nm, (c) gel electrophoresis image of the polymer coated Fe_3O_4 IONPs on 2 % agarose gel, 100 volts applied for 60 mins, (d) gel electrophoresis image of the polymer coated Fe_3O_4 IONPs with TAMRA (Tetramethylrhodamin) flourophor on 2 % agarose gel 100 volts applied for 60mins

2.6.1 Synthesis of core shell magnetic NPs

Synthesis of core shell MNPs is done with addition of cobalt and manganese metals; the synthesis approach was followed by slightly modifying the protocol published by Sun et al. [140, 142]. In a seed mediated synthesis of metal doped magnetic NPs, such as Co-ferrite NPs and Mn-ferrite NPs the metals precursor was taken to the half of the amount taken for iron precursor. In brief 0.7 g of $Fe(acac)_3$, 0.25 g of cobalt acetylacetonate $Co(acac)_3$, 2.58 g of 1-2 hexadecanediol, 1.69 g of OLAC, 1.6 g OLAM, and 20 mL of benzyl ether were taken in 100 mL 2 neck round flask then this mixture was heated upto 120 ^oC under nitrogen environment and then degassed for 10 min, after this the temperature of the flask was raised to 200 ^oC at rate of 3.3 ^oC/min, then the mixture was kept stirring at this temperature for 120 mins then again raised to 300 ^oC with same rate 3.3 ^oC/min, at 300 ^oC the mixture was kept stirring for 60 mins. After this the heating source removed and the mixture allowed to come down to room temperature and later cleaned from unused precursors and surfactants. These cleaned cobalt ferrites seeds are dried to be used to synthesize core shell MNPs.

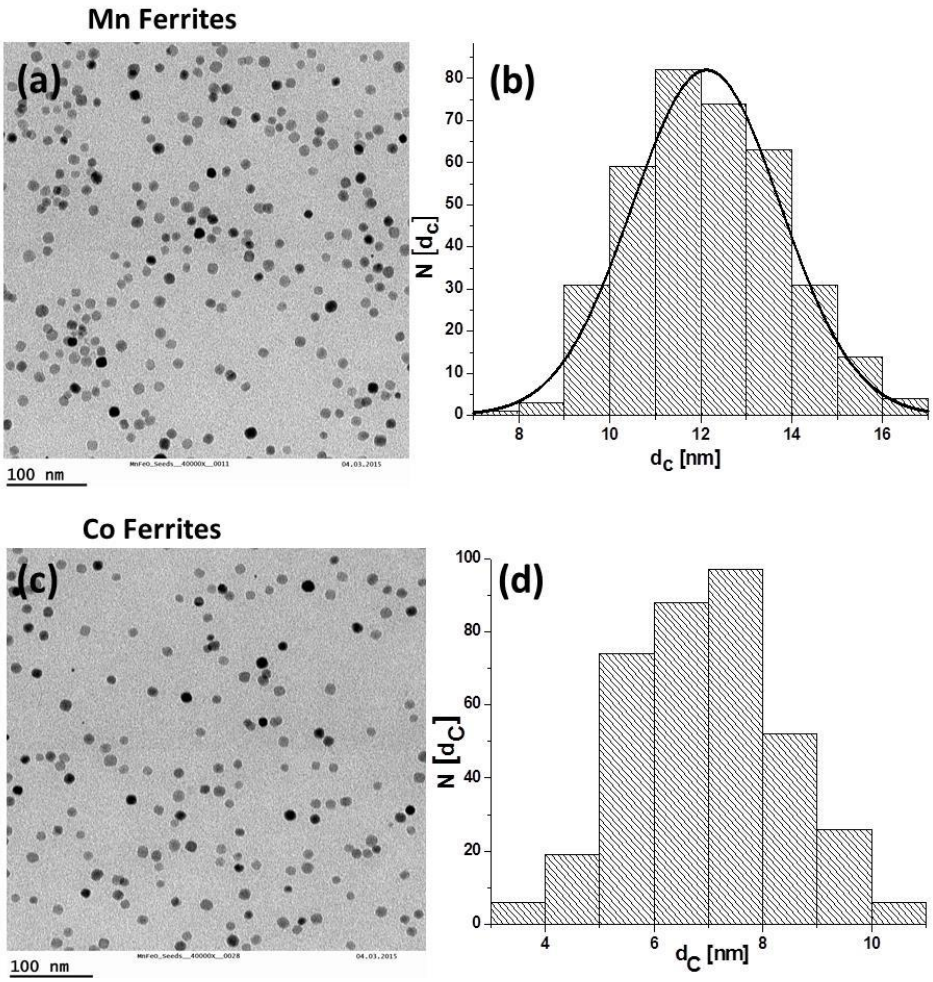

Figure 2.16: (a) & (b) Mn ferrites seeds TEM image and size distribution 10.28±1.67 nm, (c) & (d) Co ferrites seeds TEM image and size distribution histogram 6.98±1.39 nm

The growth of manganese ferrtites shell around the cobalt ferrites (seeds/core) is done by adding 40 mg of cobalt ferrites (already synthesized seeds dispersed in chloroform), to the 100 mL flask which include 0.7 g of $Fe(acac)_3$, 0.25 g of manganese acetylacetonate $Mn(acac)_3$, 2.58 g of 1-2 hexadecanediol, 1.69 g of OLAC, 1.6 g OLAM, and 20 mL of benzyl ether, which already heated and maintained at 120 ^oC under nitrogen environment and then degassed for few seconds to remove chloroform, after this the temperature of the flask was raised to 200 ^oC at rate of 3.3 ^oC/min, then the mixture was kept stirring at this temperature for 120 mins then again raised to 300 ^oC with same rate 3.3 ^oC/min, at 300 ^oC the mixture was kept stirring for 30 mins. The core and shell can be also cobalt ferrites or manganese ferrties or vice versa or of same metals. The cleaning and surface modification will be followed as explained earlier. The TEM images and size distribution histogram of these synthesized seeds is presented in Figure 2.16 and core shell MNPs in Figure 2.17.

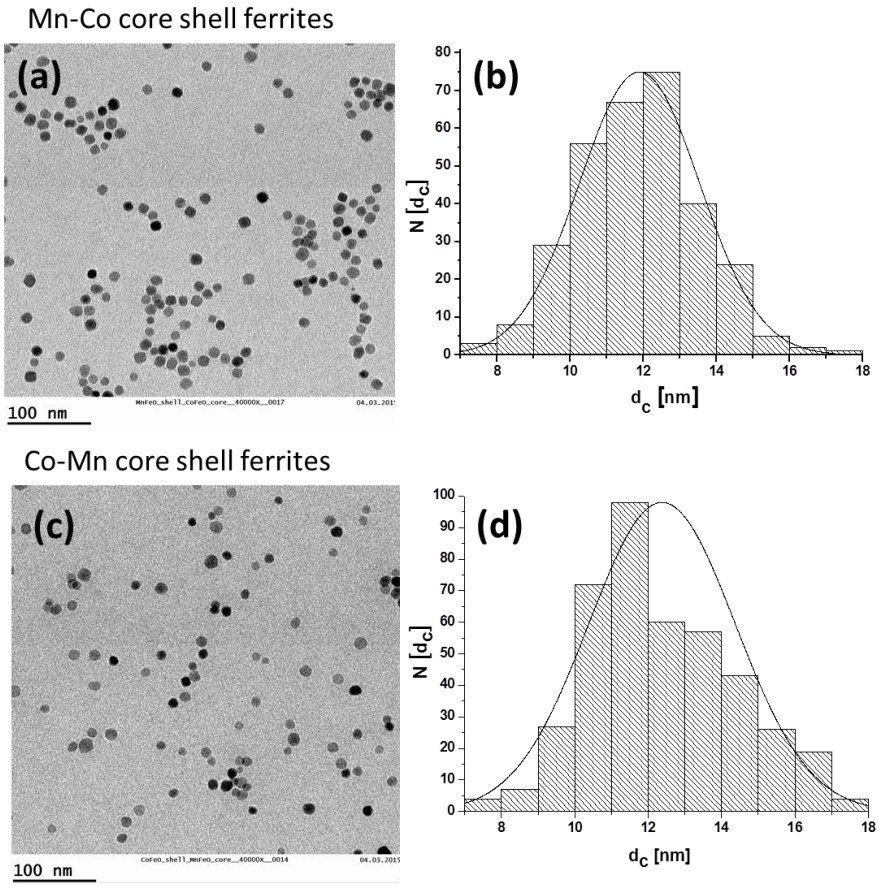

Figure 2.17: (a and b) Mn-Co composite core shell ferrites TEM image and size distribution 11.89±1.64 nm (c and d) Co-Mn composite ferrites TEM image and size distribution histogram 12.45±2.09 nm

2.7 Synthesis and polymer coating of plasmonic NPs

During this study silver and gold NPs (4 nm each) were synthesised, the synthesis method and characterization is presented below.

2.7.1 Synthesis and surface modification of silver NPs

The synthesis of the 4 nm Silver NPs (Ag NPs) was done following the synthesis route published by Pfeiffer and co-workers[143]. Briefly, first, sodium S-dodecylthiosulfate, as ligand is prepared for the stabilization of silver NPs during and after the synthesis. The Ag NPs were synthesized in ethanol with the presence of this ligand. For the preparation of sodium S-dodecylthiosulfate ligand initially 5.187 mL of 1-bromododecane was dissolved in 50 mL ethanol at 50 °C, in another falcon tube sodium thiosulfate pentahydrate 6.21 g was dissolved in 15 mL of water and then this was added in the previously prepared mixture of 1-bromododecane and ethanol. The mixture of ethanol, sodium thiosulfate pentahydrate and 1-bromododecane was refluxed for 3 hours 80 ^{o}C and after allowed to cool down at room temperature. This mixture was left for overnight to obtain white precipitates (sodium S-dodecylthiosulfate) was extracted using filter paper.

The extracted white crystals ligand (sodium S-dodecylthiosulfate) of amount 390 mg was dissolved in 90 mL ethanol in a round flask at 50 °C. Then 282 mg of $AgNO_3$ (silver nitrate) was added to the solution and stirred for 10 min. The mixture becomes white initially then after 10 mins sodium borohydride (318 mg) in 15 mL ethanol was added and the mixture turns almost black immediately. After another 5 min of stirring 74 mg ascorbic acid dissolved in 2 mL of ethanol added in the mixture then left for stirring for 3 h. Afterwards the reaction was cooled down to room temperature. Ag NPs were extracted and cleaned initially by adding water to the solution and centrifugation at 3000 rpm (1620 rcf) for 15 mins, the Ag NPs will be precipitated and the supernatant was discarded, these NPs again dissolved in ethanol and centrifuged again for 15 min at same speed and last 3rd wash was done with acetone. After washing with acetone the precipitated particles were dried and dissolved in chloroform. These silver NPs in chloroform can further be cleaned with hydrophobic syringe filters. The basic characterization data is shown below in figure Figure 2.18.

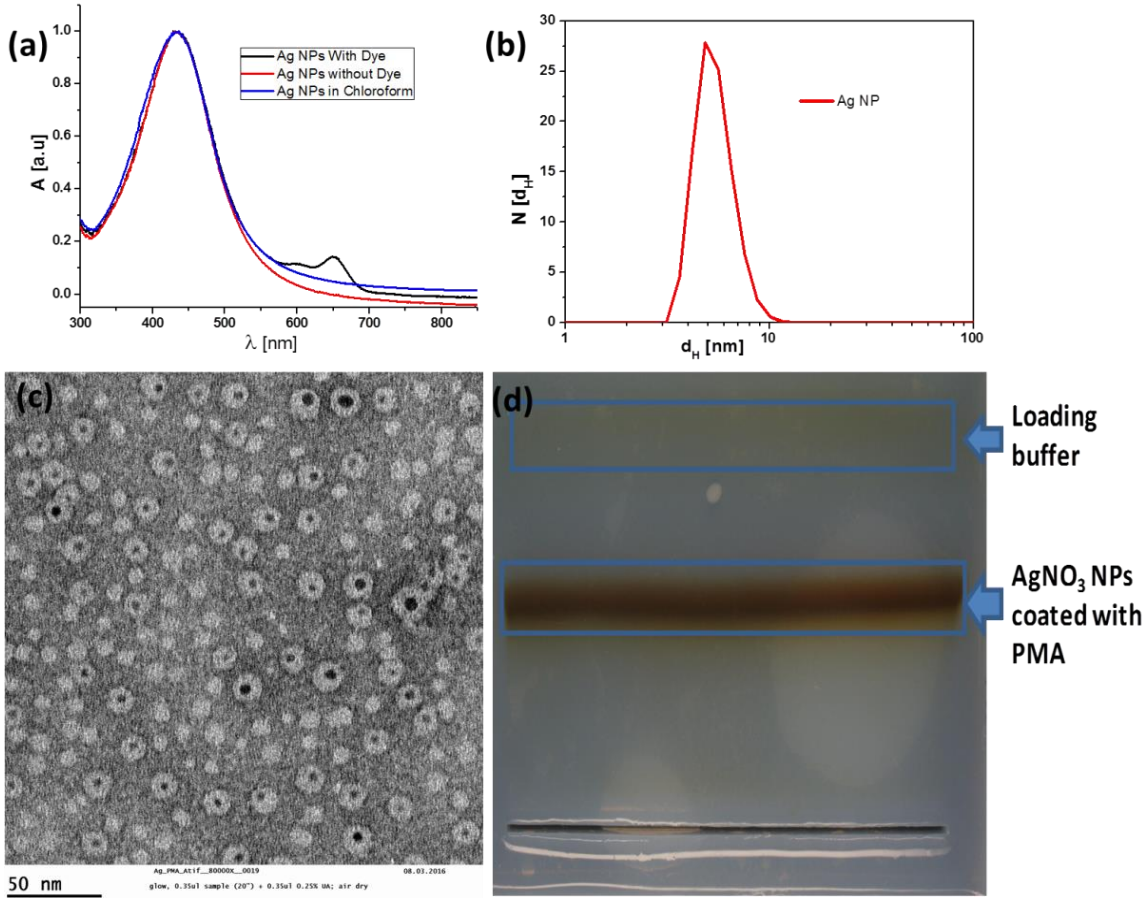

Figure 2.18: 4 nm Silver NPs (a) absorption spectra before and after polymer coating, (b) hydrodynamic (d_H) size in number using DLS zetasizer 5.16±0.45 nm, (c) TEM image in water after polymer coating, and (d) gel electrophoresis image of the polymer coated Ag NPs on 2 % agarose gel when 100 volts applied.

4 nm Ag NPs were polymer coated with and without flourophor attached with polymer (PMA). The attached flourophor (fluorescent dye) was named as Cyanine 5-amine (Cy5). The modification of the polymer with Cy5 dye is done as already described in the literature by Lin et al. [101]. The absorption or excitation peak of Cy5 dye lies at 649 nm and emission peak lies at 665 nm, there is a lot more detail available at Lumiprobe [144]. The polymer coating of 4 nm Ag NPs is done with same standard protocol as prescribed earlier, the cleaning of Ag NPs from free micelles and free dye is done using gel electrophoresis and later with ultracentrifugation. The basic characterization is shown below in Figure 2.19.

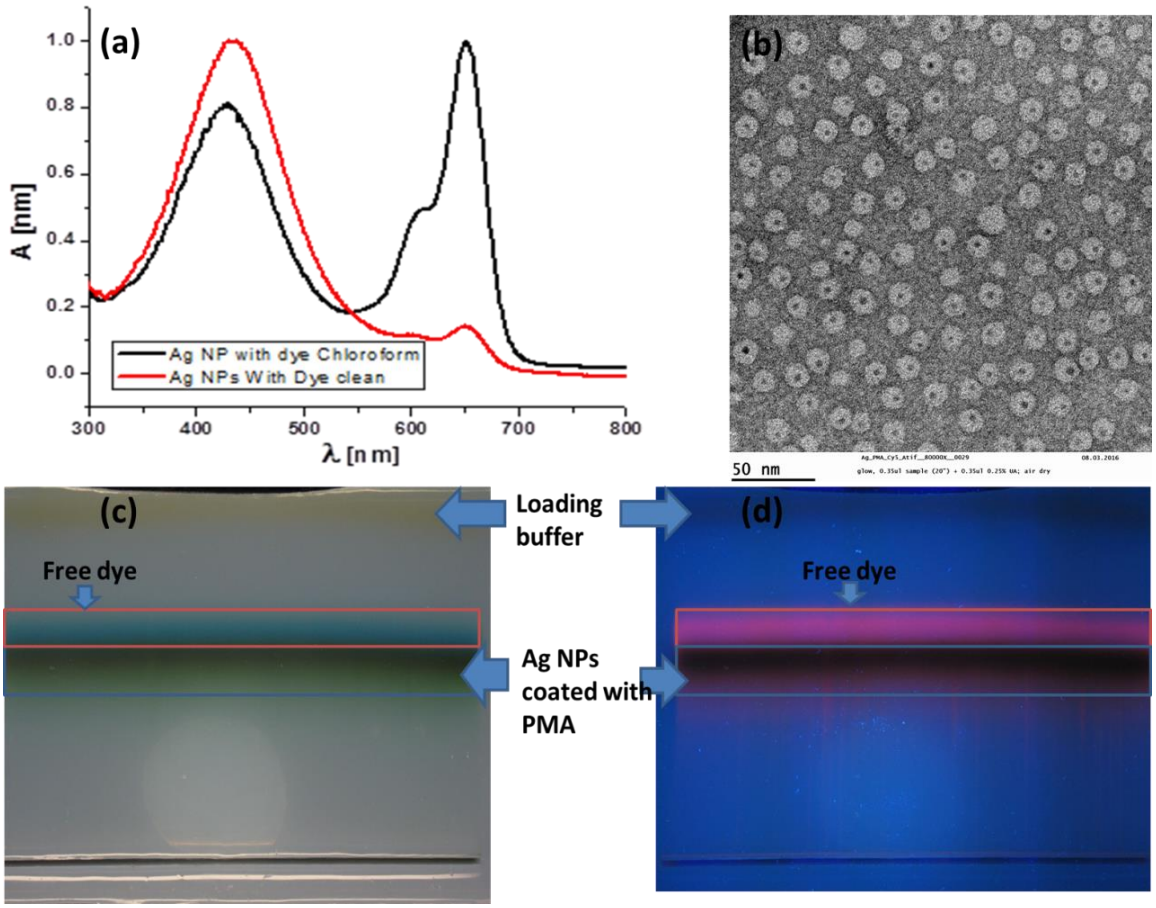

Figure 2.19: 4 nm Ag NPs polymer coated with Cy5 dye (a) absoption spectra before after polymer coating with dye, (b) TEM image in water after polymer coatin, (c) and (d) gel electrophoresis image of the polymer coated Ag-Cy5 NPs on 2 % agarose gel with and without UV light

2.7.2 Synthesis and polymer coating of gold NPs

4 nm GNPs were synthesised following the protocols reported by Brust and others [145]. The detailed step by step synthesis procedure with pictures is also shown in the published article[101,146,147]. Briefly 300 mg gold salt, i.e., hydrogen tetrachloroaurate (III) was dissolved in 25 mL of MilliQ water in a glass vial and 2.17 g of tetraoctylammonium bromide (TOAB) was dissolved in a round flask with 80 mL of toluene. Then both mixtures

were taken in 500 mL separation funnel and gently mixed for 5 mins. The mixture of these two phases gold salt of yellow color and TOAB in toluene becomes red which indicates the formation of tetraoctylammonium-gold pairs. When almost all the gold precursor is transferred to organic phase, then slowly the water phase (lower part) in separation funnel discarded, the red organic solution transferred into the 500 mL round flask, meanwhile a solution of 334 mg sodium borohydride in 25 mL of milliQ water was prepared in a flacon tube, this borohydride works as reducing agent for gold precursors. This all solution of borohydride added drop wise to the vigorously stirring red colour gold solution. The nucleation of GNPs was observed by formation of some bubbles and change of colour of solution from red to red-violet. This solution was left stirring for 1 h.

For the further cleaning of gold NPs the red-violet solution was taken to another clean 500 mL separation funnel and 10 mM solution of HCl was added and gently shaked for 1 min then the aqueous phase discarded then 10 mM of NaOH solution added and shaked for 1 min then again aqueous phase discarded, finally this cleaning method repeated with only milliQ waterfor three times. After cleaning by water this gold NPs solution taken into the flask and then left for stirring overnight. The overnight stirring is done for Oswald ripening get better average size and monodispersity of gold NPs.

The stability of gold NPs is further enhanced by adding 10 mL of dodecenthiol (DDT) in the mixture solution and left for stirring for 3 hours at 65 ^{o}C. The very good binding affinity of thiol (DDT) to gold would replace the Br^{-} ions and results in DDT-layered GNPs. The GNPs solution was allowed to cooled down at room temperature by removing the heating source but kept under stirring. To remove large agglomerates the solution was cleaned by centrifugation at 2000 rpm (720 rcf) for 5minutes, then supernatant was collected and taken to another bottle and methanol was added till the mixture becomes cloudy then the same centrifugation step was repeated. The supernatant was removed and the precipitates NPs were redissolved in chloroform for further polymer coating and phase transfer to water. The plasmonic peak of 4 nm gold NPs is usually around 518 nm, the absorbance spectra and other characterization of the synthesized NPs is shown below in Figure 2.20.

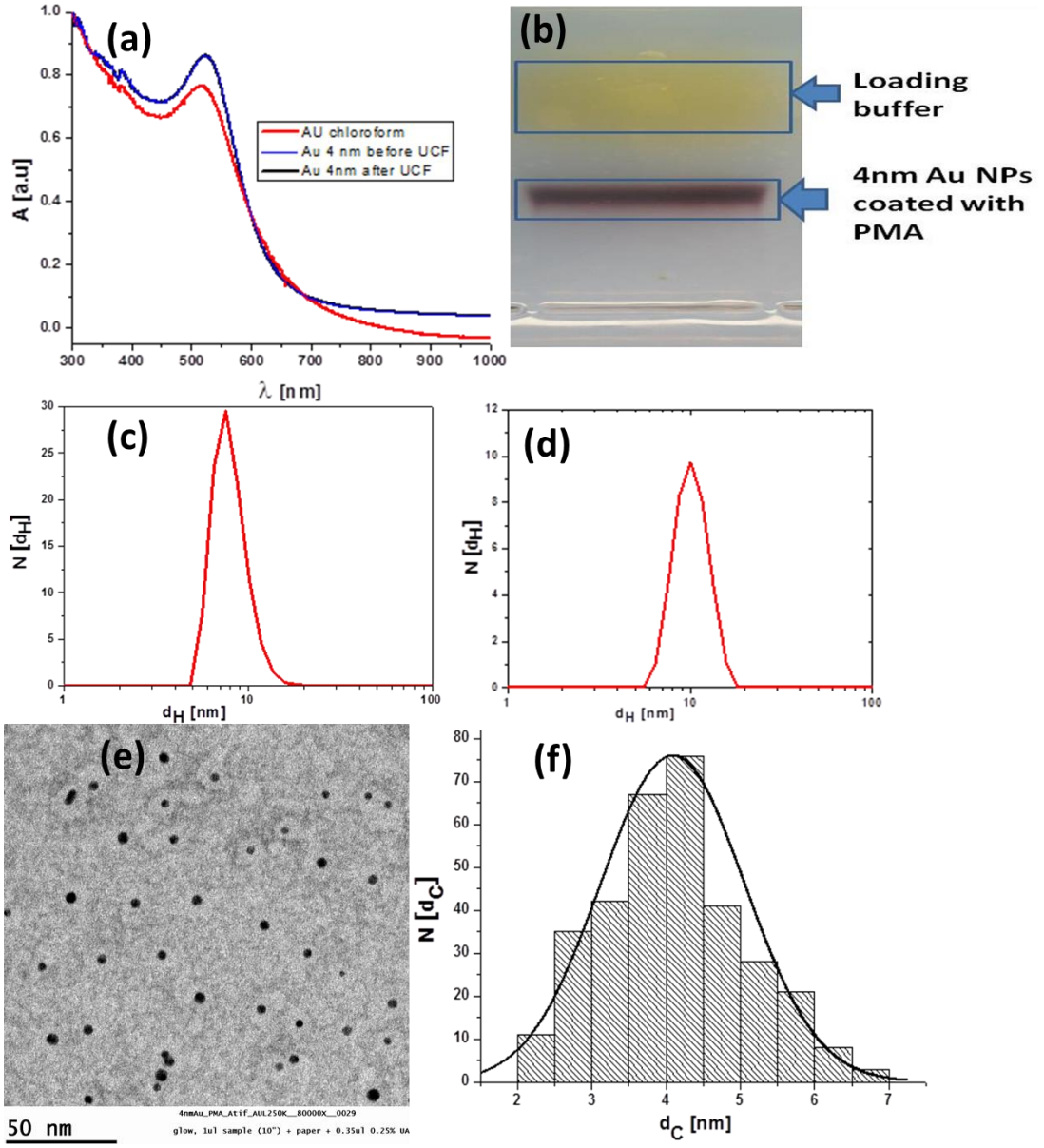

Figure 2.20: 4 nm Gold NPs (a) UV-Vis absoption spectra in chloroform (red), in water before micelles cleaning (blue), in water after micelles cleaning (black) by ultracentrifugation is represented, (b) gel electrophoresis image of the polymer coated Au NPs on 2 % agarose gel, while applying 100 Volts for 1 hour, (c) hydrodynamic (d_H) size in number using DLS zetasizer 8.13±0.17 nm, (d) hydrodynamic (d_H) size in intensity using DLS zetasizer (e) TEM image in water after polymer coating (f) size distribution 4.09±0.97 nm

2.8 Synthesis and polymer coating of TiO_2 NPs

TiO_2 NPs have been synthesized following the published protocol Murray et al. [148] with some slight modifications. Initially TiF_4 and $TiCl_4$ precursors are prepared in the nitrogen environment. Briefly 0.494 g of TiF_4, 5.64 g of oleic and 20 mL of 1-ODE, mixed together in a glass vial heated to 80 °C with stirring until orange brown color solution was presented and $TiCl_4$ precursor solution consists of 0.76 g $TiCl_4$, 5.64 g OLAC, in 20 mL 1-

ODE, and presents dark brown color. Both solutions were mixed together in another glass vial with a total volume of 10 mL in equal ratio.

Synthesis of TiO2 NPs is also carried out in oxygen free environment with nitrogen schlenk line in a glove box. Initially 8 g of OLAM, 0.42 g of OLAC and 10.2 mL of 1-ODE were mixed in a 100 mL glass flask then vacuumed at 120°C for 30 mins. Then the temperature of the glass flask mixture reduced to 60 °C, vacuum was also turned OFF and at this temperature with nitrogen flux 1.5 mL of TiF_4 /$TiCl_4$ precursor (1:1 mix ratio by volume) was injected quickly and the temperature of this mixture was quickly heated to 290 °C within approximately 10 mins, and kept this temperature for 10 mins to produce the seeds crystals. Then 8 mL from precursor mixture of TiF4/TiCl4 was added drop wise to this solution at injection rate of 0.3 mL/min. After the complete injection of 8 mL TiF4/TiCl4 precursor the heating source was removed and a blue color solution was allowed to cool down at room temperature. The cleaning of NCs from unused precursors and free ligands was done first by adding ca. 5 mL toluene along with synthesized NCs solution in a 50 mL falcon tube and then centrifuging it at speed of approximately 1100 rpm (300 rcf) for 5minutes. The precipitated blue colored TiO_2 again dispersed in 20 mL toluene and sonicated for 5mins with addition of ca. 50-100 µL of OLAM. Then the solution was again centrifuged at same speed of 1100 rpm (300 rcf) to get rid of insoluble surfactants, ligands and agglomerated particles, this time supernatant was collected and again precipitated following the addition 20 mL of methanol. This blue color precipitated TiO_2 NPs were again dissolved in 20 mL chloroform for further surface modification and ligand exchange.

These TiO_2 NPs are capped and stabilized with OLAM and OLAC as surfactant ligands. The stability of these TiO_2 NPs was further enhanced using ligand exchange approach [149] by removing most of the OLAM and OLAC surfactants and replacing by 1-tetradecylphosphonic acid (TDPA). The OLAM and OLAC was removed by the precipitation cleaning method in combination with ethanol or methanol several times until to redisperse TiO_2 NPs in chloroform becomes difficult. Then 2 mL of chloroform was added to this blue precipitation. Later 1 mL already prepared 0.2M solution of TDPA in chloroform was added drop wise under magnetic stirring at room temperature till the blue solution turned to transparent. The sample was kept stirring overnight at 60-65^{o}C this temperature helps ligand exchange. Then after the final cleaning of NPs is done with same precipitation method using methanol and centrifugation at the speed of 1100 rpm for 5 min, blue precipitation was dissolved in chloroform and cleaned by methanol another time. Finally, the TiO_2 NPs were redispersed in chloroform to get final TDPA capped TiO_2 NPs. After ligand exchange, the

TiO_2 NPs are much stable than previously capped ligands (OLAC, OLAM) which helps further surface modification or polymer coating.

The polymer coating of the TiO_2 NPs is done with same standard procedure explained earlier with slight changes in the temperature at which the polymer and NPs were mixed and chloroform removed using rotavap. The temperature bath was kept at 60^{o}C and slowly with lower pressure difference the chloroform is removed. The characterization data of TiO_2 NPs is shown in Figure 2.21.

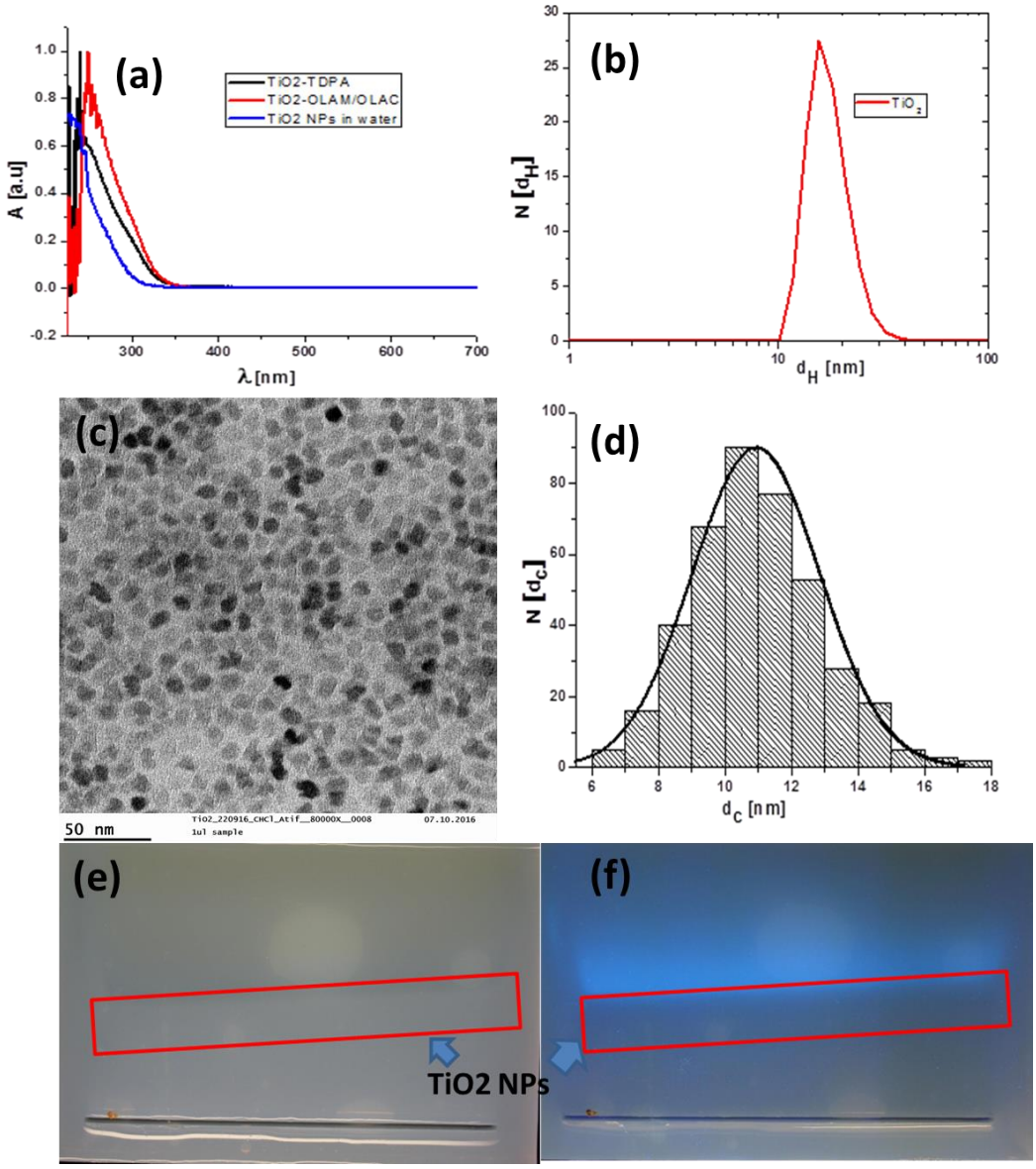

Figure 2.21: TiO2 NPs (a) absoption spectra with UV-Vis with OLAC/OLAM lignads(red), with TDPA ligand (black) after ligand exchange, and NPs after polymer coating in water (blue), (b) hydrodynamic (dH) size in number using DLS zetasizer 10.34±4.7 nm, (c) TEM image in chlorform, (d) size distribution histogram 10.94±1.92 nm, (e) and (f) gel electrophoresis image of the polymer coated TiO_2 NPs on 2 % agarose gel with and without UV-light, when applied voltage was 100 volts for 60 mins

2.9 TiO_2 NPs for in vivo study

TiO_2 NPs were used to perform various in vivo studies (detailed in section 1.6.1) during this research work. These NPs were in the shape of cube, rods plates and bipyramids, and were initially cleaned and surface engineering was performed via ligand exchange approach to made suitable for polymer coating, then all these NPs (various batches) was polymer coated to transfer them in water for biocompatibility, cleaned from free polymer, sterilized and characterized. TiO_2 NPs in cube shape was synthesised as presented in previous section 2.8. The polymer coating was performed for each of these NPs after doing ligand exchange with TDPA. This ligand exchange procedure has already been explained in previous section. Characterization of TiO_2 NPs of different shapes (cube, plates, rods and bipyramids is presented in Figure 2.22 and Figure 2.23.

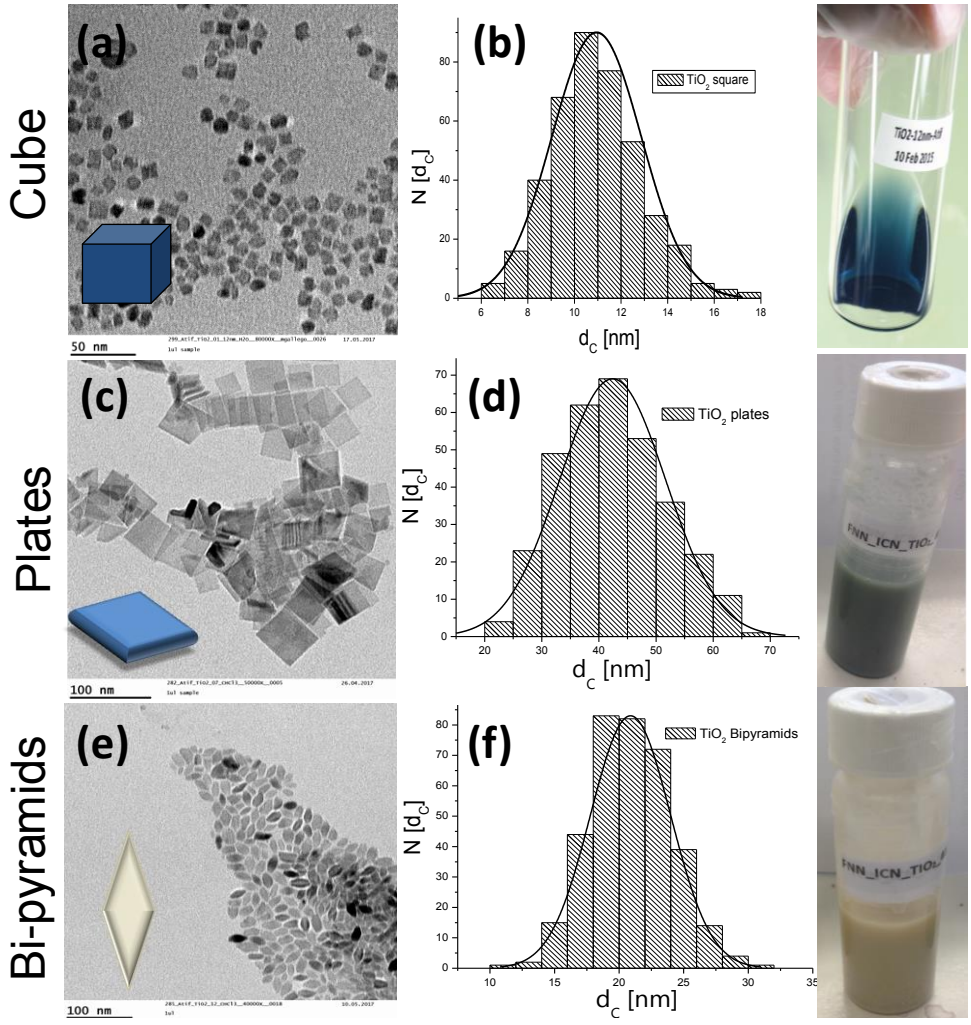

Figure 2.22: TEM images and size distribution histogram of TiO_2 (a) cube shape, (b) size 10.94±1.92 nm, (c) plates, (d) size 42.45±3.1 nm, (e) bipyramids, and (f) size 20.88±3.10 nm

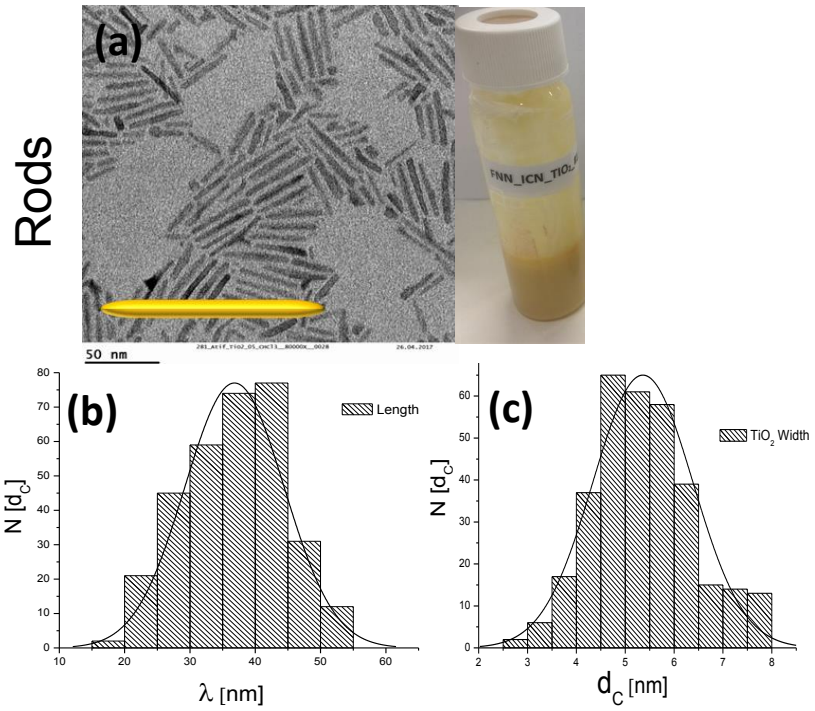

Figure 2.23: (a) TEM image TiO2 nanorods and of size distribution histogram, (b) length 61.10±19.11 nm, and (c) width 5.37±1.04 nm

2.9.1 Mass spectroscopy of TiO_2 NPs

The mass spectroscopy of all of these TiO_2 NPs was performed using inductively coupled plasma mass spectrometer Agilent 7900 (ICP-MS). TiO_2 NPs distribution in 12week old, female, NFR mice was investigated in blood, brain, lung, liver, both kidneys and spleen at different time points, to quantify this biodistribution. The Quantitative analysis (µM or mg/mL) was performed before administration of TiO_2 NPs and after the administration of TiO2 by collecting the samples of different organs. TiO_2 is very robust and does not transform easily into ionic form therefore each of these samples was digested with hydrofluoric (HF) acid in controlled environment followed by initial digestion with nitric acid. Later these samples additionally digested in aqua-regia (a combination of hydrochloric acid and nitric acid in ratio 3:1). Few of the ICP-MS characterization is presented Table 2.1

Table 2.1: TiO_2 sample concentration (µM or mg/mL), using ICP-MS before administration to mice

Sample name	**Total TiO_2 mg/mL (from ICP-MS)**	**mmol/mL**	**NP/L**	**NP/mL**	**µM**
TiO_2 (Cube)	5.015835151	1.50E-06	9.06E+17	9.06E+14	**1.504**
TiO_2 (plates)	1.787016475	2.24E-07	1.35E+17	1.35E+14	**0.224**
TiO_2 (rods)	2.086340712	1.04E-06	6.28E+17	6.28E+14	**1.043**
TiO_2 (bipyramids)	1.420933583	2.96E-07	1.78E+17	1.78E+14	**0.296**

2.10 Characterization of CdSe/CdS QRs, AuCu nanocubes and Fe_3O_4 nanospheres

CdSe/CdS nanorods, AuCu nanocubes and Fe_3O_4 nanospheres were polymercoated using the standard procedure explained in section 1.7. The characterization of these NPs is presented below in Figure 2.24

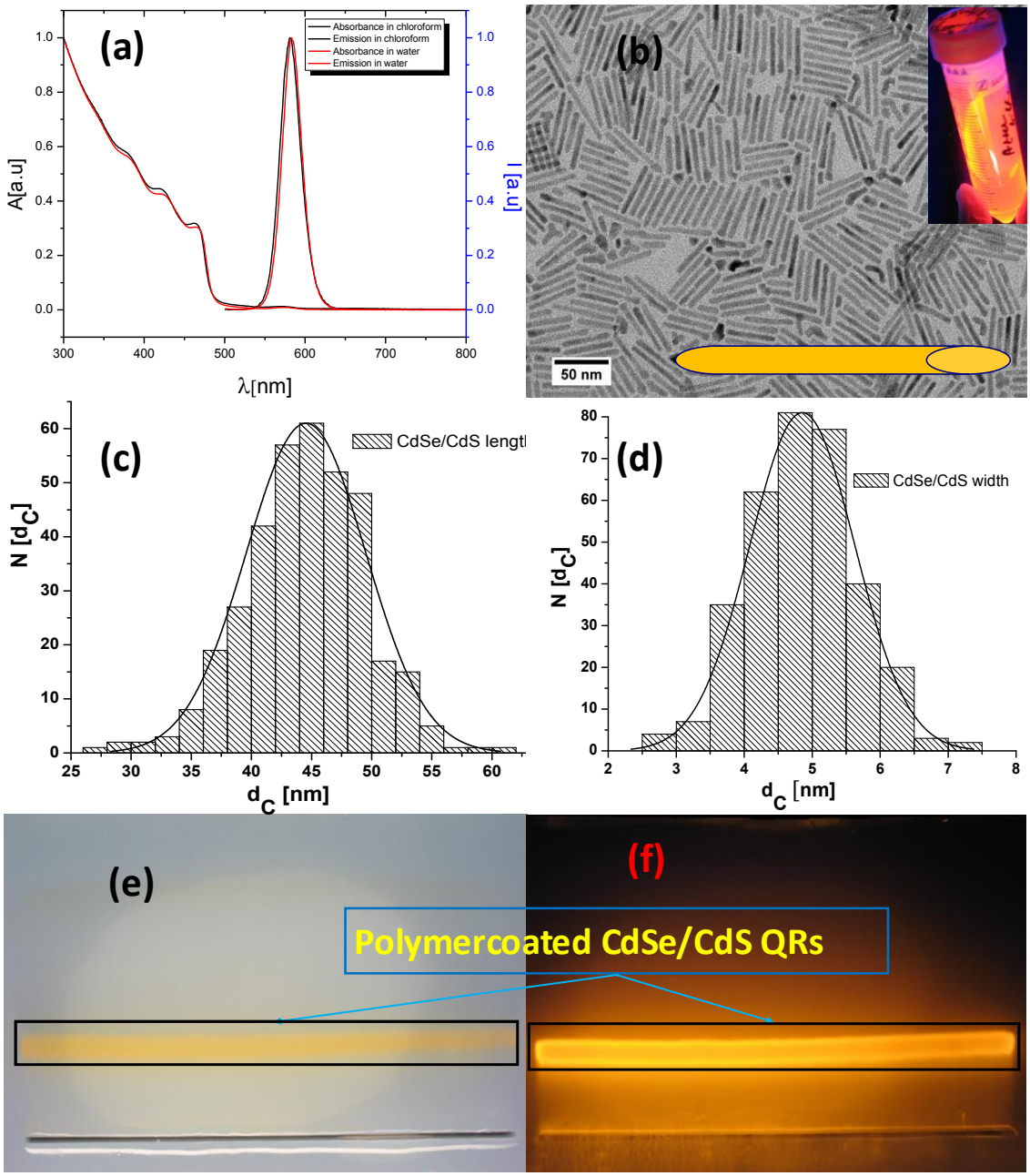

Figure 2.24: CdSe/CdS QRs characterization (a) absorption and emission spectra before and after polymer coating (b) TEM image (c) size distribution histogram (length) 44.50±4.90 nm (d) size distribution histogram (width) 4.85±0.77 nm (e) & (f) gel electrophoresis images of polymer coated QRs on 2% agarose gel without and with UV exposure respectively

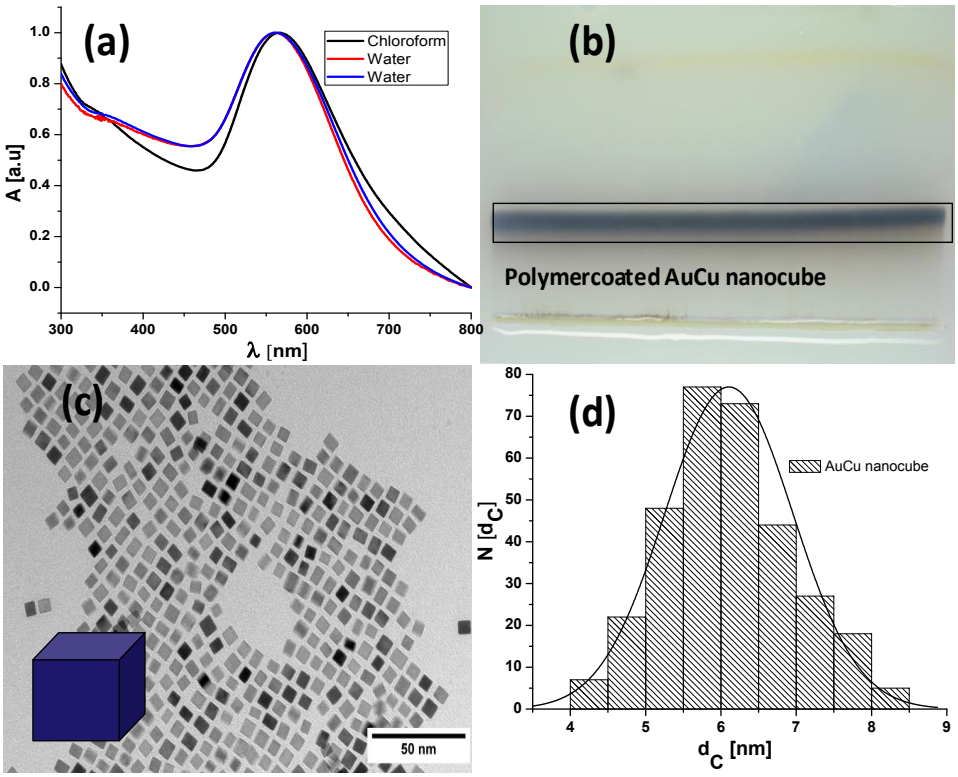

Figure 2.25: Characterization of AuCu nanocubes (a) absorption spectra before (black) and after polymer coating, (red: Before ultracentrifugation and blue: After ultracentrifugation for micelles cleaning) (b) gel electrophoresis image of AuCu nanocubes after PC, (c) TEM image, (d) size distribution histogram 6.10±0.85 nm

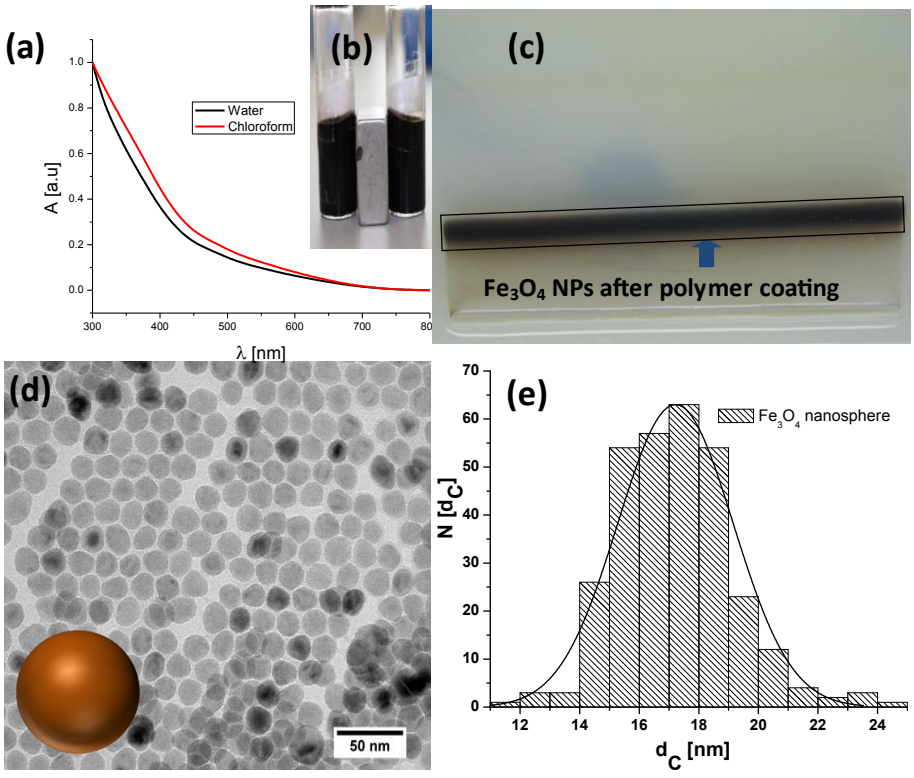

Figure 2.26: Characterization of Fe_3O_4 nanospheres (a) absorption spectra before and after polymer coating, (b) magnetic behaviour of the Fe_3O_4, and (c) gel electrophoresis image of Fe_3O_4 nanocubes after PC (d) TEM image (e) Size distribution histogram 17.21±1.93 nm

2.10.1 XRD pattern of AuCu nanocube

AuCu nanocube was further characterized by XRD; the acquired pattern is presented below in Figure 2.27 along with the reference XRD pattern of AuCu in different ratio of Au to Cu. The obtained XRD pattern clearly indicates the diffraction pattern matches with the pattern of pure Au as well as the patterns of different Au-Cu alloys with a higher ratio of Au as compared to Cu. It is difficult to conclude the exact ratio of Au to Cu in this structure but it clearly indicates that the particles are more Au enriched in comparison to Cu.

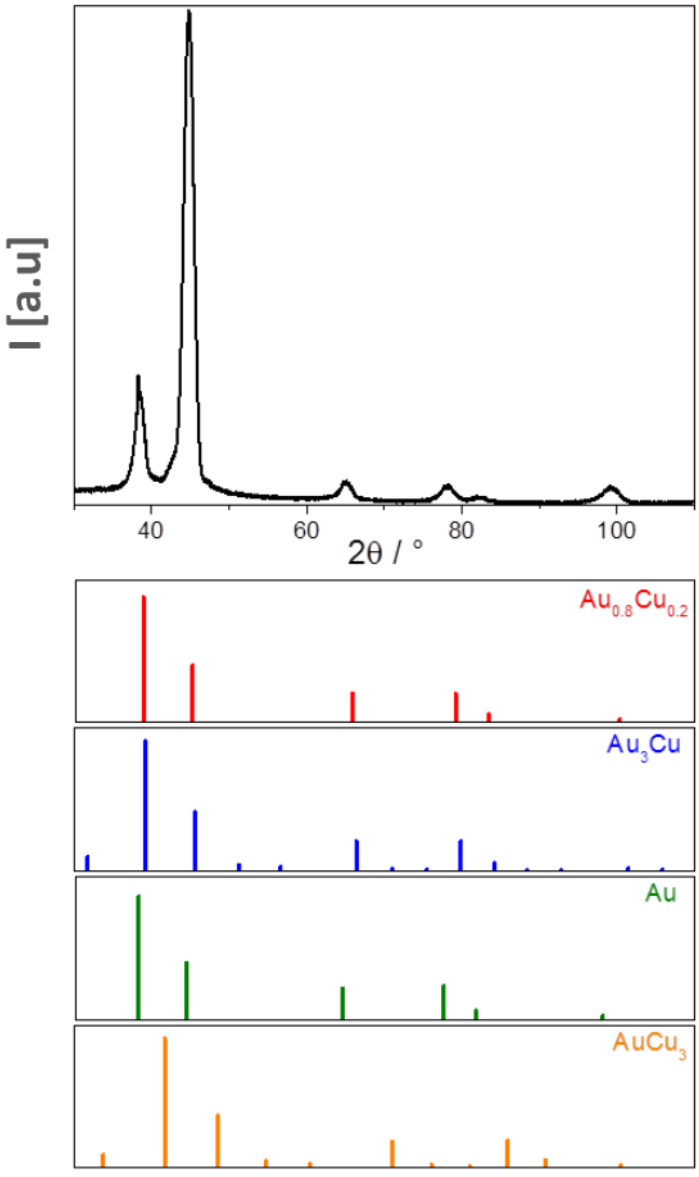

Figure 2.27: Diffraction pattern of the synthesized AuCu nanocubes with reference peak patterns AuCu in different patterns.

2.10.2 XRD pattern of Fe_3O_4 nanospheres

Fe_3O_4 nanospheres was further analysed by XRD to investigate the present status of iron oxide crystal structure in the particles. The obtained XRD pattern Fe_3O_4 nanospheres is presented in Figure 2.28 along with reference diffraction pattern of magnetite, maghemite and hematite. The comparison between obtain pattern of Fe_3O_4 nanospheres and reference patterns reveals that the obtained reflexes suit the pattern of magnetite and maghemite well whereby it can be concluded that one of these phases or a mix is formed. Regarding the hematite phase, it can be seen that the main reflex as well as the reflexes at higher 2Θ-values are not in agreement with the obtained diffraction pattern. Hence, it can be said that the hematite structure is not part of the synthesized product.

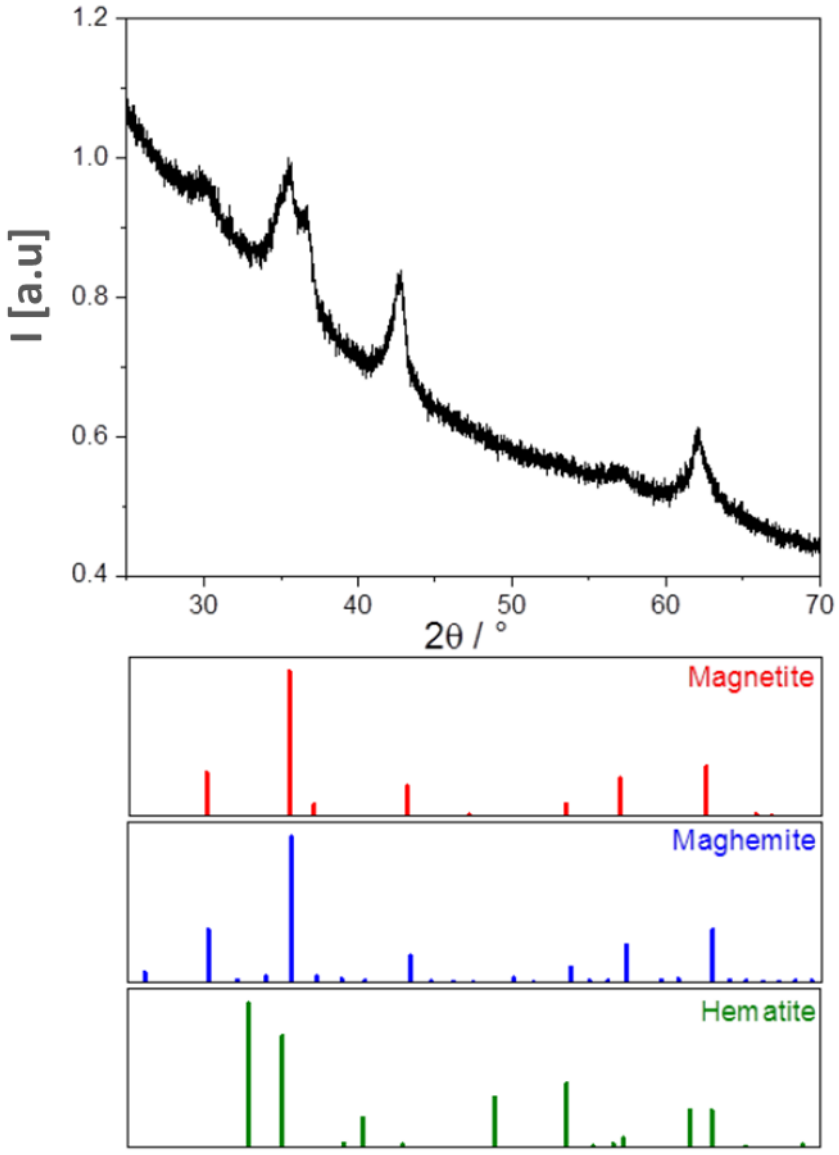

Figure 2.28: Diffraction pattern of Fe_3O_4 nanospheres with reference peak patterns of different oxides of iron from database.

2.11 Effect of QD on bacterial growth

The effect of 4 different water soluble QDs (i.e. CdS, ZnS and manganese doped CdS and ZnS) on the Pseudomonas putida and Escherichia coli were tested in controlled environment. These test performed in a carbonate buffer with relatively low ionic strength to prevent agglomeration. The highest tested concentration was 60 mg/L and no effect was observed over 24 hours. The only negative effect was caused by ionic form of Cd^{2+} (control), but in the concentration (60 mg/L) that was really high. All these QDs were also characterized in the exposure media (DLS size, zeta potential, CPS and UV-Vis). These tests were executed with 1, 10, 25 and 60 mg/L of each of the QD with Pseudomonas putida and E. coli. Cd and Zn in ionic form were used as control.

2.11.1 Bacterial culture and growth conditions

Gram-negative Pseudomonas putida and Escherichia coli were obtained from the Czech Collection of Microorganisms, Masaryk University, Brno, Czech Republic. The bacterial inocula were always prepared fresh from a single colony growing overnight in a soya nutrient broth (Sigma Aldrich) at 27 °C for P. putida and at 37 ^{o}C for E. coli. The cultures were centrifuged at 5000 rpm, 4 ^{o}C for 10 minutes to remove the medium and transfer to carbonate buffer as described below.

2.11.2 Carbonate buffer

The carbonate buffer is a combination of two salt Na_2CO_3 (1.05 mg/L), $NaHCO_3$ (167.16 mg/L) and pH is 8.

2.11.3 Bacterial growth exposed to QDs

The bacterial density was measured by optical density OD = 0.3 at 600 nm (OD600) by using a UV–Vis spectrophotometer for exposing to QDs. Each QD suspension was added to fresh bacterial culture in order to obtain final concentrations of 0.001, 0.01, 0.025 and 0.06 mg/L. The cell growth without QDs was considered as a control. Each concentration was produced in triplicate in a 24-well plate. Following step, the plates were kept in the incubator as growth conditions. The samples were taken after 6 hours and 24 hours in each sampling point to perform two bacterial viability assays (1) spot test. The method was described as below.

2.11.4 Spot test

The test was also described by Suppi et al.[70] and Aruoja et al.[71] in 2015. In this work, the agar plate was prepared by agar with soya broth. Then samples (5 µl) from bacterial growth exposed to QD were pipetted on the agar plates. The plates were incubated for 24 hours as growth condition and visualized the results on each spot.

Table 2.2: Visuals of bacterial growth in colonies by spot test. The results of P. putida exposed to QD for 24h in carbonate buffer. The bacterial growth was recorded as no effects with "0", positive effects with "+" and negative marks "-".

	Pseudomonas putida							
mg/ml	**0.001**		**0.01**		**0.025**		**0.06**	
Time (h)	2	24	2	24	2	24	2	24
Control	0	0	0	0	0	0	0	0
CdS	0	0	0	0	0	0	0	0
CdS-Mn	0	0	0	0	0	0	0	0
ZnS	0	0	0	0	0	0	0	0
Mn-ZnS	0	0	0	0	0	0	0	0
Zn^{2+}	0	0	0	0	0	0	0	0
Cd^{2+}	0	0	0	0	0	0	0	–
	Escherichia coli							
Control	0	0	0	0	0	0	0	0
CdS	0	0	0	0	0	0	0	0
CdS-Mn	0	0	0	0	0	0	0	0
ZnS	0	0	0	0	0	0	0	0
Mn-ZnS	0	0	0	0	0	0	0	0
Zn^{2+}	0	0	0	0	0	0	0	0
Cd^{2+}	0	0	0	0	0	0	0	0

2.12 Characterization of CdS, ZnS, Mn-CdS and ZnS

The characterization (size, zeta potential) of CdS, ZnS, and manganese doped CdS, ZnS QDs was performed in the exposure media. It was decided to do these tests with 1, 10, 25 and 60 mg/L of each of this QDs. Size was measured using DLS-zetasizer, each of triplicate samples is plotted. The collected data is presented below

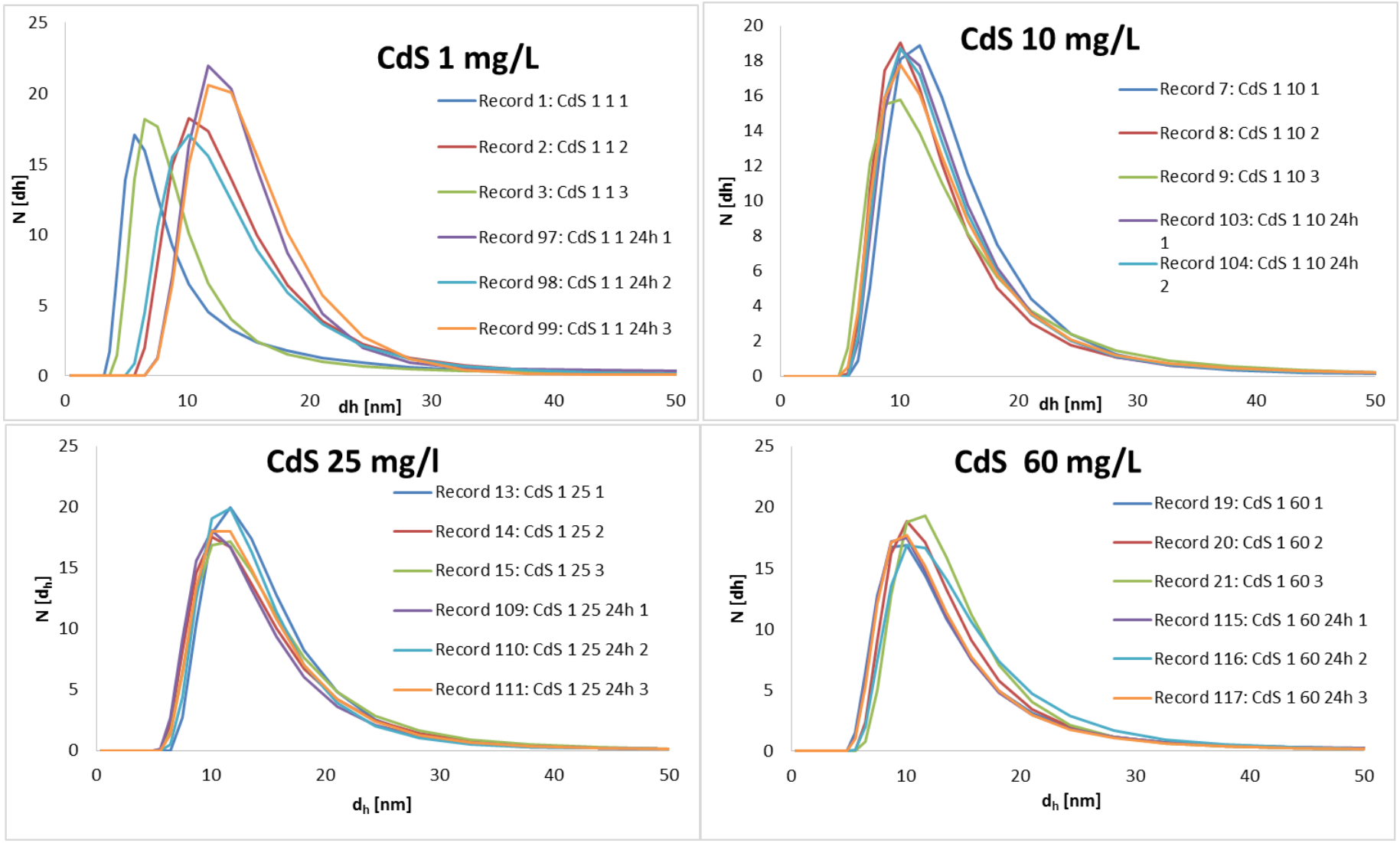

Figure 2.29: CdS QDs size measured in carbonate buffer using DLS zetasizer with different salt concentration (i.e. 1, 10, 25 and 60 mg/L) at different time points, i.e., t_0=0 hour and t_{24}= 24 hour

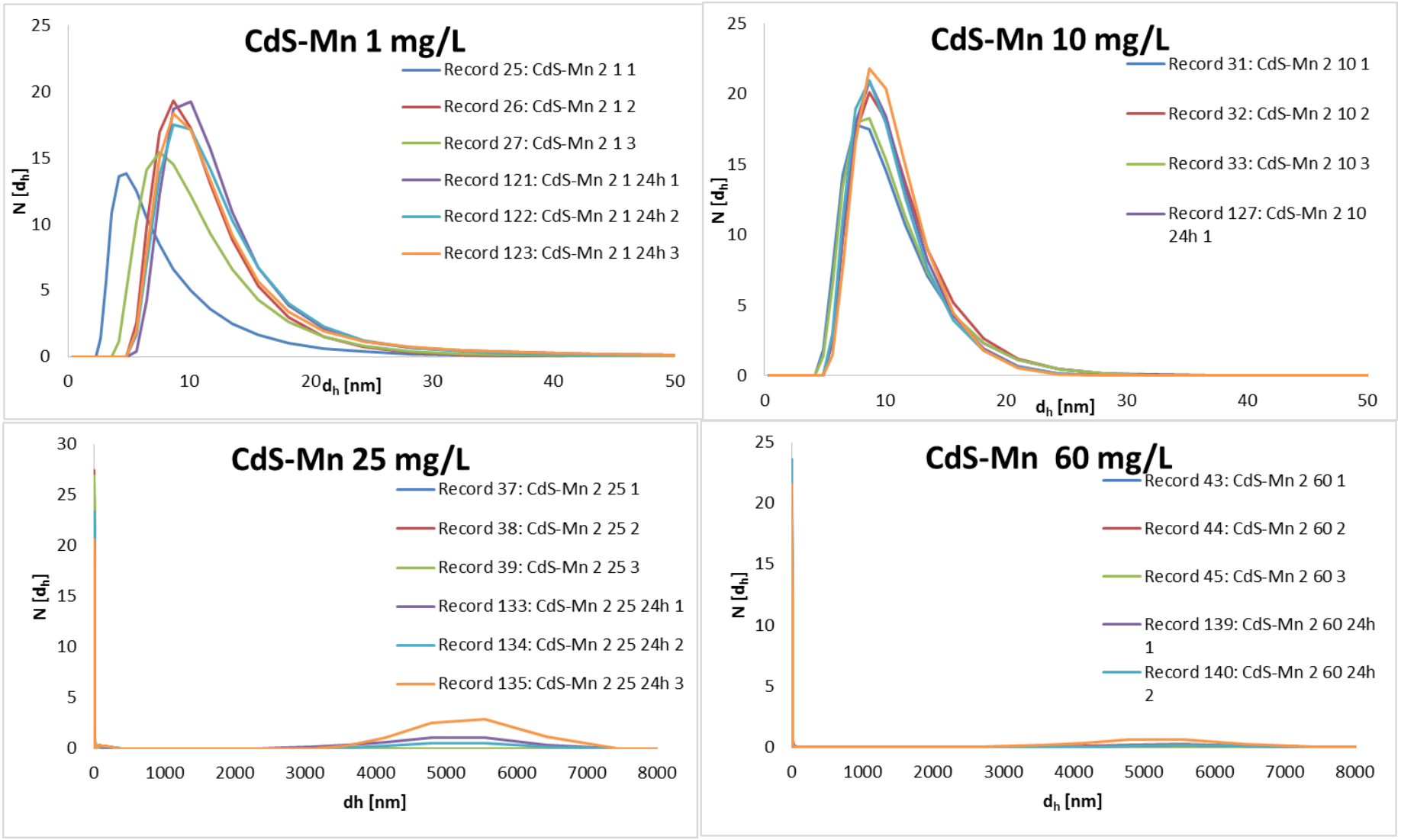

Figure 2.30: Manganese doped CdS QDs size measured in carbonate buffer using DLS zetasizer with different salt concentration (i.e. 1, 10, 25 and 60 mg/L) at different time points, i.e., t_0=0 hour and t_{24}= 24 hour

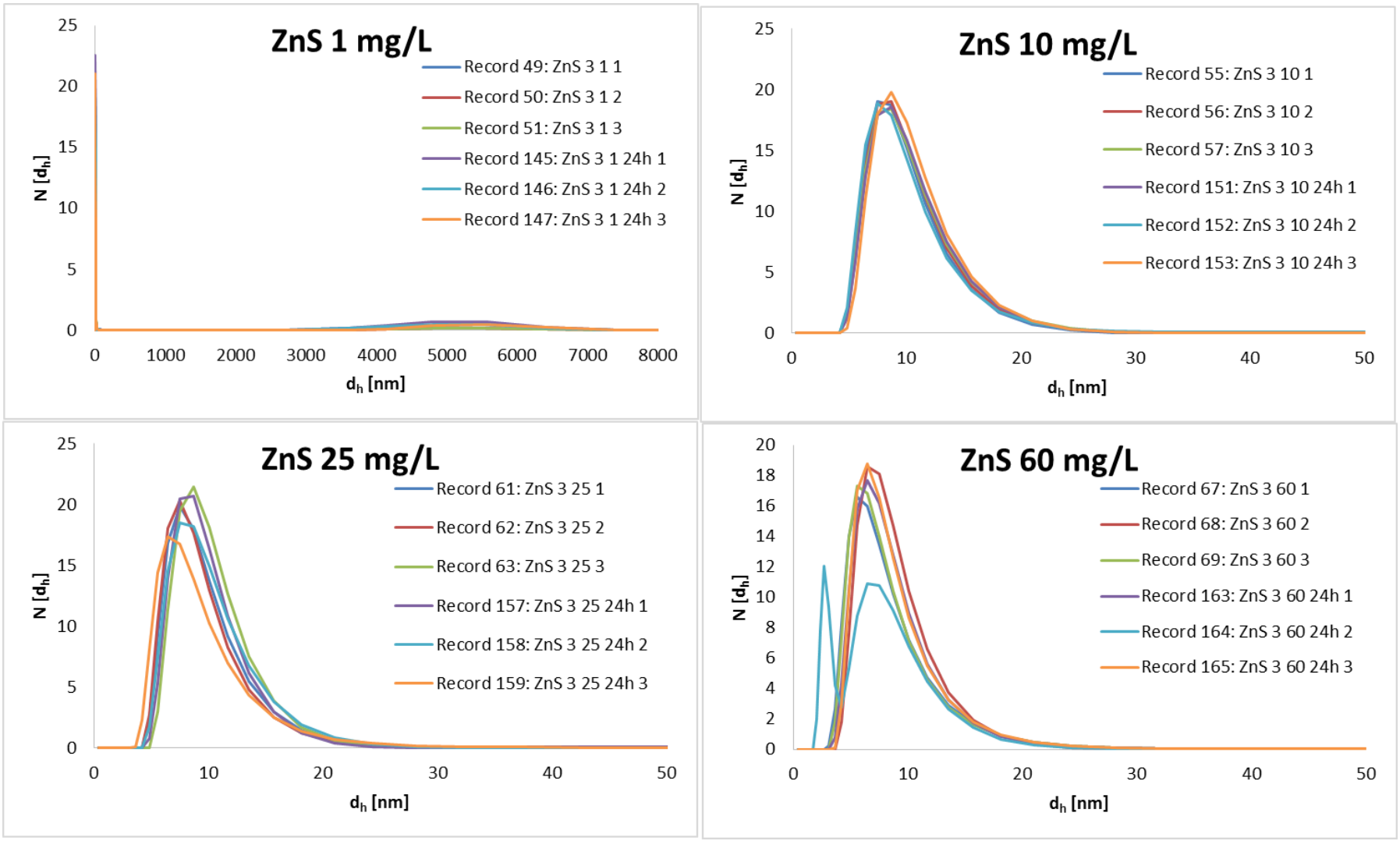

Figure 2.31: ZnS QDs size measured in carbonate buffer using DLS zetasizer with different salt concentration (i.e. 1, 10, 25 and 60 mg/L) at different time points, i.e., t0=0 hour and t24= 24 hour

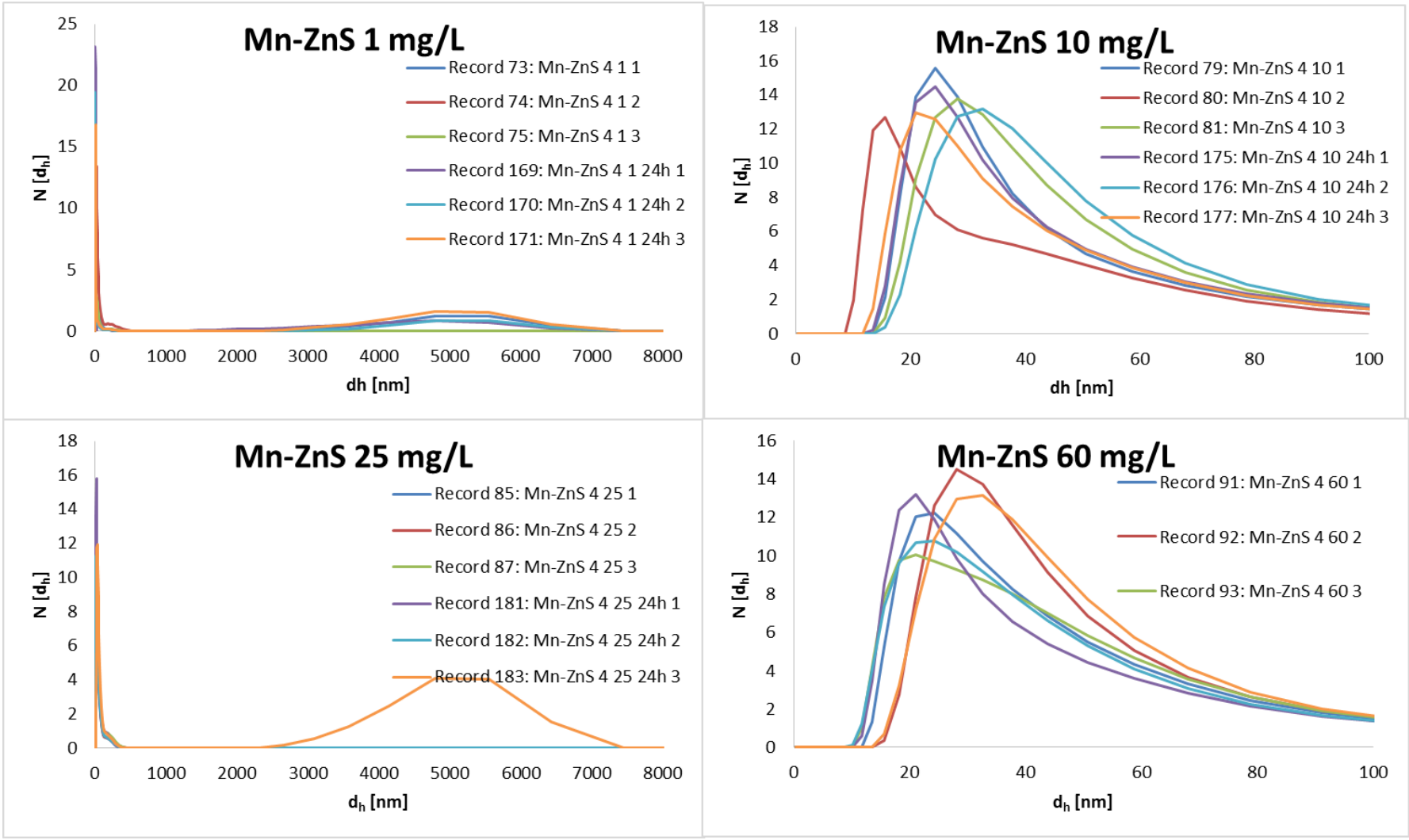

Figure 2.32: Manganese doped ZnS QDs size measured in carbonate buffer using DLS zetasizer with different salt concentration (i.e. 1, 10, 25 and 60 mg/L) at different time points, i.e., t0=0 hour and t24= 24 hour

Figure 2.33: Zeta potentials for CdS, Mn-CdS, ZnS, and Mn-ZnS, that are averages of triplicate samples, 1, 10, 25 and 60 mg/L in carbonate buffer (the same medium where the bacterial test was performed) at time 0 and after 24h

3. Conclusions and Outlook

During the presented study different kinds of NPs were synthesized including fluorescent QDs, magnetic, plasmonic (gold and silver), and titanium oxide NPs. All of these NPs were capped with hydrophobic surfactants which allow them to get easily dissolved in organic solvents like chloroform, toluene, hexane, etc. The characteristics of the synthesized NPs are significantly dependent on the size, shape, material and its composition. The size and shape growth relies predominantly on the surfactants or ligands that are present in the solution along with the allowed reaction time during the synthesis in a controlled environment, e.g., temperature. There are number of unused precursor, compounds and ligands after the completion of synthesis that needs to be removed to get clean NCs for further use. The cleaning of NPs from unused free ligands, surfactants, and precursors was done with polar-nonpolar precipitation method for example using ethanol or methanol as the NPs are dispersed in the chloroform, toluene or hexane. These hydrophobic NPs are insoluble in polar solvents or aqueous media including ethanol, methanol, and water, etc. In all biological applications the NPs should be water soluble and stable for at least time line of the experiments. In order to transfer these NPs from organic phase to aqueous phase these NPs were made soluble in water by some special capping method which gets linked to the hydrophobic surface of NPs and the outer side of this capping agent must be compatible with aqueous medium which allows or helps these NPs to get dissolved. This process of capping or phase transfer is also known as polymer coating. In this study the hydrophilic backbone poly(isobutylene-alt-maleic anhydride) was attached with hydrophobic comb like side chains of dodecylamine (DDA). This polymer PMA helps to transform these NPs to aqueous medium or cell media. The supplementary or some additional surface alteration functionalization (bioconjugation, fluorescent dye) can easily be performed on these PMA coated NPs directly by modification of the amphiphilic polymer before the coating or after polymer coating, e.g., by modification of the coated NPs via the EDC chemistry and activation of the free carboxylic groups on the surface of particles. The cleaning of the NPs and QDs from empty polymer after polymer coating or surface modification was carried out by gel electrophoresis and ultracentrifugation. These approaches results to achieve clean and pure NPs with good monodispersity. To analyze different phyisco-chemical characteristics and colloidal stability of these NPs and QDs, UV-Vis spectroscopy, fluorescence spectroscopy, DLS zetasizer, zeta potentional, ICP-MS and TEM techniques has been used.

4. Publications

The described data of thesis is based on my publications during my Ph.D. study from 2014 to 2018; a list of them is presented below. Each publication is briefly summarized along with giving the contribution of the author. The released publications and submitted manuscripts are appended.

4.1 List of articles

[A1] Chakraborty, I.; de Aberasturi, D. J.; Pazos-Perez, N.; Guerrini, L.; Masood, A.; Alvarez-Puebla, R. A.; Parak, W. J., Ion-Selective Ligands: How Colloidal Nano-and Micro-Particles Can Introduce New Functionalities. Zeitschrift für Physikalische Chemie, 2018, (paper attached).

Scientists working in the field of nanotechnology are introducing new and novel methodologies to develop hybrid micro and NPs with multipurpose functionalities that are gaining attention in a variety of fields biomedicine, nanobiotechnology, electronics, and sensing. The large surface area gives them superior age as compared to their bulk counterpart. A wide variety of functionalities can be employed on the surface of these micro and NPs which lead to novel materials with interesting properties. This approach of attachment of specific molecules (ion selective ligands) is demonstrated in this review study, which presents the advantages with examples of this ion selective ligands attachment to different NPs or incorporation inside the microparticles (microcapsules). This review demonstrates in the first section the chemistry about linking ion-selective ligands with NPs of various sizes. Example of NPs and microcapsules attached with ion-selective ligands is presented in the later sections along with the influence of these ion-selective ligands on the properties attached together. For example, Gd ions and ^{111}In ions are widely accepted as contrast agent for MRI and radioactivity respectively when attached with ion-selective ligand leads to new physicochemical properties (size, solubility, etc.), which influence the interaction with cells, i.e., biodistribution, toxicity, etc.

The author performed the literature survey, corrections, and proof-reading of the manuscript during the write-up and revision stage.

[A2] Huhn, J.; Carrillo-Carrion, C.; Soliman, M. G.; Pfeiffer, C.; Valdeperez, D.; **Masood, A.**; Chakraborty, I.; Zhu, L.; Gallego, M.; Yue, Z.; Carril, M.; Feliu, N.; Escudero, A.; Alkilany, A.; Pelaz, B.; del Pino, P.; Parak, W. J.; Selected Standard Protocols for the Synthesis, Phase Transfer, and Characterization of Inorganic Colloidal nanoparticles. *Chem. Mater.* **29,** 399–461 (2016), (paper attached)

The nanotechnology research is in discussion more aggressively for the last couple of decades and a lot of literature is available about the synthetic approaches that lead formation to nanomaterials. The two main pillars lead to about nanotechnology research and application consist of fruitful synthesis and characterization of NCs or colloidal NPs according to requirements for certain applications. There is a vast availability of scientific literature which describes the synthesis and characterization techniques of different kind of nanomaterials, which include plasmonic NPs, magnetic NPs, and quantum dots, etc. The existing scientific article and reports hardly explain the step by step synthesis approaches and methods in details, therefore, it is sometimes much harder to reproduce the illustrated synthesized NCs with closely resembling characteristics or similar characterized data of synthesized NPs or quantum dots available in the same literature. The aim of this article was to elaborate synthesis and characterization of most commonly and widely used colloidal nanocrystal. In this article, the synthesis, the characterization, the purification, and the phase transfer of different colloidal NPs and QDs from the organic phase to aqueous or aqueous phase to organics phase to meet the requirements according to the applications is illustrated step by step in pictorial and schematic representation.

The author added and wrote up the complete description about synthesis and characterization of CdS (cadmium sulfide) QDs with step by step pictorial demonstration of synthesis in the oxygen-free environment. All the characterization and graph for CdS QDs was done by the author. The author also did the literature survey corrections and proof reading of the article during drafting and revision phase.

[A3] Feliu N.; Hühn J.; Zyuzin M. V.; Ashraf S.; Valdeperez D.; **Masood A.**; Said A. H.; Escudero A.; Pelaz B.; Gonzalez E.; Duarte M. A. C.; Roy S.; Chakraborty I.; Lim M. L.; Sjöqvist S.; Jungebluth P.; Parak W. J.; Quantitative uptake of colloidal particles by cell cultures, Sci. .Total Environ. 2016, 568, 819 (paper attached)

During a couple of decades, the nanotechnology has gained a lot of attention from industrial to biomedical application. In one area of biomedical applications, the NPs which are colloidally stable in aqueous or cell media are exposed to different kind of cells. This review article reveals and elaborates about the colloidal NPs and their applications in biological environment such as exposing the NPs to cells. The focus in this article is about basic perceptions highlighting the uptake of colloidal NPs by cells which can be implemented in different studies of the cell, e.g., the behavior of different cell lines with respect to a different kind of NPs. These studies can be helpful to study and analyze the response in terms of toxicity of NPs in cells this review article also elaborates how NPs are interacting with

targeted cells. Mostly NPs in the range of nm to few micrometers are taken by cells using endocytosis method. The main focus of this article describes that majority of colloidal NPs are endocytosed with adherents cells.

The author did the literature survey, corrections proof-reading of the manuscript during drafting phase of this article.

[A4] Huehn, J.; Fedeli, C.; Zhang, Q.; **Masood, A**.; Del Pino, P.; Khashab, N. M.; Papini, E.; Parak, W. J.; Dissociation coefficients of protein adsorption to nanoparticles as quantitative metrics for description of the protein corona: A comparison of experimental techniques and methodological relevance. *Int. J. Biochem. Cell Biol.* **75,** 148–161 (2016), (paper attached)

In this review article, the attachment of proteins with NPs is discussed with estimation of an important parameter "dissociation coefficient" which describes the attachment of proteins quantitatively. Proteins are usually attached chemically to the binding site of the NPs, the number of attached proteins are dependent on the concentration of proteins with respect to exposed NPs. The attachment of proteins with NPs is also referred as adsorption of proteins. The adsorption of proteins and formation of protein corona at the binding sites or surface of NPs colloids is defined by a chemical reaction. This is quantitative measurement is done through Henderson-Hasselbach equation, which tells how many proteins are adsorbed per nanoparticle in proportion to the concentration of protein available in the solution with NPs. In this article, multiple techniques are compared to describe and to give a brief description of dissociation coefficient using 130 different experiments. In conclusion by comparing all the results from different estimation techniques the Zeta potential is the main factor which affects the adsorption of proteins on the surface of NPs.

The author did literature research, corrections and amendments to the manuscript, and the editing of the manuscript before submission.

[A5] Jungemann, A. H.; Feliu, N.; Bakaimi, I.; Hamaly M.; AlKilany, A.; Chakraborty, I.; **Masood, A.;** Casula, M. F.; Kostopoulou, A.; Oh, E.; Susumu, K.; Stewart, M. H.; Medintz, I.; Stratakis, E.; Parak, W. J.; Kanaras, A. G., The Role of Ligands in the Chemical Synthesis and Applications of Inorganic Nanoparticles" Chemical Reviews, **in writing process**

Nanoparticles (NPs) have gained a lot of attention in last decades because of their unique properties, which originate from a combination of their characteristics such as chemical composition, size, shape, surface chemistry and the type of surface coating. A very vital factor contributing to the properties of NPs is the suitable choice of surface ligands,

which is directly correlated to the choice of the application. This review will emphasize the role of the ligands in determining the formation, properties, and applications of NPs.

The author did the literature survey, corrections proof-reading of the manuscript during drafting phase of this article.

5. Abbreviations

Ag	-	Silver
$AgNO_3$	-	Silver nitrate
AMF	-	Alternating magnetic field
Au	-	Gold
ca.	-	Circa
CdSe	-	Cadmium selenide
CdTl	-	Cadmium telluride
$CHCl_3$	-	Chloroform
Co	-	Cobalt
Cr	-	Chromium
Cu	-	Copper
D_C	-	Critical diameter
DDA	-	Dodecylamine
D_S	-	Crictical diameter size superparamagnetic NPs
EDC	-	N-(3-dimethylaminopropyl)-N'-ethylcarbodiimide
EDTA	-	Ethylenediamintetraacetic acid
E_{dw}		the domain wall energy
Fe	-	Iron
FeO	-	Iron oxide
FM particle	-	Ferro- or Ferri-magnetic particle
GaAs	-	Gallium arsenide
GaN	-	Gallium Nitride
$HAuCl_4$	-	Hydrogen tetrachloroaurate(III) hydrate (Gold Salt)
HF	-	Hydrofluoric acid
Hg	-	Mercury
HgS	-	Mercury sulfide
HOMO	-	highest occupied molecular orbital
IBD	-	Inverse Beta decay
InAs	-	Indium arsenide
InGaAs	-	Indium gallium arsenide
InP	-	Indium phosphide
IONP	-	Iron oxide NPs
LS	-	Liquid scintillator
LSPR	-	Localized surface plasmon resonance
LUMO	-	least unoccupied molecular orbital
MD	-	Multiple domain
mins	-	Minutes
Mn	-	Manganese
MnZnS	-	Manganese zinc sulfide
MNP	-	Magnetic NPs
MRI	-	Magnetic resonance imaging
NaI(Tl)	-	Sodium Iodide Thallium activated
NC(s)	-	Nanocrystal(s)
Ni	-	Nickle
NM(s)	-	Nanomaterial(s)

NP(s)	-	Nanoparticle(s)
OLAC	-	Oleic acid
OLAM	-	Oleylamine
PbS	-	Lead(II) sulfide
PbSe	-	Lead selenide
PC	-	Polymer coating
PEG	-	polyethylene glycol
PPO	-	(2, 5-diphenyloxazole)
SD	-	Single domain
SNPs	-	spherical NPs
SPM	-	Superparamagnetic
TAMRA	-	Tetramethylrhodamine flourophor dye
TBE	-	Tris-borate-EDTA
TDPA	-	Tetradecylphosphonic acid
$TiCl_4$	-	Titanium (IV) chloride
TiF_4	-	Titanium (IV) fluoride
TiO_2	-	Titanium dioxide
Tris	-	tris(hydroxymethyl)aminomethane
TRPL	-	Time resolved photo luminescence spectroscopy
UCF	-	Ultra centrifugation
UV	-	Ultra violet
UV-Vis	-	Ultra violet visible
ZnS	-	Zinc sulfide
ZnSe	-	Zinc Selenide
ΔE_{MS}	-	external magnetostatic energy (stray field)

6. Chemicals and techniques

There are various chemicals and filters were used for the synthesis, surface modification and cleaning of NPs

Sigma-Aldrich

Oleic acid (OLAC, Sigma Aldrich, #364525), 1-Octadecane (ODE, Technical grade 90%, O806), Sulfur (#414980), Cadmium Oxide (#202894), sodium borohydride (#71321), dodecylamine (DDA, #325163), Tetraoctylammonium bromide (#29413-6), PMA (#531278), 1-Bromododecance (#B65551), Oleylamine (#O7805), 1-Dodecanthiol (#471364), Silver nitrate (#209139), 1-2 Hexadecandiol (#213748), Benzyl ether (#108014), Cobalt(II) acetylacetonate (#227129), Manganese (II) acetylacetonate (#245763), Sodium Thiosulfate pentahydrate (#217247),

Carl Roth

Toluene (#9558.2 and 9065.2), Chloroform (#Y015.2), n-Hexane (# 7573.1), Ethanol (#9065.2 and T171.2), Methanol (#8388.6), Tetrahydrofuran (#CP82.1), Sodium hydroxide (#6771.1), Dialysis membrane (MW = 50 kDa, # 1893.1), Hydrochloric acid (#4625.2), Millipore Syringe filter (0.22 µm, # P818.1), Ratilabo syringe filter PTFE (#P816.1), Acetone (#5025.6),

Alfa –Aeser

Hydrogen tetrachlooaurate (III) hydrate (#16903-35-8), 1-Octadecene (Technical grade 90%, #L11004), Tetradecylphosphonic acid (# A17511), 1-Dodecylamine (#A15515)

ACROS

Titanium (IV) fluoride (#7783633), Tris Base (#BP152-1)

Strem Chemicals

Titanium(IV) chloride ($TiCl_4$, Strem, #221150), Iron (III) Acetylacetonate (#26-2300)

Lumiprobe GmbH

Cyanine5 amine (#430C0)

Milipore

Amicon centrifuge filter (#UFC910024)

The following Techniques were used for analysis, quantification, cleaning, purification and characterization of the NPs.

4. UV-Vis spectroscopy and Agilent Technologies 8453 UV-Vis
5. Fluorometer Horiba FluoroLog FL-1039.
6. Dynamic light scattering (DLS) Malvern Zetasizer Nano ZS.
7. Gel electrophoresis Bio Rad PowerPac Basic.
8. Rotavap (Laborota 4000, Heidolph).
9. Centrifuge Verifuge 3.0RS, Hettich Universal 320R, Heraeus™ Fresco™ 21 Microcentrifuge
10. Transmission electron microscopy (TEM) JEOL JEM-1400PLUS.
11. Inductively coupled plasma mass spectrometry. Agilent 7900 ICP-MS.
12. Bruker D8 Advance for XRD analysis

Appendix

Wissenschaftlicher Werdegang

Persönliche Angaben

Vorname: Atif Familienname: Masood

Geburtsdatum: 16. Jan 1981, Geburtsort: Mirpurkhas, Pakistan

Staatsangehörigkeit : Pakistanish

Ausbildung

10/2014-08/2018 **Doktorarbeit, Physik. Philipps-Universität Marburg**

AG. Biophotonik (Prof. W. J. Parak), Fachbereich Physik.

Thema: Synthesis and the Surface Modification of Inorganic Nanoparticles for Application in Physics and Medicine.

Betreuer Prof. Dr.Wolfgang.*J*.Parak

12/2003 - 09/2005 ***M.Sc. Medical Physics*.** Pakistan Institute of Engineering and Applied Sciences, Islamabad**,** Fachbereich: Department of Physics and Applied Mathematics

Thema: Effects of Temperature on NaI(Tl) scintillation detector

03/1999 - 05/2003 ***B.E Electronics Engineering,*** Mehran University of Engineering and Technology, Jamshoro, Pakistan**,** Fachbereich Department of Electronics Engineering

Wissenschaftliche Veröffentlichungen

- Chakraborty, I., Jimenez de Aberasturi, D., Pazos-Perez, N.Masood A., et al. Ion-Selective Ligands How Colloidal Nano- and Micro-Particles Can Introduce New Functionalities. Zeitschrift für Physikalische Chemie, 2018. doi 10.1515/zpch-2018-1172
- Huehn, J.; Carrillo-Carrion, C.; Soliman, M. G.; Pfeiffer, C.; Valdeperez, D.; **Masood, A.**; Chakraborty, I.; Zhu, L.; Gallego, M.; Yue, Z.; Carril, M.; Feliu, N.; Escudero, A.; Alkilany, A.; Pelaz, B.; del Pino, P.; Parak, W. J.; Selected Standard Protocols for the Synthesis, Phase Transfer, and Characterization of Inorganic Colloidal Nanoparticles. *Chem. Mater.* **29,** 399–461 (2016).
- Feliu N.; Hühn J.; Zyuzin M. V.; Ashraf S.; Valdeperez D.; **Masood A.**; Said A. H.; Escudero A.; Pelaz B.; Gonzalez E.; Duarte M. A. C.; Roy S.; Chakraborty I.; Lim M. L.; Sjöqvist S.; Jungebluth P.; Parak W. J.; Quantitative uptake of colloidal particles by cell cultures, Sci. .Total Environ. 2016, 568, 819).

- Huehn, J.; Fedeli, C.; Zhang, Q.; **Masood, A**.; Del Pino, P.; Khashab, N. M.; Papini, E.; Parak, W. J.; Dissociation coefficients of protein adsorption to nanoparticles as quantitative metrics for description of the protein corona A comparison of experimental techniques and methodological relevance. *Int. J. Biochem. Cell Biol.* **75,** 148–161 (2016).

7. References

1. Guisbiers, G., Mejía-Rosales, S., & Leonard Deepak, F. (2012). Nanomaterial properties: size and shape dependencies. *Journal of Nanomaterials*, *2012*.
2. Elnashaie, S. S., Danafar, F., & Rafsanjani, H. H. (2015). *Nanotechnology for chemical engineers*. Springer.
3. Angioletti-Uberti, S. (2017). Theory, simulations and the design of functionalized nanoparticles for biomedical applications: A Soft Matter Perspective. npj Computational Materials, 3(1), 48.
4. El-Sayed, M. A. (2004). Small is different: shape-, size-, and composition-dependent properties of some colloidal semiconductor nanocrystals. Accounts of chemical research, 37(5), 326-333.
5. Fernandez-Ibanez, P., Blanco, J., Malato, S., & De Las Nieves, F. J. (2003). Application of the colloidal stability of TiO2 particles for recovery and reuse in solar photocatalysis. *Water Research*, *37*(13), 3180-3188.
6. Neeleshwar, S., Chen, C. L., Tsai, C. B., Chen, Y. Y., Chen, C. C., Shyu, S. G., & Seehra, M. S. (2005). Size-dependent properties of CdSe quantum dots. *Physical Review B*, *71*(20), 201307
7. Ashoori, R. C. (1996). Electrons in artificial atoms. *Nature*, *379*(6564), 413.
8. Ramírez, H. Y., Flórez, J., & Camacho, Á. S. (2015). Efficient control of coulomb enhanced second harmonic generation from excitonic transitions in quantum dot ensembles. *Physical Chemistry Chemical Physics*, *17*(37), 23938-23946.
9. Akbari, B., Tavandashti, M. P., & Zandrahimi, M. (2011). Particle size characterization of nanoparticles–a practicalapproach. *Iranian Journal of Materials Science and Engineering*, *8*(2), 48-56.
10. Lu, A. H., Salabas, E. E., & Schüth, F. (2007). Magnetic nanoparticles: synthesis, protection, functionalization, and application. *Angewandte Chemie International Edition*, *46*(8), 1222-1244.
11. Dave, S. R., & Gao, X. (2009). Monodisperse magnetic nanoparticles for biodetection, imaging, and drug delivery: a versatile and evolving technology. *Wiley Interdisciplinary Reviews: Nanomedicine and Nanobiotechnology*, *1*(6), 583-609.
12. Sun, Y., & Xia, Y. (2002). Shape-controlled synthesis of gold and silver nanoparticles. *Science*, *298*(5601), 2176-2179.
13. Huang, X., Jain, P. K., El-Sayed, I. H., & El-Sayed, M. A. (2008). Plasmonic photothermal therapy (PPTT) using gold nanoparticles. *Lasers in medical science*, *23*(3), 217.
14 Soliman, M.; Parak, W. Gold Nanoparticles: Synthesis, Surface Modification and Functionalization for Biomedical Applications, Thesis dissertation, Philipps-Universität Marburg., 2016.
15. Daraio, C., & Jin, S. (2012). Synthesis and patterning methods for nanostructures useful for biological applications. In *Nanotechnology for Biology and Medicine* (pp. 27-44). Springer, New York, NY.

16. Pacioni, N. L., Borsarelli, C. D., Rey, V., & Veglia, A. V. (2015). Synthetic routes for the preparation of silver nanoparticles. In *Silver Nanoparticle Applications* (pp. 13-46). Springer, Cham.

17. Wang, Y., & Xia, Y. (2004). Bottom-up and top-down approaches to the synthesis of monodispersed spherical colloids of low melting-point metals. Nano Letters, 4(10), 2047-2050.

18. Singh, P., Kim, Y. J., Zhang, D., & Yang, D. C. (2016). Biological synthesis of nanoparticles from plants and microorganisms. *Trends in biotechnology*, *34*(7), 588-599.

19. Reimann, S. M., & Manninen, M. (2002). Electronic structure of quantum dots. Reviews of modern physics, 74(4), 1283.

20 Unni, M., Uhl, A. M., Savliwala, S., Savitzky, B. H., Dhavalikar, R., Garraud, N., & Rinaldi, C. (2017). Thermal decomposition synthesis of iron oxide nanoparticles with diminished magnetic dead layer by controlled addition of oxygen. ACS nano, 11(2), 2284-2303.

21. Thanh, N. T., Maclean, N., & Mahiddine, S. (2014). Mechanisms of nucleation and growth of nanoparticles in solution. Chemical reviews, 114(15), 7610-7630.

22. LaMer, V. K., & Dinegar, R. H. (1950). Theory, production and mechanism of formation of monodispersed hydrosols. *Journal of the American Chemical Society*, *72*(11), 4847-4854.

23. Jadhav, S. A., Brunella, V., & Scalarone, D. (2015). Polymerizable ligands as stabilizers for nanoparticles. Particle & Particle Systems Characterization, 32(4), 417-428.

24. Li, J., & Zhu, J. J. (2013). Quantum dots for fluorescent biosensing and bio-imaging applications. *Analyst*, *138*(9), 2506-2515.

25. Bhatia, S. (2016). Nanoparticles types, classification, characterization, fabrication methods and drug delivery applications. In Natural Polymer Drug Delivery Systems (pp. 33-93). Springer, Cham.

26. Ekimov, A. I., & Onushchenko, A. A. (1981). Quantum size effect in three-dimensional microscopic semiconductor crystals. Jetp Lett, 34(6), 345-349.

27. Walling, M. A., Novak, J. A., & Shepard, J. R. (2009). Quantum dots for live cell and in vivo imaging. International journal of molecular sciences, 10(2), 441-491.

28. Yu, W. W., & Peng, X. (2002). Formation of high-quality CdS and other II–VI semiconductor nanocrystals in noncoordinating solvents: tunable reactivity of monomers. *Angewandte Chemie International Edition*, *41*(13), 2368-2371.

29. Zhu, J. J., Li, J. J., Huang, H. P., & Cheng, F. F. (2013). *Quantum dots for DNA biosensing* (pp. 9-24). Springer Berlin Heidelberg.

30. Tisdale, W. A., & Zhu, X. Y. (2011). Artificial atoms on semiconductor surfaces. *Proceedings of the National Academy of Sciences*, *108*(3), 965-970.

31. Medintz, I. L., Uyeda, H. T., Goldman, E. R., & Mattoussi, H. (2005). Quantum dot bioconjugates for imaging, labelling and sensing. Nature materials, 4(6), 435.

32. Mutavdžić, D., Xu, J., Thakur, G., Triulzi, R., Kasas, S., Jeremić, M., ... & Radotić, K. (2011). Determination of the size of quantum dots by fluorescence spectroscopy. *Analyst*, *136*(11), 2391-2396.

33. Mansur, H. S., Mansur, A. A., & González, J. C. (2011). Synthesis and characterization of CdS quantum dots with carboxylic-functionalized poly (vinyl alcohol) for bioconjugation. *Polymer*, *52*(4), 1045-1054.

34. Zhang, J. Z. (2000). Interfacial charge carrier dynamics of colloidal semiconductor nanoparticles. Journal of Physical Chemistry, 104, (31), 7239-7253

35. Reiss, P., Protiere, M., & Li, L. (2009). Core/shell semiconductor nanocrystals. *small*, *5*(2), 154-168.

36. Shen, G., Cho, J. H., Yoo, J. K., Yi, G. C., & Lee, C. J. (2005). Synthesis of single-crystal CdS microbelts using a modified thermal evaporation method and their photoluminescence. *The Journal of Physical Chemistry B*, *109*(19), 9294-9298.

37. Mo, Y. M., Tang, Y., Gao, F., Yang, J., & Zhang*, Y. M. (2012). Synthesis of fluorescent CdS quantum dots of tunable light emission with a new in situ produced capping agent. *Industrial & Engineering Chemistry Research*, *51*(17), 5995-6000.

38. Panda, S. K., Hickey, S. G., Demir, H. V., & Eychmüller, A. (2011). Bright White-Light Emitting Manganese and Copper Co-Doped ZnSe Quantum Dots. Angewandte Chemie, 123(19), 4524-4528.

39. Smith, B. A., Zhang, J. Z., Joly, A., & Liu, J. (2000). Luminescence decay kinetics of Mn 2+-doped ZnS nanoclusters grown in reverse micelles. *Physical Review B*, *62*(3), 2021.

40. Sun, L., Yan, C., Liu, C., Liao, C., Li, D., & Yu, J. (1998). Study of the optical properties of Eu3+-doped ZnS nanocrystals. *Journal of alloys and compounds*, *275*, 234-237.

41. Proshchenko, V., & Dahnovsky, Y. (2015). Long-lived emission in Mn doped CdS, ZnS, and ZnSe diluted magnetic semiconductor quantum dots. *Chemical Physics*, *461*, 58-62.

42. Chen, O., Shelby, D. E., Yang, Y., Zhuang, J., Wang, T., Niu, C., ... & Cao, Y. C. (2010). Excitation-Intensity-Dependent Color-Tunable Dual Emissions from Manganese-Doped CdS/ZnS Core/Shell Nanocrystals. *Angewandte Chemie International Edition*, *49*(52), 10132-10135.

43. Halder, G., & Bhattacharyya, S. (2015). Plight of mn doping in colloidal CdS quantum dots to boost the efficiency of solar cells. *The Journal of Physical Chemistry C*, *119*(24), 13404-13412.

44. Liu, L., Huang, M., Lan, Z., Wu, J., Shang, G., Liu, G., & Lin, J. (2014). Efficient Mn-doped CdS quantum dot sensitized solar cells based on SnO 2 microsphere photoelectrodes. *Journal of Materials Science: Materials in Electronics*, *25*(2), 754-759.

45. Nanda, J., Sapra, S., Sarma, D. D., Chandrasekharan, N., & Hodes, G. (2000). Size-selected zinc sulfide nanocrystallites: synthesis, structure, and optical studies. *Chemistry of Materials*, *12*(4), 1018-1024.

46. Abdallah, S., Al-Hosiny, N., & Badawi, A. (2012). Photoacoustic study of CdS QDs for application in quantum-dot-sensitized solar cells. *Journal of Nanomaterials*, *2012*, 108.

47. Reines, F., & Cowan, C. L. (1991). The neutrino. In *Neutrinos And Other Matters: Selected Works of Frederick Reines* (pp. 548-551).

48. Dolgov, A. D. (2002). Neutrinos in cosmology. *Physics Reports*, *370*(4-5), 333-535.

49. Tavernier, S. (2010). *Experimental techniques in nuclear and particle physics*. Springer Science & Business Media.

50. Froggatt, C. D., Muheim, F., & Smith, P. F. (2008). Neutrinos in particle physics, astrophysics and cosmology. CRC Press.

51. Lucio, J. L., Rosado, A., & Zepeda, A. (1985). Characteristic size for the neutrino. Physical Review D, 31(5), 1091.

52. Vogel, P., & Beacom, J. F. (1999). Angular distribution of neutron inverse beta decay, $\bar{\nu}$ e+ p→ e++ n. Physical Review D, 60(5), 053003.

53. Super-Kamiokande, http://www.ps.uci.edu/~superk/superk_detector.html

54. Leo, W. R., Techniques for Nuclear and Particle Physics Experiments, 1994 (2nd ed.). Springer, ISBN 978-3540572800

55. Handy, N. C., & Tozer, D. J. (1999). Excitation energies of benzene from Kohn–Sham theory. *Journal of computational chemistry*, *20*(1), 106-113.

56. Jaffe, H. H., & Miller, A. L. (1966). The fates of electronic excitation energy. *Journal of Chemical Education*, *43*(9), 469.

57. Priestley, E. B., & Haug, A. (1968). Phosphorescence spectrum of pure crystalline naphthalene. *The Journal of Chemical Physics*, *49*(2), 622-629.

58. Aberle, C., Li, J. J., Weiss, S., & Winslow, L. (2013). Optical properties of quantum-dot-doped liquid scintillators. *Journal of Instrumentation*, *8*(10), P10015.

59. Winslow, L., & Simpson, R. (2012). Characterizing quantum-dot-doped liquid scintillator for applications to neutrino detectors. *Journal of Instrumentation*, *7*(07), P07010.

60. Biggin, H. C., Chen, N. S., Ettinger, K. V., Fremlin, J. H., Morgan, W. D., Nowotny, R., ... & Harvey, T. C. (1974). Cadmium by in vivo neutron activation analysis. *Journal of Radioanalytical Chemistry*, *19*(2), 207-214.

61. Park, J. M., Kim, H. J., Hwang, Y. S., Kim, D. H., & Park, H. W. (2014). Scintillation properties of quantum-dot doped styrene based plastic scintillators. *Journal of Luminescence*, *146*, 157-161.

62. Tam, A. K., Boyraz, O., Unangst, J., Nazaretas, P., Schreuder, M., & Nilsson, M. (2018). Quantum-dot doped polymeric scintillation material for radiation detection. *Radiation Measurements*, *111*, 27-34.

63. Wang, Y., Zhao, Q., Han, N., Bai, L., Li, J., Liu, J., ... & Wang, S. (2015). Mesoporous silica nanoparticles in drug delivery and biomedical applications. Nanomedicine: Nanotechnology, Biology and Medicine, 11(2), 313-327.

64. Lai, C. Y., Trewyn, B. G., Jeftinija, D. M., Jeftinija, K., Xu, S., Jeftinija, S., & Lin, V. S. Y. (2003). A mesoporous silica nanosphere-based carrier system with chemically removable CdS nanoparticle caps for stimuli-responsive controlled release of neurotransmitters and drug molecules. Journal of the American Chemical Society, 125(15), 4451-4459.

65. Quan, Z., Wang, Z., Yang, P., Lin, J., & Fang, J. (2007). Synthesis and characterization of high-quality ZnS, ZnS: Mn2+, and ZnS: Mn2+/ZnS (core/shell) luminescent nanocrystals. Inorganic chemistry, 46(4), 1354-1360.

66. Kar, S., Biswas, S., & Chaudhuri, S. (2005). Catalytic growth and photoluminescence properties of ZnS nanowires. Nanotechnology, 16(6), 737.

67. Zhai, X., Zhang, X., Chen, S., Yang, W., & Gong, Z. (2012). Oleylamine as solvent and stabilizer to synthesize shape-controlled ZnS nanocrystals with good optical properties. Colloids and Surfaces A: Physicochemical and Engineering Aspects, 409, 126-129.

68. Li, L. S., Pradhan, N., Wang, Y., & Peng, X. (2004). High quality ZnSe and ZnS nanocrystals formed by activating zinc carboxylate precursors. *Nano Letters*, *4*(11), 2261-2264.

69. Zhang, W., Li, Y., Zhang, H., Zhou, X., & Zhong, X. (2011). Facile synthesis of highly luminescent Mn-doped ZnS nanocrystals. Inorganic chemistry, 50(20), 10432-10438.

70. Suppi, S., Kasemets, K., Ivask, A., Künnis-Beres, K., Sihtmäe, M., Kurvet, I., ... & Kahru, A. (2015). A novel method for comparison of biocidal properties of nanomaterials to bacteria, yeasts and algae. Journal of hazardous materials, 286, 75-84.

71. Aruoja, V., Pokhrel, S., Sihtmäe, M., Mortimer, M., Mädler, L., & Kahru, A. (2015). Toxicity of 12 metal-based nanoparticles to algae, bacteria and protozoa. Environmental Science: Nano, 2(6), 630-644.

72. Fan, Z., & Lu, J. G. (2005). Zinc oxide nanostructures: synthesis and properties. Journal of nanoscience and nanotechnology, 5(10), 1561-1573.

73. Wang, Z. L. (2004). Nanostructures of zinc oxide. Materials today, 7(6), 26-33.

74. Abdelmonem, A. M., Pelaz, B., Kantner, K., Bigall, N. C., del Pino, P., & Parak, W. J. (2015). Charge and agglomeration dependent in vitro uptake and cytotoxicity of zinc oxide nanoparticles. Journal of inorganic biochemistry, 153, 334-338.

75. Talam, S., Karumuri, S. R., & Gunnam, N. (2012). Synthesis, characterization, and spectroscopic properties of ZnO nanoparticles. ISRN Nanotechnology, 2012.

76. Oliva, J., Diaz-Torres, L., Torres-Castro, A., Salas, P., Perez-Mayen, L., & De la Rosa, E. (2015). Effect of TEA on the blue emission of ZnO quantum dots with high quantum yield. Optical Materials Express, 5(5), 1109-1121.

77. Kool, P. L., Ortiz, M. D., & van Gestel, C. A. (2011). Chronic toxicity of ZnO nanoparticles, non-nano ZnO and ZnCl2 to Folsomia candida (Collembola) in relation to bioavailability in soil. Environmental Pollution, 159(10), 2713-2719.

78. Adam, N., Leroux, F., Knapen, D., Bals, S., & Blust, R. (2014). The uptake of ZnO and CuO nanoparticles in the water-flea Daphnia magna under acute exposure scenarios. Environmental pollution, 194, 130-137.

79. Gilbert, B., Fakra, S. C., Xia, T., Pokhrel, S., Mädler, L., & Nel, A. E. (2012). The fate of ZnO nanoparticles administered to human bronchial epithelial cells. ACS nano, 6(6), 4921-4930.

80. Raut, S. B., & Thorat, P. V. (2015). A Review on Preparation, Characterization and Application of Zinc Oxide (ZnO) Nanoparticles by Green Synthesis Method.

81 Singh, B., Singh, S., Singh, J., Saini, G. S. S., Mehta, D. S., Singh, G., ... & Kaura, A. (2015). Understanding the adsorption behavior of surface active molecules on ZnO nanostructures by experimental and first-principles calculations. Physical Chemistry Chemical Physics, 17(45), 30450-30460.

82. Yue, Q., Cheng, J., Li, G., Zhang, K., Zhai, Y., Wang, L., & Liu, J. (2011). Fluorescence property of ZnO nanoparticles and the interaction with bromothymol blue. Journal of fluorescence, 21(3), 1131-1135.

83. de Mello Donegá, C. (2011). Synthesis and properties of colloidal heteronanocrystals. Chemical Society Reviews, 40(3), 1512-1546.

84. Talapin, D. V., Nelson, J. H., Shevchenko, E. V., Aloni, S., Sadtler, B., & Alivisatos, A. P. (2007). Seeded growth of highly luminescent CdSe/CdS nanoheterostructures with rod and tetrapod morphologies. Nano letters, 7(10), 2951-2959.

85. Matsuishi, K., Yuasa, A., Arai, G., & Mori, T. (2014). Structural and optical properties of CdSe nanostructures (nanoparticles, nanoparticle-and nanosheet-superlattices) fabricated using organic molecules as a template. In IOP Conference Series: Materials Science and Engineering (Vol. 54, No. 1, p. 012007). IOP Publishing.

86. Issa, B., Obaidat, I. M., Albiss, B. A., & Haik, Y. (2013). Magnetic nanoparticles: surface effects and properties related to biomedicine applications. International journal of molecular sciences, 14(11), 21266-21305.

87. Harabech, M., Leliaert, J., Coene, A., Crevecoeur, G., Van Roost, D., & Dupré, L. (2017). The effect of the magnetic nanoparticle's size dependence of the relaxation time constant on the specific loss power of magnetic nanoparticle hyperthermia. Journal of Magnetism and Magnetic Materials, 426, 206-210.

88. Gubin, S. P., Koksharov, Y. A., Khomutov, G. B., & Yurkov, G. Y. E. (2005). Magnetic nanoparticles: preparation, structure and properties. Russian Chemical Reviews, 74(6), 489-520.

89. Spaldin, N. (2003). Magnetic materials. Fundamentals and Device.

90. Coey, J. M. (2010). Magnetism and magnetic materials. Cambridge University Press.

91. Zheng, X. G., Xu, C. N., Nishikubo, K., Nishiyama, K., Higemoto, W., Moon, W. J., ... & Otabe, E. S. (2005). Finite-size effect on Néel temperature in antiferromagnetic nanoparticles. Physical Review B, 72(1), 014464.

92. Mørup, S., Madsen, D. E., Frandsen, C., Bahl, C. R., & Hansen, M. F. (2007). Experimental and theoretical studies of nanoparticles of antiferromagnetic materials. Journal of Physics: Condensed Matter, 19(21), 213202.

93. Ortega, D., & Pankhurst, Q. A. (2013). Magnetic hyperthermia. Nanoscience, 1(60), e88.

94. Fridkin, V., Ducharme S., Ferroelectricity at the Nanoscale: Basics and Applications, Springer Science & Business Media, Oct 2013

95. Kolhatkar, A. G., Jamison, A. C., Litvinov, D., Willson, R. C., & Lee, T. R. (2013). Tuning the magnetic properties of nanoparticles. International journal of molecular sciences, 14(8), 15977-16009.

96. Figuerola, A., Di Corato, R., Manna, L., & Pellegrino, T. (2010). From iron oxide nanoparticles towards advanced iron-based inorganic materials designed for biomedical applications. Pharmacological Research, 62(2), 126-143.

97. Di Marco, M., Guilbert, I., Port, M., Robic, C., Couvreur, P., & Dubernet, C. (2007). Colloidal stability of ultrasmall superparamagnetic iron oxide (USPIO) particles with different coatings. International journal of pharmaceutics, 331(2), 197-203.

98. Kumar, N., & Kumbhat, S. (2016). Essentials in nanoscience and nanotechnology. John Wiley & Sons.

99. Gupta, A. K., & Gupta, M. (2005). Synthesis and surface engineering of iron oxide nanoparticles for biomedical applications. Biomaterials, 26(18), 3995-4021.

100. Baaziz, W., Pichon, B. P., Fleutot, S., Liu, Y., Lefevre, C., Greneche, J. M., ... & Begin-Colin, S. (2014). Magnetic iron oxide nanoparticles: reproducible tuning of the size and nanosized-dependent composition, defects, and spin canting. The Journal of Physical Chemistry C, 118(7), 3795-3810.

101. Lin, C. A. J., Sperling, R. A., Li, J. K., Yang, T. Y., Li, P. Y., Zanella, M., ... & Parak, W. J. (2008). Design of an amphiphilic polymer for nanoparticle coating and functionalization. Small, 4(3), 334-341.

102. Zhang, Y., Kohler, N., & Zhang, M. (2002). Surface modification of superparamagnetic magnetite nanoparticles and their intracellular uptake. Biomaterials, 23(7), 1553-1561.

103. Osaka, T., Matsunaga, T., Nakanishi, T., Arakaki, A., Niwa, D., & Iida, H. (2006). Synthesis of magnetic nanoparticles and their application to bioassays. Analytical and bioanalytical chemistry, 384(3), 593-600.

104. Gao, J., Gu, H., & Xu, B. (2009). Multifunctional magnetic nanoparticles: design, synthesis, and biomedical applications. Accounts of chemical research, 42(8), 1097-1107.

105. Khan, K., Rehman, S., Rahman, H. U., & Khan, Q. (2014). Synthesis and application of magnetic nanoparticles. In Nanomagnetism (pp. 135-159). One Central Press (OCP) Manchester.

106. Ahmed, M., & Douek, M. (2013). The role of magnetic nanoparticles in the localization and treatment of breast cancer. BioMed research international, 2013.

107. Rodríguez-Luccioni, H. L., Latorre-Esteves, M., Méndez-Vega, J., Soto, O., Rodríguez, A. R., Rinaldi, C., & Torres-Lugo, M. (2011). Enhanced reduction in cell viability by hyperthermia induced by magnetic nanoparticles. International journal of nanomedicine, 6, 373.

108. Jain, P. K., Huang, X., El-Sayed, I. H., & El-Sayed, M. A. (2008). Noble metals on the nanoscale: optical and photothermal properties and some applications in imaging, sensing, biology, and medicine. Accounts of chemical research, 41(12), 1578-1586.

109. Dreaden, E. C., Alkilany, A. M., Huang, X., Murphy, C. J., & El-Sayed, M. A. (2012). The golden age: gold nanoparticles for biomedicine. Chemical Society Reviews, 41(7), 2740-2779.

110. Huang, X.; El-Sayed, I. H.; Qian, W.; El-Sayed, M. A., Cancer Cell Imaging and Photothermal Therapy in the Near-Infrared Region by Using Gold Nanorods, Journal of the American Chemical Society 2006, 128, 2115-2120

111. Khlebtsov, N. G., & Dykman, L. A. (2010). Optical properties and biomedical applications of plasmonic nanoparticles. Journal of Quantitative Spectroscopy and Radiative Transfer, 111(1), 1-35.

112. Huang, X., & El-Sayed, M. A. (2010). Gold nanoparticles: optical properties and implementations in cancer diagnosis and photothermal therapy. Journal of advanced research, 1(1), 13-28.

113. Grammatikopoulos, S., Pappas, S. D., Dracopoulos, V., Poulopoulos, P., Fumagalli, P., Velgakis, M. J., & Politis, C. (2013). Self-assembled Au nanoparticles on heated Corning glass by dc magnetron sputtering: size-dependent surface plasmon resonance tuning. Journal of nanoparticle research, 15(2), 1446.

114. Peng, S., McMahon, J. M., Schatz, G. C., Gray, S. K., & Sun, Y. (2010). Reversing the size-dependence of surface plasmon resonances. Proceedings of the National Academy of Sciences, 107(33), 14530-14534.

115. Ashraf, S., Pelaz, B., del Pino, P., Carril, M., Escudero, A., Parak, W. J., ... & Carrillo-Carrion, C. (2016). Gold-based nanomaterials for applications in nanomedicine. In Light-Responsive Nanostructured Systems for Applications in Nanomedicine (pp. 169-202). Springer, Cham.

116. Yang, P., Portalès, H., & Pileni, M. P. (2011). Dependence of the localized surface plasmon resonance of noble metal quasispherical nanoparticles on their crystallinity-related morphologies. The Journal of chemical physics, 134(2), 024507.

117. Soliman, M. G., Pelaz, B., Parak, W. J., & Del Pino, P. (2015). Phase transfer and polymer coating methods toward improving the stability of metallic nanoparticles for biological applications. Chemistry of Materials, 27(3), 990-997.

118. West, J. L., & Halas, N. J. (2003). Engineered nanomaterials for biophotonics applications: improving sensing, imaging, and therapeutics. Annual Review of Biomedical Engineering, 5(1), 285-292.

119. Zhan, W., Wang, J., Wang, H., Zhang, J., Liu, X., Zhang, P., ... & Sun, S. (2017). Crystal Structural Effect of AuCu Alloy Nanoparticles on Catalytic CO Oxidation. Journal of the American Chemical Society, 139(26), 8846-8854.

120. Wang, G., Xiao, L., Huang, B., Ren, Z., Tang, X., Zhuang, L., & Lu, J. (2012). AuCu intermetallic nanoparticles: surfactant-free synthesis and novel electrochemistry. Journal of Materials Chemistry, 22(31), 15769-15774.

121. Lan, Y., Lu, Y., & Ren, Z. (2013). Mini review on photocatalysis of titanium dioxide nanoparticles and their solar applications. Nano Energy, 2(5), 1031-1045.

122. Anselmann, R. (2001). Nanoparticles and nanolayers in commercial applications. Journal of Nanoparticle Research, 3(4), 329-336.

123. Gázquez, M. J., Bolívar, J. P., Garcia-Tenorio, R., & Vaca, F. (2014). A review of the production cycle of titanium dioxide pigment. Materials Sciences and Applications, 5(07), 441.

124. Zhao, Y., Li, C., Liu, X., Gu, F., Jiang, H., Shao, W., ... & He, Y. (2007). Synthesis and optical properties of TiO2 nanoparticles. Materials Letters, 61(1), 79-83.

125. Jacobs, J. F., Van de Poel, I., & Osseweijer, P. (2010). Sunscreens with titanium dioxide (TiO 2) nano-particles: A societal experiment. Nanoethics, 4(2), 103-113.

126. Weir, A., Westerhoff, P., Fabricius, L., Hristovski, K., & Von Goetz, N. (2012). Titanium dioxide nanoparticles in food and personal care products. Environmental science & technology, 46(4), 2242-2250.

127. Ibhadon, A. O., & Fitzpatrick, P. (2013). Heterogeneous photocatalysis: recent advances and applications. Catalysts, 3(1), 189-218.

128. Malekshahi Byranvand, M., Nemati Kharat, A., Fatholahi, L., & Malekshahi Beiranvand, Z. (2013). A review on synthesis of nano-TiO2 via different methods. Journal of nanostructures, 3(1), 1-9.

129 Gupta, S., & Tripathi, M. (2012). A review on the synthesis of TiO2 nanoparticles by solution route. Open Chemistry, 10(2), 279-294.

130. Mäkelä, J. M., Haapanen, J., Harra, J., Juuti, P., & Kujanpää, S. (2017). Liquid Flame Spray—A Hydrogen-Oxygen Flame Based Method for Nanoparticle Synthesis and Functional Nanocoatings. KONA Powder and Particle Journal, 34, 141-154.

131. Sánchez-Quiles, D., & Tovar-Sánchez, A. (2014). Sunscreens as a source of hydrogen peroxide production in coastal waters. Environmental Science & Technology, 48(16), 9037-9042.

132. Skocaj, M., Filipic, M., Petkovic, J., & Novak, S. (2011). Titanium dioxide in our everyday life; is it safe?. Radiology and oncology, 45(4), 227-247.

133. Charles, S., Jomini, S., Fessard, V., Bigorgne-Vizade, E., Rousselle, C., & Michel, C. (2018). Assessment of the in vitro genotoxicity of TiO2 nanoparticles in a regulatory context. Nanotoxicology, 12(4), 357-374.

134. Albanese, A., Tang, P. S., & Chan, W. C. (2012). The effect of nanoparticle size, shape, and surface chemistry on biological systems. Annual review of biomedical engineering, 14, 1-16.

135. Iavicoli, I., Leso, V. E. R. U. S. C. K. A., Fontana, L. U. C. A., & Bergamaschi, A. (2011). Toxicological effects of titanium dioxide nanoparticles: a review of in vitro mammalian studies. Eur Rev Med Pharmacol Sci, 15(5), 481-508.

136. Pellegrino, T., Kudera, S., Liedl, T., Muñoz Javier, A., Manna, L., & Parak, W. J. (2005). On the development of colloidal nanoparticles towards multifunctional structures and their possible use for biological applications. small, 1(1), 48-63.

137. Yang, Y., Chen, O., Angerhofer, A., & Cao, Y. C. (2008). On doping CdS/ZnS core/shell nanocrystals with Mn. Journal of the American Chemical Society, 130(46), 15649-15661.

138. Kaiser, U., Sabir, N., Carrillo-Carrion, C., del Pino, P., Bossi, M., Heimbrodt, W., & Parak, W. J. (2015). Förster resonance energy transfer mediated enhancement of the fluorescence lifetime of organic fluorophores to the millisecond range by coupling to Mn-doped CdS/ZnS quantum dots. Nanotechnology, 27(5), 055101.

139. Sun, S., & Zeng, H. (2002). Size-controlled synthesis of magnetite nanoparticles. Journal of the American Chemical Society, 124(28), 8204-8205.

140. Sun, S., Zeng, H., Robinson, D. B., Raoux, S., Rice, P. M., Wang, S. X., & Li, G. (2004). Monodisperse mfe2o4 (m= fe, co, mn) nanoparticles. Journal of the American Chemical Society, 126(1), 273-279.

141. Xie, J., Peng, S., Brower, N., Pourmand, N., Wang, S. X., & Sun, S. (2006). One-pot synthesis of monodisperse iron oxide nanoparticles for potential biomedical applications. Pure and applied chemistry, 78(5), 1003-1014.

142. Zhang, Q., Castellanos-Rubio, I., Munshi, R., Orue, I., Pelaz, B., Gries, K. I., ... & Pralle, A. (2015). Model driven optimization of magnetic anisotropy of exchange-coupled core–shell ferrite nanoparticles for maximal hysteretic loss. *Chemistry of Materials*, *27*(21), 7380-7387.

143. Caballero-Díaz, E., Pfeiffer, C., Kastl, L., Rivera-Gil, P., Simonet, B., Valcárcel, M., ... & Parak, W. J. (2013). The toxicity of silver nanoparticles depends on their uptake by cells and thus on their surface chemistry. Particle & Particle Systems Characterization, 30(12), 1079-1085.

144. Cyanine 5 amine (Cy5), Lumiprobe, https://www.lumiprobe.com/p/cy5-amine

145. Brust, M., Walker, M., Bethell, D., Schiffrin, D. J., & Whyman, R. (1994). Synthesis of thiol-derivatised gold nanoparticles in a two-phase liquid–liquid system. Journal of the Chemical Society, Chemical Communications, (7), 801-802.

146. Sperling, R. A., Pellegrino, T., Li, J. K., Chang, W. H., & Parak, W. J. (2006). Electrophoretic separation of nanoparticles with a discrete number of functional groups. Advanced Functional Materials, 16(7), 943-948.

147. Hühn, J., Carrillo-Carrion, C., Soliman, M. G., Pfeiffer, C., Valdeperez, D., Masood, A., ... & Carril, M. (2016). Selected standard protocols for the synthesis, phase transfer, and characterization of inorganic colloidal nanoparticles. Chemistry of Materials, 29(1), 399-461.

148. Gordon, T. R., Cargnello, M., Paik, T., Mangolini, F., Weber, R. T., Fornasiero, P., & Murray, C. B. (2012). Nonaqueous synthesis of TiO2 nanocrystals using TiF4 to engineer morphology, oxygen vacancy concentration, and photocatalytic activity. Journal of the American Chemical Society, 134(15), 6751-6761.

149. Cozzoli, P. D., Kornowski, A., & Weller, H. (2003). Low-temperature synthesis of soluble and processable organic-capped anatase TiO2 nanorods. Journal of the American Chemical Society, 125(47), 14539-14548.

Publications

Indranath Chakraborty, Dorleta Jimenez de Aberasturi, Nicolas Pazos-Perez, Luca Guerrini, Atif Masood, Ramon A. Alvarez-Puebla, Neus Feliu and Wolfgang J. Parak*

Ion-Selective Ligands: How Colloidal Nano- and Micro-Particles Can Introduce New Functionalities

https://doi.org/10.1515/zpch-2018-1172
Received March 2, 2018; accepted April 8, 2018

Abstract: Colloidal nano- and micro-particles can introduce new properties and functionalities to existing materials and thus are a valuable building block for the construction of novel materials. This is discussed for the case of ion-selective ligands, hence molecules that can bind specifically ions of one type. First, in case ion-selective fluorescent ligands are attached to the surface of particles, these fluorophores sense the local ion concentration at the particle surface and not the bulk ion concentration. Thus, the ion-response of the ligands can be tuned by attaching them to the surface of particles. Second, in case ligands specific for particular ions are bound to the surface of particles, these ions can provide contrast and thus the particles can be imaged. This involves for example Gd-ions, which provide contrast for magnetic resonance imaging (MRI), and ^{111}In-ions, which provide contrast for imaging of radioactivity. By attaching the ligands to the surface of particles, their physicochemical properties (as for example size and solubility) are changed, which affects their interaction with cells and, consequently, biodistribution. Attachment of ion-chelators for imaging to particles thus allows for tuning their

***Corresponding author: Wolfgang J. Parak,** Faculty of Physics, Center for Hybrid Nanostructures (CHyN), Universität Hamburg, Hamburg, Germany; and CIC Biomagune, San Sebastian, Spain, e-mail: wolfgang.parak@uni-hamburg.de
Indranath Chakraborty: Faculty of Physics, Center for Hybrid Nanostructures (CHyN), Universität Hamburg, Hamburg, Germany
Dorleta Jimenez de Aberasturi: CIC Biomagune, San Sebastian, Spain
Nicolas Pazos-Perez and Luca Guerrini: Universitat Rovira i Virgili, Department of Physical and Inorganic Chemistry – EMaS, Tarragona, Spain
Atif Masood: Faculty of Physics, Philipps Universität Marburg, Marburg, Germany
Ramon A. Alvarez-Puebla: Department of Physical Chemistry, Universitat Rovira i Virgili, Tarragona, Spain; and ICREA, Barcelona, Spain
Neus Feliu: Faculty of Physics, Center for Hybrid Nanostructures (CHyN), Universität Hamburg, Hamburg, Germany; and Department of Laboratory Medicine (LABMED), Karolinska Institutet, Stockholm, Sweden

biodistribution. Third, ion-specific ligands can be also attached to the surface of magnetic particles. In this case ions bound to the ligands can be extracted with magnetic field gradients and magnetic separation becomes possible. Therefore, magnetic particles provide a handle to the ligands, which enables the extraction of ions from solution. These examples demonstrate how the attachment of different types of colloidal particles to one existing class of molecules, ion-selective ligands, can open new fields of applications of these molecules.

Keywords: ion-selective ligands; microparticles; nanoparticles; surface chemistry.

1 Introduction

Colloidal micro- and nanoparticles (NPs) are of greatest interest to the scientific community owing to their distinctive properties that could potentially contribute to promising applications in energy [1], biomedicine [2], electronics and sensing [3]. Their small size gives them a high surface area-to-volume ratio and facilitates the interaction with several kinds of chemical species. The functional properties from the NPs can either arise from the NP cores (such as for example plasmonic properties of Au NPs), or the surface coatings around the NP cores. Also, the combination of core and coating functionalities is possible [4]. For some applications such as imaging, where small size is required, the use of colloidal NPs with the size of a few 10 nm is a promising approach. However, for other applications such as drug delivery, micrometer-sized polyelectrolyte capsules as NPs carriers may be more suitable [5]. The size of these capsules ranges from hundreds of nanometers to a few micrometers, depending on the size of the template which is used for the synthesis [6].

In this review, an overview will be given on how the functional properties of NP cores can add additional functionality to an existing class of materials, ion-selective ligands. Hereby ion-selective ligands will be integrated into NPs. The chemistry of linking ion-selective ligands with NPs of different size will be discussed in the first section. In the subsequent sections, examples of nanometer- and micrometer-sized particles functionalized with ion-selective ligands will be discussed and, also, we will examine how the presence of the NPs affects the properties of the ion-selective ligands.

1.1 Attachment of ion-selective ligand to the surface of colloidal nanoparticles

Often inorganic NPs are synthesized in organic surfactant mixtures, which render hydrophobic, preventing water solubility [7]. However, for several applications,

especially for biomedical purposes, it is necessary to use water-soluble NPs. Different ways enabling the transfer of NPs from an organic to an aqueous solvent are conceivable, including ligand exchange [8], silica-shell encapsulation [9] or polymer encapsulation [10–12]. All of them are commonly used strategies, but, in this article, focus will be given to the polymer encapsulation method. Hereby originally hydrophobic NPs are over-coated with an amphiphilic polymer [13]. This does not only provide the advantage to disperse originally hydrophobic NPs in aqueous solution, but also allows integration of molecules with different functionalities, such as ion-selective ligands, into the polymer shell around the particles [13]. This gives the possibility to build selective particles with multiple functionalities due to the properties inherited from the inorganic NP core and those originating from the ligand molecules which are integrated into the polymer shell [4]. The polymer shell provides high colloidal stability, which prevents the NPs from agglomeration. This is important to keep the functionality of the attached ligands, as agglomeration would reduce the effective surface area of the NPs and thus decrease the number of accessible ligands.

In the following section one prominent example of an amphiphilic polymer used for polymer coating of NPs is detailed [7]. The hydrophilic backbone of this amphiphilic polymer consists of maleic anhydride rings [poly(isobutylene-*alt*-maleic anhydride). To this backbone, hydrophobic sidechains (amine-terminated hydrocarbons) are covalently attached *via* amide bond formation. The amphiphilic polymer is wrapped around the hydrophobically capped NPs by intercalation of the hydrocarbon chains present in both species [13]. Thus the hydrophilic backbone of the polymer is facing outside and determines the surface chemistry of the NPs. After transfer to an aqueous solvent the anhydride rings open, resulting in the presence of carboxylic groups at the surface of the NP, which warrants for water-solubility [13]. The polymer can be pre-functionalized with (ion-selective) ligands before the actual coating process (pre-modification), which is advantageous for the attachment of hydrophobic ligands. The polymer which is already attached to the NP surface also can be post-modified with additional (ion-selective) ligands containing e.g. a free amino group enabling the formation of amide bonds. For this procedure, 1-ethyl-3-(3-dimethylaminopropyl) carbodiimide] (EDC) is commonly used to activate the carboxyl groups [14]. A scheme of the polymer with multiple functionalized molecules is shown in Figure 1.

1.2 Loading of ion-selective ligands into poly-electrolyte microcapsules

Poly-electrolyte microcapsules are an example for bigger NPs, most often ranging from a few 100 nm to a few micrometers. The walls of the capsules are assembled

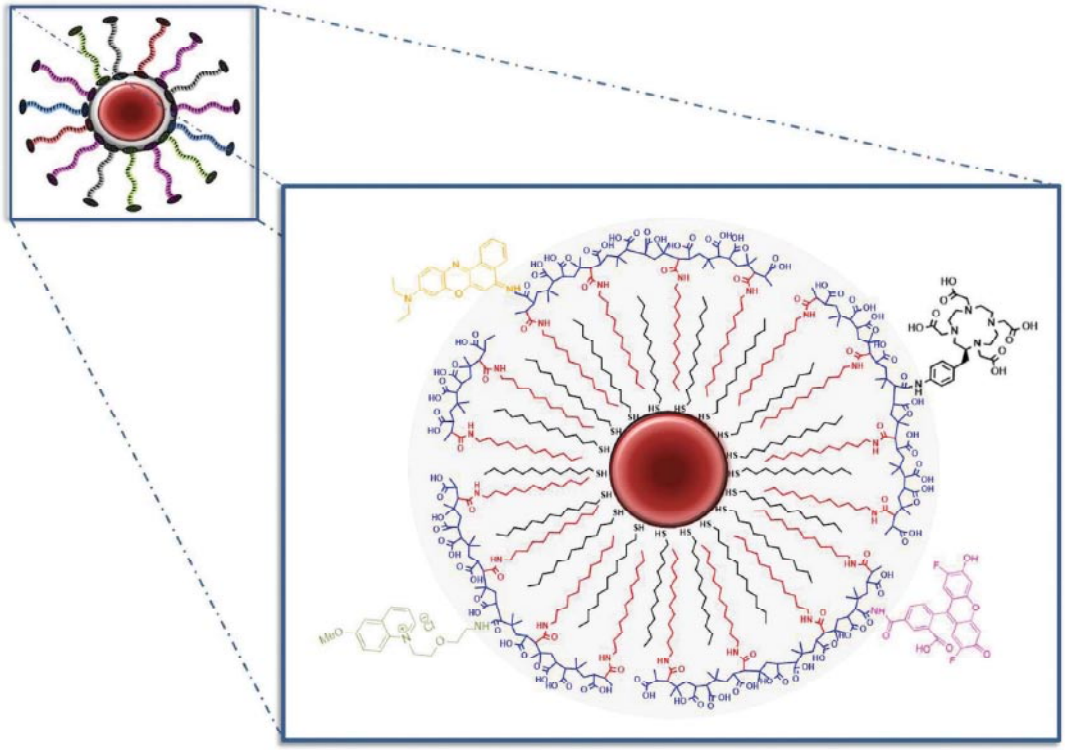

Fig. 1: Schematic illustration of the structure of a NP coated with an amphiphilic polymer, which is functionalized with ion-selective ligands. The enlarged image shows the structure of the amphiphilic polymer, consisting of a hydrophilic backbone (drawn in blue) and hydrophobic side chains (drawn in red). The hydrocarbon chains are covalently linked to the carboxylic groups of the hydrophilic polymer backbone *via* amide bonds. The side chains are intercalating the hydrophobic surfactants of the NP surface (drawn in black). Other functional (ion-selective) ligand molecules containing a primary amino group can be linked directly to the unreacted carboxylic groups of the polymer *via* amide bond formation (drawn in orange, violet, green and black).

by the so-called layer-by-layer (LBL) technique, in which oppositely charged polyelectrolytes are deposited subsequently around a template core, such as calcium carbonate [15]. After the dissolution of the template, a permeable membrane around a cavity is formed [16]. The cavities can be loaded with a large variety and high quantity of cargo (e.g. ion specific ligands) [17, 18]. Large molecules such as proteins will be readily kept inside the cavity as they are big enough so that their diffusion outside capsules is prevented. Small molecules, like most ion-specific ligands, need to be linked to macromolecules such as dextran [19] or have to be embedded inside micelles [20] in order to be retained in the capsule cavities. Moreover, the walls of the capsules can also be functionalized with NPs or other molecules such as fluorescent dyes or ion specific ligands. Here, the functionality can be embedded in-between the polyelectrolyte layers *via* electrostatic interac-

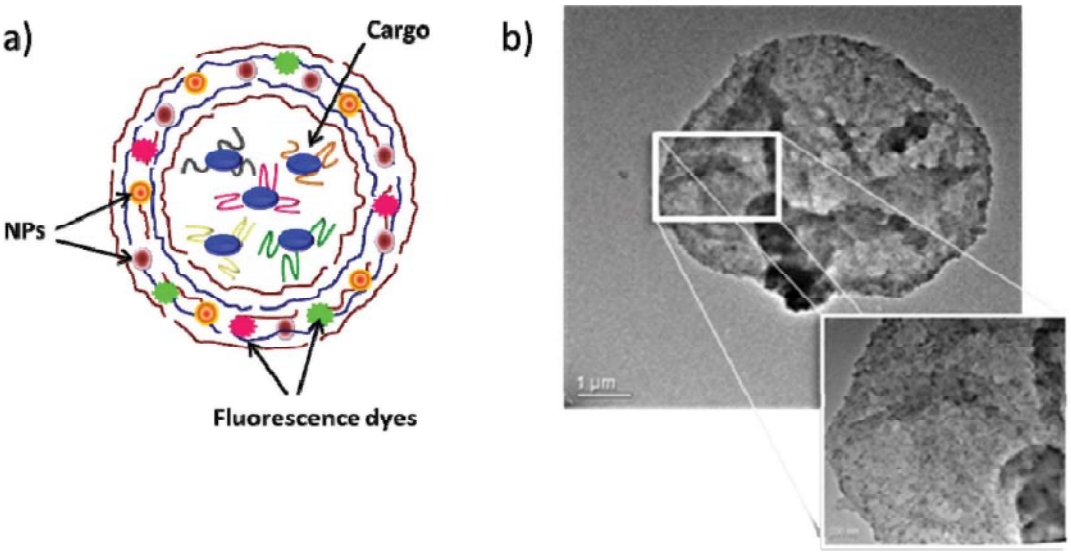

Fig. 2: (a) Schematic illustration of a capsule with walls assembled by LBL deposition of negatively (brown) and positively (blue) charged polyelectrolytes. Different types of NPs (orange and red) and molecules like ion-selective ligands and fluorophores (pink and green) are embedded in the wall. The cavity of the capsule is loaded with a cargo (blue) equipped with additional (ion-selective) ligands. (b) A transmission electron microscopy (TEM) image of a capsule with magnetic Fe_2O_3 NPs in its wall. In the enlarged excerpt individual NPs can be recognized.

tion or can be covalently bound to one of the polyelectrolytes. A sketch of the NP geometry is shown in Figure 2.

2 Ion sensing using ion-selective ligands bound to colloidal particles

There are many ion-selective ligands available and used in literature. Typically, in case of ion-selective fluorophores, after binding of the respective target ion to the fluorophore, the intensity or spectrum of the fluorescence emission is changed, which forms the bases for concentration-determination of these ions [21]. In case ion-selective ligands are attached to NPs, their properties change and thus new sensing schemes arise [22–24]. Fluorescence-based detection of ions by molecular recognition with ion-selective fluorophores can be tuned with non-fluorescent NPs such as Au NPs. Here the NPs serve as carriers and the active fluorescence readout is directly provided by the ion-selective fluorophores functionalized on the NP surface. Attachment of the ligand-selective fluorophores to carrier NPs has several advantages. First, hydrophobic ion-selective fluorophores can be used, which by themselves would not be soluble in aqueous

solution. By connecting the ligands (i.e. the fluorophores) to the surface of water-soluble NPs they adopt the physicochemical properties (e.g. solubility, polarity) of the NPs and thus can be used in aqueous environment. In other words, the originally hydrophobic ligands are converted to hydrophilic entities by attaching them to hydrophilic NPs. Second, multiple functionalization at the NP surface with different ion-selective ligands is possible, enabling the simultaneous detection of various specimens with a single system. Third, the presence of the NP surface changes the conditions in close proximity to the ion-selective fluorophores [25]. Herein the major factor is the charge of the NP surface, as it directly influences the distribution of ions around a NP by attraction of counter ions due to Debye–Hückel screening. An ion-selective fluorophore closely attached to the surface of a NP thus generates an ion-dependent fluorescence response which differs from the response that the free fluorophore would generate for the same bulk ion concentration. In other words, an ion-selective fluorophore closed to the surface of a NP senses the local ion concentration at the NP surface, which can be very different from the bulk ion concentration, see Figure 3 [26, 27]. Theoretical models include calculations based on the solution of the Poisson–Boltzmann equation [28–30] or more accurate tools based on the classical density functional theory (DFT) [31]. However, to our knowledge, there is still a lack of synergy between those theoretical models and recent experimental studies.

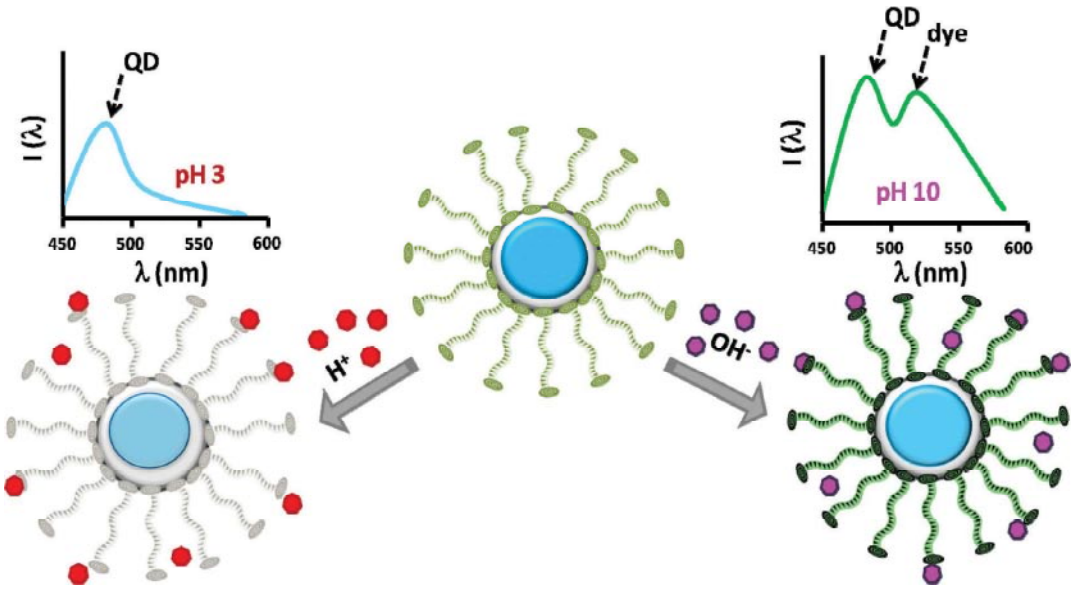

Fig. 3: Example of a FRET-based pH-sensor formed by an underlying QD and OG as an ion-sensitive ligand in the polymer shell (cf. Figure 1 about the geometry) around it. Scheme of the sensor mechanism under different pH conditions, including the fluorescence spectra of the OG-functionalized QDs at 450 nm excitation [26].

Nevertheless, the response of an ion-selective fluorophore close to a NP surface to the presence of ions will be different to the one of a free ion-selective fluorophore. By variation of the distance between the ion-selective fluorophore and the NP surface its response can be tuned. In case the distance between the NP surface and the dye molecule is increased *via* a molecular spacer, the vicinity of the dye becomes more similar to the bulk conditions regarding local ion concentration [27]. This strategy was effectively carried out for the case of a negatively charged NP surface and a Cl^- sensitive dye [32]. Herein the charge was generated by carboxylic groups which were part of the amphiphilic polymer (as depicted in Figure 1) that enabled the transfer of the Au NPs to an aqueous solvent. The carboxylic groups also served as anchor points for the attachment of Cl^--sensitive dye molecules. Those were either directly linked to the NP surface or with a spacer molecule in-between *via* amide bond formation. In this way the presence of the underlying NP surface allows for tuning of the response characteristics of attached ion-selective ligands.

3 *In vivo* imaging using metal ions bound *via* ion-selective ligands to colloidal nanoparticles

Magnetic resonance imaging (MRI) is one of the most powerful techniques in diagnostic clinical medicine and biomedical research to enhance the contrast between normal and diseased tissues or to indicate organ functions or blood flow [33]. Many metals which belong to the lanthanide and transition metal series have paramagnetic properties, which make them likely candidates for MRI contrast agents [34]. Regarding the large variety of metals and compounds tested, Gd(III) has been established as one of the best contrast agents due to its large magnetic moment [35]. However, Gd(III) needs to be chelated by ion selective ligands, as free Gd is toxic [36]. In this approach NPs modified with Gd-selective ligands are a great alternative for imaging [37]. γ-emitters such as ^{111}In can be used for radioactive imaging, but also here toxicity needs to be taken into account. Chelators, i.e. ion-selective ligands, like diethylenetriaminepentacetate (DTPA) and 1,4,7,10-tetraazacyclododecane-1,4,7,10-tetraacetic acid (DOPA) have been used frequently for chelating Gd(III) and In(III). In case those chelators are attached to the surface of NPs [4, 38], for example by the already described amphiphilic polymer (see Figure 4), the physicochemical properties of the chelator change to the ones of the underlying NP. This affects the biodistribution of the chelator. A free metal ion-chelator complex will have a different biodistribution that a metal ion-chelator complex bound to the surface of an NP [38].

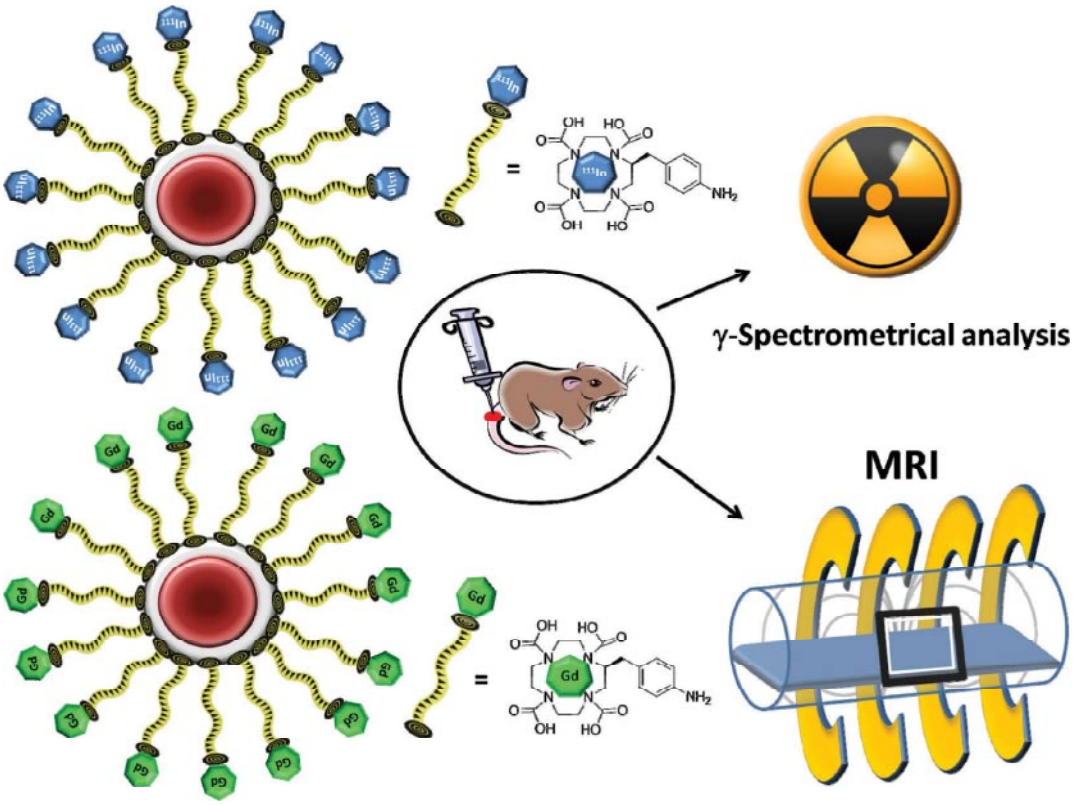

Fig. 4: Schematics of chelator functionalized NPs for different contrast based bio-imaging modalities.

Having the ability to tune the biodistribution (and in this way also potentially targeted delivery) of such contrast agents offers useful opportunities for imaging applications.

4 Magnetic separation of ions caught by ion-selective ligands using colloidal nanoparticles

Platinum group metals (PGMs) are widely used in car catalytic converters [39–41]. Palladium together with platinum is the most used metal for catalyst devices. Platinum, palladium, and rhodium are generally fixed in the washcoat surface of catalytic converters [42]. Due to their high economic value it is desirable to recover these metals once catalytic converters are disposed. In the typical PGMs recovery process, PGMs are extracted from scraps by smelting them with collec-

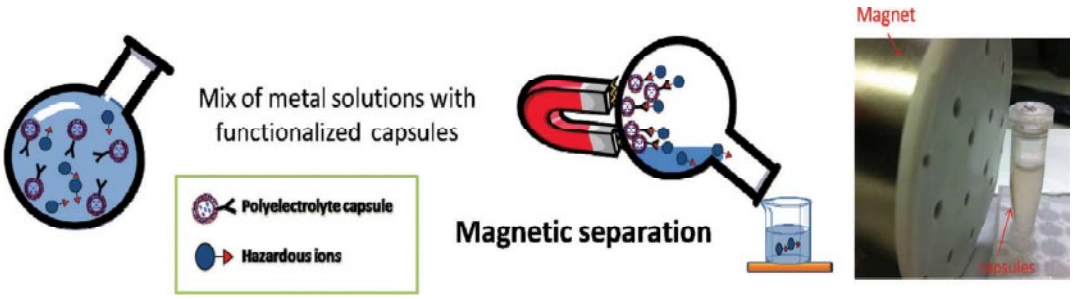

Fig. 5: Schematic illustration of ion adsorption process using magnetic capsules.

tor metals such as copper, or dissolving the scraps in strong acids [43]. Once the metals are extracted, those of interest are typically dissolved in aqueous solution. Therefore, in order to be reused, a selective recovery must be done. First, different metal ions have to be recognized, which for example is possible by ion-selective ligands such as thriacrown ester compounds. Extraction could now be facilitated by linkage of the ion-selective ligands to the surface of magnetic NPs [44]. The magnetic NPs would add a "handle" to the ion-selective ligands, which allows for "pulling them out" by magnetic field gradients, Figure 5. One of the major problems is, that magnetic NPs which are not agglomerated are difficult to extract by magnetic field gradients, as their magnetic moment is too small. For small NPs randomly directed Brownian forces at room temperature are larger than directed magnetic forces which would be achieved for example by a handheld household magnet. However, if NPs are agglomerated, a large part of the active surface, i.e. the ion-selective ligands may not be accessible and the rate of adsorption of ions will decrease. Therefore, NPs should rather stay dispersed in solution [45, 46]. Using multilayer polyelectrolyte capsules containing magnetic NPs in their walls [47] and ion-selective ligands in their cavity, the above mentioned problem might be solved. By linking several magnetic NPs to the matrix of one carrier, magnetic separation of the NPs would be facilitated. By applying an external magnetic field the separation of such capsules from the aqueous phase has been demonstrated to be fast and easy (see Figure 5) [48]. Thus, the property of ion-selective ligands to bind to PGMs can be supplemented by a "handle" if linked to magnetic NPs.

5 Conclusions

In this work different examples of NPs functionalized with ion-selective ligands either on their surface, or in their cavities, were presented. Connection to the NPs gave the ion-sensitive ligands new properties and thus enlarged their perspective

fields of applications. These examples demonstrate how the attachment of different types of colloidal NPs to one existing class of molecules, ion-selective ligands, can open new fields of applications of these molecules.

Acknowledgements: This work was supported by the Deutsche Forschungsgemeinschaft (grant DFG grant PA 794/25-1). IC acknowledges the Alexander von Humboldt foundation. This work was funded by the Spanish Ministerio de Economia y Competitividad (CTQ2014-59808R, CTQ2017-88648-R, RYC2015-19107 and RYC2016-20331), the Generalitat de Cataluña (2017SGR883), and the Universitat Rovira i Virgili (2017PFR-URV-B2-02 and 2017EXIT-08). NF acknowledges the Swedish Governmental Agency for Innovation Systems (VINNOVA). AM acknowledges the Higher Education Commission (HEC) and Deutscher Akademischer Austauschdienst (DAAD).

References

1. Q. Zhang, E. Uchaker, S. L. Candelaria, G. Cao, Chem. Soc. Rev. **42** (2013) 3127.
2. O. V. Salata, J. Nanobiotechnol. **2** (2004) 3.
3. P. C. Ray, Chem. Rev. **110** (2010) 5332.
4. Z. Ali, A. Z. Abbasi, F. Zhang, P. Arosio, A. Lascialfari, M. F. Casula, A. Wenk, W. Kreyling, R. Plapper, M. Seidel, R. Niessner, J. Knoll, A. Seubert, W. J. Parak, Anal. Chem. **83** (2011) 2877.
5. H. Mohwald, H. Lichtenfeld, S. Moya, A. Voigt, H. Baumler, G. Sukhorov, F. Caruso, E. Donath, Macromol. Symp. **145** (1999) 75.
6. Y. Wang, A. S. Angelatos, F. Caruso, Chem. Mater. **20** (2008) 848.
7. J. Hühn, C. Carrillo-Carrion, M. G. Soliman, C. Pfeiffer, D. Valdeperez, A. Masood, I. Chakraborty, L. Zhu, M. Gallego, Z. Yue, M. Carril, N. Feliu, A. Escudero, A. M. Alkilany, B. Pelaz, P. del Pino, W. J. Parak, Chem. Mater. **29** (2017) 399.
8. A. M. Smith, H. Duan, M. N. Rhyner, G. Ruan, S. Nie, Phys. Chem. Chem. Phys. **8** (2006) 3895.
9. T. Ung, L. M. Liz-Marzán, P. Mulvaney, J. Phys. Chem. B **103** (1999) 6770.
10. T. Pellegrino, L. Manna, S. Kudera, T. Liedl, D. Koktysh, A. L. Rogach, S. Keller, J. Rädler, G. Natile, W. J. Parak, Nano Lett. **4** (2004) 703.
11. W. Wang, X. Ji, A. Kapur, C. Zhang, H. Mattoussi, J. Am. Chem. Soc. **137** (2016) 14158.
12. W. Wang, A. Kapur, X. Ji, B. Zeng, D. Mishra, H. Mattoussi, Bioconjug. Chem. **27** (2016) 2024.
13. C.-A. J. Lin, R. A. Sperling, J. K. Li, T.-Y. Yang, P.-Y. Li, M. Zanella, W. H. Chang, W. J. Parak, Small **4** (2008) 334.
14. R. A. Sperling, T. Pellegrino, J. K. Li, W. H. Chang, W. J. Parak, Adv. Funct. Mater. **16** (2006) 943.
15. G. Decher, Science **277** (1997) 1232.
16. P. Rivera Gil, L. L. del Mercato, P. del Pino, A. Muñoz Javier, W. J. Parak, Nano Today **3** (2008) 12.

17. L. J. De Cock, S. De Koker, B. G. De Geest, J. Grooten, C. Vervaet, J. P. Remon, G. B. Sukhorukov, M. N. Antipina, Angew. Chem. Int. Ed. **49** (2010) 6954.
18. S. De Koker, B. G. De Geest, S. K. Singh, R. De Rycke, T. Naessens, Y. Van Kooyk, J. Demeester, S. C. De Smedt, J. Grooten, Angew. Chem. Int. Ed. **48** (2009) 8485.
19. O. Kreft, A. M. Javier, G. B. Sukhorukov, W. J. Parak, J. Mater. Chem. **17** (2007) 4471.
20. W. Tong, Y. Zhu, Z. Wang, C. Gao, H. Möhwald, Macromol. Rapid Commun. **31** (2010) 1015.
21. O. S. Wolfbeis, Sens. Actuators B Chem. **29** (1995) 140.
22. B. Hötzer, I. L. Medintz, N. Hildebrandt, Small **8** (2012) 2297.
23. M. J. Ruedas-Rama, J. D. Walters, A. Orte, E. A. H.Hall, Anal. Chim. Acta **751** (2012) 1.
24. S. Carregal-Romero, E. Caballero-Díaz, L. Beqa, A. M. Abdelmonem, M. Ochs, D. Hühn, B. S. Suau, M. Valcarcel, W. J. Parak, Annu. Rev. Anal. Chem. **6** (2013) 53.
25. S. Jailani, G. V. Franks, T. W. Healy, J. Am. Ceram. Soc. **91** (2008) 1141.
26. F. Zhang, E. Lees, F. Amin, P. Rivera_Gil, F. Yang, P. Mulvaney, W. J. Parak, Small **7** (2011) 3113.
27. F. Zhang, Z. Ali, F. Amin, A. Feltz, M. Oheim, W. J. Parak, ChemPhysChem **11** (2010) 730.
28. H. Ohshima, T. W. Healy, L. R. White, J. Colloid Interface Sci. **90** (1982) 17.
29. J. J. Lopez-Garcia, J. Horno, C. Grosse, Phys. Chem. Chem. Phys. **3** (2001) 3754.
30. H. Ohshima, J. Colloid Interface Sci. **323** (2008) 92.
31. J. Z. Wu, Z. D. Li, Annu. Rev. Phys. Chem. **58** (2007) 85.
32. A. Riedinger, F. Zhang, F. Dommershausen, C. Röcker, S. Brandholt, G. U. Nienhaus, U. Koert, W. J. Parak, Small **6** (2010) 2590.
33. M. P. Morales, O. Bomati-Miguel, R. P. De Alejo, J. Ruiz-Cabello, S. Veintemillas-Verdaguer, K. O'Grady, J. Magn. Magn. Mater. **266** (2003) 102.
34. P. Sharma, S. Brown, G. Walter, S. Santra, B. Moudgil, Adv. Colloid Interface Sci. **123–126** (2006) 471.
35. S. Aime, C. Cabella, S. Colombatto, S. Geninatti Crich, E. Gianolio, F. Maggioni, J. Magn. Reson. Imaging **16** (2002) 394.
36. A. N. Oksendal, P. A. Hals, J. Magn. Reson. Imaging **3** (1993) 157.
37. A. Bianchi, L. Calabi, F. Corana, S. Fontana, P. Losi, A. Maiocchi, L. Paleari, B. Valtancoli, Coord. Chem. Rev. **204** (2000) 309.
38. W. G. Kreyling, A. M. Abdelmonem, Z. Ali, F. Alves, M. Geiser, N. Haberl, R. Hartmann, S. Hirn, D. J. De Aberasturi, K. Kantner, G. Khadem-Saba, Nat. Nanotechnol. **10** (2015) 619.
39. T. N. Angelidis, E. Skouraki, Appl. Catal. A Gen. **142** (1996) 387.
40. C. Nowottny, W. Halwachs, K. Schügerl, Sep. Purif. Technol. **12** (1997) 135.
41. M. Baghalha, G. H. Khosravian, H. R. Mortaheb, Hydrometallurgy **95** (2009) 247.
42. M. Moldovan, S. Rauch, G. M. Morrison, M. Gomez, M. Antonia Palacios, Surf. Interface Anal. **35** (2003) 354.
43. M. Faisal, Y. Atsuta, H. Daimon, K. Fujie, Asia Pac. J. Chem. Eng. **3** (2008) 364.
44. C. T. Yavuz, J. T. Mayo, W. Y. William, A. Prakash, J. C. Falkner, S. Yean, L. Cong, H. J. Shipley, A. Kan, M. Tomson, D. Natelson, Science **314** (2006) 964.
45. K. Mandel, F. Hutter, Nano Today **7** (2012) 485.
46. G. De Las Cuevas, J. Faraudo, J. Camacho, J. Phys. Chem. C **112** (2008) 945.
47. A. Z. Abbasi, L. Gutiérrez, L. L. del Mercato, F. Herranz, O. Chubykalo-Fesenko, S. Veintemillas-Verdaguer, W. J. Parak, M. P. Morales, J. M. González, A. Hernando, P. de la Presa, J. Phys. Chem. C **115** (2011) 6257.
48. B. Zebli, A. S. Susha, G. B. Sukhorukov, A. L. Rogach, W. J. Parak, Langmuir **21** (2005) 4262.

Science of the Total Environment 568 (2016) 819–828

Contents lists available at ScienceDirect

Science of the Total Environment

journal homepage: www.elsevier.com/locate/scitotenv

Quantitative uptake of colloidal particles by cell cultures

Neus Feliu [a,b], Jonas Hühn [a], Mikhail V. Zyuzin [a], Sumaira Ashraf [a], Daniel Valdeperez [a], Atif Masood [a], Alaa Hassan Said [a,f], Alberto Escudero [a,g], Beatriz Pelaz [a], Elena Gonzalez [a,c], Miguel A. Correa Duarte [c], Sathi Roy [a], Indranath Chakraborty [d], Mei L. Lim [b], Sebastian Sjöqvist [b], Philipp Jungebluth [h], Wolfgang J. Parak [a,e,*]

[a] Department of Physics, Philipps University Marburg, Marburg, Germany
[b] Department for Clinical Science, Intervention and Technology (CLINTEC), Karolinska Institutet, Stockholm, Sweden
[c] University of Vigo, Vigo, Spain
[d] Department of Chemistry, University of Illinois at Urbana Champaign, Urbana, IL, USA
[e] CIC biomaGUNE, San Sebastian, Spain
[f] Physics Department, Faculty of Science, South Valley University, Egypt
[g] Instituto de Ciencia de Materiales de Sevilla, CSIC — Universidad de Sevilla, Seville, Spain
[h] Department of Thoracic Surgery, Thoraxklinik, Heidelberg University, Heidelberg, Germany

HIGHLIGHTS

- Colloids are endocytosed by cells.
- Distinguishing internalized (endocytosed) *versus* membrane-attached colloids
- The importance of metrics in the context of quantification of internalized colloids
- Correlation of cellular uptake of colloids with their physicochemical properties
- Immersion in biological fluids changes the physicochemical properties of colloids.
- Stability of colloids upon internalization

ARTICLE INFO

Article history:
Received 20 December 2015
Received in revised form 29 May 2016
Accepted 30 May 2016
Available online 13 June 2016

Keywords:
Nanoparticles
Uptake
Colloids
Cellular internalization
Toxicity
Gold particles
Quantum dots
Nanosafety

ABSTRACT

The use of nanotechnologies involving nano- and microparticles has increased tremendously in the recent past. There are various beneficial characteristics that make particles attractive for a wide range of technologies. However, colloidal particles on the other hand can potentially be harmful for humans and environment. Today, complete understanding of the interaction of colloidal particles with biological systems still remains a challenge. Indeed, their uptake, effects, and final cell cycle including their life span fate and degradation in biological systems are not fully understood. This is mainly due to the complexity of multiple parameters which need to be taken in consideration to perform the nanosafety research. Therefore, we will provide an overview of the common denominators and ideas to achieve universal metrics to assess their safety. The review discusses aspects including how biological media could change the physicochemical properties of colloids, how colloids are endocytosed by cells, how to distinguish between internalized *versus* membrane-attached colloids, possible correlation of cellular uptake of colloids with their physicochemical properties, and how the colloidal stability of colloids may vary upon cell internalization. In conclusion three main statements are given. First, in typically exposure scenarios only part of the colloids associated with cells are internalized while a significant part remain outside cells attached to their membrane. For quantitative uptake studies false positive counts in the form of only adherent but not internalized colloids have to be avoided. pH sensitive fluorophores attached to the colloids, which can discriminate between acidic endosomal/lysosomal and neutral extracellular environment around colloids offer a possible solution. Second, the metrics selected for uptake studies is of utmost importance. Counting the internalized colloids by number or by volume may lead to significantly different results. Third, colloids may change their physicochemical properties along their life cycle, and appropriate characterization is required during the different stages.

* Corresponding author at: Department of Physics, Philipps University Marburg, Marburg, Germany.
E-mail address: wolfgang.parak@physik.uni-marburg.de (W.J. Parak).

http://dx.doi.org/10.1016/j.scitotenv.2016.05.213
0048-9697/

1. Introduction

Due to the increased industrial usage of nanoparticles (NPs) and microparticles (hereafter, both will be simply referred as particles or colloids), our environment is increasingly exposed to such colloids (Mani et al., 2015). Nowadays, a wide range of nanomaterials are engineered for a variety of purposes, including medical applications. In addition to that, a lot of waste is mechanically and biologically degraded into small colloidal fragments (Sharma et al., 2015). Based on that, evaluation of potential risk of colloids associated to human exposure, production, fate, toxicity, *etc.*, became important aspects to investigate. A variety of studies addressing the interactions of colloids with cells and mechanism of their toxicity are found. In order to understand how biological environment copes with exposure to colloids, it is important to understand the basic mechanisms. A first step into this direction is to correlate the physicochemical properties of colloids to their effects on human health and environment, as well as for desired application. Such particle-cell studies will also benefit the development of future nanomedicines, *i.e.* providing guidelines facilitating specific delivery to the target sides. One important aspect is the amount of internalized particles. One may assume that in general toxicity of particles is bigger for internalized than for extracellular particles. Therefore, a better understanding of the uptake routes of colloids in cells is required, which will lead to comprehend and develop the targeting strategies for successful delivery systems.

While many exposure scenarios are complex, studying the uptake of colloids with well-defined properties with cell systems and to analyze their effects *in vitro* are a good start towards a fundamental understanding. Such approaches can be used for the investigation of main mechanisms, but obviously the complexity of *in vivo* cell environments cannot be emulated to a full extent. In other words, in basic *in vitro* studies complexity is sacrificed for simplicity.

In general, when cells are exposed to colloids of sizes ranging from nanometer to lower micrometer scale, they take the majority of these particles mostly through endocytosis-like mechanisms (Nazarenus et al., 2014; Iversen et al., 2011; Sahay et al., 2010). However, there are a few studies claiming that colloids could also translocate through the cell membrane *via* a passive mechanisms, such as transient pore formation. While under some restricted conditions (*i.e.* very small size) such scenarios may exist, endocytosis is the dominant pathway of particle entry in cells.

The sensing and entry portal responsible for the cellular uptake of colloids depends, to some extend, on the physicochemical properties of the materials (Lerch et al., 2013; Meng et al., 2011; Schweiger et al., 2012). There are many basic physicochemical properties of colloids such as size, shape, surface charge, stiffness, catalytic reactivity, *etc.* However, many of them are interconnected (Rivera Gil et al., 2013). Changes in one physicochemical property can significantly affect other properties of the colloids. In general it is thus not straight forward to design studies in which only one physicochemical parameter is varied, while the others are kept constant. Furthermore, the properties of particles may change over time (Bastus et al., 2008; Casals et al., 2014, 2010; Soenen et al., 2015). This in particular becomes true in case colloids have been internalized by cells (Kreyling et al., 2015; Feliu et al., 2016a). In this way the particle properties are dependent on multiple parameters and for this reason, knowledge is still not comprehensive (Krug, 2014). Those factors are very important to be consider when evaluating the potential use of colloids for biomedical application, as well as for evaluating their possible risks of usage (nanosafety profile). Still, while in general conclusions on how physicochemical properties of colloids relate with cellular effects, including uptake are reported frequently in literature, we emphasize that further investigation on nanoparticle-cell interaction is required (Torrano et al., 2013).

Also the metrics to define the amount of colloids to which cells are exposed, is still subject to interpretation. On the other hand, the metrics to quantify the uptake of colloids by cells is crucial for quantitative analysis (Taylor et al., 2014; Feliu et al., 2016b; Oberdörster et al., 2005). In fact different groups apply different metrics, which complicates meta-analytic comparison among different literature results. In this review a brief discussion of these aspects will be explored, with the aims to find out a common denominators and ideas to achieve a universal metrics to assess the interaction of colloids by cells (see Scheme 1).

In the present review the toxicology responses of cells to particles are not deeply discussed, neither targeting strategies for directing the biodistribution of particles. Instead, focus is given about pointing out selected fundamental concepts concerning the cellular uptake of colloids. However the aspects discussed could be applied in the context toxicology, targeting, *etc.*

2. Colloids are endocytosed by cells

On regard to endocytosis, there are many different endocytosis-pathways that might be involved (Canton and Battaglia, 2012; Mayor and Pagano, 2007; Conner and Schmid, 2003). Textbooks report two main endocytic pathways occurring in cells. Phagocytosis is mainly employed for phagocytic cells such as macrophages, or epithelial cells. Pinocytosis employs for most eukaryotic cells. This endocytic pathway can be further divided in different subcategories, such as macropinocytosis, clathrin- and caveolae-mediated endocytosis, as well as clathrin- and caveolae-independent endocytosis (Yameen et al., 2014). Endocytosis is the predominant pathway for particle entry into cells. Importantly, colloids can also be exocytosed. The intracellular localization and final destination of colloids will depend on the uptake mechanisms (pathways) (Beddoes et al., 2015). The pathway will be determined by the different properties such size, shape, surface chemistry, *etc.* of colloids, and by the type of cells that are exposed. Both, the synthetic and biological identities of the material (Fadeel et al., 2013) have a key role in determining how cells sense colloids and how this dictates their uptake mechanisms (Florez et al., 2012; He et al., 2010). This applies for both, passive and active delivery strategies. We refer to passive cell delivery as the "nonspecific" uptake processes that merely depends on the basic physicochemical properties of the particles, whereas for active or targeted delivery to cells, we refer to particles carrying specific delivery agents, such as ligand, peptides, *etc.* (Yameen et al., 2014). Several examples in the literature showing the different uptake mechanisms that occurs when NPs are exposed to or are in contact with cells are summarized in Table 1.

While mechanistic insight into the cellular internalization of colloids is essential for the development of successful nanotherapeutics, the best approach on how to design colloids to control and dictate the uptake mechanism by cells, is still under investigation. Nowadays there is still an open discussion on the efficiency and efficacy of targeting motifs on particles for achieving the desired target. In the light of the current literature, it is still not possible to give a reliable prediction of the most likely endocytic uptake pathways for a colloid with known physicochemical properties. However, it is well established that after the endocytic uptake of colloids, they are initially located and encapsulated in highly acidic intracellular vesicles and not free in the cytosol (Delehanty et al., 2010; Medintz et al., 2005), *cf.* Fig. 1. In general, endocytosis of colloids frequently culminates with lysosome internalization (Stern et al., 2012). There are some cases reporting that ultra-small colloids could enter cells *via* transient pores in the cell membrane and thus directly enter the cytosol (Lin and Alexander-Katz, 2013; Wang et al., 2012; Shi et al., 2011). However, those cases are exceptions based on particular physicochemical properties as already stated above. For the vast majority of colloids, they are engulfed first by membrane-based vesicles, from which they can be in certain cases released. There are reports about endosomal escape (Delehanty et al., 2010; Medintz et al., 2005), which can lead to translocation of the particles to the cytosol. The question remaining is to know how to control such processes and

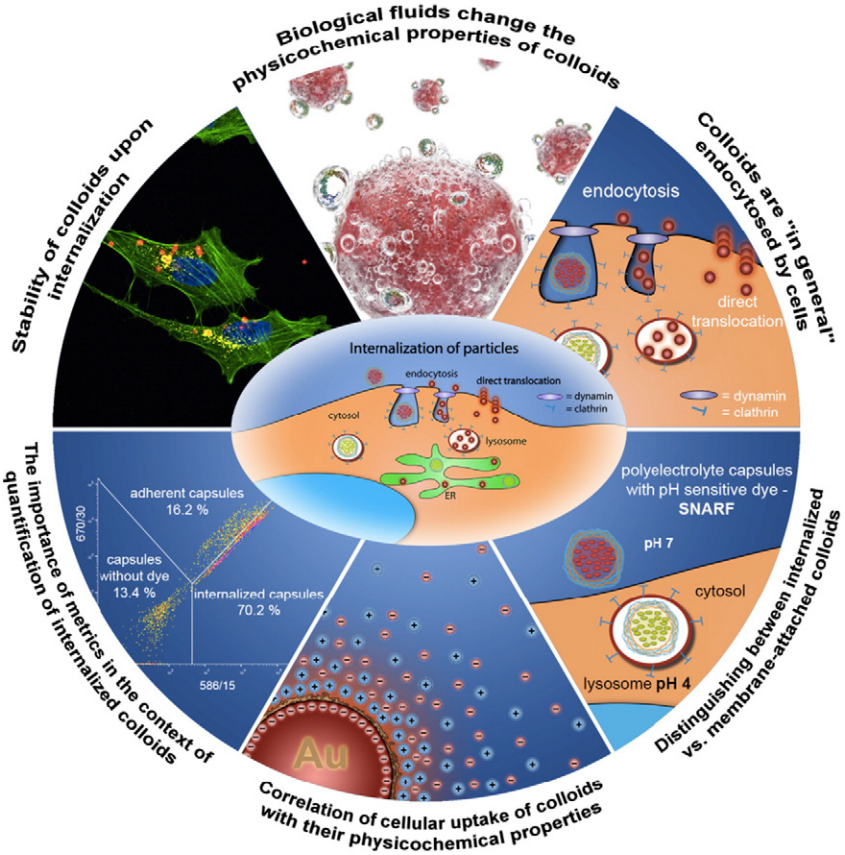

Scheme 1. Overview of the differents aspects to be consider when evaluating quantitative uptake of colloidal particles by cell cultures.

to learn about the transformation and effects of particles inside the vesicles. Several strategies liberate sequestered colloids (within vesicles) have been proposed. For instance, Delehanty et al. demonstrated that an amphiphilic peptide linked to quantum dots (QD) could mediate the rapid QD uptake by endocytosis, followed by a slower efficient endosomal release to the cytosol (Delehanty et al., 2010; Mattoussi et al., 2012). However, the dynamic transformation process that occurs to the particle inside the vesicles that determine its final fate remains unknown. Efforts in that direction are needed to find out new strategies that will allow studying such complex system.

3. Distinguishing internalized (endocytosed) *versus* membrane-attached colloids

As colloids are generally incorporated by cells upon *in vitro* exposure, protocols are required to quantify uptake. In principle, this looks like a straight forward task. Based on the physicochemical properties of the colloids such as the chemical composition, size, fluorescence, *etc.*, and on the cellular structure of interest several techniques have been proposed including microscopic approaches and elemental analysis. In the case of fluorescent colloids, their uptake can be quantified in terms of intracellular fluorescence (Hühn et al., 2013), which is possible by flow cytometry or optical microscopy. In the case of inorganic colloids their uptake can be quantified by transmission electron microscopy (TEM) or in terms of atomic concentrations of the inorganic elements by mass spectrometry (Mahmoudi et al., 2013). For mainly organic or polymeric particles TEM provides less contrast than for particles comprising high atomic weight compounds such as gold. Also mass spectroscopy is easiest to be performed on particles composed out of elements which are not typically present in cells. Some of these methods have no lateral or limited resolution. Classical element analysis *via* mass spectroscopy does not provide any lateral resolution in case it is not combined with local ablation of material. Also flow cytometry typically does not provide information about the location of the particles, it merely registers fluorescent event. Optical microscopy on the other hand allows for lateral resolution, which however is limited by the refraction limit of a few 100 nm. Therefore, in the particular case of small colloids, it is most of the time not directly possible to discriminate between the actual internalized colloids and the colloids just adherent to the outer cell membrane. Thorough rinsing may not be robust enough to remove the adherent colloids before quantification measurements, more rigorous purification techniques such as the use of enzymes (*e.g.* trypsin) should be used. Etching of metal particles remaining attached to the outer cell membrane has been used to improve rinsing (Braun et al., 2014). Nevertheless, these techniques may have effects on the cell membrane altering cellular behaviour. Therefore, additional strategies to quantify uptake are desirable. Welsher and Yang recently developed a multi resolution three-dimensional methodology to monitor the cellular uptake of peptide NPs by using two-photon microscopy. The technique allows for visualizing single NP uptake by cells and transport in vesicles *via* live tracking. The authors evaluated and quantified the deceleration of NP as they approached the cellular membrane, revealed the details of the early cellular uptake dynamics of NPs, and in this way demonstrated the feasibly of the technology (Welsher and Yang, 2014). Further application and development on that direction will enable valuable knowledge on NPs uptake and delivery.

Alternatively, as endocytosis-like mechanisms are responsible for internalization of colloids inside cells, this knowledge allows for distinguishing between endocytosed and adhered colloids. First, upon immunostaining of endosomes/lysosomes, co-localization analysis provides information whether colloids are inside these intracellular vesicles and have been therefore internalized (Kastl et al., 2013; Parakhonskiy et al., 2015), *cf.* Fig. 1b. Second, endocytosed colloids reside in acidic intracellular vesicles. By using pH-sensitive fluorophores, internalization of

Table 1
Mechanisms for cellular uptake of particles.

Reference	Nanoparticles	Size (physical diameter)	Zeta potential (mV)	Cell	Exposure conditions	Mechanism of uptake	Comments
Zielinski et al. (2016)	Silica-indocyanine 44 green/poly (ε-caprolactone) (PCL) NPs.	80–100 nm	−19.9 ± 1.2	Murinemicroglial cells (N9)	$3.8 \cdot 10^{10}$/mL particles in DMEM	Macropinocytosis and phagocytosis	The uptake of PLLA NPs was less prominent compared to the uptake of PCL particles in both microglia cell conditions, which is possibly due to differences in the surface charge of the NPs.
	Silica-indocyanine green/poly (ε-caprolactone-poly L-lactide) 46 (PLLA) NPs.		−27.7 ± 1.5		3.3×10^{10} particles in 1 mL DMEM		
Huefner et al. (2014)	Citrate-capped spherical Au NPs	40, 60 nm and 100 nm	−27.7 ± 1.5	Undifferentiated (UDC) and differentiated (DC) SH-SY5Y cells, a human neuroblastoma cell line.	Incubated with citrate-capped spherical Au NPs (40, 60 and 100 nm) at a concentration of 200,000 particles per cell, independent of particle size for 24 h and 48 h.	Endocytosis	The cellular uptake is dependent on size and incubation time.
Gliga et al. (2014)	Citrate coated Ag NPs PVP coated Ag NPs PVP uncoated Ag NPs	10, 40, and 75 nm 10 nm 50 nm		Normal bronchial epithelial cell line (BEAS-2B)	Exposed to10 μg/mL of each of the Ag NPs dispersions for 24 h.	Endocytosis	Small Ag NPs (10 nm) are cytotoxic for human lung cells. The toxicity observed is associated with the rate of intracellular Ag release, a 'Trojan horse' effect.
Dalal et al. (2016)	Polyacrylate coated folate functionalized CdSe/ZnS core-shell quantum dots (QD) of varied multivalency such as:	Hydrodynamic diameter		Human cervical cancer cell line HeLa and KB cells.	Incubated with 30 μL QD samples for 3 h.	(Endocytosis)	Lower multivalency (typically <10) of NPs is important for efficient subcellular targeting and multivalency plays an important role for cellular endocytosis.
	QD (folate)10	~35–40	−20			Caveolae	
	QD (folate)20	~40–45	−20			Caveolae and clathrin	
	QD (folate)40	~45–50	−17			Clathrin	
	QD (folate)110	~45–50	−14			Clathrin	
Forte et al. (2016)	Fluorescein isothiocyanate PS NPs (NP44)	44 nm	−37.57 ± 0.46	Gastric adenocarcinoma (AGS) cells	Incubated with 10 μg/mL NP dispersions in serum-free medium (1 h at 37 °C)	Clathrin-mediated endocytosis pathway	NP44 accumulate rapidly and more efficiently in the cytoplasm of AGS as compared to NP100
	Rhodamine PS NPs (NP100)	100 nm	−34.97 ± 0.62				
Lai et al. (2015)	Stem cell membrane-camouflaged	141.1, 391.1, and 282.9 nm in DI H_2O, 25%, and		TRAMP-C1 and immortalized murine	STM-SPIO NPs were added to the cells at final Fe	Phagocytosis	A coating of STM on the SPIO NPs significantly decreased the

	superparamagnetic iron oxide NPs (STM-SPIO NPs)	50% serum, respectively.		macrophages (RAW246.7 cell)	concentrations of 10, 20 or 30 μg/mL and were then incubated for 4 h.		macrophage uptake.
Russ et al. (2016)		Hydrodynamic diameter		RAW 264.7	Fullerene suspensions were added at a concentration of 4 μg/mL and incubated for 3 h.	Diffusion	Marginal uptake of C_{60} clusters through endocytosis/pinocytosis. Passive diffusion into membranes provides a significant source of biologically-available nanomaterial.
	Tb@C60 fullerenes	99.31 nm	−64.3				
	C60 fullerene NPs	91.13 nm	−44.3				
Cesbron et al. (2015)	Au NPs assisted by monolayer functionalization with HA2/TAT peptides.	5 and 10 nm		HeLa cells,	HeLa cells were incubated with Au NPs (6 nM) capped with 5% CALNN-TAT and 95% thiol-PEG (mole) for 10 min, 2 h, and 24 h.	Macropinocytosis	Peptide-capped Au NPs including either or both of TAT and HA2 peptides within their self-assembled monolayer lead to increased cellular uptake.
Feuser et al. (2016)	Superparamagnetic poly methyl methacrylate NPs			Murine fibroblast (L929) cells and chronic myeloid leukemia cells in blast crisis (K562)	MNPsPMMA and MNPsPMMA-FA NPs were incubated at a low temperature (4 °C), blocking receptor-mediated endocytosis mechanisms and at 37 °C with a concentration of 100 μg/mL for 2 h.	Folate receptor-mediated endocytosis	Cellular uptake assays showed a higher uptake of MNPsPMMA-FA than MNPsPMMA in K562 cells when incubated at 37 °C. On the other hand, MNPsPMMA-FA showed a low uptake when endocytosis mechanisms were blocked at low temperature (4 °C), suggesting that the MNPsPMMA-FA uptake was mediated by endocytosis.
	With folic acid (MNPsPMMA-FA)	134 ± 3.5 nm	−38 mV ± 4.5				
	Without folic acid (MNPsPMMA)	104 ± 3.9 nm	−37 mV ± 4.8				
Cheng et al. (2015)	Au NPs capped with polyethylene glycol-5000 (PEG-5000)		(In DMEM)	RAW 264.7 (phagocytic cells) and Hep G2 cells (nonphagocytic cells)	The dose of 50 μg/mL of Au NPs was used and cells were incubated for 24 h in DMEM.	Caveolin-mediated endocytosis major in both cells (for 5.20 nm NPs). Scavenger receptor-mediated endocytosis major in RAW 264.7 cells (for 50 nm). Caveolin-mediated endocytosis major in Hep G2 cells (for 50 nm).	As NP size increases, the protein corona exhibits strong inhibitory effect on the uptake level of Au NPs. Additionally, more significant inhibitory effects of the protein corona on the uptake level of Au NPs are observed in phagocytic cells than in nonphagocytic cells.
		5.1 ± 1.1 nm	−6.9 ± 0.7				
		20.5 ± 1.9 nm	−6.7 ± 0.8				
		50.7 ± 5.6 nm	−3.9 ± 0.3				
			(In c-DMEM)		The dose of 50 μg/mL of Au NPs was used and cells were incubated for 24 h in c-DMEM.	Caveolin-mediated endocytosis major in both cells (for 5.20 nm NPs). Clathrin-mediated endocytosis major in both cells (for 50 nm).	
		5.1 ± 1.1 nm	−6.5 ± 1.1				
		20.5 ± 1.9 nm	−4.8 ± 1.0				
		50.7 ± 5.6 nm	−3.4 ± 0.9				

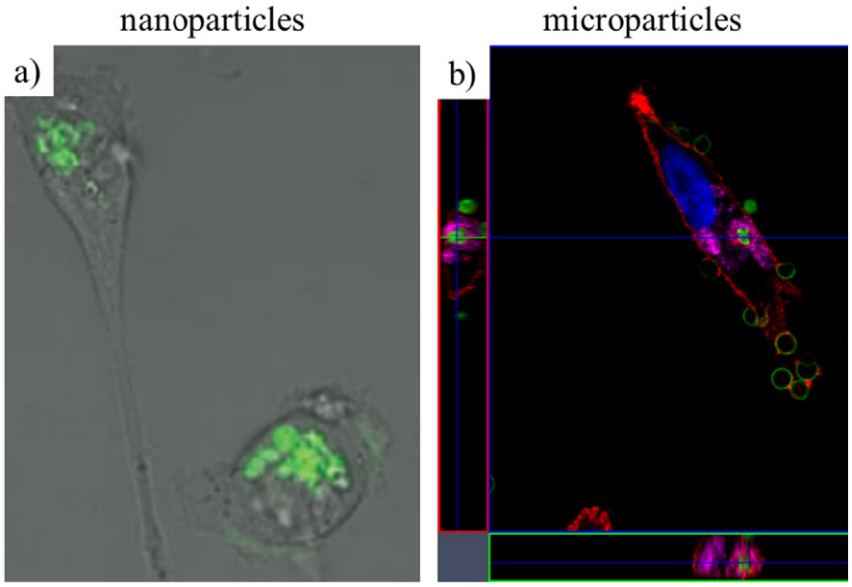

Fig. 1. Spontaneous internalization of colloids by adherent cell lines predominantly is mediated *via* endocytic pathways. a) Nanoparticles, as shown here, are green fluorescent colloidal quantum dots are located in intracellular vesicles after their uptake by cells. Image adopted from Parak et al. (2002). b) Also microparticles (colloids), as shown here, are polymer capsules with green fluorescent surface enter inside cell by endocytosis-like pathways and are finally located in intracellular vesicles. Here the cell membranes are stained red, nuclei in blue, and lysosomal membranes forming the border of the intracellular vesicles in violet. Image adopted from Kastl et al. (2013).

colloids could be detected based on pH changes in their local acidic environment (Kreft et al., 2007; Muñoz_Javier et al., 2008; Semmling et al., 2008; Hartmann et al., 2015), *cf.* Fig. 2. Experimental data in this direction in fact indicate that colloids may reside a significant time adhered to the outer cell membrane before being internalized (Semmling et al., 2008; Hartmann et al., 2015).

4. The importance of metrics in the context of quantification of internalized colloids

In order to assess the quantification of internalized colloids, it is important to select the appropriate metrics and relevant doses for accurate risk assessment (Oberdörster et al., 2005). Strategies to develop standardized dosages for comparable nanosafety studies are important. One approach that has been recommended for those evaluations it is based on the use of surface-weighted particle dosing referenced to the biologically relevant factor as for instance "*per cell*" or "*per cell surface*" (Taylor et al., 2014).

An example for the importance of choosing the appropriate metrics is shown in Fig. 3, where two typical uptake studies for colloids are presented. Even though both studies demonstrate that positively charged colloids are more internalized by cells, still the data cannot be directly compared. In one study (*cf.* Fig. 3a) the amount of particles is quantified in terms of fluorescence intensity, assuming that the fluorescence of one

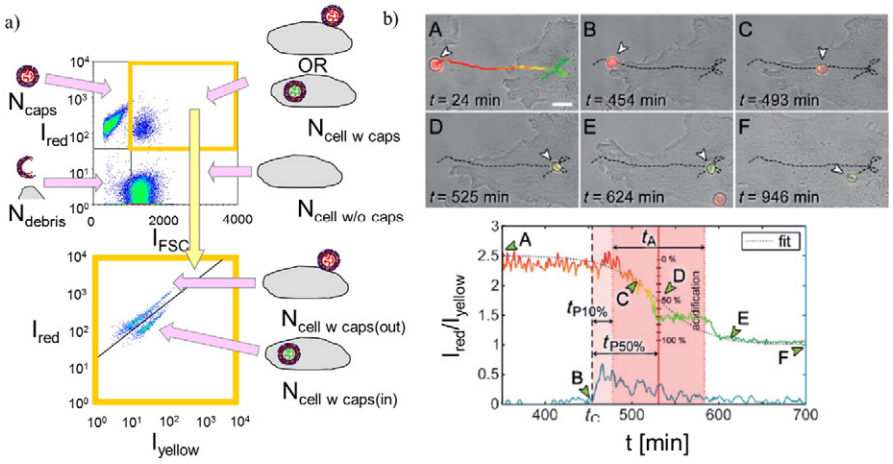

Fig. 2. Microparticles in the form of polymeric capsules with permeable shells were filled with the pH-sensitive fluorophore seminaphthorhodafluor (SNARF) leading to yellow fluorescence (here depicted in green false color) in case of acidic, and to red fluorescence in case of neutral or alkaline environment. In this way location of the colloids inside intracellular vesicles with acidic pH can be distinguished from presence of colloids in neutral/slightly acidic extracellular environment. a) Cells which have been incubated with colloids were investigated with flow cytometry, detecting intensities of forward scattering (I_{FSC}), red fluorescence (I_{red}), and yellow fluorescence (I_{yellow}). Based on scattering and fluorescence one can identify cells without associated colloids ($N_{cell\_w/\_caps(in)}$) from cells with associated colloids ($N_{cell\_w\_caps(out)}$). However, only the use of pH-sensitive fluorescence allowed for distinguishing cells with adhered ($N_{cell\_w\_caps(in)}$) from cells with internalized colloids ($N_{cell\_w\_caps(out)}$). Figure adopted from Semmling et al. (2008). b) Bright field overlaid with fluorescence image of cells exposed to colloids. After the microparticle first has touched the cell it moves along the outer cell membrane, as demonstrated by its red fluorescence indicating neutral/slightly alkaline extracellular environment. Onset of endocytosis can be observed by the color change from red to yellow fluorescence. Analysis of time-dependent fluorescence changes I_{red}/I_{yellow} allows for visualizing and quantifying of colloids and tracking the internalization process. Figure adopted from Hartmann et al. (2015).

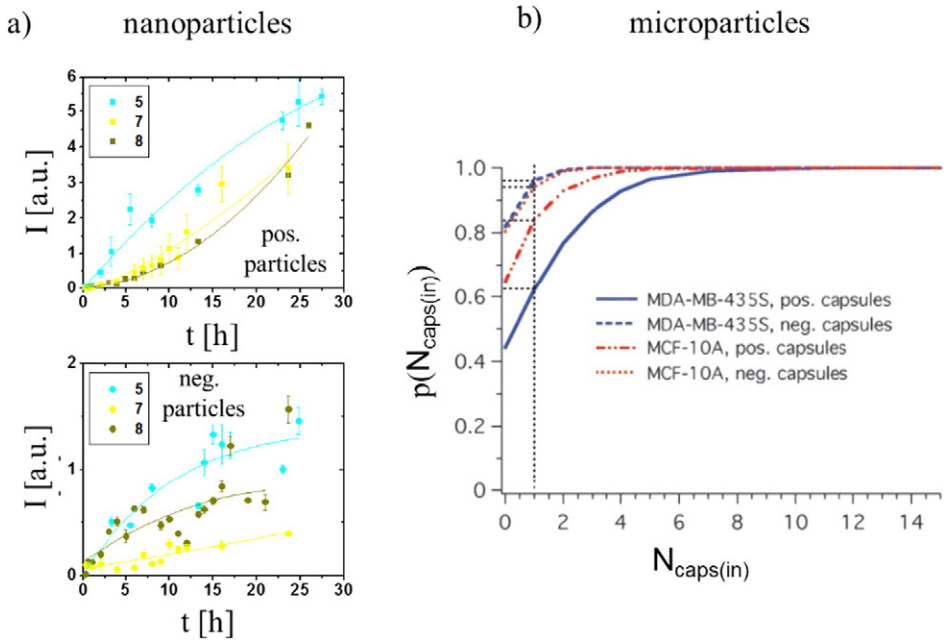

Fig. 3. Cellular uptake of colloids. a) Cells were incubated with gold nanoparticles (Au NPs) with negatively or positively charged polymer shell with an integrated fluorescence label. Uptake of colloids was quantified in terms of time-dependent fluorescence intensity I(t) on cells. The image demonstrates that Au NPs, exposed in complete media (serum) are taken up to a lower amount than in serum-free media. Under all comparable conditions, the positively charged Au NPs were incorporated in higher extend by cells than the negatively charged NPs. Image adopted from Hühn et al. (2013). b) MDA-MB-435S and MCF-10A cell lines were incubated for 1 h with micrometer sized polymeric capsules. Then uptake of capsules incorporated in each cell $N_{caps(in)}$ was determined and the cumulative distribution function $p(N_{caps(in)})$ was calculated. The more right-shifted this function is, the higher the amount of capsules per cell. Due to the micrometer size of the colloids, optical microscopy allowed to distinguish between internalized and outer adherent colloids. Image adopted from Muñoz Javier et al. (2006).

cell scales linearly with the number of incorporated colloids. In the other study, the cellular uptake was directly determined by the number of colloids internalized by each cell (*cf.* Fig. 3b). While both approaches are based on reasonable metrics, they cannot be directly compared.

Colloids of different size, ranging from *ca* 10 nm (*cf.* Fig. 3a) to a few μm (*cf.* Fig. 3b) were used for these studies. It is important to empathize that as the molar mass (besides the density) will scale with the volume of the colloids, one incorporated "big" particles is equal in mass to

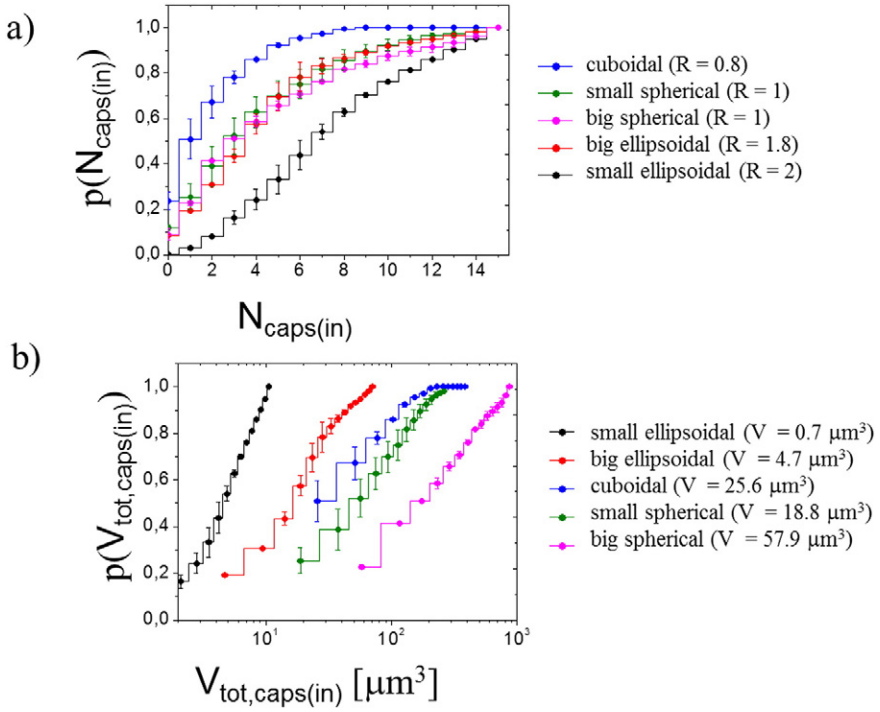

Fig. 4. Microparticles in the form of polymeric capsules with different aspect ratio R and capsule volume V were added to cells by colocalization with immuno-labelled lysosome. The number of internalized capsules per cell $N_{caps(in)}$ was determined and displayed as a) cumulative distribution function $p(N_{caps(in)})$, or b) as cumulative distribution function $p(V_{tot,caps(in)})$, with $V_{tot,caps(in)} = N_{caps(in)} \cdot V$. The image has been adopted from Parakhonskiy et al. (2015).

several incorporated "smaller" particles. Thus, if the particle uptake is quantified in terms of incorporated mass, a very different metrics is applied (Feliu et al., 2016b). This is demonstrated in Fig. 4 (Parakhonskiy et al., 2015). In this study, colloids with different aspect ratio were investigated. Data shown in Fig. 4a demonstrate that colloids with high aspect ratio (*e.g.* prolate ellipsoids) are incorporated to a higher extent by cells than colloids with low aspect ratio (*e.g.* oblate ellipsoids), in terms of internalized particles per cell $N_{caps(in)}$ used as metrics. This effect suggests that particle uptake increases with the aspect ratio. However, the colloids with different aspect ratio have different volume. For delivery applications, the amount of delivered cargo will increase with the total volume $V_{tot,caps(in)}$ delivered per cell. This volume is defined as the number of particles per cell, times the volume of a single particle. In case the same data are plotted using the totally delivered volume as metric, a different dependence is observed, *cf.* Fig. 4b. In this case particle uptake increases with particle volume. Thus, displaying the same data with different metrics can suggest quite different correlation. In this way, for all uptake studies, it is important to think about the metrics that fits best with the application.

Even if the same metrics is being used, it remains difficult to compare the different uptake studies. Often the read-out, such as the intracellular fluorescence intensity after incorporation of fluorescent colloids, will depend on the used set-up, the photo-physical properties of the colloids, *etc.* Other parameters, such as the time needed for internalization may be a good measure, as times can be directly compared. Having this in mind, one example in this direction has been recently demonstrated, *cf.* Fig. 2b (Hartmann et al., 2015). As discussed, the use of pH-sensitive fluorophores attached to colloids allows for determining the pH of the local environment around the particles. Upon endocytosis, the pH temporally decreases upon continuous fusion with highly acidic vesicles with the intracellular vesicles in which the colloids are incorporated. Thus, read-out of the local pH around the particles can provide information about the "stage" of endocytosis of each particle. This allows to determine whether the endocytosis "begins" or "is finished", and thus defining the characteristic times needed for particle endocytosis can allow for a direct comparison of two different experiments (Hartmann et al., 2015). By applying standardized experimental designs the times for internalization could be compared for different types of colloids, cell model systems, *etc.*

5. Correlation of cellular uptake of colloids with their physicochemical properties

While, as mentioned above, in many studies some colloids only attached to the outer cell membrane are counted as false positive in the uptake assays (counted as internalized colloids), still there is an agreement in the literature about some basic statements about correlation of the uptake with some physicochemical properties (Nazarenus et al., 2014). Obviously, colloidal stability plays an important role, as the physicochemical properties such as effective size or shape of colloids drastically change upon agglomeration. For well-dispersed colloids in general smaller colloids (>a few nm) are internalized to a higher extent than larger ones (Chithrani et al., 2006). Also, the role of shape has been investigated extensively by many groups. In general, sharp elongated colloids are better endocytosed than flat colloids (Parakhonskiy et al., 2015; Yoo et al., 2010; Shimoni et al., 2013). There are few studies that demonstrated the influence of the stiffness of colloids on their uptake by cells. Nevertheless, there is an indication that soft materials are internalized faster (Hartmann et al., 2015; Bedard et al., 2009; Sun et al., 2015). Another influential parameter is the charge. The influence of charge has been investigated already for decades using biological molecules as model colloids (Mutsaers and Papadimitriou, 1988; Ghinea and Simionescu, 1985). In general, positively charged colloids are better incorporated by cells than negatively charged ones, which is true for a large variety of colloids with different size, chemical composition, *etc.* (Fig. 3) (Schweiger et al., 2012; Hühn et al., 2013; Muñoz Javier et al., 2006; Jiang et al., 2010), but there are exceptions too. For instance, in a study by Zhang and Monteiro-Riviere it was found that negatively charged carboxylic coated quantum dots (QDs) (QD655-COOH) were internalized by HEK cells in greater extent than the respective positively charged-PEG-amine coated QDs (Zhang and Monteiro-Riviere, 2009). Conceptually, it could be discussed that systemically delivered colloids that are less internalized by cells (in general negative or neutral colloids), could be longer retained in blood circulation (extended half-live) than those colloids that are more internalized by cells (in general positive colloids), and thus become potential candidates for specific delivery. In contrast, Kim et al. showed that by combining both, experimental *in vitro* data and mathematical modelling, positive colloids could be used successfully for drug delivery due to their higher internalization by proliferating cells. Still, this study indicates that negatively charged colloids may be better candidates for delivering drugs into the tissue than the positively charged ones, because they diffuse faster (Kim et al., 2010).

The presence of proteins upon exposure, such as under serum-containing culture conditions, slows down the uptake of colloids (Hühn et al., 2013; Muñoz Javier et al., 2006), *cf.* Fig. 3a. For relating particle uptake with the physicochemical properties of the particles, thus the physicochemical properties of the particles under the used exposure conditions need to be considered, as will be discussed in the following.

6. Immersion in biological fluids changes the physicochemical properties of colloids

As described above, to some extent, the uptake of colloids by cells can be correlated with the colloids' physicochemical properties. However, most of the time physicochemical properties are dealt with in a static way. Analysis of the interaction between biological fluids and colloidal particles suggests that even if the particles are made of homogenous material, they should be seen as an hybrid material, due to the possible changes in their physicochemical properties upon interaction with the biological medium (Rivera Gil et al., 2013). A large number of publications indicates that the protein corona tends to stabilize colloidal particles. For example, adsorption of human serum albumin (HSA, the most abundant plasma protein) on the surface of gold nanoparticles prevents particle aggregation, even at high temperatures (Goy-Lopez et al., 2012). The formation of the protein corona depends on several factors, some of them are physicochemical properties of colloids such as size and charge. The size of the particles changes its surface activity and thus can alter the nature of biologically active proteins (Goy-Lopez et al., 2012; Lundqvist et al., 2008). The formation of the protein corona can affect both the colloidal stability and the uptake of cells, as toxicity (Westmeier et al., 2016a, 2016b. Cedervall et al. (2007) reported that protein adsorption on the particle's surface depends not only on the physicochemical properties of the nanoparticles, but also on the protein affinity to the particles, the so-called protein identity. They showed that albumin and fibrinogen associate and dissociate better than many other proteins present in the biological systems. The authors proved that the protein corona could be studied with the different techniques such as surface plasmon resonance (SPR), isothermal titration calorimetry (ITC), or size exclusion chromatography (SEC). External factors such as temperature or incubation time of particles with the proteins also play an important role (Mahmoudi et al., 2013; Weidner et al., 2015). Higher amount of adsorbed proteins were detected on the particle's surface after longer incubation time (20 min). However, at higher temperatures, the incubation time seems to be less important. A possible reason might be the denaturation of proteins during the incubation process at high temperature.

To be colloidally stable, particles should present repulsive forces between each other. These forces can be produced by introducing charge or steric repulsion (Takeuchi et al., 2013) on the surface of the particle. Salts are one of the major components of biological fluids. In contrast to proteins, salts can be a reason for colloids to lose their stability. The

negative surface charge of carboxylate groups (-COO^-) can be screened by the absorption of counter ion such as Ca^{2+}. This leads to a loss of electrostatic repulsion between the particles, resulting in particle aggregation (Boldt et al., 2006). Agglomerated particles have a bigger effective size than individually dispersed particles, and thus these changed physicochemical properties should be considered for correlative particle uptake studies.

7. Stability of colloids upon internalization

Further changes in particle properties may happen upon interaction with cells. Recent work has demonstrated that physicochemical properties of colloids can undergo significant changes upon cellular uptake (Kreyling et al., 2015). In fact, inorganic particles cores (Soenen et al., 2015; Kolosnjaj-Tabi et al., 2015), organic particle components and surface coatings (Kreyling et al., 2015), as well as the protein corona (Chanana et al., 2013; Wang et al., 2013; Bargheer et al., 2015a, 2015b) may be subject to dissolution, exchange, or degradation processes. This is demonstrated in Fig. 5. Here, nanoparticles and microparticles were modified with ovalbumin (OVA). OVA hereby had been conjugated with a fluorophores, whose emission was quenched before incorporation by cells. However, onset of fluorescence could be detected after particle uptake by cells. This was referred to a partial digestion of OVA by proteolytic enzymes, present in endosome/lysosomes, which resulted in increased distance between the cleaved peptide fragments and attached OVA conjugated, and thus to revoke the fluorescence quenching (Chanana et al., 2013; Rivera_Gil et al., 2009). This example clearly demonstrates that the properties of colloids can significantly change upon their uptake by cells. In fact, the biological activity of colloids should be rather correlated to their properties after than before cellular incorporation. The ideal scenario will be to develop new approaches and techniques to evaluate and characterize the physicochemical properties of colloids upon cell internalization such as surface composition, size, degeneration, charge, *etc.* (Feliu et al., 2016a).

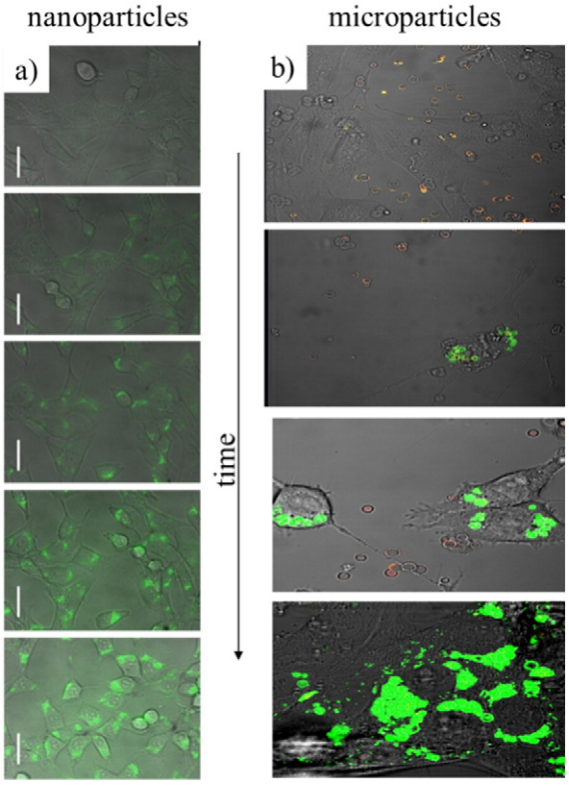

Fig. 5. a) Gold nanoparticles were covered with fluorescence-labelled ovalbumin, of which fluorescence is quenched. Upon cellular internalization proteolytic digestions of ovalbumin results in cancelling fluorescence quenching. Image adopted from Chanana et al. (2013). b) Polymer capsules with biodegradable shell were filled with fluorescence-labelled ovalbumin, of which fluorescence is quenched. Upon cellular internalization proteolytic digestions of the capsule shell and subsequently of ovalbumin results in cancelling fluorescence quenching. Image adopted from Rivera_Gil et al. (2009).

8. Conclusions

Despite a large variety of materials, sizes, *etc.* some general statements about the *in vitro* interaction of colloids with cells can be made (Nazarenus et al., 2014). These similarities were here examplified by showing similar outcomes for nanoparticles and microparticles. Thus, one can generally summarize the interaction of colloids with adherent cell lines to the statement that colloids are endocytosed and depending on the chemical nature of the colloids they might be degraded intracellularly. This is true for most of the particles and cell lines. On the other hand, details are more complex. The detailed uptake mechanisms, as well as in quantity and kinetics, and the intracellular fate of the colloids strongly depend on the individual properties of the colloids and cells to an extent, that so far many details cannot be predicted in a comprehensive way.

Acknowledgements

This work was supported by the European Commission (grant FutureNanoNeeds) grant agreement no. 604602 to WJP. NF acknowledges funding from the Lars Hiertas Minne Fundation (Sweden), SA, BP and IC acknowledge a fellowship from the Alexander von Humboldt Fundation (Germany). AE acknowledges Junta de Andalucía (Spain) for a Talentia Postdoc Fellowship, co-financed by the European Union Seventh Framework Programme, grant agreement no 267226. AHS acknowledges the Egyptian government (Ministry of Higher Education, Mission). The project was also supported by the Dr. Dorka-Stiftung (Germany) to PJ.

References

Bargheer, D., et al., 2015a. The distribution and degradation of radiolabelled SPIOs and quantum dots in mice. Beilstein J. Nanotechnol. 6, 111–123.
Bargheer, D., et al., 2015b. The fate of a designed protein corona on nanoparticles in vitro and in vivo. Beilstein J. Nanotechnol. 6, 36–46.
Bastus, N.G., et al., 2008. Reactivity of engineered inorganic nanoparticles and carbon nanostructures in biological media. Nanotoxicology 2 (3), 99–112.
Bedard, M.F., et al., 2009. On the mechanical stability of polymeric microcontainers functionalized with nanoparticles. Soft Matter 5 (1), 148–155.
Beddoes, C.M., Case, C.P., Briscoe, W.H., 2015. Understanding nanoparticle cellular entry: a physicochemical perspective. Adv. Colloid Interf. Sci. 218, 48–68.
Boldt, K., et al., 2006. Comparative examination of the stability of semiconductor quantum dots in various biochemical buffers. J. Phys. Chem. B 110 (5), 1959–1963.
Braun, G.B., et al., 2014. Etchable plasmonic nanoparticle probes to image and quantify cellular internalization. Nat. Mater. 13 (9), 904–911.
Canton, I., Battaglia, G., 2012. Endocytosis at the nanoscale. Chem. Soc. Rev. 41 (7), 2718–2739.
Casals, E., et al., 2010. Time evolution of the nanoparticle protein corona. ACS Nano 4 (7), 3623–3632.
Casals, E., et al., 2014. Programmed iron oxide nanoparticles disintegration in anaerobic digesters boosts biogas production. Small 10 (14), 2801–2808.
Cedervall, T., et al., 2007. Understanding the nanoparticle-protein corona using methods to quantify exchange rates and affinities of proteins for nanoparticles. Proc. Natl. Acad. Sci. U. S. A. 104 (7), 2050–2055.
Cesbron, Y., et al., 2015. TAT and HA2 facilitate cellular uptake of gold nanoparticles but do not lead to cytosolic localisation. PLoS One 10 (4).
Chanana, M., et al., 2013. Physicochemical properties of protein-coated gold nanoparticles in biological fluids and cells before and after proteolytic digestion. Angew. Chem. Int. Ed. 52 (15), 4179–4183.
Cheng, X.J., et al., 2015. Protein corona influences cellular uptake of gold nanoparticles by phagocytic and nonphagocytic cells in a size-dependent manner. ACS Appl. Mater. Interfaces 7 (37), 20568–20575.
Chithrani, B.D., Ghazan, A.A., Chan, C.W., 2006. Determining the size and the shape dependence of gold nanoparticle uptake into mammalian cells. Nano Lett. 6 (4), 662–668.
Conner, S.D., Schmid, S.L., 2003. Regulated portals of entry into the cell. Nature 422 (6927), 37–44.
Dalal, C., Saha, A., Jana, N.R., 2016. Nanoparticle multivalency directed shifting of cellular uptake mechanism. J. Phys. Chem. C 120 (12), 6778–6786.

Delehanty, J.B., et al., 2010. Delivering quantum dot-peptide bioconjugates to the cellular cytosol: escaping from the endolysosomal system. Integr. Biol. 2 (5–6), 265–277.
Fadeel, B., et al., 2013. Bridge over troubled waters: understanding the synthetic and biological identities of engineered nanomaterials. Wiley Interdiscip. Rev. Nanomed. Nanobiotechnol. 5 (2), 111–129.
Feliu, N., et al., 2016a. In vivo degradation and the fate of inorganic nanoparticles. Chem. Soc. Rev. 45, 2440–2457.
Feliu, N., et al., 2016b. Nanoparticle dosage-a nontrivial task of utmost importance for quantitative nanosafety research. Wiley Interdiscip. Rev. Nanomed. Nanobiotechnol.
Feuser, P.E., et al., 2016. Superparamagnetic poly(methyl methacrylate) nanoparticles surface modified with folic acid presenting cell uptake mediated by endocytosis. J. Nanopart. Res. 18, 104.
Florez, L., et al., 2012. How shape influences uptake: interactions of anisotropic polymer nanoparticles and human mesenchymal stem cells. Small 8 (14), 2222–2230.
Forte, M., et al., 2016. Polystyrene nanoparticles internalization in human gastric adenocarcinoma cells. Toxicol. in Vitro 31, 126–136.
Ghinea, N., Simionescu, N., 1985. Anionized and cationized hemeundecapeptides as probes for cell surface charge and permeability studies. J. Cell Biol. 100, 606–612.
Gliga, A.R., et al., 2014. Size-dependent cytotoxicity of silver nanoparticles in human lung cells: the role of cellular uptake, agglomeration and Ag release. Part. Fibre Toxicol. 11.
Goy-Lopez, S., et al., 2012. Physicochemical characteristics of protein-NP bioconjugates: the role of particle curvature and solution conditions on human serum albumin conformation and fibrillogenesis inhibition. Langmuir 28 (24), 9113–9126.
Hartmann, R., et al., 2015. Stiffness-dependent in vitro uptake and lysosomal acidification of colloidal particles. Angew. Chem. Int. Ed. 54 (4), 1365–1368.
He, C., et al., 2010. Effects of particle size and surface charge on cellular uptake and biodistribution of polymeric nanoparticles. Biomaterials 31 (13), 3657–3666.
Huefner, A., et al., 2014. Gold nanoparticles explore cells: cellular uptake and their use as intracellular probes. Methods 68 (2), 354–363.
Hühn, D., et al., 2013. Polymer-coated nanoparticles interacting with proteins and cells: focusing on the sign of the net charge. ACS Nano 7 (4), 3253–3263.
Iversen, T.G., Skotland, T., Sandvig, K., 2011. Endocytosis and intracellular transport of nanoparticles: present knowledge and need for future studies. Nano Today 6 (2), 176–185.
Jiang, X., et al., 2010. Specific effects of surface amines on polystyrene nanoparticles in their interactions with mesenchymal stem cells. Biomacromolecules 11 (3), 748–753.
Kastl, L., et al., 2013. Multiple internalization pathways of polyelectrolyte multilayer capsules into mammalian cells. ACS Nano 7 (8), 6605–6618.
Kim, B., et al., 2010. Tuning payload delivery in tumour cylindroids using gold nanoparticles. Nat. Nanotechnol. 5 (6), 465–472.
Kolosnjaj-Tabi, J., et al., 2015. The one year fate of iron oxide coated gold nanoparticles in mice. ACS Nano 9 (8), 7925–7939.
Kreft, O., et al., 2007. Polymer microcapsules as mobile local pH-sensors. J. Mater. Chem. 17, 4471–4476.
Kreyling, W.G., et al., 2015. In vivo integrity of polymer-coated gold nanoparticles. Nat. Nanotechnol. 10 (7), 619–623.
Krug, H.F., 2014. Nanosafety research—are we on the right track? Angew. Chem. Int. Ed. 53 (46), 12304–12319.
Lai, P.Y., et al., 2015. Biomimetic stem cell membrane-camouflaged iron oxide nanoparticles for theranostic applications. RSC Adv. 5 (119), 98222–98230.
Lerch, S., et al., 2013. Polymeric nanoparticles of different sizes overcome the cell membrane barrier. Eur. J. Pharm. Biopharm. 84 (2), 265–274.
Lin, J.Q., Alexander-Katz, A., 2013. Cell membranes open "doors" for cationic nanoparticles/biomolecules: insights into uptake kinetics. ACS Nano 7 (12), 10799–10808.
Lundqvist, M., et al., 2008. Nanoparticle size and surface properties determine the protein corona with possible implications for biological impacts. Proc. Natl. Acad. Sci. U. S. A. 105 (38), 14265–14270.
Mahmoudi, M., et al., 2013. Temperature: the "ignored" factor at the nanobio interface. ACS Nano 7 (8), 6555–6562.
Mani, T., et al., 2015. Microplastics profile along the Rhine River. Sci. Rep. 5, 17988.
Mattoussi, H., Palui, G., Na, H.B., 2012. Luminescent quantum dots as platforms for probing in vitro and in vivo biological processes. Adv. Drug Deliv. Rev. 64 (2), 138–166.
Mayor, S., Pagano, R.E., 2007. Pathways of clathrin-independent endocytosis. Nat. Rev. Mol. Cell Biol. 8, 603–612.
Medintz, I.L., et al., 2005. Quantum dot bioconjugates for imaging, labelling and sensing. Nat. Mater. 4 (6), 435–446.
Meng, H., et al., 2011. Aspect ratio determines the quantity of mesoporous silica nanoparticle uptake by a small GTPase-dependent macropinocytosis mechanism. ACS Nano 5 (6), 4434–4447.
Muñoz Javier, A., et al., 2006. Combined atomic force microscopy and optical microscopy measurements as a method to investigate particle uptake by cells. Small 2 (3), 394–400.
Muñoz_Javier, A., et al., 2008. Uptake of colloidal polyelectrolyte coated particles and polyelectrolyte multilayer capsules by living cells. Adv. Mater. 20 (22), 4281–4287.
Mutsaers, S., Papadimitriou, J., 1988. Surface charge of macrophages and their interaction with charged particles. J. Leukoc. Biol. 44 (1), 17–20.
Nazarenus, M., et al., 2014. In vitro interaction of colloidal nanoparticles with mammalian cells: what have we learned thus far? Beilstein J. Nanotechnol. 5, 1477–1490.
Oberdörster, G., Oberdörster, E., Oberdörster, J., 2005. Nanotoxicology: an emerging discipline evolving from studies of ultrafine particles. Environ. Health Perspect. 113 (7), 823–839.
Parak, W.J., et al., 2002. Cell motility and metastatic potential studies based on quantum dot imaging of phagokinetic tracks. Adv. Mater. 14 (12), 882–885.
Parakhonskiy, B., et al., 2015. The influence of the size and aspect ratio of anisotropic, porous CaCO3 particles on their uptake by cells. J. Nanobiotechnol. 13 (1), 53.
Rivera Gil, P., et al., 2013. The challenge to relate the physicochemical properties of colloidal nanoparticles to their cytotoxicity. Acc. Chem. Res. 46 (3), 743–749.
Rivera_Gil, P., et al., 2009. Intracellular processing of proteins mediated by biodegradable polyelectrolyte capsules. Nano Lett. 9 (12), 4398–4402.
Russ, K.A., et al., 2016. C-60 fullerene localization and membrane interactions in RAW 264.7 immortalized mouse macrophages. Nanoscale 8 (7), 4134–4144.
Sahay, G., Alakhova, D.Y., Kabanov, A.V., 2010. Endocytosis of nanomedicines. J. Control. Release 145 (3), 182–195.
Schweiger, C., et al., 2012. Quantification of the internalization patterns of superparamagnetic iron oxide nanoparticles with opposite charge. J. Nanobiotechnol. 10 (1), 28.
Semmling, M., et al., 2008. A novel flow-cytometry-based assay for cellular uptake studies of polyelectrolyte microcapsules. Small 4 (10), 1763–1768.
Sharma, V.K., et al., 2015. Natural inorganic nanoparticles—formation, fate, and toxicity in the environment. Chem. Soc. Rev. 44 (23), 8410–8423.
Shi, X., et al., 2011. Cell entry of one-dimensional nanomaterials occurs by tip recognition and rotation. Nat. Nanotechnol. 6, 714–719.
Shimoni, O., et al., 2013. Shape-dependent cellular processing of polyelectrolyte capsules. ACS Nano 7 (1), 522–530.
Soenen, S.J., et al., 2015. (Intra)cellular stability of inorganic nanoparticles: effects on cytotoxicity, particle functionality, and biomedical applications. Chem. Rev. 115 (5), 2109–2135.
Stern, S.T., Adiseshaiah, P.P., Crist, R.M., 2012. Autophagy and lysosomal dysfunction as emerging mechanisms of nanomaterial toxicity. Part. Fibre Toxicol. 9.
Sun, H.L., et al., 2015. The role of capsule stiffness on cellular processing. Chem. Sci. 6 (6), 3505–3514.
Takeuchi, H., Omogo, B., Heyes, C.D., 2013. Are bidentate ligands really better than monodentate ligands for nanoparticles? Nano Lett.
Taylor, U., et al., 2014. Rational design of gold nanoparticle toxicology assays: a question of exposure scenario, dose and experimental setup. Nanomedicine 9 (13), 1971–1989.
Torrano, A.A., et al., 2013. A fast analysis method to quantify nanoparticle uptake on a single cell level. Nanomedicine 8 (11), 1815–1828.
Wang, T., et al., 2012. Cellular uptake of nanoparticles by membrane penetration: a study combining confocal microscopy with FTIR spectroelectrochemistry. ACS Nano 6 (2), 1251–1259.
Wang, F.J., et al., 2013. The biomolecular corona is retained during nanoparticle uptake and protects the cells from the damage induced by cationic nanoparticles until degraded in the lysosomes. Nanomed. Nanotechnol. Biol. Med. 9 (8), 1159–1168.
Weidner, A., et al., 2015. Preparation of core-shell hybrid materials by producing a protein corona around magnetic nanoparticles. Nanoscale Res. Lett. 10, 1–11.
Welsher, K., Yang, H., 2014. Multi-resolution 3D visualization of the early stages of cellular uptake of peptide-coated nanoparticles. Nat. Nanotechnol. 9 (3), 198–203.
Westmeier, D., et al., 2016a. The bio-corona and its impact on nanomaterial toxicity. Eur. J. Nanomedicine 7, 153–168.
Westmeier, D., Stauber, R.H., Docter, D., 2016b. The concept of bio-corona in modulating the toxicity of engineered nanomaterials (ENM). Toxicol. Appl. Pharmacol. 299, 53–57.
Yameen, B., et al., 2014. Insight into nanoparticle cellular uptake and intracellular targeting. J. Control. Release 190, 485–499.
Yoo, J.W., Doshi, N., Mitragotri, S., 2010. Endocytosis and intracellular distribution of plga particles in endothelial cells: effect of particle geometry. Macromol. Rapid Commun. 31 (2), 142–148.
Zhang, L.W., Monteiro-Riviere, N.A., 2009. Mechanisms of quantum dot nanoparticle cellular uptake. Toxicol. Sci. 110, 138–155.
Zielinski, J., et al., 2016. Evaluation of endocytosis of silica particles used in biodegradable implants in the brain. Nanomedicine 1603–1613.

The International Journal of Biochemistry & Cell Biology 75 (2016) 148–161

Contents lists available at ScienceDirect

The International Journal of Biochemistry & Cell Biology

journal homepage: www.elsevier.com/locate/biocel

Review article

Dissociation coefficients of protein adsorption to nanoparticles as quantitative metrics for description of the protein corona: A comparison of experimental techniques and methodological relevance

Jonas Hühn[a], Chiara Fedeli[b], Qian Zhang[a], Atif Masood[a], Pablo del Pino[c], Niveen M. Khashab[d], Emanuele Papini[b,*], Wolfgang J. Parak[a,c,*]

[a] Fachbereich Physik, Philipps Universität Marburg, Marburg, Germany
[b] Department of Biomedical Science, University of Padova, Padova, Italy
[c] CIC biomaGUNE, San Sebastian, Spain
[d] Smart Hybrid Materials (Shms) Laboratory, Advanced Membranes and Porous Materials center, King Abdullah University of Science and Technology (KAUST), Thuwal, Saudi Arabia

ARTICLE INFO

Article history:
Received 31 October 2015
Received in revised form
28 December 2015
Accepted 28 December 2015
Available online 31 December 2015

Keywords:
Protein corona
Dissociation constant
Hill model
Nanoparticles

ABSTRACT

Protein adsorption to nanoparticles is described as a chemical reaction in which proteins attach to binding sites on the nanoparticle surface. This process is defined by a dissociation coefficient, which tells how many proteins are adsorbed per nanoparticle in dependence of the protein concentration. Different techniques to experimentally determine dissociation coefficients of protein adsorption to nanoparticles are reviewed. Results of more than 130 experiments in which dissociation coefficients have been determined are compared. Data show that different methods, nanoparticle systems, and proteins can lead to significantly different dissociation coefficients. However, we observed a clear tendency of smaller dissociation coefficients upon less negative towards more positive zeta potentials of the nanoparticles. The zeta potential thus is a key parameter influencing protein adsorption to the surface of nanoparticles. Our analysis highlights the importance of the characterization of the parameters governing protein–nanoparticle interaction for quantitative evaluation and objective literature comparison.

Contents

* Corresponding authors.
E-mail addresses: emanuele.papini@unipd.it (E. Papini), wolfgang.parak@physik.uni-marburg.de (W.J. Parak).

http://dx.doi.org/10.1016/j.biocel.2015.12.015
1357-2725/

1. Introduction

Proteins in solution may adsorb to surfaces. This phenomenon has been investigated with a long history for extended (and in general planar) surfaces. One example in this direction are intended protein coatings of cell culture substrates to improve cell growth such as fibronectin, laminin, polyornithine (Hindie et al., 2011; Keselowsky et al., 2003; Jung et al., 2009; Min et al., 2013). Even when cell culture substrates are not coated intentionally, proteins from serum-containing media adsorb to the surface and thus provide coating. Formation of such protein films can be for example measured with ellipsometry (Vroman and Lukosevicius, 1964). With nanotechnological tools such coatings can nowadays even be directly visualized, for example by scratching the surface with the tip of an atomic force microscope (AFM) (Domke et al., 2000). Protein coatings can drastically change the physicochemical properties of surfaces (Vroman, 1962). Hereby already early work has demonstrated that protein coatings are not a static entity, but may undergo continuous adsorption and desorption, in which originally adsorbed proteins desorb and other adsorb. This is nowadays described in the context of the Vroman effect (Jung et al., 2003; Noh and Vogler, 2007). The order in which proteins may adsorb to a surface has been quantified for many examples. For example human fibrinogen (FIB) binds stronger than human serum albumin (Vroman and Adams, 1969).

From the physicochemical point of view adsorption and desorption can be interpreted as a chemical reaction

$$n \cdot P + S \leftrightarrow P_n S \tag{1}$$

in which the educts are proteins P in solution and the free surface S, and the product is a protein-surface complex P_nS in the form of a protein-layer bound to the surface. Such chemical reaction can be quantified in terms of a dissociation equilibrium coefficient or apparent dissociation coefficient

$$K_D = \frac{c^n(P) \cdot c(S)}{c(P_n S)} \tag{2}$$

which describes in dependence of the protein concentration $c(P)$ *etc.* whether in equilibrium the reaction will be shifted towards free or adsorbed proteins (del Pino et al., 2014). According to the Hill model (Hill et al., 1910) in equilibrium N of N_{max} binding sites of the surface for proteins will be occupied.

$$\frac{N}{N_{max}} = \frac{1}{1 + (K'_D/c(P))^n} \tag{3}$$

Hereby

$$K'_D = (K_D)^{1/n} \tag{4}$$

is the protein concentration at which half of the surface is saturated with proteins. In this way also K'_D can be used in as similar way as K_D as quantifier for protein adsorption to surfaces. In the context of Eq. (3), n is the Hill coefficient. Dissociation coefficients are thus a convenient way to quantify protein adsorption of different surfaces.

While being textbook knowledge for planar surfaces, these concepts have gained new interest in the context of colloidal nanoparticles (NPs). In case NPs are dispersed in protein containing media, also for this geometry protein adsorption may occur, which is termed the formation of a protein corona (Cedervall et al., 2007; Docter et al., 2015a). In the last decade, it has been demonstrated experimentally that the protein corona plays a crucial role in the interaction of the NPs with cells. As outermost part of the NP the protein corona largely determines the "biological identity" of a NP (Fadeel et al., 2013; Docter et al., 2015b). Adsorption of proteins (and likely other macromolecules) from the host changes the actual physico-chemical nature of the NPs, which can change general features of the nanosurface "seen" by soluble and cellular biological actors, like surface charge or hydrophobicity. Dependence of the corona formation on several NP parameters such as size (Goy-Lopez et al., 2012; Lundqvist et al., 2008; Deng et al., 2011; Huang et al., 2013), charge (Hühn et al., 2013; Feliu et al., 2012), shape (Albanese et al., 2012), surface chemistry (Pelaz et al., 2015), *etc.* and on external parameters such as pH (Moerz et al., 2015), temperature (Mahmoudi et al., 2013; Lesniak et al., 2010) *etc.* has been investigated. It is also known that the protein corona is no static entity, but undergoes dynamic changes during the lifetime of a NP from the first contact with extracellular medium until having reached the final location inside cells (Casals et al., 2010; Tenzer et al., 2013; Chanana et al., 2013).

However, besides changing the physico-chemical properties of NPs the protein corona may also directly interfere with biological signal cascades. Indeed, virtually any biological macromolecule is "full" with information, encoded by its structural determinants, substantially dictating its ability to bind to other molecules, free in solution or expressed on cells. In this respect, it is to be remembered that often protein-mediated binding to other molecules leads to the activation of normally inactive self-amplifying cascades of biological and pathological paramount relevance, like, for example, the coagulation (Tavano et al., 2010) and the complement cascades (Banda et al., 2014). Another related aspect to be closely monitored when considering new nanoparticle properties induced by the protein corona, is the interaction with phagocytic cells (Segat et al., 2011; Fedeli et al., 2013, 2015). Indeed, there may be induction of an improved or a reduced ability to evade, or obstacle, the clearance of the formed nanoentity by macrophages placed in organs like the liver and the spleen. This is of utmost importance, since the intensity of these phenomena influences the blood circulation half-life and hence the efficacy of a nanotheranostic formulation.

Despite joint efforts by many research groups to investigate the protein corona there are still some important questions. This involves for example the geometry of the protein corona. While in some studies formation of monolayers are claimed, others report thick coronas and multiple shell formation (Maiolo et al., 2015). One general problem for unravelling the remaining secrets is that though numerous studies exist, many of them are hard to compare, as there is a lack of quantitative parameters which could be used as metrics for direct comparison.

In Fig. 1, transmission electron microscopy (TEM) data are presented, in which the protein corona adsorbed to NPs is visualized with negative staining. These data correspond nicely with the monolayer hypothesis, as shown in Table 1.

Similar to planar surfaces, also in case of NPs the strength with which proteins bind to the surface of NPs can be quantified by determining the protein concentration $K'_D = (K_D)^{1/n}$ at which half of the NP surface is saturated with proteins (del Pino et al., 2014). K'_D values thus could be used as quantifier to compare protein corona formation for different NPs and different proteins under equilibrium conditions. K'_D values regarding the protein corona have been determined by several groups. The aim of this review article is to describe the different methods with which these values have been experimentally obtained and to compare the results obtained for different NPs and proteins.

2. Description of experimental techniques

2.1. Fluorescence correlation spectroscopy (FCS) and dynamic light scattering (DLS)

Protein adsorption to NPs can be directly observed by measuring changes in hydrodynamic diameter d_h. The more proteins adsorb on the surface of one NP, the bigger the NP-protein complex and thus the hydrodynamic diameter of the NP becomes. Hydrodynamic

Table 1
Protein adsorption quantified for different NPs, buffers, temperatures T (RT = room temperature), and methods. As NP materials FePt, Au, Ag, Cu, CdSe/ZnS, SiO_2, TiO_2, CeO_2 Al_2O_3, ZnO, γ-Fe_2O_3, $MnFe_2O_4$/$CoFe_2O_4$ core/shell hybrids (Zhang et al., 2015a), starch, HES (hydroxyethyl starch), PPy (polypyrol), and PS (polystyrene) were investigated. NP surface coatings involve OT (1-octanethiol), brOT (branched version of OT, 3,7-dimethyloctane-1-thiol), MPA (mercaptopropionic acid), MUA (11-mercaptoundecanoic acid), MUS (11-mercapto-1-undecanesulfonate), OA (oleic acid), DPA (D-penicillamine), DHLA (dihydrolipoic acid), GSH (glutathione), CTAB (cetyltrimethylammonium bromide), MHPC (myristoyl hydroxyl-phosphatidylcholine), Asp (aspartate), Gly (glycine), Leu (leucine), Lys (lysine), Ser (serine), PMA (modified poly (isobutylene alt-maleic anhydride), where 75% of the anhydride rings were reacted with dodecylamine) (Lin et al., 2008), P(−) (PMAPHOS-stat-PLMA) (Hühn et al., 2013; Geidel et al., 2011), P(+) (PTMAEMA-stat-PLMA) (Hühn et al., 2013; Geidel et al., 2011), AMP (amphiphilic polymer), PAA (polyacrylic acid), PAH (poly-allylamine hydrochloride), PEG (polyethylene glycol), and PVAm (Poly(vinyl-amine)). In some cases the same materials or the coatings were further chemically modified to add carboxylate (—COOH) or amine ($—NH_2$) groups. A large set of proteins was investigated, including HSA (human serum albumin), HSAsuc (succinylated HSA), HSAam (aminated HSA), BSA (bovine serum albumin), FIB (human fibrinogen), apo-Tf (apo-transferrin), apoA-I (apolipoprotein A-I), apoE3 (apolipoprotein E3), apoE4 (apolipoprotein E4), HRG (human Histidine Rich Glycoprotein), Kin 1 (human Kininogen 1), A1AT (Alpha-1-antitrypsin), HaG (Haptoglobin), and C3 (complement component 3). Incubation of NPs with proteins was carried out in different media, *i.e.* H_2O, PB (100 mM phosphate buffer), PBS (phosphate buffered saline, pH = 7.4), PBST (10 mM Na_2HPO_4, 2 mM KH_2PO_4, 137 mM NaCl, 2.7 mM KCl, 0.005% Tween 20, pH 7.4), RPMI 1640 (GIBCO brl, code number 11875-085), HEPES (20 mM HEPES buffer, pH 7.4), and MOPS (5 mM 3-morpholinopropane-1-sulfonic acid buffer, pH 7). The radius r_c of the (spherical) inorganic cores of the NPs was determined by transmission electron microscopy (TEM). For the FePt NPs reported here (Röcker et al., 2009; Jiang et al., 2010; Maffre et al., 2011), the r_c data are taken from Lehmann et al. (2010). In case of rod-shaped or ellipsoid NPs the radii of the short and long axis are given. SiO_2 NPs of amorphous silica were synthesized and characterized as described previously by Fedeli et al. (2015). The protein corona was quantified with different methods. In case of FCS (fluorescence correlation spectroscopy) $r_h(0)$ and $r_h(N_{max})$ are the hydrodynamic radii of the NPs without adsorbed proteins and upon saturation of the NP surface with proteins, respectively, as determined by FCS using the Hill model. Thus $\Delta r_h = r_h(N_{max}) - r_h(0)$ is the thickness of the protein corona. The Hill coefficient n controls the steepness of the binding curve, N_{max} is the maximum number of proteins adsorbing onto a single NP, and K'_D represents the concentration of protein molecules at half coverage. FCS measurements are described in a series of publications from the Nienhaus group (Röcker et al., 2009; Jiang et al., 2010; Maffre et al., 2011).

	Protein	NP core	NP coating/modification	r_c (nm)	$r_h(0)$ (nm)	ζ (mV)	Buffer	T (°C)	Method	K_D (μM)	$K'_D = (K_D)^{1/n}$ (μM)	N_{max}	n	Δr_h (nm)	Report
1	HSA	FePt	PMA	1.6 ± 0.2	5.6 ± 0.2	−44 ± 3	PBS	RT	FCS	3.1[a]	5.1 ± 1.3	27 ± 4	0.7 ± 0.1	3.3 ± 0.3	Röcker et al., 2009
2	HSA	FePt	PMA	1.6 ± 0.2	6.0 ± 0.1	−44 ± 3	PBS	RT	FCS	7.9[a]	9.9 ± 4.7	27 ± 3	0.9 ± 0.2	3.3 ± 0.3	Maffre et al., 2011
3	HSA	FePt	PMA	1.6 ± 0.2	5.4 ± 0.1	−44 ± 3	PBS	RT	FCS	2.7[a]	4.1 ± 0.8	15.2 ± 0.8	0.7 ± 0.1	2.6 ± 0.1	Pelaz et al., 2015
4	HSA	Au	P(−)	2.3 ± 0.6	7.9 ± 0.2	−39.8 ± 10	PBS	RT	FCS	1.4[a]	1.5 ± 0.8	32 ± 4	0.8 ± 0.3	2.5 ± 0.3	Hühn et al., 2013
5	HSA	Au	P(+)	2.3 ± 0.6	5.1 ± 0.1	+9.7 ± 8.9	PBS	RT	FCS	1[a]	1.0 ± 0.3	35 ± 3	0.8 ± 0.3	4.3 ± 0.4	Hühn et al., 2013
6	HSA	CdSe/ZnS	PAA	3 × 6	7.9 ± 0.3		PBS	RT	FCS	18[a]	37 ± 12	44 ± 8	0.8 ± 0.2	3.2 ± 0.4	Röcker et al., 2009
7	HSA	CdSe/ZnS	PAA	5.0	9.3 ± 0.2	−27 ± 2	PBS	RT	FCS	13[a]	24.8 ± 3.8	–	0.8 ± 0.1	3.2 ± 0.7	Maffre et al., 2014
8	HSA	CdSe/ZnS	DPA	5.0	6.1 ± 0.1	−27 ± 2	PBS	RT	FCS	0.3[a]	0.31 ± 0.06	–	1.0 ± 0.2	2.8 ± 0.4	Maffre et al., 2014
9	HSA	CdSe/ZnS	DHLA	5.0	4.8 ± 0.2	−31 ± 4	PBS	RT	FCS	3.5[a]	6 ± 3	–	0.7 ± 0.1	3.2 ± 0.8	Maffre et al., 2014
10	HSA	CdSe/ZnS	Cysteamine	–	6.3 ± 0.4	+29 ± 4	H_2O	RT	FCS	0.004[a]	0.025 ± 0.007	–	1.5 ± 0.4	4.4 ± 0.4	Maffre et al., 2014
11	HSA	Fe_3O_4	PMA	4.0 ± 0.6	6.8 ± 0.2	−55 ± 3	PBS	RT	FCS	1.3[a]	1.5 ± 0.5	33.0 ± 4.0	0.6 ± 0.2	3.6 ± 0.5	Pelaz et al., 2015
12	HSA	Au	DHLA	–	2.9 ± 0.1	−37 ± 3	PBS	RT	FCS	0.1[a]	0.08 ± 0.02	–	0.8 ± 0.1	–	Shang et al., 2014
13	HSA	Ag	DHLA	0.7 ± 0.2	1.1 ± 0.2	−51 ± 1	PBS	RT	FCS	–	0.37 ± 0.2	–	–	–	Shang et al., 2012
14	HSA	FePt	PMA-0.75 kDa PEG	1.6 ± 0.2	6.5 ± 0.1	−17.8 ± 0.5	PBS	RT	FCS	1.9[a]	2.0 ± 1.0	9.0 ± 1.0	0.9 ± 0.3	1.4 ± 0.2	Pelaz et al., 2015
15	HSA	FePt	PMA-5 kDa PEG	1.6 ± 0.2	7.9 ± 0.2	−28 ± 1	PBS	RT	FCS	1[a]	1.0 ± 0.4	14.0 ± 2.0	1.5 ± 0.8	1.5 ± 0.3	Pelaz et al., 2015
16	HSA	FePt	PMA-10 kDa PEG	1.6 ± 0.2	9.7 ± 0.2	−14.3 ± 0.4	PBS	RT	FCS	1.4[a]	1.4 ± 0.7	21.0. ± 3.0	1.1 ± 0.8	1.5 ± 0.3	Pelaz et al., 2015
17	HSA	FePt	PMA-glucose	1.6 ± 0.2	5.4 ± 0.1	−25 ± 3	PBS	RT	FCS	1.9[a]	2.3 ± 0.3	18.3 ± 0.7	0.8 ± 0.1	3.0 ± 0.1	Pelaz et al., 2015
18	HSA	FePt	PMA	1.7 ± 0.3	5.5 ± 0.3	−45 ± 2	PBS	13	FCS	4[a]	10 ± 4	31 ± 5	0.6 ± 0.1	3.7 ± 0.4	Mahmoudi et al., 2013
19	HSA	FePt	PMA	1.7 ± 0.3	6.0 ± 0.1	−45 ± 2	PBS	23	FCS	5.2[a]	6.3 ± 2.2	30 ± 3	0.9 ± 0.2	3.3 ± 0.2	Mahmoudi et al., 2013

Table 1 (*Continued*)

	Protein	NP core	NP coating/modification	r_c (nm)	$r_h(0)$ (nm)	ζ (mV)	Buffer	T (°C)	Method	K_D (μM)	$K'_D = (K_D)^{1/n}$ (μM)	N_{max}	n	Δr_h (nm)	Report
20	HSA	FePt	PMA	1.7 ± 0.3	6.0 ± 0.1	−45 ± 2	PBS	43	FCS	0.9[a]	0.8 ± 0.4	23 ± 2	0.7 ± 0.2	2.8 ± 0.2	Mahmoudi et al., 2013
21	HSA	Au	–	8	–	–	–	RT	FQ	18	–	–	–	–	Naveenraj et al., 2010
22	HSA	SiO_2	–	12	–	−18.8	RPMI 1640	37	Free protein	>1	–	–	–	–	Fedeli et al., 2015
23	HSA	TiO_2	–	1.8	–	+47.0 ± 1.0	PBST	25	SPR	>0.066 <0.094[b]	–	–	–	–	Canoa et al., 2015
24	HSA	CeO_2	–	6.5	–	+26.5 ± 0.5	PBST	25	SPR	>0.025 <0.045[b]	–	–	–	–	Canoa et al., 2015
25	HSA	Al_2O_3	–	–	–	+20.3 ± 0.2	PBST	25	SPR	2.5 ± 0.5[c]	–	–	–	–	Canoa et al., 2015
26	HSA	HES	–	–	−275 ± 26	−34 ± 3	H_2O	25	ITC	1.25	–	0.114	–	–	Winzen et al., 2015
27	HSA	HES	—COOH	–	−200 ± 20	−34 ± 3	H_2O	25	ITC	2.5	–	0.156	–	–	Winzen et al., 2015
28	HSA	HES	—NH_2	–	−256 ± 26	−27 ± 3	H_2O	25	ITC	2	–	0.184	–	–	Winzen et al., 2015
29	HSA	CdSe/ZnS	DHLA	2.6 ± 0.4	5	−25 ± 2	PBS	RT	FCS	6.4 ± 3.6	–	9.5 ± 0.8	0.8 ± 0.1	3.3 ± 0.6	Klapper et al., 2015
30	HSA	CdSe/ZnS	MHPC	2.6 ± 0.4	6.8 ± 0.9	−9.3 ± 0.5	PBS	RT	FCS	400 ± 70	–	15 ± 2	0.7 ± 0.2	3.3	Klapper et al., 2015
31	HSA	Fe_3O_4	PAA	3.85 ± 0.45	24.2 ± 4.1	−46.2	PBS	RT	CE	1.4 ± 0.11	–	–	1	–	Zeng et al., 2014
32	HSA	Fe_3O_4	PAA	4.05 ± 0.5	29 ± 5.9	−43.8	PBS	RT	CE	5.1 ± 0.18	–	–	1.1	–	Zeng et al., 2014
33	HSA	Au	Asp	8 ± 2	10.5 ± 1	−31 ± 3	PBS	25	FQ	0.000032[d]	–	–	–	4.5 ± 0.5	Cai and Yao, 2014
34	HSA	Au	Gly	20 ± 4	23.5 ± 0.5	−32 ± 1	PBS	25	FQ	0.00067[d]	–	–	–	5.5 ± 1	Cai and Yao, 2014
35	HSA	Au	Lys	5.5 ± 2	7.5 ± 1.5	−26 ± 1	PBS	25	FQ	0.00071[d]	–	–	–	4.5 ± 3	Cai and Yao, 2014
36	HSA	Au	Ser	8 ± 1	7.5 ± 0.5	−34 ± 2	PBS	25	FQ	0.00091[d]	–	–	–	3 ± 0.5	Cai and Yao, 2014
37	HSA	Au	Leu	12.5 ± 3.5	13.5 ± 1	−35 ± 3	PBS	25	FQ	0.00012[d]	–	–	–	4.5 ± 1.5	Cai and Yao, 2014
38	HSAsuc	CdSe/ZnS	DHLA	5.0	4.8 ± 0.2	−31.2 ± 0.8	PBS	RT	FCS	4.6[a]	19 ± 8	89 ± 8	0.52 ± 0.04	8.1 ± 0.6	Treuel et al., 2014
39	HSAsuc	Au	DHLA	0.7 ± 0.15	3.2 ± 0.1	−37 ± 3	PBS	RT	FCS	0.1[a]	0.034 ± 0.008	12.5 ± 0.6	0.7 ± 0.1	1.9 ± 0.2	Shang et al., 2014
40	HSAam	CdSe/ZnS	DHLA	5.0	5.6 ± 0.1	−31.2 ± 0.8	PBS	RT	FCS	40.8[a]	22 ± 3	31 ± 1	1.2 ± 0.1	4.6 ± 0.1	Treuel et al., 2014
41	HSAam	Au	DHLA	0.7 ± 0.15	3.2 ± 0.1	−37 ± 3	PBS	RT	FCS	1.1[a]	1.2 ± 0.4	5.6 ± 0.4	0.7 ± 0.1	2.4 ± 0.2	Shang et al., 2014
42	BSA	Starch	–	20–25	–	–	–	20	FQ	0.0053	–	–	–	–	Ji et al., 2015
43	BSA	Starch	–	20–25	–	–	–	30	FQ	0.0055	–	–	–	–	Ji et al., 2015
44	BSA	Starch	–	20–25	–	–	–	37	FQ	0.0062	–	–	–	–	Ji et al., 2015
45	BSA	Au	–	1.25 ± 0.25	–	–	PB	25	ITC	1.3	–	1.5	–	–	Chakraborty et al., 2011
46	BSA	Au	CTAB	4 × 10	–	–	PB	25	ITC	0.085	–	2	–	–	Chakraborty et al., 2011
47	BSA	$MnFe_2O_4$/ $CoFe_2O_4$	PMA	6.9 ± 0.7	9.6 ± 0.4	−31.8 ± 1.3	Vaccum/H_2O	RT	TEM	–	–	–	–	4.2	This study
48	BSA	ZnO	–	3.75	–	–	H_2O	9	FQ	0.000000066	–	–	–	–	Bhogale et al., 2013
49	BSA	ZnO	–	3.75	–	–	H_2O	25	FQ	0.0000001	–	–	–	–	Bhogale et al., 2013
50	BSA	ZnO	–	3.75	–	–	H_2O	37	FQ	0.0006	–	–	–	–	Bhogale et al., 2013

Table 1 (*Continued*)

	Protein	NP core	NP coating/modification	r_c (nm)	$r_h(0)$ (nm)	ζ (mV)	Buffer	T (°C)	Method	K_D (μM)	$K'_D = (K_D)^{1/n}$ (μM)	N_{max}	n	Δr_h (nm)	Report
51	BSA	Cu	–	3.75	–	–	H_2O	9	FQ	0.2	–	–	–	–	Bhogale et al., 2014
52	BSA	Cu	–	3.75	–	–	H_2O	25	FQ	0.08	–	–	–	–	Bhogale et al., 2014
53	BSA	Cu	–	3.75	–	–	H_2O	37	FQ	0.05	–	–	–	–	Bhogale et al., 2014
54	BSA	Cu	–	3.75	–	–	H_2O	42	FQ	0.015	–	–	–	–	Bhogale et al., 2014
55	BSA	Ag	–	–	31	–	H_2O	4	FQ	0.00006	–	–	–	–	Mariam et al., 2011
56	BSA	Ag	–	–	31	–	H_2O	28	FQ	0.000000055	–	–	–	–	Mariam et al., 2011
57	BSA	Ag	–	–	31	–	H_2O	37	FQ	0.0000000066	–	–	–	–	Mariam et al., 2011
58	BSA	Ag	–	–	31	–	H_2O	42	FQ	0.00000000009	–	–	–	–	Mariam et al., 2011
59	BSA	Au	Citrate	25.6 ± 3.4	26 ± 1.3	−49 ± 8	H_2O	RT	FCS	256 ± 50	–	295 ± 30	0.4 ± 0.1	4.6 ± 2.4	Dominguez-Medina et al., 2012
60	BSA	Au	Citrate	25.5 ± 3.5	26 ± 2	−50	H_2O	RT	FCS	600	–	–	0.6	5 ± 2	Dominguez-Medina et al., 2013
61	BSA	Au	–	7.5 ± 0.5	–	–	–	RT	FQ	27	–	–	0.95		Naveenraj et al., 2010
62	BSA	Au	PAA	10.8 ± 1.3	–	−70	H_2O	4	FQ	0.00033	–	–	0.93		Boulos et al., 2013
63	BSA	Au	PAH	10.8 ± 1.3	–	+49	H_2O	4	FQ	0.000058	–	–	0.57		Boulos et al., 2013
64	BSA	Au	PEG	10.8 ± 1.3	–	−5	H_2O	4	FQ	0.00036	–	–	1.36		Boulos et al., 2013
65	BSA	Au	PAA	8 × 27	–	−70	H_2O	4	FQ	0.000105	–	–	1.3		Boulos et al., 2013
66	BSA	Au	PAH	8 × 27	–	+49	H_2O	4	FQ	0.000068	–	–	1.2		Boulos et al., 2013
67	BSA	Au	PEG	8 × 27	–	−5	H_2O	4	FQ	0.0002	–	–	1.3		Boulos et al., 2013
68	BSA	Au	PAH	8 × 27	–	+49	H_2O	4	FQ[e]	0.0041	–	–	–		Boulos et al., 2013
69	BSA	Au	PAA	8 × 27	–	−70	MOPS	4	FQ	0.000103	–	–	–		Boulos et al., 2013
70	BSA	Au	PAH	8 × 27	–	+49	MOPS	4	FQ	0.000042	–	–	–		Boulos et al., 2013
71	BSA	Au	PEG	8 × 27	–	−5	MOPS	4	FQ	0.000072	–	–	–		Boulos et al., 2013
72	BSA	Au	PAA	10.5 × 171	–	−70	H_2O	4	FQ	0.000082	–	–	1.1		Boulos et al., 2013
73	BSA	Au	PAH	10.5 × 171	–	+49	H_2O	4	FQ	0.000036	–	–	0.7		Boulos et al., 2013
74	BSA	Au	PEG	10.5 × 171	–	−5	H_2O	4	FQ	0.00012	–	–	1.2		Boulos et al., 2013
75	BSA	Au	PAA	8 × 27	–	−70	MOPS	RT	ACE	13	–	–	2.3		Boulos et al., 2013
76	BSA	Au	PEG	8 × 27	–	−5	MOPS	RT	ACE	65	–	–	2.3		Boulos et al., 2013
77	BSA	Au	MUS	2.3 ± 0.6	5.4 ± 0.1	–	PBS	22	FQ	0.0005[d]	–	–	–	~7	Huang et al., 2014

Table 1 (*Continued*)

	Protein	NP core	NP coating/modification	r_c (nm)	$r_h(0)$ (nm)	ζ (mV)	Buffer	T (°C)	Method	K_D (μM)	$K'_D = (K_D)^{1/n}$ (μM)	N_{max}	n	Δr_h (nm)	Report
78	BSA	Au	MUS/brOT	2.4 ± 0.5	6.3 ± 1.2	–	PBS	22	FQ	0.00074[d]	–	–	–	~ 7	Huang et al., 2014
79	BSA	Au	MUS/OT	2 ± 0.4	4.7 ± 0.5	–	PBS	22	FQ	0.011[d]	–	–	–	~ 8.5	Huang et al., 2014
80	BSA	Au	MPA/brOT	2.9 ± 0.2	5.3 ± 0.2	–	PBS	22	FQ	0.005[d]	–	–	–	~ 5	Huang et al., 2014
81	BSA	Au	MPA/OT	2.9 ± 0.2	5 ± 0.3	–	PBS	22	FQ	0.013[d]	–	–	–	~ 7	Huang et al., 2014
82	BSA	Au	Asp	8 ± 2	10.5 ± 1	−31 ± 3	PBS	25	FQ	0.00029[d]	–	–	–	4 ± 0.5	Cai and Yao, 2014
83	BSA	Au	Gly	20 ± 4	23.5 ± 0.5	−32 ± 1	PBS	25	FQ	0.000024[d]	–	–	–	5.5 ± 0.5	Cai and Yao, 2014
84	BSA	Au	Leu	12.5 ± 3.5	13.5 ± 1	−35 ± 3	PBS	25	FQ	0.00015[d]	–	–	–	4 ± 1.5	Cai and Yao, 2014
85	BSA	Au	Lys	5.5 ± 2	7.5 ± 1.5	−26 ± 1	PBS	25	FQ	0.00071[d]	–	–	–	2.5 ± 1.5	Cai and Yao, 2014
86	BSA	Au	Ser	8 ± 1	7.5 ± 0.5	−34 ± 2	PBS	25	FQ	0.00071[d]	–	–	–	3.5 ± 0.5	Cai and Yao, 2014
87	BSA	Fe_3O_4	PAA	4	23.8	−26.55	BBS	RT	ACE	7.9 ± 0.21	–	–	3.3 ± 0.3	0.8	Li et al., 2010
88	BSA	Fe_3O_4	PAA	5	–	–	BBS	RT	ACE	0.19 ± 0.0073	–	–	2.4 ± 0.3	–	Li et al., 2010
89	BSA	Au	Citrate	2.5	11.3	–	BBS	RT	ACE	0.23 ± 0.019	–	–	2.3 ± 0.4	–	Li et al., 2010
90	BSA	Au	Citrate	5	18.9	–	BBS	RT	ACE	0.095 ± 0.0068	–	–	1.2 ± 0.1	–	Li et al., 2010
91	BSA	PS	COOH	30	32.1 ± 0.7	−39.8 ± 3.9	HEPES	25	ITC	4.17	–	–	–	6 ± 0.7	Fleischer and Payne, 2014
92	BSA	PS	COOH	30	32.1 ± 0.7	−39.8 ± 3.9	PBS	RT	FQ	0.00056[d]	–	–	–	6 ± 0.7	Fleischer and Payne, 2014
93	BSA	PS	NH_2	29	31.7 ± 0.6	40.3 ± 4	HEPES	25	ITC	25	–	–	–	31.7 ± 0.6	Fleischer and Payne, 2014
94	BSA	PS	NH_2	29	31.7 ± 0.6	40.3 ± 4	PBS	RT	FQ	0.0013[d]	–	–	–	31.7 ± 0.6	Fleischer and Payne, 2014
95	BSA	PPy	PVAm	67 ± 12	93 ± 21.5	13.5	PBS	RT	CE	0.115 ± 0.005	–	–	1.355 ± 0.078	10	Au and Armes, 2012
96	BSA	CdSe/ZnS	GSH	–	–	–	BBS	RT	CE	8.8	–	–	2.6	–	Wang et al., 2015
97	FIB	FePt	PMA	1.7 ± 0.3	5.8 ± 0.6	−44.1 ± 0.3	PBS	RT	FCS	0.1[a]	0.03 ± 0.01	65 ± 5	0.7 ± 0.1	20.0 ± 1.0	Pelaz et al., 2015
98	FIB	FePt	PMA-10 kDa PEG	1.7 ± 0.3	9.8 ± 0.5	−14.3 ± 0.4	PBS	RT	FCS	0.5[a]	0.14 ± 0.004	18 ± 4	0.4 ± 0.1	8.1 ± 1.6	Pelaz et al., 2015
99	FIB	SiO_2	–	12	–	−18.8	RPMI 1640	37	Free protein	0.028 ± 0.012	–	27 ± 3	–	–	Fedeli et al., 2015
100	FIB	TiO_2	–	1.8	–	47.0 ± 1.0	PBST	25	SPR	>0.00074 <0.000206[b]	–	–	–	–	Canoa et al., 2015
101	FIB	CeO_2	–	6.5	–	26.5 ± 0.5	PBST	25	SPR	>0.000037 <0.000047[b]	–	–	–	–	Canoa et al., 2015
102	FIB	Al_2O_3	–	7	–	20.3 ± 0.2	PBST	25	SPR	>0.010.9 <0.0167[b]	–	–	–	–	Canoa et al., 2015
103	FIB	γ-Fe_2O_3	–	5	–	–	–	25	FQ	0.045	–	–	–	–	Zhang et al., 2015b
104	FIB	γ-Fe_2O_3	–	5	–	–	–	30	FQ	0.09	–	–	–	–	Zhang et al., 2015b
105	FIB	γ-Fe_2O_3	–	5	–	–	–	37	FQ	0.14	–	–	–	–	Zhang et al., 2015b
106	FIB	Au	MUA	2.8	14.4 ± 0.3	−40.8 ± 1.51	H_2O	25	Bound protein	–	2.25	1	2.31	–	Deng et al., 2013
107	FIB	Au	MUA	7.1	23.9 ± 0.3	−41.2 ± 1.31	H_2O	25	Bound protein	–	1.3	2	1.2	–	Deng et al., 2013

Table 1 (*Continued*)

	Protein	NP core	NP coating/modification	r_c (nm)	$r_h(0)$ (nm)	ζ (mV)	Buffer	T (°C)	Method	K_D (μM)	$K'_D = (K_D)^{1/n}$ (μM)	N_{max}	n	Δr_h (nm)	Report
108	FIB	Au	MUA	15.7	46 ± 3	−46.2 ± 2.78	H_2O	25	Bound protein	–	3.5	128	0.75	–	Deng et al., 2013
109	FIB	Au	MUA	32.5	90 ± 1	−40.7 ± 2.84	H_2O	25	Bound protein	–	4.3	1124	1.1	–	Deng et al., 2013
110	apo-Tf	Fe_3O_4	OA/AMP	5	7.45 ± 2.75	−40.4 ± 0.3	PBS	37	CE	0.233 ± 0.1	–	–	–	–	Ashby et al., 2013
111	apo-Tf	FePt	PMA	1.6 ± 0.2	5.1 ± 0.2	−44 ± 3	PBS	RT	FCS	254[a]	26 ± 6	23 ± 3	1.7 ± 0.2	7.0 ± 0.4	Jiang et al., 2010
112	apo-Tf	FePt	PMA	1.7 ± 0.3	5.0 ± 0.2	−45 ± 2	PBS	22	FCS	7[a]	16 ± 6	40 ± 6	0.7 ± 0.1	9.3 ± 0.7	Mahmoudi et al., 2013
113	apo-Tf	FePt	PMA	1.7 ± 0.3	5.1 ± 0.2	−45 ± 2	PBS	9	FCS	4.7[a]	13 ± 4	47 ± 7	0.6 ± 0.1	10.0 ± 0.8	Mahmoudi et al., 2013
114	apo-Tf	FePt	PMA	1.7 ± 0.3	5.3 ± 0.1	−45 ± 2	PBS	43	FCS	3.1[a]	5 ± 1	17 ± 2	0.7 ± 0.1	5.7 ± 0.4	Mahmoudi et al., 2013
115	apoA-I	FePt	PMA	1.6 ± 0.2	6.0 ± 0.1	−44 ± 3	PBS	RT	FCS	140[a]	140 ± 60	52 ± 10	1.0 ± 0.3	4.8 ± 1.4	Maffre et al., 2011
116	apoA-I	HES	–	–	275 ± 26	−34 ± 3	H_2O	25	ITC	0.003	–	10 ± 4	–	–	Winzen et al., 2015
117	apoA-I	HES	—COOH	–	200 ± 20	−34 ± 3	H_2O	25	ITC	0.0053	–	6 ± 3	–	–	Winzen et al., 2015
118	apoA-I	HES	$—NH_2$	–	256 ± 26	−27 ± 3	H_2O	25	ITC	0.185	–	8 ± 6	–	–	Winzen et al., 2015
119	apoA-I	Fe_3O_4	OA/AMP	5	7.45 ± 2.75	−40.4 ± 0.3	PBS	37	CE	0.155 ± 0.001	–	–	–	–	Ashby et al., 2013
120	apoE3	CdSe/ZnS	DHLA	2.6 ± 0.4	5	−25 ± 2	PBS	RT	FCS	0.06 ± 0.01	–	19 ± 1	1.7 ± 0.2	8.2 ± 0.3	Klapper et al., 2015
121	apoE3	CdSe/ZnS	MHPC	2.6 ± 0.4	6.8 ± 0.9	−9.3 ± 0.5	PBS	RT	FCS	430 ± 120	–	28 ± 1	1.5 ± 0.2	8.2	Klapper et al., 2015
122	apoE4	FePt	PMA	1.6 ± 0.2	6.0 ± 0.1	−44 ± 3	PBS	RT	FCS	0.004[a]	0.021 ± 0.003	65 ± 3	1.4 ± 0.2	5.7 ± 0.2	Maffre et al., 2011
123	β-Casein	Fe_3O_4	PAA	3.85 ± 0.45	24.2 ± 4.1	−46.2	PBS	RT	CE	0.23 ± 0.0085	–	–	2.7	–	Zeng et al., 2014
124	β-Casein	Fe_3O_4	PAA	4.05 ± 0.5	29 ± 5.9	−43.8	PBS	RT	CE	4.6 ± 0.093	–	–	1.3	–	Zeng et al., 2014
125	Calmodulin	Fe_3O_4	PAA	3.85 ± 0.45	24.2 ± 4.1	−46.2	PBS	RT	CE	0.28 ± 0.024	–	–	0.4	–	Zeng et al., 2014
126	Calmodulin	Fe_3O_4	PAA	4.05 ± 0.5	29 ± 5.9	−43.8	PBS	RT	CE	0.015 ± 0.0006	–	–	2.1	–	Zeng et al., 2014
127	Myoglobin	Fe_3O_4	PAA	3.85 ± 0.45	24.2 ± 4.1	−46.2	PBS	RT	CE	1.8 ± 0.11	–	–	1.3	–	Zeng et al., 2014
128	Myoglobin	Fe_3O_4	PAA	4.05 ± 0.5	29 ± 5.9	−43.8	PBS	RT	CE	4 ± 0.27	–	–	1.4	–	Zeng et al., 2014
129	Cytochrome C	Fe_3O_4	PAA	3.85 ± 0.45	24.2 ± 4.1	−46.2	PBS	RT	CE	18 ± 4.8	–	–	1.9	–	Zeng et al., 2014
130	Cytochrome C	Fe_3O_4	PAA	4.05 ± 0.5	29 ± 5.9	−43.8	PBS	RT	CE	2.9 ± 0.091	–	–	1.1	–	Zeng et al., 2014
131	C3	CdSe/ZnS	DHLA	2.6 ± 0.4	5	−25 ± 2	PBS	RT	FCS	0.015 ± 0.001	–	8.9 ± 0.4	2.1 ± 0.2	14.6 ± 0.2	Klapper et al., 2015
132	C3	CdSe/ZnS	MHPC	2.6 ± 0.4	6.8 ± 0.9	−9.3 ± 0.5	PBS	RT	FCS	201 ± 30	–	14 ± 2	1.3 ± 0.1	14.6	Klapper et al., 2015
133	A1AT	Fe_3O_4	OA/AMP	5	7.45 ± 2.75	−40.4 ± 0.3	PBS	37	CE	1.01 ± 0.1	–	–	–	–	Ashby et al., 2013
134	HaG	Fe_3O_4	OA/AMP	5	7.45 ± 2.75	−40.4 ± 0.3	PBS	37	CE	0.612 ± 0.074	–	–	–	–	Ashby et al., 2013
135	HRG	SiO_2	–	12	–	−18.8	RPMI 1640	37	Free protein	0.0024 ± 00011	–	30 ± 2	–	–	Fedeli et al., 2015
136	Kin 1	SiO_2	–	12	–	−18.8	RPMI 1640	37	Free protein	0.0046 ± 0.0013	–	47 ± 2	–	–	Fedeli et al., 2015

[a] In case of FCS experiments the measured data are K'_D and n, and K_D was calculated from these two parameters. Measurement of free protein or NP-bound protein concentrations are based on removal of NP-protein complexes by centrifugation and fitting of data using a one-site equilibrium equation or Hill model equation to obtain K_D and N_{max} values (Fedeli et al., 2015), or K'_D values (Deng et al., 2013). For SPR (surface plasmon resonance) data (Canoa et al., 2015), K_D values can be calculated from the binding and dissociation kinetics, obtained using increasing protein ligand concentrations in PBST, and fitting the binding or dissociation curves with Langmuir or bivalent analyte models.

[b] NPs were coupled to alginate (GLC), NeutrAvidin (NLC) or bare gold (BGD) supports and the two extreme values of the range are here indicated.

[c] In the case of HSA-Al_2O_3 binding K_D could not be determined using NLC and BGD supports, likely for interfering phenomena, and high density GLC supports (GLCH) were employed in two different experiments (the two obtained values are reported). In case of TEM imaging of the negative-stained HSA corona the $r_h(0)$ and $r_h(N_{max})$ values were determined by TEM, and the zeta-potential in H_2O.

[d] K_D values were assumed as $K_D = 1/K_{SV}$.

[e] FQ data were experimentally corrected for Inner Filter Effect by using BSA-presaturated NPs.

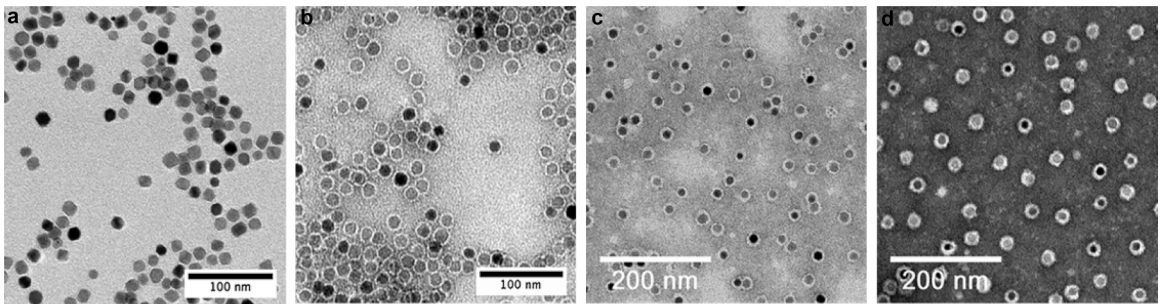

Fig. 1. TEM images of $MnFe_2O_4$ NPs with $CoFe_2O_4$ shell ($MnFe_2O_4/CoFe_2O_4$). (a) NPs as synthesized in chloroform. (b) NPs after transfer to water with a polymer shell (PMA) (Zhang et al., 2015a), imaged with negative staining (Pelaz et al., 2015). (c) NPs after transfer to water with a polymer shell (PMA) and addition of a PEG layer (M_W = 10 kDa), imaged with negative staining. d) NPs after transfer to water with a polymer shell (PMA) and addition of bovine serum albumin (BSA) (Zhang et al., 2015a), imaged with negative staining. Note that here BSA was linked chemically to the NP surface with EDC (1-ethyl-3-(3-dimethylaminopropyl)carbodiimide) chemistry. However, the BSA corona upon adsorption was shown to be the same using gel electrophoresis, *cf.* Fig. 2. The core radius of the NPs as dissolved in chloroform was $r_c = 6.9 \pm 0.7$ nm. The diameter of the NPs as visualized with the negative staining was (b) $r_h(0) = 9.6 \pm 0.4$ nm, (c) 12.4 ± 1.0 nm, and (d) 13.8 ± 1.5 nm, as determined from images of >300 NPs. The thickness of the polymer shell (PMA) thus is 9.6 nm − 6.9 nm = 2.7 nm. The thickness of the PEG shell added to the polymer coating is 12.4 nm − 9.6 nm = 2.8 nm. And the thickness of the layer of adsorbed BSA molecules on top of the polymer shell is Δr_h = 13.8 nm − 9.6 nm = 4.2 nm.

diameters can be determined *via* measurements of the diffusion coefficient of NPs, related by the Stokes–Einstein equation. Diffusion coefficients can be measured *via* observation of NPs diffusing in and out of a test volume from the autocorrelation function of signal fluctuation. Signal of the NPs can be obtained by light scattering (DLS) or by fluorescence of the NPs (FCS) (Liedl et al., 2005; Nienhaus et al., 2013). The resulting data set $d_h(c(P))$ of hydrodynamic diameters determined at different protein concentrations $c(P)$ can be fitted with the Hill model, yielding the protein concentration in which half of the NP surface is saturated with protein K'_D, the maximum number N_{max} of proteins which can be bound per NP, and the Hill coefficient n (del Pino et al., 2014). The group of Nienhaus et al. has used such FCS measurements to determine protein adsorption of several proteins to different NP surfaces (Hühn et al., 2013; Pelaz et al., 2015; Mahmoudi et al., 2013; Röcker et al., 2009; Jiang et al., 2010; Maffre et al., 2011, 2014; Treuel et al., 2014; Klapper et al., 2015). Notably FCS measurements can be performed *in situ*, that is unbound proteins do not have to be separated, as fluorescence originates only from fluorescent NPs. In case of DLS, similar measurements are complicated by light scattering also from free proteins. In general such measurements are also limited to small NPs, as size changes of big NPs upon adsorption by proteins would be too low to be detected with reasonable experimental error.

2.2. Detection of free or NP-bound proteins

There are several biochemical methods for the characterization of the protein corona which are based on the rapid separation of unbound proteins and the NP-protein complexes by centrifugation and the subsequent measurement of the free protein left in the supernatant or of the proteins in the purified NP-protein complexes by any sensitive enough methods (absorbance, fluorescence or colorimetric protein assays). Combining flow field-flow fractionation (F4) with centrifugation, as an open channel separation technique, has proved to be very valuable for the dissociation-based screening of NP-protein interaction (Giddings, 1993). F4 separates compounds based on their size and shape and has already been employed to study antibodies binding affinity to receptors and to cleanup nonspecifically bound proteins from the surface of microbeads that are used in affinity pull-down assay (Li et al., 2008; Korn et al., 2011). Most recently, centrifugation coupled with F4 technique was utilized to purify the protein corona formed on superparamagnetic iron oxide nanoparticles (SPIONs) after incubation with ImmunoglobulinG (IgG)/albumin-depleted human serum (Ashby et al., 2013). Optimal fitting of free protein concentration according to the one-site equilibrium equation, being the NPs molar concentration known, allows for obtaining K_D and N_{max} values. This has been recently demonstrated for the interaction of human Histidine Rich Glycoprotein (HRG), human Kininogen 1 (Kin 1) and FIB with SiO_2-NPs (Fedeli et al., 2015). However such method, being based on the measurement of what is left free, is limited by the accuracy of the protein determination assays and by the affinity and binding capability of the NPs to be analyzed. Low affinity (high K_D) and/or low capacity (low N_{max}) binding may introduce a too high experimental error to get reasonable quantitative information. For example, the affinity of HSA for SiO_2-NPs could be just extrapolated (>1 μM) and the N_{max} was not defined (Fedeli et al., 2015). Alternatively, the amount of NP-bound protein can be determined after nanoparticle washings with any suitable method, as above, and plotted *versus* free protein (deduced) by fitting data with the Hill model (Deng et al., 2013). In such approach, compared to the measurement of the free protein, even binding characterized by low affinity or capacity can be measured accurately since the measure is not subtractive. However, since further steps are required to eliminate any un-bound residual proteins, this procedure may suffer from some degree of dissociation of NPs-bound proteins, during the dilution in ligand free media, used for washings. In fact, this is a critical aspect of both approaches, that is, due to the progressive concentration of NPs during the pelleting procedure, the equilibrium between NPs and solutes are altered to some extent (del Pino et al., 2014), so that the final value of the obtained K_D may be underestimated. Another aspect to be considered is that there may be temperature changes of the system during the procedure. In particular, the temperature kept during the incubation of NPs with proteins (which can be set as desired) may be required to be changed during the following centrifugation steps, usually performed at temperatures between 0 and 4 °C, in order to avoid overheating of the rotors. This technical aspect may affect K_D values as well, since the kinetical constants characterizing the NP-protein conjugates may be temperature dependent (Mahmoudi et al., 2013). A strong point of this methodology is that it is robust, label-free and needs few theoretic assumptions.

2.3. Surface plasmon resonance (SPR)

Real-time SPR is another label-free technique usable, where K_D can be deduced by the analysis of the kinetics of association and dissociation of the ligands from the complex (K_D can be indeed properly defined as the ratio between the dissociation K_{off} constant and the association K_{in} constant in defined temperature conditions). This technique also has the advantage of detecting

phenomena inducing alteration of the structure (denaturation) of bound proteins, which influence the thermodynamics of the interaction and that must be considered for the final K_D determination. However, since this methodology implies the chemical coupling of NPs or proteins to the solid support (cheap) of the SPR device a major problem might be the interference of the chemical nature of this supporting matrix with protein-NP interaction. Canoa et al. (2015) applied SPR to obtain the affinity values of FIB and HSA for TiO_2, CeO_2, Al_2O_3 NPs and found that, in most cases, they were not grossly influenced by the different supports. However, there were exceptions (HSA interaction with Al_2O_3-NPs) in which the choice of the support was found to be very critical. This case indicates that different supporting matrixes should be screened and carefully selected to have reliable results.

2.4. Isothermal titration calorimetry (ITC)

ITC is a very informative label-free method that allows for obtaining both affinity and maximal binding capacity of a certain ligand to NPs, by the detection of the generated, or adsorbed, heat. The measured thermal exchanges may be due to the formation of protein-NPs complexes but also to possible protein denaturation events that also contribute in determining K_D values.

2.5. (Affinity) Capillary electrophoresis (ACE, CE) and related methods

In few cases the ACE technique was used to assess NP-protein interaction. In this approach the velocity of NPs in an applied electric field (Boulos et al., 2013) is a parameter related to the mean NP charge (Pyell et al., 2015a,b), if other hydrodynamic features are not modified. Since in capillary electrophoresis no matrix, as in gel electrophoresis, is used, increase in hydrodynamic diameters has less effect than in case of gel electrophoresis, in which conjugates of biological molecules and NPs may be sorted predominantly by size (Parak et al., 2002, 2003; Sperling et al., 2006; Pellegrino et al., 2007). The charge change due to protein binding to NPs hence modifies their electrophoretic mobility, which in this way reflects the amount of bound proteins. Hence, the relative changes in the retention of the NP-protein conjugates as a function of the protein dose can be a parameter for protein binding to NPs and can be fitted with appropriate mathematical models, like the Hill model (Li et al., 2010), in order to obtain K_D and n as fit parameters. This method has several advantages. It is label-free and, being non-optical, does not suffer for alterations such as the IFE (Inner Filter Effect) that may be acting in fluorescence quenching (FQ) experiments. There is also no purification from unbound proteins required, and thus ACS can be performed *in situ*. However, it has been shown that ACE may not work if positive NPs are to be tested, possibly due to interfering interactions with the capillary material (silica), and is sensitivity to the formation of aggregated NP/protein complexes which affects hydrodynamic diameters. In case a solid matrix is used during electrophoresis such as in gel electrophoresis, then NP-protein conjugates can be also sorted by size (Sperling et al., 2006; Pellegrino et al., 2007), *cf.* Fig. 2.

2.6. Fluorescence quenching (FQ)

Upon formation of protein-NP complex P_nS (here the substrate S is the NP) in case of intrinsically fluorescent NPs the NP fluorescence, or in case of fluorescent proteins (*i.e.* proteins containing tryptophan, tyrosine and phenylalanine) the protein fluorescence can be quenched. Quenching under equilibrium conditions can be described by the Hill model, leading to K_D and n as fit parameters (Lacerda et al., 2010). In case of very low quencher concentrations (*i.e.* in the case fluorescence of the proteins and the NPs is quenched

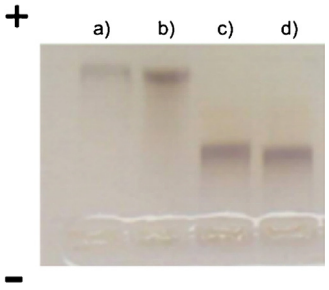

Fig. 2. $MnFe_2O_4$ NPs with $CoFe_2O_4$ shell ($MnFe_2O_4/CoFe_2O_4$) NPs (Zhang et al., 2015a) were coated with the PMA polymer shell. The NPs were incubated with (a) water, (b) EDC, (c) EDC and BSA (TEM image shown in Fig. 1), and (d) BSA. After applying an electric field the negatively charged NPs migrated from the wells towards the plus pole. Due to the size increase by BSA the BSA containing samples are retarded on the gel.

the NPs and the proteins are the quenchers, respectively) nonequilibrium quenching can be described by the Stern–Volmer equation (Stern and Volmer, 1919; Moon et al., 1965). In this approach the quenching efficiency depends on the degree of shielding of the fluorophores by the quenchers, and thus reveals the relative accessibility of quenchers to the fluorophores, which is done by a diffusion model (Lacerda et al., 2010; Sandro et al., 2005; Huang et al., 2014). The Stern–Volmer constant K_{SV} can be considered to be reciprocal to the dissociation constant $K_D \approx 1/K_{SV}$, though actually K_D refers to equilibrium and $1/K_{SV}$ to nonequilibrium conditions. The Stern–Volmer model is based on a diffusion model and only applies for the case that all fluorophores have equal access to the quenchers, that is there are no cooperative or noncooperative effects. In this case of $n = 1$ (*i.e.* noncooperative binding) the Hill and the Stern–Volmer model can be formally merged as shown in the following. The initially added NPs with concentration $c_0(S)$ divide after addition to the proteins in free NPs without attached proteins with concentration $c(S)$ and in the NPs with adsorbed proteins with concentration $c(P_nS)$:

$$c_0(S) = c(S) + c(P_nS) \tag{5}$$

In case the proteins are the quenchers for the NP fluorescence the ratio I_0/I of the NP fluorescence without and the NP fluorescence with proteins added is described by the Stern–Volmer equation.

$$\frac{I_0}{I} = 1 + K_{SV} \cdot c(P) \tag{6}$$

As the fluorescence intensity I of the NPs is proportional to the NP concentration $c(S)$, Eq. (6) can be rewritten to

$$\frac{c_0(S)}{c(S)} = \frac{I_0}{I} = 1 + K_{SV} \cdot c(P) \tag{7}$$

Insertion of Eq. (5) leads to

$$\frac{c(S) + c(P_nS)}{c(S)} = 1 + K_{SV} \cdot c\,(P) \Rightarrow K_{SV} = \frac{c(P_nS)}{c(S) \cdot (P)} = 1/K_D\,(\text{in Eq. (2) with } n = 1) \tag{8}$$

While in Table 1 the $1/K_{SV}$ values (from the Stern–Vollmer model) are enlisted as K_D values (from the Hill model), one has to be aware that this is only true in case $n = 1$ is assumed, quencher concentrations need to be low, and equilibrium and nonequilibrium conditions are mixed. In general FQ may be also overestimated due to the Inner Filter Effect (IFE) caused by light absorption or scattering (Boulos et al., 2013). Also, not all NPs may quench fluorescence of adsorbed proteins with the same efficiency. For sufficient quenching the fluorescent parts of the proteins have to come close enough to the inorganic part of the NP surface (such as Au or Ag

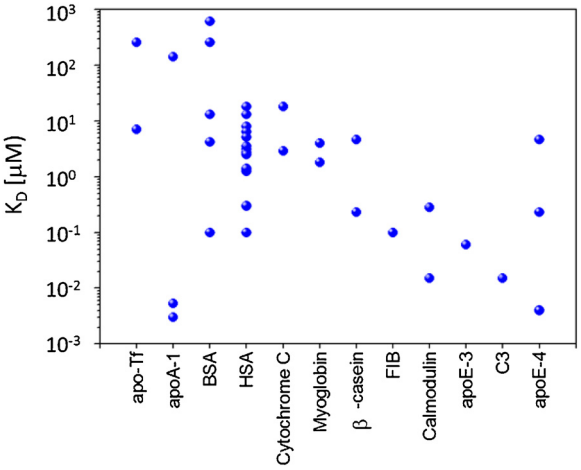

Fig. 3. K_D values from Table 1 for different proteins. In order to get comparable conditions only NPs with —COOH groups on their surface (citrate, DPA, DHLA, PMA, PAA) with zeta potential $\zeta < -25$ mV, at room temperature (RT, 22 °C, 25 °C) were considered. Data obtained with FQ measurements are excluded from this graph.

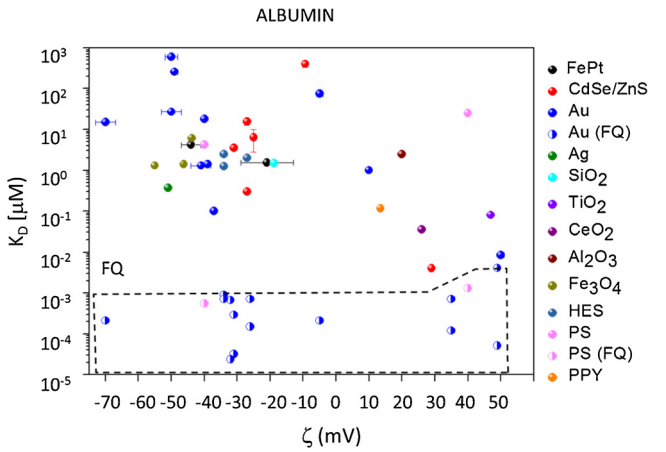

Fig. 4. K_D values from Table 1 relative to albumin-NP binding plotted *versus* the zeta potential of the NPs. Values obtained using NPs made with the indicated materials are represented irrespectively of size, shape, or further coating and chemical modification, and are uniquely expressed as a function of their zeta potential. Obviously reported K_D values not implemented with determined zeta potential of the NPs in the study could not be used for this analysis. The dashed line-delimited area groups all data that were obtained with FQ, while points outside this area correspond to all other methodologies (*cf.* Table 1).

surfaces) (Dulkeith et al., 2005) and thus polymer shells around the NP cores may significantly reduce quenching. In case of NP (*i.e.* QD) quenching, one needs to make sure that protein solutions do not contain other molecules as some ions, as those also may quench the fluorescence of QDs (Susha et al., 2006).

3. Results

Results obtained from more than 130 different datasets with different NPs, proteins, and methods are summarized in Table 1. This table is representative for one general problem in literature concerning investigation of the protein corona. Most authors are using very different systems and thus it is hard to compare data. In this review, we focus on K_D values, which represent absolute numbers and thus should be comparable. However, due to the different NP materials, modifications and different detection methods, it is even hard to find strong correlations in the set of K_D data presented in Table 1. In general, K_D values as obtained with FQ as method are smaller than the ones as measured with different techniques. In fact, for obtaining this table we simply set $K_{SV} = 1/K_D$ (*cf.* Eq. (8)), despite the fact that in general both values are not equivalent and this approximation can be used only for certain conditions. Thus, values as obtained with FQ will not be involved in the analysis as given below. A second problem hampering direct comparison of different studies is lack of NP characterization. In several studies experimental determination of the colloidal properties, as in particular state of dispersion (*i.e.* analysis of potential NP agglomeration) and about basis parameters such as the zeta potential are missing. In those studies it is hard to relate the protein-binding properties of the NPs to their physicochemical parameters.

First we analyzed different K_D values of proteins. In order to achieve comparable conditions we limited this analysis to highly negatively charged NPs at room temperature, excluding data obtained with FQ. The results are displayed in Fig. 3. While for some proteins there is only one of few values available some tendencies in the K_D values in-between different protein species can be observed. In agreement with the classical Vroman data K_D values for FIB are in general orders of magnitude lower than that for HSA. FIB thus is a stronger binder to negatively charged NP surfaces than HSA. Still surprisingly there are enormous differences between data obtained in different studies.

Next we attempted to analyze dependencies on physicochemical parameters of NPs. As albumins (HSA and BSA) are the most studied proteins, in Table 1 we first screened these data for potential dependencies of the K_D values with physicochemical NP properties. As most evident parameter we identified the zeta potential ζ. In Fig. 4, the K_D values are plotted for both bovine and human albumins, assumed to behave similarly, *versus* the zeta potential of the respective NPs. In spite of scattering of data, reasonable considering the many other variables involved (materials, coatings, size and methodologies), there is a clear trend for lower K_D values towards less negative and more positive zeta potentials.

However, as anticipated above in commenting Table 1, this graphical representation allows to appreciate better how, while the majority of methodologies seem to generate data in the same rough direction, data obtained with FQ show a peculiar and divergent distribution. Not only the absolute values of K_D are orders of magnitudes lowers than those determined with other approaches, in some cases within the same study and exactly with the same NPs (Fleischer and Payne, 2014), but also no clear changes were reported as a function of the zeta potential. Although IFE, if not properly evaluated, may be responsible for K_D underestimations, this is not enough to account for the observed divergence with values from alternative methods. This analysis demonstrates that data obtained with FQ experiments are significantly different from those obtained with other methods, and suggests caution in assuming that K_D can be deduced from K_{SV}. In Fig. 5, the K_D values characterizing HSA/BSA interaction with NPs, omitting FQ derived ones for the reasons above motivated, are analyzed for different NP materials. This allowed to confirm the trend above evidenced of an affinity improvement of albumin for positively charged NPs, independently on the material or the coating chemistry, further supporting the importance of the z potential in governing albumin-NP association. However, in the case of the three organic NPs that could be analyzed (HSE, PS and PPy) no clear trend could be seen. In fact, in the only homogeneous comparison possible (PS) the charge switch from negative to positive charge of the NP, obtained by —COOH or $-NH_2$ groups coupling, determined a sensible increase of the K_D, indicating an affinity decrease, opposite to the trend observed for other NP types. On the other hand, positive PPy NPs coated with a cationic polymer bind BSA with an affinity apparently one-two order of magnitude stronger than those seen in the other organic NPs here compared, in line with data obtained with other NPs.

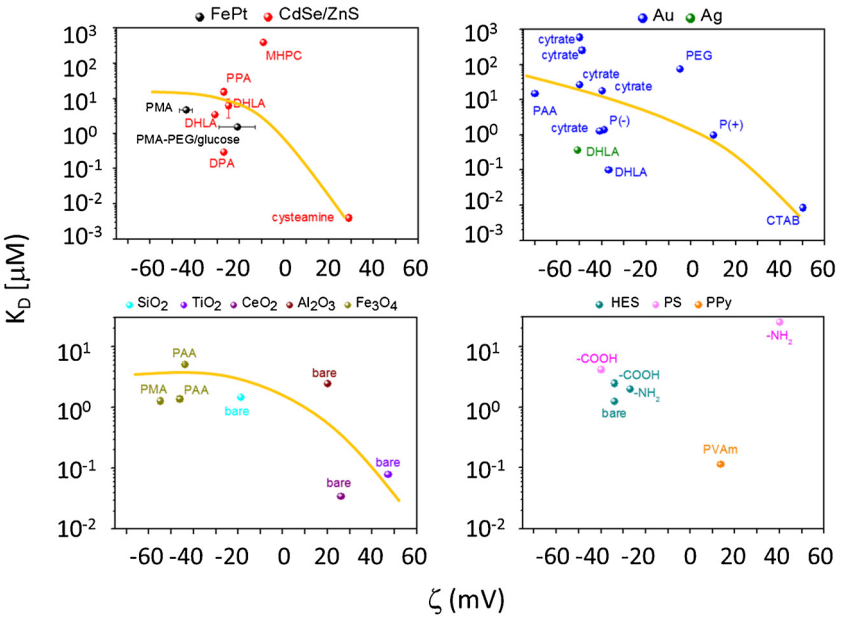

Fig. 5. Data from Fig. 4 divided into different subgroups. All K_D values of Fig. 4 were split into four groups: FePt and CdSe/ZnS NPs; metal NPs (Au and Ag); oxides and organic NPs. The surface coating or chemical modification of the bare material is indicated near to the respective data point. "bare" indicates the pristine material surface. The yellow line guides the eye to follow the trend of data, without analytical rational behind the shape of the curve.

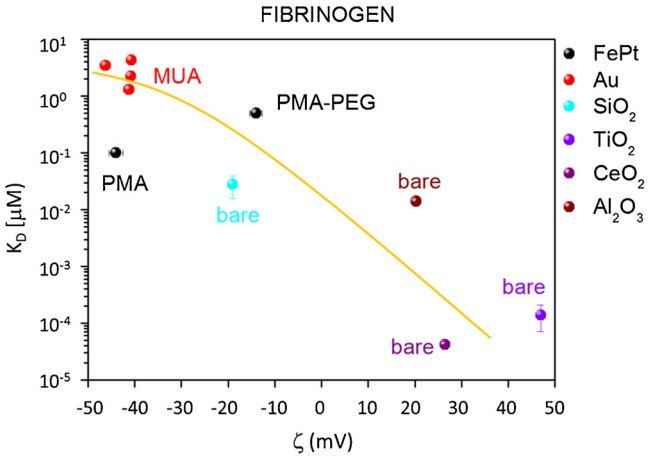

Fig. 6. Fibrinogen K_D values from Table 1 plotted *versus* the zeta potential of the NPs. The surface coating or chemical modification of the bare material, when present, is indicated near to any data point. "bare" indicates the pristine material surface. These data are taken from several studies (Pelaz et al., 2015; Fedeli et al., 2015; Deng et al., 2013; Canoa et al., 2015). The yellow line acts merely as a guide to the eye to follow the trend of data, without analytical rational behind the shape of the curve.

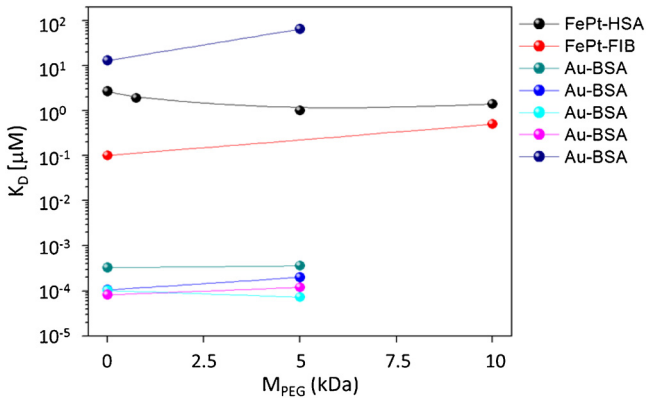

Fig. 7. K_D values from Table 1 plotted *versus* the degree of PEGylation of the NPs. The PEGylation is described *via* the molecular mass M_{PEG} of the attached PEG molecules. No attached PEG is referred to as $M_{PEG} = 0$. These data are taken from several studies (Pelaz et al., 2015; Boulos et al., 2013). From the data set of Boulos et all the data with PAA (*i.e.* $M_{PEG} = 0$) and with 5 kDa PEG are compared (Boulos et al., 2013). The lines connecting the data points act merely as a guide to the eye to follow the trend of data, without analytical rational behind the shape of the curve.

Hence, due to the paucity of data and to the conflicting results, no conclusion can be drawn and more quantitative data are necessary.

The same analysis as for albumins (HSA, BSA) was also done for FIB, *cf.* Fig. 6. Although the data set for this protein is smaller, and negative and positive NPs are all chemically different, the graph clearly suggests that, as for albumins, there is a tendency to lower K_D values for FIB for more positive NPs. In this case, quantitative homogeneous data would greatly help to confirm the trend. With all the caveats emerged, the available data indicate that zeta-potential of the NPs thus seems to be a very influential parameter.

In Table 1, there are also some sets of data in which the effect of PEGylation within one series of NPs is investigated (Pelaz et al., 2015; Boulos et al., 2013). Surprisingly, in the case of albumin, K_D values are weakly influenced by PEGylation. Data plotted in Fig. 6 are relative to a set of data in which the same particles (FePt) coated only with PMA or with PMA plus a further layer of PEG with increasing molecular weights are compared (Pelaz et al., 2015). Interestingly, while for BSA K_D and N_{max} values only slightly changed, for FIB K_D increased 5 times and N_{max} decreased sensibly in PEGylated NPs compared to the PMA-coated. Considering that the isoelectric points of albumin and FIB are similar (4.7 and 5.5, respectively), and that hence both proteins are negatively charged in the experimental condition used (pH around 7), this information suggests that zeta potential and PEG polymer coating are not the unique factors governing the K_D and the binding capacity of a NPs to proteins, *cf.* Fig. 7. The kind of protein, and its specific biochemical and structural properties are also very important factors. Also temperature dependence has been investigated in several studies. However, comparison of these data does not suggest any trend, *cf.* Fig. 8.

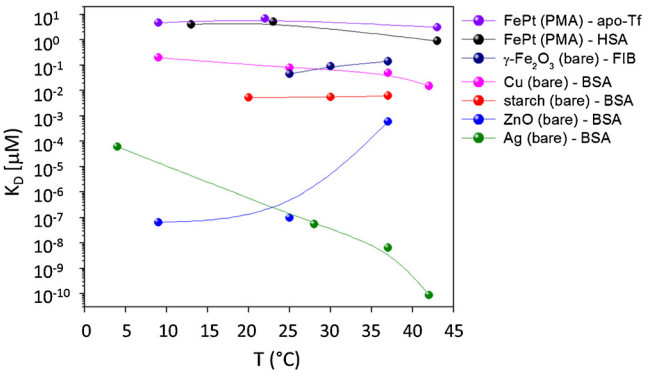

Fig. 8. K_D values from Table 1 plotted *versus* the temperature upon incubation of the NPs with proteins. These data are taken from several studies (Mahmoudi et al., 2013; Ji et al., 2015; Bhogale et al., 2013; Mariam et al., 2011; Zhang et al., 2015b). The material forming the NPs and the binding protein are indicated. Coatings are within brackets. The lines connecting the data points act merely as a guide to the eye to follow the trend of data, without analytical rational behind the shape of the curve.

4. Conclusions

For the use of NPs towards biological applications the characterizations of the proteins selectively adsorbed to proposed NP formulations is a recognized central aspect. Thanks to increasingly sophisticated proteomic and bio-informatics approaches, the list of specific biofluid proteins (especially from serum or plasma) found on various NPs is becoming more and more long and detailed. However, it is still to be remembered that the dynamic association and dissociation of a protein to and from the NP surface, is the first essential phenomenon governing the formation of the NPs' protein corona, and that its quantitative characterization is critically important. The dissociation constant (K_D) is a useful and intuitive thermodynamic parameter related to the efficacy, or affinity, of a given molecule to bind to NPs. In fact, the K'_D value ($K_D = K'_D$ for $n = 1$), the reciprocal of the association constant (K'_A), corresponds to the concentration of a certain protein ligand resulting in half saturation (50%) of the NPs maximal binding capacity (N_{max}), in the absence of other potential binders which may compete for attachment to the NP surface. Hence, the lower the K_D, the higher the affinity and, in the end, the lower the concentrations of a solute necessary to significantly cover the NPs surface. Clearly, for a systematic studies K_D values need to be determined with single purified protein ligands, while, within the context of complex protein mixtures, the actual concentrations of the potential protein binders and their reciprocal competitions for the NP surface will lead to the final binding extent of any ligand and hence to the actual corona composition. Nevertheless, the determination of both K_D and N_{max} values characterizing all the main corona-forming proteins may be an obliged step to understand and even simulate, with appropriate models, the corona composition at equilibrium and possibly to predict its evolution in changing physiological environments. Affinity determination is strongly desirable also because it would allow for objective and quantitative comparisons of the performance and features of different NPs and corona components, studied in different investigations.

With this perspective, in this review we have done a detailed literature survey, screening for those studies in which the interaction of proteins with NPs was approached in a quantitative way and wherefrom K_D values could be evinced and compared. In doing this we also described the different available methodologies that were applied, evaluating their strong points or their critical aspects and limitations. Data analysis and comparison indicated that, in spite of many years effort, only for few proteins like albumin and fibrinogen larger sets of data have been produced, while in other cases, the information is more limited and sometime sporadic. This is understandable, due to the extreme variability of the NPs developed or studied by the various groups. In some other cases, like for HRG, the protein was only recently identified as a functionally important actor in the corona of a single NP type (SiO_2-NPs). At the same time, considering that NPs proteoma are available in several cases, our analysis indicates that we are only beginning to approach protein-NP interactions with a quantitative attitude.

With the above limitations, data comparison allowed us to draw some conclusions. First, the zeta-potential, which is related to the surface charge of the NPs, was found to be a strongly influential parameter determining protein binding. In fact, a general trend of increased affinity, or decreased K_D, in the case of moderately negative or positive NPs could be seen. Importantly, however, in agreement with some specific experiments present in one study, our vast comparison confirmed that among all possible methods used to obtain K_D, the Fluorescence Quenching approach (FQ) strongly underestimates K_D values and deviates from the above found trend.

A final consideration deserves the classical distinction between hard and soft NP coronas. The hard corona is popularly defined as the layer of bound proteins irreversibly or strongly bound to the NP while, in opposition, the soft corona is assumed to be formed by reversibly or weakly bound proteins. However, one can image a whole spectrum of affinities for different pairs of NP and proteins, as clearly emerged from our survey, with K_D values gradually ranging from mM to pM. This fact makes it difficult and also arbitrary to establish a clear-cut border between hard and soft binding. K_D values, being a continuous parameter, and being the ratio between the kinetics dissociation constant and the kinetics association constants, may be a more appropriate and less subjective way to define and to compare the strength and the reversibility of different NP-ligand complexes.

In the same way reversible *versus* irreversible binding may be the reason for differences in K_D values as obtained with the different experimental methods. Here the time scale on which measurements take place in relation to the time needed to reach equilibrium is of importance (Maffre et al., 2014). Reversible *versus* irreversible binding has only be scarcely discussed in literature. Treuel et al. have demonstrated that in case of ligand capped negatively charged NPs, that is NPs with a very thin shell rich in —COOH, protein binding is full reversible (Treuel et al., 2014). They refer this to the fact that in this case protein binding is fully controlled by electrostatic forces. In buffer the charge of the NP surface and the proteins is screened, and thus only local electrostatic interaction plays a role. In this way adhesion is driven by positive patches on the protein surface that bind to the negatively charged NP surface. Binding thus is dominated by Coulomb energy. This was demonstrated by modifying the charge of HSA by chemical modification, followed by determining K_D constants of the modified proteins (Maffre et al., 2014; Treuel et al., 2014). In contrast, for NPs coated with an amphiphilic polymer binding is also influenced by entropy (Mahmoudi et al., 2013; Tay et al., 2014), which may be due to the hydrophobic parts in the inside of the polymer shell. This in turn may lead to some irreversible binding of proteins (Maffre et al., 2014).

Acknowledgements

This work was supported by the European Commission (projects FutureNanoNeeds to WJP, CheTherDel to EP and NANOPHOTO to EP) and by the University of Padova (projects Ex 60% 2010–2015 and PRAT 2011 to EP). The authors are grateful to Prof. Dr. Hermann Gaub for stimulating discussions.

References

Albanese, A., Tang, P.S., Chan, W.C.W., 2012. The effect of nanoparticle size, shape, and surface chemistry on biological systems, in annual review of biomedical engineering. Annu. Rev. (Palo Alto) 14, 1–16.

Ashby, J., et al., 2013. Dissociation-based screening of nanoparticle–protein interaction via flow field-flow fractionation. Anal. Chem. 85 (15), 7494–7501.

Au, K.M., Armes, S.P., 2012. Heterocoagulation as a facile route to prepare stable serum albumin-nanoparticle conjugates for biomedical applications: synthetic protocols and mechanistic insights. ACS Nano 6 (9), 8261–8279.

Banda, N.K., et al., 2014. Mechanisms of complement activation by dextran-coated superparamagnetic iron oxide (SPIO) nanoworms in mouse versus human serum. Part. Fibre Toxicol. 11.

Bhogale, A., et al., 2013. Systematic investigation on the interaction of bovine serum albumin with ZnO nanoparticles using fluorescence spectroscopy. Colloids Surf. B: Biointerfaces 102, 257–264.

Bhogale, A., et al., 2014. Comprehensive studies on the interaction of copper nanoparticles with bovine serum albumin using various spectroscopies. Colloids Surf. B: Biointerfaces 113, 276–284.

Boulos, S.P., et al., 2013. Nanoparticle–protein interactions: a thermodynamic and kinetic study of the adsorption of bovine serum albumin to gold nanoparticle surfaces. Langmuir 29 (48), 14984–14996.

Cai, H.A.X., Yao, P., 2014. Gold nanoparticles with different amino acid surfaces: serum albumin adsorption, intracellular uptake and cytotoxicity. Colloids Surf. B: Biointerfaces 123, 900–906.

Canoa, P., et al., 2015. A quantitative binding study of fibrinogen and human serum albumin to metal oxide nanoparticles by surface plasmon resonance. Biosens. Bioelectron. 74, 376–383.

Casals, E., et al., 2010. Time evolution of the nanoparticle protein corona. ACS Nano 4 (7), 3623–3632.

Cedervall, T., et al., 2007. Understanding the nanoparticle–protein corona using methods to quantify exchange rates and affinities of proteins for nanoparticles. Proc. Natl. Acad. Sci. U. S. A. 104 (7), 2050–2055.

Chakraborty, S., et al., 2011. Contrasting effect of gold nanoparticles and nanorods with different surface modifications on the structure and activity of bovine serum albumin. Langmuir 27 (12), 7722–7731.

Chanana, M., et al., 2013. Physicochemical properties of protein-coated gold nanoparticles in biological fluids and cells before and after proteolytic digestion. Angew. Chem. Int. Ed. 52 (15), 4179–4183.

del Pino, P., et al., 2014. Protein corona formation around nanoparticles-from the past to the future. Mater. Horiz. 1, 301–313.

Deng, Z.J., et al., 2011. Nanoparticle-induced unfolding of fibrinogen promotes Mac-1 receptor activation and inflammation. Nat. Nanotechnol. 6 (1), 39–44.

Deng, J., et al., 2013. Molecular interactions of different size AuNP-COOH nanoparticles with human fibrinogen. Nanoscale 5 (17), 8130–8137.

Docter, D., et al., 2015a. The nanoparticle biomolecule corona: lessons learned – challenge accepted? Chem. Soc. Rev. 44, 6094–6121.

Docter, D., et al., 2015b. No king without a crown – impact of the nanomaterial–protein corona on nanobiomedicine. Nanomedicine 10 (3), 503–519.

Dominguez-Medina, S., et al., 2012. In situ measurement of bovine serum albumin interaction with gold nanospheres. Langmuir 28 (24), 9131–9139.

Dominguez-Medina, S., et al., 2013. Adsorption of a protein monolayer via hydrophobic interactions prevents nanoparticle aggregation under harsh environmental conditions. ACS Sustain. Chem. Eng. 1 (7), 833–842.

Domke, J., et al., 2000. Substrate dependent differences in morphology and elasticity of living osteoblasts investigated by atomic force microscopy. Colloids Surf. B 19 (4), 367–379.

Dulkeith, E., et al., 2005. Gold nanoparticles quench fluorescence by phase induced radiative rate suppression. Nanoletters 5 (4), 585–589.

Fadeel, B., et al., 2013. Bridge over troubled waters: understanding the synthetic and biological identities of engineered nanomaterials. Wiley Interdiscipl. Rev.: Nanomed. Nanobiotechnol. 5 (2), 111–129.

Fedeli, C., et al., 2013. Catastrophic inflammatory death of monocytes and macrophages by overtaking of a critical dose of endocytosed synthetic amorphous silica nanoparticles/serum protein complexes. Nanomedicine 8 (7), 1101–1126.

Fedeli, C., et al., 2015. The functional dissection of the plasma corona of SiO_2-NPs spots histidine rich glycoprotein as a major player able to hamper nanoparticles capture by macrophages. Nanoscale 7 (42), 17710–17728.

Feliu, N., et al., 2012. Stability and biocompatibility of a library of polyester dendrimers in comparison to polyamidoamine dendrimers. Biomaterials 33 (7), 1970–1981.

Fleischer, C.C., Payne, C.K., 2014. Secondary structure of corona proteins determines the cell surface receptors used by nanoparticles. J. Phys. Chem. B 118 (49), 14017–14026.

Geidel, C., et al., 2011. A general synthetic approach for obtaining cationic and anionic inorganic nanoparticles via encapsulation in amphiphilic copolymers. Small 7 (20), 2929–2934.

Giddings, J.C., 1993. Field-flow fractionation: analysis of macromolecular, colloidal, and particulate materials. Science 260, 1456–1465.

Goy-Lopez, S., et al., 2012. Physicochemical characteristics of protein-NP bioconjugates: the role of particle curvature and solution conditions on human serum albumin conformation and fibrillogenesis inhibition. Langmuir 28 (24), 9113–9126.

Hill, A.V., Brown, T.G., Roaf, H.E., 1910. The possible effects of the aggregation of the molecules of hemoglobin on its dissociation curves. J. Physiol. 40 (Suppl.), i–vii.

Hindie, M., et al., 2011. Pre-osteoblasts on poly(L-lactic acid) and silicon oxide: influence of fibronectin and albumin adsorption. Acta Biomater. 7 (1), 387–394.

Huang, R., et al., 2013. Protein–nanoparticle interactions: the effects of surface compositional and structural heterogeneity are scale dependent. Nanoscale 5 (15), 6928–6935.

Huang, R.X., et al., 2014. Effects of surface compositional and structural heterogeneity on nanoparticle–protein interactions: different protein configurations. ACS Nano 8 (6), 5402–5412.

Hühn, D., et al., 2013. Polymer-coated nanoparticles interacting with proteins and cells: focusing on the sign of the net charge. ACS Nano 7 (4), 3253–3263.

Ji, N., et al., 2015. Study on the interaction between bovine serum albumin and starchnanoparticles prepared by isoamylolysis and recrystallization. Colloids Surf. B: Biointerfaces 128, 594–599.

Jiang, X., et al., 2010. Quantitative analysis of the protein corona on FePt nanoparticles formed by transferrin Binding. J. R. Soc. Interface 7, S5–S13.

Jung, S.-Y., et al., 2003. The Vroman effect: a molecular level description of fibrinogen displacement. J. Am. Chem. Soc. 125 (42), 12782–12786.

Jung, S.Y., et al., 2009. A biologically active sequence of the laminin alpha 2 large globular 1 domain promotes cell adhesion through syndecan-1 by inducing phosphorylation and membrane localization of protein kinase C delta. J. Biol. Chem. 284 (46), 31764–31775.

Keselowsky, B.G., Collard, D.M., Garcia, A.J., 2003. Surface chemistry modulates fibronectin conformation and directs integrin binding and specificity to control cell adhesion. J. Biomed. Mater. Res. Part A 66A (2), 247–259.

Klapper, Y., et al., 2015. Low affinity binding of plasma proteins to lipid-coated quantum dots as observed by in situ fluorescence correlation spectroscopy. Nanoscale 7 (22), 9980–9984.

Korn, M., et al., 2011. Development of stable isotope dilution assays for ochratoxin A in blood samples. Anal. Biochem. 419, 88–94.

Lacerda, S.H., et al., 2010. Interaction of gold nanoparticles with common human blood proteins. ACS Nano 4 (1), 365–379.

Lehmann, A.D., et al., 2010. Fluorescent-magnetic hybrid nanoparticles induce a dose-dependent increase in proinflammatory response in lung cells in vitro correlated with intracellular localization. Small 6 (6), 753–762.

Lesniak, A., et al., 2010. Serum heat inactivation affects protein corona composition and nanoparticle uptake. Biomaterials 31 (36), 9511–9518.

Li, J., et al., 2008. Multiplexed affinity-based protein complex purification. Anal. Chem. 80, 7068–7074.

Li, N., et al., 2010. Probing nanoparticle–protein interaction by capillary electrophoresis. Anal. Chem. 82 (17), 7460–7466.

Liedl, T., et al., 2005. Fluorescent nanocrystals as colloidal probes in complex fluids measured by fluorescence correlation spectroscopy. Small 1 (10), 997–1003.

Lin, C.-A.J., et al., 2008. Design of an amphiphilic polymer for nanoparticle coating and functionalization. Small 4 (3), 334–341.

Lundqvist, M., et al., 2008. Nanoparticle size and surface properties determine the protein corona with possible implications for biological impacts. Proc. Natl. Acad. Sci. U. S. A. 105 (38), 14265–14270.

Maffre, P., et al., 2011. Characterization of protein adsorption onto FePt nanoparticles using dual-focus fluorescence correlation spectroscopy. Beilstein J. Nanotechnol. 2, 374–383.

Maffre, P., et al., 2014. Effects of surface functionalization on the adsorption of human serum albumin onto nanoparticles – a fluorescence correlation spectroscopy study. Beilstein J. Nanotechnol. 5, 2036–2047.

Mahmoudi, M., et al., 2013. Temperature: the "ignored" factor at the NanoBio interface. ACS Nano 7 (8), 6555–6562.

Maiolo, D., et al., 2015. Nanomedicine delivery: does protein corona route to the target or off road? Nanomedicine 10, 3231–3247.

Mariam, J., Dongre, P.M., Kothari, D.C., 2011. Study of interaction of silver nanoparticles with bovine serum albumin using fluorescence spectroscopy. J. Fluoresc. 21 (6), 2193–2199.

Min, S.K., et al., 2013. Titanium surface coating with a laminin-derived functional peptide promotes bone cell adhesion. Biomed. Res. Int. 2013, article ID 638348.

Moerz, S.T., et al., 2015. Formation mechanism for stable hybrid clusters of proteins and nanoparticles. ACS Nano 9 (7), 6696–6705.

Moon, A.Y., Poland, D.C., Scheraga, H.A., 1965. Thermodynamic data from fluorescence spectra. I. The system phenol-acetate. J. Phys. Chem. 69, 2960–2966.

Naveenraj, S., et al., 2010. The interaction of sonochemically synthesized gold nanoparticles with serum albumins. J. Pharm. Biomed. Anal. 53 (3), 804–810.

Nienhaus, G.U., Maffre, P., Nienhaus, K., 2013. Studying the protein corona on nanoparticles by FCS. Methods Enzymol. 519, 115–137.

Noh, H., Vogler, E.A., 2007. Volumetric interpretation of protein adsorption: competition from mixtures and the Vroman effect. Biomaterials 28 (3), 405–422.

Parak, W.J., et al., 2002. Conjugation of DNA to silanized colloidal semiconductor nanocrystaline quantum dots. Chem. Mater. 14 (5), 2113–2119.

Parak, W.J., et al., 2003. Conformation of oligonucleotides attached to gold nanocrystals probed by gel electrophoresis. Nanoletters 3 (1), 33–36.

Pelaz, B., et al., 2015. Surface functionalization of nanoparticles with polyethylene glycol: effects on protein adsorption and cellular uptake. ACS Nano 9 (7), 6996–7008.

Pellegrino, T., et al., 2007. Gel electrophoresis of gold-DNA nanoconjugates. J. Biomed. Biotechnol., 1–9, AN: 26796.

Pyell, U., et al., 2015a. Characterization of gold nanoparticles with different hydrophilic coatings via capillary electrophoresis and Taylor dispersion analysis. Part I: determination of the zeta potential employing a modified analytic approximation. J. Colloid Interface Sci. 450, 288–300.
Pyell, U., et al., 2015b. Characterization of hydrophilic coated gold nanoparticles via capillary electrophoresis and Taylor dispersion analysis. Part II: determination of the hydrodynamic radius distribution – comparison with asymmetric flow field-flow fractionation. J. Colloid Interface Sci. 457, 131–140.
Röcker, C., et al., 2009. A quantitative fluorescence study of protein monolayer formation on colloidal nanoparticles. Nat. Nanotechnol. 4 (9), 577–580.
Sandro, M.G., et al., 2005. High-affinity approach for the synthesis of fluorophore appended protein nanoparticle assemblies. Chem. Commun., 2832–2834.
Segat, D., et al., 2011. Proinflammatory effects of bare and PEGylated ORMOSIL-PLGA- and SUV-NPs on monocytes and PMNs and their modulation by f-MLP. Nanomedicine 6 (6), 1027–1046.
Shang, L., et al., 2012. Ultrasmall fluorescent silver nanoclusters: protein adsorption and its effects on cellular responses. Nano Res. 5 (8), 531–542.
Shang, L., et al., 2014. Nanoparticles interacting with proteins and cells: a systematic study of protein surface charge effects. Adv. Mater. Interfaces 1 (2).
Sperling, R.A., et al., 2006. Electrophoretic separation of nanoparticles with a discrete number of functional groups. Adv. Funct. Mater. 16 (7), 943–948.
Stern, O., Volmer, M., 1919. Über die Abklingungszeit der Fluoreszenz. Phys. Z. 20, 183–188.
Susha, A.S., et al., 2006. Luminescent CdTe nanocrystals as ion probes and pH sensors in aqueous solutions. Colloids Surf. A: Physicochem. Eng. Asp. 281, 40–43.
Tavano, R., et al., 2010. Procoagulant properties of bare and highly PEGylated vinyl-modified silica nanoparticles. Nanomedicine 5 (6), 881–896.
Tay, C.Y., et al., 2014. Back to basics: exploiting the innate physico-chemical characteristics of nanomaterials for biomedical applications. Adv. Funct. Mater. 24, 5936–5955.
Tenzer, S., et al., 2013. Rapid formation of plasma protein corona critically affects nanoparticle pathophysiology. Nat. Nanotechnol. 8 (10), 772-U1000.
Treuel, L., et al., 2014. Impact of protein modification on the protein corona on nanoparticles and nanoparticle–cell interactions. ACS Nano 8 (1), 503–513.
Vroman, L., 1962. Effect of adsorbed proteins on wettability of hydrophilic and hydrophobic solids. Nature 196 (4853), 476.
Vroman, L., Adams, A.L., 1969. Findings with recording ellipsometer suggesting rapid exchange of specific plasma proteins at liquid/solid interfaces. Surf. Sci. 16, 438.
Vroman, L., Lukosevicius, A., 1964. Ellipsometer recordings of changes in optical thickness of adsorbed films associated with surface activation of blood clotting. Nature 204 (495), 701.
Wang, J.H., et al., 2015. In-capillary self-assembly study of quantum dots and protein using fluorescence coupled capillary electrophoresis. Electrophoresis 36 (14), 1523–1528.
Winzen, S., et al., 2015. Complementary analysis of the hard and soft protein corona: sample preparation critically effects corona composition. Nanoscale 7 (7), 2992–3001.
Zeng, S., et al., 2014. Protein binding for detection of small changes on a nanoparticle surface. Analyst 139 (6), 1364–1371.
Zhang, Q., et al., 2015a. Model driven optimization of magnetic anisotropy of exchange-coupled core–shell ferrite nanoparticles for maximal hysteretic loss. J. Mater. Chem.
Zhang, H., et al., 2015b. Interaction of gamma-Fe_2O_3 nanoparticles with fibrinogen. Spectrochim. Acta A. Mol. Biomol. Spectrosc. 151, 40–47.

CHEMISTRY OF MATERIALS

Article

pubs.acs.org/cm

Selected Standard Protocols for the Synthesis, Phase Transfer, and Characterization of Inorganic Colloidal Nanoparticles

Jonas Hühn,[†] Carolina Carrillo-Carrion,[‡] Mahmoud G. Soliman,[†] Christian Pfeiffer,[†] Daniel Valdeperez,[†] Atif Masood,[†] Indranath Chakraborty,[†] Lin Zhu,[†] Marta Gallego,[‡] Zhao Yue,[†] Monica Carril,[‡,§] Neus Feliu,[†,▼] Alberto Escudero,[†,∥] Alaaldin M. Alkilany,[⊥] Beatriz Pelaz,[†,#] Pablo del Pino,[†,#] and Wolfgang J. Parak*[,†,‡,▽]

[†]Fachbereich Physik, Philipps Universität Marburg, 35037 Marburg, Germany

[‡]CIC biomaGUNE, 20009 San Sebastian, Spain

[§]Ikerbasque, Basque Foundation for Science, 48011 Bilbao, Spain

[∥]Instituto de Ciencia de Materiales de Sevilla, CSIC − Universidad de Sevilla, 41092 Seville, Spain

[⊥]Faculty of Pharmacy, The University of Jordan, Amman 11942, Jordan

[#]Centro Singular de Investigación en Química Biológica y Materiales Moleculares (CiQUS) y Departamento de Física de Partículas, Universidade de Santiago de Compostela, 15782 Santiago de Compostela, Spain

[▽]Institute of Nano Biomedicine and Engineering, Key Laboratory for Thin Film and Microfabrication Technology of the Ministry of Education, Department of Instrument Science and Engineering, School of Electronic Information and Electrical Engineering, Shanghai Jiao Tong University, 800 Dongchuan Rd., Shanghai 200240, China

[▼]Experimental Cancer Medicine (ECM), Department of Laboratory Medicine, Karolinska Institutet, Huddinge, Stockholm, Sweden

Supporting Information

ABSTRACT: Synthesis, characterization, and applications of colloidal nanoparticles have been a prominent topic of current research interests within the last two decades. Available reports in the literature that describe the synthesis of colloidal nanoparticles are abundant with various degrees of reproducibility and simplicity. Moreover, different methods for the characterization of colloidal nanoparticle's basic properties are employed, resulting in conflicting results in many cases. Herein, we describe "in detail" selected standard protocols for the synthesis, purification, and characterization of various types of colloidal inorganic nanoparticles including gold nanoparticles, silver nanoparticles, iron oxide nanoparticles, and quantum dots. This report consists of five main parts: The first and the second parts are dedicated to describing the synthesis of various types of hydrophobic and hydrophilic nanoparticles in organic solvents and in aqueous solutions, respectively. The third part describes surface modification of nanoparticles with a focus on ligand exchange reactions, to allow phase transfer of nanoparticles from aqueous to organic solvents and vice versa. The fourth and the fifth parts describe various general purification and characterization techniques used to purify and characterize nanoparticles, respectively. Collectively, this contribution does not aim to cover all available protocols in the literature to prepare inorganic nanoparticles but rather provides detailed synthetic procedures for important inorganic nanocrystals with a full description of their purification and characterization process.

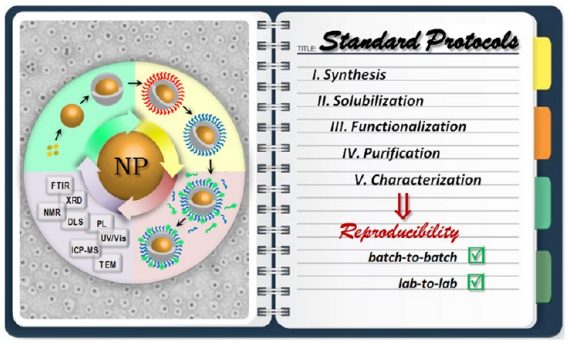

INTRODUCTION

Colloidal inorganic nanoparticles (NPs) gained an extensive interest recently due to their fascinating electronic, catalytic, optical, magnetic, and biological properties, which enable a novel material chemistry and a wide range of promising applications. Continuous development in understanding the fundamental physics, chemistry, and applications of these inorganic NPs originates from the availability of facile and reproducible synthetic protocols. The literature is abundant with a large number of synthetic protocols, which focus typically on controlling the nanoparticle (NP) size and shape in addition to purity, crystallinity, stability, and monodispersity.[1] However, the preparation of high quality inorganic NPs is still challenging and needs fine-tuning. For example, the widely used Frens protocol fails to prepare large citrate-capped gold NPs

Special Issue: Methods and Protocols in Materials Chemistry

Received: November 10, 2016
Revised: December 10, 2016
Published: December 12, 2016

DOI: 10.1021/acs.chemmater.6b04738
Chem. Mater. 2017, 29, 399−461

(>50 nm) with acceptable monodispersity.[2] Recent modification to the Frens method by adapting the seed-mediated approach allowed for the synthesis of citrate-capped gold and silver NPs with excellent monodispersity and large diameter (up to 100 nm as described in Section 2).[3,4] More importantly, the reproducibility of available reports is an issue in some cases, which may originate from highly sensitive systems, and thus fluctuations of any variable, such as the source of some chemicals, may have a significant impact on the reaction products. Another reason for the observed irreproducibility is the unexpressed "critical details" and "tricks" in the published reports. With this in mind and based on our own experience, we aim in this contribution to compile reproducible, simple, and detailed synthetic protocols that enable the synthesis and characterization of high quality inorganic NPs. Accordingly, Sections 1 and 2 in this contribution focus on the synthesis of hydrophobic and hydrophilic inorganic NPs including gold, silver, iron oxide, and quantum dots.

Usually "as prepared" NPs need further modification to control their hydrophilicity, hydrophobicity, colloidal stability, biocompatibility, biological recognition, and many other properties. Powerful surface modification reactions and strategies are available in the literature, including ligand exchange, ligand modification, polymer coating, and silanization,[5,6] as well as controlled bioconjugation.[7] Due to the importance of surface functionalization, we describe ligand exchange reactions in three sections (Sections 3, 4, and 5) and a polymer coating strategy in Section 6. The described ligand exchange reactions might be employed to control the properties of the NPs such as (i) improving the colloidal stability and interaction with biological compartments (e.g., ligand exchange of citrate-capped Au = gold (Au) NPs with thiolated polyethylene glycol in Section 3); (ii) facilitating the phase transfer of NPs from water to organic solvent (e.g., ligand exchange of citrate-capped Au NPs with dodecylamine/polyethylene glycol mix in Section 4); and (iii) facilitating the phase transfer of NPs from organic solvent to water (e.g., ligand exchange of alkanethiol capped Au NPs with 3-mercaptopropionic acid in Section 5). Another universal strategy of surface functionalization is detailed in Section 6, in which a polymer coating is employed to change hydrophobic inorganic NPs into highly charged NPs, rendering their surface hydrophilic and allowing their transfer to the aqueous solution. It is worth mentioning that the described surface functionalization strategies herein are general and can be applied to NPs of other materials, sizes, and shapes.

Similar to the synthesis of organic small molecules or polymers, the preparation of inorganic NPs requires a careful postsynthesis purification to get rid of "impurities", which can be any leftover reactants, free surfactant/capping agents, or undesired reaction products. The purification of NP solution is critical in many cases and should be considered as a vital step. For example, free cationic surfactants in gold nanorods (Au NRs) suspensions are responsible for cellular toxicity and in first order not the Au NRs themselves, highlighting the importance of using "purified" Au NR solution prior to biological evaluations/applications.[8] Another example is the presence of free recognition ligands (unbound) in NP solution, which should compete with bound ligand on the NPs for interaction with the designated target, which complicates interpretation of results and may result in serious artifacts. Despite the clear importance of the purification process, it is often overlooked in the literature and only briefly described in many published reports. With this in mind, we tried to focus on this important topic through designating a separate section that describe various methods of NP purification including filtration, centrifugation, dialysis, size exclusion chromatography, and electrophoresis (see Section 7).

After synthesis and purification of NPs, proper characterization is essential to confirm the NP's structural, photophysical, and colloidal properties, as detailed in Sections 8, 9, and 10, respectively. Structural characterization of NPs involves probing the quantitative and qualitative composition of NPs, size and shape determination of inorganic core and organic shell using electron microscopy, analysis of NP crystallinity using X-ray diffraction (XRD), quantification of the organic shell weight percentage on single NPs using thermogravimetric analysis, and confirming the chemical structure of the organic shell on the surface of NPs using nuclear magnetic resonance (NMR) analysis and infrared spectroscopy.

Photophysical characterization of NPs is very important, since it is the basis of various applications. For example, plasmon absorption and scattering of Au NPs allow sensing, imaging, and analytical applications of these nanostructures. The fluorescence phenomenon of quantum dots (QDs) is the basis for their use in imaging, tracking, and cellular labeling applications. Considering the importance of careful evaluation to the photophysical properties of NPs, it is addressed separately in Section 9, which includes characterization of Au NP's optical absorption and determination of NP concentration based on their absorption spectra. Also fluorescence spectroscopy as a tool to characterize QDs and to calculate their quantum yields is detailed with examples.

Characterization of the colloidal properties of NPs such as hydrodynamic diameter using dynamic light scattering (DLS) and effective surface charge using laser Doppler anemometry is very critical and thus included in Section 10. For example, measuring hydrodynamic diameters is an effective tool to follow NP aggregation, dissolution, and interaction with proteins or other ligands. Moreover, evaluation of the effective surface charge of NPs can be employed to confirm specific surface functionalization, such as ligand exchange, polymer overcoating, and protein adsorption. In Section 10, following NP aggregation as a function of salt addition or the solution's pH is discussed and detailed with examples of gold and silver NPs with various surface chemistries. Finally, characterization of the acidity/basicity of NPs by determination of their pK_a and number of acidic or basic groups on single NPs using pH titration and laser Doppler anemometry is described.

1. SYNTHESIS AND CHARACTERIZATION OF HYDROPHOBIC INORGANIC NPs IN ORGANIC SOLVENT

1.1. General Considerations. All glassware was first cleaned with detergent followed by aqua regia and carefully rinsed with Milli-Q water and acetone to guarantee an extremely cleaned glass surface. Aqua regia oxidizes and dissolves residual organic and inorganic impurities, which may interfere with the synthesis of NPs. Aqua regia solution is prepared by mixing 3 volume parts of hydrochloric acid (HCl) with 1 volume part of nitric acid (HNO_3) and should be used fresh. Aqua regia is a corrosive and strong oxidizing agent that should be prepared with care in a well-ventilated fume cupboard with protective clothing, goggles, and gloves.

Sections 1.2−1.8 describe the detailed synthesis of various types of NPs (Au, Ag, FePt, Fe_3O_4, Sn, CdSe, CdSe/ZnS, and

DOI: 10.1021/acs.chemmater.6b04738
Chem. Mater. 2017, 29, 399−461

CdS) in hydrophobic organic solvents. In these syntheses, the inorganic NP cores are stabilized by a shell of organic hydrophobic ligands (Figure 1), which ensures colloidal

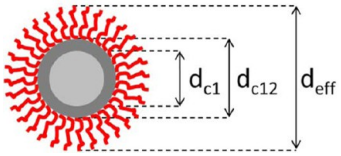

Figure 1. Scheme showing an inorganic NP, which consists of an inorganic core and an organic hydrophobic ligand shell (drawn in red). The inorganic core here is composed of a core/shell structure of two different materials (first material is the inner core drawn in light gray, and the second material is the inorganic shell drawn in dark gray).

stability of NPs in organic solvents such as toluene or chloroform. The effective NP diameter (d_{eff}) is the sum of the inorganic core diameter (d_c) and the thickness of the stabilizing ligand shell (l_{ligand}) as per eq 1. In case the NP core is comprised of (n) layers of different materials (e.g., core−shell NPs), the diameter of the first inner material is referred to as d_{c1} and the diameter of the core after the second material is referred to as d_{c12}. The diameter of the core after the nth material is referred to as $d_{c12...n}$).

$$d_{eff} = d_c + 2 \times l_{ligand} \quad (1)$$

1.2. Synthesis of Hydrophobic Au NPs (≈4 or 7 nm core diameter). *Dodecanethiol-Stabilized Au NPs (≈4 nm core diameter).* Hydrophobic Au NPs were synthesized according to the Brust−Schiffrin two-phase method,[9] with some modifications, as previously published.[10] The reaction was carried out at room temperature (RT) under ambient conditions. An aqueous phase with gold precursor (a yellow translucent solution containing $AuCl_4^-$ ions) was prepared by dissolving 300 mg (0.9 mmol) of hydrogen tetrachloroaurate (III) ($HAuCl_4$, 99.9%, Alfa Aesar no. 12325) in 25 mL of Milli-Q water. An organic phase containing 2.170 g (3.9 mmol) of tetraoctylammonium bromide (TOAB, $N(C_8H_{17})_4^+Br^-$, Sigma-Aldrich no. 294136) dissolved in 80 mL of toluene (Fluka 89682) was prepared immediately afterward.

The two solutions, i.e., the aqueous and the organic phases, were mixed in a 500 mL separation funnel (cf. Figures 2 and 3) and shaken vigorously for about 5 min. Upon mixing, $AuCl_4^-$ ions (in the aqueous yellow phase) were gradually transferred into the organic toluene phase, forming tetraoctylammonium tetrachloroaurate ion pairs ($N(C_8H_{17})_4^+AuCl_4^-$) as per eq 2. Within this process, the initial colorless toluene phase (tol)

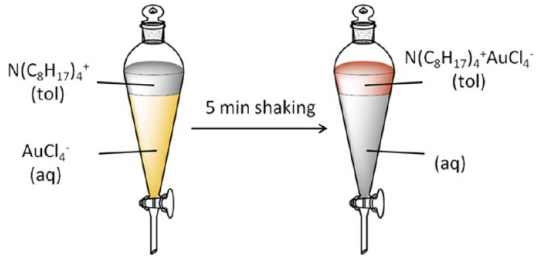

Figure 2. Scheme of the process of transferring $AuCl_4^-$ ions from the aqueous phase to the organic phase through the formation of tetraoctylammonium tetrachloroaurate ion pairs.

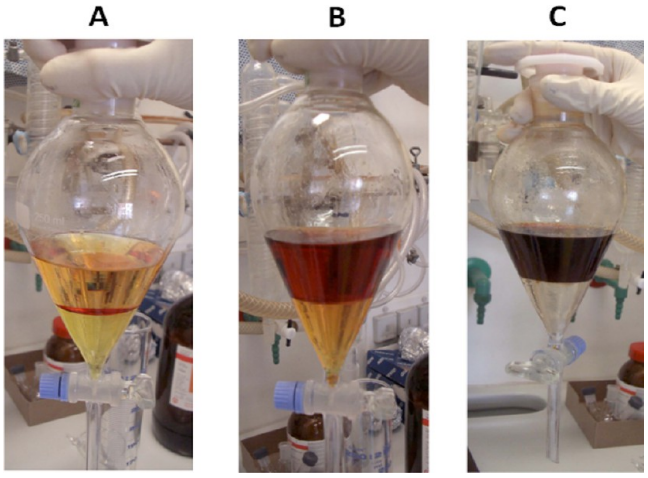

Figure 3. Photographs of the biphasic system showing the process of transferring $AuCl_4^-$ ions from the aqueous phase (lower phase) to the organic phase (upper phase) through the formation of tetraoctylammonium tetrachloroaurate ion pairs (dark red phase in C).

turned into a deep orange color, while the initial yellow color of the aqueous phase (aq) turned colorless (see Figure 3A−C).

$$HAuCl_4(aq) + N(C_8H_{17})_4^+Br^-(tol) \rightarrow N(C_8H_{17})_4^+AuCl_4^-(tol) + HBr(aq) \quad (2)$$

The aqueous solution (at the bottom) was discarded, and the organic phase containing gold precursors was transferred to a 250 mL round flask.

In addition to the gold precursor solution, a solution with a strong reducing agent was prepared as follows: In a beaker, 334 mg of sodium borohydride ($NaBH_4$, 98%, Sigma-Aldrich no. 452882) was dissolved in 25 mL of Milli-Q water under vigorous stirring. The prepared solution should be used immediately after preparation due to the fast decomposition of sodium borohydride as per eq 3. Observing small bubbles due to the formation of hydrogen is common.

$$BH_4^-(aq) + 3H_2O \rightarrow B(OH)_3(aq) + 3H_2(\uparrow) + H^+ + e^- \quad (3)$$

In order to obtain Au NPs, the freshly prepared solution of sodium borohydride was added dropwise within 1 min to the vigorously stirred organic phase containing the gold precursor (see Figures 4 and 5). Hereby the Au(III) precursor is reduced to Au(0) forming Au NPs. A few seconds after the addition of borohydride the color changed from deep orange (Au(III) precursor) to red-violet (tetraoctylammonium bromide capped Au NPs, TOAB-Au NPs).

$$n \times Au^{3+}(tol) + 3n \times e^- \rightarrow Au_n \quad (4)$$

The solution was kept stirring for about 1 h in order to reduce remaining gold ions (Figure 5).

After 1 h of stirring at RT, the mixture was transferred into a separation funnel. The aqueous phase was discarded, and the organic phase was washed with 25 mL of 10 mM HCl (aq), 25 mL of 10 mM NaOH (aq), and 3 times with 25 mL Milli-Q water (cf. Figure 4). For the washing steps the solution used for washing (i.e., HCl, NaOH, or H_2O) was added in the funnel to the organic phase, and the mixture was shaken. After separation of the organic and aqueous phase the aqueous phase at the

DOI: 10.1021/acs.chemmater.6b04738
Chem. Mater. 2017, 29, 399−461

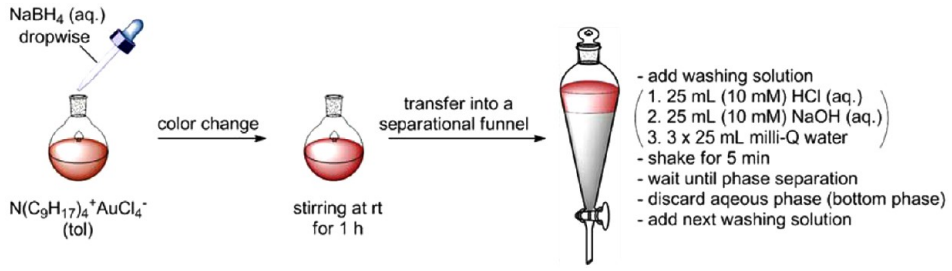

Figure 4. Synthesis of 4 nm TOAB-Au NPs is based on the reduction of Au(III) to elemental Au(0) by the addition of $NaBH_4$. After the formation of Au clusters, the NP suspension is washed several times with aqueous solutions.

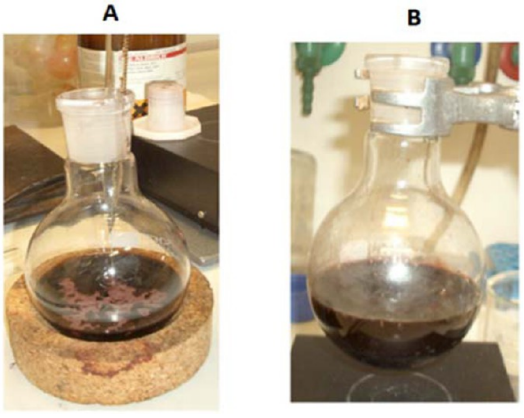

Figure 5. Reduction process of gold ions by sodium borohydride.

bottom was discarded. Washing steps are necessary to get rid of residual precursors and salts (Figure 6).

After discarding the aqueous phase from the last washing step, the remaining deep red, organic solution (ca. 80 mL) was transferred to a 250 mL round-bottom flask and stirred overnight to get thermodynamically stable NPs with narrow size distribution, mediated by Ostwald ripening[11−13] (cf. Figure 7).

After the synthesis of TOAB-Au NPs, a ligand exchange procedure was carried out, in order to obtain dodecanethiol-stabilized Au NPs (DDT-Au NPs). TOAB-Au NPs are stabilized by weakly adsorbed TOAB molecules at the surface of Au NPs, which can be desorbed by various stresses, such as dilution or repeated centrifugation. In order to get more stable Au NPs, TOAB can be exchanged with alkanethiols (e.g., dodecanethiol) that assemble strongly on the surface of gold due to the strong Au−S bond.[14,15]

For the ligand exchange procedure, 10 mL of 1-dodecanethiol (DDT, 98%, Sigma-Aldrich no. 471364) was added to the TOAB-Au NPs in toluene (ca. 80 mL) (Figures 8 and 9). The solution was heated to 65 °C and stirred for 2 h to facilitate the ligand exchange and finally stirred at RT to cool down. During this process, the mercapto group in dodecanethiol molecules displaces the TOAB,[16] yielding dodecanethiol-stabilized Au NPs.

The solution of DDT-Au NPs was poured into several 40 mL vials and centrifuged at 900 rcf for 5 min, in order to remove larger agglomerates. The supernatant containing the well-dispersed DDT-Au NPs was collected and pooled, and the agglomerates (i.e., the precipitate) were discarded. DDT-Au NPs were then precipitated using methanol (99.8%, Sigma, no. 322415) as a nonsolvent. For this, about 20 mL of DDT-Au NPs solution was placed in 40 mL glass vials, followed by the

Figure 6. Purification of TOAB-Au NPs. Upper toluene phase containing TOAB-Au NPs is washed with aqueous solutions (HCl, NaOH, and Milli-Q water) in the lower phase to remove excess sodium borohydride and other residual chemicals. (A) Photograph of the two phases immediately after shaking: note that the two phases are not completely separated. (B) Photograph of the two phases after they were allowed to separate, forming a transparent aqueous phase at the bottom and a deep red organic phase at the top containing TOAB-Au NPs.

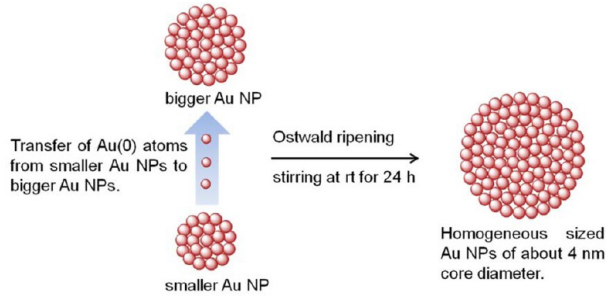

Figure 7. Ostwald ripening phenomena result in TOAB-Au NPs with a narrow size distribution. Smaller Au NPs in inhomogeneous population in terms of size dissolve and end up in bigger Au NPs.

gradual addition of methanol until the solution turned cloudy. The solution was then centrifuged at 900 rcf for 5 min, in order to precipitate the DDT-Au NPs. After this step of centrifugation, the supernatant turned colorless, and DDT-Au

DOI: 10.1021/acs.chemmater.6b04738
Chem. Mater. 2017, 29, 399−461

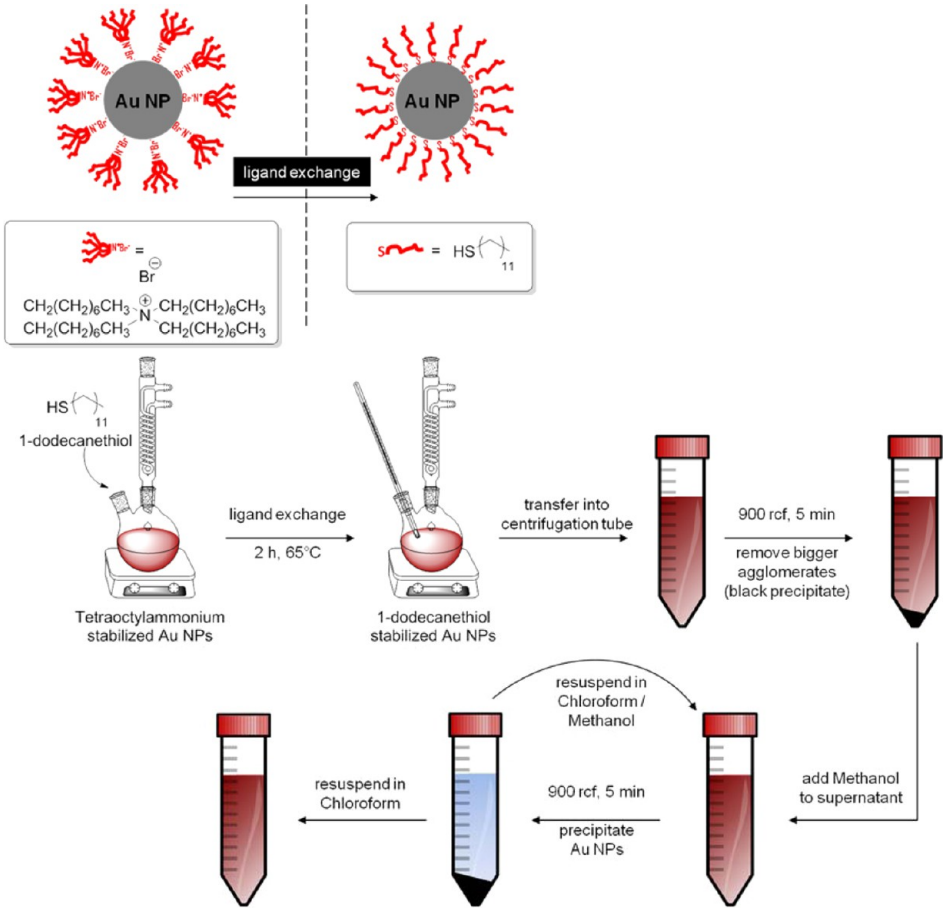

Figure 8. Ligand exchange on TOAB-Au NPs with dodecanethiol leading to the formation of DDT-stabilized Au NPs.

Figure 9. Au NPs are stirred after the addition of DDT while the temperature is controlled by a thermometer that is embedded in the reaction flask.

NPs were collected on the bottom of the centrifugation tube. In case of incomplete collection of DDT-Au NPs, additional methanol can be added, in order to increase the polarity of the medium and thus promoting the precipitation of the DDT-Au NPs, cf. Figure 10. After discarding the supernatant (which contains excess DDT and the replaced TOAB), the collected DDT-Au NPs were resuspended in chloroform. Similarly, DDT-Au NPs in chloroform were precipitated by the addition of methanol (a large enough amount to induce turbidity), followed by centrifugation for 5 min at 900 rcf to precipitate and collect DDT-Au NPs. After discarding the supernatant, collected DDT-Au NPs were resuspended in chloroform, leading to the final solution of DDT-Au NPs.

The described cleaning procedure by the addition of methanol (i.e., nonsolvent) narrows the size distribution of the DDT-Au NPs. Upon the addition of only a little methanol, bigger Au NPs precipitate, whereas the smaller Au NPs remain in the supernatant. This size selective precipitation allows for collecting NPs with similar sizes and discarding extremely small NPs (Figure 10).[17] It is worth noting here that the use of excess methanol should be avoided, since this will coprecipitate excess ligand molecules in solution along with the collected NPs, and thus hinder the purification.[18]

Synthesis of Au NPs in the Presence of Hexanoic Acid: Hexanoic Acid-Stabilized Au NPs (≈4 nm core diameter). In a 25 mL round-bottom flask a solution of 29 μL (231 nmol) of hexanoic acid (Sigma-Aldrich, no. 153745) dissolved in 2 mL of toluene was mixed with 25 mg (97.2 mmol) of tetrabutylammonium borohydride (TBAB, 98%, Alfa Aesar, no. A17494) dissolved in 1 mL of didodecyldimethylammonium bromide (DDAB, 99%, Alfa Aesar, no. B22839) stock solution (100 mM in toluene) at RT. In addition, a solution of 500 μL (25 μmol) of $HAuCl_4$ (Sigma-Aldrich, no. 254169) (50 mM in DDAB stock) and 2 mL of DDAB stock was added fast under vigorous stirring. The solution was left for ripening for 1 h, stirring at RT before further use.

DOI: 10.1021/acs.chemmater.6b04738
Chem. Mater. 2017, 29, 399−461

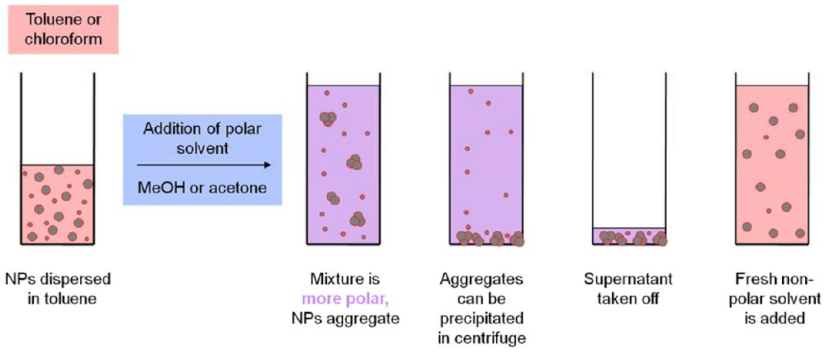

Figure 10. Size selective precipitation method to purify DDT-Au NPs and narrow their particle size distribution. The addition of a polar nonsolvent (methanol or acetone, drawn in blue) to DDT-Au NPs in hydrophobic solvent (e.g., toluene or chloroform, drawn in red) results in agglomeration and precipitation of large DDT-Au NPs. Collected precipitates of large DDT-Au NPs are redispersed in fresh hydrophobic solvent resulting in DDT-Au NPs with higher monodispersity. Smaller DDT-Au NPs remaining in supernatant are discarded.[17]

Synthesis of Au NPs in the Presence of Decanoic Acid: Decanoic Acid-Stabilized Au NPs (≈7 nm core diameter). For this purpose, a solution of 43 mg (250 μmol) of decanoic acid (Sigma-Aldrich, no. C1875) dissolved in 2.5 mL of toluene and a solution of 25 mg (97.2 mmol) of TBAB dissolved in 1 mL of DDAB stock solution (100 mM in toluene) were added in a 25 mL flask. Then a solution of 500 μL (25 μmol) of $HAuCl_4$ (50 mM in DDAB stock) and 2 mL of DDAB stock were added to the mixture quickly and under vigorous stirring and left for ripening for 1 h stirring at RT before further use.

It is worth noting that the synthesis of Au NPs in the presence of hexanoic or decanoic acid results in weakly capped NPs with these ligands, which can be considered as "intermediate NPs" ready for further ligand exchange with thiol capped molecules. However, the use of these fatty acids ensures a narrow size distribution of the prepared Au NPs as described by Jana et al.[19]

1.3. Synthesis of Hydrophobic Ag NPs (≈4 nm core diameter). Also silver NPs (Ag NPs) can be synthesized in organic solvents.[20] The herein described synthesis of Ag NPs is similar to the synthesis of Au NPs as described in Section 1.2. Mari et al. reported an effective protocol to prepare alkanethiol-stabilized Ag NPs (≈4.2 nm in core diameter).[21] The first step was the synthesis of an alkyl thiosulfate (namely, sodium *S*-dodecylthiosulfate) as a ligand precursor as per eq 5.

$$Na_2S_2O_3{\cdot}5H_2O + CH_3(CH_2)_{11}Br \rightarrow CH_3(CH_2)_{11}S_2O_3^{-}Na^{+} + NaBr + 5H_2O \quad (5)$$

Sodium thiosulfate pentahydrate (6.21 g (25 mmol, 1.0 equiv), Sigma-Aldrich, no. 217247) was dissolved in 50 mL of Milli-Q water. In addition, 5.19 mL (25 mmol, 1.0 equiv) of 1-bromododecane (Sigma-Aldrich, no. B65551) was dissolved in 50 mL of ethanol. The combined solutions were stirred under reflux for 3 h. The mixture was cooled down to RT, and the resulting crystals of sodium *S*-dodecylthiosulfate were filtered using a funnel with a proper filter paper. Another crystallization step was performed, where sodium *S*-dodecylthiosulfate was dissolved in as little ethanol as possible under heating (~45 °C) and left in a crystallization beaker for cooling to RT. In this manner, purification of the product was obtained by allowing the solution to gradually cool and be saturated with the compound. The product of interest crystallized, and unwanted contaminations remained in the liquid phase. Finally, the sodium *S*-dodecylthiosulfate crystals were filtered as previously described, and the final product was dried in vacuum (cf. Figure 11). Importantly, the synthesis should be done in a fume hood and under controlled laboratory conditions.

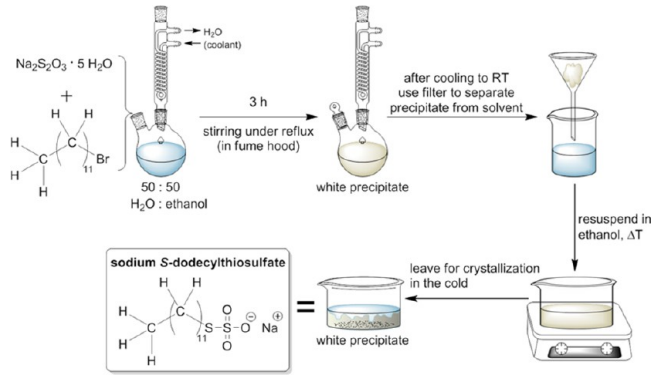

Figure 11. Schematic illustration of the chemical synthesis of sodium *S*-dodecylthiosulfate as a ligand precursor to stabilize Ag NPs.

For the synthesis of Ag NPs, 390 mg (1.26 mmol, 0.75 equiv) of sodium *S*-dodecylthiosulfate in 90 mL of ethanol was heated up to 50 °C. To this solution was added 282 mg (1.68 mmol, 1.0 equiv) of $AgNO_3$ (Sigma-Aldrich, no. 209139), and the resulting mixture was stirred for a further 10 min. A color change was observed; the white solution turned brown after a few minutes (cf. Figure 12). A total of 318 mg (8.4 mmol, 5.0 equiv) of sodium borohydride ($NaBH_4$ 98%, Sigma-Aldrich, no. 452882) was dissolved in 15 mL of ethanol and added to the mixture, which turned almost black immediately (cf. Figure 12). After 5 min, 74 mg (0.42 mmol, 0.25 equiv) of ascorbic acid (Sigma-Aldrich, no. 255564) was added, and the mixture was stirred at 50 °C for a further 3 h. As the reaction mixture reached RT, the solution with the Ag NPs was transferred into centrifuge tubes, and the Ag NPs were collected at the tube bottom by centrifuging at 3000 rcf for 15 min. After discarding the supernatant, the Ag NPs were resuspended in Milli-Q water and again collected by sedimentation (3000 rcf, 15 min). This washing step was repeated two more times using ethanol and then acetone (cf. Figure 12). After that, the Ag NPs were dried under reduced pressure, which led to gray powder. For further use, the NPs were resuspended in chloroform.

1.4. Synthesis of Hydrophobic FePt NPs (≈4 nm core diameter). The synthesis of ≈4 nm core diameter FePt NPs as carried out here was described first by Sun et al.[22] This reaction needs to be carried out in a water- and oxygen-free atmosphere

DOI: 10.1021/acs.chemmater.6b04738
Chem. Mater. 2017, 29, 399−461

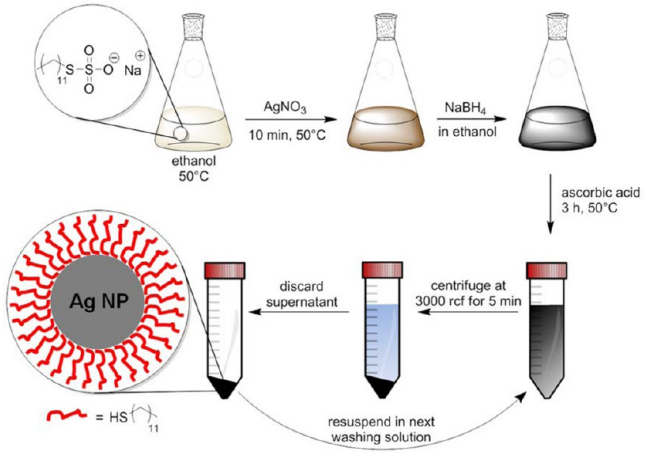

Figure 12. Graphic scheme of the synthesis and purification of dodecanethiol-stabilized Ag NPs (DDT-Ag NPs).

(e.g., Schlenk line and/or glovebox). In a typical synthesis, platinum(II) acetylacetonate (197 mg, 0.5 mmol, 1 eq, ABCR, no. AB 121416), 1,2-hexadecanediol (390 mg, 1.5 mmol, 3 equiv, Sigma-Aldrich, no. 213748) and dioctylether (20 mL, Sigma-Aldrich, no. 249599) were mixed in a three-neck flask, a magnetic bar was added, and the mixture was heated to 100 °C. The temperature was controlled by a temperature sensor immersed in the solution (cf. Figure 13). When the desired

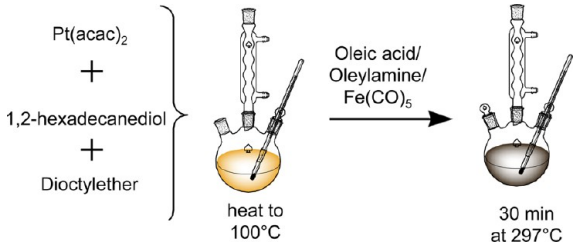

Figure 13. Schematic illustration of the chemical synthesis of 4 nm core diameter FePt NPs. The synthesis was carried out under water exclusion and N_2 atmosphere in a three neck flask equipped with seal septa to be able to add all reagents under oxygen and water free conditions.

temperature was reached, the solution presented a light yellow color. Then, oleic acid (OA, 0.16 mL, 0.5 mmol, 1 equiv, Sigma-Aldrich, no. O1008), oleylamine (OLA, 0.17 mL, 0.5 mmol, 1 equiv, Sigma-Aldrich, no. O7805), and $Fe(CO)_5$ (0.13 mL, 1 mmol, 2 equiv, Sigma-Aldrich, no. 481718) were added. After the addition of the Fe precursor, the color of the solution turned to light brown. The reaction was heated under reflux (297 °C) for 30 min (cf. Figure 13). At this temperature, the solution started to boil, and some fumes were observed. Moreover, the color of the solution changed to deep brown, indicating the formation of NPs. After 30 min of heating, the reaction mixture was allowed to cool down to RT by removing the heating source.

For purification, the solution of FePt NPs was transferred to two centrifuge tubes of 50 mL, and ethanol (40 mL, Carl Roth, no. 64-17-5) was added to induce precipitation of the NPs. The NPs were separated by centrifugation (5 min, 2700 rcf) (cf. Figure 14). The brown colored supernatant containing byproducts was discarded, and the black NP precipitate was dispersed in hexane (25 mL) in the presence of OA (0.05 mL)

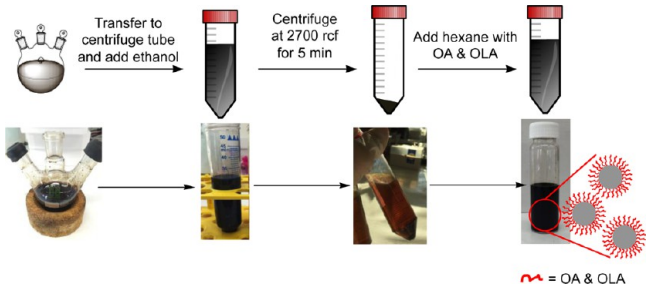

Figure 14. Graphic scheme (upper panel) and photographs (lower panel) of FePt NP purification steps after synthesis.

and OLA (0.05 mL), in order to provide the NP colloidal stability for long storage periods.

1.5. Synthesis of Hydrophobic Fe_3O_4 NPs (≈4 nm core diameter). The synthesis of Fe_3O_4 NPs as outlined here was initially published by Sun et al. in 2003,[23] with a procedure to obtain monodisperse NPs with variable composition: MFe_2O_4, M being a metal that can be iron, cobalt, or manganese, allowing variation in the magnetic properties. This protocol allows for the synthesis of NPs with a tunable diameter from 3 to 20 nm by changing the initial reaction conditions, or via a postsynthesis seed-mediated approach. In the present report only the synthesis of 4 nm core size Fe_3O_4 NPs is presented and detailed (cf. Figure 15). To prepare these NPs, 706.4 mg (2

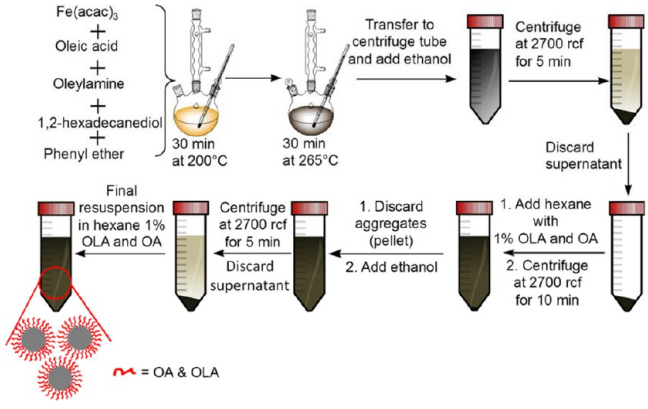

Figure 15. General scheme of the synthesis and purification of Fe_3O_4 NPs. After the initial synthesis, both large aggregates and solvent impurities are removed by centrifugation, obtaining NPs that are finally stabilized by OLA and OA.

mmol, 1 equiv) of the metal precursor iron(III) acetylacetonate ($Fe(acac)_3$; 99%, Strem Chemicals, no. 26-2300) was dissolved in 20 mL of diphenyl ether (Sigma-Aldrich, no. P24101) in the presence of 6 mmol of OA (3 equiv, 90%, Sigma-Aldrich, no. 364525), 6 mmol of OLA (3 equiv, Aldrich, no. O7805), and 10 mmol of 1,2-hexadecanediol (5 equiv, Sigma-Aldrich, no. 52270). The process needs to be carried out in an oxygen- and water-free atmosphere (glovebox and/or Schlenk line), where the mixture was stirred at 200 °C for 30 min. The mixture was then heated up to 265 °C for another 30 min to induce thermal decomposition and thus the formation of NPs (cf. Figure 15). The Fe_3O_4 NP dispersion was then cooled down to RT and was taken away from the water- and oxygen-free ambient. In this preparation, 1,2-hexadecanediol acts as reducing agent to reduce the metal precursor into Fe_3O_4 NPs that are stabilized with oleic acid and oleylamine. For purification, the dark brown dispersion was equally distributed into two 50 mL centrifuge

DOI: 10.1021/acs.chemmater.6b04738
Chem. Mater. 2017, 29, 399−461

tubes, and then 25 mL of ethanol (Roth, no. 5054.2) was added to each tube, and the NPs were centrifuged at 2700 rcf for 5 min. Supernatants were discarded, and the Fe_3O_4 NPs were collected at the bottom of the centrifugation vial. The Fe_3O_4 NPs were resuspended in a mixture of hexane with 1% (v/v) OA and OLA. Additional centrifugation at 2700 rcf for 10 min is necessary to get rid of any undispersed residue/aggregates. The resulting supernatants were transferred to clean vials, and a new washing step with ethanol was performed at 2700 rcf for 5 min (cf. Figure 15). The final Fe_3O_4 NPs with a core diameter of ≈4 nm forming the pellet were finally redispersed into hexane supplemented with 1% OA and OLA.

1.6. Synthesis of Hydrophobic Sn NPs (≈11 nm core diameter). The synthesis of monodisperse Sn NPs with a core diameter of 11 nm as reported here was first published by Kravchyk et al. in 2013.[24] The protocol employs the reaction of $LiN(Si(CH_3)_3)_2$ with a solution of oleylamine (OLA) and $SnCl_2$ at 180 °C, followed by the reduction of Sn(II) to elemental tin using diisobutylaluminum hydride (DIBAH) (Figure 16). The reaction was completely performed inside a

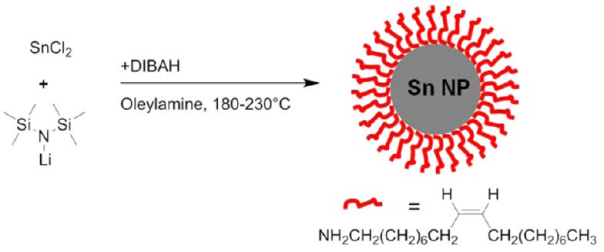

Figure 16. Synthesis of monodispersed Sn NPs.

glovebox under N_2 atmosphere. Importantly, all glassware should be dried using heat and vacuum as the reaction is sensitive to water. The described reaction is violent; thus, it should be carried out with caution, and safety regulations should be considered.

A 250 mL three neck flask was equipped with a reflux condenser, stirring bar, and two additional seal septa with one thermal sensor connected to a magnetic stirrer with heating capability. A total of 24.6 mL of OLA (Sigma-Aldrich, ≥98%, no. HT-OA100) was filled into the flask using a 20 mL syringe and was stirred under vacuum at 140 °C for 1.5 h. After cooling the solvent down to 50 °C, 94.8 mg (0.5 mmol, 1.0 equiv) of $SnCl_2$ (Sigma-Aldrich, no. 208256) was added, and the mixture was again dried under vacuum at 140 °C for 30 min. Meanwhile, 601 mg (3.6 mmol, 7.2 equiv) of $LiN(Si(CH_3)_3)_2$ (Sigma-Aldrich, no. 324620) was dissolved in 3 mL of toluene using a small beaker. The mixture of OLA and $SnCl_2$ was heated up to 180 °C under N_2 atmosphere, followed by the injection of $LiN(SiMe_3)_2$ in toluene solution. After 10 s, 0.6 mL (0.6 mmol, 1.2 equiv) of a 1.0 M solution of DIBAH dissolved in tetrahydrofuran (THF, Sigma-Aldrich, no. 214981) was injected, which induced a color change to dark brown. The reaction mixture was further stirred for 1 h before putting the flask into an ice bath to cool it down. During this, at about 150 °C, 10 mL of toluene were added, and the flask was extracted out of the glovebox and immediately held into an ice bath to speed up the cooling process (cf. Figure 17).

When the Sn NP solution had cooled to RT, it was transferred into two 50 mL centrifuge tubes and mixed with 40 mL of ethanol, which led to precipitation of the Sn NPs. The sample was centrifuged at 3000 rcf for 5 min, in order to

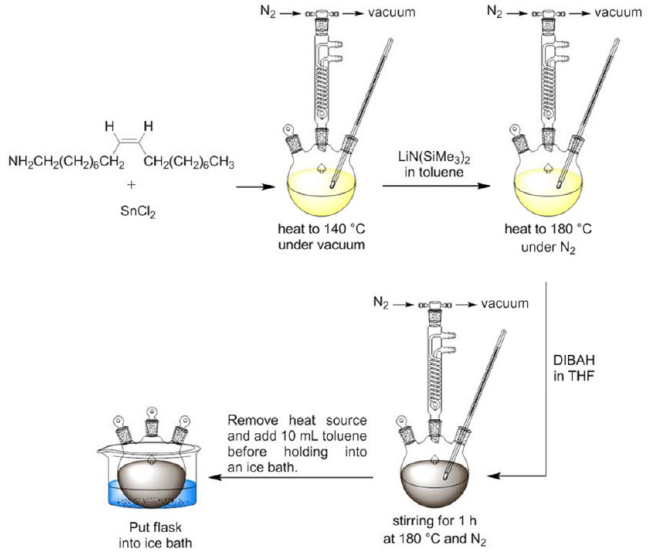

Figure 17. Schematic illustration of the chemical synthesis of 11 nm Sn NPs. The synthesis was carried out under water exclusion and N_2 atmosphere in a three neck flask equipped with a seal septa to be capable of adding all reagents and guarantee oxygen- and water-free conditions. For drying the solvent OLA and $SnCl_2$, the reflux condenser was equipped with a three-way valve to be able to switch between N_2 and vacuum. Before extracting the flask out of the glovebox, the thermal sensor and reflux condenser were removed, and all three necks were closed using the seal septa.

separate the NPs from the solvent. The NPs were collected, and the supernatant was discarded. Next, the Sn NPs were resuspended in a solution of oleic acid (OA) in chloroform (~6 mL, 1 mL OA/50 mL $CHCl_3$), which led to a ligand exchange from OLA to OA. Finally, a second precipitation step was performed by adding 10 mL of ethanol to the solution and centrifugation at 3000 rcf for 5 min and resuspension in 10 mL of $CHCl_3$ to generate a long-term stable solution of Sn NPs (cf. Figure 18).

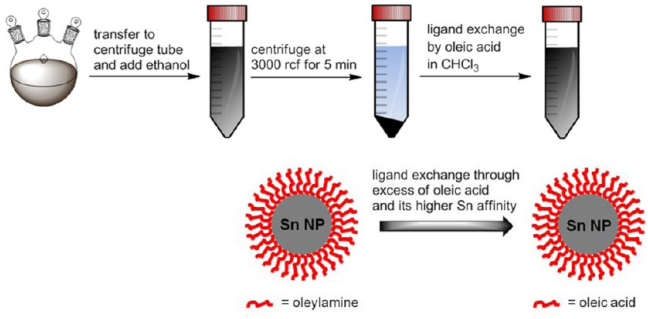

Figure 18. Purification of Sn NPs and OLA ligand exchange with OA.

1.7. Synthesis of Hydrophobic CdSe and CdSe/ZnS NPs (≈2−10 nm core diameter). CdSe NPs, so-called quantum dots (QDs), of different sizes were synthesized using CdO as a precursor, via the procedure described by Peng's group,[25] with minor modification in reaction temperature/time, in order to achieve a better control of the size of the NPs. To improve the quantum yield and long-term stability of these fluorescent NPs, coating of the CdSe NPs with a shell of ZnS was employed[26,27] using diethylzinc and hexamethyldisilathiane as zinc and sulfur sources, respectively.[28]

DOI: 10.1021/acs.chemmater.6b04738
Chem. Mater. 2017, 29, 399−461

Synthesis of CdSe cores: In a typical synthesis, 0.03 g of cadmium oxide (CdO, Sigma-Aldrich no. 202894), 0.11 g of hexylphosphonic acid (HPA, Sigma-Aldrich no. 750034), and 3.5 g of trioctylphosphine oxide (TOPO, Sigma-Aldrich no. 223301) were loaded into a 100 mL glass three-neck flask connected to a nitrogen line (see Figure 19). The mixture was

Figure 19. Setup for the synthesis of CdSe/ZnS NPs. The photo shows a three-neck flask equipped with a heating mantle, a reflux condenser, an addition funnel, a thermometer connected to a temperature controller, and a nitrogen flow.

degassed at 120 °C for 20 min and then heated to 300−320 °C under nitrogen atmosphere for 15 min to allow the complete dissolution of CdO in HPA and TOPO leading to a clear and colorless solution, which indicates that a Cd−HPA/TOPO complex has been formed. In case the CdO did not dissolve completely, (i.e., the solution did not turn transparent), some more HPA needs to be added.

Then, the temperature of the solution was cooled down to 270 °C by setting the temperature controller to this temperature and waiting for around 10−15 min. When the desired temperature was reached, 1.2 mL of selenium stock solution was swiftly injected with a syringe. The selenium stock solution was prepared by dissolving 0.0255 g of selenium powder (Se, Sigma-Aldrich no. 229865) in 1.5 mL of trioctylphosphine (TOP, Sigma-Aldrich no. 718165), to produce a 0.215 M stock solution of trioctylphosphine selenide (Se−TOP). After injection, the temperature dropped by roughly 20 °C and was maintained then at 250 °C throughout the synthesis of the CdSe cores. At 3−5 min after the injection, the color of the solution turned from colorless to yellow, indicating the nucleation of CdSe NPs. Upon further grown of the NPs this color gradually turned to yellow-orange, orange, red, and finally dark red 30−40 min after the injection.

CdSe NP growth was monitored by taking aliquots from the reaction flask every 5 min. Aliquot solutions were diluted with chloroform, and their UV/visible absorption spectra were recorded (cf. Figure 20). Even when the growth rate varied slightly from synthesis to synthesis, it was always sufficiently

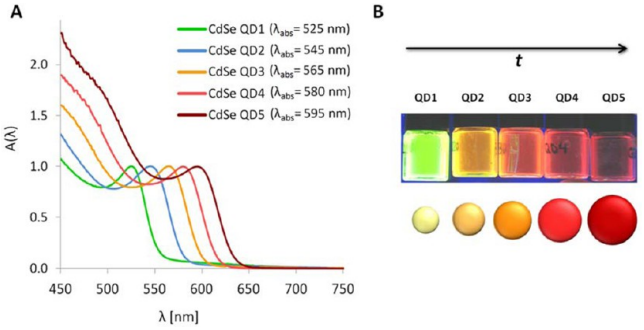

Figure 20. Monitoring the growth of CdSe NPs by (A) recording the UV/visible absorption spectra $A(\lambda)$ of aliquot samples that were taken from the reaction flask at different time intervals followed by dilution with chloroform. The peak in the spectrum at wavelength λ_{abs} is due to the excitation of the first exciton.[30] The spectra were normalized to the absorption at the first exciton peak. Upon growth of CdSe NPs, the absorption peak shifts to higher wavelength, as shown here in the five spectra recorded after different time points (t = 5 min, 10 min, 15 min, 20 min, 30 min). (B) The solutions of the CdSe NPs are fluorescent with tunable excitation wavelength that were red upon growth of NPs.

slow so that the synthesis could be stopped whenever the first exciton peak in the absorption spectrum reached the desired value, which could be easily correlated to the NPs' average size through calibration curves available in the literature.[29] Once the cores had reached the desired size, either the reaction could be stopped by removing the heating mantle to let the solution cool down to RT with the resulting NPs purified as described below or optionally the temperature could be maintained at 250 °C and the synthesis was continued further to grow a ZnS shell on the prepared CdSe cores.

For ZnS shell growth, a shell of ZnS can be optionally grown around the CdSe cores; see Figure 21. Once CdSe NPs have reached the desired size, they can be directly passivated by growing a ZnS shell, without the need of isolating the CdSe NPs from the crude solution.[31] For CdSe cores with a size of d_c = 3.82 nm in diameter, 1.5 mL of the overcoating stock solution (Zn/S/TOP solution) was added dropwise to the mixture under vigorous stirring through the addition funnel over a period of ≈10 min. It is important that the addition is done dropwise in order to avoid nucleation of ZnS NPs. The Zn/S/TOP stock solution was prepared by adding equimolar amounts of the Zn and S precursors in TOP, that is, 1.75 mL of diethylzinc solution ($ZnEt_2$ 1 M in hexane, Sigma-Aldrich no. 296112) and 0.37 mL of hexamethyldisilathiane ($(TMS)_2S$, Sigma-Aldrich no. 283134) in 10.38 mL of trioctylphosphine (TOP, Sigma-Aldrich no. 718165). Note that the Zn/S/TOP stock solution can be separated and frozen into aliquots to be used in the next synthesis, being stable once frozen for at least six months. After the addition of Zn/S/TOP solution, the mixture was left to cool down to 90 °C by removing the heating mantle, and then this temperature was maintained and the solution stirred for 3 h more. Finally, the solution was cooled down to RT by turning the heating off, and the NP suspension was transferred to a glass vial and diluted with 10 mL of anhydrous chloroform.

The amount of added Zn/S/TOP stock solution depends on the CdSe core size and the desired thickness of the ZnS shell. The amount of Zn and S precursors (i.e., Zn/S/TOP stock solution) needed for growing a ZnS shell of desired thickness can be estimated. First, from the wavelength of the first exciton peak λ_{abs} in the absorption spectrum of the CdSe cores, the

DOI: 10.1021/acs.chemmater.6b04738
Chem. Mater. 2017, 29, 399−461

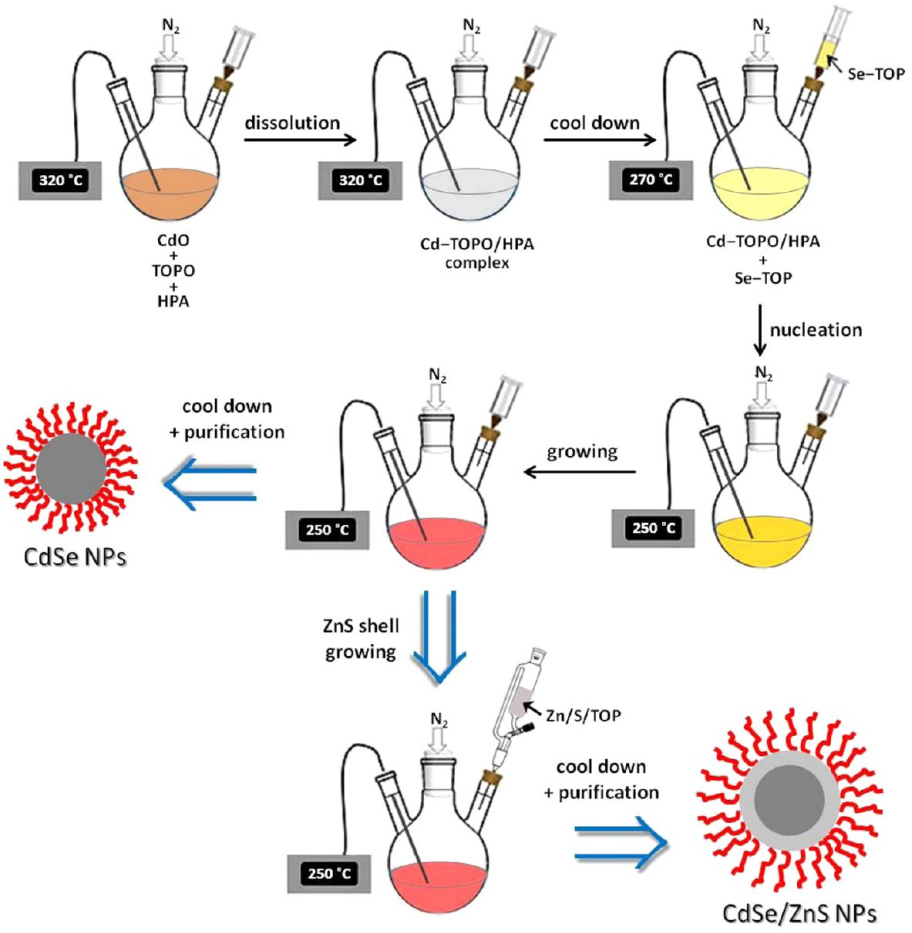

Figure 21. Schematic illustration of the synthesis of CdSe and CdSe/ZnS NPs.

diameter of the cores d_c is estimated via an empirical formula by Yu et al.,[29] which correlates CdSe NPs core size (d_c) with the corresponding wavelength of the first exciton peak (λ_{abs}):

$$d_c = (1.6122\ \text{nm} \times 10^{-9}\text{nm}^{-4}) \times {\lambda_{abs}}^4 - (2.6575 \times 10^{-6}\text{nm}^{-3}) \times {\lambda_{abs}}^3 + (1.6242 \times 10^{-3}\text{nm}^{-2}) \times {\lambda_{abs}}^2 - 0.4277 \times \lambda_{abs} + 41.57\ \text{nm} \quad (6)$$

According to the literature, a number of ZnS monolayers between 1 and 2 is usually the optimum for getting the maximum quantum yield in CdSe/ZnS NPs.[26,31,32] In case of too thin layers, the passivation effect is not significant. In case of too thick layers, the ZnS shell may crack due to differences in the lattice constants between CdSe and ZnS, resulting in poor quantum yields. In this work 1.2 monolayers were selected as the desired thickness of ZnS on CdSe NPs. According to the bulk lattice parameters of ZnS, the thickness of one single ZnS monolayer is 0.31 nm, defined as the distance between consecutive planes along the [002] axis in bulk wurtzite ZnS.[26] Therefore, the thickness of the ZnS shell corresponding to 1.2 monolayers is 0.37 nm (cf. Figure 1).

By knowing the diameter of the CdSe core (d_{c1}) from eq 6 (as the inorganic part comprises here a core and a shell the innermost core is termed d_{c1} instead of d_c) and the desired thickness of the ZnS shell ($d_{c12} - d_{c1}$) = 2 × 0.37 nm = 0.74 nm, the diameter d_{c12} of the CdSe/ZnS core/shell NP can be calculated ($d_{c12} = d_{c1} + 0.74$ nm). The volume of the ZnS shell V_{c2} around one CdSe core thus is the volume of one CdSe NP ($V_{c1} = (\pi/6){d_{c1}}^3$), subtracted from the volume of one CdSe/ZnS NP ($V_{c12} = (\pi/6){d_{c12}}^3$), cf. eq 22.

For example, sample QD4 in Figure 20 corresponds to CdSe NPs with λ_{abs} = 580 nm. According to eq 6, d_{c1} = 3.82 nm, and thus d_{c12} = 3.82 nm + 0.74 nm = 4.56 nm. This leads to volumes V_{c1} = 29.19 nm^3 and $V_{c2} = V_{c12} - V_{c1}$ = 20.46 nm^3 of the CdSe core and the ZnS shell, respectively. The ratio of the shell volume to the core volume thus is V_{c2}/V_{c1} = 0.70. As there are Cd atoms only in the core ($N_{Cd/NP}$ per NP) and Zn atoms only in the shell ($N_{Zn/NP}$ per NP), the amount of Cd and Zn in one NP scales according to eqs 7, 8, 28, and 29 with the volume of the CdSe core (ratio of Cd:Se = x:y = 1) and the ZnS shell (ratio of Zn:S = x:y = 1), respectively:

$$N_{Cd/NP} = \rho_{CdSe} \times V_{c1} \frac{N_A}{\left(M_{Cd} + \left(\frac{1}{1}\right) \times M_{Se}\right)} \quad (7)$$

$$N_{Zn/NP} = \rho_{ZnS} \times V_{c2} \frac{N_A}{\left(M_{Zn} + \left(\frac{1}{1}\right) \times M_{S}\right)} \quad (8)$$

Hereby M_{Cd} = 112.4 g/mol, M_{Se} = 79.0 g/mol, M_{Zn} = 65.4 g/mol, and M_S = 32.1 g/mol are the molar masses of cadmium, selenium, zinc, and sulfur, respectively. ρ_{CdSe} = 5.82 g/cm^3 and ρ_{ZnS} = 4.09 g/cm^3 are the bulk densities of CdSe and ZnS, respectively. Thus, the ratio of Zn to Cd atoms in one CdSe/ZnS NP is

DOI: 10.1021/acs.chemmater.6b04738
Chem. Mater. 2017, 29, 399−461

$$\frac{N_{Zn/NP}}{N_{Cd/NP}} = \left(\frac{V_{c2}}{V_{c1}}\right) \times \left(\frac{\rho_{ZnS}}{\rho_{CdSe}}\right) \times \left(\frac{M_{Cd} + M_{Se}}{M_{Zn} + M_S}\right) = 1.38 \times \left(\frac{V_{c2}}{V_{c1}}\right) \quad (9)$$

In the case of the sample QD4 in Figure 20 with λ_{abs} = 580 nm this leads to N_{Zn}/N_{Cd} = 1.38 × 0.70 ≈ 0.96. The amount n_{Cdsol} of Cd added in form of CdO as precursor during the synthesis of the CdSe cores is known. In the particular case of the synthesis described here it was n_{Cdsol} = 0.234 mmol (mass of added CdO = 0.03 g, M_W(CdO) = 128.4 g/mol). The amount of Zn needed in the reaction solution thus is $n_{Znsol} = n_{Cdsol} \times (N_{Zn}/N_{Cd})$ = 0.234 mmol × 0.96 ≈ 0.22 mmol. Note that this calculation assumes that all added Cd ends up in the CdSe core. The Zn concentration in the Zn/S/TOP stock solution is c_{Zn} = 1 M × 1.75 mL/(1.75 mL + 0.37 mL + 10.38 mL) = 0.14 M. Thus, in order to inject n_{Znsol} = 0.22 mmol Zn, the volume $V_{Zn/S/TOPsol} = n_{Znsol}/c_{Zn}$ = 0.22 mmol/0.14 M ≈ 1.5 mL needs to be dropwise injected.

Note that this calculation only provides a rough estimate of the amount of Zn/S/TOP stock solution, which is needed for growing the ZnS shell. In fact, during growth of the ZnS shell small aliquots may be taken and the fluorescence analyzed. Shell growth is continued until the quantum yield of the NPs no longer increases.

Purification of CdSe or CdSe/ZnS NPs: 10 mL of anhydrous methanol were added to 10 mL of the NP suspension, which caused flocculation of the NPs. The NPs were then precipitated by centrifugation (5000 rcf, 5 min). Then, the supernatant was discarded and the NP precipitate at the bottom of the vial was resuspended in chloroform. This purification process was repeated two more times (cf. Figure 22). After the last

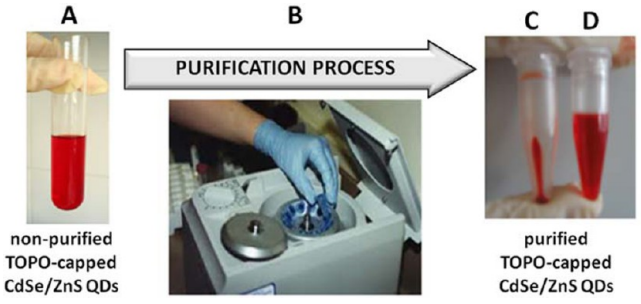

Figure 22. Purification process of the CdSe or CdSe/ZnS QDs by centrifugation and washing with methanol. (A) Vial with NPs dispersed in chloroform. (B) Centrifugation of the NP suspension after the addition of methanol. (C) Precipitated QDs after centrifugation. (D) QDs solution after removal of supernatant in C and redispersion in chloroform.

centrifugation, the supernatant should be colorless and the NPs should be all precipitated on the bottom of the Eppendorf tube in which centrifugation had been carried out. If the supernatant is still colored, the addition of more methanol is needed in order to increase the polarity of the medium, promoting the precipitation of the NPs. Finally, the purified QD NPs (TOPO-capped CdSe or CdSe/ZnS QDs) were dispersed in 10 mL of anhydrous chloroform and stored in the dark.

1.8. Synthesis of Hydrophobic CdS NPs (≈2 nm core diameter). Hydrophobic CdS NPs were synthesized by adapting the original method described by Yu and Peng.[33] For the synthesis, a mixture of 4 g including 12.8 mg (0.10 mmol, 2 equiv) of cadmium oxide (Sigma, no. 202894), 85 mg (0.30 mmol, 6 equiv) of oleic acid (OA, Sigma, no. 364525), and 3.90 g (15.3248 mmol, 306.5 equiv) of octadecane (ODE, Technical grade 90%, Alfa Aesar, no. L11004) were weighed and mixed in a 50 mL three-neck round-bottom flask. Then, the mixture was heated to 120 °C and stirred under nitrogen environment, followed by degassing under vacuum for 5 min, cf. Figure 23.

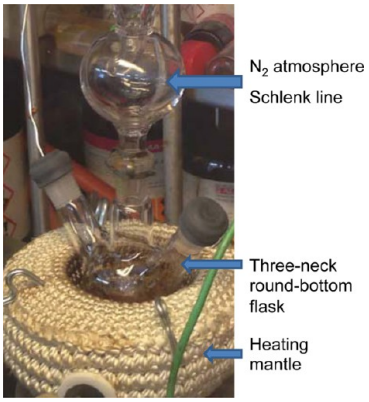

Figure 23. Reaction setup used for heating the mixture of CdO, oleic acid, and ODE.

This mixture was then heated to 300 °C, while a solution of sulfur (0.0016 g, 0.05 mmol, 1 equiv, Sigma, no. 414980) in 2 g of ODE was prepared in a separated glass vial. Since it is very difficult to measure such a small quantity of sulfur, a stock solution was prepared instead by dissolving 8 mg of sulfur in 10 g of octadecane (ODE, Technical grade 90%, Alfa Aesar, no. L11004). To efficiently dissolve the sulfur in ODE, the mixture was heated to 85 °C under stirring.

When the mixture of CdO, OA, and ODE reached 300 °C, the CdO started to decompose, and the initial brownish colored solution started turning into a transparent solution, cf. Figure 24. When the solution became completely transparent, the previously prepared sulfur solution was quickly injected using a syringe, cf. Figure 25.

After injection of the sulfur-ODE solution, the temperature of the mixture dropped to 240 °C. In the case that the required size of the QDs was d_c ≈ 2 nm, the heating mantle was

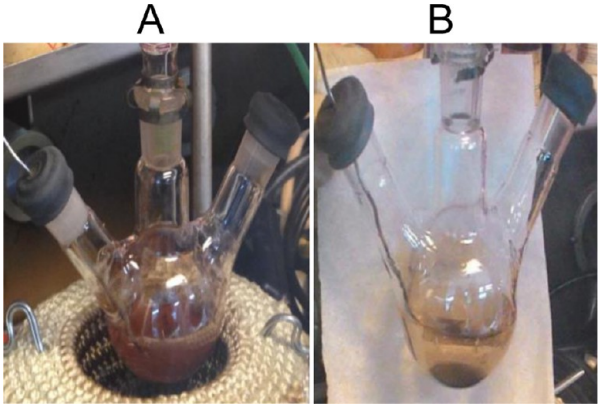

Figure 24. Color change of the mixture before (A) and after (B) decomposition of CdO.

DOI: 10.1021/acs.chemmater.6b04738
Chem. Mater. 2017, 29, 399−461

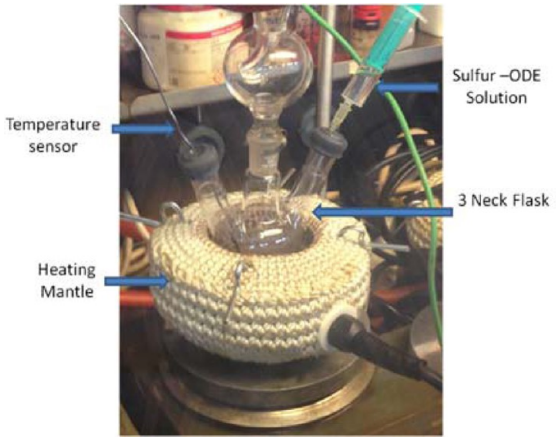

Figure 25. Injection of the sulfur−ODE solution at 300 °C.

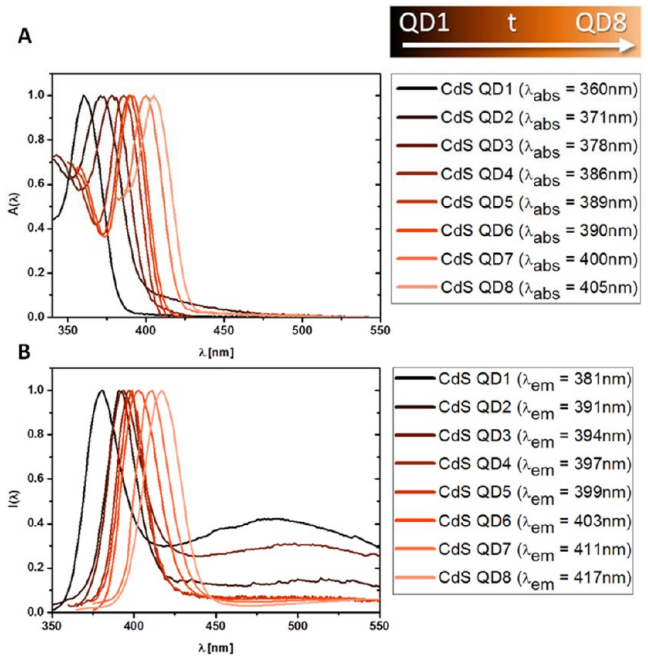

Figure 27. Growth of CdS QDs. Absorption spectra (A) and emission spectra (B) were recorded by taking small aliquots from the reaction solution at different time points (QD1−8). The spectra were normalized to the exciton peak, $A(\lambda_{abs})$ for absorbance and $I(\lambda_{em})$ for emission. Note that upon growth of the QDs, the peak shifts toward higher wavelength.

removed just before injecting the sulfur−ODE solution, and the solution was left undisturbed to cool down to RT under the same stirring conditions, cf. Figure 26. In the case the required size of the QDs was bigger than 2 nm, the temperature of the solution was allowed to recover up to 250 °C after injection of the sulfur−ODE solution. Depending on the required size of the QDs, the solution was kept for 1−15 min at 250 °C (i.e., longer times for bigger QDs), cf. Figure 27. The formation of the QDs could be observed by the change of the solution color, from transparent to light yellow. When the desired size (i.e., the envisaged absorption/emission wavelength of the QDs) was achieved, the heating mantle was removed and the solution was allowed to cool down to RT.

After cooling down to RT, the solution was transferred into a centrifuge tube. To purify the QDs from ODE, OA, and nonreacted Cd or CdO, 20 mL of acetone was added and mixed together until the mixture became cloudy. The cloudy mixture was then centrifuged at 2500 rcf for 10 min. The QDs were precipitated, and the supernatant was discarded. The precipitated QDs could be redispersed in organic solvent (e.g., chloroform, toluene, etc.). For further cleaning of the QDs, a 1:1 volumetric ratio of chloroform and methanol was used to precipitate the QDs. This process was repeated 1−3 times, until the precipitated QDs were like white powder, in order to ensure the purity of the QDs. Finally, the solvent was evaporated and the QDs were dissolved in toluene.

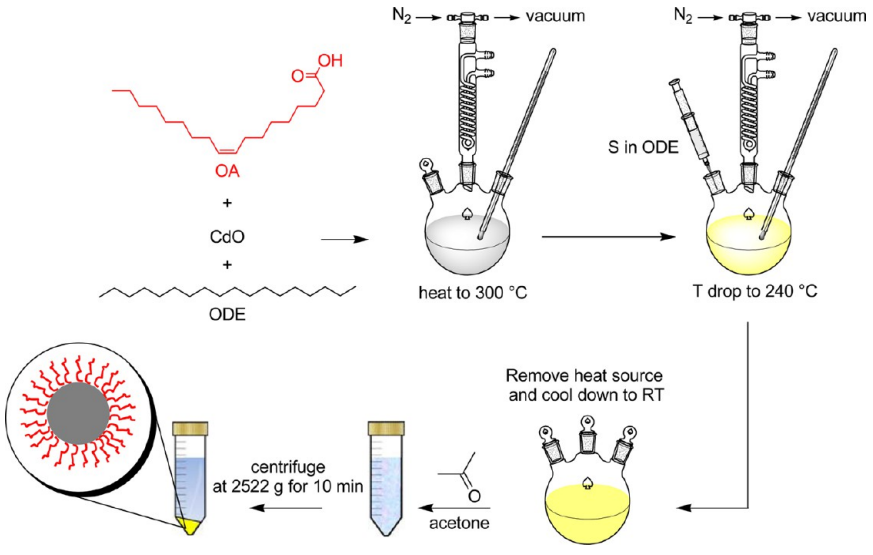

Figure 26. Schematic illustration of the chemical synthesis of hydrophobic CdS NPs ($d_c \approx 2$ nm) is shown. OA, CdO, and ODE were mixed and heated at 300 °C resulting in a color change from brown to transparent. The sulfur solution in ODE was rapidly injected to induce the formation of NPs as evident from the change from transparent to light yellow (QDs). The QDs were purified (1−3 times) by addition of acetone or methanol followed by precipitation and centrifugation.

DOI: 10.1021/acs.chemmater.6b04738
Chem. Mater. 2017, 29, 399−461

2. SYNTHESIS OF INORGANIC NPs IN AQUEOUS SOLUTION LEADING TO HYDROPHILIC NPs

2.1. General Considerations. As detailed in Section 1.1, all glassware was first cleaned with detergent followed by aqua regia and carefully rinsed with Milli-Q water and acetone to guarantee extremely clean glass surfaces.

In this chapter NPs are prepared in aqueous media and thus capped by a shell of hydrophilic ligands to maintain their colloidal stability; see Figure 28. In particular, in this chapter

$$L_{eff} = L_c + 2 \times l_{ligand} \quad \text{(Equation 10)}$$

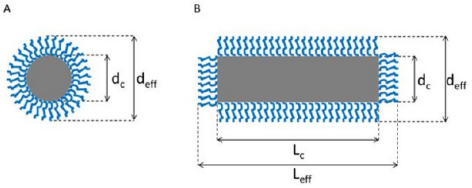

Figure 28. Sketch of (A) spherical and (B) rod-shaped inorganic NPs, comprising an inorganic core (drawn in gray) and an organic hydrophilic ligand shell (drawn in blue). In the case of nanorods, their shape is described by a cylinder with length L_c of the inorganic core and L_{eff} of the NP including the organic ligand shell and with diameter d_c of the inorganic core and d_{eff} of the whole NP.

the synthesis of different materials such as Au and Ag with different shapes is described. In case the NP cores are not of spherical shape, their geometry needs to be described by parameters other than just the core diameter (cf. Figure 28). While this is complex in the form of irregularly shaped NP cores, some other cores can be described best by simple three-dimensional objects such as tubes, ellipsoids, cubes, etc. As described in Section 1.1 the ligand shell adds to the size of the whole NP. Thus, in the case of an elongated object, apart from the diameter also the effective length is higher than the core lengths; see eq 1 and eq 10.

$$L_{eff} = L_c + 2 \times l_{ligand} \quad (10)$$

2.2. Synthesis of Hydrophilic Au NPs (≈5−100 nm core diameter). Since the first systematic preparation of Au NPs in aqueous media by Turkevich[34] and then by Frens,[2] significant efforts have been exerted during the past decade to fabricate monodisperse Au NPs with controlled size and shape using wet chemical methods.[35−39] In the following sections we will detail recent synthetic protocols that present improved outcomes compared to the traditional Frens method in several aspects: higher monodispersity and reaction yield of prepared Au NPs, as well as superior tunability and control over NP size and size distribution.

Citrate-capped spherical Au NPs (Cit-Au NPs) can be prepared in aqueous media by reducing gold ions using sodium citrate (SC) as reducing agent and stabilizer. Turkevich et al. and Frens were the first to prepare monodisperse Cit-Au NPs in aqueous solution in a controlled way.[2,40] However, these protocols fail to produce Au NPs with large diameters (d_c > 50 nm) with acceptable monodispersity. By controlling the reaction conditions (temperature, pH, stirring speed, etc.), stoichiometry of the reagents (gold salt to SC ratio), and addition of additives, recent protocols produce different sizes of Cit-Au NPs (up to 200 nm with excellent monodispersity) as reported by Bastus et al.[3] Synthetic protocols for spherical Cit-Au NPs with core diameter of 5 nm, 13 nm, 20 nm, 25 nm, 50 nm, and 100 nm are described below.

Synthesis of Cit-Au NPs (5 nm core diameter). Cit-Au NPs with a core diameter of around 5 nm were synthesized by following the protocol reported by Piella et al.[38] Briefly, 150 mL of 2.2 mM sodium citrate (SC, 0.33 mmol, 13.2 equiv, Sigma-Aldrich, no. W302600), 0.1 mL of 2.5 mM tannic acid (TA, 0.25 μmol, 0.01 equiv, Alfa Aesar, no. A17022) (the use of traces of tannic acid helps for the growing of homogeneous seeds; as tannic acid is used at a very small concentration, the predominant capping agent is citric acid), and 1 mL of 150 mM potassium carbonate (K_2CO_3, 0.15 mmol, 6 equiv, Sigma-Aldrich, no. P5833) were placed in a 250 mL three-necked round-bottomed flask connected with a condenser to prevent the evaporation of the solvent and were heated up with a heating mantle under vigorous stirring. When the temperature reached 70 °C, 1 mL of 25 mM tetrachloroauric acid ($HAuCl_4$, 25 μmol, 1 equiv, Strem Chemicals, no. 16903-35-8) was quickly injected. The color of the solution changed quickly to purple and then to red in 2 min (see Figure 29). The solution was kept at 70 °C for 5 min more, in order to ensure a complete reduction of gold ions.

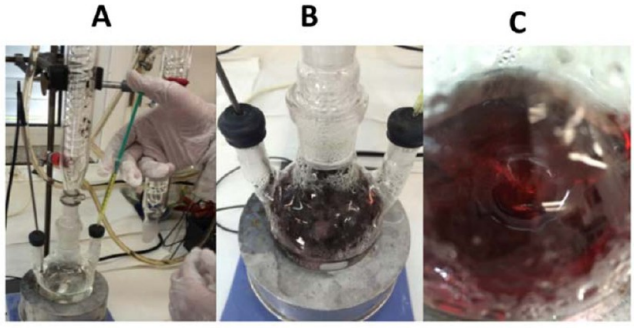

Figure 29. Synthesis of Cit-Au NPs of ≈5 nm in diameter. Photographs showing the reaction flask. (A) Before gold injection (note the yellow gold salt solution inside the syringe). (B) Immediately after injection of gold salt solution (the solution color changed from pale to purple in less than 10 s after the gold addition). (C) Few minutes (ca. 2 min) after injection of gold salt solution; the red color indicates the formation of the Cit-Au NPs.

The reduction of a gold salt by sodium citrate in general is described in eq 11. This equation represents all the following methodologies to obtain spherical Cit-Au NPs. A sketch of the reaction is shown in Figure 30.

$$\begin{aligned} &n\cdot HAuCl_4(aq) + n\cdot(^{-}OCOCH_2)_2C(OH)COO^{-})(aq) \\ &\rightarrow 4n\cdot Cl^{-}(aq) + 4n\cdot H^{+}(aq) + Au^{0}{}_n + n \\ &\cdot(^{-}OCOCH_2)_2CO(aq) + n\cdot CO_2(\uparrow) \end{aligned} \quad (11)$$

Synthesis of Cit-Au NPs (13 nm core diameter). Cit-Au NPs with a core diameter of ≈13 nm were synthesized by following the protocol reported by Schulz et al.[37] Briefly, 144 mL of Milli-Q water were placed in a 250 mL three-necked round-bottomed flask connected with a condenser and heated up until boiling (ca. 100 °C) with a heating mantle. Then, a mixture of sodium citrate (3.5 mL of 60 mM, 0.21 mmol, 8.4 equiv) and citric acid (1.5 mL of 60 mM, Acros, no. A0350656) was added and kept under vigorous stirring (450 rpm) for 30 min. Two parameters are crucial in this reaction to get a narrow

DOI: 10.1021/acs.chemmater.6b04738
Chem. Mater. 2017, 29, 399−461

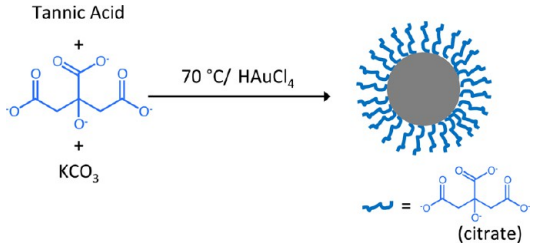

Figure 30. Schematic representation of the synthesis of 5 nm Cit-Au NPs in water.

size distribution: the final pH (which is kept constant by the addition of the buffer citrate/citric) and the heating time (30 min), in which citrate is partially oxidized. To this solution, 0.1 mL of 30 mM ethylenediaminetetraacetic acid (EDTA, 0.003 mmol, 0.12 equiv, Sigma-Aldrich, no. EDS) was injected quickly, followed by the addition of 1 mL of 25 mM hydrogen tetrachloroaurate(III) dissolved in water (0.025 mmol, 1 equiv). After ca. 60 s the color of the mixture changed from pale yellow to dull blue and then to wine-red, which is indicative of the formation of Cit-Au NPs (see Figure 31). After

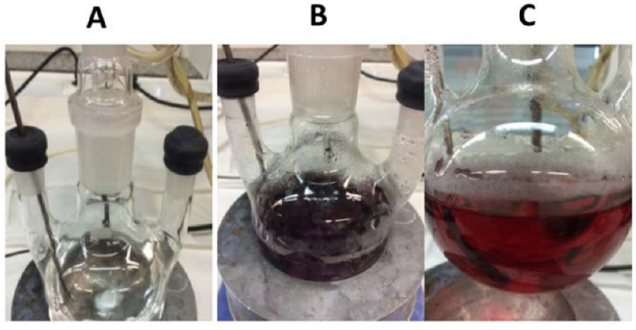

Figure 31. Synthesis of Cit-Au NPs of ≈13 nm in diameter. Photographs showing the reaction flask (A) before gold injection, (B) after injection of gold salt and EDTA solutions when the solution color changed to purple/blue, and (C) shortly (ca. 1 min) after injection, when the red color showed up, indicating the formation of Cit-Au NPs.

that, the heating was switched off (but not the stirring). When the temperature of the mixture had cooled down to 95 °C, the flask with the NP suspension was immersed in ice in order to stop the reaction. It is worth mentioning that this method allows for a fine-tuning of Cit-Au NP size by employing a seed-mediated approach to grow larger NPs. For example, after the synthesis of Au NPs with 13 nm core diameter as described above, the NP suspension may be cooled down to 95 °C, and upon injection of 1 mL of $HAuCl_4$ (25 mM) to this seed solution in the same flask bigger NPs may be grown, similar to using 18 nm seeds, as explained in more detail later in this section.

Synthesis of Cit-Au NPs (18 nm core diameter). Spherical NPs were synthesized following a modified protocol reported by Bastus et al.[3] Briefly, 150 mL of a 1.32 mM sodium citrate solution (0.2 mmol, 8 equiv) was added to a 250 mL three-necked round-bottom flask connected with a condenser and heated up until boiling with a heating mantle under vigorous stirring. After 5 min of boiling, 1.5 mL of 25 mM tetrachloroauric acid ($HAuCl_4$, 0.025 mmol, 1 equiv) was injected. A color change was immediately observed from pale yellow to light blue and then to soft red (see Figure 32). The solution was further boiled for 10 min to allow the NPs to grow and then cooled down with stirring to RT. The resultant Cit-Au NPs had a core diameter of $d_c \approx 18$ nm.

Synthesis of Cit-Au NPs ($18 < d_c < 100$ nm core diameter). Cit-Au NPs (18 nm core diameter) were used as seeds to prepare larger Cit-Au NPs. After preparing 18 nm Cit-Au NPs as described above, the solution was cooled down to 90 °C, and 1 mL of 25 mM $HAuCl_4$ (0.025 mmol, 1 equiv) was injected (see Figure 33). The solution was stirred for 30 min, and this

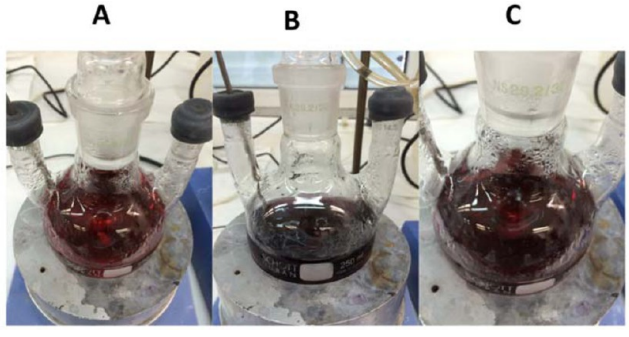

Figure 33. Synthesis of Cit-Au NPs of ≈25 nm in diameter using 18 nm seeds and the seed-mediated approach. Real photographs showing the color change at different stages: (A) 18 nm Au NPs seeds; (B) after injection of gold salt solution where the solution color changed to purple; and (C) after three injections (30 min reaction time between injections) to prepare Cit-Au NPs of 25 nm in diameter.

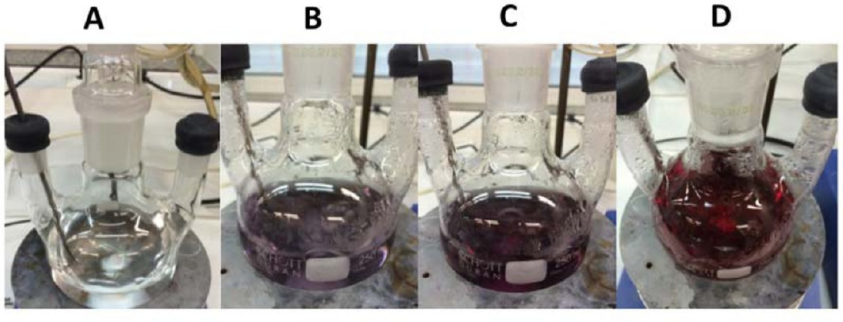

Figure 32. Synthesis of Cit-Au NPs of ≈18 nm in diameter. Real photographs showing the color change at different stages: (A) before gold injection; (B) after injection of gold salt solution where the solution color changed to light blue and then to purple in (C), and finally to red color indicating the formation of Cit-Au NPs in (D).

DOI: 10.1021/acs.chemmater.6b04738
Chem. Mater. 2017, 29, 399−461

process was repeated twice (total three injections of gold salt *per* growth step). Importantly, the temperature was set constant to 90 °C during the whole growing steps. Notice that the temperature is minimally affected by the addition of 1 mL into the 150 mL reaction. After that, the sample was diluted by extracting 55 mL of sample and adding 53 mL of Milli-Q water and 2 mL of 60 mM sodium citrate (0.12 mmol, 4.8 equiv), which temporarily drops the temperature, and thus, the mixture requires ca. 15 min to reach the temperature set in the heating mantle (i.e., 90 °C). Then, by three consecutive gold additions (0.025 mmol, 1 equiv, each) separated by 30 min intervals as described above, Cit-Au NPs with 25 nm were obtained. Likewise, 25 nm Cit-Au NPs were grown to 50 nm, and later they were grown to 100 nm, by using the approach described above (i.e., growing from 18 to 25 nm Cit-Au NPs; see Figure 90 for UV/vis absorption spectra of different growing steps). After the synthesis, the Cit-Au NPs can be stored for further modification in the presence of free citrate in the solution to ensure colloidal stability of Cit-Au NPs for long time periods (months).

2.3. Synthesis of Hydrophilic Ag NPs (≈15 nm core diameter). Ag NPs can be synthesized with different capping agents in aqueous solution to yield a Ag core of different sizes and shapes.[41] Citric acid has been used as the most common capping agent. Synthesizing highly monodisperse citrate-capped silver NPs (Cit-Ag NPs) has been a challenge for long time. There are plenty of synthetic routes developed to synthesize Cit-Ag NPs.[4,41−44] In this section, we briefly describe the synthesis of Cit-Ag NPs (15 nm in diameter) as developed by Bastus et al.[4] The described procedure employs tannic acid (TA) (basically its phenolic hydroxyl groups) as well as citric acid as reducing agents. The use of a small amount of tannic acid controls the size during the growth process, yielding unprecedented narrow size distributions. TA acts as both a reducing agent and a size control agent. The advantage of this method is that, by varying the concentration of TA, a wide size range of highly monodisperse Cit-Ag NPs can be synthesized.

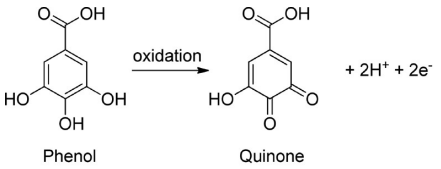

(12)

$$Ag^{+} + e^{-} \rightarrow Ag^{0} \quad (13)$$

To synthesize 15 nm Cit-Ag NPs, 100 mL of aqueous solution of sodium citrate (SC) and tannic acid (TA) were taken in a three-neck round-bottom flask such that the final concentration of SC and TA are 5 mM and 0.1 mM, respectively. At this stage the solution looks colorless, as it can be seen in the photographs given in Figure 34A. The flask was heated with a heating mantle (with a magnetic stirrer), and a condenser was used to avoid the evaporation of solvent. When the solution started boiling, 1 mL of an aqueous solution of 25 mM $AgNO_3$ was rapidly injected into the solution. The color of the solution immediately turned to bright yellow (cf. Figure 34B), confirming the formation of NPs. After cooling down the solution, it was centrifuged at 5000 rcf for 10 min in order to precipitate the NPs. Then, the supernatant was removed and the NP precipitate was redispersed in 0.25 mM sodium citrate solution to get the purified Cit-Ag NPs.

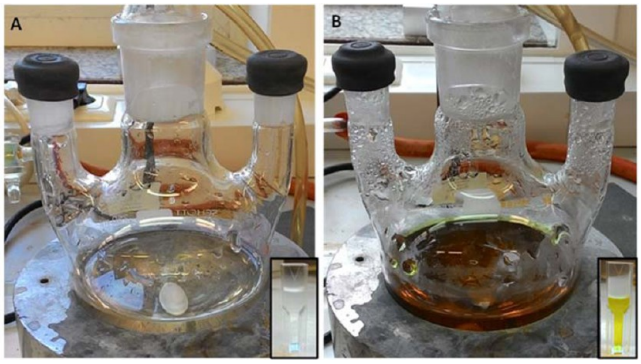

Figure 34. Synthesis of Cit-Ag NPs of ≈15 nm in core diameter. Photographs showing the solution color (A) before and (B) after injection of silver nitrate solution. Yellow solution color in B indicates the formation of Cit-Ag NPs. For more clarity, a photograph of a cuvette containing the solution is given in the inset.

2.4. Synthesis of Rod-Shaped Au NPs (variable size). Rod-shaped Au NPs (gold nanorods, Au NRs) with the longitudinal surface plasmon resonance (SPR) located at λ_{SPR} = 650, 800, 830, and 1050 nm were prepared by a seed-mediated method following previously published protocols.[35,45]

The wet-synthesis method to prepare Au NRs was pioneered by the groups of Murphy[46] and El Sayed[47] in the early 2000s. In general, a solution of small gold seeds (NPs of $d_c \approx 3-4$ nm in diameter) is synthesized in the presence of the cationic surfactant hexadecyltrimethylammonium bromide (CTAB), and silver ions. These seeds are further grown in a growth solution that contains more gold ions, silver ions, and CTAB. The gold ions in the growth solution are partially reduced to Au(I) to allow complete reduction to Au(0) only at the surface of the added seeds, in order to promote growth of Au NRs and to prevent undesired nucleation and formation of nanospheres as side product. The presence of silver ions improves the shape yield and controls the final aspect ratio (length to width ratio) of the nanorods. CTAB is the shape-directing agent that promotes the unidirectional growth and acts simultaneously as a capping agent to form CTAB-capped gold nanorods (CTAB-Au NRs).[48] The shape and size of the prepared Au nanorods can be tuned primarily by varying silver nitrate levels, but generally by controlling the reaction conditions and the level of used chemicals (cf. Table 1 and Table 2).

The traditional protocols to prepare CTAB-Au NRs indicate the use of a high concentration of CTAB (0.1 M), which is cytotoxic and thus limits the use of CTAB-Au NRs in biomedical applications.[49] Significant effort has been done to prepare CTAB-Au NRs in low-CTAB growth solution. In 2012, Murray's group proved that the presence of aromatic additives

Table 1. Synthesis of CTAB-Au NRs in the Presence of 5-Bromosalicylic Acid, with Different SPR Wavelengths λ_{SPR} As Detailed in the Text[a]

λ_{SPR} [nm]	V_{HCl_sol} [mL]	pH	V_{AgNO3_sol} [mL]	V_{AA_sol} [mL]	V_{NP_sol} [mL]
650	0	3.05	6	1	0.8
825	0	2.00	18	2	0.4

[a] V_{HCl_sol} refers to the volume of HCl, which was used to optimize the pH of the growth solution. V_{AgNO3_sol} refers to the volume of added $AgNO_3$ solution. V_{AA_sol} refers to the volume of added ascorbic acid solution. V_{NP_sol} refers to the volume of added NP seed solution.

DOI: 10.1021/acs.chemmater.6b04738
Chem. Mater. 2017, 29, 399−461

Table 2. Synthesis of CTAB-Au NRs in the Presence of Sodium Oleate, with Different SPR Wavelengths λ_{SPR} Using Protocol 2 As Detailed in the Text[a]

λ_{SPR} [nm]	V_{HCl_sol} [mL]	pH	V_{AgNO3_sol} [mL]	V_{AA_sol} [mL]	V_{NP_sol} [mL]
790	2.4	1.68	18	1.25	0.4
1050	5	1.2	24	1.25	0.8

[a] V_{HCl_sol} refers to the volume of HCl, which was used to optimize the pH of the growth solution. V_{AgNO3_sol} refers to the volume of added $AgNO_3$ solution. V_{AA_sol} refers to the volume of added ascorbic acid solution. V_{NP_sol} refers to the volume of added seed NP solution.

in the growth solution reduces the required amount of CTAB to half (this procedure will be termed Protocol 1 below).[35] In 2013, the same group published a modified method in which the CTAB concentration was reduced to 0.037 M. This methodology employs a binary surfactant mixture: CTAB and sodium oleate (NaOL) (this procedure will be termed Protocol 2 below).[45]

Synthesis of the Seed Solution. A seed solution was prepared by mixing 5 mL of 0.5 mM $HAuCl_4$ (0.5 mmol, 1 equiv) with 5 mL of 0.2 M CTAB (200 mmol, 396 equiv, Sigma-Aldrich, no. H9151) in a 40 mL tube. To this solution, 0.6 mL of 0.01 M freshly prepared $NaBH_4$ (10 mmol, 19.8 eq, Sigma-Aldrich no. 71321) was added under stirring. The solution color changed immediately to brownish-yellow (cf. Figure 35). The seed solution, containing ~4 nm core diameter Au NPs capped with CTAB, was vigorously stirred at 1200 rpm for 2 min and kept at 25 °C.

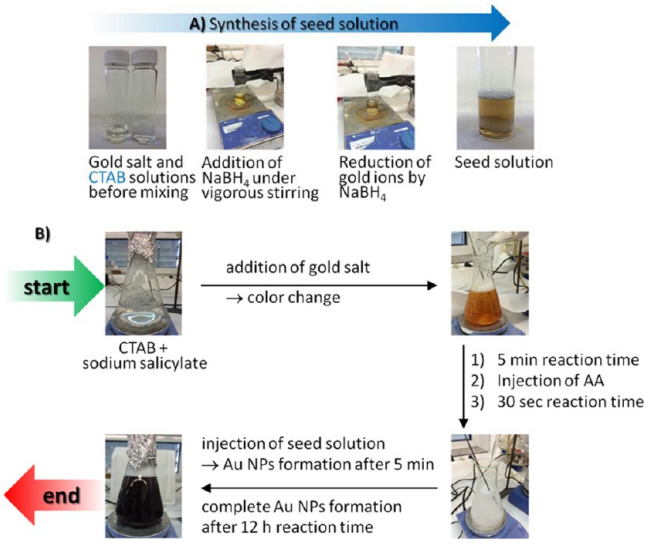

Figure 35. Photographs of steps involved in the preparation of CTAB-Au NRs, using wet chemical seed-mediated method (in the presence of sodium salicylate). (A) Preparation of CTAB-capped seeds. (B) Growth of CTAB-Au NRs.

Protocol 1: Synthesis of CTAB Capped Gold Nanorods (CTAB-Au NRs) in the Presence of 5-Bromosalicylic Acid. This protocol[35] was used to prepare CTAB-Au NRs with longitudinal surface plasmon resonance at λ_{SPR} = 650 and 825 nm. For this purpose, 9.0 g of CTAB (24.6 mmol, 98.5 equiv) and 0.8 g of sodium salicylate (5 mmol, 20 equiv, Sigma, no. S3007) in the case of λ_{SPR} = 650 nm or 1.1 g of 5-bromosalicylic acid (5 mmol, 20 equiv, Sigma, no. 461814) in case of λ_{SPR} = 825 nm were dissolved in 250 mL of warm water (60 °C) in a 500 mL Erlenmeyer flask. The solution was allowed to cool to 30 °C, and then silver nitrate dissolved in water ($AgNO_3$, 4 mM) was added as per Table 1. The mixture was kept undisturbed at 30 °C for 15 min, after which 250 mL of aqueous 1 mM $HAuCl_4$ solution (0.25 mmol, 1 equiv) was added. After 15 min of slow stirring (400 rpm), ascorbic acid solution was added (64 mM) as per Table 1. The solution was stirred for 30 s, until it became colorless. The color change is due to the incomplete reduction of Au(III) to Au(I) by ascorbic acid. Finally, seed solution (freshly prepared as described above) was injected into the growth solution as per Table 1. The solution was mixed gently and left undisturbed overnight, to allow for a compete growth of CTAB-Au NRs. CTAB-Au NRs were collected by centrifugation, and the supernatant was discarded. The centrifuged CTAB-Au NRs pellets were finally redispersed in water.

(Protocol 2): Synthesis of CTAB Capped Gold Nanorods (CTAB-Au NRs) in the Presence of Sodium Oleate. This protocol[45] was used to prepare CTAB-Au NRs with longitudinal surface plasmon resonance at λ_{SPR} = 790 and 1050 nm. For this purpose, 7.0 g of CTAB (19.1 mmol, 76.6 equiv) and 1.234 g of sodium oleate (NaOL, 4 mmol, 16.2 equiv, Sigma-Aldrich, no. O7501) were dissolved in 250 mL of Milli-Q water at 50 °C. After dissolving the reactants, the solution was cooled down to 30 °C; then, a specific amount of $AgNO_3$ (4 mM) was added as per Table 2, and the solution was kept at 30 °C for 15 min. To this solution, 250 mL of 1 mM $HAuCl_4$ (0.25 mmol, 1 equiv) were added, and the solution color changed from dark yellow to colorless during 90 min of stirring at 700 rpm. To control the aspect ratio of Au NRs, HCl (37 wt % in water, 12.1 M, Sigma-Aldrich, no. 320331) was added to adjust the pH as per Table 2. The solution was stirred at 400 rpm for 15 min. After this, 1.25 mL of 0.064 M ascorbic acid (0.08 mmol, 0.32 equiv) was added, and the solution was vigorously stirred for 30 s. Finally, a small amount of seed solution was injected into the growth solution as per Table 1. The solution was stirred for 30 s and kept at 30 °C, without stirring overnight, to allow a compete growth of CTAB-Au NRs. Finally, the CTAB-Au NRs were collected by centrifugation, and the supernatant was discarded. The centrifuged CTAB-Au NRs pellets were redispersed in water.

2.5. Synthesis of Star-Shaped Au NPs (≈70 nm diameter, distance from tip to tip). Gold nanostars can be prepared following an unpublished modification of the protocol reported by Vo-Dihn.[50] Typically, gold nanostars are grown using spherical gold NPs as seeds and using Ag^+ ions as blocking facet agents. These Ag^+ ions promote the tip growth on the surface of the spherical NPs. The reduction of the gold salt at RT using ascorbic acid promotes the seed growth instead of independent nucleation.[20]

Briefly, in a clean glass vial, 20 mL of an aqueous solution of 0.25 mM $HAuCl_4$ (5 μmol, 1 equiv) was mixed with 0.03 mL of 1 M HCl (0.03 mmol, 6 equiv) and 1.5 mL of Au NPs of 13 nm diameter, as prepared according to the protocol given in Section 2.2. To this mixture, 0.15 mL of 1 mM $AgNO_3$ (0.15 μmol, 0.03 equiv) and 0.15 mL of 66.67 mM ascorbic acid (10 μmol, 2 equiv) were added simultaneously. After 1 min, 1 mL of an aqueous solution of 10 mg/mL α-metoxy-ω-thiol-poly(ethylene glycol (mPEG-SH; molecular weight M_w = 750 Da, 13.3 μmol, 2.67 equiv, Rapp polymer, no. 12750-40) and 0.05 mL of 2 M sodium hydroxide (NaOH, 0.1 mmol, 20 equiv, Carl Roth no. 6771.3) were added simultaneously (cf. Figure

DOI: 10.1021/acs.chemmater.6b04738
Chem. Mater. 2017, 29, 399−461

36). After that, the solution was immersed in ice in order to stop the reaction. The NPs can be stored as prepared or purified by centrifugation (15 min, 4000 rcf).

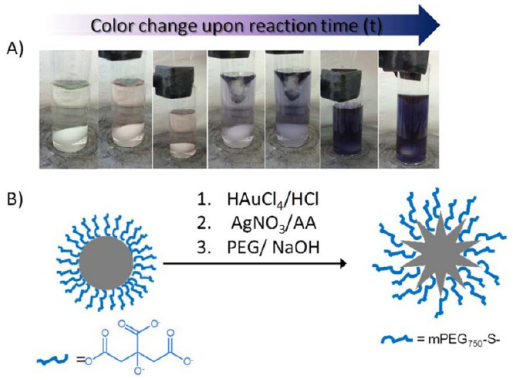

Figure 36. (A) Synthesis process of PEG-coated star-shaped Au NPs. After addition of $AgNO_3$ and AA, the solution color changed from soft red to light blue in a few seconds and then to dark blue, which is indicating the formation of gold nanostars. (B) The cartoon demonstrates the seed mediated growth of spherical gold NPs (seeds) into star-shaped Au NPs. The final surface functionalization of the resulting NPs is PEG-SH, as mediated by displacement of physically adsorbed citrate ions by chemically assembled PEG-S^- molecules via the strong S–Au bond.

3. LIGAND EXCHANGE PROCEDURES FOR HYDROPHILIC NPs MAINTAINING THEIR HYDROPHILIC CHARACTER

3.1. General Considerations. Often the original hydrophilic ligands used for the synthesis of NPs in aqueous solutions are not adequate to maintain excellent colloidal stability and/or not the ligand of choice for a desired application. The original ligands can be replaced in a ligand exchange procedure based on a superior affinity of the displacing ligand and/or concentration difference.[51] The general scheme of the ligand exchange process is depicted in Figure 37. Despite the availability of various examples in the literature, this section will describe a few selected examples.

3.2. Ligand Exchange on Citrate-Capped Au NPs with Bis(*p*-sulfonatophenyl)-phenylphosphine. The citrate ions are physically adsorbed on the surface of citrate-caped Au NPs; i.e., the ligands are only weakly associated with the Au NPs' surface. For example, citrate ligands tend to desorb from the

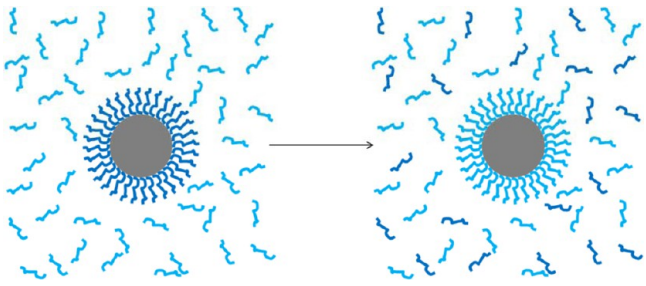

Figure 37. Ligand exchange reaction at the surface of Au NPs. After synthesis, the depicted Au NP core is capped by hydrophilic ligands (drawn in dark blue). In the case Au NPs are incubated with new ligands in excess (drawn in light blue), the new ligands can displace the original ones.

surface of Cit-Au NPs upon dialysis, dilution, or repeated centrifugation, resulting in irreversible aggregation. In other words, Cit-Au NPs are not stable for a long time and further processing/applications. There are many strategies to improve the colloidal stability of Cit-Au NPs, including exchanging citrate molecules with ligands that provide superior stability or specific functionality. Au NPs of 5 and 10 nm core diameter were used to perform the ligand exchange reaction by displacing citrate ions on the gold surface with bis(*p*-sulfonatophenyl)-phenylphosphine as described previously by Pellegrino et al.[52,53]

In order to perform the ligand exchange, bis(*p*-sulfonatophenyl)phenylphosphine dihydrate dipotassium salt (150 mg (281 μmol, 1.0 equiv; Strem Chemicals, no. 15-0463) was dissolved in 500 mL of suspension of Cit-Au NPs (d_c = 5 nm (c_{NP} = 8.3 nM) or d_c = 10 nm (c_{NP} = 9.0 nM), BBI Solutions, no. 15702 and no. 15703, or synthesized according to Section 2.2). The resulting solution was stirred at RT for 2 days, cf. Figure 38. After this, the mixture was concentrated to

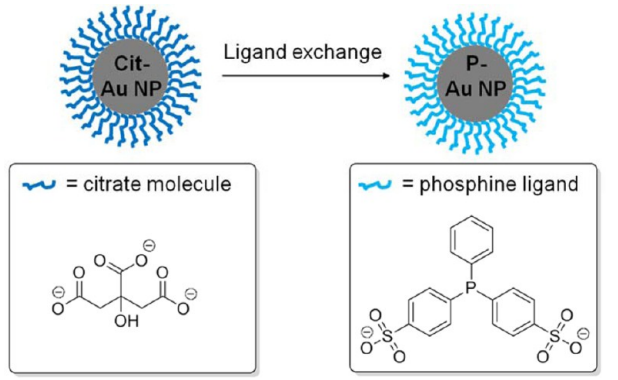

Figure 38. Scheme of the ligand exchange on Cit-Au NPs of different size with bis(*p*-sulfonatophenyl)-phenylphosphine. Spherical Cit-Au NPs of d_c = 5 and 10 nm core size stabilized by citrate molecules (drawn as dark blue ligands) were modified by bis(*p*-sulfonatophenyl)-phenylphosphine molecules (drawn as light blue ligands). The resulting P-Au NPs have improved colloidal stability.

approximately 2 mL, cf. Section 7.2. For that, the solution was centrifuged at 3000 rcf for 5 min using centrifuge filters (Merck Millipore, 100 kDa, 15 mL). Next, the concentrated Cit-Au NP suspension was diluted in phosphine solution (3 mg of bis(*p*-sulfonatophenyl)phenylphosphine dihydrate dipotassium salt per 10 mL of Milli-Q water) to 15 mL. Then, the solution was concentrated to 2 mL using centrifuge filters as described previously. Importantly, in order to ensure an excess of phosphine (by decreasing the amount of citrate molecules), the dilution and concentration step was repeated three times. Finally, this leads to phosphine-capped Au NPs (P-Au NPs) that are suspended in 3 mg/10 mL phosphine solution.

3.3. Ligand exchange of citrate-capped Au NPs with thiolated polyethylene glycol. PEGylation, i.e., coating the surface of NPs with an organic shell composed of polyethylene glycol (PEG), is among the most used strategies to improve the colloidal stability of Au NPs in both polar and nonpolar solvents, due to the amphiphilic character of PEG. Moreover, PEGylation is essential for various biomedical applications as it enhances the biocompatibility of NPs and alters their in vitro cellular interaction and in vivo pharmacokinetics.[54] Usually, linear thiolated PEG polymers with molecular weight in the range of 0.75 to 10 kDa are employed to PEGylate Cit-Au

DOI: 10.1021/acs.chemmater.6b04738
Chem. Mater. 2017, 29, 399–461

NPs.[55−57] Thiol moieties are necessary to ensure strong attachment of PEG chains to the surface of Au NPs via the strong Au−S bond forming a self-assembled monolayer of PEG on the Au NP surface. In a typical experiment, PEG-SH is dissolved in distilled water (e.g., 10 mg·mL^{-1}) and added in excess (ca. 5−15 PEG per nm^2 of NP surface A_c) to ensure full coverage of PEG on the surface of Au NPs.[56] After ca. 2 min stirring, NaOH (2 M) is added dropwise to increase the pH value to 8−9 (to deprotonate thiol groups in PEG-SH and thus increase their reactivity). Samples are stirred overnight at RT, followed by centrifugation (at least three steps) to collect the PEG-capped Au NPs (PEG-Au NPs). Notice that the centrifugal force has to be adapted to d_c (bigger colloids require less centrifugal force). For instance, for PEG-Au NPs with $d_c \approx 14$ nm, 30 min at ca. 15 000 rcf was sufficient to obtain clear supernatants and to pellet all PEG-Au NPs containing excess. Purified PEG-Au NPs can be stored (ideally at 4 °C) for extended periods of time (years) without losing their colloidal stability and preserving the initial optical properties (i.e., UV/vis absorption spectrum). Figure 39 illustrates the PEGylation method for Cit-Au NPs with thiolated PEG molecules, resulting in PEG-Au NPs.

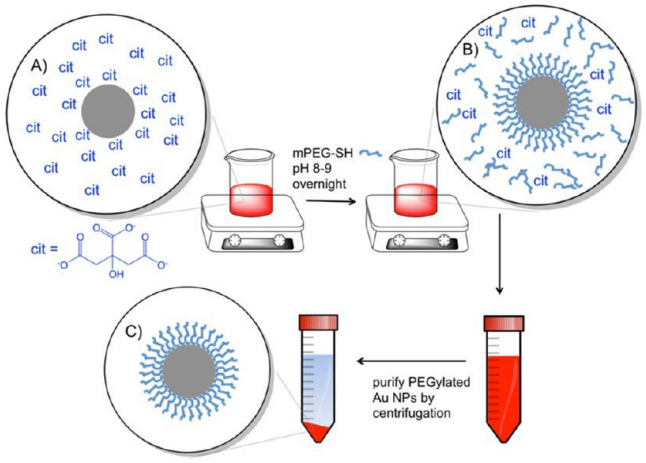

Figure 39. (A) Cit-Au NPs in solution with physically adsorbed and excess free citrate molecules. (B) Addition of mPEG-SH at basic pH to promote displacement of citrate molecules by mPEG-SH. (C) Purification by centrifugation in which PEGylated NPs are purified from free citrate molecules and mPEG-SH in the supernatant.

4. LIGAND EXCHANGE PROCEDURES TO TRANSFER HYDROPHILIC NPs FROM AQUEOUS SOLUTION TO ORGANIC SOLVENT AND THUS TO RENDER THEM HYDROPHOBIC

4.1. General Considerations. The synthesis of Au NPs with complex shapes and/or large size is usually carried out in aqueous media. However, some applications require hydrophobic Au NPs, for example, in the cases the NPs are to be embedded into an organic matrix as in the case of molecular electronics. With this in mind, a significant effort was devoted to developing facile postsynthesis surface functionalization protocols that modify the surface of hydrophilic Au NPs with hydrophobic ligands (surface hydrophobization) (Figure 40).[58] In this section we will describe three examples in which Au NPs were typically prepared in water (Cit-Au NPs, CTAB-Au NRs, and star-shaped PEG-Au NPs as per Section 2.3), followed by

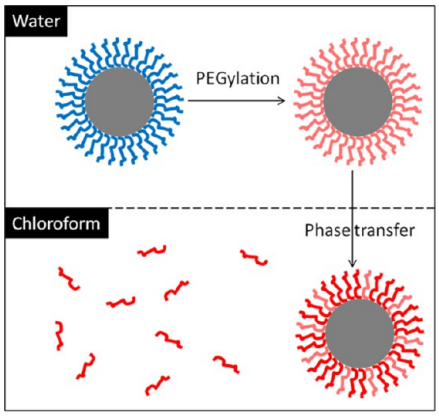

Figure 40. Hydrophobization of Au NPs via two-stage functionalization: (1) PEGylation in water (upper panel) by displacement of hydrophilic ligands (drawn in blue) by PEG-SH molecules (drawn in light red), followed by phase transfer into chloroform containing alkylamines (drawn in dark red).

surface PEGylation, which is an intermediate step prior to phase transfer of the NPs to organic solvent containing alkylamines.[57,59] We found that PEGylation is crucial to initiate phase transfer without NP aggregation due to the unique solubility of PEG in both aqueous and organic media, which provides excellent colloidal stability for NPs in both media. For more insights into the mechanism of phase transfer, the original references should be consulted as cited.

4.2. Ligand Exchange on Citrate-Capped Au NPs with PEG-SH Followed by Phase Transfer of PEG-Capped Au NPs to Chloroform Containing Dodecylamine. Herein, a protocol to transfer Cit-Au NPs, as prepared in Section 2.2, from water to chloroform is detailed.[57] As prepared Cit-Au NPs were first coated with mPEG-SH (M_W = 750 Da, Rapp Polymer, no. 12750-40), as described in detail in Section 3.3, followed by purification and concentration (range of ca. c_{NP} = 50−200 nM in distilled water). Then, typically 1 mL of the concentrated solution of PEG-Au NPs was mixed with 5 mL of chloroform (Carl Roth, no. Y015.2) containing dodecylamine (DDA) as per Table 3. DDA was added in excess of ~2.5 × 10^6 DDA molecules *per* NP, in order to promote partial/full exchange of PEG by DDA. This resulted in a two-phase system with the aqueous phase containing the PEGylated NPs on top and the organic phase with the DDA at the bottom (cf. Figure 41A). Both phases were mixed by magnetic stirring (ca. 800 rpm), until the NPs were transferred to the chloroform phase

Table 3. Phase Transfer of Spherical Cit-Au NPs with Various Core Diameters (d_c)[a]

d_c [nm]	c_{NP} [nM]	c_{DDA} [M]	c_{PEG}/c_{NP}	c_{DDA}/c_{NP}
5	200	0.1	1 × 10^4	2.5 × 10^6
13	200	0.2	2 × 10^4	5 × 10^6
20	200	0.4	3 × 10^4	10 × 10^6
25	150	0.4	3 × 10^4	13 × 10^6
50	100	0.4	20 × 10^4	20 × 10^6
100	50	0.4	50 × 10^4	40 × 10^6

[a] c_{NP} and c_{DDA} refer to the concentration of NPs and DDA, respectively. The ratios c_{PEG}/c_{NP} and c_{DDA}/c_{NP} describe the number of PEG and DDA molecules added per Au NP, respectively. Detailed procedure to determine Au NP concentration c_{NP} can be found in Sections 8.2 and 9.2.

DOI: 10.1021/acs.chemmater.6b04738
Chem. Mater. 2017, 29, 399−461

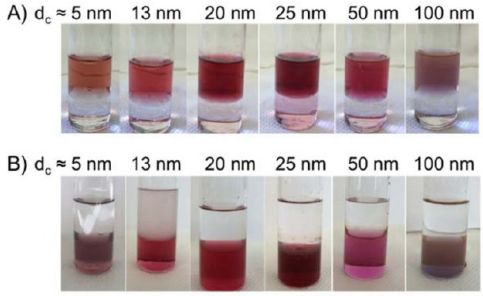

Figure 41. Phase transfer of PEG-Au NPs from water (upper layers in all vials) to chloroform containing DDT (lower layers in all vials). (A) Photographs of biphasic system after ligand exchange of Cit-Au NPs with PEG in water. (B) Photographs of biphasic system after phase transfer of PEG-Au NPs to the chloroform layer with DDT. Different vials correspond to Au NPs with different core diameters as labeled.

(Figure 41B). The transferred Au NPs were cleaned twice by centrifugation in order to remove free DDA and PEG molecules (i.e., the supernatant was discarded, and the NP pellet was redispersed in chloroform). The same protocol can be employed to phase transfer Cit-Au NPs with various core diameters as per Table 3.

4.3. Ligand Exchange on CTAB-Capped Au NRs with PEG-SH Followed by Phase Transfer of PEG-Capped Au NPs to Chloroform Containing Dodecylamine. CTAB-Au NRs can be transfered to the chloroform phase using a similar protocol as for Cit-Au NPs as described in Section 4.2.[57] Initially, free CTAB in excess in "as prepared" CTAB-Au NRs suspensions was removed by centrifugation (5000 rcf, 30 min), and the supernatant was discarded. The resultant NP pellets were then resuspended in water, and another round of purification was performed. To the purified CTAB-Au NRs, PEG-SH (mPEG-SH, M_W = 750 Da, Rapp Polymer, no. 12750-40) was added as per Table 4 and mixed for 2 min. Then, the pH was adjusted to ca. 8−9 by dropwise addition of NaOH (2 M). The solution was left under stirring at RT overnight, to allow for self-assembly of PEG-SH on the Au NRs to form PEG-Au NRs. The PEG-Au NRs were then purified by centrifugation (5000 rcf, 30 min, twice). A significant decrease in ζ-potential, from 40 mV (CTAB-Au NRs) to 10 mV (PEG-Au NRs), was observed, confirming a partial ligand exchange.[57] Finally, a solution of DDA in chloroform (volume ratio 5:1 chloroform to aqueous solution of NPs) was added (cf. Table 4), leading to a two-phase system, which was stirred overnight at RT. After stirring for ca. 12 h, PEG-Au NPs transferred to the chloroform phase (Figure 42). Au NRs in chloroform were cleaned twice by centrifugation to remove free DDA and PEG molecules and were finally redispersed in chloroform. The same protocol can be employed to phase transfer CTAB-Au NPs with various aspect ratios as per Table 4.

Table 4. Phase Transfer of CTAB-Au NRs with Various Aspect Ratios and λ_{SPR}[a]

λ_{SPR} [nm]	c_{PEG}/c_{NR}	c_{DDA} [M]
650	3×10^4	0.4
790	8×10^4	0.4
825	8×10^4	0.4
1050	8×10^4	0.4

[a] c_{NR}, c_{PEG}, and c_{DDA} refer to the concentrations of Au NRs, PEG, and DDA, respectively. The ratio c_{PEG}/c_{NR} describes the number of PEG molecules added per Au NR. A detailed procedure to determine the Au NR concentration c_{NP} can be found in Section 8.2.

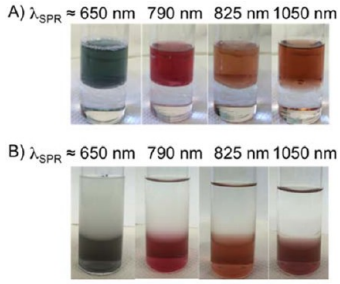

Figure 42. Phase transfer of PEG-Au NRs from water (upper layers in all vials) to chloroform containing DDT (lower layers in all vials). (A) Photographs of the biphasic system after ligand exchange of CTAB-Au NRs with PEG in water. (B) Photographs of the biphasic system after phase transfer of PEG-Au NRs to the chloroform layer with DDT. Different vials correspond to Au NRs with different aspect ratios and λ_{SPR} as labeled.

4.4. Phase Transfer of Star-Shaped PEG-Capped Au NPs to Chloroform Containing Dodecylamine. The protocol in Section 2.5 describes the synthesis of star-shaped Au NPs, which are capped with PEG molecules as prepared. Thus, these NPs can be directly transferred from aqueous media to chloroform containing DDA (0.2 M), similar to the phase transfer of PEG-Au NPs and PEG-Au NRs as detailed in Section 4.2 and Section 4.3. The phase transfer is shown in Figure 43.

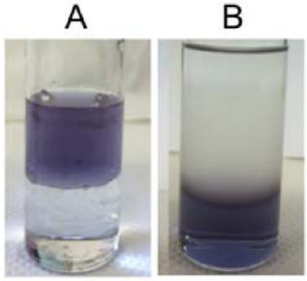

Figure 43. Phase transfer of star-shaped Au NPs from water (upper layers) to chloroform containing DDT (lower layers). Photographs of biphasic system before (A) and after (B) phase transfer from water to chloroform.

5. LIGAND EXCHANGE PROCEDURES TO TRANSFER HYDROPHOBIC NPs INTO AQUEOUS SOLUTION AND THUS TO RENDER THEM HYDROPHILIC

5.1. General Considerations. For most biological applications, dispersion of NPs in the aqueous phase is required. Thus, proper surface modification of hydrophobic NPs, which have been originally synthesized in organic solvent, is needed to allow their stable dispersion in aqueous media. Ligand exchange is a powerful approach to displace the original hydrophobic ligands by hydrophilic versions (Figure 44).[19,60] This section describes procedures to modify the surface of hydrophobic Au NPs and Ag NPs with hydrophilic ligands.

5.2. Ligand Exchange on DDT-Au NPs with 3-Mercaptopropionic Acid (MPA) or 11-Mercaptoundecanoic Acid (MUA). Here we describe the detailed procedure for synthesizing Au NPs, protected by weakly bound ligands, and

DOI: 10.1021/acs.chemmater.6b04738
Chem. Mater. 2017, 29, 399−461

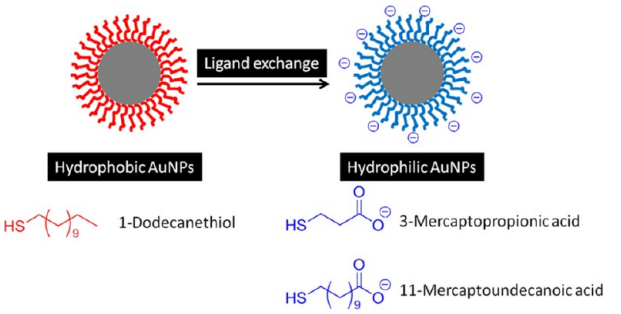

Figure 44. Ligand exchange on hydrophobic NPs (capped with hydrophobic ligands drawn in red) with hydrophilic ligands (drawn in blue). The chemical structures of 1-dodecanethiol, 3-mercaptopropionic acid, and 11-mercaptoundecanoic acid are shown.

how to perform the following ligand exchange to mercapto-carbonic acids like mercaptopropionic acid (MPA) or mercaptoundecanoic acid (MUA), which due to their mercapto-groups are strong ligands, cf. Figure 45. The protocol

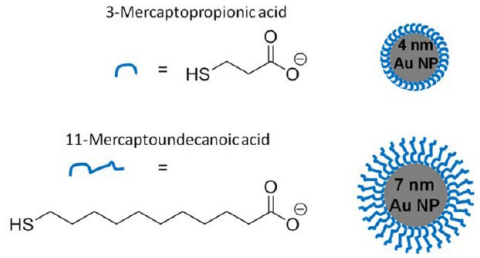

Figure 45. Sketch of the final Au NPs stabilized by MPA in case of d_c = 4 nm Au NPs and MUA in case of 7 nm Au NPs.

for synthesizing precursor Au NPs stabilized by hexanoic or decanoic acid (cf. Section 1.2), as well as the additional ligand exchange to MPA or MUA, was previously described, and we refer to the original protocols for more information.[19,61]

Ligand Exchange on DDT-Au NPs (4 nm) with Mercaptopropionic Acid. To DDT-Au NPs (d_c = 4 nm) in chloroform (as synthesized per Section 1.2) was added MPA dissolved in CH_2Cl_2 (dichloromethane) (500 μL in 2 mL), and the mixture was left to react in an ultrasonic bath for 90 min at RT to allow for ligand exchange. The MPA-Au NPs were then transferred into a 50 mL centrifuge tube, 20 mL of methanol was added, and the mixture was centrifuged at 3000 rcf for 5 min. The supernatant was removed, and the sedimented Au NPs were resuspended in 20 mL of methanol and centrifuged. The washing procedure was done four times in total. After the last washing step, the supernatant was discarded, and the Au NP pellet (at the bottom of the centrifugation tube) was dispersed in 15 mL of Milli-Q water, which led to a dark red solution. Finally, the MPA-Au NPs were washed twice using centrifuge filters (Merck Millipore, 100 kDa, 15 mL) and a speed of 3000 rcf for 5 min to get rid of free MPA (cf. Section 7.2).

Ligand Exchange on DDT-Au NPs (7 nm) with Mercaptoundecanonic Acid. To DDT-Au NPs (d_c = 7 nm) in chloroform (as synthesized per Section 1.2) was added 91 mg (417 μmol) of MUA, and the resulting mixture was first stirred at 60 °C for 30 min and then put into an ultrasonic bath at RT for another hour to allow for ligand exchange. MUA-Au NPs were precipitated by the addition of 40 mL of methanol, transferred into a centrifuge tube, and sedimented at 3000 rcf for 10 min to collect the MUA-Au NPs. The supernatant was discarded, and the solid Au NP pellet was resuspended in another 40 mL of methanol and again centrifuged. This washing procedure was repeated 3 times, and the MUA-Au NPs were finally purified by column chromatography using a Sepharose (CL-4B) column and 25 mM aqueous sodium hydroxide as the mobile phase (cf. Section 7.3).

5.3. Phase Transfer of DDT-Ag NPs from Chloroform to Water Using 3-Mercaptopropionic Acid (MPA) or 11-Mercaptoundecanoic Acid (MUA). This protocol implies the phase transfer of DDT-Ag NPs with MPA or MUA to render Ag NPs with a hydrophilic surface and thus to resuspend them in aqueous solution with satisfactory colloidal stability (Figure 46).[62] Briefly, DDT-Ag NPs in chloroform (10 mL of

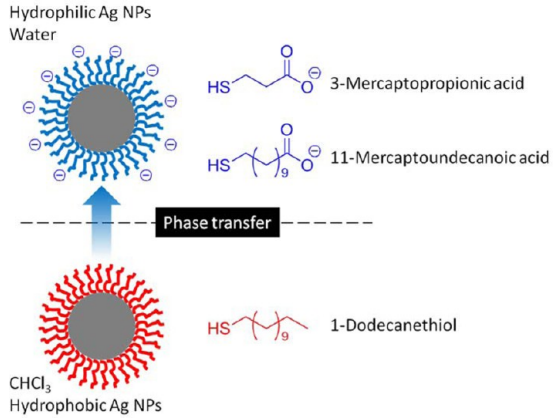

Figure 46. Phase transfer of DDT-Ag NPs from chloroform to water using 3-mercaptopropionic acid (MPA) or 11-mercaptoundecanoic acid (MUA).

0.5 mg/mL, cf. Section 1.3) were placed in a 250 mL round-bottom flask. MPA (7.3 mmol, 636 μL) or MUA (7.3 mmol, 1.59 g) was dissolved in 130 mL of Tris-Borate-EDTA (TBE) buffer (0.5×) (Sigma-Aldrich, no. T3913). In the case of MUA, the buffer mixture had to be dissolved by placing it into an ultrasonic bath for 45 min. Then aqueous buffer solution was added to the chloroform organic phase, and both phases were mixed thoroughly until a phase transfer of Ag NPs to the aqueous layer at the top of the vial was observed. The two phases were then transferred into a 40 mL glass vial and centrifuged at 900 rcf for 20 min to precipitate the excess ligands as white solid on the bottom of the vial and simultaneously to separate the two liquid layers. The aqueous phase, including the MPA-Ag NPs or MUA-Ag NPs on top of the biphasic system, was removed by a pipet and further washed three times with Milli-Q water using centrifuge filters (Merck Millipore, 100 kDa, 15 mL) at 3000 rcf for 5 min.

6. POLYMER COATING TO TRANSFER HYDROPHOBIC NPs INTO AQUEOUS SOLUTION AND THUS TO RENDER THEM HYDROPHILIC

6.1. General Considerations. This section describes the phase transfer of hydrophobic alkanethiol-capped NPs to the aqueous phase by overcoating the NPs with an amphiphilic polymer that interacts strongly with the self-assembled alkane monolayer on the NPs' surface and provides a hydrophilic character that enables efficient transfer of NPs from organic solvent to water phase (cf. Figure 47). In other words, the hydrophobic NPs are encapsulated inside the hydrophobic

DOI: 10.1021/acs.chemmater.6b04738
Chem. Mater. 2017, 29, 399−461

cavity of the polymer micelles with independence on the type of the inorganic core material.[63,64]

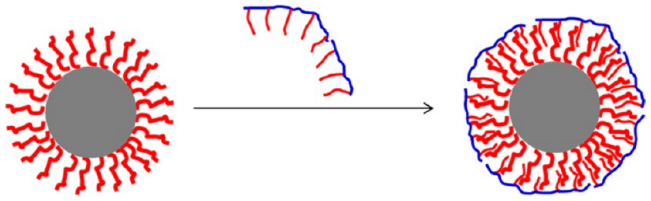

Figure 47. NP cores (drawn in gray) that are capped with hydrophobic ligands (drawn in red) are modified with an amphiphilic polymer (hydrophilic backbone drawn in blue and hydrophobic side chains drawn in red). The NP core is embedded in the resulting polymer micelle, resulting in a hydrophilic nanoparticle surface.

6.2. Synthesis of the Amphiphilic Polymer: Poly(isobutylene-*alt*-maleic anhydride)-*graft*-dodecyl, PMA-*g*-dodecyl. In principle, there are many potential amphiphilic polymers which can be used for polymer coating of NPs. In this section emphasis is given to an amphiphilic polymer which is based on a backbone of poly(isobutylene-*alt*-maleic anhydride), functionalized with dodecylamine, yielding dodecylamine hydrophobic side chains through formation of amide bonds upon reaction with the maleic anhydride rings (PMA). The anhydride rings that have not been reacted with dodecylamine open in contact with water, forming negatively charged carboxyl groups and, thus, providing colloidal stability to the NPs in aqueous solutions. This chemistry allows for preparation of the amphiphilic polymers with additional functionalities (e.g., by attaching organic fluorophores).[65]

The synthetic PMA has been reported in previous work.[10,66] A 250 mL round-bottom flask received 3.084 g (20 mmol expressed as monomer, cf. Figure 48) of poly(isobutylene-*alt*-maleic anhydride) (average M_w ∼ 6000 g/mol of whole polymer, molecular weight of one PMA monomer unit M_{PMA} ∼ 154 g/mol, Sigma, no. 531278). Then, 2.70 g (15 mmol) of dodecylamine (DDA, ≥ 98%, Fluka, no. 44170) was dissolved in 100 mL of anhydrous tetrahydrofuran (THF, ≥99.9%, Aldrich, no. 186562). Note, each polymer monomer unit comprises an anhydride ring. The ratio of dodecylamine/anhydride rings was chosen in a way that $R_{chain/mon}$ = 75% (15 mmol out of 20 mmol), to allow for 75% anhydride rings coupled with dodecylamine and 25% intact anhydride rings. It is very important to use anhydrous organic solvents in order to maintain the maleic anhydride rings active during the synthesis, i.e., to prevent hydrolysis. This solution was then added to the poly(isobutylene-*alt*-maleic anhydride), and the mixture was sonicated for ca. 20 s, followed by heating to 55−60 °C for 3 h under stirring. This mixture was initially cloudy, and only after a while of heating it turned transparent. Next, the solution was concentrated to 30−40 mL by evaporation of THF under reduced pressure in a rotary evaporator, and the mixture was heated under reflux overnight. Finally, the solvent was completely evaporated under reduced pressure in a rotary evaporator, and the dried polymer powder was dissolved in V_{P_sol} = 40 mL of anhydrous chloroform (≥99%, Sigma, no. 372978), yielding a solution 0.5 M in monomer concentration, c_P. It is important to keep this polymer solution under anhydrous conditions so that the remaining maleimide rings do not yet hydrolyze.

The final molar mass of one polymer unit M_P comprises the molar mass M_{PMA} of one PMA monomer and the molar mass M_{DDA} = 185 g/mol of one DDA side chain times the number of side chains per monomer; see eq 14.

$$M_P = M_{PMA} + R_{chain/mon} \times M_{DDA} \quad (14)$$

For $R_{chain/mon}$ = 0.75, the value of M_P = 154 g/mol + 0.75 × 185 g/mol ≈ 293 g/mol is obtained.

During the polymer synthesis molecules that are soluble in THF and which bear a $-NH_2$ group can be integrated into the polymer. This can be done by adding those amine-containing molecules (like dyes or spacer molecules like polyethylene glycol) together with the dodecylamine to the PMA. By this $R_{chain/mon}$ = 75% of the anhydride rings will react with the NH_2 group of the dodecylamine, as described above, and some of the

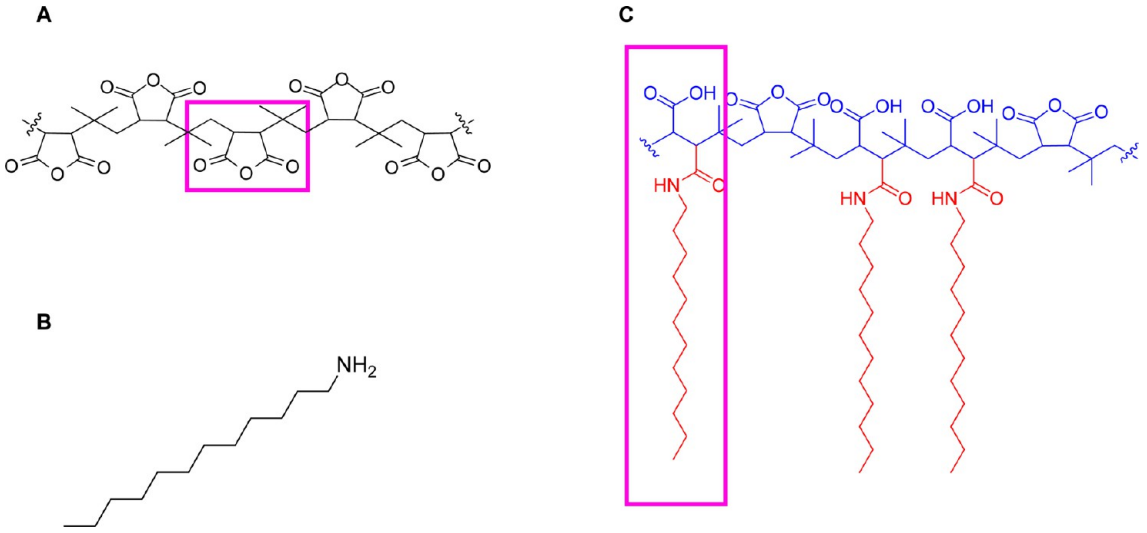

Figure 48. Synthesis of poly(isobutylene-*alt*-maleic anhydride)-*graft*-dodecyl, PMA-*g*-dodecyl. (A) Poly(isobutylene-*alt*-maleic anhydride) is used as hydrophilic backbone (the purple box shows one monomer unit). (B) Dodecylamine is used as hydrophobic side chain. The amphiphilic polymer was obtained by reaction of the hydrophilic backbone with hydrophobic side chains. (C) Structure of the amphiphilic polymer (PMA-*g*-dodecyl). The purple box in C shows a monomer unit with attached side chain (of molar mass M_P). The hydrophobic and hydrophilic parts are drawn in red and blue, respectively.

DOI: 10.1021/acs.chemmater.6b04738
Chem. Mater. 2017, 29, 399−461

remaining PMA monomers with the additional functional molecules. Typically not more than $R_{func/mon}$ = 5% of the anhydride rings should be modified with functional molecules, as otherwise the polymer coating procedure as described in Section 6.3 may no longer work. A list with modified polymers that has been reported in literature is provided in Section 6.3.

6.3. Phase Transfer of Alkanethiol-Capped NPs from Chloroform to Water Using PMA-*g*-dodecyl Polymer. DDT-Au NPs in chloroform were mixed with PMA-*g*-dodecyl dissolved in chloroform. The mixture was stirred manually for 5 min at RT, and then the solvent (i.e., chloroform) was completely evaporated in a rotary evaporator under heating at 40 °C to force the polymer to wrap around the NPs, as illustrated in Figure 49. A few milliliters of anhydrous

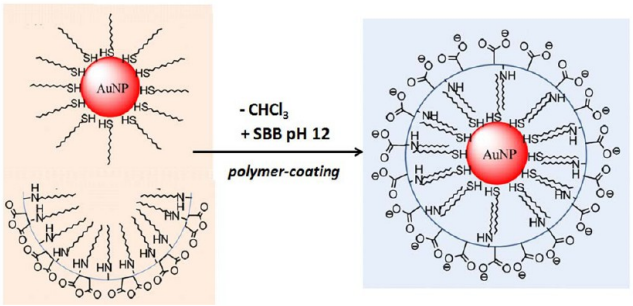

Figure 49. Phase transfer of DDT-Au NPs from chloroform (left) to water (right) using PMA-*g*-dodecyl polymer.

chloroform were added to the flask to reconstitute the solid film, and again the solvent was removed under reduced pressure. This step was carried out 3 times in order to obtain a homogeneous coating. After the last step, the remaining solid film in the flask film was reconstituted in alkaline sodium borate buffer (50 mM, pH 12 adjusted with NaOH) under vigorous stirring until the solution turned clear, cf. Figure 50. Sonication

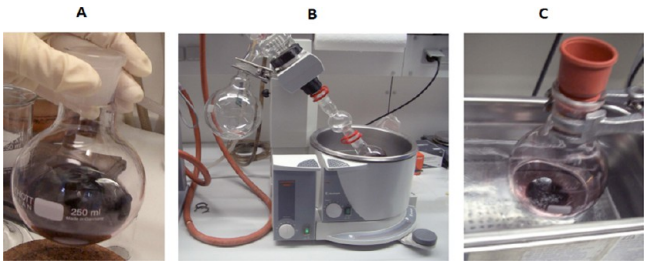

Figure 50. Phase transfer of DDT-Au NPs (d_c = 4.2 nm) from chloroform to water using PMA-*g*-dodecyl polymer. Photographs of (A) DDT-Au NPs in chloroform after addition of the polymer solution dissolved in chloroform, (B) chloroform evaporated using a rotary evaporator, and (C) sonication after the addition of sodium borate buffer (pH 12).

can be optionally used to facilitate the dispersion. In the last step, the remaining anhydride rings get hydrolyzed in alkaline conditions resulting in carboxylate groups that allow reconstitution in water with excellent colloidal stability. This approach can be employed to transfer various types of NPs with different sizes from water to chloroform as per Table 5.

A key point in this procedure is the calculation of the amount of polymer N_P (in terms of monomer units), which needs to be added to the NPs. The amount of polymer per NP scales with the effective surface area A_{eff} of one NP and with the amount of NPs. In the case of spherical NPs A_{eff} is given as the surface of a sphere (cf. Figure 1):

$$A_{eff} = 4\pi \times \left(\frac{d_{eff}}{2}\right)^2 = \pi \times {d_{eff}}^2 \quad (15)$$

Nanorods were considered as cylinders with diameter d_{eff} and length L_{eff} to simplify the calculations (cf. Figure 2), and thus the effective surface of one rod-shaped NP becomes

$$A_{eff} = 2\pi \times \left(\frac{d_{eff}}{2}\right) \times L_{eff} = \pi \times d_{eff} \times L_{eff} \quad (16)$$

In a solution with volume V_{NP_sol} and NP concentration c_{NP} the number of moles of NPs is $n_{NP} = c_{NP} \cdot V_{NP\_sol}$; i.e., the total number of NPs $N_{NP} = n_{NP} \times N_A$ (N_A = Avogadro's number). The total effective surface area of all NPs in solution thus is

$$A_{total\_eff} = N_{NP} \times A_{eff} = c_{NP} \times V_{NP\_sol} \times N_A \times A_{eff} \quad (17)$$

The number of monomer units that needs to be added per nm^2 of effective surface area ($R_{P/Area}$) is an important value that should be determined experimentally for any polymer coating protocol, as it may depend on the core material, core diameter, surface capping, etc. of the NPs. The number of polymer monomers N_P that needs to be added to the NP suspension thus is

$$N_P = R_{P/Area} \times A_{total\_eff} \quad (18)$$

For a polymer stock solution of monomer concentration c_P, the volume V_{P_sol} needs to be added to the NP suspension.

$$V_{P\_sol} = \frac{n_P}{c_P} = \frac{N_P/N_A}{c_P} = \frac{R_{P/Area} \times A_{total\,eff}}{N_A \times c_P} = \frac{R_{P/Area} \times A_{eff} \times c_{NP} \times V_{NP\_sol}}{c_P} \quad (19)$$

The polymer coating procedure should be carried out in sufficiently diluted NP suspension. In the case of NPs with d_c < 10 nm we typically use a NP concentration of around c_{NP} = 1 μM. In case of bigger NPs, lower NP concentrations should be used.

To give an example of the above calculation: A batch of hydrophobic Au NPs synthesized according to Section 1.2 have a core diameter of d_c = 4.2 nm, and a ligand length of dodecanethiol of l_{ligand} = 1 nm was assumed. The Au NPs were suspended at a concentration of c_{NP} = 1 μM in a volume of V_{NP_sol} = 7.1 mL. For the polymer coating procedure the amount of polymer added per effective NP surface was chosen as $R_{P/Area}$ = 100 nm^{-2}. The polymer was dissolved in a stock solution with monomer concentration c_P = 0.05 M. In this way with the help of eq 1, eq 15, and eq 19 the amount V_{P_sol} of polymer solution, which needs to be added to the NP suspension of volume V_{NP}, can be calculated:

$$d_{eff} = d_c + 2 \times l_{ligand} = 4.2\ \text{nm} + (2 \times 1\ \text{nm}) = 6.2\ \text{nm}$$

$$A_{eff} = \pi \times {d_{eff}}^2 = \pi \times (6.2\ \text{nm})^2 = 121\ \text{nm}^2$$

$$V_{P\_sol} = (R_{P/Area} \times A_{eff} \times c_{NP} \times V_{NP\_sol})/c_P = (100\ \text{nm}^{-2} \times 121\ \text{nm}^2 \times 1\ \mu\text{M} \times 7.1 \times \text{mL})/0.05\ \text{M} = 1.7\ \text{nm}$$

DOI: 10.1021/acs.chemmater.6b04738
Chem. Mater. 2017, 29, 399−461

Table 5. List of Parameters Used To Overcoat Various NPs with PMA-*g*-dodecyl Polymer[a]

NP material	shape	d_c [nm]	L_c [nm]	l_{ligand} [nm]	synthesis described in section	$R_{chain/mon}$	$R_{P/Area}$ [nm^{-2}]	ref
Au	sphere	4.2	-	1.0	1.2	75%	100	10
Au	sphere	25	-	1.0	2.2, 4.2	75%	3000	57
Au	sphere	50	-	1.0	2.2, 4.2	75%	3000	57
Au	sphere	50	-	1.0	2.2, 4.2	75%	3000	57
Au	sphere	100	-	1.0	2.2, 4.2	75%	4000	-
Au	rod	15	40	1.0	2.4, 4.3	75%	3000	-
Au	rod	15	63	1.0	2.4, 4.3	75%	3000	57
Au	rod	30	100	1.0	2.4, 4.3	75%	3000	-
Au	rod	12	83	1.0	2.4, 4.3	75%	3000	57
Ag	sphere	4.2		1.0	1.3	75%	100	62
FePt	sphere	4	-	1.0	1.4	75%	100	67
Fe_3O_4	sphere	4	-	1.0	1.5	75%	100	-
CdSe/ZnS	sphere	2−10		1.2	1.7	75%	100	64, 68

[a]In some of the examples[57] the original NPs were not capped with hydrophobic ligands and thus were capped with DDT previous to the polymer coating procedure.

A list of polymer coating conditions for a variety of NP materials is given in Table 5. Parameters for NPs coated with functionalized polymers are listed in Table 6 and Table 7.

7. PURIFICATION OF HYDROPHILIC NPs

7.1. General Considerations. Generally, NPs should be purified from excess of free reactants, byproducts, and ligand molecules in the solution. The selection of a purification technique for a NP solution depends on many variables such as colloidal stability of NPs during purification, efficiency of the purification process, the desired purity level, size and nature of molecules/ligands to be removed, and availability of the respective purification techniques. Unfortunately, there is no universal purification tool for any generic NP solution, but indeed proper purification techniques should be carefully selected for each reaction, to ensure efficient separation between NPs (products) and free excess reactants (impurities). Purification, on the other hand, also may change the properties of the NPs, e.g., modify their ligand shell.[18]

As an xample, the polymer coating procedure in Section 6.3 employs excess polymer in the reaction, which must be removed afterward (post-synthesis purification). It is worth mentioning that avoiding excess addition of polymer may result in incomplete coating and thus induce NP aggregation. The free residual polymer in aqueous solution forms polymeric micelles, with a hydrophobic cavity and a hydrophilic surface, cf. Figure 51.[100] They are stable assemblies of several polymer molecules, in which the hydrophobic tails point toward the inside of the micelle, and the hydrophilic backbones are exposed to the outside. Thus, they can be thought of as "empty" polymer shells without embedded inorganic NPs. The polymer micelles have the size of a few nanometers, and thus it is hard to be separated from NPs with similar size using size exclusion chromatography. However, efficient separation could be achieved by other separation methods such as gel electrophoresis and ultracentrifugation (cf. Section 7.5).

Purification is paramount for many applications. In case of cytotoxicity studies it is required to ensure that any effect is related to the NPs and not to residuals in solution. Also, for quantitative labeling, empty micelles will compete with polymer coated NPs for binding to the same target; however, without any label (i.e., the NP core) inside and, thus, without being detected. Note that polymeric micelles are hard to detect, as the amphiphilic polymer itself does not have any specific absorption of light and also is not fluorescent. In case the polymer has been modified with organic fluorophores, these micelles can be detected by their fluorescence.[100] In addition negative staining of the polymer allows for visualizing empty polymer micelles with transmission electron microscopy, cf. Section 7.5.

7.2. Filtration, Ultrafiltration, and Dialysis. The synthesis of NP synthesis in many occasions is associated with the formation of large aggregates/agglomerates due to NP aggregation, which can be removed from solution by simple filtration via a syringe membrane filter (0.22 μm pore size, Carl Roth, no. KY62.1) as per Figure 52. In case the NP solution does not pass easily through the filter, addition of water to the NP solution, i.e., dilution, may help.

Ultrafiltration can be employed to purify and to concentrate NPs. Ultrafiltration also allows for exchange of the suspending media, for example, from buffer to water or vice versa. Briefly, NP suspension is placed in the centrifuge filter (available from various suppliers, e.g., Vivaspin 20 from Sartorius or Amicon Ultra 4 mL Centrifugal Filters), with typically 100 000 Da molecular weight cutoff (MWCO). The pores of the filter are big enough to be passed through by small molecules but retain the NPs. Upon centrifugation the filtrate that contains free ligands/reactants is collected in the outer vial below the filter membrane, and the NP suspension is concentrated in the inner vial. Fresh solvent can be added to the NP concentrate, and the filtration can be repeated for several rounds of clean up as required (Figure 53 and Figure 54). Note that excessive purification/concentration may induce NPs aggregation, which can also block the filter.

Dialysis is a widely used method to purify NP suspensions from free impurities. The method is described in Figure 55. The NP suspension is put in a semipermeable membrane dialysis bag with defined pore size and molecular weight cutoff (MWCO), which then is placed in a beaker filled with a large volume of fresh buffer/solvent. Molecules smaller than the MWCO can penetrate the membrane and diffuse out from the dialysis bag to the bulk solution in the beaker. Dialysis is driven by the concentration gradient between the dialysis bag and the concentration in the beaker. Thus, the process occurs until equilibrium is achieved. At this point, the bath needs to be replaced with fresh solvent. Dialysis is easy to perform and in fact is a "gentle" treatment for the NPs, since no mechanical stress is placed on NPs (the case of centrifugation as an

DOI: 10.1021/acs.chemmater.6b04738
Chem. Mater. 2017, 29, 399−461

Table 6. List of Parameters Used for Overcoating Various NPs with PMA-*g*-dodecyl or Functionalized PMA-*g*-dodecyl Polymers[a]

NP core material	shape	d_c [nm]	L_c [nm]	l_{ligand} [nm]	$R_{chain/mon}$	$R_{cross/mon}$	$R_{func/mon}$	added functionality	$R_{P/Area}$ [nm^{-2}]	d_h [nm]	ζ [mV]	ref
Au	sphere	2.36 ± 0.48	-	1.0	75%	0	0	-	200	-	-	61
Au	sphere	3.2 ± 0.5	-	-	75%	0	0	-	100−200	13.9	-	66
Au	sphere	3.2 ± 0.5	-	-	100%	0	0	-	100−200	-	-	66
Au	sphere	3.2 ± 0.5	-	-	100%	0	0	-	100−200	-	-	66
Au	sphere	3.2 ± 0.5	-	-	100%	0	0	-	100−200	-	-	66
Au	sphere	3.2 ± 0.5	-	-	100%	0	0	-	100−200	11.4	-	66
Au	sphere	3.8	-	1.2	75%	0	0	-	200	9.0	−45	69
Au	sphere	4.0	-	1.0	100%	7%	0	-	147, 295	-	-	64
Au	sphere	4.0	-	1.0	100%	8%	0	-	310	-	-	64
Au	sphere	4.0	-	1.0	100%	10%	0	-	92, 100	-	-	64
Au	sphere	4.0	-	1.0	100%	10%	0	-	92, 100	-	-	70
Au	sphere	4.0	-	-	100%	10%	0	-	100	-	-	17
Au	sphere	4.0	-	-	100%	10%	0	_	100	-	-	17
Au	sphere	4.0	-	1.0	75%	0	0	-	100	-	-	10
Au	sphere	4.0	-	1.0	75%	0	1%	Fluoresceinamine	100	-	-	10
Au	sphere	4.0	-	1.0	75%	0	4%	Galactose	100	-	-	10
Au	sphere	4.0	-	1.0	75%	0	4%	Biotin	100	-	-	10
Au	sphere	4.0	-	-	75%	0	2%	Amino-MQAE + CV	50−100	9.6 ± 0.6	-	71
Au	sphere	4.0	-	-	75%	0	2%	NH_2-PEG-Amino-MQAE + CV	50−100	10.6 ± 0.6	-	71
Au	sphere	4.0	-	-	75%	0	2%	NH_2-PEG-Amino-MQAE + CV	50−100	11.0 ± 0.6	-	71
Au	sphere	4.0	-	-	75%	0	2%	NH_2-PEG-Amino-MQAE + CV	50−100	13.2 ± 0.6	-	71
Au	sphere	4.0	-	-	75%	0	-	NH_2-PEG-NH-SNARF	100	-	-	72
Au	sphere	4.0	-	1.0	75%	0	4%	Cresyl violet	100	-	-	73
Au	sphere	4.0	-	1.2	75%	0	0	-	100	13.2	-	74
Au	sphere	4.0	-	1.2	75%	0	0	-	100	24.6	-	74
Au	sphere	4.0	-	1.6	75%	0	0	-	100	13.9 ± 1.2	−27.6 ± 5.6	75
Au	sphere	4.0	-	-	75%	0	0	-	100	26.8	−61.1	76
^{198}Au (neutron irradiated)	sphere	4.2 ± 0.5	-	1.1	75%	0	2%	ATTO590	100	-	-	65
^{198}Au (neutron irradiated)	sphere	4.2 ± 0.5	-	1.1	75%	0	3%	ABz-DOTA + Gd^{3+}	100	-	-	65
^{198}Au (neutron irradiated)	sphere	4.2 ± 0.5	-	1.1	75%	0	3%	ABz-DOTA + $^{111}In^{3+}$	100	-	-	65
Au	sphere	4.4 ± 0.6	-	-	75%	0	0	-	100	-	-	77
Au	sphere	4.4 ± 1.1	-	1.2	75%	0	1%	Dy647	200	11.7	−38	78
Au	sphere	4.4 ± 0.6	-	1.2	75%	0	2%	ATTO633 Crystal Violet	100	-	-	79
Au	sphere	4.6	-	3.25	100%	10%	0	-	100	11.7	-	80
Au	sphere	4.6	-	6.9	100%	10%	0	-	100	-	-	80
Au	sphere	4.6	-	9.95	100%	10%	0	-	100	-	-	80
Au	sphere	4.6	-	12.65	100%	10%	0	-	100	-	-	80
Au	sphere	4.6	-	8.5	100%	10%	0	-	100	-	-	80
Au	sphere	4.6	-	12.35	100%	10%	0	-	100	-	-	80
Au	sphere	4.6	-	11.55	100%	10%	0	-	100	-	-	80
Au	sphere	4.6	-	17.8	100%	10%	0	-	100	-	-	80
Au	sphere	4.6	-	3.95	100%	10%	0	-	100	13.5	-	80

DOI: 10.1021/acs.chemmater.6b04738
Chem. Mater. 2017, 29, 399−461

Table 6. continued

NP core material	shape	d_c [nm]	L_c [nm]	l_{ligand} [nm]	$R_{chain/mon}$	$R_{cross/mon}$	$R_{func/mon}$	added functionality	$R_{P/Area}$ [nm^{-2}]	d_h [nm]	ζ [mV]	ref
Au	sphere	4.6	-	5.95	100%	10%	0	-	100	15.6	-	80
Au	sphere	4.6	-	8.2	100%	10%	0	-	100	17.9	-	80
Au	sphere	4.6	-	12.1	100%	10%	0	-	100	18.5	-	80
Au	sphere	4.6	-	15.1	100%	10%	0	-	100	18.6	-	80
Au	sphere	4.6	-	2.2	100%	10%	-	-	100	-	-	81
Au	sphere	4.6	-	1.0	75%	0	-	-	100	-	-	82
Au	sphere	4.6 ± 1.1	-	1.6	75%	0	-	-	50	12.6 ± 1.1	−31.9 ± 5.2	83
Au	sphere	4.6 ± 1.0	-	1.0	75%	0	-	-	100	19 ± 1	−(55 ± 6)	84
Au	sphere	4.6 ± 1.0	-	1.0	75%	0	2%	Cresyl violet + PEG	100	40 ± 5	−(10 ± 5)	84
Au	sphere	4.6 ± 1.0	-	1.0	75%	0	2%	Cresyl violet + PEG-CPP1	100	60 ± 7	−(11 ± 5)	84
Au	sphere	4.6 ± 1.0	-	1.0	75%	0	2%	Cresyl violet + PEG-CPP2	100	35 ± 5	−(13 ± 4)	84
Au	sphere	4.7 ± 0.8	-	-	75%	0	0	-	-	-	-	85
Au	sphere	4.8 ± 0.7	-	1.2	75%	0	2%	ATTO590	50	-	-	86
Au	sphere	4.8 ± 0.9	-	1.2	75%	0	3%	ABz-DOTA	100	13.0 ± 0.8	−46 ± 16	87
Au	sphere	5	-	-	100%	0	0	-	-	21 ± 3	−(19.1 ± 0.4)	54
Au	sphere	5	-	-	100%	0	0	-	-	31.0 ± 0.2	−(10.1 ± 0.6)	54
Au	sphere	5	-	1	75%	0	0	-	100	24.2 ± 2.6	−42.7 ± 2.3	88
Au	sphere	6.0	-	-	75%	0	0	-	100	-	-	10
Au	sphere	6.89 ± 1.25	-	1.0	75%	0	0	-	600	-	-	61
Au	rod	11 ± 2	77.3 ± 12.8	-	75%	0	0	-	3000	29.6 ± 0.5	−(33.5 ± 0.3)	57
Au	sphere	12.6	-	1.2	75%	0	1%	ATTO-590	400	20.9 ± 1.2	-	89
Au	sphere	24 ± 3	-	-	75%	0	0	-	3000	27.0 ± 0.2	−(25.7 ± 0.5)	57
Au	rod	24 ± 5	92.3 ± 14.8	-	75%	0	0	-	3000	9.0 ± 0.2	−(29.2 ± 0.4)	57
Au	sphere	50 ± 7	-	-	75%	0	0	-	3000	43 ± 1	−(34 ± 2)	57
Au	sphere	60 ± 8	-	-	75%	0	0	-	3000	47 ± 1	−(28.4 ± 0.3)	57
Au	star	-	-	-	75%	0	2%	Tamra	150	-	-	90
Ag	sphere	3.8	-	1.2	75%	0	0	-	200	8.9	−35	69
Ag	sphere	4.2 ± 0.4	-	1.0	75%	0	0	-	100	12 ± 3	−(31 ± 1)	62
Ag	sphere	4.2 ± 0.4	-	1.0	75%	0	0	-	100	13 ± 4	−(41 ± 1)	62
Ag	sphere	4.2 ± 0.4	-	1.0	75%	0	0	-	100	12 ± 3	−(10.9 ± 0.4)	62
Ag	sphere	4.2	-	-	75%	0	0	-	-	12 ± 2.7	−31 ± 1.3	91
CdSe	sphere	2.6	-	1.2	75%	0	0.1−5%	ATTO590	50	-	-	92
CdSe	sphere	4.7	-	-	100%	10%	0	-	100	-	-	80
CdSe (Q dot 705 ITK)	sphere	9.4 ± 0.7	-	-	75%	0	4%	EuC + PEG-Cy5-biotin	130	-	-	93
CdSe (Q dot 655 ITK)	sphere	9.6 ± 0.6	-	-	75%	0	4%	EuC + PEG-Cy5-biotin	125	-	-	93
CdSe/ZnS	sphere	-	-	-	100%	10%	0	-	-	5.5 ± 1.3	-	94
CdSe/ZnS	sphere	-	-	-	100%	10%	0	-	-	10.8 ± 1.4	-	94
CdSe/ZnS (Evindent QD490)	sphere		-	-	100%	0	0	-	100−200	16.9	-	66
CdSe/ZnS (Evident QD610)	sphere		-	-	100%	0	0	-	100−200	23.6	-	66
CdSe/ZnS	sphere		-	-	75%	0	0	-	-	-	-	85
CdSe/ZnS	sphere		-	-	75%	0	0	-	-	-	-	85
CdSe/ZnS	sphere	2.1	-	1.2	75%	0	2%	ATTO590	100	-	-	86
CdSe/ZnS	sphere	2.35	-	1.7	75%	0	0	-	100	-	-	10

DOI: 10.1021/acs.chemmater.6b04738
Chem. Mater. 2017, 29, 399−461

Table 6. continued

NP core material	shape	d_c [nm]	L_c [nm]	l_{ligand} [nm]	$R_{chain/mon}$	$R_{cross/mon}$	$R_{func/mon}$	added functionality	$R_{P/Area}$ [nm^{-2}]	d_h [nm]	ζ [mV]	ref
CdSe/ZnS	sphere	2.56	-	-	75%	0	2%	ATTO590	100	-	-	65
CdSe/ZnS	sphere	2.56	-	-	75%	0	3%	ABz-DOTA + Gd^{3+}	100	-	-	65
CdSe/ZnS	sphere	2.56	-	-	75%	0	3%	ABz-DOTA + $^{111}In^{3+}$	100	-	-	65
CdSe/ZnS	sphere	2.7 ± 0.4	-	1.2	75%	0	2 to 0.06%	ATTO5950	100	-	-	68
CdSe/ZnS	sphere	2.8	-	1.1	75%	0	0.1−5%	ATTO590	50	-	-	92
CdSe/ZnS	sphere	2.9 ± 0.3	-	1	75%	0	0	-	500	16.5 ± 0.3	−18.1 ± 0.4	95
CdSe/ZnS (Evidot 490)	sphere	3.2	-	-	75%	0	0	-		10	-	96
CdSe/ZnS (Evidot 520)	sphere	3.3	-	-	75%	0	0	-	-	12	-	96
CdSe/ZnS (Evidot 540)	sphere	3.4	-	-	75%	0	0	-	-	12.4	-	96
CdSe/ZnS	sphere	4.2	-	1.0	100%	10%	0	-	-	-	-	97
CdSe/ZnS	sphere	4.4	-	1.0	100%	10%	0	-	-	-	-	97
CdSe/ZnS (Evidot 580)	sphere	4.4	-	-	75%	0	0	-	-	13.4	-	96
CdSe/ZnS	sphere	4.6 ± 0.9	-	1.2	75%	0	0	-	100	11.9 ± 5.6	−29.0 ± 5.6	98
CdSe	sphere	4.7	-	-	100%	10%	0	-	100	-	-	80
CdSe/ZnS	sphere	4.7 ± 0.9	-	-	75%	0	0	-	100	11.4 ± 3.2	18.3 ± 1.4	99
CdSe/ZnS	sphere	4.7 ± 1	-	1.1	75%	0	2%	Dy495	70	-	−28 ± 4	87
CdSe/ZnS	sphere	4.7 ± 1	-	1.1	75%	0	2%	Dy636	70	-	−33 ± 3	87
CdSe/ZnS	sphere	5.3	-	7.6	100%	10%	0	-	100	13.3	-	80
CdSe/ZnS	sphere	5.3	-	8.75	100%	10%	0	-	100	-	-	80
CdSe/ZnS	sphere	5.3	-	9.55	100%	10%	0	-	100	-	-	80
CdSe/ZnS	sphere	5.3	-	10.3	100%	10%	0	-	100	-	-	80
CdSe/ZnS	sphere	5.3	-	13.75	100%	10%	0	-	100	-	-	80
CdSe/ZnS	sphere	5.3	-	10.25	100%	10%	0	-	100	-	-	80
CdSe/ZnS	sphere	5.3	-	10.65	100%	10%	0	-	100	-	-	80
CdSe/ZnS	sphere	5.3	-	10.5	100%	10%	0	-	100	-	-	80
CdSe/ZnS	sphere	5.3	-	11.95	100%	10%	0	-	100	-	-	80
CdSe/ZnS	sphere	5.3	-	10.05	100%	10%	0	-	100	16.8	-	80
CdSe/ZnS	sphere	5.3	-	10.15	100%	10%	0	-	100	17.7	-	80
CdSe/ZnS	sphere	5.3	-	11.15	100%	10%	0	-	100	18	-	80
CdSe/ZnS	sphere	5.3	-	12.45	100%	10%	0	-	100	18.2	-	80
CdSe/ZnS	sphere	5.3	-	14.45	100%	10%	0	-	100	18.4	-	80
CdSe/ZnS	sphere	5.3	-	-	75%	5%	1%	ATTO590	70	-	-	100
CdSe/ZnS	sphere	5.3	-	-	75%	5%	0	-	70	-	-	100
CdSe/ZnS	sphere	5.3	-	-	75%	0	5%	ATTO590	70	-	-	73
CdSe/ZnS	sphere	5.6	-	1.0	100%	10%	0	-	-	-	-	97
CdSe/ZnS	sphere	6.2 ± 0.3	-	1	75%	0	0	-	500	21.7 ± 0.4	−20.4 ± 1.4	95
CdSe/ZnS	sphere	6.4	-	1.0	100%	10%	0	-	-	-	-	97
CdSe/ZnS	sphere	7.0	-	1.0	100%	6%	0	-	10, 15	19 ± 2	-	64
									20, 60	24 ± 2		
CdSe/ZnS	sphere	7.0	-	1.0	100%	10%	0	-	100	19 ± 2	-	64
										24 ± 2		
CdSe/ZnS	sphere	7.0	-	1.0	100%	10%	0	-	100	19 ± 2	-	70
										24 ± 2		

DOI: 10.1021/acs.chemmater.6b04738
Chem. Mater. 2017, 29, 399−461

Table 6. continued

NP core material	shape	d_c [nm]	L_c [nm]	l_{ligand} [nm]	$R_{chain/mon}$	$R_{cross/mon}$	$R_{func/mon}$	added functionality	$R_{P/Area}$ [nm^{-2}]	d_h [nm]	ζ [mV]	ref
CdSe/ZnS	sphere	7.0	-	-	100%	10%	0	-	100	-	-	17
CdS/Mn:ZnS/ZnS	sphere	4.4 ± 0.7	-	1.2	75%	0	2%	ATTO633	150	-	-	101
CdS/ZnS/ZnS	sphere	4.5 ± 0.8	-	1.2	75%	0	2%	ATTO633	150	-	-	101
CdTe	sphere	6.3	-	2.8	100%	10%	0	-		-	-	80
Co	rod	5.0 ± 1.1	52.3 ± 7.9	-	75%	0	0	0	5200	-	-	102
$Co_{0.5}Fe_{2.5}O_3$	sphere	15.3 ± 1.6	-	-	75%	0	-	-	300	19.8 ± 2.1	−30.5 ± 0.6	103
$Co_{0.5}Fe_{2.5}O_3/Mn_{0.3}Fe_{2.7}O_3$	sphere	12.9 ± 1.4	-	-	75%	0	-	-	300	19.5 ± 0.4	−31.9 ± 1.4	103
$CoPt_3$	sphere	8.0	-	1.0	100%	10%	0	-	100	-	-	64
Fe_3O_4	sphere	3.8	-	1.2	75%	0	0	-	200	12.3	−54	69
Fe_3O_4	sphere	5.5	-	-	75%	0	0	-	200	9.0	-	104
Fe_3O_4	sphere	8.0	-	-	75%	0	0	-	200	12.0	-	104
Fe_3O_4	sphere	8	-	-	75%	0	0	-	-	145 ± 2	-	105
Fe_3O_4	sphere	8	-	-	75%	0	0	-	-	178 ± 7	-	105
Fe_3O_4	sphere	8.0 ± 1.1	-	1.0	75%	0	0.75%	DY-636	100	6.2 ± 0.2	−(55 ± 3)	67
Fe_2O_3	sphere	9.2	-	1.0	100%	10%	0	-	100, 519	-	-	64
Fe_2O_3	sphere	9.2	-	1.0	100%	13%	0	-	93, 182, 260	-	-	64
Fe_2O_3	sphere	10.8 ± 0.12	-	-	75%	0	0	-	50	22.1 ± 7.1	−38.0 ± 5.6	106
Fe_2O_3	sphere	10.8 ± 0.5	-	1.2	75%	0	2%	ATTO590	50	-	-	65
Fe_2O_3	sphere	10.8 ± 0.5	-	1.2	75%	0	3%	ABz-DOTA + Gd^{3+}	50	-	-	65
Fe_2O_3	sphere	10.8 ± 0.5	-	1.2	75%	0	3%	ABz-DOTA + $^{111}In^{3+}$	50	-	-	65
Fe_2O_3	sphere	10.8 ± 0.12	-	-	100%	0	0	-	100−200	-	-	66
Fe_3O_4	sphere	12.0	-	-	75%	0	0	-	200	15.0	-	104
Fe_2O_3	sphere	13.0	-	1.0	75%	0	0	-	100	-	-	10
FePt	sphere		-	-	75%	0	2%	DY-636	300	-	-	107
FePt	sphere	3.1 ± 0.4	-	1.0	75%	0	0.75%	DY-636	100	4.2 ± 0.2	−(44 ± 3)	67
FePt	sphere	3.1 ± 0.4	-	1.0	75%	0	0.75%	DY-636 + Glucose	100	4.6 ± 0.6	−(25 ± 3)	67
FePt	sphere	3.1 ± 0.4	-	1.0	75%	0	0.75%	DY-636 + PEG (750 Da)	100	4.8 ± 0.5	−(17.8 ± 0.5)	67
FePt	sphere	3.1 ± 0.4	-	1.0	75%	0	0.75%	DY-636 + PEG (5 kDa)	100	6.5 ± 0.7	−(28 ± 1)	67
FePt	sphere	3.1 ± 0.4	-	1.0	75%	0	0.75%	DY-636 + PEG (10 kDa)	100	10.6 ± 0.9	−(14.3 ± 0.4)	67
FePt	sphere	3.1 ± 0.4	-	1.0	75%	0	0.75%	DY-636	100	4.2 ± 0.2	−(44 ± 3)	67
FePt	sphere	3.2 ± 0.4	-	1.1	75%	0	0−2%	ATTO590	200	11.2	-	108
FePt	sphere	3.2 ± 0.4	-	1.2	75%	0	2%	ATTO633 Crystal Violet	100	-	-	79
FePt	sphere	3.5 ± 0.6	-	-	75%	0	0	-	-	9 ± 5	−(66 ± 2)	109
$Mn_{0.3}Fe_{2.7}O_3$	sphere	13.9 ± 1.9	-	-	75%	0	-	-	300	16.8 ± 0.9	−32.4 ± 1.6	103
$Mn_{0.3}Fe_{2.7}O_3/Co_{0.5}Fe_{2.5}O_3$	sphere	13.8 ± 1.3	-	-	75%	0	-	-	300	17.1 ± 0.58	−30.7 ± 1.5	103
$Mn_{0.3}Fe_{2.7}O_3/Co_{0.5}Fe_{2.5}O_3$	sphere	14.3 ± 1.5	-	-	75%	0	-	-	300	17.8 ± 0.9	−31.8 ± 1.3	103
$MnFe_2O_3$	sphere	4.5	-	1.0	100%	10%	0	-	100	-	-	110
$MnFe_2O_3$	sphere	6.0	-	1.0	100%	10%	0	-	100	-	-	110
$MnFe_2O_3$	sphere	7.5	-	1.0	100%	10%	0	-	100	-	-	110
PbS	sphere	3.0 ± 0.4	-	1.2	75%	0	2%	Rhodamine 123 Rhodamine 6G Rhodamine B	100	-	-	79

DOI: 10.1021/acs.chemmater.6b04738
Chem. Mater. 2017, 29, 399−461

Table 6. continued

NP core material	shape	d_c [nm]	L_c [nm]	l_{ligand} [nm]	$R_{chain/mon}$	$R_{cross/mon}$	$R_{func/mon}$	added functionality	$R_{P/Area}$ [nm^{-2}]	d_h [nm]	ζ [mV]	ref
								Oregon Green cadaverine Cresyl Violet Crystal Violet amino-ATTO590 amino-DY636 Nile Red amino-ATTO633				
$NaYF_4$:Yb^{3+}, Er^{3+}	sphere	22.7	-	1.1	75%	0	75%	-	100	34	−53	111
ZnO	sphere	6.9 ± 1.5	-	1.1	75%	0	-	-	100	18 ± 2	−(35 ± 4)	112

[a] $R_{chain/mon}$ describes the percentage of anhydride rings of PMA that has been used for linking hydrophobic side chains (dodecyl chains). Note that in some references a slightly different polymer was used, in which there is one hydrophobic side chain in addition to each anhydride ring, and thus $R_{chain/mon}$ = 100%[17,64,80,94,100,110] and thus $R_{chain/mon}$ + $R_{cross/mon}$ + $R_{func/mon}$ > 100%. $R_{cross/mon}$ describes the percentage of anhydride rings that have been used for addition of a crosslinker.[64] $R_{func/mon}$ describes the percentage of anhydride rings that have been used to add organic functionalities such as fluorophores. The following fluorophores have been integrated into PMA, as given together with their excitation wavelength and the extinction coefficient at their excitation wavelength: (i) ATTO590 (λ_{ext} = 590 nm, ε = 1.2 × 10^5 M^{-1} cm^{-1}), (ii) DY-636 (λ_{ext} = 645 nm, ε = 1.9 × 10^5 M^{-1} cm^{-1}), (ii) SNARF (λ_{ext} = 514 nm, ε = depends on pH), (iv) Amino-MQAE (λ_{ext} = 350 nm, ε = 2.8 × 10^3 M^{-1} cm^{-1}), (v) Cresyl Violet (CV) (λ_{ext} = 590 nm), (vi) Oregon Green (λ_{ext} = 494 nm, ε = 7.02 × 10^4 M^{-1} cm^{-1}), (vii) 3-hydroxyflavone dye (FE) (λ_{ext} = 410 nm), (viii) Fluoresceinamine (λ_{ext} = 515 nm), (ix) Cy5-biotin (λ_{ext} = 649 nm), (x) Rhodamine 123 (λ_{ext} = 505 nm, ε = 8.52 × 10^4 M^{-1} cm^{-1}), (xi) Rhodamine 6G (λ_{ext} = 530 nm, ε = 1.16 × 10^5 M^{-1} cm^{-1}), (xii) Rhodamine B (λ_{ext} = 555 nm, ε = 1.07 × 10^5 M^{-1} cm^{-1}), (xiii) Nile Red (λ_{ext} = 555 nm, ε = 3.8 × 10^4 M^{-1} cm^{-1}), (xiv) Crystal Violet (λ_{ext} = 590 nm, ε = 8.7 × 10^4 M^{-1} cm^{-1}), (xv) ATTO633 (λ_{ext} = 630 nm, ε = 1.3 × 10^5 M^{-1} cm^{-1}), and (xvi) Tamra (λ_{ext} = 544 nm). Hydrodynamic diameter (d_h) and zeta-potential ζ values are provided (cf. Section 10).

DOI: 10.1021/acs.chemmater.6b04738
Chem. Mater. 2017, 29, 399−461

Table 7. List of Amphiphilic Polymers Other than PMA Which Have Been Used for the Overcoating of Hydrophobic NPs[a]

NP core material	d_c [nm]	polymer	M_w(polymer) [g/mol]	$R_{P/Area}$ [nm^{-2}]	d_h [nm]	ζ [mV]	ref
Au	4.0	PEO	600000				113
Au	3.8	PDMAEMA-*stat*-PLMA (11:89)	9950	≥50			114
Au	3.8	PDMAEMA-*stat*-PLMA (19:81)	11000	≥50			114
Au	3.8	PDMAEMA-*stat*-PLMA (20:80)	8650	≥50			114
Au	3.8	PDMAEMA-*stat*-PLMA (38:62)	9500	≥50	22 ± 13	+(28 ± 15)	114
Au	3.8	PDMAEMA-*stat*-PLMA (47:53)	46200	≥50			114
Au	3.8	PDMAEMA-*stat*-PLMA (51:49)	47000	≥50			114
Au	3.8	PDMAEMA-*stat*-PLMA (53:47)	11000	≥50	7 ± 2	+(30 ± 14)	114
Au	3.8	PDMAEMA-*stat*-PLMA (64:36)	12000	≥50			114
Au	3.8	PDMAEMA-*stat*-PLMA (73:27)	6500	≥50			114
Au	3.8	PDMAEMA-*stat*-PLMA (75:25)	46000	≥50			114
Au	3.8	PDMAEMA-*stat*-PLMA (76:24)	7000	≥50	28 ± 21	+(31 ± 6)	114
Au	3.8	PMAPHOS(OMe)$_2$-*stat*-PLMA (21:79)	10500	≥50			114
Au	3.8	PMAPHOS(OMe)$_2$-*stat*-PLMA (25:75)	8000	≥50			114
Au	3.8	PMAPHOS(OMe)$_2$-*stat*-PLMA (35:65)	11800	≥50	13 ± 3	−(25 ± 5)	114
Au	3.8	PMAPHOS(OMe)$_2$-*stat*-PLMA (40:60)	9500	≥50	11 ± 4	−(21 ± 9)	114
Au	3.8	PMA-*g*-D1 (68:32)	6000	≥50	10.6 ± 0.7	−(24 ± 4)	114
CdSe/ZnS	4	PDMAEMA-*stat*-PLMA (38:62)	9500	50			114
CdSe/ZnS	4	PDMAEMA-*stat*-PLMA (53:47)	11000	50			114
CdSe/ZnS	4	PDMAEMA-*stat*-PLMA (76:24)	7000	50			114
CdSe/ZnS	4	PDMAEMA-*stat*-PLMA (35:65)	11800	50			114
CdSe/ZnS	4	PDMAEMA-*stat*-PLMA (40:60)	9500	50			114
CdSe/ZnS	4	PDMAEMA-*stat*-PLMA (68:32)	6000	50			114
Au	4.6 ± 1.1	PMAPHOS-*stat*-PLMA	9000	50	11 ± 3	−(40 ± 10)	115
Au	4.6 ± 1.1	PTMAEMA-*stat*-PLMA	16300	50	13 ± 3	+(10 ± 9)	115
Au	4.6 ± 1.1	PMAPHOS-*stat*-PLMA-*stat*-PDI	9500	50	13 ± 6	−(23 ± 8)	115
Au	4.6 ± 1.1	PTMAEMA-*stat*-PLMA-*stat*-PDI	17800	50	7 ± 2	+(17 ± 1)	115

[a]For the polymer materials the ratio of charged (x) to uncharged (y) monomer units in the polymer is noted as (x:y).

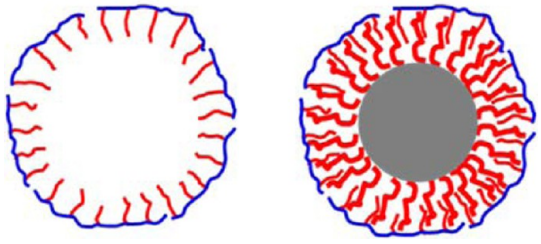

Figure 51. Empty polymer micelles (left) versus polymer-coated Au NPs (right). Due to similar size, separation using size exclusion chromatography is not efficient.

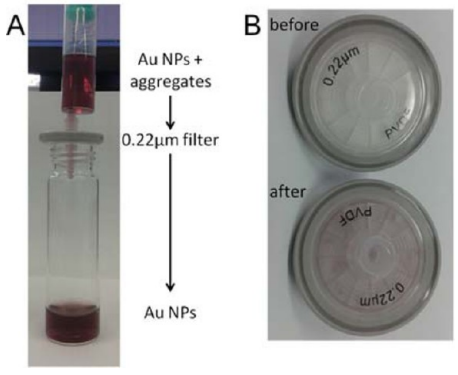

Figure 52. (A) Purification of PMA-*g*-dodecyl capped Au NPs (≈4 nm core diameter, cf. Section 1.2, Section 6.3) from aggregates via filtration using a syringe filter. (B) After filtration the aggregates can be seen in the filter by the naked eye.

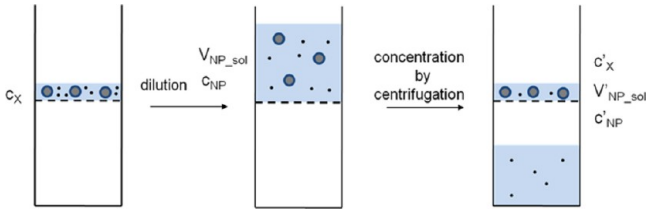

Figure 53. Ultrafiltration of hydrophilic NPs (drawn as gray spheres with blue surface) using a centrifugal filter. The NP suspension contains impurities (small black dots) of concentration c_X. First, the NP suspension is diluted with fresh solvent to a volume (V_{NP_sol}), resulting in NP concentration of c_{NP}. Upon centrifugation only solvent and the small impurities pass through the filter membrane, which results in an increase in NP concentration ($c'_{NP} = c_{NP} \cdot V'_{NP\_sol}/V_{NP\_sol}$) and a decrease in impurities concentration ($c'_X = c_X \cdot V_{NP\_sol}/V'_{NP\_sol}$).

example). However, it is time-consuming and has lower efficiency compared to ultrafiltration. In addition, due to osmotic pressure upon dialysis, the volume of the NP suspension in the dialysis bag may increase, resulting in dilution of the NP suspension.

7.3. Size Exclusion Chromatography. In size exclusion chromatography (SEC), a NP suspension is run through a porous gel matrix driven by gravity or by pressure. The separation mechanism is based on the interaction between the NPs and the pores of the gel: "small" NPs can enter the pores and are thus retained, whereas "large" NPs are excluded from the pores and thus pass the gel faster without interaction. In this way "large" NPs are eluted first, and "small" NPs take longer to diffuse into and out of the pores and thus are eluted later, cf. Figure 56. "Small" and "large" sizes of NPs are relative

DOI: 10.1021/acs.chemmater.6b04738
Chem. Mater. 2017, 29, 399−461

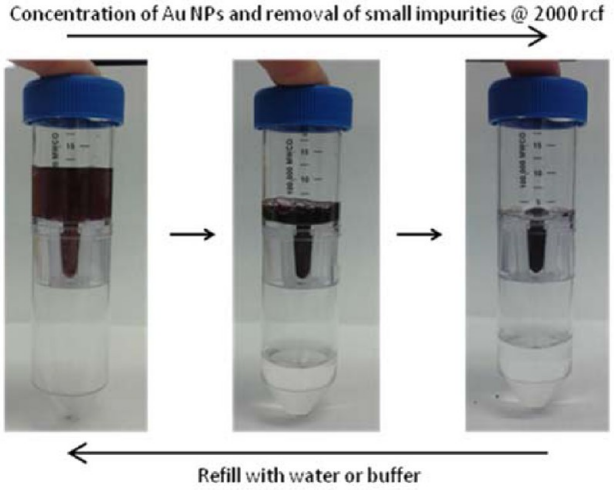

Figure 54. Ultrafiltration using a centrifugal filter to purify and concentrate Au NPs. (PES (Polyethersulfon-membrane centrifugal filter with 100 kDa MWCO, Sartorius Stedim, no. VS2042).

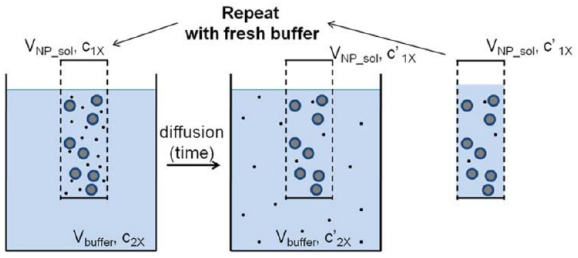

Figure 55. Dialysis of hydrophilic NPs (drawn as gray spheres with blue surface) using dialysis bag of volume V_{NP_sol}. Besides the NPs there are also small impurities of concentration c_{1X} in the NP suspension. The dialysis bag is placed into a bath solution of volume V_{buffer}, in which there are no impurities, i.e., $c_{2X} = 0$. Upon diffusion impurities move from the dialysis bag into the bath. At equilibrium, concentration of impurities in the dialysis bag is reduced to c'_{1X} ($c'_{1X} = c_{1X} \times V_{NP\_sol}/(V_{NP\_sol} + V_{buffer})$).

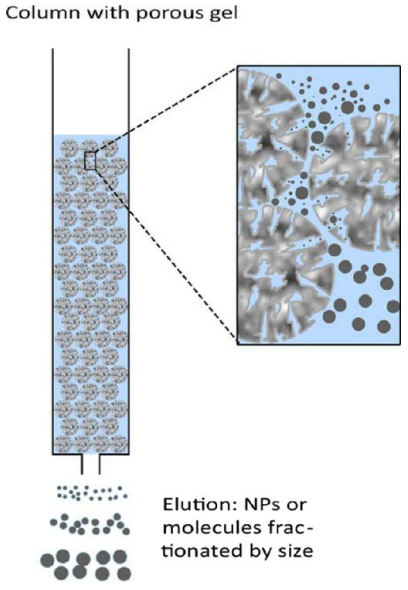

Figure 56. Principle of size exclusion chromatography. Small impurities enter the pores of gel beads and are thus retarded, whereas larger NPs are eluted faster.

to the size of the pores of the gel; i.e., the pore size has to be selected based on the size of the NPs in the sample. The gel beads used to form the gel matrix have to be inert, i.e., the NPs must not react and/or stick to them. SEC is frequently used for desalting, i.e., small ions are retained, whereas the sample, such as proteins, is eluted.[116,117] In this way SEC can be also be used to purify NPs from smaller excess molecules (e.g., salt or capping agent) in solution. For quantitative analysis, SEC columns need to be calibrated to estimate the hydrodynamic diameter d_h of NPs.[80]

The possibility of assembling a SEC column in a high performance liquid chromatography (HPLC) system (cf. Figure 57) allows for an automatic sample injection and

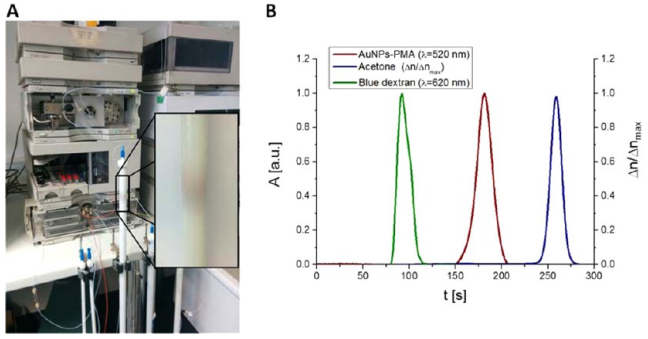

Figure 57. (A) Elution of PMA-*g*-dodecyl-capped Au NPs (≈4 nm core diameter, cf. Section 1.2, Section 6.3) via high performance liquid chromatography (HPLC; Agilent 1100 Series) on a size exclusion chromatography column (75 cm length and 1.5 cm diameter) filled with Sephacryl S400HR as stationary phase and sodium borate buffer pH = 9 as mobile phase. The flow rate was set as 0.5 mL·min^{-1}. The inset shows the red band of eluted Au NPs. (B) Size exclusion chromatograph of PMA-*g*-dodecyl-capped Au NPs (≈4 nm diameter, cf. Section 1.2, Section 6.3) using similar conditions in *A*. The normalized absorption *A* at 520 nm is plotted versus the elution time of the Au NPs (dark red curve). For column calibration, peaks of blue dextran shown as normalized absorption at 620 nm (drawn in green) and acetone shown as normalized changes of the refractive index (blue) are also represented on the chromatogram as reference of the range of the column retention time at these working conditions. In the case of the acetone the changes of the refractive index are measured via an internal reference cell and a sample cell set in the instrument. Both are initially flushed with the mobile phase until the refractive index is the same in both cells, and at this moment the zero value is adjusted. Once the measurement starts, the reference cell stays closed and the column eluate flows through the sample cell. The final signal is expressed as Refractive Index Units (RIU), being the difference Δn between the refractive index in the sample cell and the refractive index in the reference cell.

collection, a customizable constant pressure all over the sample run, and the possibility of multiple programmed detectors. Optimizing parameters related to the stationary phase, the column dimensions, the mobile phase, or the process flow allows fine-tuning of the separation quality. It is important to note that a prefiltering step of NP suspension prior to sample injection is important.

7.4. Gel Electrophoresis. Gel electrophoresis is based on the mobility of charged molecules in a gel matrix under applied electric field. The higher the charge of the molecules, the faster they migrate through the gel.[118] The bigger the molecules, the slower they can pass the pores in the gel and the slower they migrate.[53] In this way, assuming similar surface charge density, "large" NPs run slower in gel than "small" NPs.[52] Separation of

DOI: 10.1021/acs.chemmater.6b04738
Chem. Mater. 2017, 29, 399−461

NPs with various particle sizes can be optimized by adjusting the concentration of the gel and thus the gel mean pore size.[52]

For gel preparation (here 2% (w/v) agarose), 3 g of agarose powder (Invitrogen, no. 15510027, "Agarose UltraPure") was dissolved in 150 mL of 0.5× TBE buffer (44.5 mM Tris-borate and 1 mM ethylenediaminetetraacetic acid (EDTA), pH = 8.3, Sigma-Aldrich, no. T3913) in a 500 mL Erlenmeyer flask. The solution was then covered with a watch−glass and heated in a microwave oven at 380 W for 8 min until the solution started to boil. The flask was swirled to help all agarose powder to dissolve and was then heated again to the boiling point. The hot and clear agarose solution was poured in a 10 × 15 cm gel tray leveled in a gel caster (BioRad). A comb (1, 2, 15, 20, or 30 wells) was placed into the gel, and the whole device was covered with an alumina or polyethylene foil. The gel was allowed to cool down to RT and to solidify, which typically takes 1 h, cf. Figure 58. After solidification the comb was

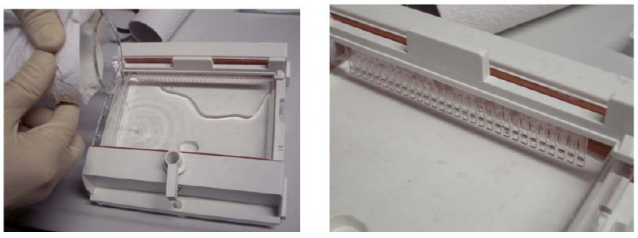

Figure 58. Boiling agarose solution is poured in the gel tray, and a template comb is inserted. The gel then is allowed to cool down and solidify at RT.

removed and the gel was taken out of the casting device and placed into the electrophoresis device (BioRad Subcell GT wide mini), which was filled with 0.5× TBE buffer until the whole gel was covered.

Prior to loading into the wells of the gel, the NPs were first mixed with about 20% by volume with loading buffer (30% glycerol in 0.5× TBE with 0.3% Orange G). Glycerol increases the viscosity so that the NP suspension can be better filled into the wells of the gel. The yellow/orange color of Orange G allows for observing a fast migrating band as control on the gel. The NP suspension was carefully pipetted into the wells of the gel, i.e., into the holes made by the removed template comb, cf. Figure 59A. The wells should not be filled too high, and the NP suspension should not be too concentrated, as otherwise the band upon running electrophoresis may be smeared out. Once the gel had been loaded with NP suspension the electrophoresis devices were connected to a power source (BioRad Power Pac 1000) and run at a constant voltage of typically 100 V, corresponding to a potential gradient of 10 V/cm. The NPs were then run on the 2% agarose gels for 30−100 min under the following conditions: 100 V, 500 mA, 250 W, 0.5× TBE buffer. In case the NPs are charged, they migrate toward the oppositely charged pole, cf. Figure 59B. The speed of migration depends on the charge and hydrodynamic diameter of the NPs. In this way different NP species can be separated as different bands on the gel. The more homogeneous the size and charge distribution of one NP species, the sharper the corresponding NP band is. The longer the running time, the better the separation of the NP bands.

Afterward, the gel was taken out from the tray and a digital picture was taken (BioRad Gel Doc), showing the gel under visible or UV light. In the case the NPs did not migrate

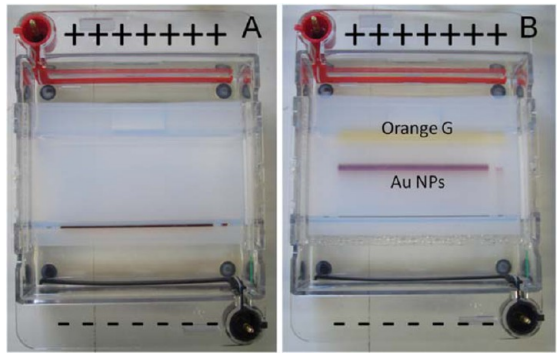

Figure 59. Photographs of an agarose gel filled with anionic Au NPs (≈4 nm diameter, cf. Section 1.2, Section 6.3) (A) before and (B) after electrophoresis. The NP sample is loaded in the well seen on the bottom of the image and can be seen by the red color of the Au NPs as labeled. PMA-coated Au NPs are negatively charged, and thus they migrate toward the positive pole when an electric field is applied, i.e., in the shown image toward the top of the image. Orange G is a small negatively charged molecule and thus migrates faster than Au NPs toward the positive pole. Yellow and red bands in the gel correspond to the Orange G and Au NPs, respectively.

sufficiently, the gel was run for another 30 min and another photograph was taken after the additional running time. For imaging, the gel was placed on a white plastic plate to enhance the contrast and was inserted into the chamber of the imaging device, cf. Figure 60.

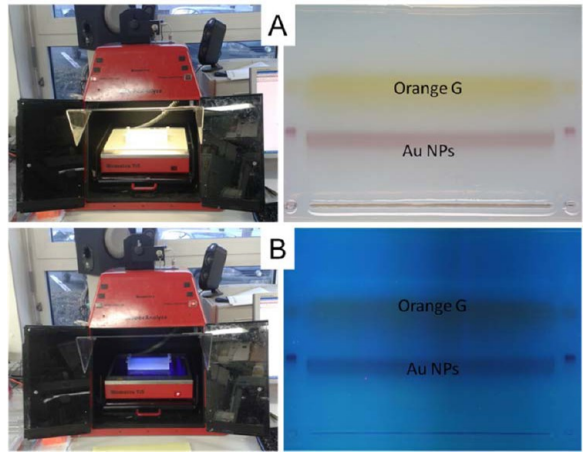

Figure 60. Photographs of the BioRad Gel Doc imaging device, which was used to take pictures of gel containing Orange G and Au NPs bands (in Figure 59), under white light (A) or under UV illumination (B). In both A and B: The gel inside the imaging device is shown on the left and the resulting images on the right. In case of white light illumination the yellow band of Orange G and the red band of Au NPs can be seen. Since Orange G and the Au NPs are nonfluorescent, no fluorescence can be observed under UV illumination.

Gel electrophoresis can be used for purification of NP samples. Free impurities such as surfactants, molecules, or polymer micelles typically migrate faster than NPs. By taking out the NP band from the gel, an NP suspension purified from empty polymer micelles can be obtained. The band of the NPs was cut with a knife and then put into a dialysis bag tube (Spectra/Pro 6 dialysis tubing, 50 kDa MWCO, 34 mm flat width, Spectralabs, no. 132544). The gel-filled bag was then put into the electrophoresis cell filled with fresh 0.5× TBE buffer,

DOI: 10.1021/acs.chemmater.6b04738
Chem. Mater. 2017, 29, 399−461

and voltage (100 V) was applied, typically for 20 min. Due to the applied voltage the NPs migrated out of the gel, but they remained trapped inside the dialysis bags. Once the NPs had been migrated out of the gel pieces and the voltage was switched off, the dialysis bags were taken out of the electrophoresis cell, and the suspension of NPs was pipetted out of the bags, cf. Figure 61. For concentration and buffer exchange of this NP suspension ultrafiltration was applied as reported in Section 7.2.

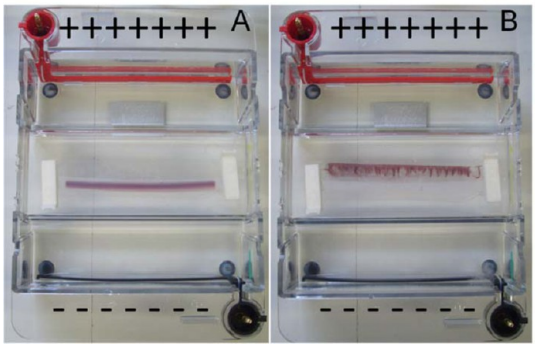

Figure 61. Recovering Au NPs from a gel band. (A) The extracted band contains Au NPs (≈4 nm diameter, cf. Section 1.2, Section 6.3) and was placed inside a dialysis bag, which was placed into the electrophoresis cell. (B) After applying an electric field the Au NPs migrated out of the gel band but remained trapped inside the dialysis bag.

7.5. Ultracentrifugation. A major method for NP purification is centrifugation. NPs with density higher than the density of the solvent may be precipitated by gravity or centrifugal forces, whereas lighter impurities (surfactants, ions, capping agents, polymers, etc.) remain in the supernatant and thus can be removed by supernatant decantation. The NP pellet is then resuspended in fresh medium/solvent, cf. Figure 62. This procedure works well for NPs that are large or dense

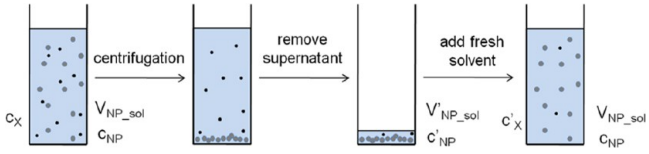

Figure 62. Purification via repeated centrifugation of a suspension of NPs (drawn in gray) of initial volume V_{NP_sol} and a concentration of c_{NP}. Small impurities (drawn in black) with concentration c_X are presented initially in the suspension. Upon centrifugation the NPs form a pellet, whereas the impurities remain in solution. The supernatant with the impurities is removed. Fresh solvent is added to result in a decreased final concentration of impurities $c'_X = c_X \cdot V'_{NP\_sol}/V_{NP\_sol}$.

enough to be precipitated by using a tabletop centrifuge (e.g., Au NPs of $d_c > 15$ nm at 10000 rcf). In the case of smaller NPs, ultracentrifugation with much higher centrifugation speed is needed. The duration and centrifugal forces depend on the NPs' size, shape, and density, as well as on solvent-related parameters such as solvent density/viscosity. Moreover, the colloidal stability of NPs during centrifugation is a very important parameter to be considered when selecting the centrifugation settings. Collectively, optimum centrifugation settings for a specific NP suspension should be evaluated experimentally. For example, PMA-*g*-dodecyl capped Au NPs (≈4 nm core diameter, cf. Section 1.2, Section 6.3) required centrifugation at 85 000 rcf (Thermo Scientifiv ultracentrifuge equipped with a SureSpin 630 rotor in combination with 36 mL PET thin-walled tubes (Thermo Scientific, no. 75000471)) for 3 h. After centrifugation, a red pellet was observed, and the supernatant was discarded. Three centrifugation cycles were found to be necessary to purify PMA-*g*-dodecyl capped Au NPs from empty PMA-*g*-dodecyl micelles (cf. Figure 62). After the third centrifugation step, the Au NPs were suspendet in Milli-Q water and filtered through a hydrophilic syringe filter (0.22 μm, cf. Section 7.2).

Various purification methods may result in different purification efficiencies. For example, we did find that purification of PMA-*g*-dodecyl capped Au NPs using ultracentrifugation is more efficient than the gel electrophoresis method. Interestingly, some empty polymer micelles may remain in solution after electrophoresis, whereas the NP sample was virtually free of empty micelles after three ultracentrifugation cycles, cf. Figure 63.

8. CHARACTERIZATION OF STRUCTURAL PROPERTIES OF THE NPS

8.1. General Comments about the Composition of the NPs. As outlined in Sections 1−6, NPs described in this report are composed of an inorganic core and an organic shell. The total mass of one NP (m_{NP}) involves the mass of the inorganic core (m_c) and the mass of the organic surface coating. As inorganic cores can be conveniently imaged with transmission electron microscopy (TEM, cf. Section 8.3), the mass of one NP core can be obtained. In addition to the NPs' core material density, the NP core volume V_c should be calculated using NP dimensions as obtained from TEM images (core diameter (d_c) in the case of spherical NPs and core diameter (d_c) and length (L_c) in the case of rod-shaped NPs). Note that without additional staining (cf. Section 8.4) the organic shell does not provide contrast in regular TEM, and thus only the inorganic cores are visible. In the case of spheres and rods (assumed to have the shape of a cylinder) the volume of one NP core is

$$V_c(\text{sphere}) = \left(\frac{4\pi}{3}\right) \times \left(\frac{d_c}{2}\right)^3 = \left(\frac{\pi}{6}\right) \times {d_c}^3 \quad (20)$$

$$V_c(\text{rod}) = \pi \times \left(\frac{d_c}{2}\right)^2 \times L_c = \left(\frac{\pi}{4}\right) \times {d_c}^2 \times L_c \quad (21)$$

If the core is built in core/shell geometry (cf. Figure 1), the volume V_{c2} of the shell is

$$V_{c2}(\text{sphere}) = V_{c12}(\text{sphere}) - V_{c1}(\text{sphere}) = \left(\frac{\pi}{6}\right) \times ({d_{c12}}^3 - {d_{c1}}^3) \quad (22)$$

In the case the core is composed out of material of density ρ_c, the mass of one NP core is

$$m_c = \rho_c \times V_c \quad (23)$$

For most inorganic NP materials their densities can be found in the literature. In first order the bulk densities of the materials can be assumed. The molar mass of an NP core thus is

$$M_c = m_c \times N_A \quad (24)$$

DOI: 10.1021/acs.chemmater.6b04738
Chem. Mater. 2017, 29, 399−461

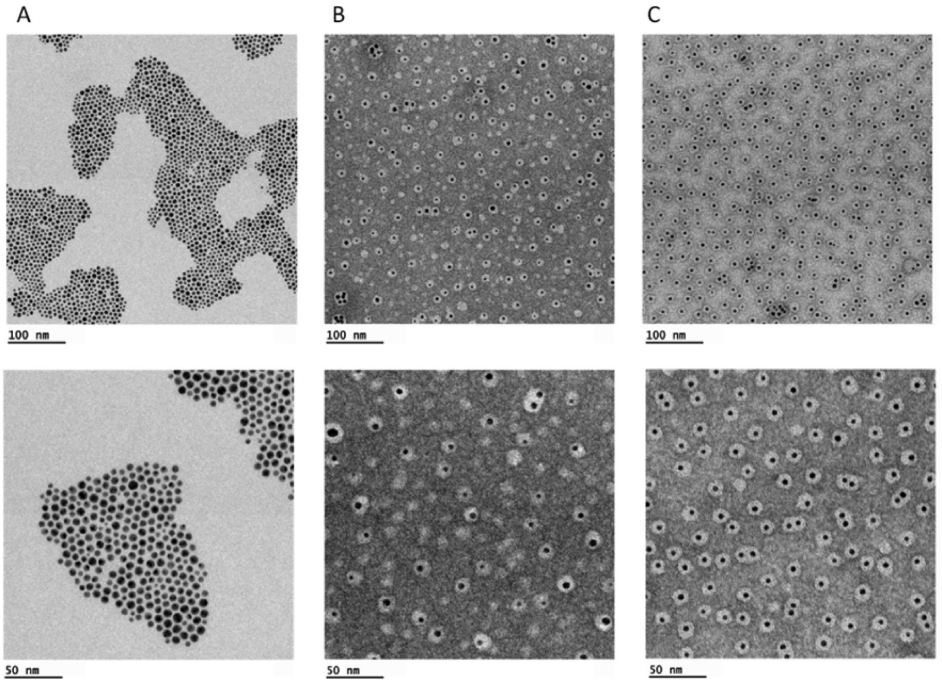

Figure 63. Transmission electron microscopy (TEM) images of PMA-*g*-dodecyl capped Au NPs (≈4 nm core diameter, cf. Section 1.2). (A) TEM images of the DDT-Au NPs (cf. Section 8.3) before coating with PMA-*g*-dodecyl polymer at two magnifications in upper and lower panels. (B) TEM images after negative staining (cf. Section 8.4) of the PMA-*g*-dodecyl capped Au NPs purified by gel electrophoresis (cf. Section 7.4) at two magnifications in upper and lower panels (Note: some empty polymer micelles can be seen (gray spots without black NP inside)). (C) TEM images of the PMA-*g*-dodecyl capped Au NPs purified by ultracentrifugation at 65 000 × *g* three times at two magnifications in upper and lower panels (Note: the sample is virtually free of empty polymer micelles). The scale bars in the top and bottom rows represent 100 and 50 nm, respectively.

In the case the core is composed out of one element X, then each NP core includes $N_{X/NP}$ atoms of X. M_X is the molar mass of element X.

$$N_{X/NP} = \frac{M_c}{M_X} = \rho_c \times V_c \times \frac{N_A}{M_X} \tag{25}$$

To give an example, for a spherical Au NP with core diameter d_c = 4.2 nm, $V_c = (\pi/6) \times (4.2\ \text{nm})^3 \approx 38.8\ \text{nm}^3$. Given the bulk density of Au of $\rho_{Au} = 19.3\ \text{g/cm}^3$, the mass of one Au core thus is $m_c = 19.3\ \text{g/cm}^3 \times 38.8\ \text{nm}^3 \approx 750\ \text{g}\cdot(10^{-9}\ \text{m}/10^{-2}\ \text{m})^3 = 7.5 \times 10^{-19}$ g. The molar mass of a Au core thus is $M_c = m_c \times N_A = 7.5 \times 10^{-19}\ \text{g} \cdot 6.02 \times 10^{23}\ \text{mol}^{-1} \approx 4.5 \times 10^5\ \text{g/mol}$. Given the molar mass of Au M_{Au} = 197 g/mol, one Au core thus comprises approximately $N_{Au/NP} = M_c/M_{Au} = 4.5 \times 10^5\ \text{g}\cdot\text{mol}^{-1}\ /197\ \text{g}\cdot\text{mol}^{-1} \approx 2284 \approx 2300$ Au atoms.

In the case the core is composed out of two elements X and Y with the stoichiometry X_xY_y (i.e., for Fe_3O_4, x = 3 and y = 4), then each NP core includes $N_{X/NP}$ and $N_{Y/NP}$ atoms of X and Y, respectively. M_X and M_Y are the molar masses of the two elements.

$$M_c = N_{X/NP} \times M_X + N_{Y/NP} \times M_Y \tag{26}$$

$$\frac{N_{X/NP}}{N_{Y/NP}} = \frac{x}{y} \tag{27}$$

Thus, $M_c = N_{X/NP} \times M_X + N_{X/NP} \times (y/x) \times M_Y$, leading to

$$N_{X/NP} = \frac{M_c}{M_X + \left(\frac{y}{x}\right) \times M_Y} = \rho_c \times V_c \times \frac{N_A}{M_X + \left(\frac{y}{x}\right) \times M_Y} \tag{28}$$

$$N_{Y/NP} = \frac{M_c}{M_Y + \left(\frac{x}{y}\right) \times M_x} = \rho_c \times V_c \times \frac{N_A}{M_y + \left(\frac{x}{y}\right) \times M_x} \tag{29}$$

To give an example, for a spherical Fe_3O_4 NP with core diameter d_c = 4.2 nm, $V_c = (\pi/6) \times (4.2\ \text{nm})^3 \approx 38.8\ \text{nm}^3$. Given the bulk density of Fe_3O_4 of $\rho_{Fe3O4} = 5\ \text{g/cm}^3$, the mass of one Fe_3O_4 core thus is $m_c = 5\ \text{g/cm}^3 \times 38.8\ \text{nm}^3 = 194\ \text{g} \times (10^{-9}\ \text{m}/10^{-2}\ \text{m})^3 \approx 1.9 \times 10^{-19}$ g. The molar mass of a Fe_3O_4 core thus is $M_c = m_c \times N_A = 1.9 \times 10^{-19}\ \text{g}\cdot 6.02 \times 10^{23}\ \text{mol}^{-1} \approx 1.2 \times 10^5$ g/mol. Given the molar masses of iron M_{Fe} = 55.8 g/mol and of oxygen M_O = 16 g/mol, one Fe_3O_4 core thus comprises approximately $N_{Fe/NP} = M_c/(M_{Fe} + (4/3) \times M_O) = 1.2 \times 10^5\ \text{g}\cdot\text{mol}^{-1}/(55.8\ \text{g}\cdot\text{mol}^{-1} + (4/3) \times 16\ \text{g}\cdot\text{mol}^{-1}) = 1556 \approx 1600$ iron atoms, and $N_{O/NP} = M_c/(M_O + (3/4) \times M_{Fe}) = 1.2 \times 10^5\ \text{g}\cdot\text{mol}^{-1}/(16\ \text{g}\cdot\text{mol}^{-1} + (3/4) \times 55.8\ \text{g}\cdot\text{mol}^{-1}) = 2074 \approx 2100$ oxygen atoms.

8.2. Determination of NP Concentrations by Elemental Analysis. With inductively coupled plasma coupled with either mass spectrometry (ICP-MS) or optical emission spectroscopy (ICP-OES), quantitative elemental analysis can be performed. Dilution and acid digestion are required prior to analysis. For example, in the case of metal NPs, such as Au or

DOI: 10.1021/acs.chemmater.6b04738
Chem. Mater. 2017, 29, 399−461

Ag, 50 μL of the sample was added to 200 μL of aqua regia (i.e., concentrated HCl (35 wt %) and HNO_3 (67 wt %) in 3:1 volume ratio), and then it was left for digestion (oxidation of metallic cores into their corresponding ions) for about 30 min. The digestion step diluted the sample by a dilution factor of 5× prior to further dilution by a factor of 10× with HCl solution (2 wt % HCl) prior to their injection into ICP-MS (total dilution factor of 50×). A high dilution factor in acidic media is required to stabilize metallic ions and to improve the analytical detection limit, as well as to ensure a qualitative and quantitatively equal background signal for all samples. Samples with high levels of acid might harm the ICP-MS machinery.

For calibration, the autotuning solution from Agilent for ICP-MS 7500cs with a standard concentration of 1 μg/L of Ce, Co, Li, Mg, Tl, and Y was used to set the general background, as well as to calibrate the electrical field of the lenses and the magnetic quadrupole field in strength and frequency before the actual run. The oxidation level (less than 0.8%) and double charge rate (less than 1.8%) were also measured using this tuning solution.

All vials and working materials either were cleaned using freshly prepared aqua regia for 2 h followed by boiling in Milli-Q water or consisted of sterile and clean nonreusable consumables. The samples were introduced into the ICP-MS setup through a Perfluoroalkoxy-Alkane (PFA) based micro-flow spray chamber, where the aqueous sample was nebulized, introduced to the argon gas flow, and transported to the torch, where it was ionized in an argon-plasma of around 6000 °C. After ionization the sample was presorted using an omega lens, element-wise separated in the quadrupole field through the mass to charge ratio, again sorted using kinetic barriers and a charged lens system, and finally detected with either an analog or a digital detector depending on the count rate. It is important to mention that the working mode of the instrument and flow of Ar gas also affected the analysis.

Before each run, a proper calibration was needed with an appropriate standard. The ICP-MS setup was calibrated by using an Agilent standard of corresponding ions (all the standards of corresponding ions should be available prior to the measurement). For example, in the case of Au NPs the element to be detected is Au. The Agilent Au standard has 1000 mg/L Au concentration from which eight solutions of concentration 2500, 1000, 500, 250, 100, 50, 25, and 10 parts per billion (1 ppb = 10^{-9} = 1 μg detected Au/1 kg water (density ρ_{H2O} = 1 kg/L), corresponding to a gold concentration C_{Au} = 1 μg/L) were prepared along with a blank using the same low matrix (aqueous 2 wt % HCl) as diluent. The calibration curve was constructed using concentration points of the aforementioned standard solutions. The syringe and tubings were washed thoroughly at the end of each run (for gold, extensive rinsing is needed as it often sticks to the tube). The calibration curve and the sample results were used to calculate the concentration of measured elements in the corresponding samples considering the used dilution factor (Final concentration = dilution factor × measured concentration).

With TEM studies the volume of one NP core V_c (the core that contains the detected element) can be determined, leading to the total number of atoms X per NP ($N_{X/NP}$) (cf. Section 8.3). By knowing the elemental concentration of metallic ions X in a sample c_X, the concentration of NPs in the sample can be determined:

$$c_{NP} = c_X / N_{X/NP} \quad (30)$$

For example, to determine the concentration of Fe_3O_4 NP in a sample (c_{NP}) we need to determine the elemental concentration of iron c_{Fe} in the sample and the number of Fe atoms per NP as per eq 28: $N_{Fe/NP} = \rho_{Fe3O4} \times V_c \times N_A/(M_{Fe} + (4/3) \times M_O) = \rho_{Fe3O4} \times (\pi/6) \times d_c^3 \times V_c \times N_A/(M_{Fe} + (4/3)\cdot M_O)$. The concentration of Fe_3O_4 NP in the sample now can be calculated as follows: $c_{NP} = c_{Fe}/N_{Fe/NP}$.

8.3. Transmission Electron Microscopy of NP Cores. Transmission electron microscopy (TEM) analysis allows a direct measure of the size and shape of NPs. The organic ligand shell typically does not provide sufficient electron contrast, and thus in TEM images only the inorganic part of the NPs can be seen. However, special techniques can be employed to visualize the organic shell around NPs as described in Section 8.4.

All images in this section were obtained using a Philips CM 100 electron microscope operated at an accelerating voltage of 100 kV or on a JEOL JEM-1400PLUS TEM operated at an accelerating voltage of 120 kV. The NPs were deposited from a dilute solution onto a 3−4 nm thick film of amorphous carbon supported on a 400 mesh copper grid (Ted Pella Inc., no. 01822-F). One drop (2 μL) of NP suspension was deposited onto the grid, and the solvent was evaporated at RT. In the case of NPs suspended in water, the grids were kept under ethanol vapor for 1−2 days prior to sample deposition. This treatment made the carbon film more hydrophilic and improved the adsorption of the NPs on it. The microscope magnification was calibrated with a calibration grid (Grating Replica, Waffle, 2160 l/mm, on 3 mm grid, Ted Pella Inc., no. 607).

From TEM images several parameters can be extracted. First, the shape of the NPs can be determined, which is important in the case of nonspherical NPs such as rods, stars, etc. Second, the frequency distribution (histograms) of NP core diameter d_c (and length L_c in case of rod-shaped NPs) can be determined to calculate the NP's dimensions. Figures 64−76 show TEM images of NP samples prepared in this work, along with their size distribution histograms. To determine the size distribution histograms, dimensions of several NPs were measured from their TEM images using ImageJ 1.42 (freely available software from https://imagej.nih.gov/ij/). As a representative sample, at least 100 NPs were analyzed for each size distribution histogram, from which the mean diameter of the NPs (d_c) and its standard deviation (as indicator of polydispersity) could be calculated. Third, the state of agglomeration can be observed

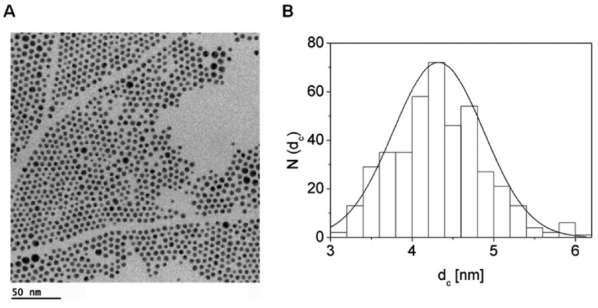

Figure 64. (A) TEM image of hydrophobic DDT-Au NPs (capped with dodecanethiol, ≈4 nm core diameter, cf. Section 1.2) dried on a grid from a chloroform suspension. The scale bar corresponds to 50 nm. (B) Size distribution histogram, plotted as number of NPs $N(d_c)$ that have a core diameter of d_c. From this histogram the mean NP diameter and its standard deviation was determined to be d_c = (4.3 ± 0.4) nm.

DOI: 10.1021/acs.chemmater.6b04738
Chem. Mater. 2017, 29, 399−461

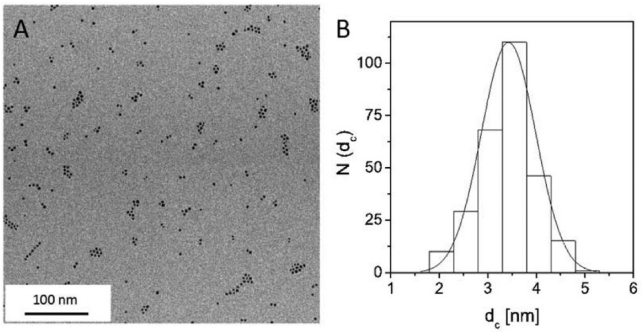

Figure 65. (A) TEM image of hydrophobic FePt NPs (capped with OA and OLA, ≈4 nm core diameter, cf. Section 1.4) dried on a grid from a chloroform suspension. The scale bar corresponds to 100 nm. (B) Size distribution histogram, plotted as number of NPs $N(d_c)$ that have a core diameter of d_c. From this histogram the mean NP diameter and its standard deviation were determined to be $d_c = (3.4 \pm 0.6)$ nm.

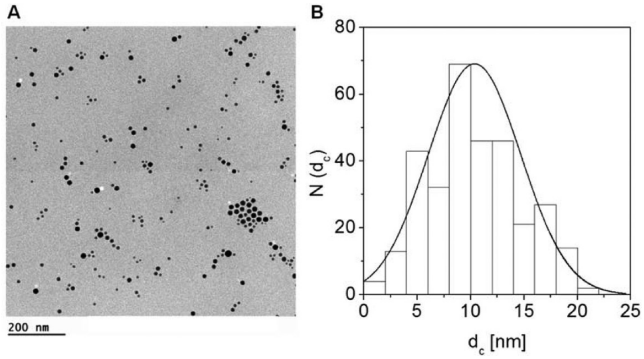

Figure 67. (A) TEM image of hydrophobic Sn NPs (capped with oleic acid, ≈ 11 nm core diameter, cf. Section 1.6) dried on a grid from a chloroform suspension. The scale bar corresponds to 200 nm. (B) Size distribution histogram, plotted as number of NPs $N(d_c)$ that have a core diameter of d_c. From this histogram the mean NP diameter and its standard deviation were determined to be $d_c = (10 \pm 4)$ nm.

(note that TEM works with dried samples, and thus even NPs, which are individually dispersed in solution, may cluster on the TEM grids due to drying-induced assembly). Drying-induced clustering on the TEM grids can be reduced by depositing diluted NP suspensions on the TEM grids, using treated grids (cationic or anionic surfaces), or optimizing the rate of drying. In contrast, when TEM grids are prepared with higher concentration of NPs, the NPs can self-assemble into 2-dimensional lattices, cf. Figure 64. Fourth, from TEM images with self-assembled NPs the thickness of the organic coating/shell around the inorganic NP cores can be estimated as half the minimum distance between the two adjacent inorganic NP cores.[80,85,119] However, for TEM imaging the NPs have to be deposited on a substrate, and the solution in which the NPs are dispersed must be evaporated. The thickness of the organic layer is likely to be reduced due to the drying-induced shrinkage. For example, organic hydrophobic tails of two adjacent NPs can intercalate, and polymeric shells on NPs can shrink upon desolvation. For these reasons, the measured thickness of the organic coating around the NP cores as determined from TEM is likely to be underestimated, and therefore, the values obtained in this way have to be interpreted as lower limits.

8.4. Transmission Electron Microscopy of NPs Including Their Organic Shell. As shown in the previous sections, TEM imaging is used to determine the size (d_c) and shape (rods, spheres, stars, etc.) of NP cores composed of various materials such as Au, Ag, Fe_3O_4, FePt, etc. The inorganic cores of the NPs appear almost black due to the strong electron-scattering character of these materials. However, as it has been previously discussed, these NPs are modified with different organic ligands, which increase the effective diameter of the NPs (e.g., d_{eff}). Such organic shells have low electron scattering character and thus do not show sufficient contrast to be visible in regular TEM images. In order to investigate the thickness of these organic coatings (e.g., l_{ligand}), negative staining is needed. Heavily electron-scattering compounds (e.g., uranyl acetate, ammonium molibdate, or osmium tetroxide) may be used to stain the background of TEM grids and indirectly allow the visualization of the organic shell around NPs.[120] Ideally, negative staining contrast agents form a homogeneous dark background, and thus the organic shells around NPs appear as bright corona (i.e., negative staining) around the dark inorganic cores (cf. Figure 77)

The technique can be visualized as to balance the competition between the sample and the staining agent to reach the grid surface. Therefore, for a successful negative staining it may be important to take into account several sample parameters such as, for example, the overall particle charge or its diffusion rate together of the chosen stain. This translates into the need of different approaches to achieve homogeneous negative contrast for different samples. For PEGylated Au NPs (cf. Section 2.2 and Section 3.3), as shown in Figure 77, a sample preparation protocol reported by Harris[120] was

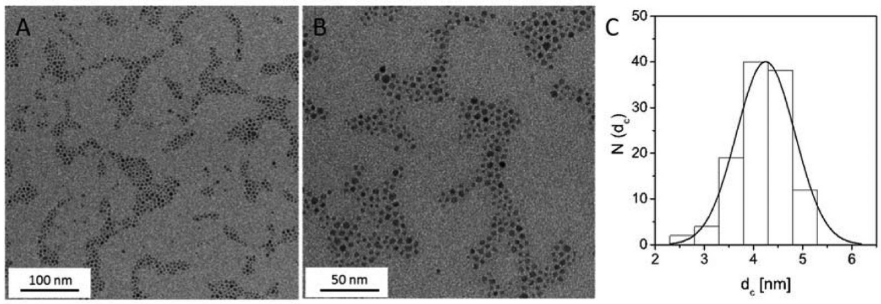

Figure 66. TEM image of hydrophobic Fe_3O_4 NPs (capped with OA and OLA, ≈4 nm core diameter, cf. Section 1.5) dried on a grid from a chloroform suspension. (A) The scale bar corresponds to 100 nm, and (B) the scale bar corresponds to 50 nm. (C) Size distribution histogram, plotted as number of NPs $N(d_c)$ that have a core diameter of d_c. From this histogram the mean NP diameter and its standard deviation were determined to be $d_c = (4.2 \pm 0.6)$ nm.

DOI: 10.1021/acs.chemmater.6b04738
Chem. Mater. 2017, 29, 399−461

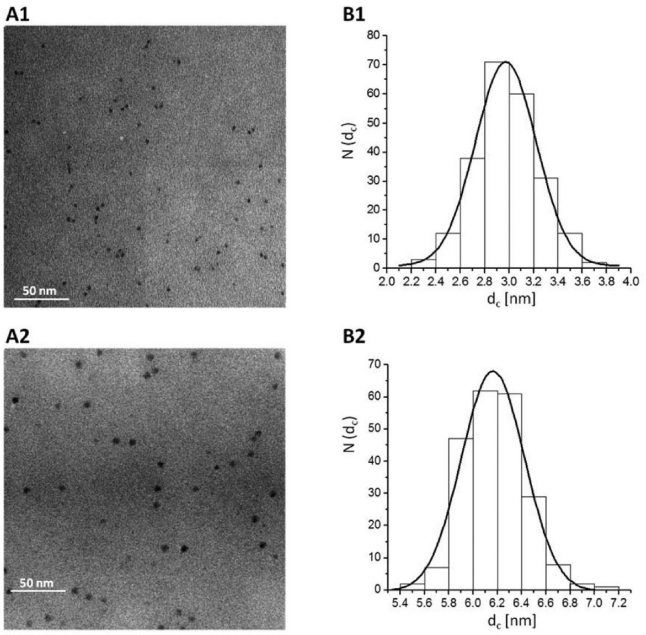

Figure 68. (A) TEM image of hydrophobic CdSe/ZnS NPs (capped with TOPO, ≈4 nm core diameter, cf. Section 1.7) dried on a grid from a chloroform suspension. The scale bar corresponds to 50 nm. (B) Size distribution histogram, plotted as number of NPs $N(d_c)$ that have a core diameter of d_c. A1 and B1 correspond to CdSe/ZnS NPs of ≈3 nm in diameter. From the histogram in B1, the mean NP diameter and its standard deviation were determined to be $d_c = (3.0 \pm 0.2)$ nm. A2 and B2 correspond to CdSe/ZnS NPs of ≈6 nm in diameter. From the histogram in B2, the mean NP diameter and its standard deviation were determined to be $d_c = (6.2 \pm 0.3)$ nm.

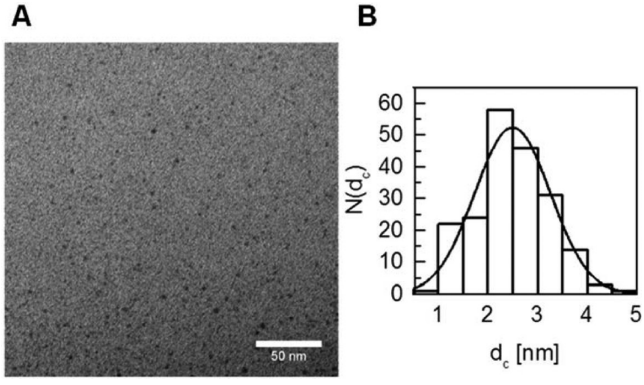

Figure 69. (A) TEM image of hydrophobic CdS NPs (capped with oleic acid and to some extent with octadecane, ≈2 nm core diameter, cf. Section 1.8) dried on a grid from a chloroform suspension. The scale bar corresponds to 50 nm. (B) Size distribution histogram, plotted as number of NPs $N(d_c)$ that have a core diameter of d_c. From this histogram the mean NP diameter and its standard deviation were determined to be $d_c = (2.5 \pm 0.8)$ nm. Note that for NPs of such a very small size, the size measurement as determined by TEM has to be interpreted with care, as NPs with ultrasmall size may not provide sufficient contrast and thus are not counted.

optimized as follows:[56] Samples were prepared on carbon film 400 copper mesh grids purchased from Electron Microscopy Sciences (Hatfield, U.S.A.). To enhance the hydrophilicity of grids and to impart them with negative charge, the specimen grids were exposed to glow-discharge treatment under air plasma for 20 s (2.0×10^{-1} atm and 30 mA), using a MED 020 modular high vacuum coating system (BAL-TEC AG, Balzers, Fürstentum Liechtenstein). Negatively charged carbon grids were used within 5 min after treatment to ensure hydrophilicity. 0.35 μL sample droplet of NP solution with NP concentration ranging from 10 nM (for Au cores of 14 nm diameter) to 1.5 nM (for Au cores of 30 nm diameter) of PEGylated Au NPs was placed on the grid, allowed to incubate for 20 s to 1 min (the smaller the particle size, the lower the incubation time) followed by 0.35 μL droplet of 0.25% weight/volume (w/v) uranyl acetate aqueous solution. The grid was air-dried overnight before actual TEM imaging.

8.5. X-ray Diffraction. With X-ray diffraction (XRD) the diameter d_{crys} of the crystalline part of the NP core can be determined. For this, a diffractogram has to be recorded. Briefly, and in most of the cases, a NP powder solid sample is irradiated with monochromatic X-ray radiation, and the diffraction (i.e., the change of the direction of the elastically scattered radiation) is recorded. For a crystalline material, diffraction occurs only for several angles, named Bragg's angles (Θ). Such angles are associated with crystallographic planes, which depend on the unit cell parameter of the analyzed material. In a typical XRD experiment, the intensity (i.e., number of counts in the detector for a determined Θ) is plotted versus the double of the diffraction angle (2Θ). The number and position of peaks in a powder diffractogram can be used for phase identification, since every individual crystalline compound has its own "fingerprint", which is determined by its crystallographic structure. The intensity of the peaks (i.e., the number of counts in the detector for a determined 2Θ) is related to the atomic positions in the crystalline unit cell, and the width of every peak is connected with the crystallite size and microstrain in the corresponding crystallographic direction.

The crystallite size for a crystalline direction, determined by a crystallographic plane and a Bragg's angle (Θ), can be estimated with the Scherrer equation:

$$d_{crys} = \frac{K\lambda}{\beta \cos \Theta} \tag{31}$$

where d_{crys} is the crystallite size. K is the shape factor or Scherrer constant, which varies in the range $0.89 < K < 1$, and usually $K = 0.9$. λ is the wavelength of the X-ray (for Cu Kα = 0.15418 nm). β is the line broadening at half the maximum intensity (fwhm). Θ is the Bragg's angle of the analyzed peak.

For single crystal NPs, the crystallite size d_{crys} estimated by the Scherrer equation is expected to be very similar to the geometric particle size d_c as determined by other characterization techniques such as TEM.[122] In the case of polycrystalline NPs, the obtained crystalline sizes are much smaller than the actual NP size.

Here, X-ray diffraction (XRD) studies were carried out using a Panalytical X'Pert Pro diffractometer equipped with an X-Celerator detector. The NPs were deposited on a silicon sample holder. In this instrument a Θ:Θ Bragg–Brentano geometry is used, in which the sample is fixed, the tube rotates at a rate Θ°/min, and the detector rotates at the same rate of Θ°/min. In Figure 78 data obtained with dodecanethiol-capped Au NPs (≈4 nm core diameter, cf. Section 1.2) overcoated with PMA (cf. Section 6.3) are shown. The XRD pattern indicates that the analyzed NPs consisted of *fcc* Au crystals (PDF card number: 00-004-0784).

The peak corresponding to the (111) plane (2Θ around 38.5°) was used to determine the crystallite size. It should be taken into account that Θ values (and not 2Θ) should be used, as well as radian units (and not degrees), especially for the β

DOI: 10.1021/acs.chemmater.6b04738
Chem. Mater. 2017, 29, 399−461

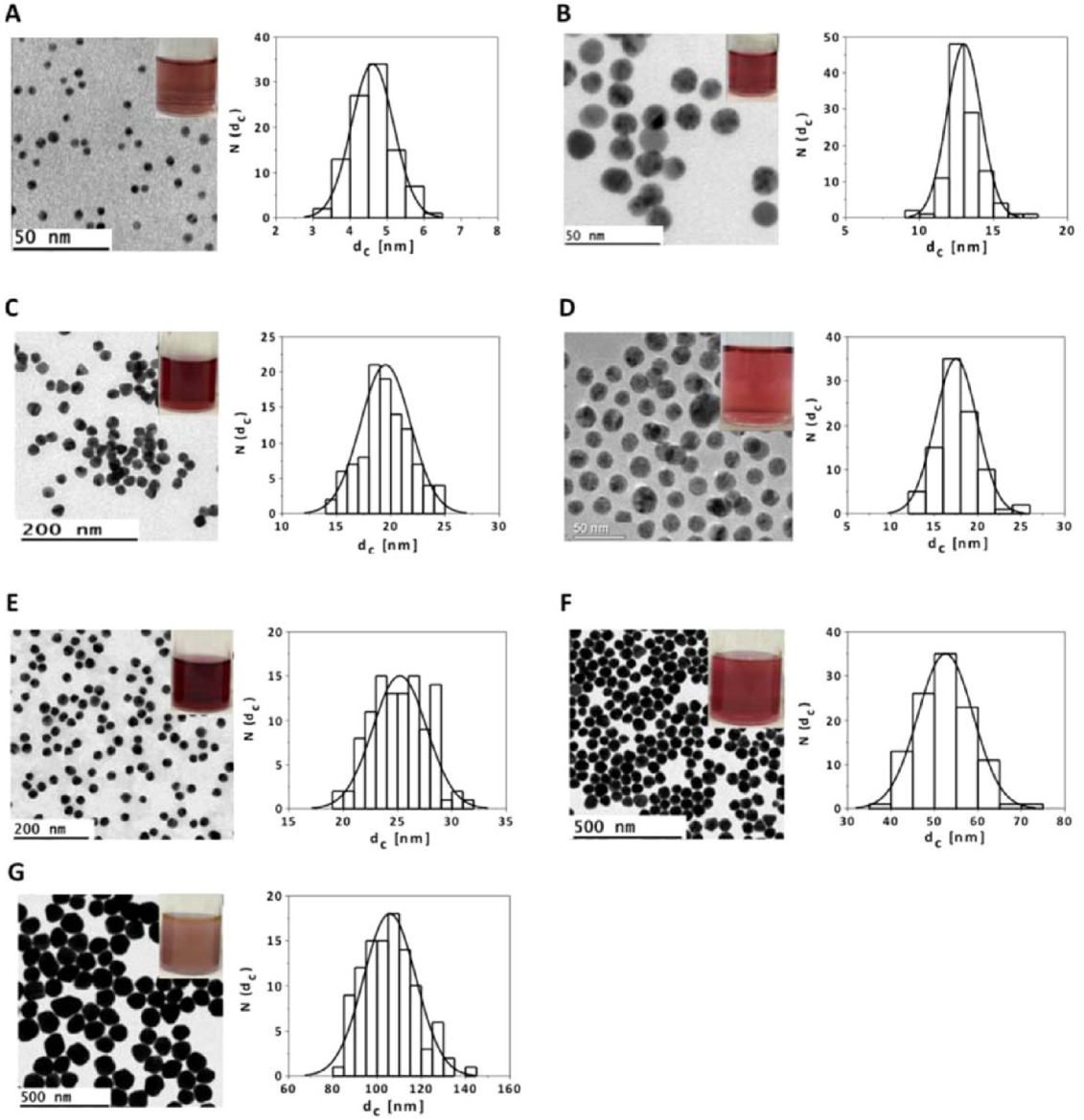

Figure 70. TEM images of Cit-Au NPs (cf. Section 2.2) dried on a grid from a suspension of NPs in water and their corresponding size distribution histograms, plotted as number of NPs $N(d_c)$ that have a core diameter of d_c. From these histograms, the mean NP diameter d_c and its standard deviation were determined for each preparation. Insets show images of glass vials filled with Cit-Au NPs suspension of each preparation. (A) Cit-Au NPs with $d_c = (4.6 \pm 0.5)$ nm; the scale bar corresponds to 50 nm. (B) Cit-Au NPs with $d_c = (13 \pm 1)$ nm; the scale bars correspond to 50 nm. (C) Cit-Au NPs with $d_c = (19 \pm 2)$ nm; the scale bar corresponds to 200 nm. (D) Cit-Au NPs with $d_c = (17 \pm 3)$ nm; the scale bar corresponds to 50 nm. (E) Cit-Au NPs, ≈25 nm core diameter, grown on 18 nm seeds, $d_c = (25 \pm 2)$ nm; the scale bar corresponds to 200 nm. (F) Cit-Au NPs with $d_c = (53 \pm 6)$ nm, the scale bar corresponds to 500 nm. (G) Cit-Au NPs with $d_c = (106 \pm 12)$ nm; the scale bar corresponds to 500 nm.

(fwhm) value. The first step consisted of the appropriate plot of the desired peak (intensity I versus Θ). The determination of the full width at half-maximum (fwhm) value was carried out by fitting the peak. In most of the cases a GauSamp function provides accurate results (cf. Figure 79).

In the presented case, the following values were obtained: $\Theta = 19.198°$; fwhm = 1.457° = 0.0255 rad. Thus, according to eq 31, $d_{crys} = (K \times \lambda)/(\beta \cdot \cos(\Theta)) = (0.9 \times 0.15418\ \text{nm})/(0.0255 \times \cos(19.198°)) = 5.7$ nm. In this way the crystallite size determined from the width of the (111) peak was $d_{crys} = 5.7 \pm 0.2$ nm, in acceptable agreement with the TEM data (cf. Figure 64 and the actually determined value for the batch used here was $d_c = 4.3$ nm).

8.6. Thermogravimetric Analysis of NPs. Thermogravimetric analysis (TGA) measures the mass of a sample, while its temperature is continuously increased. Upon decomposition of parts of the sample its mass decreases and thus allows for analyzing the composition of the sample. In the case of inorganic NPs upon heating the solvent may be evaporated, as the organic shell around the NP surface may decompose. In this section, calculation of the weight contribution of the organic coating on NPs to the total weight of the NPs will be detailed.

In Figure 80A the TGA analysis carried out on DDT-Au NPs (≈ 4 nm core diameter, cf. Section 1.2) is shown. A suspension of the hydrophobic NPs in chloroform was added dropwise to an alumina sample holder, and the solvent was evaporated in an oven at 40 °C. The process was repeated until around $m_{NP\_pel} \approx 2$ mg of NPs were deposited on the sample holder. TGA was performed in air at a heating rate of 5 °C·min^{-1}, using a Q600 TA Instrument.

DOI: 10.1021/acs.chemmater.6b04738
Chem. Mater. 2017, 29, 399−461

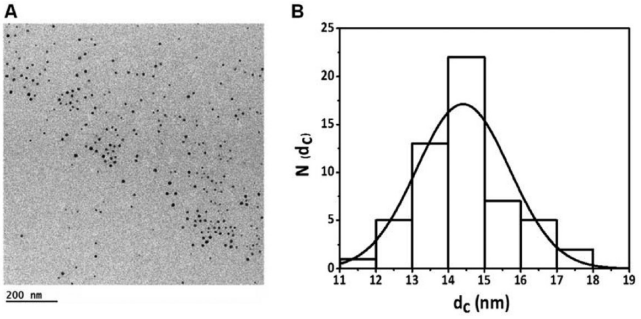

Figure 71. (A) TEM image of Cit-Ag NPs (cf. Section 2.3) dried on a grid from a suspension of NPs in water. The scale bar corresponds to 200 nm. (B) Size distribution histogram, plotted as number of NPs $N(d_c)$ that have a core diameter of d_c. From this histogram the mean NP diameter d_c and its standard deviation were determined to be d_c = (15 ± 1) nm.

The TGA curve corresponding to the dodecanethiol-capped Au NPs (Figure 80A) showed a very slight loss (<1%) in the 25−150 °C range, as expected from hydrophobic NPs. An abrupt loss (around 18%) took place between 150 and 300 °C, which should be caused by the decomposition of the DDT. No changes in the mass were observed at higher temperatures. Based on these data, an estimation of the amount of the organic coating ($m_{NP,org}$, comprising the original DDT ligand in this case) deposited on the NPs surface can be determined. The diameter of the inorganic Au core of this batch of Au NPs had been determined to be d_c = 4.3 nm. The mass m_{NP} of one NP comprises the mass of the inorganic core m_c and the mass of the organic coating $m_{NP,org}$:

$$m_{NP} = m_c + m_{NP,org} \quad (32)$$

In the present case according to eq 20 and eq 23 the volume V_c and the mass m_c of one NP core could be calculated. For a spherical Au NP with core diameter d_c = 4.3 nm, $V_c = (\pi/6) \times (4.3\ \text{nm})^3 \approx 41.6\ \text{nm}^3$. Given the bulk density of Au of ρ_{Au} = 19.3 g/cm^3, the mass of one Au core thus is $m_c = 19.3\ \text{g/cm}^3 \times 41.6\ \text{nm}^3 \approx 803\ \text{g} \times (10^{-9}\ \text{m}/10^{-2}\ \text{m})^3 \approx 8.0 \times 10^{-19}$ g (cf. Section 8.1).

In the data shown in Figure 80A, the absolute weights for the NP pellet ($m_{NP\_pel}(T)$) were m_{NP_pel}(25 °C) = 1.744 mg (mass at RT), m_{NP_pel}(150 °C) = 1.730 mg, m_{NP_pel}(340 °C) = 1.424 mg, and m_{NP_pel}(700 °C) = 1.421 mg (final mass). We considered that at 700 °C only the NP cores were present. The number of cores (and thus of NPs) in the sample thus was $N_c = m_{NP\_pel}(700\ °C)/m_c = 1.421 \times 10^{-3}\ \text{g}/8.0 \times 10^{-19}\ \text{g} = 1.77 \times 10^{15} \approx 1.8 \times 10^{15}$. We attributed the mass of the organic coating (DDT) to the mass lost upon heating from 150 to 340 °C: $m_{NP,org\_pel} = m_{NP\_pel}(150\ °C) - m_{NP\_pel}(340\ °C)$ = 1.730 mg − 1.424 mg = 0.306 mg. Thus, the mass of the organic coating around one NP is $m_{NP,org} = m_{NP,org\_pel}/N_c = 0.306 \times 10^{-3}\ \text{g}/1.8 \times 10^{15} \approx 1.7 \times 10^{-19}$ g. Therefore, the whole mass of one Au NP is according to eq 32 $m_{NP} = m_c + m_{NP,org} = 8.0 \times 10^{-19}\ \text{g} + 1.7 \times 10^{-19}\ \text{g} \approx 9.7 \times 10^{-19}$ g. The organic coating thus contributed $m_{NP,org}/m_{NP} = 1.7 \times 10^{-19}\ \text{g}/9.7 \times 10^{-19}\ \text{g} \approx$ 17% of the mass of one NP.

The TGA analysis of the DDT-Au NPs overcoated with PMA (cf. Section 6.3) is shown in Figure 80B. The PMA-Au NPs, which were suspended in water were cleaned by ultracentrifugation (cf. Section 7.2). In this case, the sample was dried before analysis, and around $m_{NP\_pel} \approx 1$ mg of pelleted PMA coated NPs were placed in an alumina sample holder. TGA was also performed in air at a heating rate of 5 °C·min^{-1}, using the same Q600 TA Instrument.

The TGA curve of the DDT-Au NPs overcoated with PMA showed a slight weight loss (around 5%) in the 25−150 °C range, which can be ascribed to the release of absorbed water. An additional abrupt loss (around 26%) took place between 150 and 300 °C, which should be caused by the decomposition of the dodecanethiol and/or the amphiphilic polymer poly(isobutylene-*alt*-maleic anhydride)-*graft*-dodecyl (PMA). Almost no changes in the mass were observed at higher temperatures. As in the previous hydrophobic sample, the TGA data could be used to estimate the mass of organic coating $m_{NP,org}$ of one Au NP. The mass of an Au NP core was calculated as described above to be 8.0×10^{-19} g.

The absolute weights $m_{NP\_pel}(T)$ in Figure 80B were m_{NP_pel}(25 °C) = 1.032 mg (mass at RT), m_{NP_pel}(150 °C) = 0.990 mg, m_{NP_pel}(340 °C) = 0.711 mg, m_{NP_pel}(700 °C) = 0.693 mg (final mass). As in the previous sample, we considered that at 700 °C only the NP cores were present. The number of cores (and thus of NPs) in the sample thus was $N_c = m_{NP\_pel}(700\ °C)/m_c = 0.693 \times 10^{-3}\ \text{g}/8.0 \times 10^{-19}\ \text{g} = 8.66 \times 10^{14} \approx 8.7 \times 10^{14}$. We attributed the mass of the organic coating to the mass lost upon heating from 150 to 340 °C: $m_{NP,org\_pel} = m_{NP\_pel}(150\ °C) - m_{NP\_pel}(340\ °C) = 0.990$ mg − 0.711 mg = 0.279 mg. Thus, the mass of the organic coating around one NP was $m_{NP,org} = m_{NP,org\_pel}/N_c = 0.279 \times 10^{-3}\ \text{g}/8.7 \times 10^{14} = 3.21 \times 10^{-19}\ \text{g} \approx 3.2 \times 10^{-19}$ g. Thus, the whole mass of one Au NP was according to eq 32 $m_{NP} = m_c + m_{NP,org} = 8.0 \times 10^{-19}\ \text{g} + 3.2 \times 10^{-19}\ \text{g} \approx 11.2 \times 10^{-19}$ g. The organic coating thus contributed $m_{NP,org}/m_{NP} = 3.2 \times 10^{-19}\ \text{g}/11.2 \times 10^{-19}\ \text{g} \approx 29\%$ of the mass of one NP. The contribution of the organic coating for the dodecanethiol-capped Au NPs overcoated with PMA was thus higher than for the hydrophobic DDT-Au NPs, as expected. Note that for bigger NP cores the percentage contribution of the organic coating would be much lower, but in the case of very small NPs it is highly relevant.

The TGA analysis of dried PMA (cf. Section 6.2) is shown in Figure 81. Note that PMA decomposed from 200 to ca. 500 °C; however, in the PMA-coated Au NPs (Figure 80B) the main mass loss took place from 200 to 300 °C, and the mass of the sample remained almost constant above this temperature. The mass loss observed in the PMA polymer above ca. 350 °C may thus have corresponded to the evaporation of impurities, which may have originated from the precursors used for its synthesis. By using ultracentrifugation (cf. Section 7.2), such impurities can be removed from the coated NPs.

Based on these data some quantitative analysis concerning the organic surface coating can be performed. In the case of the DDT capped Au NPs the number $N_{DDT/NP}$ of DDT molecules per Au NP can be calculated, by assuming that the organic surface coating only comprises DDT.

$$m_{NP,org} = m_{NP,DDT} \quad (33)$$

Using the molar mass of DDT $M_{ligand} = M_{DDT}$ = 202.40 Da thus leads to

$$N_{DDT/NP} = (m_{NP,org}/M_{ligand}) \times N_A \quad (34)$$

For the DDT-Au NPs (d_c = 4.3 nm) as analyzed here with TGA the following result was obtained as described above: $m_{NP,org} = 1.7 \times 10^{-19}$ g. Thus, $N_{DDT/NP} = (m_{NP,org}/M_{DDT}) \times N_A = (1.7 \times 10^{-19}\ \text{g}/202.40\ \text{g·mol}^{-1}) \times 6.02 \times 10^{23}\ \text{mol}^{-1} = 506$ DDT molecules are assumed to be situated at the surface of the DDT-Au NPs. The surface of one Au core is

DOI: 10.1021/acs.chemmater.6b04738
Chem. Mater. 2017, 29, 399−461

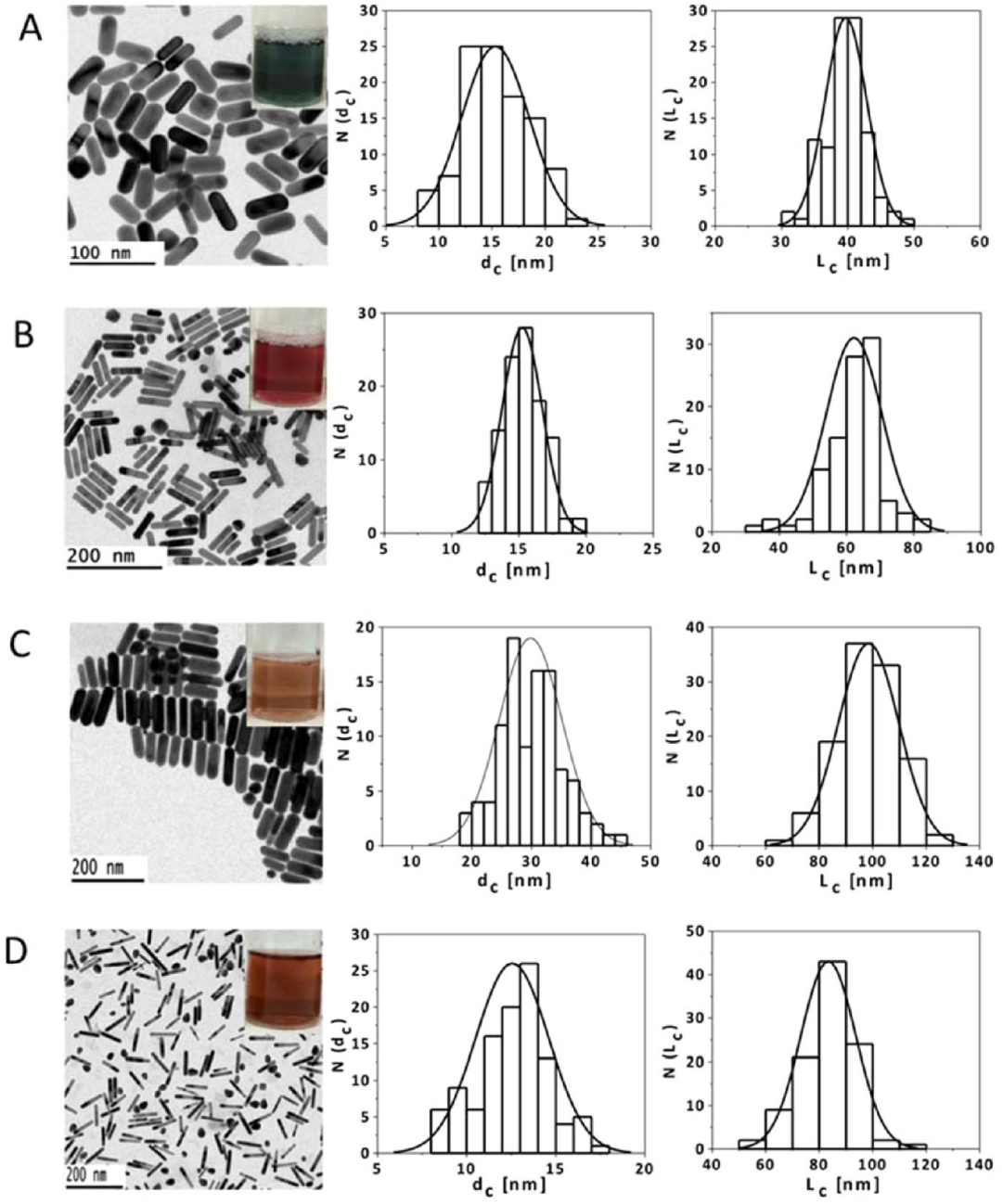

Figure 72. TEM images of CTAB- Au NRs (cf. Section 2.4) dried on a grid from a suspension of NPs in water and the corresponding size distribution histograms, plotted as number of NPs $N(d_c)$ that have a core diameter of d_c (histograms to the left) or as number of NPs $N(L_c)$ that have a core length of L_c (histograms to the right). From these histograms the mean NP diameter d_c and its standard deviation, as well as the mean length L_c and its standard deviation, were determined for each preparation. Insets show images of glass vials filled with CTAB-Au NRs suspension of each preparation. (A) λ_{SPR} = 650 nm, d_c = (16 ± 5) nm, and L_c = (40 ± 3) nm; the scale bar corresponds to 100 nm. (B) λ_{SPR} = 825 nm, d_c = (15 ± 1) nm, and L_c = (62 ± 8) nm; the scale bar corresponds to 200 nm. (C) λ_{SPR} = 790 nm, d_c = (30 ± 5) nm, and L_c = (98 ± 11) nm; the scale bar corresponds to 200 nm. (D) λ_{SPR} = 1050 nm, d_c = (13 ± 2) nm, and L_c = (83 ± 10) nm; the scale bar corresponds to 200 nm. λ_{SPR} corresponds to their surface plasmon peak.

$$A_c = 4\pi \times (d_c/2)^2 = \pi \cdot d_c^{\,2} \tag{35}$$

and thus in the present case $A_c = \pi \cdot (4.3\ \text{nm})^2 \approx 58.1\ \text{nm}^2$. In this way the surface area which is occupied by each DDT molecule is

$$A_{c,DDT} = A_c / N_{DDT/NP} \tag{36}$$

In the present case each DDT molecule covers $A_{c,DDT}$ = 58.1 $\text{nm}^2/506 \approx 0.11\ \text{nm}^2$ surface area. This is less than observed for the highest packing density of alkanethiols on the regular smooth Au(111) surface of 0.214 nm^2.[123] The discrepancy might be explained by several arguments. Due to the highly curved surface more thiols may be bound per surface area according to a radius-of-curvature effect, which leaves more space for the alkyl chains pointing toward solution.[53] Due to the typical size distribution of Au cores (such as shown in Figure 64), there is a part of the NPs with d_c smaller than the average value and thus with a higher surface-to-volume ratio,

DOI: 10.1021/acs.chemmater.6b04738
Chem. Mater. 2017, 29, 399−461

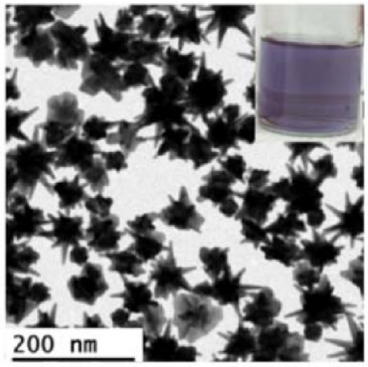

Figure 73. TEM image of hydrophilic star-shaped Au NPs (cf. Section 2.5) dried on a grid from a suspension of NPs in water. The scale bar corresponds to 200 nm. The inset shows glass vials filled with a suspension of star-shaped Au NPs.

and thus more thiols can bind. Despite purification there still may be excess ligand (DDT) in solution. The ligand exchange from TOAB-Au NPs to DDT-Au NPs may have been incomplete, leading to the presence of ligands others than DDT on the Au surface. In addition, the assumed monolayer formation of DDT may not be completely true, and some more DDT may be attached to the NPs, for example, due to intercalation. TGA thus helps to verify assumptions about the structure of NPs.

Also for the PMA coated Au NPs some quantitative analysis can be performed.[124] In this case the mass of the organic surface coating around one NP comprises the underlying DDT layer $m_{NP,DDT}$ and the PMA-based polymer $m_{NP,P}$ wrapped around it.

$$m_{NP,org} = m_{NP,DDT} + m_{NP,P} \quad (37)$$

According to the TGA results in this section the DDT contributes to 17% of the mass of one DDT-Au NP, whereas the DDT plus PMA-based polymer contributes to 29% of the mass of one PMA-Au NP. Thus, based on the TGA data of $m_{NP,org} = 3.2 \times 10^{-19}$ g for PMA-Au NPs the following contributions can be calculated: $m_{NP,DDT} = (17\%/29\%) \times m_{NP,org} = (17/29) \times 3.2 \times 10^{-19}$ g $\approx 1.9 \times 10^{-19}$ g and $m_{NP,P} = ((29\%-17\%)/29\%) \times m_{NP,org} = (12/29) \times 3.2 \times 10^{-19}$ g $\approx 1.3 \times 10^{-19}$ g. By using the molar mass of one polymer monomer (cf. eq 14), the number of polymer monomers bound per NP can be calculated as

$$N_{P/NP} = (m_{NP,P}/M_P) \times N_A \quad (38)$$

Using the value of $M_P = 293$ g/mol for PMA-based polymers as calculated in Section 6.2 leads to $N_{P/NP} = (m_{NP,P}/M_P) \times N_A = (1.3 \times 10^{-19}$ g/293 g/mol$) \times 6.02 \times 10^{23}$ mol$^{-1} \approx 270$ polymer monomer units bound to each PMA-Au NP. This value can be now compared to the number of polymer monomer units $N_{P/NP(added)}$ that have been added to each DDT-Au NP during the formation of PMA-Au NPs.

$$N_{P/NP(added)} = R_{P/Area} \times A_{eff} \quad (39)$$

In the present case the following parameters were used: $l_{ligand} = l_{DDT} = 1$ nm (cf. Table 5), resulting in $d_{eff} = d_c + 2 \times l_{ligand} = 4.3$ nm $+ 2 \times 1$ nm $= 6.3$ nm, and thus according to eq 15 in $A_{eff} = \pi \cdot d_{eff}^2 = \pi \cdot (6.3$ nm$)^2 \approx 124$ nm^2. Therefore, $N_{P/NP(added)} = R_{P/Area} \times A_{eff} = 100$ nm$^{-2} \times 124$ nm$^2 = 12\,400$ polymer monomer units had been added per NP upon the polymer coating procedure. The fact that $N_{P/NP} \ll N_{P/NP(added)}$ demonstrates that most added polymer actually has not bound to the NPs, and thus purification of NP solutions from excess polymer is crucial.

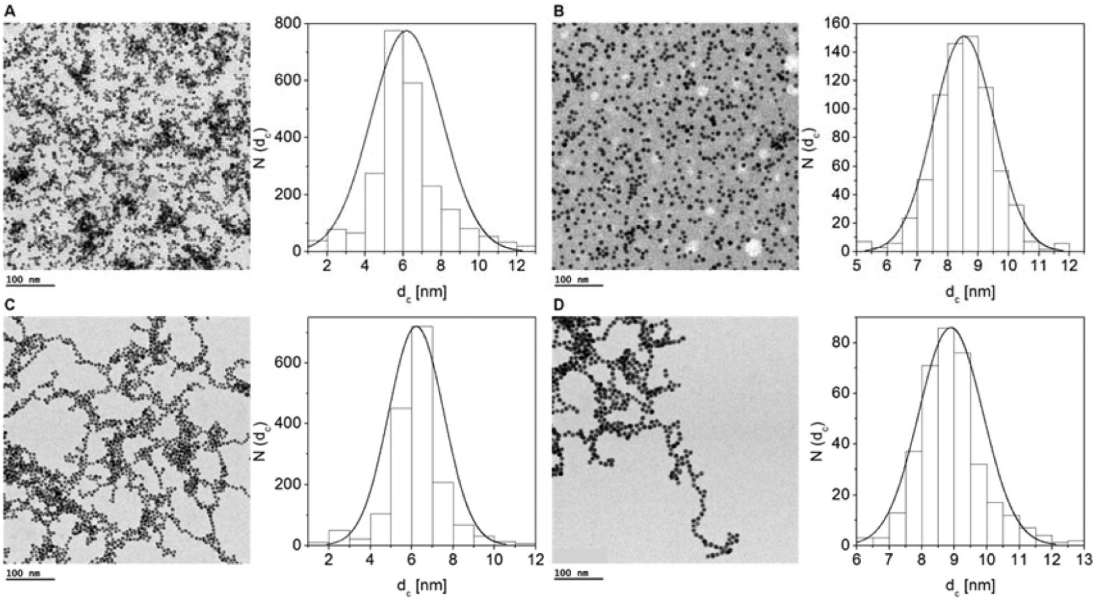

Figure 74. TEM images of Cit-Au NPs (cf. Section 2.2) dried on a grid from a suspension of NPs in water and their corresponding size distribution histograms before (A zand C) and after (B and D) ligand exchange with bis(*p*-sulfonatophenyl)-phenylphosphine (cf. Section 3.2). Histograms are plotted as number $N(d_c)$ of NPs which have a core diameter d_c. From these histograms the mean NP diameter d_c and its standard deviation were determined. All scale bars correspond to 100 nm. (A) Cit-Au NPs before ligand exchange with $d_c = (6.0 \pm 1.1)$ nm. (B) Au NPs after exchanging the original citrate capping ions with bis(*p*-sulfonatophenyl)-phenylphosphine with, $d_c = (8.7 \pm 1.0)$ nm. (C) Cit-Au NPs before ligand exchange with $d_c = (6.3 \pm 0.8)$ nm. (E) Au NPs after exchanging the original citrate capping ions with bis(*p*-sulfonatophenyl)-phenylphosphine with $d_c = (8.9 \pm 0.8)$ nm.

DOI: 10.1021/acs.chemmater.6b04738
Chem. Mater. 2017, 29, 399−461

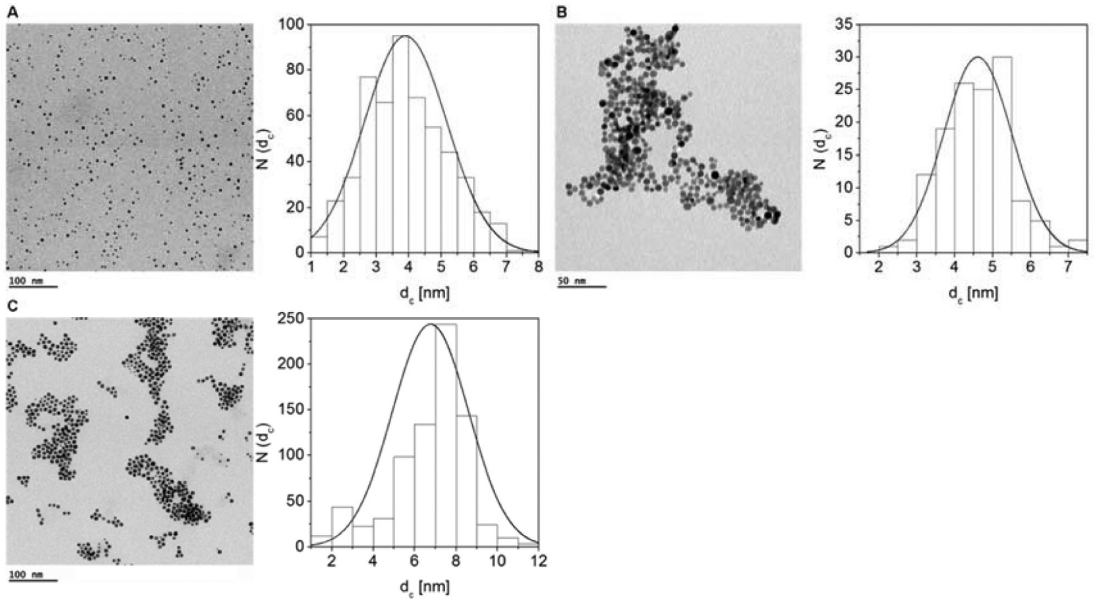

Figure 75. TEM images of PMA-Au NPs, made by DDT-Au NPs (cf. Section 1.2), which have been transferred to aqueous solution using PMA-*g*-dodecyl polymer coating or ligand exchange method (cf. Section 6.3 and Section 5.2, respectively) and dried on a grid from a suspension of NPs in water, along with corresponding size distribution histograms. Histograms are plotted as number of NPs $N(d_c)$ that have a core diameter d_c to calculate the mean NP diameter d_c and its standard deviation. (A) PMA-Au NPs (DDT-Au NPs after coating with PMA-*g*-dodecyl polymer, Section 6.3) with $d_c = (4.1 \pm 1.1)$ nm; the scale bar corresponds to 100 nm. (B) Au NPs originally capped with hexanoic acid, ≈4 nm core diameter, after ligand exchange with mercaptopropionic acid (cf. Section 5.2), $d_c = (4.4 \pm 0.9)$ nm; the scale bar corresponds to 50 nm. (C) Au NPs originally capped with decanoic acid, ≈7 nm core diameter, after ligand exchange with mercaptoundecanonic acid (cf. Section 5.2), $d_c = (7.1 \pm 1.3)$ nm; the scale bar corresponds to 100 nm.

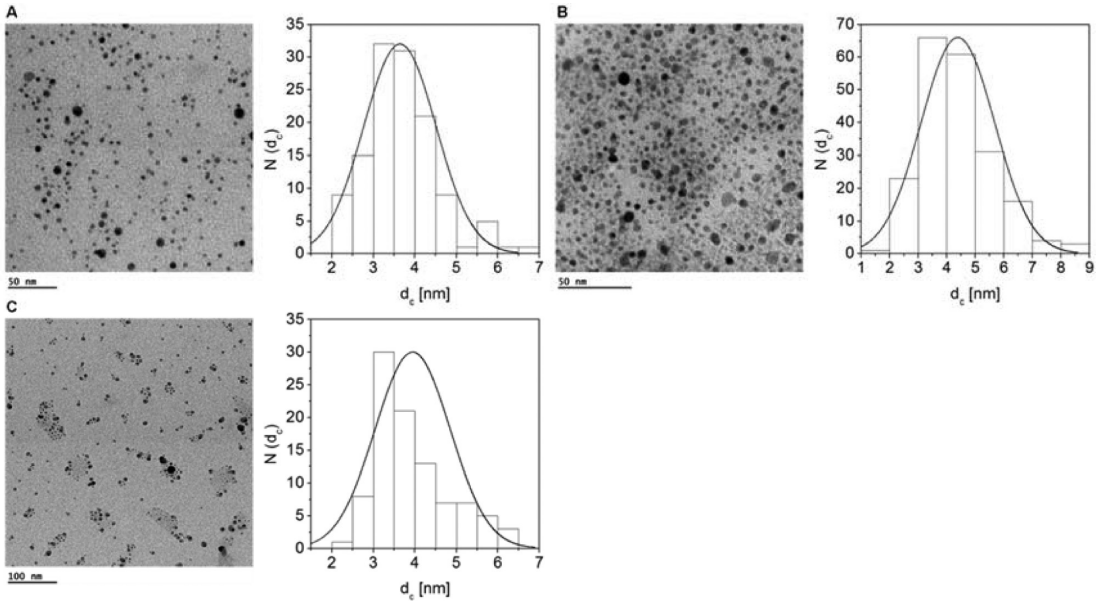

Figure 76. TEM images of hydrophobic Ag NPs originally capped with dodecanethiol of ≈4 nm core diameter (cf. Section 1.3), which have been transferred to aqueous solution using PMA-*g*-dodecyl polymer coating or the ligand exchange method (cf. Section 6.3 and Section 5.2, respectively) and dried on a grid from a suspension of NPs in water. Histograms are plotted as number of NPs $N(d_c)$ that have a core diameter d_c to calculate the mean NP diameter d_c and its standard deviation. (A) PMA-Ag NPs (DDT-Ag NPs after coating with PMA-*g*-dodecyl polymer, Section 6.3) with $d_c = (3.6 \pm 0.9)$ nm; the scale bar corresponds to 50 nm. (B) Ag NPs after ligand exchange with mercaptopropionic acid (cf. Section 5.3), $d_c = (4.4 \pm 1.3)$ nm; the scale bar corresponds to 50 nm. (C) Ag NPs after ligand exchange with mercaptoundecanonic acid (cf. Section 5.3), $d_c = (4.4 \pm 1.3)$ nm; the scale bar corresponds to 100 nm.

8.7. Infrared Spectroscopy. Fourier transform infrared spectroscopy (FTIR) allows for analyzing the chemical structure of the organic shell around NP cores. As a vibrational spectroscopy with a specific vibrational fingerprint for specific functional groups, FTIR can be used to qualitatively describe the organic shell around NPs and thus can be employed to follow up surface functionalization or ligand exchange. Moreover, deviations in typical vibrational features of adsorbing functional groups on the surface of NPs can be used to describe the type and orientation of organic ligand−core interaction. In

DOI: 10.1021/acs.chemmater.6b04738
Chem. Mater. 2017, 29, 399−461

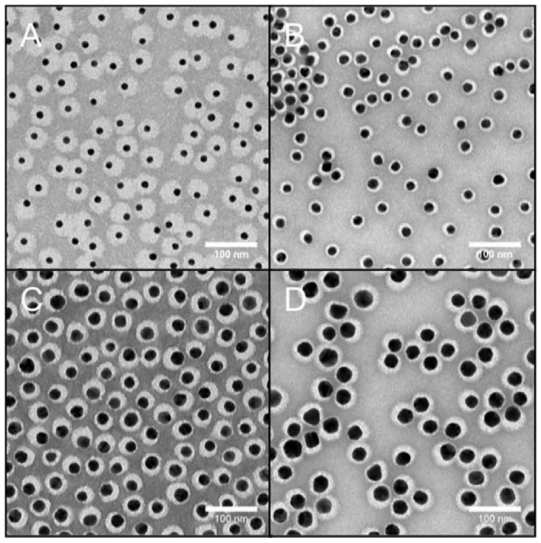

Figure 77. Visualizing the PEG shell around PEG-Au NPs using TEM imaging and the negative staining technique with uranyl acetate[56] (cf. Section 2.2 and Section 3.3). (A) Au cores (d_c = 13.7 ± 0.7 nm) plus an organic shell of PEG (10 kDa, l_{ligand} = 11.8 ± 1.2 nm) results in d_{eff} = 37.4 ± 2.5 nm. (B) Au cores (d_c = 18.9 ± 1.9 nm) plus an organic shell of PEG (1 kDa, l_{ligand} = 3.2 ± 0.4 nm) results in d_{eff} = 25.4 ± 2.1 nm. (C) Au cores (d_c = 23.5 ± 1.7 nm) plus an organic shell of PEG (5 kDa, l_{ligand} = 11.8 ± 1.5 nm) results in d_{eff} = 37.4 ± 1.5 nm. (D) Au cores (d_c = 30.1 ± 2.6 nm) plus an organic shell of PEG (3 kDa, l_{ligand} = 7.7 ± 1.0 nm) results in d_{eff} = 45.6 ± 3.6 nm. Mean and corresponding standard deviation values of the core (d_c), ligand shell (l_{ligand}), and the effective size (d_{eff}) were obtained by analyzing several negative staining TEM micrographs (>1000 NPs) as described by del Pino et al.[56] TEM images were segmented using Matlab (Mathworks) and Cellprofiler.[121] The scale bars are 100 nm.

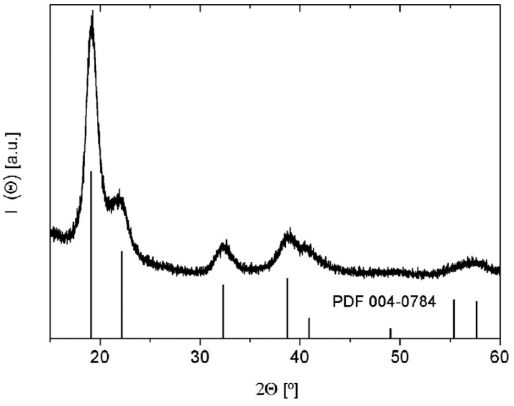

Figure 78. XRD diagram $I(\Theta)$ of polymer coated Au NPs (≈4 nm core size, cf. Section 1.2 and Section 6.3). The PDF pattern of cubic gold has also been included.

the present work FTIR analysis of DDT-Au NPs (≈4 nm core diameter, cf. Section 1.2) before and after overcoating with PMA (cf. Section 6.3), as well as for free PMA as control, were carried out and compared. Spectra were measured with a Thermo Nicolet 6700 FT-IR. Sample purity is essential, and thus initial the DDT-Au NP sample was purified as described above (cf. Section 1.2) and PMA-coated Au NPs (cf. Section 6.3) were purified following the protocol mentioned above (cf. Section 7.5), while PMA was used directly as-synthesized (cf. Section 6.2). DDT-Au NPs and PMA solutions were dissolved in chloroform, and they were left to evaporate to get solid

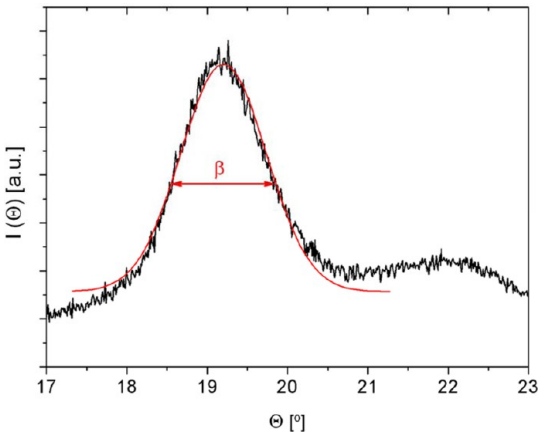

Figure 79. XRD diagram $I(\Theta)$ of the (111) plane of polymer coated Au NPs (≈4 nm core size, cf. Section 1.2 and Section 6.3). The red line represents the GauSamp fit of the peak. This graph is a part of the graph shown in Figure 78.

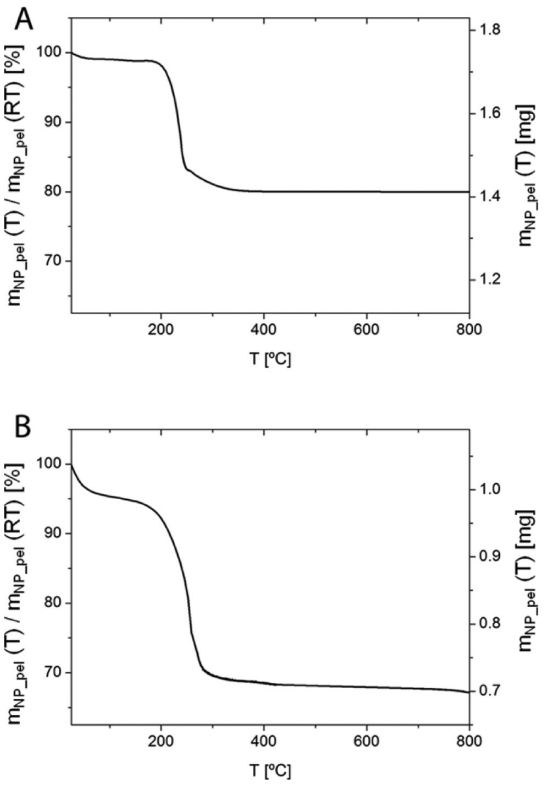

Figure 80. TGA analyses of DDT-Au NPs (A) and DDT-Au NPs overcoated with PMA (B). In both graphs, $m_{NP\_pel}(T)$ describes the mass of the NP pellet at temperature T. The masses are normalized to the mass $m_{NP\_pel}(RT)$ at RT. The same scale in the left y-axis is used to facilitate the comparison. For both samples d_c = 4.3 nm.

samples, whereas the aqueous solution of PMA-coated Au NPs was lyophilized prior to the preparation of the KBr pellets. These pellets were prepared at a 1% concentration of the sample, i.e., m_{NP_pel} = 2 mg of the dried NP sample was mixed with 200 mg of KBr, grinding until a homogeneous mixture was obtained, and finally the pellet was formed by using a hand press. For the measurements, 50 scans were recorded with a Thermo Nicolet 6700 FT-IR, and the presented FTIR spectra of 50 scans at 4 cm^{-1} resolution were averaged. Data are presented in Figure 82.

DOI: 10.1021/acs.chemmater.6b04738
Chem. Mater. 2017, 29, 399−461

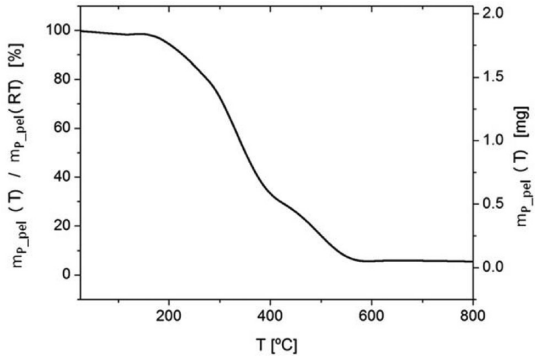

Figure 81. TGA analysis of PMA. $m_{P\_pel}(T)$ describes the mass of the PMA at temperature T. The mass is normalized to the mass $m_{P\_pel}(RT)$ at RT.

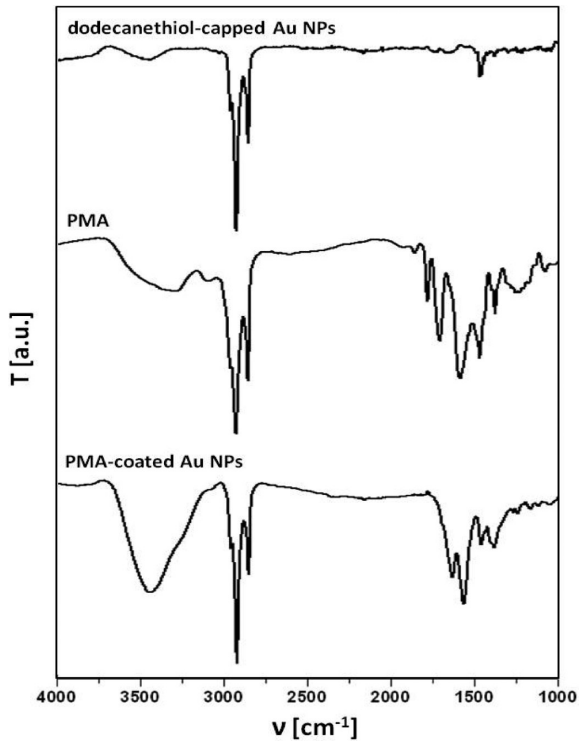

Figure 82. FTIR spectrum (transmission mode $T(\nu)$, i.e., transmission T versus wavenumber ν) of DDT-Au NPs of ≈4 nm core diameter before and after overcoating with PMA. The spectrum of free PMA is shown as control.

The DDT-Au NPs exhibited only three significant peaks. The strong peaks at 2923 and 2853 cm^{-1} were assigned to the asymmetric and symmetric C−H stretching of the alkyl chain, respectively, and the peak at 1460 cm^{-1} was assigned to the bending vibrations of C−H. In contrast, the PMA polymer (cf. Figure 48) presented more peaks. The strong peaks at 2925 and 2854 cm^{-1} were assigned to the asymmetric and symmetric C−H stretching of the alkyl chains. The broad and weak adsorption peak from 3200−3600 cm^{-1} corresponded to the presence of the O−H stretching resonance of the carboxylic acids formed after the anhydride opening. The two peaks at 1780 and 1705 cm^{-1} were characteristic of the cyclic anhydride with 5-membered rings. The peak of the symmetric stretching vibrations of C═O from the carboxylic groups overlapped with the peak at 1705 cm^{-1}. At 1583 cm^{-1} the symmetric stretching vibrations of N—C═O of the amide groups appeared. The 1468 and 1375 cm^{-1} peaks were assigned to the angular deformation of CH_2 and CH_3, respectively. When the DDT-Au NPs were overcoated with the amphiphilic PMA polymer, the IR spectrum of the resulting PMA-coated Au NPs had the same peaks as the DDT-Au NPs and some additional peaks from the PMA, such as the peaks at 1635 and 1565 cm^{-1} assigned to the symmetric stretching vibrations of C═O from the carboxylic groups and N—C═O from the amide groups, respectively. Here, again the 1466 and 1384 cm^{-1} peaks from the angular deformation of CH_2 and CH_3 appeared, respectively. Additionally, there was a broad and intense band from 3000−3600 cm^{-1} corresponding the O—H stretching resonance of the carboxylic acids formed when the NPs had been transferred to water and then all the anhydride rings had been opened. Collectively, FTIR results indicated the surface modification (overcoating) of DDT-Au NPs with PMA.

In summary, FTIR analysis of NPs allows for knowing which ligands and chemical groups are present on the NP surface. This serves to confirm that the functionalization strategy (e.g., polymer coating or ligand exchange/displacement) worked properly.

8.8. Nuclear Magnetic Resonance. Nuclear magnetic resonance spectroscopy (NMR) is a powerful tool to probe the chemical structure of the organic shell around the inorganic NP core. NMR is mainly used to provide evidence on the presence and orientation of organic molecules/ligands around NPs. NMR works well to analyze small molecules, but it may get complicated in the case of large constructs, due to the heterogeneity and reduced flexibility of the analyzed constructs.

In the present work we analyzed the NMR spectra of PMA before and after the coating of ≈4 nm DDT-Au NPs (cf. Section 1.2 and Section 6.3). A ^1H NMR spectrum of PMA in $CDCl_3$ (i.e., chloroform where the proton ^1H was substituted by a deuteron D = ^2H) was first measured. As expected nonresolved broad bands were observed as a result of the size distribution of the starting poly(isobutylene-*alt*-maleic anhydride)-*graft*-dodecyl and the random distribution of dodecylamine moieties along the polymer chain. In this situation it was possible to distinguish broad singlets (br s) between 3.66 and 2.63 ppm corresponding to −C*H*− protons, 1.69−0.92 ppm corresponding to −CH_2− protons, and 0.90−0.80 ppm corresponding to −CH_3− protons (cf. Figure 83A). A ^{13}C NMR spectrum was also measured observing good resolution for nonquaternary carbon atoms due to their higher signal intensity compared to quaternary ones such as C═O, for instance (cf. Figure 83B). The peak assignment both in ^1H and ^{13}C NMR was based on the chemical shift (δ) and was aided by 2D HSQC experiment (heteronuclear single quantum correlation) edited for distinguishing CH_2 signals from CH and CH_3.

^1H NMR of PMA coated Au NPs (≈ 4 nm core diameter, cf. Section 1.2) was measured in water with 15% of deuterium oxide, using a sequence for suppressing water signal. When PMA was coating the Au NPs, there were no longer cyclic anhydrides present and two separate peaks were observed for −C*H* protons: those linked to amide groups and kept inside the hydrophobic core, and those linked to carboxylic groups and exposed to the water phase. Those nuclei had very different environments and hence different chemical shifts. Interestingly, when this spectrum was compared with that of PMA treated with NaOH to open all the anhydride groups and measured under the same conditions (H_2O with 15% D_2O) a somehow

DOI: 10.1021/acs.chemmater.6b04738
Chem. Mater. 2017, 29, 399−461

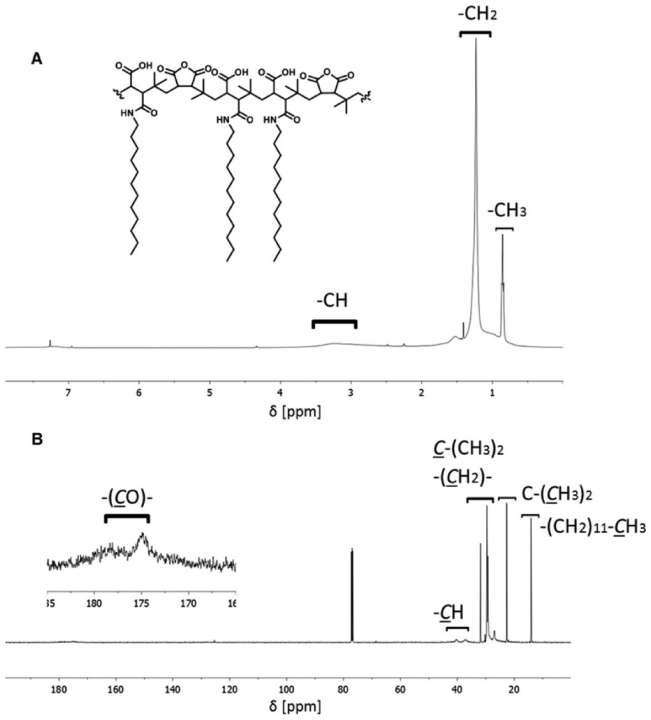

Figure 83. (A) ^{1}H NMR spectrum of PMA in $CDCl_3$. (B) ^{13}C NMR spectrum of PMA in $CDCl_3$; the zoomed area shows the peaks for the carbonyl groups.

different profile was observed. The CH peak was barely visible, and only the CH_2 and CH_3 peaks were clearly visible, although the ratio between them was modified ($CH_2/CH_3 \approx 2$ in PMA coated Au NPs vs $CH_2/CH_3 \approx 1$ in PMA after NaOH treatment). This shows that PMA molecules arranged differently when free in solution (i.e., forming empty polymer micelles) or when on the surface of Au NPs, but it is difficult to extract further structural information from these experiments.

In summary, NMR spectroscopy can give further evidence of the presence of PMA on the surface of Au NPs of ≈4 nm and can also be used to check the purity of those NPs by confirming the absence of other organic molecules such as organic solvents or glycerol from the filters. However, the heterogeneity of PMA polymer and the poor ability of some of the protons to resonate when linked to Au NPs led to poor resolution spectra that could only be interpreted from a qualitative point of view.

^{1}H and ^{13}C spectra were recorded in a Bruker 500 MHz spectrometer. Chemical shifts are reported in parts per million (ppm) relative to the residual signal of the solvent used, and are listed below:

PMA (cf. Figure 83). ^{1}H NMR (500 MHz, $CDCl_3$) δ 3.66−2.63 (br s, CH), 1.69−0.92 (m, CH_2), 0.90−0.80 (m, CH_3). ^{13}C NMR (126 MHz, $CDCl_3$) δ 178.08, 174.80, 173.92, 77.00, 40.36, 37.19, 31.86, 30.25, 29.59, 29.30, 29.14, 28.78, 26.98, 22.62, 14.05.

PMA coated Au NPs (cf. Figure 84A). ^{1}H NMR (500 MHz, D_2O) δ 3.66 (br s, CH), 2.64 (br s, CH), 1.68 (br s, CH_2), 1.31 (br s, CH_2), 0.89 (br s, CH_3).

PMA after basic treatment (cf. Figure 84B). ^{1}H NMR (500 MHz, D_2O) δ 2.40 (br s, CH), 1.08 (br s, CH_2), 0.67 (br s, CH_3).

9. CHARACTERIZATION OF THE PHOTOPHYSICAL PROPERTIES OF NPs

9.1. UV/Vis Absorption Spectroscopy. UV/vis absorption spectroscopy is an easy and simple method to characterize important properties of colloidal NPs. Several types of NPs, such as quantum dots or plasmonic NPs, have particular features (i.e., resonance peaks) in their absorption spectra, which provide important information regarding NP size, size distribution, and shape. Moreover, UV/vis absorption spectroscopy can be used to determine the concentration of NPs (cf. Section 9.2) and to follow colloidal growth and stability (cf. Section 10.1).

To record absorption spectra for NPs, several issues need to be considered. First, a blank has to be recorded for the pure solvent, which needs to be subtracted from the NP absorption spectrum. Typically (unless, for example, IR absorbing NPs such as gold nanorods are investigated) NP suspensions are transparent at high wavelengths. Spherical Au NPs of a few nm in size have their plasmon absorption peak around 520 nm (cf. Table 8) and do not absorb light at higher wavelengths of ca. 800−1200 nm. In case the measured "absorption" in this range does not converge to zero, in fact scattering and not absorption has been detected. This most likely is due to partial agglomeration of the NP sample (cf. Section 10.1). Thus, before further analysis based of the UV/vis absorption spectra of a NP solution, it has to be made sure that the absorption in the spectra converges toward zero in this range (ca. 800−1200 nm). In case the NPs are well dispersed this should be automatically the case after automated subtraction of the offset. However, in case the offset function does not work, a constant offset may be subtracted manually, until the absorption for high wavelengths (ca. 800−1200 nm, in case there are no absorption

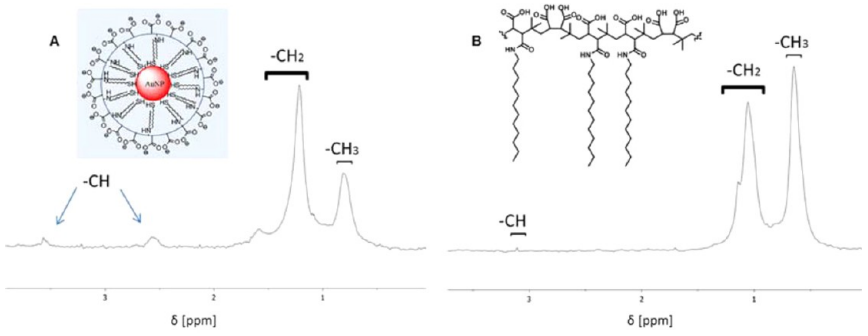

Figure 84. (A) ^{1}H NMR spectrum of PMA coated Au NPs of ≈4 nm core diameter in 15% D_2O/H_2O mixture. (B) ^{1}H NMR of PMA in 15% D_2O/H_2O mixture after treatment with base to open all anhydride groups.

DOI: 10.1021/acs.chemmater.6b04738
Chem. Mater. 2017, 29, 399−461

Table 8. Values of Surface Plasmon Resonance Maximum Wavelength (λ_{max}) and Molecular Extinction Coefficients, ε_{NP}, (cf. Section 9.2) of Cit-Au NPs of Different Sizes in Water[a]

d_c [nm]	source	λ_{SPR} [nm]	ε_{NP} [$M^{-1}\cdot cm^{-1}$]
4.2	Section 1.2, Section 6.3	516	8.70×10^6
5	BBI solutions	518	9.70×10^6
10	BBI solutions	520	9.55×10^7
15	BBI solutions	523	3.64×10^8
30	BBI solutions	526	3.58×10^9
50	BBI solutions	532	1.93×10^{10}

[a]Extinction coefficients were provided from the manufacturer.

features of the NPs in this range) converges to zero; see Figure 85.

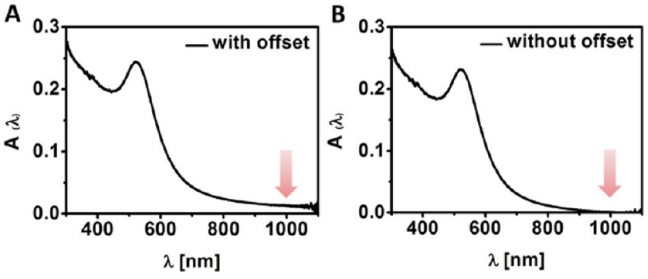

Figure 85. Absorption spectra (absorption (A) as a function of the wavelength λ) of ≈4 nm core diameter Au NPs (cf. Section 1.2) coated with PMA in water (cf. Section 6.3). (A) The "raw spectra" include an offset at higher wavelengths. (B) Processed spectra by subtracting the absorption at higher wavelengths from the whole spectra. Processed spectra provide more accurate comparison between different spectra with different offset levels.

Next, it is important to use a cuvette of an appropriate material. Plastic cuvettes may be incompatible with organic solvents (e.g., acetone and chloroform), which should be avoided to eliminate artifacts in recording absorption spectra of NPs. Moreover, cuvettes are not transparent in the whole UV/vis absorption spectrum. In case that the absorbance at small wavelengths (<300 nm) is important, the material of the used cuvette plays an important role. Plastic cuvettes are not transparent at short wavelengths (<250 nm) and thus should be avoided in these cases. Even glass cuvettes show significant absorption at short wavelengths. The use of quartz cuvettes is standard practice to minimize cuvette-related absorption at short wavelengths (see Figure 86).

Proper sample dilution is essential to record accurate UV/vis spectra of NP solutions. If the sample is very concentrated, the recorded spectra will be noisy, due to saturation of the instrument detector. Moreover, quantification will not be possible since absorbance readings will be out of the linear range of the concentration−absorbance relationship.

The absorption $A(\lambda)$ is the logarithmic ratio of the intensity of the incident light beam I_0 to the intensity of the transmitted light beam $I_t(\lambda)$. For this reason the absorption also has no units. In the case the path length of the cuvette is l_{sol} = 1 cm, the absorption is also referred to as optical density (OD) of the solution.

$$A(\lambda) = \log(I_0/I_t(\lambda)) \quad (40)$$

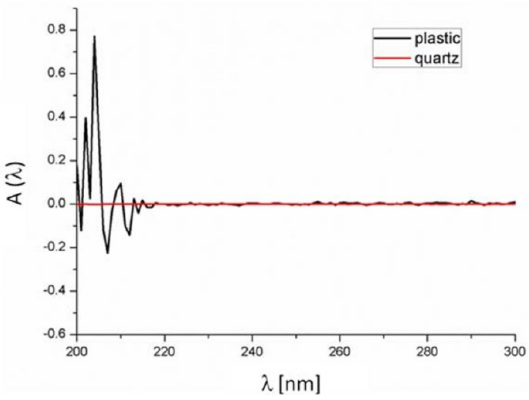

Figure 86. Absorption spectrum $A(\lambda)$ of water (with water as blank) recorded in plastic or quartz cuvette. Note the cuvette-related absorption when a plastic cuvette was used at short wavelength.

In the case the transmitted light is ten times less, due to the decadic logarithm, the absorption is a factor of 2 higher. Thus, for high absorption rates the intensity of the transmitted light becomes very low and can no longer be correctly detected.

Figure 87 shows the UV/vis absorption spectra of Au NPs as a function of sequential dilution, as recorded on an Agilent

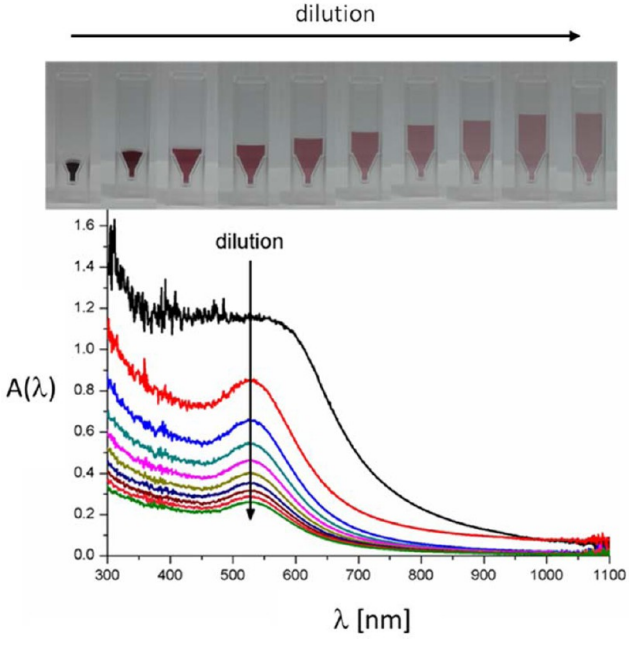

Figure 87. Concentrated aqueous solution of Au NPs was stepwise diluted, which can be seen by the fading color in the solution (upper panel) and deceasing absorption intensity (lower panel). High NP concentration (black curve) resulted in high absorption, and thus λ_{max} cannot even be identified due to detector saturation that results in peak broadening and distortion.

8450 UV/vis spectrometer. At high NP concentrations, the absorption spectrum is noisy and distorted at lower wavelengths, where the absorption is high and exceeding the capacity of the detector. Thus, absorption spectra need to be recorded at sufficiently low concentrations by accurate dilution with solvent. Typical optical densities should not exceed 0.5, and at higher absorption the shape of the spectrum may be an artifact.

DOI: 10.1021/acs.chemmater.6b04738
Chem. Mater. 2017, 29, 399−461

Despite the strong plasmon optical extinction of Ag NPs and Au NPs, NPs from other materials may have no features in their UV/vis absorption spectra. Figure 88 shows as examples of

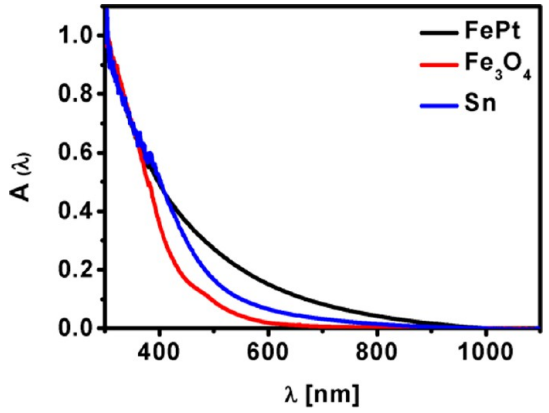

Figure 88. Normalized absorption spectra $A(\lambda)$ of FePt NPs (black curve) (cf. Section 1.4), Fe_3O_4 NPs (red curve) (cf. Section 1.5), and Sn NPs (blue curve) (cf. Section 1.6). All NPs are dispersed in chloroform. Due to the absence of plasmon resonance, the absorption spectra do not contain defined peaks or characteristics.

such cases the absorption spectra for ≈4 nm FePt (cf. Section 1.4), ≈4 nm Fe_3O_4 (cf. Section 1.5), and ≈11 nm Sn (cf. Section 1.6) NPs dispersed in organic solvent. These NP solutions have higher absorption in the UV region (with no peaks), which converges to zero in the IR.

Plasmonic NPs (such as Au NPs, Ag NPs) have characteristic absorption peaks due to the surface resonance plasmon (SPR) phenomenon in the UV/vis−NIR region. Plasmonic NPs may have one or even more SPR peaks, depending on the shape and architecture of the NPs.[125−127] The characteristic absorption peaks are responsible for the distinctive bright color of NP solutions. The spectral position and shape of the surface plasmon absorption peak depends on a variety of factors, such as NP material, size, size-distribution, shape, surface chemistry, and state of aggregation, as well as of the solvent. Figure 89A

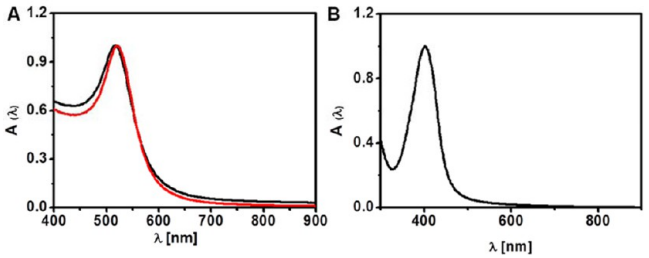

Figure 89. Normalized UV/vis absorption spectra of (A) Cit-Au NPs ≈ 13 nm core diameter (black line) versus Cit-Au NPs ≈ 20 nm core diameter (red line). (B) Cit-Ag NPs ≈ 15 nm core diameter. Au NPs and Ag NPs suspensions in water were prepared as detailed in Section 2.2 and Section 2.3, respectively.

shows a red shift of the SPR maximum (λ_{SPR}) to higher wavelength when the size of Au NPs is increased from 13 to 20 nm (size dependency). Figure 89B shows the absorption spectra of citrate capped spherical Ag NPs in the violet/UV (λ_{SPR} = 415 nm) as compared to Au NPs with the same size (15 and 13 nm respectively) that absorb green light (λ_{SPR} = 520 nm) (NP material dependency).

The size-dependency of λ_{SPR} for Au NPs is well documented with a general trend predicting a red shift of the absorption (λ_{SPR}) as the NP diameter increases. Figure 90 shows a red shift

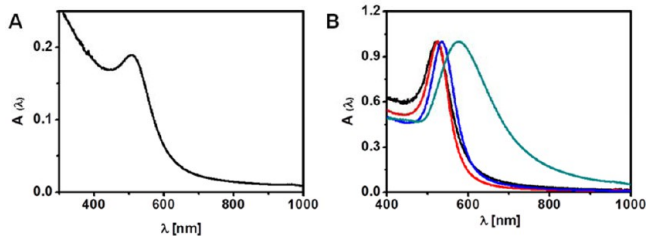

Figure 90. Normalized UV/vis absorption spectra of Cit-Au NPs (cf. Section 2.2) with core diameters of ≈5 nm (A), 18 nm (B, black line), 25 nm (B, red line), 50 nm (B, blue line), and 100 nm (B, green line). The corresponding TEM images of these NPs are shown in Figure 70 A,D−G.

of the SPR maximum (λ_{SPR}) to higher wavelength, when Cit-Au NPs increase in size from 5 to 100 nm. In case of Cit-Au NPs (green curve in B), the size distribution of the NPs is poor, i.e., there are NPs of different sizes in solution, and the absorption peak becomes broader. Thus, a sharp SPR peak is a good indication of narrow size distribution of the core diameter d_c. Figure 91 and Table 8 show a red shift of the SPR maximum wavelength (λ_{SPR}) to higher wavelengths, when commercially available Cit-Au NPs increased in size from 5 to 50 nm.

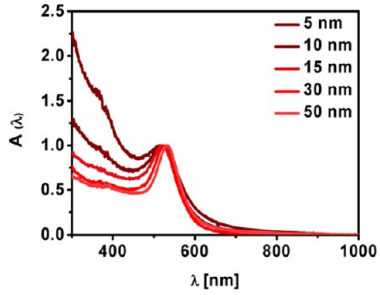

Figure 91. Normalized UV/vis absorption spectra of commercial Cit-Au NPs in water from BBI solutions (cf. Section 2.2) with core diameters of 5, 10, 15, 30, and 50.

The shape dependence of the SPR peak is well documented and reported in the literature. For example, rod-shaped Au NPs have two SPR peaks, as the oscillation of electrons in the conduction band can occur around either the short axis or the long axis, resulting in the so-called transverse and longitudinal peaks, respectively. While in case of Au NPs the transverse plasmon peak is located generally in the visible region (~520 nm), the longitudinal peak can be tuned to be in the visible−near infrared (vis−NIR) region of the spectrum (600−1200 nm) as shown in Figure 92A. Spectra for star-shaped Au NPs exhibit one peak in the vis−NIR as shown in Figure 92B.

Finally, the surface plasmon peak can change dramatically upon agglomeration due to the plasmon coupling of aggregated NPs.[128] This will be discussed in more detail in Section 10.1.

The UV/vis absorption spectrum of NPs may also change in dependence of the surface capping, as well as on the solvents in which the NP are suspended. This is demonstrated in Figure 93.

Quantum dots have a characteristic absorption peak in their spectrum due to the formation of electron−hole pairs

DOI: 10.1021/acs.chemmater.6b04738
Chem. Mater. 2017, 29, 399−461

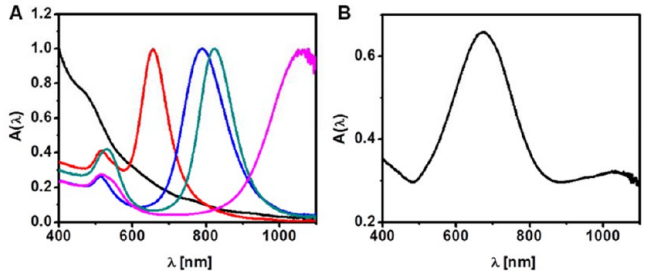

Figure 92. Normalized UV/vis absorption spectra of (A) Au NRs (cf. Section 2.4), with λ_{SPR} = 650 nm (red curve), 790 nm (blue curve), 825 nm (green curve), 1050 nm (pink curve), and the original spherical Au seeds used to grow the nanorods (black curve). For TEM images of these Au NRs cf. Figure 72. (B) Star-shaped Au NPs with λ_{SPR} = 690 nm (cf. Section 2.5). For TEM images of these NPs cf. Figure 73.

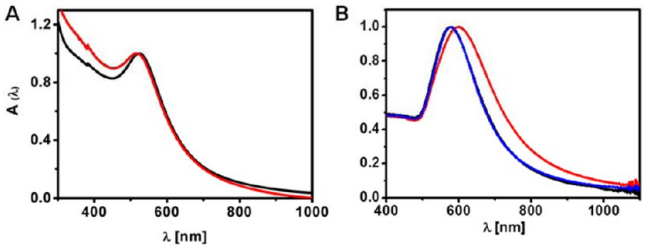

Figure 93. Normalized UV/vis absorption spectrum of Au NPs capped with different surface coatings and suspended in different solvents. (A) Au NPs with core diameter of ≈4 nm (cf. Section 1.2), either capped with DDT and suspended in chloroform (black curve) or after being overcoated with PMA (cf. Section 6.3) and suspended in water (red curve). (B) Au NPs with core diameter of ≈100 nm (cf. Section 2.2) either with the original citrate capping as recorded in water (black) or after their phase transfer to chloroform by ligand exchange with dodecylamine and PEG (cf. Section 4.3) (red curve), and finally after retransfer to water by PMA coating (cf. Section 6.3) (blue curve). The black and blue curves are almost superimposed in B.

(excitons) upon absorption.[129−132] In the case of semiconductor NPs with very sharp size distribution, multiple exciton peaks can be observed.[133−135] The absorption spectra of CdSe/ZnS and CdS NPs are shown in Figure 94.

The spectral position of the first exciton peak, which corresponds to the energy gap between the ground states of the valence and conduction band, is extremely size dependent. This is due to the quantum confinement of light-generated

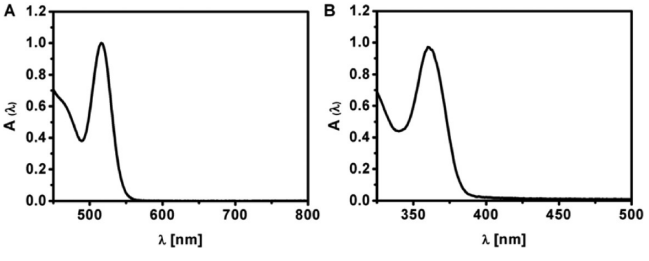

Figure 94. (A) Normalized UV/vis absorption spectrum of CdSe/ZnS quantum dots with core diameter of ≈4 nm (cf. Section 1.7; Figure 68) as recorded in toluene with λ_{max} = 516 nm. (B) Normalized UV/vis absorption spectrum of CdS quantum dots with core diameter of ≈2 nm (cf. Section 1.8; Figure 69) as recorded in toluene with λ_{max} = 360 nm.

electron−hole pairs.[136−139] The smaller a QD becomes, the bigger the energy gap and thus the shorter the wavelength of the first exciton peak. Equation 6 correlates the wavelength λ_{max} of the first exciton peak in the absorption spectrum with the core NP diameter d_c. Values have been listed for several QD materials.[29,140] Note that in Yu et al. data are only provided for QDs with a single semiconductor core. However, as demonstrated in Section 1.7, quantum dots can also be grown with several semiconductor shells around the semiconductor core. For example, the values for CdSe NPs in the Yu et al. table cannot be directly applied for CdSe/ZnS NPs, as the ZnS shell will shift the absorption peak λ_{abs} to higher wavelength. If this wavelength is used with eq 6, the resulting d_c for the CdSe core in CdSe/ZnS is overestimated. However, and since the ZnS shell contributes to the size of the inorganic part of the NPs, this error in the calculation is often tolerated.

9.2. Determination of NP Concentrations from Absorption Spectra. The NP concentration of NP suspension c_{NP} can be obtained from the Beer−Lambert's law, which correlates the absorption A (from the UV/vis absorption spectrum) with c_{NP} as follows:

$$A(\lambda) = \varepsilon_{NP}(\lambda) \times l_{sol} \times c_{NP} \quad (41)$$

Both the molar extinction coefficient ($\varepsilon_{NP}(\lambda)$) and thus the absorption ($A(\lambda)$) depend on the wavelength λ and the solvent. l_{sol} is the path length of the cuvette in which the absorbance has been measured, i.e., the distance that the light passes in the NP suspension during measurements. As mentioned in Section 9.1, a blank spectrum of the solvent should be measured first and subtracted from the sample spectrum, in order to eliminate absorption from the cuvette and the solvent. In order to determine the NP concentration c_{NP} of a sample, the absorption $A(\lambda)$ is measured at wavelength λ in a cuvette of path length l_{sol}. It is important to correct the offset of the absorption spectra as detailed in Figure 85). In the case that $\varepsilon_{NP}(\lambda)$ is known, the NP concentration can be calculated according to eq 41.

In the case of NPs which do not have specific peaks in their absorption spectra (such as FePt, Fe_3O_4, Sn, etc.), $\varepsilon_{NP}(\lambda)$ usually is not reported in the literature. In this case the absorption $A(\lambda)$ of an NP suspension is recorded, and then the NP concentration c_{NP} in this solution is determined by ICP-MS (cf. Section 8.2). The molar extinction coefficient can then be calculated as $\varepsilon_{NP}(\lambda) = A(\lambda)/(c_{NP} \times l_{sol})$. Once $\varepsilon_{NP}(\lambda)$ is known, the NP concentration in the following samples can be determined by absorption instead of ICP-MS analysis, which is less time-consuming and cheaper.

For plasmonic NPs or QDs, values for the molar extinction at λ_{SPR} (wavelength of the surface plasmon resonance) or λ_{max} (first exciton peak), respectively, are available in the literature. For Au NPs some molar extinction values λ_{SPR} are given in Table 8. An extended table has been reported by Haiss et al.[141] Also in the case of QDs, lists of molar extinction values are reported in literature.[29,142] In Figure 95 an example for the concentration determination of a solution of Au NPs is given.

NP concentration values obtained via absorption measurements have to be interpreted with care, as they may be prone to significant errors. With this in mind, published reports should clearly detail calculation of NP concentration stating the used molar extinction values and the selected absorption wavelength.

In the case the molar extinction coefficient for a NP sample is recorded at one wavelength λ_1 but the extinction coefficient at

DOI: 10.1021/acs.chemmater.6b04738
Chem. Mater. 2017, 29, 399−461

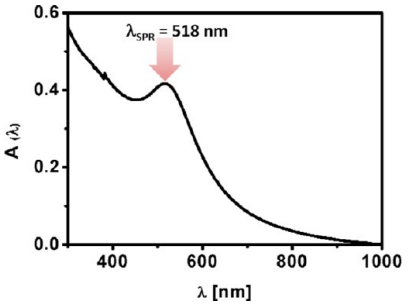

Figure 95. Absorption spectrum of ≈4 nm Au NPs (cf. Section 1.2) recorded in chloroform. The absorption at their surface plasmon peak λ_{SPR} = 518 nm is measured to be $A(\lambda_{SPR})$ = 0.42. The path length of the used cuvette was l_{sol} = 1 cm. The molar extinction coefficient $\varepsilon(\lambda_{SPR})$ = 8.7 × 10^6 M^{-1} × cm^{-1} is obtained from Table 8. Thus, the concentration of Au NPs in this solution was calculated using eq 41 as $c_{NP} = A(\lambda_{SPR})/(\varepsilon_{NP}(\lambda_{SPR}) \times l_{sol})$ = 0.42/(8.7 × 10^6 M^{-1} × cm^{-1} × 1 cm) = 0.048 × 10^{-6} M = 48 nM.

another wavelength λ_2 is needed, this can be calculated from the absorption spectrum $A(\lambda)$ according to eq 42 as

$$\varepsilon(\lambda_2) = \varepsilon(\lambda_1) \times A(\lambda_2)/A(\lambda_1) \quad (42)$$

For homogeneous NPs with characteristic features, such as Au NPs, the extinction coefficients of the Au cores are known with relatively good precision.[141] However, these values refer to the absorption related to the NP core, with an assumption that the organic coating does not contribute significantly to the total absorption (as the absorption of the inorganic core is much stronger). Thus, the extinction coefficient for the core is used for the whole NP. In the case of thin transparent ligand shells this approximation works well at higher wavelengths (vis–NIR) but not at lower wavelengths (UV) where most organic ligands possess significant absorption. Also in the case the inorganic part comprises a core and (several) shell(s), such as already mentioned in the case of CdSe/ZnS NPs, the absorption of the shell often is neglected and the extinction values for the core are used for the whole core/shell NP.

The organic shell can be modified intentionally with "absorbers", for example, in the case organic fluorophores are integrated into the polymer shell around a NP (cf. Section 6.2). In this case the absorption spectrum shows the absorption of the inorganic NP core, the absorption of the organic shell (which can be in general neglected), and the absorption of the integrated fluorophores; see Figure 96. Obviously, it is important to determine the number of fluorophores per NP, for which several methods have been proposed.[68,79,92] One of these methods is based on determining both the concentration of NP cores c_{NP} and the concentration of dyes c_{dye} from the UV/vis absorption spectra, leading to the number $N_{dye/NP} = c_{dye}/c_{NP}$ of fluorophores per NP. An example of the calculation is shown in Figure 96.

Typically the absorption spectrum of the dye will overlap with the absorption spectrum of the NP core. Thus, the dye absorption part needs to be deconvoluted from the NP core absorption part. For this purpose three UV/vis absorption spectra need to be recorded: (i) from solutions of the NPs with integrated fluorophores, (ii) of the NPs alone, and (iii) of the fluorophores alone, cf. Figure 96.[52,86] The fluorophores typically absorb only in a small spectral band, whereas the NP cores absorb continuously, optionally until a maximum wavelength. Thus, the NP core concentration can be

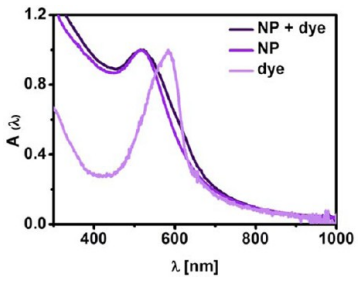

Figure 96. Normalized absorption spectra of ≈4 nm Au NPs (cf. Section 1.2; blue curve) recorded after their PMA coating and functionalization with a dye (cresyl violet perchlorate, CV) versus the spectrum free of the dye (red curve). The absorption at surface plasmon peak λ_{SPR} = 519 nm of the NPs is normalized to $A(\lambda_{SPR})$ = 1.0. The absorption of the free dye at their emission maximum $\lambda_{dye,max}$ = 583 nm is normalized to $A(\lambda_{dye,max})$ = 1.0 as well. To calculate the concentration c_{dye} of the conjugated dye, the absorption of the NPs at $\lambda_{dye,max}$ is first subtracted from the absorption of dye-modified NPs at $\lambda_{dye,max}$ ⇒ $A_{dye}(\lambda_{dye,max}) = A_{NP+dye}(\lambda_{dye,max}) - A_{NP}(\lambda_{dye,max})$ = 0.73–0.63 = 0.1. The molar extinction coefficient of NPs $\varepsilon_{NP}(\lambda_{SPR})$ = 8.7 × 10^6 $M^{-1}{\cdot}cm^{-1}$ is obtained from Table 8, and the one of CV is $\varepsilon_{dye}(\lambda_{max})$ = 8.3 × 10^4 $M^{-1}{\cdot}cm^{-1}$. The path length of the used cuvette was l_{sol} = 1 cm. Now both concentrations can be calculated according to eq 41. For the dye $c_{dye} = A_{dye}(\lambda_{dye,max})/(\varepsilon_{dye}(\lambda_{dye,max}) \times l_{sol})$ = 0.1/(8.3 × 10^4 $M^{-1}{\cdot}cm^{-1}$ × 1 cm) = 1.21 × 10^{-6} M = 1.21 μM. For the NPs $c_{NP} = A_{NP}(\lambda_{SPR})/(\varepsilon_{NP}(\lambda_{SPR}) \times l_{sol})$ = 1.0/(8.7 × 10^6 $M^{-1}{\cdot}cm^{-1}$ × 1 cm) = 0.115 × 10^{-6} M = 115 nM. By this the ratio of $N_{dye/NP} = c_{dye}/c_{NP}$ = 1.21 × 10^{-6} M/0.115 × 10^{-6} M = 10.5 dye molecules per NP can be estimated.

determined at a wavelength where the NP core, but not the fluorophore, absorbs. This can be directly done by the known molar extinction coefficient $\varepsilon_{NP}(\lambda)$ at this wavelength by measuring the absorption from the NP spectrum, leading to the concentration of NP cores c_{NP}. On the other hand, at the absorption peak of the dye there is typically also absorption of the NP core. Thus, the absorption spectrum of the NP cores only is scaled by multiplication with an appropriate factor to match the absorption spectrum of the NPs with integrated dyes at the parts, where the dyes do not absorb. Then, at the absorption peak of the dye the appropriately scaled absorption of the nonmodified NPs is subtracted from the absorption of the NPs with integrated dyes, leading to the absorption of only the dyes. In the case the molar extinction coefficient of the dyes $\varepsilon_{dye}(\lambda)$ at this absorption wavelength is known, then the dye concentration can be calculated using Lambert–Beer's law:

$$A(\lambda) = \varepsilon_{dye}(\lambda) \times c_{dye} \times l_{sol} \quad (43)$$

This methodology works better the more the characteristic absorption peaks of the NP cores and the more the dyes are spectrally shifted. An example for a calculation is shown in Figure 96.

Also data from TGA (cf. Section 8.6) can be used for estimating the number of dyes attached per NP. In the case the number of polymer units bound to the NP ($N_{P/NP}$) is known, the number of dyes bound per NP ($N_{dye/NP}$) can be derived from the amount of dye that has been added per monomer ($R_{dye/mon}$):

$$N_{dye/NP} = R_{dye/mon} \times N_{P/NP} \quad (44)$$

In the case of the PMA-Au NPs with d_c = 4.3 as discussed in Section 8.6, addition of dye to 2% of the anhydride rings ($R_{dye/mon}$ = 0.02) leads to $N_{dye/NP}$ = 0.02 × 270 = 54. This value

DOI: 10.1021/acs.chemmater.6b04738
Chem. Mater. 2017, 29, 399–461

can now be compared to the values determined with other methods. In Kaiser et al.[68] Evidot540/Catskill Green QDs (d_c = 2.7 ± 0.4 nm determined by TEM, value provided by company: 2.6 nm) were modified with 2% dye ($R_{dye/mon}$ = 0.02), and the value $N_{dye/NP}$ = 7 ± 0.7 was determined from time-resolved photoluminescence spectra. Assuming that the number of dye molecules per NP scale with the effective surface area A_{eff}, this value can be compared to the TGA data of Au: $N_{dye/NP(1)} = N_{dye/NP(2)} \times ((R_{P/Area(1)} \times A_{eff(1)})/(R_{P/Area(2)} \times A_{eff(2)})) = N_{dye/NP(2)} \times (R_{P/Area(1)}/(R_{P/Area(2)}) \times ((d_{c(1)} + 2 \times l_{ligand(1)})/(d_{c(2)} + 2 \times l_{ligand(2)}))^2$. In both cases the same amount of polymer per surface area had been added, $R_{P/ligand(1)} = R_{P/ligand(2)}$ = 100 nm^2, but the diameters are different. In the case of CdSe/ZnS, $d_{c(1)}$ = 2.7 nm and $l_{ligand(1)}$ = 1.2 nm, and in the case of Au, $d_{c(2)}$ = 4.3 nm and $l_{ligand(2)}$ = 1.0 nm. Thus, this leads to $N_{dye/NP(1)} = N_{dye/NP(2)} \times ((d_{c(1)} + 2 \times l_{ligand(1)})/(d_{c(2)} + 2 \times l_{ligand(2)}))^2 = 54 \times ((2.7\ nm + 2 \times 1.2\ nm)/(4.3\ nm + 2 \times 1.0\ nm))^2 = 54 \times (5.1/6.3)^2 \approx 35$. Thus, TGA analyses leads to a value of $N_{dye/NP}$ = 35 dye molecules per CdSe/ZnS NP, as compared to the optically determined value of $N_{dye/NP}$ = 7. For this reason, in order to estimate the error, it is convenient to use several methods in parallel for the determination of $N_{dye/NP}$.

9.3. Fluorescence Spectroscopy. NPs can be fluorescent for two reasons. First, NPs may be intrinsically fluorescent, such in the case of QDs,[143] upconverting NPs,[111] ultrasmall Au,[144] or Ag clusters.[145] Examples for fluorescence spectra of CdSe/ZnS and CdS NPs are shown in Figures 97 and 98, respectively.

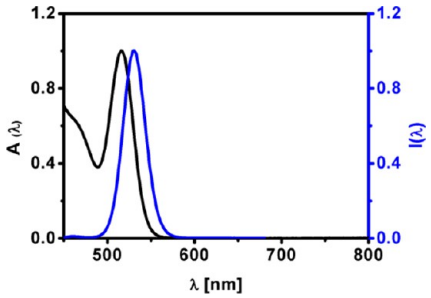

Figure 97. Normalized absorption spectrum $A(\lambda)$ (black solid line, cf. Figure 94A) and emission spectrum $I(\lambda)$ (blue solid line) of hydrophobic CdSe/ZnS NPs ($d_c \approx$ 4 nm, cf. Section 1.7) in toluene. The absorption and emission peaks are at $\lambda_{abs} \approx$ 516 nm and $\lambda_{em} \approx$ 530 nm respectively, and correspond to CdSe/ZnS NPs of ≈4 nm.

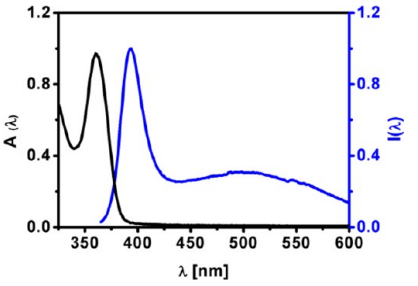

Figure 98. Normalized absorption spectrum $A(\lambda)$ (black solid line, cf. Figure 94B) and emission spectrum $I(\lambda)$ (blue solid line) of hydrophobic CdS NPs ($d_c \approx$ 2 nm, cf. Section 1.8) in toluene. The absorption and emission peaks, respectively, at $\lambda_{abs} \approx$ 360 nm and $\lambda_{em} \approx$ 390 nm correspond to CdS NPs of ≈2 nm.

Second, organic fluorophores can be integrated in the organic surface coating (cf. Section 6.2) around nonfluorescent inorganic NP cores. An example is shown in Figure 99. In this case the underlying inorganic NP core may affect the fluorescence emission of the organic fluorophores. In the case of plasmonic NPs the fluorescence of adjacent dyes may be quenched,[146] and in the case of QDs, fluorescence resonance energy transfer (FRET) may occur with the linked dyes.[86,100,147] In both cases the effects strongly depend on the distance between the organic fluorophores and the NP cores.

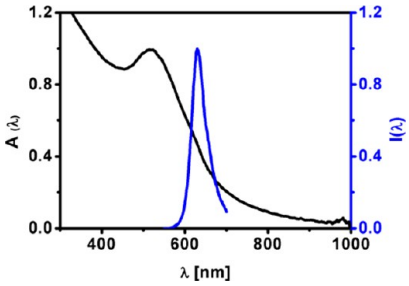

Figure 99. Normalized absorption spectrum $A(\lambda)$ (black solid line, cf. Figure 96) and emission spectrum $I(\lambda)$ (blue solid line) of hydrophilic Au NPs coated with PMA modified with cresyl violet (CV) ($d_c \approx$ 4 nm, cf. Section 1.2) as recorded in water. The absorption and emission peaks are at $\lambda_{abs} \approx$ 519 nm and $\lambda_{em} \approx$ 630 nm, respectively.

9.4. Determination of Quantum Yields. A major characteristic of fluorescent NPs is their quantum yield (Φ_F). This feature represents the ratio of the number of photons emitted through fluorescence to the number of absorbed photons. In other words, the quantum yield describes the probability that a photoexcited state gets relaxed by fluorescence rather than by another, nonradiative mechanism. As photons may be emitted in all directions, in principle, a 4π-detection geometry is required to detect absolute quantum yields.[148,149] Instead, often relative quantum yields are measured in standard 90° detection geometry. For this purpose fluorescence intensities of a dilution series of the sample (s) and a dilution series of a reference fluorophore (ref) with known absolute quantum yield Φ_{ref} are determined. From the slopes $\Delta I_{int}/\Delta A_\lambda$ of the integrated emission (I_{int}) versus absorption (A_λ) curves of the sample and the reference fluorophore, the absolute quantum yield of the NP sample can be calculated, cf. eq 45. A good description of this methodology is detailed by Horiba Jobin Yvon.[150,151]

$$\frac{\Phi_s}{\Phi_{ref}} = \frac{(\Delta I_{int}/\Delta A_\lambda)_s}{(\Delta I_{int}/\Delta A_\lambda)_s} \cdot \frac{{n_s}^2}{{n_{ref}}^2} \quad (45)$$

[Φ_s, Φ_{ref}], [$(\Delta I_{int}/\Delta A_\lambda)_s$, $(\Delta I_{int}/\Delta A_\lambda)_{ref}$], and [$n_s$, n_{ref}] refer to the quantum yield, slope of the integrated emission versus absorption curve, and refractive index of the sample and reference fluorophore, respectively. An example for determining the quantum yield of Au NPs with the attached fluorophore is provided in Figure 100.[115]

To demonstrate how to determine the quantum yield of NPs (Φ_{NP}), hydrophobic Au NPs ($d_c \approx$ 4 nm) were synthesized (cf. Section 1.2) and coated with PMA modified with $R_{dye/mon}$ = 2% tetramethylrhodamine 5-(and-6-) carboxamide cadaverine (TAMRA, no. AS-81506, Anaspec) (cf. Section 6). After their purification using gel electrophoresis (the process has been repeated twice) (cf. Section 7.4), the NPs were concentrated, washed with Milli-Q water, and filtered by passing them through a syringe membrane filter (0.22 μm pore size) (cf. Section 7.2). Cresyl violet perchlorate (CV) dissolved in

DOI: 10.1021/acs.chemmater.6b04738
Chem. Mater. 2017, 29, 399−461

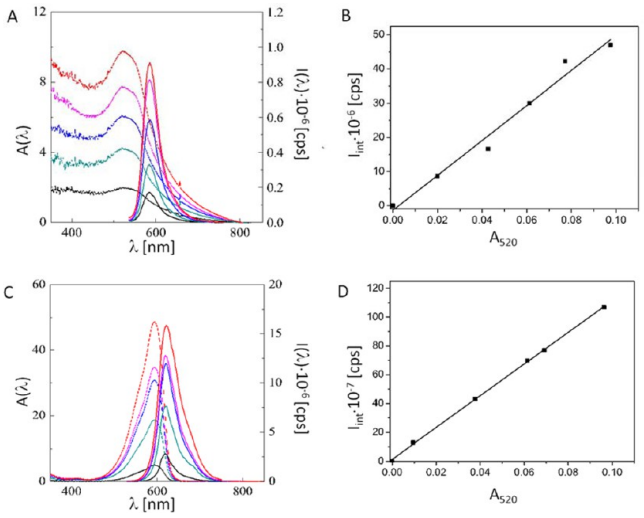

Figure 100. Determination of the quantum yield Φ_{NP} of TAMRA modified Au NPs (top row) and CV (bottom row). The graphs on the left side (A, C) represent the absorption spectra $A(\lambda)$ (dotted line, left y-axis) and emission spectra $I(\lambda)$ (full line, right y-axis) recorded at excitation wavelength λ_{exc} = 520 nm for dilution series of the Au NPs and CV. From each absorption spectrum the absorption A_{520} at 520 nm was determined. From each emission spectrum at 520 nm excitation, the integrated fluorescence intensity I_{int} was determined as the sum of all emitted fluorescence from 530 to 750 nm.

methanol was chosen as the reference dye with a known quantum yield Φ_{CVP} = 0.54 ± 0.03.[152]

To determine the quantum yield, first dilution series of both samples (NPs in water, CV in methanol) were generated. Dilution was quantified by measuring the absorption A_λ of the samples at the excitation wavelength λ_{exc} = 520 nm of TAMRA. Note that for the NP sample as for the reference dye absorption needs to be detected at the same wavelength. Ideally, the excitation wavelength of the reference dye should be similar to the fluorescent NP sample. The highest concentration of the absorption series should not exceed an optical density of 0.1, in order to avoid reabsorption and self-quenching of fluorescence, which may occur at high fluorophore concentrations. For each sample within the dilution series the integrated fluorescence emission I_{int} was determined (i.e., the intensity of the whole fluorescence peak was counted), using the excitation wavelength λ_{exc} at which the absorption A_λ had been determined before. All fluorescence emission measurements must be made with the same settings of the fluorometer. The recorded absorption $A(\lambda)$ and emission spectra $I(\lambda)$ of the dilution series are shown in Figure 100. From these curves the respective absorption A_{520} at λ_{exc} = 520 nm was determined. The integrated emission I_{int} was obtained as the sum of all fluorescence emission counts in the spectral range from 530 to 750 nm. The resulting $I_{int}(A_{520})$ curves show the linear relation between absorbance and integrated fluorescence intensity. From these graphs the slopes $\Delta I_{int}/\Delta A_{520}$ were derived. In the case of the NP and the CV sample (5.11 ± 10.4) × 10^8 cps and (110 ± 1.31) × 10^8 cps were obtained (cps = counts per second). In order to calculate the quantum yield of the NP sample according to eq 45, the refractive indexes n_{H2O} = 1.333 for water and $n_{methanol}$ = 1.3288 for methanol at 20 °C were used, yielding $\Phi_{NP} = \Phi_{CVP} \cdot \frac{(\Delta I_{int}/\Delta A_{520})_{NP}}{(\Delta I_{int}/\Delta A_{520})_{CV}} \cdot \frac{n_{H2O}^2}{n_{methanol}^2}$ = 0.025 ± 0.008. The error was estimated using Gaussian error propagation.

10. CHARACTERIZATION OF THE COLLOIDAL PROPERTIES OF THE NPs

10.1. UV/Vis Absorption Spectroscopy. The UV/vis absorption spectrum provides a fast and simple quality control measure for the colloidal stability of NPs. Several types of NPs, such as plasmonic NPs and QDs, possess characteristic peaks in their absorption spectrum (cf. Section 9.2) that can provide important information regarding size, shape, surface chemistry, and aggregation state. For example, aggregation of Au NPs is typically associated with a red shift of the SPR (λ_{SPR}) to higher wavelengths and a significant spectral broadening. Most isotropic inorganic NPs absorb in the UV/vis and not in the near IR, unless they have been designed for this purpose (e.g., rod-shaped Au NPs, Au nanostars, IR emitting QDs, etc.). Thus, absorption in the range where NPs do not typically absorb indicates NP aggregation. "Absorption" in this case is mainly light scattering due to NP agglomeration. Figure 101 shows the red shift and broadening of the plasmon absorption spectrum of Au NPs upon salt-induced aggregation.

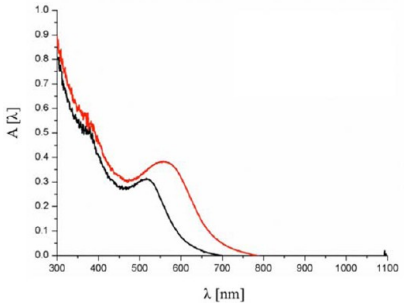

Figure 101. Absorption spectra of 5 nm core diameter Cit-Au NPs (purchased from BBI) as recorded in water (black curve) and in water supplemented with NaCl (red curve). The red shift of the SPR peak to higher wavelength and associated peak broadening is clear upon the addition of NaCl due to NP aggregation and plasmon coupling effect.

Colloidal stability is a critical property for NP dispersions, which can be maintained by ensuring repulsive force (either an electrostatic or a steric repulsion) that outweighs the attractive van der Waals forces between NPs.[5] For example, Cit-Au NPs are stabilized through electrostatic repulsion due to the presence of physically adsorbing citrate ions on the surface of Au NPs (zeta potentials of these NPs are typically negative ∼−30 mV). When salt is added, electrostatic forces are screened by counterion effects and electrostatic double layer compression, and thus NPs tend to aggregate. The higher the charge density of the NP surface, the less prone the NPs are to aggregation. Note that the surface charge of NPs may depend on the pH (cf. Section 10.4). NPs that are stabilized by steric repulsion are typically less prone to aggregation upon the addition of salt. In various biological applications, NPs are expected to be dosed into media with physiological salt levels (150 mM NaCl), and thus colloidal stability should be carefully evaluated.

By titrating the NP suspension against increasing concentrations of NaCl, one can observe the aggregation state by UV/vis absorption measurements. Such measurements in particular allow for observing the NaCl concentration at which the

DOI: 10.1021/acs.chemmater.6b04738
Chem. Mater. 2017, 29, 399−461

colloidal stability of the NPs is lost. Figures 102 and 103 show the colloidal stability of Au NPs or Ag NPs with different

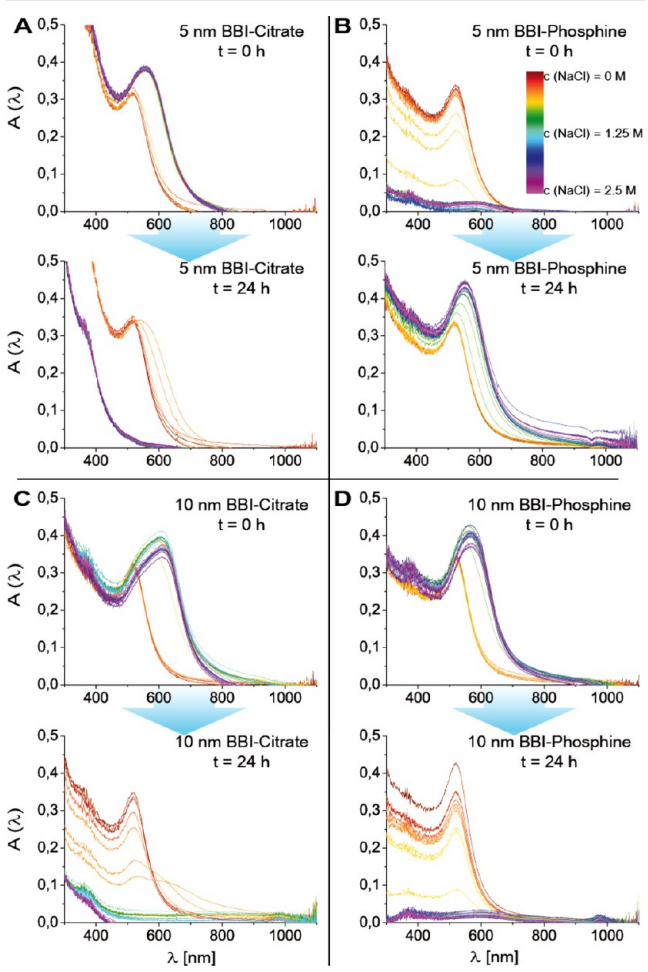

Figure 102. Absorption spectra recorded for different Au NPs in water in the presence of different concentrations of NaCl, recorded after 0 and 24 h, with $c_{NP} \approx 12$ nM. The NaCl concentrations were in the range of 0.0 to 2.5 M as illustrated using a color map. Cuvettes with freshly mixed solutions were measured at $t = 0$ h before incubating overnight at RT and measured again after $t = 24$ h. (A) ≈5 nm core diameter Cit-Au NPs purchased from BBI). (B) ≈5 nm core diameter Cit-Au NPs (purchased from BBI), after ligand exchange to bis(*p*-sulfonatophenyl)-phenylphosphine (cf. Section 3.2). (C) ≈10 nm core diameter Cit-Au NPs (purchased from BBI). (D) ≈10 nm core diameter Cit-Au NPs (purchased from BBI), after ligand exchange to bis(*p*-sulfonatophenyl)-phenylphosphine (cf. Section 3.2).

surface coatings, as judged by their UV/vis absorption spectra upon titration with NaCl aqueous solution. As agglomeration is time dependent, these measurements were carried out directly after exposure of the NPs to salt and were then repeated after 24 h. The absorption spectra were measured over a range of 300 to 1100 nm with an Agilent Technologies 8453 UV/vis spectrometer.

In most cases after 24 h the absorption peaks became broader and smaller. The increment in the peak width was due to agglomeration. The reduction in absorption intensity was due to the severe degree of aggregation that decreased the number of individually dispersed NPs due to the significant NP loss via precipitation out from the suspension. Collectively, data in Figures 102 and 103 suggest that PMA is superior to MPA and MUA in protecting NPs against salt-induced aggregation.

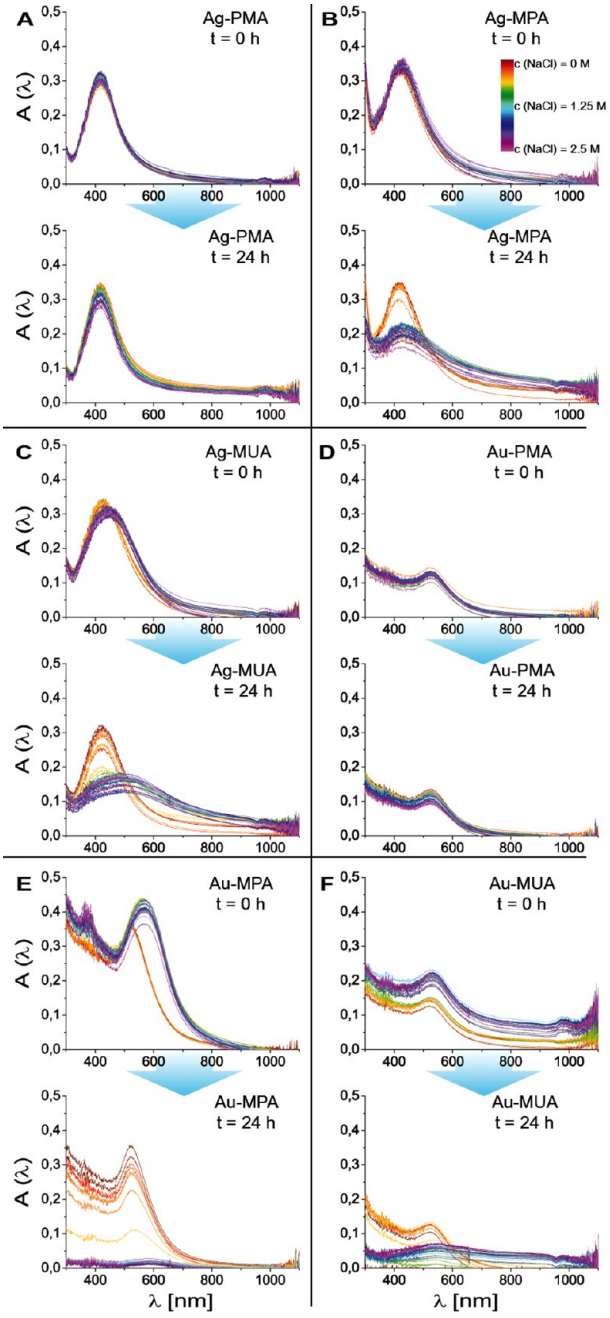

Figure 103. Absorption spectra of different NPs in water in the presence of different concentrations of NaCl recorded after 0 and 24 h, with $c_{NP} \approx 12$ nM. The NaCl concentrations were in the range of 0.0 to 2.5 M as illustrated using a color map. Cuvettes with freshly mixed solutions were measured at $t = 0$ h before incubating overnight at RT and measured again after $t = 24$ h. (A) ≈4 nm core diameter Ag NPs (cf. Section1.3) overcoated with PMA (cf. Section 6.3). (B) ≈4 nm core diameter Ag NPs (cf. Section 1.3) after ligand exchange with mercaptopropionic acid (MPA; cf. Section 5.2). (C) ≈4 nm core diameter Ag NPs (cf. Section 1.3) after ligand exchange with mercaptoundecanoic acid (MUA; cf. Section 5.2). (D) ≈4 nm core diameter Au NPs (cf. Section 1.2) overcoated with PMA (cf. Section 6.3). (E) ≈4 nm core diameter Au NPs (cf. Section 1.2) after ligand exchange with mercaptopropionic acid (MPA; cf. Section 5.2). (F) ≈4 nm core diameter Au NPs (cf. Section 1.2) after ligand exchange with mercaptoundecanoic acid (MUA; cf. Section 5.2).

10.2. Dynamic Light Scattering. There are several techniques available that are able to measure the hydrodynamic

DOI: 10.1021/acs.chemmater.6b04738
Chem. Mater. 2017, 29, 399−461

diameter d_h of NPs dispersed in solvent. Hydrodynamic diameters may differ for NPs with different core diameter d_c, capping agents/polymers, solvent, and aggregation state. For example, identical NPs with a PEG shell exhibit different d_h in water versus chloroform due to different hydration/solvation nature and polymer architecture on the NPs in each solvent. In another context, the addition of a high concentration of electrolyte to an aqueous suspension containing charged NPs may decrease the d_h of these NPs due to the counterion effect and thus a compressed electric double layer (Debye length).[153] In addition to measuring the average value of d_h, it is also important to determine the monodispersity of NP suspensions by measuring the so-called polydispersity index (PDI).[154] The PDI is an unitless parameter that measures the heterogeneity (statistical variation from the average value) in the NPs' hydrodynamic diameter in a sample. Values below 0.05 are normally not obtained, meanwhile values higher than 0.7 indicate that the sample has a very broad size distribution.

There are various techniques to measure hydrodynamic diameters of NPs.[94,155] Dynamic light scattering (DLS) is a simple, fast, and common technique to measure the hydrodynamic diameter of NPs and associated PDI.[156−158] DLS records the temporal fluctuations in scattered light, due to diffusion of NPs in solution. Using an autocorrelation function, the diffusion constant of the NPs then can be derived. By applying the Einstein−Stokes relation and using the measured diffusion constant value, the NPs' hydrodynamic diameter d_h can be calculated. Obtaining reliable size measurements of NPs of only a few nanometers in diameter using DLS is a real challenge, since the scattering signal from these small NPs is close to the noise of the detector.

It is worth mentioning that serious error in measuring the absolute size of NPs using DLS may occur and can originate from various reasons such as dirty cuvettes, contaminated solvent, using incorrect values for solvent physical parameters (e.g., viscosity and dielectric constant), improper sample concentration (too high or too low), and unstable samples during measurement. To avoid possible under- or overestimation of NP hydrodynamic size, an internal calibration with reference NPs is essential.

When carrying out DLS analysis, the obtained distributions of hydrodynamic diameters can be plotted in terms of the number of NPs $N(d_h)$ or the intensity of the scattered light $I(d_h)$ as shown in Figure 104. The intensity distribution $I(d_h)$ considers the scattering intensity of each NP fraction. Since larger NPs scatter much more than smaller NPs, the intensity distribution can provide overestimated values of hydrodynamic diameter. For example, a very low level of aggregates in a Au NP suspension will scatter extensively and thus will result in a resolved significant peak (second and third peaks in Figure 104A). Applying Mie's theory, the intensity distribution can be converted to volume or number distributions. To do so, there are several assumptions made, including that all NPs are spherical and homogeneous, which in the case of samples with broad size distribution and/or anisotropic NPs is not valid. In the number distribution, the contribution of large NP populations at low level is very minimal and does not dominate, and thus measured d_h values are closer to the d_c values as obtained by TEM. As an example, in Figure 104A, d_h obtained from the intensity distribution (first peak) is 26.07 ± 12.75 nm where d_h obtained from the number distribution in Figure 104B is 11.71 ± 3.29 nm, which is closer to the value obtained by TEM (d_c = 4.3 nm ± 0.4 nm as per Figure 64 plus the addition of the l_{ligand}; (see Figure 63B,C). Commercial DLS setups often assume the presence of several NP populations in solution, and thus fits of even one NP population may result in several distinct sizes. For example, in the intensity distribution shown in Figure 104 three peaks are observed, whereas there is only one peak in the number distribution. In fact, only one NP species is present in solution, and small agglomerates are overestimated in the intensity distribution, which then wrongfully identifies three discrete subspecies.

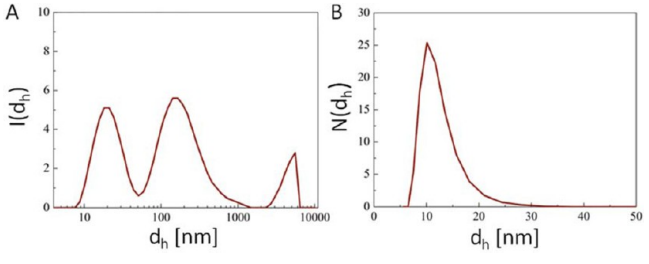

Figure 104. (A) DLS histograms of Au NPs of ≈4 nm coated with PMA measured in aqueous solution. (A) Intensity distribution $I(d_h)$ and (B) number distribution $N(d_h)$ of the hydrodynamic diameter d_h.

A significant increase in measured hydrodynamic diameter of NPs as compared to the structural diameter (i.e., $d_h \gg d_c$ for NPs without the presence of thick organic shell) is usually a strong indication of NP aggregation. In the case NPs are aggregated, the measured effective hydrodynamic diameter values describe the diameter of NP agglomerates rather than the diameter of the individual NPs. In Figure 105, aggregation

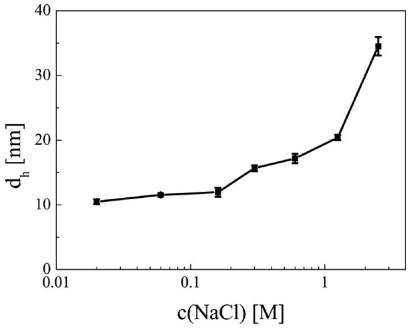

Figure 105. Hydrodynamic diameter (d_h) of 4 nm PMA-Au NPs as a function of NaCl concentration in the NP suspension.

of PMA-Au NPs upon the addition of NaCl is associated with an increase in d_h. Such measurement of hydrodynamic diameters is an essential tool to probe the colloidal stability of NPs in solution.

More examples on the salt-induced aggregation of Ag NPs and Au NPs with differing surface modification and core diameter are provided in Figure 106. Aqueous suspension of the NPs (1.0 mL; c_{NP} = 25 nM) received equal volume of NaCl (aq) (1.0 mL; concentration ranges from 0.0 to 5 M). Obviously the final NaCl concentration was hereby reduced to half of the original concentration upon mixing it with the same amount of NP stock solution. The hydrodynamic diameter d_h was measured immediately after mixing the two solutions and after a 24 h incubation time at RT (since aggregation is a time-dependent process that can be slow but significant). DLS histograms (d_h versus c_{NaCl}) and real photographs of NP suspensions in the cuvettes are shown in Figure 106, in which

DOI: 10.1021/acs.chemmater.6b04738
Chem. Mater. 2017, 29, 399−461

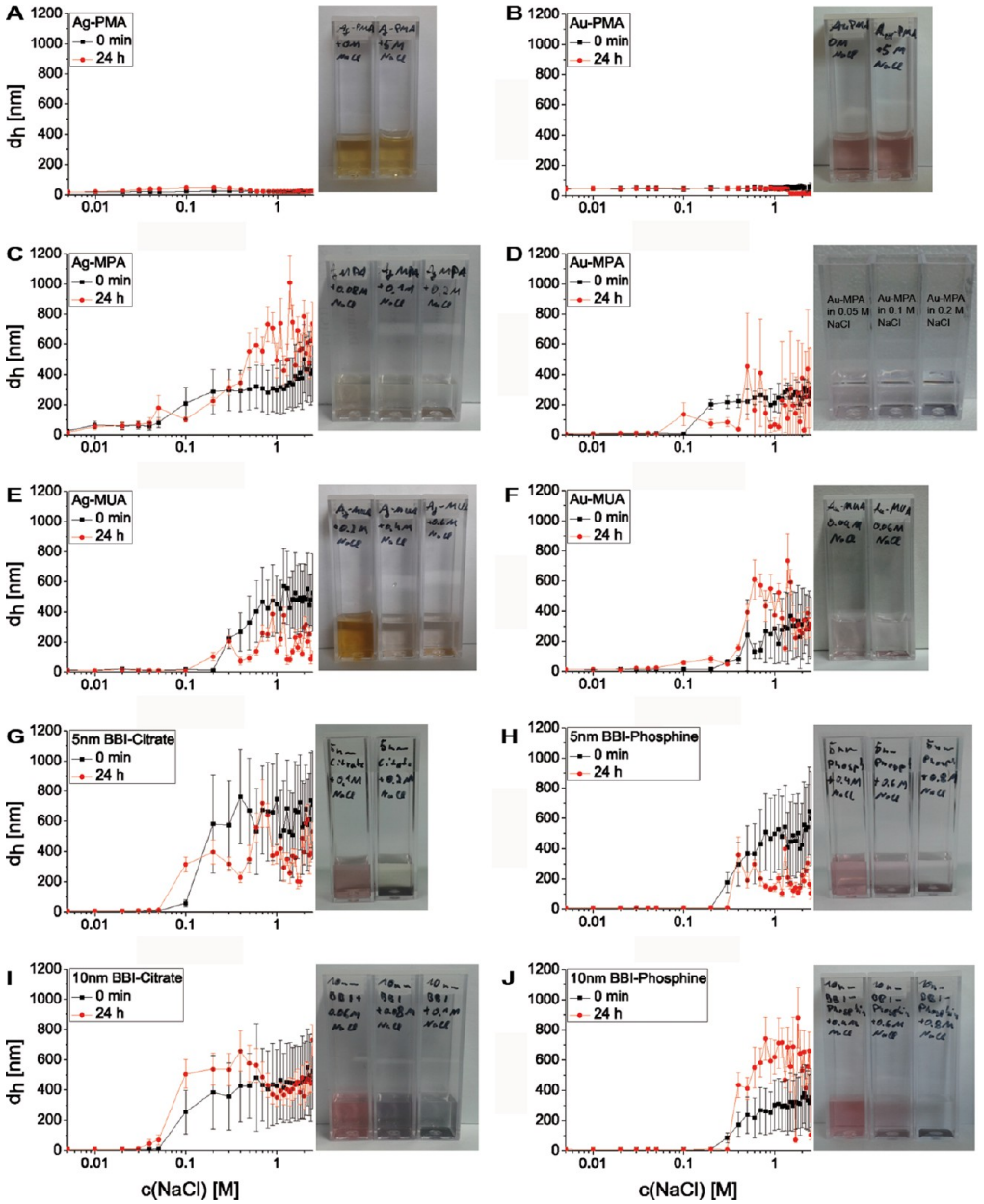

Figure 106. Ag NPs and Au NPs with differing surface modification and core diameter were exposed to different concentrations of NaCl. Hydrodynamic diameter values d_h in aqueous solution were measured directly (0 h; ■) and 24 h (●) after exposure. The behavior of the hydrodynamic diameter d_h is plotted against the NaCl concentration within a range from C_{NaCl} of 0.0 to 2.5 M. The NPs were suspended in Milli-Q water to reach a concentration of 25 nM. DLS measurements were done with a Malvern Zetasizer nano ZS. The cuvette photos represent the relevant concentrations within the range where agglomeration took place. (A) ≈4 nm core diameter Ag NPs (cf. Section 1.3) overcoated with PMA (cf. Section 6.3). (B) ≈4 nm core diameter Au NPs (cf. Section 1.2) overcoated with PMA (cf. Section 6.3). (C) ≈4 nm core diameter Ag NPs (cf. Section 1.3) after ligand exchange with MPA (cf. Section 5.2). (D) ≈4 nm core diameter Au NPs (cf. Section 1.2) after ligand exchange with mercaptopropionic acid (MPA; cf. Section 5.2). (E) ≈4 nm core diameter Ag NPs (cf. Section 1.3) after ligand exchange with MUA (cf. Section 5.2). (F) ≈ 4 nm core diameter Au NPs (cf. Section 1.2) after ligand exchange with MUA (cf. Section 5.2). (G) ≈5 nm core diameter Cit-Au NPs (purchased from BBI). (H) ≈5 nm core diameter citrate coated Au NPs (purchased from BBI), after ligand exchange to bis(*p*-sulfonatophenyl)-phenylphosphine (cf. Section 3.2). (I) ≈10 nm core diameter Cit-Au NPs (purchased from BBI). (J) ≈10 nm core diameter citrate coated Au NPs (purchased from BBI), after ligand exchange to bis(*p*-sulfonatophenyl)-phenylphosphine (cf. Section 3.2).

agglomeration can be directly observed by visible color change. In most cases aggregation of NPs at high NaCl concentrations was severe, inducing NP precipitation and sedimentation on the bottom of the cuvette. The results indicated that PMA is superior compared to MPA or MUA in protecting NPs against salt-induced aggregation. PMA coating resulted in constant hydrodynamic diameter values and suspension color even for high NaCl concentrations. Addition of NaCl to MPA or MUA coated NP resulted in increased hydrodynamic diameter values and change in suspension color, indicating NP aggregation.

Similar to NP aggregation upon salt addition, NP aggregation can be induced by changing the suspension pH. While salt screens the electric charge on the NP surface, pH may suppress ionization and thus decrease the effective surface charge density, resulting in NP aggregation (cf. Section 10.3 and Section 10.4). In Figure 107, examples on pH-induced NP

DOI: 10.1021/acs.chemmater.6b04738
Chem. Mater. 2017, 29, 399−461

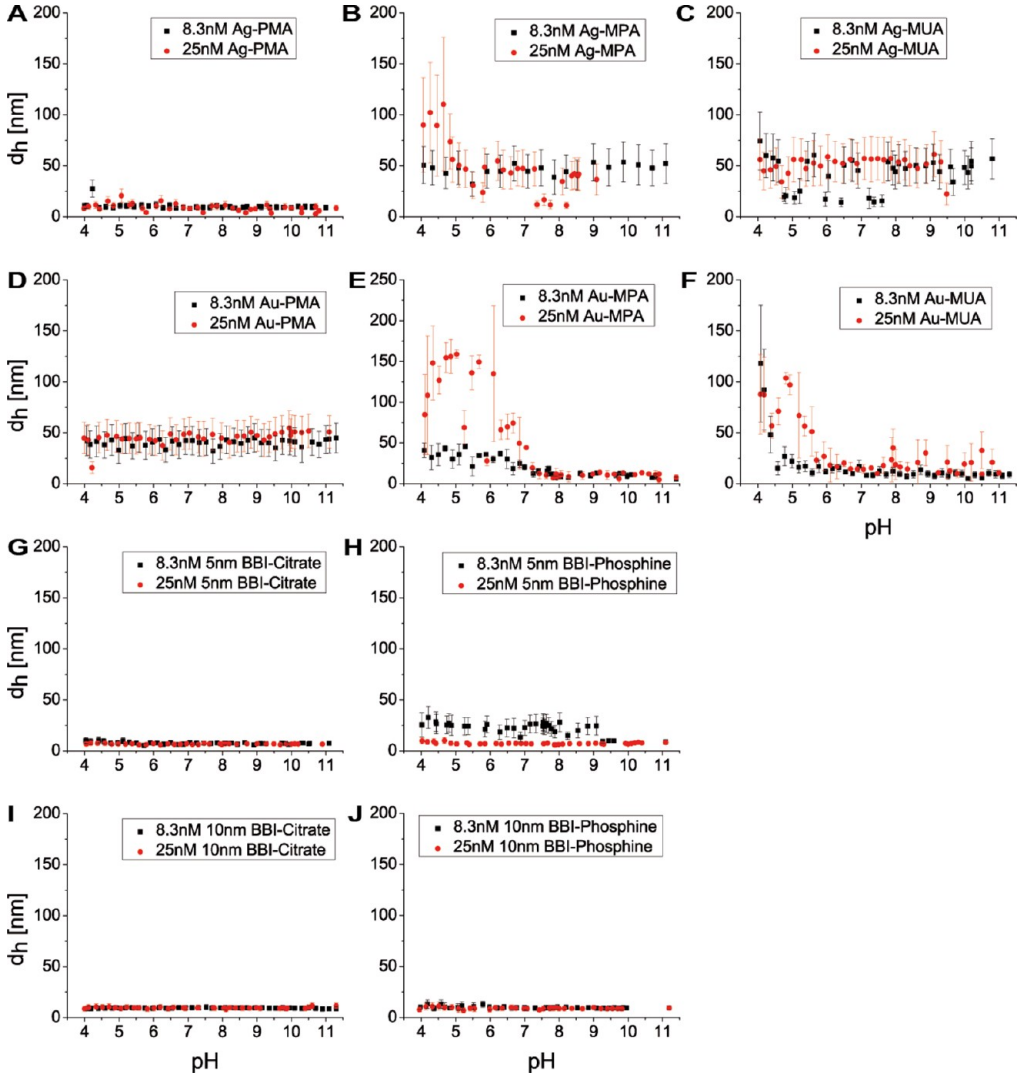

Figure 107. Titration of Ag and Au NPs suspended in 1.5 mM NaOH (aq) with a concentration of c_{NP} = 8.6 nM (■) and c_{NP} = 25 nM (●), with a total volume of 10 mL. HCl (aq) with a concentration of 12 mM was chosen as titrant and was added using a Malvern MPT-2 autotitrator within a pH range from 11 to 4. The hydrodynamic radius d_h is plotted against the pH to detect size-dependent changes and aggregation of the NPs. ≈4 nm core diameter Ag NPs (cf. Section 1.3) (A) overcoated with PMA (cf. Section 6.3), (B) after ligand exchange with MPA (cf. Section 5.2), and (C) after ligand exchange with MUA (cf. Section 5.2). ≈4 nm core diameter Au NPs (cf. Section 1.2) (D) overcoated with PMA (cf. Section 6.3) and (E) after ligand exchange with MPA (cf. Section 5.2). (F) After ligand exchange with MUA (cf. Section 5.2). ≈5 nm core diameter (G) Cit-Au NPs (purchased from BBI) and (H) after ligand exchange to bis(*p*-sulfonatophenyl)-phenylphosphine (cf. Section 3.2). ≈10 nm core diameter (I) Cit-Au NPs (purchased from BBI) and (J) after ligand exchange to bis(*p*-sulfonatophenyl)-phenylphosphine (cf. Section 3.2).

aggregation and the dependence of hydrodynamic diameter from solution pH for anionic charged NPs with different types of surface ligands are shown.

For NPs with ligands containing weak acids, such as carboxylate functional groups ($-COO^-$), the NP effective surface charge decreases at low pH (i.e., high concentration of H^+) due to protonation of the $-COO^-$ groups:

$$R{-}COOH \leftrightarrow R{-}COO^- + H^+ \tag{46}$$

This equilibrium is described by the pK_a value.

$$K_a = \frac{c(R{-}COO^-) \times c(H^+)}{c(R{-}COOH)} \tag{47}$$

$$pK_a = -\log(K_a) \tag{48}$$

Equations 47 and 48 can be combined with the Henderson–Hasselbalch equation:[159−163]

$$pK_a = -\log(K_a) = -\log\left(\frac{c(R{-}COO^-) \times c(H^+)}{c(R{-}COOH)}\right)$$
$$= -\log\left(\frac{c(R{-}COO^-)}{c(R{-}COOH)}\right) - \log(c(H^+))$$
$$= -\log\left(\frac{c(R{-}COO^-)}{c(R{-}COOH)}\right) + pH$$

leading to

$$pH = pK_a + \log\frac{c(R{-}COO^-)}{c(R{-}COOH)} \tag{49}$$

One can thus predict the percent of ionization (J_{R-COO^-}) at certain pH for weak acid as follows:

DOI: 10.1021/acs.chemmater.6b04738
Chem. Mater. 2017, 29, 399−461

$$J_{R-COO^-} = \frac{c(R-COO^-)}{c(R-COOH) + c(R-COO^-)} = \frac{1}{\frac{c(R-COOH)}{c(R-COO^-)} + 1} = \frac{1}{1 + \left(\frac{c(R-COO^-)}{c(R-COOH)}\right)^{-1}} = \frac{1}{1 + (10^{pH-pK_a})^{-1}}$$

leading to

$$J_{R-COO^-} = \frac{100\%}{1 + 10^{pK_a - pH}} \quad (50)$$

Thus, by increasing the NP suspension's pH, the denominator in eq 50 decreases and thus the percent ionized as well as the anionic surface charge density of the NP increases. Instead, by decreasing the NP suspension's pH, the denominator in eq 50 increases, and thus the anionic surface charge density of the NPs decreases. In the latter case, vanishing electrostatic repulsion between NPs induces NP aggregation and increases their effective hydrodynamic diameter at high pH values (cf. Section 10.4).

For NPs with ligands containing weak basic functional groups (e.g., R-NH_3), the NP effective surface charge increases at low pH (i.e., high concentration of H^+) due to protonation of the amine groups:

$$R-NH_4^+ \leftrightarrow R-NH_3 + H^+ \quad (51)$$

This equilibrium is described by the pK_a value.

$$K_a = \frac{c(R-NH_3) \times c(H^+)}{c(R-NH_4^+)} \quad (52)$$

$$pK_a = -\log(K_a) \quad (53)$$

This leads to the Henderson−Hasselbalch equation:

$$pH = pK_a + \log \frac{c(R-NH_3)}{c(R-NH_4^+)} \quad (54)$$

Again, one can predict the percentage of unionization (J_{R-NH_3}) at certain pH values for a weak base as follows:

$$J_{R-NH_3} = \frac{c(R-NH_3)}{c(R-NH_4^+) + c(R-NH_3)} = \frac{100\%}{1 + 10^{pK_a - pH}} \quad (55)$$

Thus, by lowering the pH of suspension containing NPs with a basic functional group, the denominator in eq 55 increases and thus the percent of un-ionized amines decreases (i.e., the ionization and cationic surface charge density of NP increases). Instead, increasing the NP suspension pH, the denominator in eq 55 decreases, and thus the percent un-ionized increases (ionization and cationic surface charge density of NP decreases). In the latter case, vanishing electrostatic repulsion between NPs induces NP aggregation and increases their effective hydrodynamic diameter at high pH values (cf. Section 10.4). There are also charged groups whose charge is independent from the pH. For ammonium salts such as *N*,*N*,*N*-trimethylammonium-2-ethyl methacrylate iodide there is full dissociation, leading to permanent positive surface charges.[114,115]

In Figure 107 the dependence of the hydrodynamic diameter of different negatively charged NPs on the pH of the solution is shown. For this the hydrodynamic diameter d_h of NPs was measured with DLS during a titration with HCl (aq). The NPs were suspended in 1.5 mM NaOH (aq), setting a total volume of 10 mL and concentrations of c_{NP} = 8.3 or 25 nM. The titrant was aqueous HCl with a concentration of 12 mM. HCl was added using a Malvern MPT-2 autotitrator and the hydrodynamic diameter was measured with a Malvern Zetasizer nano ZS DLS setup.

10.3. Laser Doppler Anemometry. As pointed out in Section 10.1 and Section 10.2, the surface charge of colloidal NPs provides colloidal stability due to electrostatic repulsion forces. Effective surface charge depends on many variables such as solvent type and its pH. In the case of NPs with known surface chemistry and geometry, titration curves (cf. Section 10.4) can be used to estimate the number of charged groups on the surface of a single NP. Alternatively, and most commonly used, the so-called zeta-potential ζ[156,157,164] of the NPs can be measured. The zeta-potential describes the electric potential of the NPs at the distance of the electrostatic screening length (which depends on the ionic strength of the aqueous solution). While in principle electric potential and electric charge are coupled via the Poisson−Boltzmann equation, the complicated geometry of NPs with inorganic core, organic shell, and adsorbed counterions, in general, does not allow for deriving the surface charge from the zeta-potential. However, the sign of the surface charge can be concluded from the sign of the measured zeta-potential. In addition, the magnitude of the zeta-potential provides a good indicator of the NP colloidal stability. Generally, zeta-potential values $|\zeta| > 20-30$ mV are required to maintain colloidal stability and prevent NP aggregation.

One way to measure zeta-potentials is laser Doppler anemometry (LDA). An electric field is applied and the velocity of charged NPs in this field is detected via the Doppler effect. From this the electrophoretic mobility, defined as the quotient of the drift velocity and the applied electric field, can be calculated. By using different models from electrophoretic mobility the zeta-potential can be estimated.[157] Often DLS and LDA are combined in the same setup, such as in the Zetasizer from Malvern. Note that for LDA special cuvettes are required, which comprise electrodes to apply the electric field. Note also that during measurements NP suspensions must cover these electrodes, and thus before measurement it has to be made sure that electrodes are functional, and if required the cuvette needs to be changed. In Figure 108 the distribution of the zeta-potential is shown for PMA-Au NPs. The zeta-potential is then taken as the mean value from the distribution function.

In Figure 109 results for zeta-potential measurements for Au and Ag NPs with different surface coatings at different pH values are shown. Due to the coupled system of an autotitrator and a Zetasizer, it was possible to use the same cuvette for d_h (DLS, cf. Section 10.2) and zeta potential (LDA) measurements before adding more acid and pursue the titration (i.e., lowering of the pH). Thus, the NP concentrations and volumes of added acid are the same as those shown in Section 10.2, as DLS and LDA measurements were performed simultaneously. The data indicate that according to eq 46 at low pH values the negatively charged $-COO^-$ groups get protonated, the zeta-potential thus becomes less negative, and thus the colloidal stability of the NPs is decreased.

10.4. pH Titration. Acid−base titration is a well-established chemical method in which pH is measured as a function of the amount of added acid or base. The resulting plot is called the titration curve, which can be used to determine the pK_a of the

DOI: 10.1021/acs.chemmater.6b04738
Chem. Mater. 2017, 29, 399−461

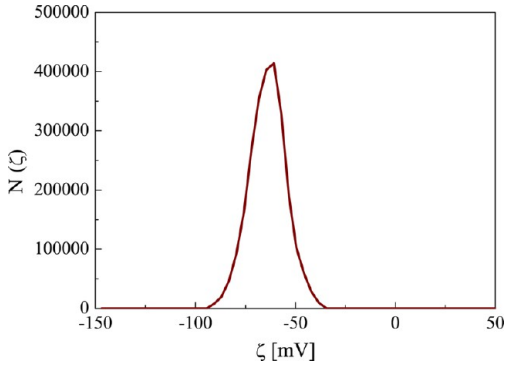

Figure 108. Distribution $N(\zeta)$ of the zeta-potential ζ as measured in water from a sample of ≈4 nm core diameter PMA-Au NPs with c_{NP}= 10 nM. The obtained mean value for the zeta potential is −48.07 ± 1.16 mV.

NPs and, more importantly, the surface density of acidic or basic ligands. Here, the principle is demonstrated for NPs with −COOH groups present on their surface. In order to determine titration curves over a large spectrum and to guarantee fully deprotonated carboxylic moieties, the NPs were first diluted in NaOH (aq) (pH = 11). The basic NP suspension was then titrated using HCl (aq) (cf. Figure 110). First, added H^+ (from HCl) can react with free OH^- (from NaOH) in suspension. This leads to the first plateau followed by the first steep drop and equivalent point (ep_1 in Figure 110). Upon consumption of all free OH^- ions, the carboxylates present on the NP surface become protonated, resulting in the second plateau (buffer plateau). Further addition of HCl leads to the second steep drop and equivalent point (ep_2 in Figure 110). Further addition of HCl leads to the third plateau at low pH. To determine the pK_a the pH value of the halfway point of the second plateau needs to be considered (∼7 in this case). In

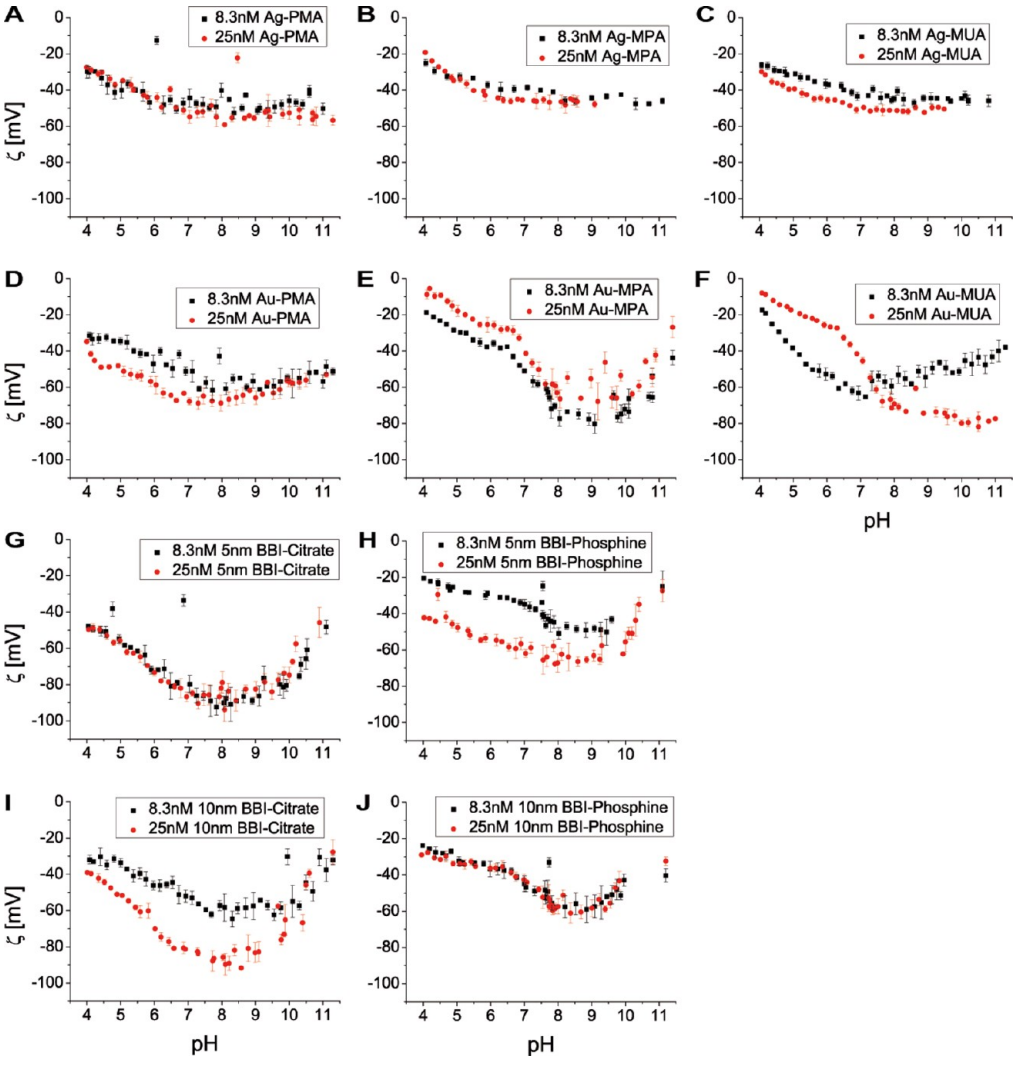

Figure 109. Titration of Ag and Au NPs suspended in 1.5 mM NaOH (aq) with a concentration of c_{NP} = 8.6 nM (■) and c_{NP} = 25 nM (●), with a total volume of 10 mL. HCl (aq) with a concentration of 12 mM was chosen as titrand and was added using a Malvern MPT-2 autotitrator within a pH range from 11 to 4. The zeta-potential ζ is plotted against the pH. These measurements were done simultaneously to the DLS measurements shown in Figure 107. ≈4 nm core diameter Ag NPs (cf. Section 1.3) (A) overcoated with PMA (cf. Section 6.3), (B) after ligand exchange with MPA (cf. Section 5.2), and (C) after ligand exchange with MUA (cf. Section 5.2). ≈4 nm core diameter Au NPs (cf. Section 1.2) (D) overcoated with PMA (cf. Section 6.3), (E) after ligand exchange with MPA (cf. Section 5.2), and (F) after ligand exchange with MUA (cf. Section 5.2). ≈5 nm core diameter (G) Cit-Au NPs (purchased from BBI) and (H) after ligand exchange to bis(*p*-sulfonatophenyl)-phenylphosphine (cf. Section 3.2). ≈10 nm core diameter (I) Cit-Au NPs (purchased from BBI) and (J) after ligand exchange to bis(*p*-sulfonatophenyl)-phenylphosphine (cf. Section 3.2).

DOI: 10.1021/acs.chemmater.6b04738
Chem. Mater. 2017, 29, 399−461

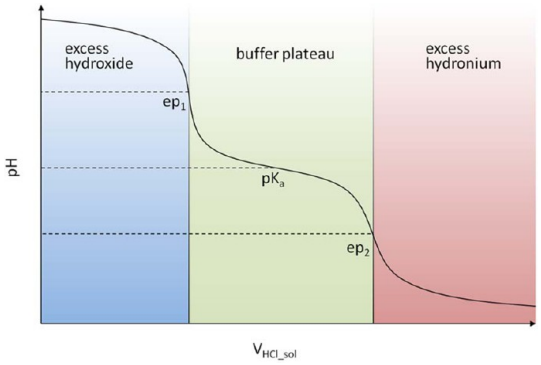

Figure 110. Illustrative titration curve of carboxylate stabilized NPs suspended in NaOH (aq) with the original volume V_{NaOH_sol} against HCl (aq), of which the volume V_{HCl_sol} has been added. The figure is adapted and modified with permission from Charron et al.[61] Copyright 2012 American Chemical Society.

this experiment, NPs were suspended in aqueous NaOH solution (1.5 mM, V_{NaOH_sol} = 10 mL) to a concentration of c_{NP} = 8.6 nM. HCl solution (2.5 mM) was added in 100 μL steps to the vigorously stirring NP suspension using the Malvern MPT-2 autotitrator. The resulting volume of the solution is V_{sol} = V_{NaOH_sol} + V_{HC_sol}. After the addition of each volume of acid the solution was given 5 s to equilibrate, and then the pH was measured using a Sartorius (PP 50) pH meter. The experiments were repeated after 24 h to confirm the data and ensure reproducibility. The pK_a value of the NPs was found to be around ≈7 as per the titration curve in Figure 110. By adding more acid the charged groups became saturated with protons, until the pH led to aggregation of the NPs at a pH of around 4−5 due to the loss of surface charge. Examples of titration curves with determined pK_a values for various NPs with different surface chemistries are shown in Figure 111.

If the concentration of NPs (c_{NP}) is known, the number of carboxyl groups on the surface of a single NP can be estimated as described by Charron et al.[61] For example, from Figure 111, the volume of HCl (ΔV_{HCl_sol}) used to protonate R−COO$^-$ on the surface of the NPs can be determined as the length of the buffer plateau.

$$\Delta V_{HCl\_sol} = V_{HCl\_sol}(ep_2) - V_{HCl\_sol}(ep_1) \quad (56)$$

Since the concentration of HCl (c_{HCl}) and the volume of initial NP suspension (V_{NP_sol} = V_{NaOH_sol}) are known, the concentration of all carboxylate ions on NPs (c_{R-COO^-}) can be calculated as follows:

$$c_{R-COO^-} \times V_{NP\_sol} = c_{HCl} \times \Delta V_{HCl\_sol} \quad (57)$$

The number of acid groups per NP ($N_{R-COO^-/NP}$) thus should be

$$N_{R-COO^-/NP} = \frac{c_{R-COO^-}}{c_{NP}} \quad (58)$$

In the case of PMA-coated NPs, $N_{R-COO^-/NP}$ can be compared with $N_{P/NP}$ as described in Section 8.6. Each polymer monomer unit in a fully deprotonated state bears one or two negative charges, in the case the PMA backbone is linked to a side chain or hydrolyses, respectively.[114]

$$N_{R-COO^-/NP} = (2 - R_{chain/mon}) \times N_{P/NP} \quad (59)$$

While in Figure 111D the second equivalence point is not in the measured pH range, roughly ΔV_{HCl_sol} ≈ 2 mL. With c_{HCl} = 2.5 mM, c_{NP} = 8.6 nM, and V_{NP_sol} = V_{NaOH_sol} = 10 mL (cf. Figure 111), this leads to $N_{R-COO^-/NP}$ = $((c_{HCl} \times \Delta V_{HCl\_sol})/V_{NP\_sol})/c_{NP}$ = $((2.5 \times 10^{-3}$ M × 2 mL)/10 mL)/ 8.6×10^{-9} M ≈ 58 000. In Section 8.6 TGA analysis of similar PMA-Au NPs (ca. 4 nm core diameter) yielded $N_{P/NP}$ = 270. Thus, with $R_{chain/mon}$ = 0.75, this leads to $N_{R-COO^-/NP}$ = $(2 - R_{chain/mon}) \times N_{P/NP}$ = (2 − 0.75) × 270 ≈ 338. The discrepancy in values can be explained by the different degrees of purification. While the PMA-Au NPs in the case of TGA analysis had been purified by ultracentrifugation ($N_{R-COO^-/NP}$ = 338), the PMA-Au NPs in the case of titration analysis ($N_{R-COO^-/NP}$ = 58 000) had been purified by gel electrophoresis only, which may result in some remaining polymer micelles, which contribute to the amount of COO$^-$ groups. These number examples point out again the necessity of applying different characterization techniques.

CONCLUSIONS

Synthetic protocols in this contribution described the preparation of hydrophobic NPs of different types (Au, Ag, FePt, Fe_3O_4, Sn, CdSe, and CdSe/ZnS). Moreover, preparation of hydrophilic Au and Ag NPs of various shapes (spheres, rods, stars) and sizes (5−100 nm) are detailed. The prepared NPs showed good monodispersity as evident from the corresponding TEM analysis. Surface functionalization strategies including ligand exchange and polymer overcoating were employed on selected NPs to control their hydrophobicity, hydrophilicity, and colloidal stability. For example, ligand exchange on citrated-capped Au NPs with alkylamine induced phase transfer from water to chloroform. On the other hand, ligand exchange on alkanethiol-capped gold NPs with 3-mercaptopropionic acid molecules facilitated the phase transfer of these NPs into aqueous phase from chloroform. Similarly, a carefully designed amphiphilic polymer was capable of overcoating alkanethiol-capped Au NPs and rendering their surface hydrophilic, allowing facile transfer into aqueous phase from chloroform.

Purification of one type of NPs (namely, PMA-*g*-dodecyl-capped Au NPs ≈ 4 nm diameter, cf. Section 1.2, Section 6.3) was evaluated using various methods: syringe filtration, ultracentrifugation, size exclusion chromatography, and gel electrophoresis. These results showed different purity levels for different purification methods (for example, ultracentrifugation resulted in fewer free polymer micelles as compared to gel electrophoresis), highlighting the importance of optimizing the purification process for a specific synthesis.

Various characterization techniques confirmed the ability to probe the structural, photophysical, and colloidal properties of NPs. For example, visualization of PEG-capped Au NPs with TEM coupled to negative staining confirmed the NP core dimension and, more importantly, a well-defined polymeric shell surrounding each NP. Thermogravimetric analysis of dodecanethiol-capped Au NPs confirmed the presence of the organic shell on NPs and allowed for quantifying its weight percentage per NP. FTIR and NMR analysis confirmed overcoating of dodecanethiol-capped Au NPs with PMA polymer, highlighting the importance of these analytical techniques to follow surface functionalization of NPs. UV/vis absorption was employed successfully to quantify the concentration of Au NPs, to follow their salt- or pH-induced aggregation by monitoring the plasmon peak shift and broadening and to quantify the loaded dye per single NP. Finally, effective surface charge analysis as measured by laser Doppler anemometry upon acid−base titration allowed for the

DOI: 10.1021/acs.chemmater.6b04738
Chem. Mater. 2017, 29, 399−461

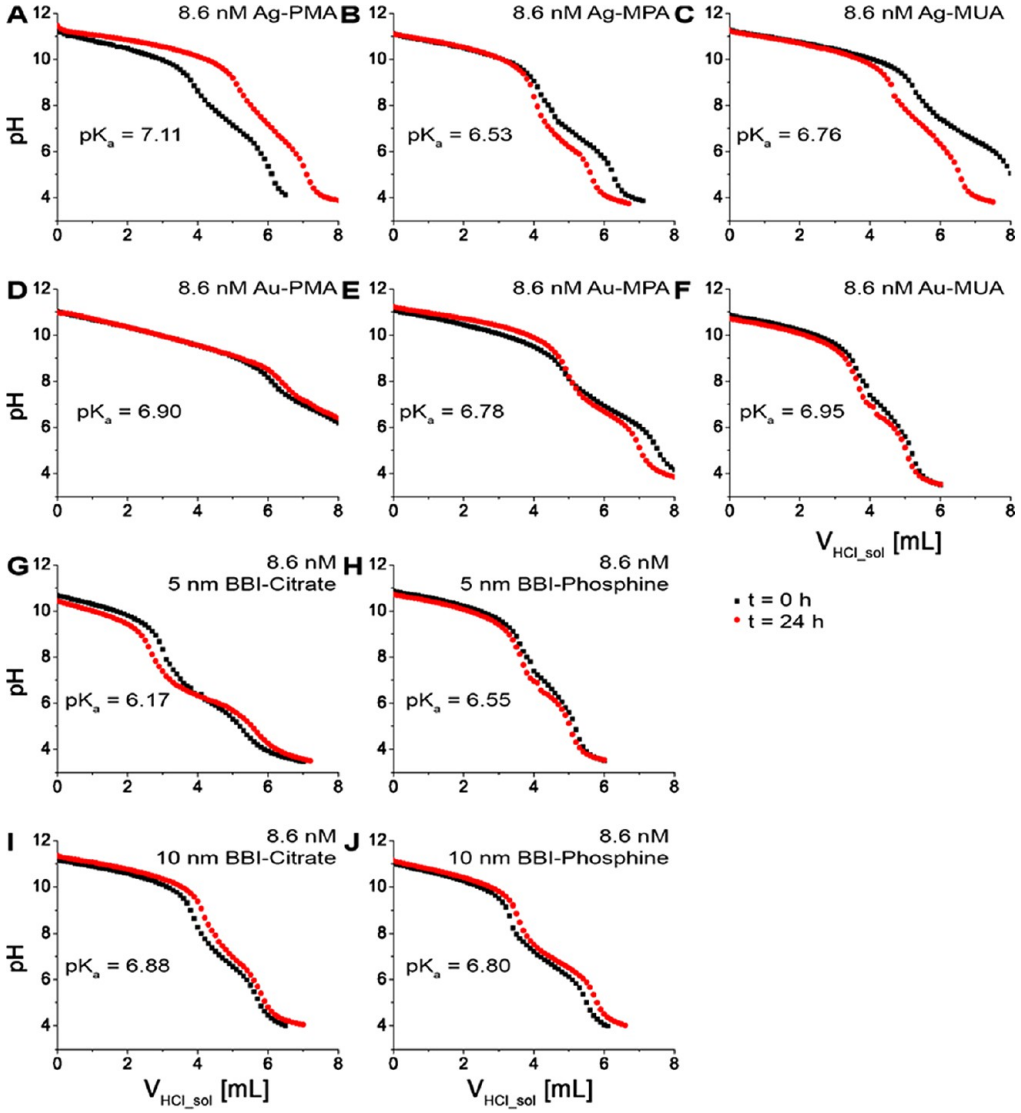

Figure 111. pH titration of Ag and Au NPs with different surface chemistries originally suspended in 1.5 mM NaOH (aq) with a concentration of c_{NP} = 8.6 nM and a total volume of V_{NaOH_sol} = 10 mL. HCl (aq) with a concentration of 2.5 mM was chosen as titrand and was added in steps of ΔV_{HCl_sol} = 100 μL to the NP suspension under vigorous stirring. After the first titration at t = 0 h (■) the experiments were repeated at t = 24 h (●). The NP samples are the same as those used in Figure 107 and Figure 109: ≈4 nm core diameter Ag NPs (cf. Section 1.3) (A) overcoated with PMA (cf. Section 6.3), (B) after ligand exchange with MPA (cf. Section 5.2), and (C) after ligand exchange with MUA (cf. Section 5.2). ≈4 nm core diameter Au NPs (cf. Section 1.2) (D) overcoated with PMA (cf. Section 6.3), (E) after ligand exchange with MPA (cf. Section 5.2), and (F) after ligand exchange with MUA (cf. Section 5.2). ≈5 nm core diameter Au NPs (G) citrate coated (purchased from BBI) and (H) after ligand exchange to bis(*p*-sulfonatophenyl)-phenylphosphine (cf. Section 3.2). ≈10 nm core diameter Au NPs (I) citrate coated (purchased from BBI) and (J) after ligand exchange to bis(*p*-sulfonatophenyl)-phenylphosphine (cf. Section 3.2).

determination of the acidity/basicity, pK_a, and number of acidic or basic groups on a single PMA-*g*-dodecyl-capped Au NP.

On purpose discrepancies in quantitative results as obtained with different characterization techniques are presented. In fact, different characterization techniques analyzed different parameters, and to relate them idealized models, like the sketches in Figure 47, have to be used. Also the degree of purity plays a major role in quantitative analysis.

To the end there is no "optimum" characterization technique. In this contribution an overview was presented about the characterization techniques routinely used in one selected laboratory and which quantitative information can be obtained from them. Collectively, the described details in this contribution should shed light on important corners in the field of inorganic NP synthesis, characterization, and surface functionalization.

■ ASSOCIATED CONTENT

Supporting Information

The Supporting Information is available free of charge on the ACS Publications website at DOI: 10.1021/acs.chemmater.6b04738.

List of symbols used (PDF)

■ AUTHOR INFORMATION

Corresponding Author

*(W.J.P.) E-mail: wolfgang.parak@physik.uni-marburg.de.

DOI: 10.1021/acs.chemmater.6b04738
Chem. Mater. 2017, 29, 399−461

ORCID

Pablo del Pino: 0000-0003-1318-6839
Wolfgang J. Parak: 0000-0003-1672-6650

Notes

The authors declare no competing financial interest.

■ ACKNOWLEDGMENTS

This work was supported by the German Research Foundation (DFG Grant PA 794/25-1) and by the European Commission (Project FutureNanoNeeds). C.C.-C. acknowledges the Spanish Ministerio de Economía y Competitividad for a Juan de la Cierva—Incorporación contract. A.E. acknowledges Junta de Andalucía (Spain) for a Talentia Postdoc Fellowship, cofinanced by the European Union Seventh Framework Programme, Grant Agreement No. 267226. M.C. acknowledges Ikerbasque for a Research Fellow position. N.F. acknowledges support funding from the Swedish Governmental Agency for Innovation Systems (Vinnova). I.C. acknowledges the Alexander Von Humboldt Foundation for postdoctoral fellowship. M.G.S. acknowledges funding from Fazit Stiftung. L.Z. acknowledges funding from Chinese Scholarship Council (CSC).

■ REFERENCES

(1) Parak, W. J. Complex Colloidal Assembly. *Science* **2011**, *334*, 1359−1360.
(2) Frens, G. Controlled Nucleation for Regulation of Particle-Size in Monodisperse Gold Solutions. *Nature, Phys. Sci.* **1973**, *241* (105), 20−22.
(3) Bastus, N. G.; Comenge, J.; Puntes, V. Kinetically Controlled Seeded Growth Synthesis of Citrate-Stabilized Gold Nanoparticles of up to 200 nm: Size Focusing versus Ostwald Ripening. *Langmuir* **2011**, *27* (17), 11098−11105.
(4) Bastus, N. G.; Merkoci, F.; Piella, J.; Puntes, V. Synthesis of Highly Monodisperse Citrate-Stabilized Silver Nanoparticles of up to 200 nm: Kinetic Control and Catalytic Properties. *Chem. Mater.* **2014**, *26* (9), 2836−2846.
(5) Pellegrino, T.; Kudera, S.; Liedl, T.; Javier, A. M.; Manna, L.; Parak, W. J. On the Development of Colloidal Nanoparticles towards Multifunctional Structures and their Possible Use for Biological Applications. *Small* **2005**, *1* (1), 48−63.
(6) Sperling, R. A.; Parak, W. J. Surface modification, functionalization and bioconjugation of colloidal inorganic nanoparticles. *Philos. Trans. R. Soc., A* **2010**, *368* (1915), 1333−1383.
(7) Montenegro, J.-M.; Grazu, V.; Sukhanova, A.; Agarwal, S.; de la Fuente, J. M.; Nabiev, I.; Greiner, A.; Parak, W. J. Controlled antibody/(bio-) conjugation of inorganic nanoparticles for targeted delivery. *Adv. Drug Delivery Rev.* **2013**, *65*, 677−688.
(8) Alkilany, A.; Murphy, C. Toxicity and cellular uptake of gold nanoparticles: what we have learned so far? *J. Nanopart. Res.* **2010**, *12* (7), 2313−2333.
(9) Brust, M.; Walker, M.; Bethell, D.; Schiffrin, D. J.; Whyman, R. Synthesis of Thiol-Derivatized Gold Nanoparticles in a 2-Phase Liquid-Liquid System. *J. Chem. Soc., Chem. Commun.* **1994**, No. 7, 801−802.
(10) Lin, C.-A. J.; Sperling, R. A.; Li, J. K.; Yang, T.-Y.; Li, P.-Y.; Zanella, M.; Chang, W. H.; Parak, W. J. Design of an Amphiphilic Polymer for Nanoparticle Coating and Functionalization. *Small* **2008**, *4* (3), 334−341.
(11) Yin, Y.; Alivisatos, A. P. Colloidal nanocrystal synthesis and the organic-inorganic interface. *Nature* **2005**, *437* (7059), 664.
(12) Viswanatha, R.; Santra, P. K.; Dasgupta, C.; Sarma, D. D. Growth mechanism of nanocrystals in solution: ZnO, a case study. *Phys. Rev. Lett.* **2007**, *98* (25), 255501.
(13) Thanh, N. T. K.; Maclean, N.; Mahiddine, S. Mechanisms of Nucleation and Growth of Nanoparticles in Solution. *Chem. Rev.* **2014**, *114* (15), 7610−7630.
(14) Pensa, E.; Cortés, E.; Corthey, G.; Carro, P.; Vericat, C.; Fonticelli, M. H.; Benítez, G.; Rubert, A. A.; Salvarezza, R. C. The Chemistry of the Sulfur−Gold Interface: In Search of a Unified Model. *Acc. Chem. Res.* **2012**, *45*, 1183−1192.
(15) Häkkinen, H. The gold−sulfur interface at the nanoscale. *Nat. Chem.* **2012**, *4*, 443−455.
(16) Fink, J.; Kiely, C. J.; Bethell, D.; Schiffrin, D. J. Self-Organization of Nanosized Gold Particles. *Chem. Mater.* **1998**, *10* (3), 922−926.
(17) Sperling, R. A.; Pellegrino, T.; Li, J. K.; Chang, W. H.; Parak, W. J. Electrophoretic Separation of Nanoparticles with a Discrete Number of Functional Groups. *Adv. Funct. Mater.* **2006**, *16* (7), 943−948.
(18) Ansar, S. M.; Mohammed, F. S.; von White, G., II; Budi, M.; Powell, K. C.; Mefford, O. T.; Kitchens, C. L. Effect of Postsynthesis Purifications on Gold and Silver Nanoparticle Ligand Coverage. *J. Phys. Chem. C* **2016**, *120*, 6842−6850.
(19) Jana, N. R.; Peng, X. Single-Phase and Gram-Scale Routes toward Nearly Monodisperse Au and Other Noble Metal Nanocrystals. *J. Am. Chem. Soc.* **2003**, *125* (47), 14280−14281.
(20) Sun, Y. Controlled synthesis of colloidal silver nanoparticles in organic solutions: empirical rules for nucleation engineering. *Chem. Soc. Rev.* **2013**, *42* (7), 2497−2511.
(21) Mari, A.; Imperatori, P.; Marchegiani, G.; Pilloni, L.; Mezzi, A.; Kaciulis, S.; Cannas, C.; Meneghini, C.; Mobilio, S.; Suber, L. High yield synthesis of pure alkanethiolate-capped silver nanoparticles. *Langmuir* **2010**, *26* (19), 15561−15566.
(22) Sun, S.; Murray, C. B.; Weller, D.; Folks, L.; Moser, A. Monodisperse FePt Nanoparticles and Ferromagnetic FePt Nanocrystal Superlattices. *Science* **2000**, *287*, 1989−1992.
(23) Sun, S.; Zeng, H.; Robinson, D. B.; Raoux, S.; Rice, P. M.; Wang, S. X.; Li, G. Monodisperse MFe_2O_4 (M = Fe, Co, Mn) Nanoparticles. *J. Am. Chem. Soc.* **2004**, *126* (1), 273−279.
(24) Kravchyk, K.; Protesescu, L.; Bodnarchuk, M. I.; Krumeich, F.; Yarema, M.; Walter, M.; Guntlin, C.; Kovalenko, M. V. Monodisperse and inorganically capped Sn and Sn/SnO2 nanocrystals for high-performance Li-ion battery anodes. *J. Am. Chem. Soc.* **2013**, *135* (11), 4199−202.
(25) Peng, Z. A.; Peng, X. Formation of High-Quality CdTe, CdSe, and CdS Nanocrystals Using CdO as Precursor. *J. Am. Chem. Soc.* **2001**, *123* (1), 183−184.
(26) Dabbousi, B. O.; Rodriguez-Viejo, J.; Mikulec, F. V.; Heine, J. R.; Mattoussi, H.; Ober, R.; Jensen, K. F.; Bawendi, M. G. (CdSe)ZnS Core-Shell Quantum Dots: Synthesis and Characterization of a Size Series of Highly Luminescent Nanocrystallites. *J. Phys. Chem. B* **1997**, *101* (46), 9463−9475.
(27) Rizzo, A.; Li, Y. Q.; Kudera, S.; Della Sala, F.; Zanella, M.; Parak, W. J.; Cingolani, R.; Manna, L.; Gigli, G. Blue light emitting diodes based on fluorescent CdSe/ZnS nanocrystals. *Appl. Phys. Lett.* **2007**, *90* (5), 051106.
(28) Song, K.-K.; Lee, S. Highly luminescent (ZnSe)ZnS core-shell quantum dots for blue to UV emission: synthesis and characterization. *Curr. Appl. Phys.* **2001**, *1* (2−3), 169−173.
(29) Yu, W. W.; Qu, L.; Guo, W.; Peng, X. Experimental Determination of the Extinction Coefficient of CdTe, CdSe, and CdS Nanocrystals. *Chem. Mater.* **2003**, *15* (14), 2854−2860.
(30) Bawendi, M. G.; Steigerwald, M. L.; Brus, L. E. The quantum mechanics of large semiconductor clusters ("quantum dots"). *Annu. Rev. Phys. Chem.* **1990**, *41*, 477−496.
(31) Talapin, D. V.; Rogach, A. L.; Kornowski, A.; Haase, M.; Weller, H. Highly Luminescent Monodisperse CdSe and CdSe/ZnS Nanocrystals Synthesized in a Hexadecylamine-Trioctylphosphine Oxide-Trioctylphospine Mixture. *Nano Lett.* **2001**, *1* (4), 207−211.
(32) Xie, R.; Kolb, U.; Li, J.; Basche, T.; Mews, A. Synthesis and Characterization of Highly Luminescent CdSe-Core CdS/Zn0.5Cd0.5S/ZnS Multishell Nanocrystals. *J. Am. Chem. Soc.* **2005**, *127* (20), 7480−7488.

DOI: 10.1021/acs.chemmater.6b04738
Chem. Mater. 2017, 29, 399−461

(33) Yu, W. W.; Peng, X. Formation of High-Quality CdS and Other II-VI Semiconductor Nanocrystals in Noncoordinating Solvents: Tunable Reactivity of Monomers. *Angew. Chem., Int. Ed.* **2002**, *41* (13), 2368−2371.
(34) Turkevich, J.; Stevenson, P. C.; Hillier, J. A study of the nucleation and growth processes in the synthesis of colloidal golde. *Discuss. Faraday Soc.* **1951**, *11*, 55−75.
(35) Ye, X.; Jin, L.; Caglayan, H.; Chen, J.; Xing, G.; Zheng, C.; Doan-Nguyen, V.; Kang, Y.; Engheta, N.; Kagan, C. R.; Murray, C. B. Improved Size-Tunable Synthesis of Monodisperse Gold Nanorods through the Use of Aromatic Additives. *ACS Nano* **2012**, *6* (3), 2804−2817.
(36) Li, N.; Zhao, P.; Astruc, D. Anisotropic Gold Nanoparticles: Synthesis, Properties, Applications, and Toxicity. *Angew. Chem., Int. Ed.* **2014**, *53* (7), 1756−1789.
(37) Schulz, F.; Homolka, T.; Bastus, N. G.; Puntes, V.; Weller, H.; Vossmeyer, T. Little Adjustments Significantly Improve the Turkevich Synthesis of Gold Nanoparticles. *Langmuir* **2014**, *30* (35), 10779−10784.
(38) Piella, J.; Bastus, N. G.; Puntes, V. Size-Controlled Synthesis of Sub-10-nanometer Citrate-Stabilized Gold Nanoparticles and Related Optical Properties. *Chem. Mater.* **2016**, *28* (4), 1066−1075.
(39) Scarabelli, L.; Sánchez-Iglesias, A.; Pérez-Juste, J.; Liz-Marzán, L. M. A "Tips and Tricks" Practical Guide to the Synthesis of Gold Nanorods. *J. Phys. Chem. Lett.* **2015**, *6* (21), 4270−4279.
(40) ENUSTUN, B.; TURKEVICH, J. COAGULATION OF COLLOIDAL GOLD. *J. Am. Chem. Soc.* **1963**, *85* (21), 3317−3328.
(41) Zeng, J.; Zheng, Y. Q.; Rycenga, M.; Tao, J.; Li, Z. Y.; Zhang, Q. A.; Zhu, Y. M.; Xia, Y. N. Controlling the Shapes of Silver Nanocrystals with Different Capping Agents. *J. Am. Chem. Soc.* **2010**, *132* (25), 8552.
(42) Li, H. S.; Xia, H. B.; Wang, D. Y.; Tao, X. T. Simple Synthesis of Monodisperse, Quasi-spherical, Citrate-Stabilized Silver Nanocrystals in Water. *Langmuir* **2013**, *29* (16), 5074−5079.
(43) Sondi, I.; Goia, D. V.; Matijevic, E. Preparation of highly concentrated stable dispersions of uniform silver nanoparticles. *J. Colloid Interface Sci.* **2003**, *260* (1), 75−81.
(44) Banerjee, S.; Loza, K.; Meyer-Zaika, W.; Prymak, O.; Epple, M. Structural Evolution of Silver Nanoparticles during Wet-Chemical Synthesis. *Chem. Mater.* **2014**, *26* (2), 951−957.
(45) Ye, X.; Zheng, C.; Chen, J.; Gao, Y.; Murray, C. B. Using Binary Surfactant Mixtures To Simultaneously Improve the Dimensional Tunability and Monodispersity in the Seeded Growth of Gold Nanorods. *Nano Lett.* **2013**, *13* (2), 765−771.
(46) Jana, N. R.; Gearheart, L.; Murphy, C. J. Wet Chemical Synthesis of High Aspect Ratio Cylindrical Gold Nanorods. *J. Phys. Chem. B* **2001**, *105* (18), 4065−4067.
(47) Nikoobakht, B.; El-Sayed, M. A. Preparation and Growth Mechanism of Gold Nanorods (NRs) Using Seed-Mediated Growth Method. *Chem. Mater.* **2003**, *15* (10), 1957−1962.
(48) Murphy, C. J.; Thompson, L. B.; Chernak, D. J.; Yang, J. A.; Sivapalan, S. T.; Boulos, S. P.; Huang, J.; Alkilany, A. M.; Sisco, P. N. Gold nanorod crystal growth: From seed-mediated synthesis to nanoscale sculpting. *Curr. Opin. Colloid Interface Sci.* **2011**, *16* (2), 128−134.
(49) Alkilany, A. M.; Nagaria, P. K.; Hexel, C. R.; Shaw, T. J.; Murphy, C. J.; Wyatt, M. D. Cellular uptake and cytotoxicity of gold nanorods: molecular origin of cytotoxicity and surface effects. *Small* **2009**, *5* (6), 701−8.
(50) Yuan, H.; Fales, A.; Vo-Dinh, T. TAT Peptide-Functionalized Gold Nanostars: Enhanced Intracellular Delivery and Efficient NIR Photothermal Therapy Using Ultralow Irradiance. *J. Am. Chem. Soc.* **2012**, *134* (28), 11358−11361.
(51) Indrasekara, A.; Wadams, R.; Fabris, L. Ligand Exchange on Gold Nanorods: Going Back to the Future. *PARTICLE & PARTICLE SYSTEMS CHARACTERIZATION* **2014**, *31* (8), 819−838.
(52) Pellegrino, T.; Sperling, R. A.; Alivisatos, A. P.; Parak, W. J. Gelelectrophoresis of Gold-DNA Nanoconjugates. *J. Biomed. Biotechnol.* **2007**, *2007*, 26796.
(53) Parak, W. J.; Pellegrino, T.; Micheel, C. M.; Gerion, D.; Williams, S. C.; Alivisatos, A. P. Conformation of oligonucleotides attached to gold nanocrystals probed by gel electrophoresis. *Nano Lett.* **2003**, *3* (1), 33−36.
(54) Lipka, M.; Semmler-Behnke, M.; Sperling, R. A.; Wenk, A.; Takenaka, S.; Schleh, C.; Kissel, T.; Parak, W. J.; Kreyling, W. G. Biodistribution of PEG-modified gold nanoparticles following intratracheal instillation and intravenous injection. *Biomaterials* **2010**, *31* (25), 6574−6581.
(55) Brandenberger, C.; Mühlfeld, C.; Ali, Z.; Lenz, A.-G.; Schmid, O.; Parak, W. J.; Gehr, P.; Rothen-Rutishauser, B. Quantitative Evaluation of Cellular Uptake and Trafficking of Plain and Polyethylene Glycol-Coated Gold Nanoparticles. *Small* **2010**, *6*, 1669−1678.
(56) del Pino, P.; Yang, F.; Pelaz, B.; Zhang, Q.; Kantner, K.; Hartmann, R.; Martinez de Baroja, N.; Gallego, M.; Möller, M.; Manshian, B. B.; Soenen, S. J.; Riedel, R.; Hampp, N.; Parak, W. J. Basic Physicochemical Properties of Polyethylene Glycol Coated Gold Nanoparticles that Determine Their Interaction with Cells. *Angew. Chem., Int. Ed.* **2016**, *55*, 5483−5487.
(57) Soliman, M. G.; Pelaz, B.; Parak, W. J.; del Pino, P. Phase transfer and polymer coating methods toward improving the stability of metallic nanoparticles for biological applications. *Chem. Mater.* **2015**, *27*, 990−997.
(58) Lista, M.; Liu, D. Z.; Mulvaney, P. Phase Transfer of Noble Metal Nanoparticles to Organic Solvents. *Langmuir* **2014**, *30* (8), 1932−1938.
(59) Serrano-Montes, A. B.; Jimenez de Aberasturi, D.; Langer, J.; Giner-Casares, J. J.; Scarabelli, L.; Herrero, A.; Liz-Marzan, L. M. A General Method for Solvent Exchange of Plasmonic Nanoparticles and Self-Assembly into SERS-Active Monolayers. *Langmuir* **2015**, *31* (33), 9205−9213.
(60) Chan, W. C. W.; Nie, S. Quantum Dot Bioconjugates for Ultrasensitive Nonisotopic Detection. *Science* **1998**, *281*, 2016−2018.
(61) Charron, G.; Hühn, D.; Perrier, A.; Cordier, L.; Pickett, C. J.; Nann, T.; Parak, W. J. On the Use of pH Titration to Quantitatively Characterize Colloidal Nanoparticles. *Langmuir* **2012**, *28* (43), 15141−15149.
(62) Caballero-Díaz, E.; Pfeiffer, C.; Kastl, L.; Rivera-Gil, P.; Simonet, B.; Valcárcel, M.; Jiménez-Lamana, J.; Laborda, F.; Parak, W. J. The Toxicity of Silver Nanoparticles Depends on Their Uptake by Cells and Thus on Their Surface Chemistry. *Particle and Particle Systems Characterization* **2013**, *30* (12), 1079−1085.
(63) Wu, M. X.; Liu, H.; Liu, J.; Haley, K. N.; Treadway, J. A.; Larson, J. P.; Ge, N.; Peale, F.; Bruchez, M. P. Immunofluorescent labeling of cancer marker Her2 and other cellular targets with semiconductor quantum dots. *Nat. Biotechnol.* **2002**, *21*, 41−46.
(64) Pellegrino, T.; Manna, L.; Kudera, S.; Liedl, T.; Koktysh, D.; Rogach, A. L.; Keller, S.; Rädler, J.; Natile, G.; Parak, W. J. Hydrophobic Nanocrystals Coated with an Amphiphilic Polymer Shell: A General Route to Water Soluble Nanocrystals. *Nano Lett.* **2004**, *4* (4), 703−707.
(65) Ali, Z.; Abbasi, A. Z.; Zhang, F.; Arosio, P.; Lascialfari, A.; Casula, M. F.; Wenk, A.; Kreyling, W.; Plapper, R.; Seidel, M.; Niessner, R.; Knoll, J.; Seubert, A.; Parak, W. J. Multifunctional Nanoparticles for Dual Imaging. *Anal. Chem.* **2011**, *83* (8), 2877−2882.
(66) Zhang, F.; Lees, E.; Amin, F.; RiveraGil, P.; Yang, F.; Mulvaney, P.; Parak, W. J. Polymer-Coated Nanoparticles: A Universal Tool for Biolabelling Experiments. *Small* **2011**, *7*, 3113−3127.
(67) Pelaz, B.; Del Pino, P.; Maffre, P.; Hartmann, R.; Gallego, M.; Rivera-Fernandez, S.; de la Fuente, J. M.; Nienhaus, G. U.; Parak, W. J. Surface Functionalization of Nanoparticles with Polyethylene Glycol: Effects on Protein Adsorption and Cellular Uptake. *ACS Nano* **2015**, *9* (7), 6996−7008.
(68) Kaiser, U.; Jimenez de Aberasturi, D.; Vazquez-Gonzalez, M.; Carrillo-Carrion, C.; Niebling, T.; Parak, W. J.; Heimbrodt, W. Determining the exact number of dye molecules attached to colloidal

DOI: 10.1021/acs.chemmater.6b04738
Chem. Mater. 2017, 29, 399−461

CdSe/ZnS quantum dots in Förster resonant energy transfer assemblies. *J. Appl. Phys.* **2015**, *117*, 024701.
(69) Joris, F.; Valdeperez, D.; Pelaz, B.; Soenen, S.; Manshian, B.; Parak, W.; De Smedt, S.; Raemdonck, K. The impact of species and cell type on the nanosafety profile of iron oxide nanoparticles in neural cells. *J. Nanobiotechnol.* **2016**, *14*, 69.
(70) Kirchner, C.; Liedl, T.; Kudera, S.; Pellegrino, T.; Muñoz Javier, A.; Gaub, H. E.; Stölzle, S.; Fertig, N.; Parak, W. J. Cytotoxicity of Colloidal CdSe and CdSe/ZnS Nanoparticles. *Nano Lett.* **2005**, *5* (2), 331−338.
(71) Riedinger, A.; Zhang, F.; Dommershausen, F.; Röcker, C.; Brandholt, S.; Nienhaus, G. U.; Koert, U.; Parak, W. J. Ratiometric Optical Sensing of Chloride Ions with Organic Fluorophore - Gold Nanoparticle Hybrids: A Systematic Study of Distance Dependency and the Influence of Surface Charge. *Small* **2010**, *6* (22), 2590−2597.
(72) Zhang, F.; Ali, Z.; Amin, F.; Feltz, A.; Oheim, M.; Parak, W. J. IIon and pH Sensing with Colloidal Nanoparticles: Influence of Surface Charge on Sensing and Colloidal Properties. *ChemPhysChem* **2010**, *11*, 730−735.
(73) Abbasi, A. Z.; Amin, F.; Niebling, T.; Friede, S.; Ochs, M.; Carregal-Romero, S.; Montenegro, J. M.; Rivera Gil, P.; Heimbrodt, W.; Parak, W. J. How colloidal nanoparticles could facilitate multiplexed measurements of different analytes with analyte-sensitive organic fluorophores. *ACS Nano* **2011**, *5*, 21−25.
(74) Amin, F.; Yushchenko, D. A.; Montenegro, J. M.; Parak, W. J. Integration of Organic Fluorophores in the Surface of Polymer-Coated Colloidal Nanoparticles for Sensing the Local Polarity of the Environment. *ChemPhysChem* **2012**, *13* (4), 1030−1035.
(75) Soenen, S. J.; Manshian, B.; Montenegro, J. M.; Amin, F.; Meermann, B.; Thiron, T.; Cornelissen, M.; Vanhaecke, F.; Doak, S.; Parak, W. J.; De Smedt, S.; Braeckmans, K. Cytotoxic Effects of Gold Nanoparticles: A Multiparametric Study. *ACS Nano* **2012**, *6* (7), 5767−5783.
(76) Pyell, U.; Jalil, A. H.; Pfeiffer, C.; Pelaz, B.; Parak, W. J. Characterization of gold nanoparticles with different hydrophilic coatings via capillary electrophoresis and Taylor dispersion analysis. Part I: Determination of the zeta potential employing a modified analytic approximation. *J. Colloid Interface Sci.* **2015**, *450*, 288−300.
(77) Pyell, U.; Jalil, A. H.; Pfeiffer, C.; Pelaz, B.; Parak, W. J.; Urban, D. A. Characterization of hydrophilic coated gold nanoparticles via capillary electrophoresis and Taylor dispersion analysis. Part II: Determination of the hydrodynamic radius distribution − Comparison with asymmetric flow field-flow fractionation. *J. Colloid Interface Sci.* **2015**, *457*, 131−140.
(78) Marisca, O. T.; Kantner, K.; Pfeiffer, h.; Zhang, Q.; Pelaz, B.; Leopold, N.; Parak, W. J.; Rejman, J. Comparison of the in Vitro Uptake and Toxicity of Collagen- and Synthetic Polymer-Coated Gold Nanoparticles. *Nanomaterials* **2015**, *5*, 1418−1430.
(79) Menendez-Miranda, M.; Costa-Fernandez, J. M.; Encinar, J. R.; Parak, W. J.; Carrillo-Carrion, C. Determination of the ratio of fluorophore/nanoparticle for fluorescence-labelled nanoparticles. *Analyst* **2016**, *141* (4), 1266−1272.
(80) Sperling, R. A.; Liedl, T.; Duhr, S.; Kudera, S.; Zanella, M.; Lin, C.-A. J.; Chang, W. H.; Braun, D.; Parak, W. J. Size Determination of (Bio-) Conjugated Water-Soluble Colloidal Nanoparticles: A Comparison of Different Techniques. *J. Phys. Chem. C* **2007**, *111* (31), 11552−11559.
(81) Harakeh, S.; Abdel-Massih, R. M.; Rivera Gil, P.; Sperling, R. A.; Meinhardt, A.; Niedwiecki, A.; Rath, M.; Parak, W. J.; Baydoun, E. The effect of PEG-coated gold nanoparticles on the anti-proliferative potential of Specific Nutrient Synergy. *Nanotoxicology* **2010**, *4*, 177−185.
(82) Van Hoecke, K.; De Schamphelaere, K. A. C.; Ali, Z.; Zhang, F.; Elsaesser, A.; Rivera Gil, P.; Parak, W. J.; Smagghe, G.; Janssen, C. R.; Howard, C. V. Ecotoxicity and uptake of polymer coated gold nanoparticles. *Nanotoxicology* **2013**, *7* (1), 37−47.
(83) Soenen, S. J.; Manshian, B. B.; Abdelmonem, A. M.; Montenegro, J.-M.; Tan, S.; Balcaen, L.; Vanhaecke, F.; Brisson, A. R.; Parak, W. J.; De Smedt, S. C.; Braeckmans, K. The Cellular Interactions of PEGylated Gold Nanoparticles: Effect of PEGylation on Cellular Uptake and Cytotoxicity. *Particle & Particle Systems Characterization* **2014**, *31*, 794−800.
(84) Kantner, K.; Ashraf, S.; Carregal-Romero, S.; Carrillo-Carrion, C.; Collot, M.; del Pino, P.; Heimbrodt, W.; Jimenez de Aberasturi, D.; Kaiser, U.; Kazakova, L. I.; Lelle, M.; Martinez de Baroja, N.; Montenegro, J.-M.; Nazarenus, M.; Pelaz, B.; Peneva, K.; Rivera Gil, P.; Sabir, N.; Schneider, L. M.; Shabarchina, L. I.; Sukhorukov, G. B.; Vazquez, M.; Yang, F.; Parak, W. J. Particle-Based Optical Sensing of Intracellular Ions at the Example of Calcium - What are the Experimental Pitfalls? *Small* **2015**, *11*, 896−904.
(85) Yu, X.; Lei, D. Y.; Amin, F.; Hartmann, R.; Acuna, G. P.; Guerrero-Martínez, A.; Maier, S. A.; Tinnefeld, P.; Carregal-Romero, S.; Parak, W. J. Distance control in-between plasmonic nanoparticles via biological and polymeric spacers. *Nano Today* **2013**, *8* (5), 480−493.
(86) Kaiser, U.; Jimenez de Aberasturi, D.; Malinowski, R.; Amin, F.; Parak, W. J.; Heimbrodt, W. Multiplexed measurements by time resolved spectroscopy using colloidal CdSe/ZnS quantum dots. *Appl. Phys. Lett.* **2014**, *104*, 041901−041904.
(87) Kreyling, W. G.; Abdelmonem, A. M.; Ali, Z.; Alves, F.; Geiser, M.; Haberl, N.; Hartmann, R.; Hirn, S.; de Aberasturi, D. J.; Kantner, K.; Khadem-Saba, G.; Montenegro, J. M.; Rejman, J.; Rojo, T.; de Larramendi, I. R.; Ufartes, R.; Wenk, A.; Parak, W. J. In vivo integrity of polymer-coated gold nanoparticles. *Nat. Nanotechnol.* **2015**, *10* (7), 619−23.
(88) Zyuzin, M. V.; Honold, T.; Carregal-Romero, S.; Kantner, K.; Karg, M.; Parak, W. J. Influence of Temperature on the Colloidal Stability of Polymer-Coated Gold Nanoparticles in Cell Culture Media. *Small* **2016**, *13*, 1723−1731.
(89) Rothen-Rutishauser, B.; Kuhn, D. A.; Ali, Z.; Gasser, M.; Amin, F.; Parak, W. J.; Vanhecke, D.; Fink, A.; Gehr, P.; Brandenberger, C. Quantification of gold nanoparticle cell uptake under controlled biological conditions and adequate resolution. *Nanomedicine* **2014**, *9* (5), 607−621.
(90) Jimenez de Aberasturi, D.; Serrano-Montes, A. B.; Langer, J.; Henriksen-Lacey, M.; Parak, W. J.; Liz-Marzán, L. M. Encoded Gold Nanostars for Multiplexed SERS Cell Differentiation. *Chem. Mater.* **2016**, *28*, 6779−6790.
(91) Manshian, B. B.; Pfeiffer, C.; Pelaz, B.; Heimerl, T.; Gallego, M.; Möller, M.; del Pino, P.; Himmelreich, U.; Parak, W. J.; Soenen, S. J. High-Content Imaging and Gene Expression Approaches To Unravel the Effect of Surface Functionality on Cellular Interactions of Silver Nanoparticles. *ACS Nano* **2015**, *9*, 10431−10444.
(92) Yakovlev, A. V.; Zhang, F.; Zulqurnain, A.; Azhar-Zahoor, A.; Luccardini, C.; Gaillard, S.; Mallet, J. M.; Tauc, P.; Brochon, J. C.; Parak, W. J.; Feltz, A.; Oheim, M. Wrapping Nanocrystals with an Amphiphilic Polymer Preloaded with Fixed Amounts of Fluorophore Generates FRET-Based Nanoprobes with a Controlled Donor/Acceptor Ratio. *Langmuir* **2009**, *25* (5), 3232−3239.
(93) Cywiński, P. J.; Hammann, T.; Hühn, D.; Parak, W. J.; Hildebrandt, N.; Löhmannsröben, H.-G. Europium-quantum dot nanobioconjugates as luminescent probes for time-gated biosensing. *J. Biomed. Opt.* **2014**, *19*, 101506.
(94) Liedl, T.; Keller, S.; Simmel, F. C.; Rädler, J. O.; Parak, W. J. Fluorescent Nanocrystals as Colloidal Probes in Complex Fluids Measured by Fluorescence Correlation Spectroscopy. *Small* **2005**, *1* (10), 997−1003.
(95) Carrillo-Carrion, C.; Parak, W. J. Design of pyridyl-modified amphiphilic polymeric ligands: Towards better passivation of water-soluble colloidal quantum dots for improved optical performance. *J. Colloid Interface Sci.* **2016**, *478*, 88−96.
(96) Niebling, T.; Zhang, F.; Ali, Z.; Parak, W. J.; Heimbrodt, W. Excitation dynamics in polymer-coated semiconductor quantum dots with integrated dye molecules: The role of reabsorption. *J. Appl. Phys.* **2009**, *106*, 104701.
(97) Hsieh, M. F.; Li, J. K. J.; Lin, C. A. J.; Huang, S. H.; Sperling, R. A.; Parak, W. J.; Chang, W. H. Tracking of Cellular Uptake of Hydrophilic CdSe/ZnS Quantum Dots/Hydroxyapatite Composites

DOI: 10.1021/acs.chemmater.6b04738
Chem. Mater. 2017, 29, 399−461

Nanoparticles in MC3T3-E1 Osteoblast Cells. *J. Nanosci. Nanotechnol.* **2009**, *9* (4), 2758−2762.
(98) Manshian, B. B.; Abdelmonem, A. M.; Kantner, K.; Pelaz, B.; Klapper, M.; Tirroni, C. N.; Parak, W. J.; Himmelreich, U.; Soenen, S. J. Evaluation of quantum dot cytotoxicity: interpretation of nanoparticle concentrations versus intracellular nanoparticle numbers. *Nanotoxicology* **2016**, *10*, 1318−1328.
(99) Soenen, S. J.; Montenegro, J.-M.; Abdelmonem, A. M.; Manshian, B. B.; Doak, S. H.; Parak, W. J.; De Smedt, S. C.; Braeckmans, K. Corrigendum to "The effect of nanoparticle degradation on poly(methacrylic acid)-coated quantum dot toxicity: The importance of particle functionality assessment in toxicology" [Acta Biomater. 10 (2014) 732−741]. *Acta Biomater.* **2015**, *12*, 362.
(100) Fernández-Argüelles, M. T.; Yakovlev, A.; Sperling, R. A.; Luccardini, C.; Gaillard, S.; Medel, A. S.; Mallet, J.-M.; Brochon, J.-C.; Feltz, A.; Oheim, M.; Parak, W. J. Synthesis and Characterization of Polymer-Coated Quantum Dots with Integrated Acceptor Dyes as FRET-based Nanoprobes. *Nano Lett.* **2007**, *7* (9), 2613−2617.
(101) Kaiser, U.; Sabir, N.; Carrillo-Carrion, C.; del Pino, P.; Bossi, M.; Heimbrodt, W.; Parak, W. J. Förster resonance energy transfer mediated enhancement of the fluorescence lifetime of organic fluorophores to the millisecond range by coupling to Mn-doped CdS/ZnS quantum dots. *Nanotechnology* **2016**, *27*, 055101.
(102) Schrittwieser, S.; Pelaz, B.; Parak, W. J.; Lentijo-Mozo, S.; Soulantica, K.; Dieckhoff, J.; Ludwig, F.; Altantzis, T.; Bals, S.; Schotter, J. Homogeneous Protein Analysis by Magnetic Core−Shell Nanorod Probes. *ACS Appl. Mater. Interfaces* **2016**, *8*, 8893−8899.
(103) Zhang, Q.; Castellanos-Rubio, I.; Munshi, R.; Orue, I.; Pelaz, B.; Gries, K. I.; Parak, W. J.; del Pino, P.; Pralle, A. Model Driven Optimization of Magnetic Anisotropy of Exchange-Coupled Core-Shell Ferrite Nanoparticles for Maximal Hysteretic Loss. *Chem. Mater.* **2015**, *27*, 7380−7387.
(104) Casula, M. F.; Floris, P.; Innocenti, C.; Lascialfari, A.; Marinone, M.; Corti, M.; Sperling, R. A.; Parak, W. J.; Sangregorio, C. Magnetic Resonance Imaging Contrast Agents Based on Iron Oxide Superparamagnetic Ferrofluids. *Chem. Mater.* **2010**, *22* (5), 1739−1748.
(105) Colombo, M.; Mazzucchelli, S.; Montenegro, J. M.; Galbiati, E.; Corsi, F.; Parak, W. J.; Prosperi, D. Protein Oriented Ligation on Nanoparticles Exploiting O6-Alkylguanine-DNA Transferase (SNAP) Genetically Encoded Fusion. *Small* **2012**, *8* (10), 1492−1497.
(106) Schweiger, C.; Hartmann, R.; Zhang, F.; Parak, W. J.; Kissel, T.; Rivera Gil, P. Quantification of the Internalization Patterns of Superparamagnetic Iron Oxide Nanoparticles with Opposite Charge. *J. Nanobiotechnol.* **2012**, *10* (1), 28.
(107) Röcker, C.; Pötzl, M.; Zhang, F.; Parak, W. J.; Nienhaus, G. U. A Quantitative Fluorescence Study of Protein Monolayer Formation on Colloidal Nanoparticles. *Nat. Nanotechnol.* **2009**, *4* (9), 577−580.
(108) Lehmann, A. D.; Parak, W. J.; Zhang, F.; Ali, Z.; Röcker, C.; Nienhaus, G. U.; Gehr, P.; Rothen-Rutishauser, B. Fluorescent-Magnetic Hybrid Nanoparticles Induce a Dose-Dependent Increase in Proinflammatory Response in Lung Cells in vitro Correlated with Intracellular Localization. *Small* **2010**, *6* (6), 753−762.
(109) Mahmoudi, M.; Abdelmonem, A. M.; Behzadi, S.; Clement, J. H.; Dutz, S.; Ejtehadi, M. R.; Hartmann, R.; Kantner, K.; Linne, U.; Maffre, P.; Metzler, S.; Moghadam, M. K.; Pfeiffer, C.; Rezaei, M.; Ruiz-Lozano, P.; Serpooshan, V.; Shokrgozar, M. A.; Nienhaus, G. U.; Parak, W. J. Temperature: The "Ignored" Factor at the NanoBio Interface. *ACS Nano* **2013**, *7* (8), 6555−6562.
(110) Tromsdorf, U. I.; Bigall, N. C.; Kaul, M.; Bruns, O. T.; Nikolic, M. S.; Mollwitz, B.; Sperling, R. A.; Reimer, R.; Hohenberg, H.; Parak, W. J.; Förster, S.; Beisiegel, U.; Adam, G.; Weller, H. Size and Surface Effects on the MRI Relaxivity of Manganese Ferrite Nanoparticle Contrast Agents. *Nano Lett.* **2007**, *7* (8), 2422−2427.
(111) Wilhelm, S.; Kaiser, M.; Wuerth, C.; Heiland, J.; Carrillo-Carrion, C.; Muhr, V.; Wolfbeis, O. S.; Parak, W. J.; Resch-Genger, U.; Hirsch, T. Water dispersible upconverting nanoparticles: effects of surface modification on their luminescence and colloidal stability. *Nanoscale* **2015**, *7* (4), 1403−1410.
(112) Abdelmonem, A. M.; Pelaz, B.; Kantner, K.; Bigall, N. C.; Del Pino, P.; Parak, W. J. Charge and agglomeration dependent in vitro uptake and cytotoxicity of zinc oxide nanoparticles. *J. Inorg. Biochem.* **2015**, *153*, 334−338.
(113) Kim, G.-M.; Wutzler, A.; Radusch, H.-J.; Michler, G. H.; Simon, P.; Sperling, R. A.; Parak, W. J. One-Dimensional Arrangement of Gold Nanoparticles by Electrospinning. *Chem. Mater.* **2005**, *17*, 4949−4957.
(114) Geidel, C.; Schmachtel, S.; Riedinger, A.; Pfeiffer, C.; Müllen, K.; Klapper, M.; Parak, W. J. A General Synthetic Approach for Obtaining Cationic and Anionic Inorganic Nanoparticles *via* Encapsulation in Amphiphilic Copolymers. *Small* **2011**, *7* (20), 2929−2934.
(115) Hühn, D.; Kantner, K.; Geidel, C.; Brandholt, S.; De Cock, I.; Soenen, S. J. H.; Rivera Gil, P.; Montenegro, J.-M.; Braeckmans, K.; Müllen, K.; Nienhaus, G. U.; Klapper, M.; Parak, W. J. Polymer-Coated Nanoparticles Interacting with Proteins and Cells: Focusing on the Sign of the Net Charge. *ACS Nano* **2013**, *7* (4), 3253−3263.
(116) Hagel, L. Gel Filtration. In *Protein Purification. Principles, High Resolution Methods and Applications*, 2nd ed.; Janson, J.-C.; Ryden, L., Eds.; John Wiley & Sons: New York, 1998; pp 79−143.
(117) Amersham_Pharmacia_Biotech. *Gel filtration - Principles and Methods*, 8th ed.; Amersham Pharmacia Biotech: 2001.
(118) Parak, W. J.; Gerion, D.; Zanchet, D.; Woerz, A. S.; Pellegrino, T.; Micheel, C.; Williams, S. C.; Seitz, M.; Bruehl, R. E.; Bryant, Z.; Bustamante, C.; Bertozzi, C. R.; Alivisatos, A. P. Conjugation of DNA to silanized colloidal semiconductor nanocrystaline quantum dots. *Chem. Mater.* **2002**, *14* (5), 2113−2119.
(119) Zanchet, D.; Micheel, C. M.; Parak, W. J.; Gerion, D.; Williams, S. C.; Alivisatos, A. P. Electrophoretic and Structural Studies of DNA-Directed Au Nanoparticle Groupings. *J. Phys. Chem. B* **2002**, *106* (45), 11758−11763.
(120) Harris, J. R. Negative Staining of Thinly Spread Biological Particulates. In *Electron Microscopy Methods and Protocols*; Humana Press: 1999; Vol. *117*.
(121) Carpenter, A.; Jones, T.; Lamprecht, M.; Clarke, C.; Kang, I.; Friman, O.; Guertin, D.; Chang, J.; Lindquist, R.; Moffat, J.; Golland, P.; Sabatini, D. CellProfiler: image analysis software for identifying and quantifying cell phenotypes. *Genome Biology* **2006**, *7* (10), R100.
(122) Borchert, H.; Shevchenko, E. V.; Robert, A.; Mekis, I.; Kornowski, A.; Grübel, G.; Weller, H. Determination of Nanocrystal Sizes: A Comparison of TEM, SAXS, and XRD Studies of Highly Monodisperse $CoPt_3$ Particles. *Langmuir* **2005**, *21* (5), 1931−1936.
(123) Dubois, L. H.; Nuzzo, R. G. Synthesis, Structure, and Properties of Model Organic-Surfaces. *Annu. Rev. Phys. Chem.* **1992**, *43*, 437−463.
(124) Fedosyuk, A.; Radchanka, A.; Antanovich, A.; Prudnikau, A.; Kvach, M. V.; Shmanai, V.; Artemyev, M. Determination of Concentration of Amphiphilic Polymer Molecules on the Surface of Encapsulated Semiconductor Nanocrystals. *Langmuir* **2016**, *32* (8), 1955−1961.
(125) Liz-Marzan, L. M. Tailoring surface plasmons through the morphology and assembly of metal nanoparticles. *Langmuir* **2006**, *22* (1), 32−41.
(126) Sepulveda, B.; Angelome, P. C.; Lechuga, L. M.; Liz-Marzan, L. M. LSPR-based nanobiosensors. *Nano Today* **2009**, *4* (3), 244−251.
(127) Barbosa, S.; Agrawal, A.; Rodriguez-Lorenzo, L.; Pastoriza-Santos, I.; Alvarez-Puebla, R. A.; Kornowski, A.; Weller, H.; Liz-Marzan, L. M. Tuning Size and Sensing Properties in Colloidal Gold Nanostars. *Langmuir* **2010**, *26* (18), 14943−14950.
(128) Vial, S.; Pastoriza-Santos, I.; Perez-Juste, J.; Liz-Marzan, L. M. Plasmon coupling in layer-by-layer assembled gold nanorod films. *Langmuir* **2007**, *23* (8), 4606−4611.
(129) Efros, A. L.; Efros, A. L. Interband Absorption of Light in a Semiconductor Sphere. *Sov. Phys. Semicond.-USSR* **1982**, *16* (7), 772−775.
(130) Takagahara, T.; Takeda, K. Theory of the quantum confinement effect on excitons in quantum dots of indirect-gap

DOI: 10.1021/acs.chemmater.6b04738
Chem. Mater. 2017, 29, 399−461

materials. *Phys. Rev. B: Condens. Matter Mater. Phys.* **1992**, *46*, 15578−15581.
(131) Vossmeyer, T.; Katsikas, L.; Giersig, M.; Popovic, I. G.; Diesner, K.; Chemseddine, A.; Eychmüller, A.; Weller, H. CdS Nanoclusters: Synthesis, Characterization, Size Dependent Oscillator Strength, Temperature Shift of the Excitonic Transition Energy, and Reversible Absorbance Shift. *J. Phys. Chem.* **1994**, *98*, 7665.
(132) Nirmal, M.; Murray, C. B.; Bawendi, M. G. Fluorescence-line narrowing in CdSe quantum dots: Surface localization of the photogenerated exciton. *Phys. Rev. B: Condens. Matter Mater. Phys.* **1994**, *50* (4), 2293−2300.
(133) Lavallard, P. Excitons in nanocrystals. *J. Cryst. Growth* **1998**, *185*, 352−359.
(134) Peng, X. G.; Manna, L.; Yang, W. D.; Wickham, J.; Scher, E.; Kadavanich, A.; Alivisatos, A. P. Shape control of CdSe nanocrystals. *Nature* **2000**, *404* (6773), 59−61.
(135) Henglein, A. Photo-Degradation And Fluorescence Of Colloidal-Cadmium Sulfide In Aqueous-Solution. *Berichte Der Bunsen-Gesellschaft-Physical Chemistry Chemical Physics* **1982**, *86* (4), 301−305.
(136) Rossetti, R.; Nakahara, S.; Brus, L. E. Quantum Size Effects in the Redox Potentials, Resonance Raman-Spectra, and Electronic-Spectra of Cds Crystallites in Aqueous-Solution. *J. Chem. Phys.* **1983**, *79* (2), 1086−1088.
(137) Ekimov, A. I.; Efros, A. L.; Onushchenko, A. A. Quantum size effect in semiconductor microcrystals. *Solid State Commun.* **1993**, *88*, 947−50.
(138) Alivisatos, A. P. Semiconductor Clusters, Nanocrystals, and Quantum Dots. *Science* **1996**, *271*, 933−937.
(139) Parak, W. J.; Manna, L.; Simmel, F. C.; Gerion, D.; Alivisatos, P. Quantum Dots. In *Nanoparticles - From Theory to Application*, 1st ed.; Schmid, G., Ed.; Wiley-VCH: Weinheim, 2004; pp 4−49.
(140) Segets, D.; Lucas, J. M.; Taylor, R. N. K.; Scheele, M.; Zheng, H.; Alivisatos, A. P.; Peukert, W. Determination of the Quantum Dot Band Gap Dependence on Particle Size from Optical Absorbance and Transmission Electron Microscopy Measurements. *ACS Nano* **2012**, *6* (10), 9021−9032.
(141) Haiss, W.; Thanh, N. T. K.; Aveyard, J.; Fernig, D. G. Determination of Size and Concentration of Gold Nanoparticles from UV-Vis Spectra. *Anal. Chem.* **2007**, *79* (11), 4215−4221.
(142) Striolo, A.; Ward, J.; Prausnitz, J. M.; Parak, W. J.; Zanchet, D.; Gerion, D.; Milliron, D. J.; Alivisatos, A. P. Molecular Weight, Osmotic Second Virial Coefficient, and Extinction Coefficient of colloidal CdSe Nanocrystals. *J. Phys. Chem. B* **2002**, *106* (21), 5500−5505.
(143) Bruchez, M., Jr.; Moronne, M.; Gin, P.; Weiss, S.; Alivisatos, A. P. Semiconductor Nanocrystals as Fluorescent Biological Labels. *Science* **1998**, *281* (5385), 2013−2016.
(144) Lin, C.-A. J.; Yang, T.-Y.; Lee, C.-H.; Huang, S. H.; Sperling, R. A.; Zanella, M.; Li, J. K.; Shen, J.-L.; Wang, H.-H.; Yeh, H.-I.; Parak, W. J.; Chang, W. H. Synthesis, Characterization, and Bioconjugation of Fluorescent Gold Nanoclusters toward Biological Labeling Applications. *ACS Nano* **2009**, *3* (2), 395−401.
(145) Huang, S.; Pfeiffer, C.; Hollmann, J.; Friede, S.; Chen, J. J.-C.; Beyer, A.; Volz, K.; Heimbrodt, W.; Montenegro Martos, J. M.; Chang, W.; Parak, W. J.; Haas, B. Synthesis and Characterization of Colloidal Fluorescent Silver Nanoclusters. *Langmuir* **2012**, *28*, 8915−8919.
(146) Dulkeith, E.; Ringler, M.; Klar, T. A.; Feldmann, J.; Muñoz Javier, A.; Parak, W. J. Gold Nanoparticles Quench Fluorescence by Phase Induced Radiative Rate Suppression. *Nano Lett.* **2005**, *5* (4), 585−589.
(147) Medintz, I. L.; Clapp, A. R.; Mattoussi, H.; Goldman, E. R.; Fisher, B.; Mauro, J. M. Self-Assembled Nanoscale Biosensors Based on Quantum Dot FRET Donors. *Nat. Mater.* **2003**, *2*, 630−638.
(148) Würth, C.; Geissler, D.; Behnke, T.; Kaiser, M.; Resch-Genger, U. Critical review of the determination of photoluminescence quantum yields of luminescent reporters. *Anal. Bioanal. Chem.* **2015**, *407*, 59−78.
(149) Huber, A.; Behnke, T.; Würth, C.; Jaeger, C.; Resch-Genger, U. Spectroscopic Characterization of Coumarin-Stained Beads: Quantification of the Number of Fluorophores Per Particle with Solid-State 19F-NMR and Measurement of Absolute Fluorescence Quantum Yields. *Anal. Chem.* **2012**, *84* (8), 3654.
(150) Jobin Yvon Horiba. *A Guide to Recording Fluorescence Quantum Yields*; Jobin Yvon Horiba: Stanmore, 2016.
(151) Williams, A. T. R.; Winfield, S. A.; Miller, J. N. Relative Fluorescence Quantum Yields Using a Computer-controlled Luminescence Spectrometer. *Analyst (Cambridge, U. K.)* **1983**, *108* (1290), 1067−1071.
(152) Magde, D.; Brannon, J. H.; Cremers, T. L.; Olmsted, J. Absolute Luminescence Yield of Cresyl Violet - Standard for the Red. *J. Phys. Chem.* **1979**, *83* (6), 696−699.
(153) Rivera Gil, P.; Jimenez de Aberasturi, D.; Wulf, V.; Pelaz, B.; del Pino, P.; Zhao, Y.; de la Fuente, J.; Ruiz de Larramendi, I.; Rojo, T.; Liang, X.-J.; Parak, W. J. The Challenge to Relate the Physicochemical Properties of Colloidal Nanoparticles to Their Cytotoxicity. *Acc. Chem. Res.* **2013**, *46* (3), 743−749.
(154) Murdock, R. C.; Braydich-Stolle, L.; Schrand, A. M.; Schlager, J. J.; Hussain, S. M. Characterization of nanomaterial dispersion in solution prior to in vitro exposure using dynamic light scattering technique. *Toxicol. Sci.* **2008**, *101* (2), 239−53.
(155) Roebben, G.; Ramirez-Garcia, S.; Hackley, V. A.; Roesslein, M.; Klaessig, F.; Kestens, V.; Lynch, I.; Garner, C. M.; Rawle, A.; Elder, A.; Colvin, V. L.; Kreyling, W.; Krug, H. F.; Lewicka, Z. A.; McNeil, S.; Nel, A.; Patri, A.; Wick, P.; Wiesner, M.; Xia, T.; Oberdorster, G.; Dawson, K. A. Interlaboratory comparison of size and surface charge measurements on nanoparticles prior to biological impact assessment. *J. Nanopart. Res.* **2011**, *13* (7), 2675−2687.
(156) Bhattacharjee, S. DLS and zeta potential − What they are and what they are not? *J. Controlled Release* **2016**, *235*, 337.
(157) Tay, C. Y.; Setyawati, M. I.; Xie, J.; Parak, W. J.; Leong, D. T. Back to Basics: Exploiting the Innate Physico-chemical Characteristics of Nanomaterials for Biomedical Applications. *Adv. Funct. Mater.* **2014**, *24*, 5936−5955.
(158) Fischer, K.; Schmidt, M. Pitfalls and novel applications of particle sizing by dynamic light scattering. *Biomaterials* **2016**, *98*, 79−91.
(159) Henderson, L. J. Concerning the relationship between the strength of acids and their capacity to preserve neutrality. *Am. J. Physiol.* **1908**, *21* (2), 173−179.
(160) Hasselbalch, K. A. Die Berechnung der Wasserstoffzahl des Blutes aus der freien und gebundenen Kohlensäure desselben, und die Sauerstoffbindung des Blutes als Funktion der Wasserstoffzahl. *Biochem. Z.* **1917**, *78*, 112−144.
(161) Po, H. N.; Senozan, N. M. The Henderson-Hasselbalch Equation: Its History and Limitations. *J. Chem. Educ.* **2001**, *78* (11), 1499.
(162) de Levie, R. The Henderson Approximation and the Mass Action Law of Guldberg and Waage. *Chem. Educ.* **2002**, *7* (3), 132−135.
(163) de Levie, R. The Henderson-Hasselbalch Equation: Its History and Limitations. *J. Chem. Educ.* **2003**, *80* (2), 146.
(164) Doane, T. L.; Chuang, C. H.; Hill, R. J.; Burda, C. Nanoparticle Zeta-Potentials. *Acc. Chem. Res.* **2012**, *45* (3), 317−326.

DOI: 10.1021/acs.chemmater.6b04738
Chem. Mater. 2017, 29, 399−461

The Role of Ligands in the Chemical Synthesis and Applications of Inorganic Nanoparticles

Journal:	*Chemical Reviews*
Manuscript ID	cr-2017-00671t
Manuscript Type:	Proposal
Date Submitted by the Author:	07-Nov-2017
Complete List of Authors:	Heuer-Jungemann, Amelie; University of Southampton, Feliu, Neus; Karolinska Institutet, Institute of Environmental Medicine Bakaimi, Ioanna; University of Southampton Hamaly, Majd; The University of Jordan, AlKilany, Alaaldin; University of Jordan Chakraborty, Indranath; Philipps-Universitat Marburg Fachbereich Chemie, Physic Masood, Atif; Philipps-Universitat Marburg Fachbereich 13 Physik Casula, Maria; Università di Cagliari, Dept. Scienze Chimiche e Geologiche and INSTM Kostopoulou, Athanasia; Foundation for Research and Technology - Hellas (FORTH), Institute of Electronic Structure and Laser (IESL) Oh, Eunkeu; Naval Research Laboratory, Optcial Sciences Division, Code 5611 Susumu, Kimihiro; Naval Research Laboratory, Optical Sciences Stewart, Michael; US Naval Research Laboratory, Chemistry Medintz, Igor; U.S. Naval Research Laboratory, Stratakis, Emmanuel; FORTH-IESL, Parak, Wolfgang; Universitaet Marburg, Fachbereich Physik; Universitaet Marburg, Fachbereich Physik Kanaras, Antonios; University of Southampton, Physics and Astronomy

CHEMICAL REVIEWS PROPOSAL TEMPLATE

The Role of Ligands in the Chemical Synthesis and Applications of Inorganic Nanoparticles

Amelie Heuer-Jungemann,[1] Neus Feliu,[2] Ioanna Bakaimi,[1] Majd Hamaly,[3] Alaaldin AlKilany,[4,5] Indranath Chakraborty,[5] Atif Masood,[5] Maria F. Casula,[6] Athanasia Kostopoulou,[7] Eunkeu Oh,[8,9] Kimihiro Susumu,[8,9] Michael H. Stewart,[9] Igor Medintz,[10] Emmanuel Stratakis,[7] Wolfgang J. Parak,[5,11] and Antonios G. Kanaras*,[1]

[1]Physics and Astronomy, Faculty of Physical Sciences and Engineering, University of Southampton, Southampton, U.K., SO171BJ; [2] Department of Laboratory Medicine (LABMED), Karolinska Institutet, Stockholm, Sweden; [3] King Hussein Cancer Center, P.O.Box 1269 Al-Jubeiha, Amman 11941 Jordan; [4] Department of Pharmaceutics & Pharmaceutical Technology, School of Pharmacy, The University of Jordan, Amman 11942, Jordan; [5] Fachbereich Physik, Philipps Universität Marburg, Marburg, Germany; [6] INSTM and Department of Chemical and Geological Sciences, University of Cagliari, Italy; [7] Institute of Electronic Structure and Laser, Foundation for Research and Technology - Hellas, Heraklion, 71110, Crete, Greece; [8] Sotera Defense Solutions, Inc., Columbia, Maryland 21046, USA; [9] Optical Sciences Division, Code 5600, U.S. Naval Research Laboratory, Washington, D.C. 20375, USA; [10] Center for Bio/Molecular Science and Engineering, Code 6900, U.S. Naval Research Laboratory, Washington, D.C. 20375, USA. [11]Fachbereich Physik und Chemie, CHyN, Universität Hamburg, 22607 Hamburg, Germany.

(1) TOPICAL OUTLINE (2-3 pages)

This review aims to be a comprehensive, authoritative, critical, and readable review of general interest to the chemistry community because it discusses the influence of surface ligands on tuning the synthesis and properties of colloidal inorganic nanoparticles and extends to the role that the ligand coating of nanoparticles plays in a broad spectrum of applications ranging from energy to biomedicine providing insights into application-targeted ligand engineering.

Significance and goals: Nanoparticles (NPs) have attracted great research interest due to their unique properties, which derive from a combination of their characteristics such as chemical composition, size, shape, and the type of surface coating. Owing to the composition of their inorganic core, metallic NPs (especially gold and silver) can exhibit

strong optical absorption and scattering, whilst semiconductor quantum dots (e.g. CdSe or CdTe, PbS) and perovskite nanoparticles (e.g. Cesium lead halides) can be highly fluorescent as a result of their electronic band structure. On the other hand, NPs synthesized from magnetic materials (e.g. iron oxide or cobalt) can exhibit unique phenomena, which are not encountered in the corresponding bulk counterparts such as superparamagnetism. These properties have rendered inorganic NPs highly interesting candidates for a vast variety of applications. A very important factor contributing to the properties of inorganic NPs is the appropriate choice of surface ligands, which is directly correlated to the choice of the application. For applications carried out in solution, the choice of nanoparticle ligand coating is critical to also enable their colloidal stability. Ligands may also infer additional functions, which in turn can influence the interactions of NPs with their surrounding environment. Thus NPs can be equipped with targeting and cargo delivery abilities engineered to be non-toxic or designed to assemble in an ordered manner.

This review will focus on the role of the ligands in determining the formation, properties, and applications of NPs. Different post-synthetic strategies to functionalize and stabilize various types of NPs (plasmonic, luminescent, magnetic, organic) that are prepared in either aqueous or organic media are highlighted. As extensive research in the field of NPs' design has demonstrated that the use of ligands during synthesis has a dramatic effect on the resulting size, dispersion, shape, crystal structure, and colloidal stability, the ligands used to assist NPs synthesis in aqueous or organic media will also be reviewed. Furthermore commonly used ligands to functionalize various types of nanoparticles for specific biomedical or energy applications will be discussed.

Our review differentiates significantly from other recent reviews in the field correlating the surface ligands both with nanoparticle synthesis and a broader spectrum of applications. Thus, it gives a complete and comprehensive picture of the ligand influence to design and use nanoparticles in complex environments. Our aim is to address the relevant literature of the last 10-15 years.

----------PROVIDE SAMPLE OUTLINE OF YOUR SECTIONS----------

1. Introduction

2. Surface stabilization of colloidal nanoparticles

2.1. Ligand coating on inorganic nanoparticles synthesized in aqueous media
- 2.1.1. Plasmonic nanoparticles
- 2.1.2. Magnetic nanoparticles
- 2.1.3. Fluorescent nanoparticles

2.2. Ligand coating on nanoparticles synthesized in organic media
- 2.2.1. Plasmonic nanoparticles
- 2.2.2. Magnetic nanoparticles
- 2.2.3. Fluorescent nanoparticles
- 2.2.4. Other nanoparticles

3. Ligand modification for stable and functional nanoparticles in complex media

3.1. Ligand coating of nanoparticles for biomedical applications
- 3.1.1. Ethyelne glycol containing ligands
- 3.1.2. Lipids
- 3.1.3. Silica
- 3.1.4. Oligonucleotides
- 3.1.5. Peptides
- 3.1.6. Proteins
- 3.1.7. Carbohydrates

3.2. Ligand coating of nanoparticles for other applications
- 3.2.1. Photodetectors
- 3.2.2. Photovoltaic devices
- 3.2.3. Light-Emitting Devices
- 3.2.4. Sensors
- 3.2.5. Memory devices
- 3.2.6. Thermoelectric applications
- 3.2.7. Catalysis

4. Conclusions and Outlook

(2) LIST OF PREVIOUS REVIEWS RELEVANT TO THE SUBJECT

(1) Ligand density quantification on colloidal inorganic nanoparticles
By: Smith, Ashley M.; Johnston, Kathryn A.; Crawford, Scott E.; et al.
ANALYST Volume: 142 Issue: 1 Pages: 11-29 Published: 2017

(2) Surface functionalization of nanoparticles for nanomedicine
By: Mout, Rubul; Moyano, Daniel F.; Rana, Subinoy; et al.
CHEMICAL SOCIETY REVIEWS Volume: 41 Issue: 7 Pages: 2539-2544 Published: 2012

(3) Functionalization of Inorganic Nanoparticles for Bioimaging Applications
By: Erathodiyil, Nandanan; Ying, Jackie Y.
ACCOUNTS OF CHEMICAL RESEARCH Volume: 44 Issue: 10 Special Issue: SI Pages: 925-935 Published: OCT 2011 (3) List review

(4) Functionalisation of nanoparticles for biomedical applications
By: Thanh, Nguyen T. K.; Green, Luke A. W.
NANO TODAY Volume: 5 Issue: 3 Pages: 213-230 Published: JUN 2010

(5) Surface modification, functionalization and bioconjugation of colloidal inorganic nanoparticles
By: Sperling, R. A.; Parak, W. J.
PHILOSOPHICAL TRANSACTIONS OF THE ROYAL SOCIETY A-MATHEMATICAL PHYSICAL AND ENGINEERING SCIENCES Volume: 368 Issue: 1915 Pages: 1333-1383 Published: MAR 28 2010

(3) LIST OF FIVE OF THE AUTHORS' PAPERS THAT ARE MOST CLOSELY RELATED TO THE REVIEW TOPIC

(1) Meyns, M.;Perálvarez, M.; Heuer-Jungemann, A.; Hertog,W.; Ibáñez,M.; Nafria,R.; Genç,A.; Arbiol,J.; Kovalenko, M. V.; Carreras,J.; Cabot, A.; Kanaras, A. G. "Polymer-Enhanced Stability of Inorganic Perovskite Nanocrystals and Their Application in Color Conversion LEDs" *ACS Appl. Mater. Interfaces* **2016**, 8 (30), 19579–19586

(2) Kymakis, E.; Spyropoulos, G. D.; Fernandes, R.; Kakavelakis, G.; Kanaras, A. G.; Stratakis, E. "Plasmonic Bulk Heterojunction Solar Cells: The Role of Nanoparticle Ligand Coating" *ACS Photonics* **2015**, 2 (6), 714-723

(3) Bartczak, D.; Muskens, O. L.; Nitti, S.; Millar, T. M.; Kanaras, A. G
"Nanoparticles for inhibition of in vitro tumour angiogenesis: Synergistic actions of ligand function and laser irradiation." *Biomater. Sci*. **2015**, 3, 733-741

(4) Fernandes,R.; Smyth,N. R.; Muskens, O.L.;Nitti, S.; Heuer-Jungemann, A.; Ardern-Jones, M. R.; Kanaras, A. G "Interactions of Skin with Gold Nanoparticles of Different Surface Charge, Shape and Functionality." *Small* **2015**, 11 (6), 713-721.

(5) Mahmoudi, M.; Meng, J.; Xue, X.; Liang, X. J.; Rahman, M.; Pfeiffer, C.; Hartmann, R.; Gil, P. R.; Pelaz, B.; Parak, W. J.;del Pino, P.; Carregal-Romero, S.; Kanaras, A. G.; Selvan, S. T. "Interaction of stable colloidal nanoparticles and cellular membranes" *Biotechnology Advances*, **2014**, 32, 679-692.

(6) Stratakis, E.; Kymakis, E. "Nanoparticle-based plasmonic organic photovoltaic devices" *Mater. Today* **2013**, 16 (4), 133-146

(7) Bartczak, D.; Kanaras A. G. "Preparation of Peptide Functionalized Gold Nanoparticles Using One Pot EDC/sulfo-NHS Coupling" *Langmuir*, **2011**, 27 (16), 10119–10123

(4) ESTIMATE OF THE NUMBER OF REFERENCES

~550 references

(5) ESTIMATE OF THE NUMBER OF DOUBLE-SPACED PAGES

~171 pages (incl. Figures and References)

(6) TENTATIVE SUBMITTAL DATE

~ December 2017